Amyloid-β Fibrils Form by Surface-Catalysed Multi-Step Nucleation

Alexander I. P. Taylor

A thesis submitted for the degree of Doctor of Philosophy

May, 2021

Department of Molecular Biology and Biotechnology

University of Sheffield

Abstract

Amyloid-β (Aβ) is a disordered peptide that aggregates to form amyloid fibrils, and non-amyloid assemblies such as globular oligomers and protofibrils. Many Aβ assemblies are neurotoxic, playing a key role in the onset of Alzheimer's disease. Mathematical analyses of Aβ self-assembly have shown that amyloids first form by primary nucleation, and then grow by progressive incorporation of monomers into the fibril structure; in addition, existing fibrils catalyse secondary nucleation events that result in positive feedback and the exponential accumulation of toxic oligomers. However, the mechanisms of primary and secondary nucleation and the structural characteristics of secondary oligomers remain unclear. In addition, current mathematical models fail to produce the correct scaling behaviours under physiological conditions, pointing to critical flaws in their description of self-assembly.

In this study, a combination of experimental biophysics and mathematical modelling was used to investigate Aβ aggregation. Both primary and secondary nucleation were found to be surface-catalysed multi-step processes, involving at least two stages: surface-dependent condensation to form a partly ordered intermediate, and slow conversion to an amyloid state. The results suggest that diverse surfaces may catalyse nucleation and oligomerisation *in vivo*, and different surfaces may condition the populations of toxic oligomers that are formed. In addition, secondary oligomers, which are usually rare but toxic species, were found to accumulate to high levels at physiological ionic strength. These oligomers are partly ordered, and appear to contain fibril-like structural motifs, suggesting a possible mechanism for secondary nucleation. Moreover, existing mathematical models fail to describe the self-assembly kinetics because they neglect nucleation intermediates, a conclusion that is relevant to other diseases caused by amyloid formation, such as Parkinson's and Huntington's disease. Thus, to accurately describe amyloid formation and oligomerisation *in vivo*, future mathematical models must incorporate multi-step nucleation with large populations of intermediates.

Acknowledgments

In the six years I've spent in this lab, I have had the pleasure to work with some really amazing people, who have contributed an enormous amount of expertise, inspiration, and humour to the enterprise. I've tried to acknowledge some more specific contributions in individual sections at the end of each chapter, but here I really wanted to thank the people who've made this an amazing experience in general.

First of all, I'd like to begin by thanking Rosie for all the support and encouragement she's provided, and some really amazing chats about science. Your door really has always been open, and it's been great to have someone to have such fantastic discussions with. I'd also like to thank Per Bullough, Jeremy Craven, and Jon Waltho for their advice and support, Svet Tzokov for his expertise with the EM, and the admin staff, especially Emily Cooper, for being an island of calm and efficiency amidst the surrounding chaos.

The amyloid group have been an amazing bunch to work with. Particular thanks go to Liam, Pete, Lianne, and Xander, who I've worked with most closely over the years - collectively and individually, you have been a constant source of fascinating conversations, expertise, enthusiasm, and silly jokes (I'm still finding nerf bullets in my bag, and I'm not sure we ever got to the bottom of whose triangle it was). I've tried to acknowledge your contributions in individual chapters, but, aside from all that, I couldn't have imagined a nicer or more engaging group of people to work with, and you really have made the whole experience worthwhile. I've also been fortunate to work with some great Master's students - Josh, Caitlin, and Alanah - who contributed to the work in this thesis, and helped make the lab such a fun place to be. The wider NMR group and the EM group have also been fantastic to work with - in particular, Henry, Aaron, Gus, Ainhoa, and Oishik, who've been a source of engaging scientific discussions, humour, and political rants in equal measure. Having worked across so many different labs, it would be impossible to name everybody else, but you've all made this a great experience, and for that I am truly grateful!

Away from the lab, I am indebted to many people for keeping me grounded throughout this PhD. I will sorely miss Tuesday pub quiz, Friday craziness, trips to Maveli and Akbar's, coffee breaks and ice cream, and that 'cake' that Gus made out of bacon. Particular mentions go to Aaron, Henry, Lianne, Xander, Caitlin, Ainhoa, Gus, Josh, and all the friends from undergrad. You've been a wonderful group of people to know, and I'm so glad we're getting back to a stage where we can all meet up in person!

Thank you to my family, especially Mum and Dad, for your love and support, and always being there for me. You have no idea how much your support has meant to me. Thanks also to Bilbo, whose reptations were an excellent source of inspiration when thinking about polymer dynamics.

Lastly, thank you to Jess. You have supported me, you have kept me sane, and you have been the most amazing person to spend my life with. Finishing this PhD would not have been possible without you.

Contents

List of Figures

List of Tables

List of Abbreviations

AA	Amyloid A
AD	Alzheimer's disease
AF4	Asymmetric flow field-flow fractionation
AFM	Atomic force microscopy
ANS	8-Anilinonaphthalene-1-sulfonic acid
APF	Annular protofibril
APP	Amyloid precursor protein
AU	Arbitrary units
AWI	Air-water interface
Aβ	Amyloid β-peptide
Aβcc	Aβ with the A21C and A30C mutations
BSA	Bovine serum albumin
CD	Circular dichroism
CDF	Cumulative density function
CHC	Central hydrophobic cluster (of the Aβ peptide)
CI	Confidence interval
CMC	Critical micellar concentration
Cryo-EM	Cryo-electron microscopy
Cryo-ET	Cryo-electron tomography
CSF	Cerebrospinal fluid
CTD	C-terminal domain
CTR	C-terminal region
dH_2O	Deionised water
DRA	Dialysis-related amyloidosis
ECM	Extracellular matrix
EDTA	Ethylenediaminetetraacetic acid

EM	Electron microscopy
EPR	Electron paramagnetic resonance
ESI	Electrospray ionisation
FCR	Fraction of charged residues
FFF	Field-flow fractionation
FI	Frit inlet
FTIR	Fourier transform infrared (spectroscopy)
HbS	Sickle cell haemoglobin
hCC	Human cystatin C
HD	Huntington's disease
HFIP	Hexafluoroisopropanol
HMW	High molecular weight
HPLC	High-performance liquid chromatography
HSA	Human serum albumin
HS-AFM	High speed atomic force microscopy
Htt	Huntingtin
HttEx1	Huntingtin exon 1
HX	Hydrogen exchange
IAPP	Islet amyloid polypeptide
IDD	Intrinsically disordered domain
IDP	Intrinsically disordered protein
IP	Initiation-propagation
IR	Infrared
KDE	Kernel density estimation
KMC	Kinetic Monte Carlo
LC-MS	Liquid chromatography mass spectrometry
LD	Langevin dynamics
LLPS	Liquid-liquid phase separation
LMW	Low molecular weight
LS	Light scattering
LS 90^{o}	Light scattering at 90^{o}
MALS	Multi-angle light scattering
MAS-NMR	Magic angle spinning NMR
MD	Molecular dynamics

MG	Molten globule
Micro-ED	Micro-electron diffraction
MPL	Mass-per-length
MRE	Molar residue ellipticity
MS	Mass spectrometry
MW	Molecular weight
MWCO	Molecular weight cut-off
NBA	Native basin of attraction
NCC	Nucleated conformational conversion
NMDAR	*N*-methyl-D-aspartate receptor
NMR	Nuclear magnetic resonance
NP	Nucleated polymerisation
NS-EM	Negative stain electron microscopy
NTD	N-terminal domain
NTR	N-terminal region
PD	Parkinson's disease
PDB	Protein Data Bank
PDF	Probability density function
PDI	Polydispersity index
PEG	Polyethylene glycol
PHF	Paired helical filaments
PI3K	Phosphatidyl-inositol-3-kinase
PMF	Probability mass function
PMG	Pre-molten globule
Poly-Q	Polyglutamine
PPII	Polyproline II (helix)
PrP	Mammalian prion protein
PrP^{Sc}	Scrapie form of the mammalian prion protein
rfKMC	Rejection-free kinetic Monte Carlo
RI	Refractive index
RMS	Root-mean-squared
ROA	Raman optical activity
ROI	Region of interest
RSS	Residual sum of squares

SANS	Small angle neutron scattering
SDM	Site-directed mutagenesis
SEC	Size exclusion chromatography
SH3	Src-homology 3
ssNMR	Solid-state NMR
STEM	Scanning transmission electron microscopy
TEM	Transmission electron microscopy
ThT	Thioflavin T
TIRFM	Total internal reflection fluorescence microscopy
TR	Turn region (of the Aβ peptide)
TTR	Transthyretin
UV	Ultraviolet
UV_{280}	Ultraviolet absorbance at 280 nm
vdW	van der Waals
WLC	Worm-like chain
α-syn	α-synuclein
β_2m	β_2-microglobulin

Mathematical Notation

Wherever possible, mathematical notation has been chosen to be as similar as possible to that used by existing studies in the literature. In particular, much of the notation is based on the conventions used by Knowles *et al.* [1–6] and Hong and Yong [7]. However, as the work in this thesis covers several fields of study, changes have been made to some of the notation to avoid certain conflicts. In addition, changes have been made to ensure that the notation is consistent with that used by Taylor *et al.* [8], the analytical results of which are discussed in Chapter 5. In line with the recommendations of the American Physical Society, the binary operators $\propto$, $\approx$, and $\sim$ are used to mean 'proportional to', 'approximately equal to', and 'approximately or asymptotically proportional to', respectively. In addition, unary $\sim$ is used to denote approximate values. The most commonly used mathematical symbols in this thesis are outlined below; those that appear infrequently are omitted from this section, but are defined elsewhere at the point of use.

c	Molar concentration (M)
c^*	Critical concentration for stability of a species (M)
C_+	$= \lambda^2/2\kappa^2$
$G(t)$	Concentration of globular oligomers (M)
I	Ionic strength (M)
$I(t)$	ThT fluorescence intensity (AU)
$J_n(t)$	Surface-catalysed primary nucleation rate per surface area ($\mathrm{m}^{-2}.\mathrm{s}^{-1}$)
k_B	Boltzmann constant ($\mathrm{J.K}^{-1}$)
k'_c	Pseudo-first-order rate parameter for conversion of oligomers (s^{-1})
k'_d	Pseudo-first-order rate parameter for disassembly of oligomers (s^{-1})
k_e^+	Polymerisation/elongation rate parameter ($\mathrm{M}^{-1}.\mathrm{s}^{-1}$)
k_e^-	Depolymerisation rate parameter (s^{-1})
k_f	Length and position-independent fragmentation rate parameter (s^{-1})
k'_g	Pseudo-first-order rate parameter for secondary oligomer generation (s^{-1})
k_n	Primary nucleation rate parameter ($\mathrm{M}^{1-n_c}.\mathrm{s}^{-1}$)

k'_n	Effective primary nucleation rate parameter, for saturable nucleation ($\mathrm{M}^{1-n_c}.\mathrm{s}^{-1}$)
k_s	Secondary nucleation rate parameter ($\mathrm{M}^{-n_s}.\mathrm{s}^{-1}$)
k'_s	Effective secondary nucleation rate parameter, for saturable nucleation ($\mathrm{M}^{-n_s}.\mathrm{s}^{-1}$)
K_{av}	Distribution coefficient for partitioning of solutes into SEC beads (*dimensionless*)
$K_{M,e}$	Effective Michaelis constant for saturable elongation (M)
$K_{M,n}$	Effective Michaelis constant for primary nucleation (M^{n_c} or $\mathrm{M}^{n_c-\varepsilon_c}$)
$K_{M,s}$	Effective Michaelis constant for secondary nucleation (M^{n_s} or $\mathrm{M}^{n_s-\varepsilon_s}$)
l	Fibril length (eg. μm) *or* instrument path length (eg. cm)
l_p	Persistence length (eg. nm)
$L_1(t)$	Effective concentration of peptide deposited as a monolayer film (M)
$L_{1,\max}$	Maximum occupancy of a monolayer film (M)
$L_+(t)$	$= L_{\mathrm{tot}}(t) - L_1(t)$
$L_{\mathrm{tot}}(t)$	Effective concentration of peptide deposited as a multilayer film (M)
$m(t)$	Free monomer concentration (M)
$M(t)$	Fibrillar monomer concentration (M)
$M_T(t)$	Total concentration of aggregated monomer (M)
M_n	Number-averaged molecular weight (Da)
M_w	Weight-averaged molecular weight (Da)
M_n^{ROI}	Number-averaged molecular weight of a region of interest (Da)
M_w^{ROI}	Weight-averaged molecular weight of a region of interest (Da)
n^*	Number of monomers in the critical nucleus
n_c	Effective order of primary nucleation
n_s	Effective (monomer) order of secondary nucleation
$\langle N \rangle$	Average size of globular oligomers
$N(t)$	Effective concentration of aggregated monomers in a non-fibrillar state (M)
N_A	Avogadro constant (mol^{-1})
$p(M)$	Probability density function of aggregate mass (Da^{-1})
$P(M)$	Cumulative density function of aggregate mass (*dimensionless*)
P_θ	Form factor in MALS (*dimensionless*)
R_a	Surface roughness (eg. nm)
R_e^+	Fold-change in k_e^+
R_g	Radius of gyration (eg. nm)
R_H	Hydrodynamic radius (eg. nm)
R'_n	Fold-change in k'_n

R'_s	Fold-change in k'_s
t_r	Retention time (eg. s)
z	AFM height measurement (eg. nm) *or* charge number
γ	Monomer-dependence of τ, ie. $\gamma = -\partial \log \tau / \partial \log m(0)$
γ_{50}	Monomer-dependence of τ_{50}, ie. $\gamma_{50} = -\partial \log \tau_{50} / \partial \log m(0)$
γ_{inf}	Monomer-dependence of τ_{inf}, ie. $\gamma_{\text{inf}} = -\partial \log \tau_{\text{inf}} / \partial \log m(0)$
γ_{lag}	Monomer-dependence of τ_{lag}, ie. $\gamma_{\text{lag}} = -\partial \log \tau_{\text{lag}} / \partial \log m(0)$
Γ	Scaling exponent relating τ_{lag} to ν_{max}, ie. $\Gamma = -\partial \log \tau_{\text{lag}} / \partial \log \nu_{\text{max}}$
ΔG	Free energy change (eg. kcal.mol^{-1})
$\Delta I(t)$	ThT fluorescence intensity change (AU)
$\Delta I_{\text{norm}}(t)$	Normalised ThT fluorescence intensity change (*dimensionless*)
ε	Molar extinction coefficient (eg. M^{-1}.cm^{-1})
ε_c	Effective order of primary nucleation in the saturating limit
ε_s	Effective (monomer) order of secondary nucleation in the saturating limit
$[\Theta]_{\text{MR}}$	Molar residue ellipticity (deg.cm^2.dmol^{-1})
κ	Macroscopic rate constant for secondary pathways (s^{-1})
λ	Macroscopic rate constant for primary pathways (s^{-1})
ν_e^+	Specific polymerisation/elongation rate of an amyloid fibril (s^{-1})
ν_e^-	Specific depolymerisation rate of an amyloid fibril (s^{-1})
ν_{max}	Maximum relative rate of fibril mass gain (s^{-1})
ρ	Mass concentration (eg. g.L^{-1})
τ	Generalised characteristic time for self-assembly (s)
τ_{50}	Half-time for self-assembly (s)
τ_{inf}	Inflection time for self-assembly (s)
τ_{lag}	Lag time for self-assembly (s)
$\Phi_n(t)$	Primary nucleation rate (M.s^{-1})
$\Phi_s(t)$	Secondary nucleation rate (M.s^{-1})

Chapter 1

Introduction

1.1 Overview of amyloids

Amyloids are fibrous, highly ordered assemblies of protein (Fig. 1.1) whose formation is associated with over fifty human diseases [9], including Alzheimer's disease (AD) [10–14], Parkinson's disease (PD) [15], and Huntington's disease (HD) [16]. These diseases, which are collectively termed amyloidoses, are often chronic, debilitating, and ultimately fatal. Many amyloidoses are age-related illnesses, and due to the increase in global life expectancy since the start of the twentieth century, they are rapidly becoming leading causes of death and disability worldwide [17–19]. Moreover, due to their severity and chronic nature, amyloid diseases impose a significant economic burden; the annual cost of AD was recently estimated at $34.7 billion in the UK [20] and $305 billion in the US [21], and the latter figure does not account for the substantial additional role of unpaid carers. As the global population continues to age, amyloid diseases are predicted to take centre stage as the predominant cause of age-related morbidity, and a significant barrier to further global development [17–19].

There is an urgent need to develop better treatments for these diseases. While the majority of therapeutic candidates to date have been targeted to specific amyloid-forming proteins, it is becoming increasingly clear that many diseases are characterised by the simultaneous formation of amyloids by several different proteins. For example, in addition to the well-established role of the amyloid β-peptide (Aβ) [10–13] and Tau [22] in the onset of AD, two other amyloidogenic proteins, α-synuclein (α-syn) [23–25] and the mammalian prion protein (PrP) [26], are also believed to be involved. Similarly, while α-syn is the primary amyloidogenic protein associated with PD [15], a role for Aβ is also supported [27]. In contrast to non-pathogenic protein polymerisation in which proteins typically adopt a limited range of conformational states, amyloid formation is also notoriously polymorphic, with a single primary sequence able to give rise to a wide variety of distinct amyloid and amyloid-related protein structures [28] (Fig. 1.1(b)). The heterogeneous and polymorphic

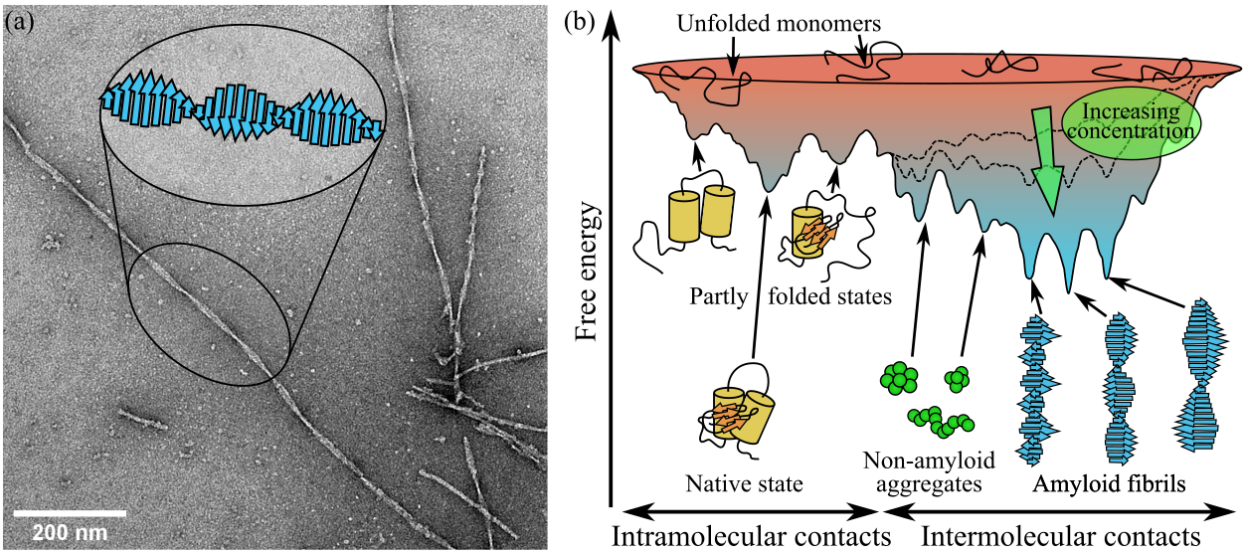

Figure 1.1: Basic characteristics of amyloid fibrils. (a) Negative stain electron micrograph of amyloid fibrils, superimposed with a simplified schematic of an amyloid fibril, showing a twisted ribbon of intermolecular β-sheets. Own image, with acquisition methods described in Section 2.7. (b) A simplified free energy surface of protein folding, misfolding, and amyloid formation. Different wells correspond to different conformational/aggregation states. The free energy of aggregates is concentration-dependent, so they are less stable at lower concentrations, as shown by the dashed lines and green arrow on the right of the free energy surface. Unfolded monomers are situated around the periphery of the folding funnel. There are multiple wells corresponding to different amyloid fibril polymorphs, with distinct structures but in principle the same primary sequence. Panel (b) is based on a similar figure in Hartl and Hayer-Hartl [30], but re-made to represent the concentration-dependence and polymorphism of protein aggregation.

nature of amyloid self-assembly presents a considerable challenge to traditional therapeutic approaches that target a limited variety of protein structures. Thus, while studies of individual amyloid species have provided crucial insights into disease mechanisms, more effective treatments for many amyloid diseases are likely to require general therapeutic approaches capable of targeting a variety of different amyloids; this, in turn, requires a general and rigorous theory of the underlying self-assembly process [9, 29].

At the same time, it has become apparent that amyloid self-assembly is a topic well-suited to yielding general physical principles [9]. Amyloid formation is not restricted to a small number of disease-causing proteins; it is a near-universal property of polypeptide chains [31]. The cross-β structure that is characteristic of amyloids, which consists of a continuous intermolecular β-sheet spanning the entire length of the filament [32, 33] (Fig. 1.1(a)), has now been induced in many non-pathogenic proteins [31, 34, 35], homopolypeptides [36], demonstrating the lack of requirement for a specific primary sequence, and even in non-polypeptide amphiphilic polymers [37]. Moreover, the physiological concentrations of many proteins are now understood to lie above their critical concentration for amyloid formation, meaning that the native state is often a metastable phenomenon [38, 39]. A schematic of the position of amyloid fibrils in protein

folding free energy surfaces, and the effect of concentration on amyloid stability, is shown in Fig. 1.1(b). The fact that such a diverse range of polypeptides can all adopt the cross-β structure has profound implications for our understanding of protein folding and disease. Amyloids require a more nuanced interpretation of Anfinsen's dogma [40]; the native state does not necessarily represent the universal thermodynamic minimum under physiological conditions [38, 39, 41], and given the existence of amyloids and their frequent polymorphism, the primary sequence does not uniquely determine the fold [28, 41]. More saliently for the study of human disease, the universality of the cross-β structure also offers the promise of developing broad-spectrum therapeutics that can be used to treat a range of amyloidoses, including those complicated by heterogeneity and structural polymorphism [42].

Interest in amyloids extends beyond their role as toxic or non-functional aggregates. Given the ubiquity, stability, and ease of assembly of the cross-β structure, it is unsurprising that many amyloids are now also understood to have biological functions [41]. Perhaps the most famous example is Curli, a Gram-negative bacterial adhesion protein [43]; however, many more examples of functional amyloids have now been found. These include yeast prions such as Sup35p [44, 45], Ure2p [46], and HET-s [47], and the human protein Pmel17 [48], which is involved in melanin biosynthesis. Thus, the ability to modulate amyloid formation may have far-reaching consequences for the treatment of a wide variety of illnesses. In addition, artificial amyloids are increasingly being investigated as potential biomaterials, due to their ease of assembly, rigidity, high tensile strength, and capacity to host large arrays of repeating functional units [41].

In addition to well-developed, ordered amyloids, there has been considerable interest in the metastable aggregate states populated during amyloid formation (Fig. 1.1(b)). These may be situated on- or off-pathway to true amyloids, and are given various names such as oligomers, spheroids, and protofibrils, depending on their gross morphology (Section 1.4). Many of these prefibrillar assemblies exhibit marked cytotoxicity [49]. For example, oligomers of the Alzheimer's-associated Aβ peptide have been shown to inhibit neuronal long-term potentiation (LTP) in rodent models [50], and oligomers of Aβ, α-syn, PrP, and several other amyloidogenic polypeptides have been shown to permeate membranes in a manner similar to bacterial pore-forming toxins [51]. Thus, there is growing evidence that pathology in some amyloidoses is largely due to the species formed during amyloid self-assembly, rather than mature amyloids [49]. Nonetheless, the pathways by which amyloids, oligomers, and other related species form are intricately linked, and autocatalytic processes such as fibril fragmentatation and secondary nucleation have been shown to generate toxic oligomers in a fibril-dependent manner [52–56]. Therefore, a detailed understanding of the mechanism and kinetics of the entire self-assembly pathway is needed to design effective therapeutics for amyloidoses.

The aim of this literature review is to provide a general overview of the structural biology and biophysics of amyloids, with particular attention to their formation mechanisms, and the implications of these mechanisms for the macroscopic self-assembly kinetics in both experimental and physiological contexts.

Particular emphasis is given to the Alzheimer's Aβ peptide, the model system used in this thesis. However, as argued above, amyloid formation is a field both in need of and well-suited for obtaining general physical principles. Therefore, the conclusions of this thesis are likely to be relevant to other amyloids, and studies of other amyloidogenic polypeptides can shed light on Aβ self-assembly mechanisms. As such, this literature review has a broader scope, examining the general characteristics of amyloid structure and self-assembly, and their underlying biophysical explanations.

1.2 Alzheimer's disease and the amyloid β-peptide

Aβ is a disordered, amyloidogenic peptide that is believed to play a causal or contributing role in the onset of Alzheimer's disease (AD). AD is the most common form of dementia, and affects around 50 million people around the world, a number that is predicted to increase to over 130 million by 2050 [18]. At present, AD is incurable and the efficacy of treatments is poor; therefore, the mechanisms of AD pathology remain the subject of intense research. Two of the most promising therapeutic targets for AD research are Tau and Aβ, amyloidogenic polypeptides whose aggregates are the dominant constituents of the intracellular neurofibrillary tangles and extracellular plaques considered characteristic of AD histopathology, respectively [57]. Aβ, the dominant component of the plaques, is derived from the amyloid precursor protein (APP), a transmembrane protein whose extracellular domain is cleaved by β-secretase and γ-secretase to release Aβ into the extracellular environment, where it then aggregates [58]. Mutations in *APP* and the presenilin genes, which encode parts of the γ-secretase complex, are strongly associated with hereditary and early-onset AD [59, 60], and an increase in copy number of the *APP* gene has been implicated as the cause of high rates of AD in people with Down's syndrome [61]. During Aβ production, β-secretase cleavage forms the N-terminus and γ-secretase cleavage forms the C-terminus of the peptide, and both proteases have variable cleavage sites giving rise to several Aβ isoforms whose terminal regions have different lengths. *In vivo*, the most abundant isoforms are Aβ(1-40), Aβ(1-42), and Aβ(11-42). The majority of Aβ isoforms aggregate to form amyloid fibrils and a variety of metastable, non-amyloid aggregates, but the Aβ(1-42) and Aβ(11-42) isoforms are more amyloidogenic than Aβ(1-40), and are considered to be more toxic [58, 62]. While evidence for direct toxicity of the amyloid fibrils formed by Aβ is scarce, prefibrillar oligomers have been shown to have a wide range of toxic effects. These include damage to lipid membranes [51, 63–68], activation of the *N*-methyl-D-aspartate receptor (NMDAR) [69], and induction of Tau hyperphosphorylation [70]. Thus, Aβ oligomer preparations are highly neurotoxic [71, 72], and oligomers are believed to be responsible for a cascade of processes that ultimately results in neuronal death and cognitive decline [73]. In addition, as mentioned in the previous section, there is now strong evidence that amyloid fibrils formed by Aβ and many other polypeptides can catalyse the formation of toxic prefibrillar oligomers, indirectly

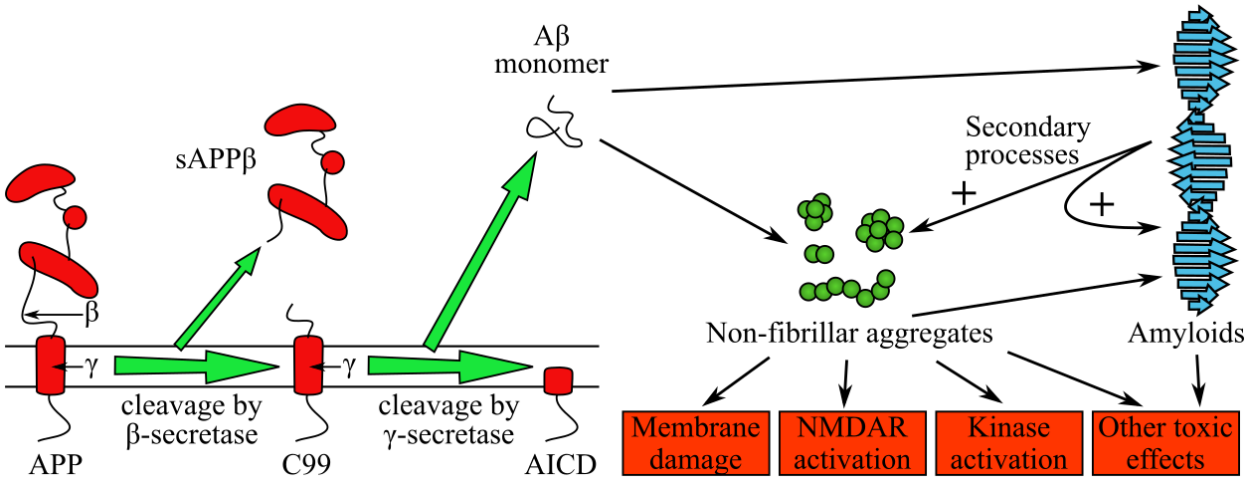

Figure 1.2: Formation, aggregation, and toxicity of Aβ. The amyloid precursor protein (APP) is a transmembrane protein that is sequentially cleaved by the β- and γ-secretases (left). Cleavage by β-secretase produces the C99 and sAPPβ fragments, and further cleavage of C99 by γ-secretase causes the release of Aβ from the membrane. The C-terminus, which is formed by γ-secretase cleavage, is part of the transmembrane domain prior to release, and is more hydrophobic than the N-terminus, which is derived from a flexible extracellular region. After its release, the Aβ monomer aggregates to form amyloids, as well as a variety of toxic aggregation intermediates and off-pathway species (right). Fibril-dependent 'secondary' processes such as fragmentation and secondary nucleation promote formation of more fibrils and non-fibrillar aggregates, creating positive feedback. Aβ aggregates then cause toxicity by a variety of mechanisms, a selection of which are represented in this figure. Based on information in Hamley [58] and Dawkins and Small [76].

contributing to toxicity and completing a positive feedback loop that results in exponential accumulation of toxic species [4,52–54,74,75]. Thus, toxicity depends on the concentration, structure, and polymorphism of both oligomers and amyloid fibrils [54], and the Aβ self-assembly pathway must be studied in its entirety in order to understand the effects of potential therapeutics on disease outcomes. The formation, aggregation, and toxicity of Aβ are summarised in Fig. 1.2.

1.3 Morphological, structural, and biophysical characteristics of amyloids

General opinion on the defining characteristics of amyloids has shifted over the years, in response to progressive advances in biochemistry and biophysics that have led to a deepening understanding of the fundamental properties that unify these assemblies and distinguish them from other proteins [41, 77]. Originally, amyloids were misidentified as lipid deposits, and later as polysaccharides by Virchow, who coined the term 'amyloid' from the Latin 'amylum' (starch), based on the observation that they stained blue with iodine [78, 79]. Shortly after, Friedrich and Kekulé showed that amyloids consisted of protein [80]; however, the first indications of their structure only appeared after advances in light microscopy and biophysical

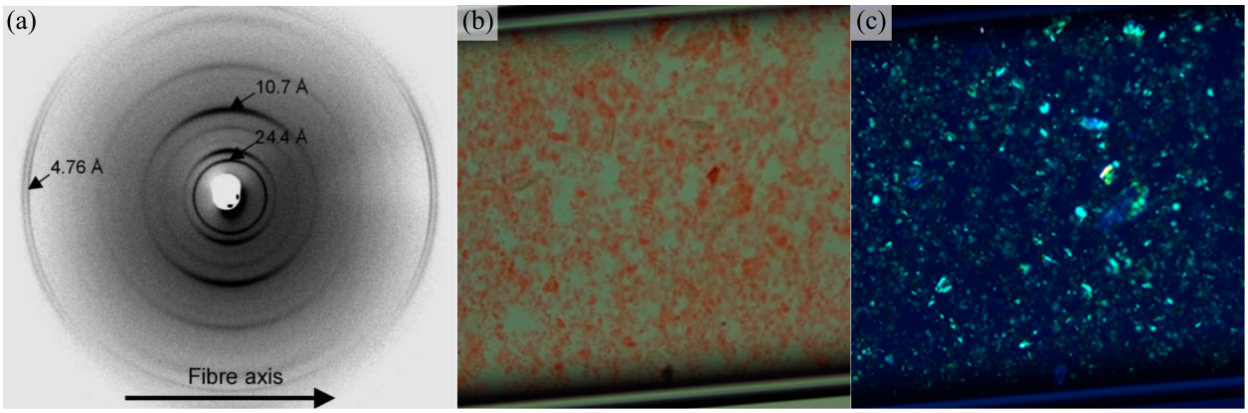

Figure 1.3: Diagnostic features of amyloid fibrils. Although the cross-β structure is arguably the unifying feature of amyloid fibrils, diagnostic experimental signs include a ∼4.7 Å ring in the X-ray fibre diffraction pattern, and birefringence when stained with Congo red and viewed under polarised light. (a) X-ray fibre diffraction pattern of partially aligned amyloid fibrils formed by the AAAK peptide, from Makin *et al.* [90]. (b-c) Light microscopy images of Aβ fibrils stained with Congo red, under (b) normal illumination and (c) polarised light, with the latter showing green birefringence indicative of cross-β structure. Panels (b-c) adapted from Aliyan *et al.* [91].

techniques in the early-to-mid 20$^{\text{th}}$ century. Several authors observed that amyloids exhibited birefringence when stained with Congo red dye, indicating a high degree of molecular alignment [81–85] now known to be caused by their repetitive cross-β structure. The cross-β structure consists of a continuous intermolecular β-sheet spanning the entire length of the filament, formed by β-strands from adjacent subunits whose polypeptide chains are oriented approximately orthogonal to the filament axis. This motif had already been identified by Astbury and colleagues [86], in their X-ray diffraction study of the denatured states of natively globular proteins, and was subsequently shown to exist in amyloids by Eanes and Glenner, who observed an intense ∼4.7 Å ring in the X-ray diffraction patterns of amyloid from human liver and spleen, indicating the presence of an extensive β-sheet [33]. In addition, both the birefringence data and early electron microscopy (EM) images led to the conclusion that amyloid was fibrous in nature [87–89]. A representative EM image of amyloid fibrils is shown in Fig. 1.1(a), and an X-ray diffraction pattern and example of Congo red birefringence are shown in Fig. 1.3.

Today, EM routinely shows that amyloids are filamentous structures with a typical length up to several microns, usually unbranched, and possessing ribbon-like, helical, or tubular morphologies [41]. In addition to binding Congo red, amyloids are also commonly detected by their ability to bind thioflavin T (ThT) [92], a dye that exhibits enhanced fluorescence when interacting with amyloid fibrils, and allows real-time quantitation of amyloid self-assembly. Significant progress has been made in the kinetic theory of amyloid self-assembly [9], and recent advances in solid-state nuclear magnetic resonance (ssNMR) spectroscopy and cryo-electron microscopy (cryo-EM) have provided atomic-resolution structural models, revealing a

plethora of hitherto unforeseen features [77]. This more intricate, quantitative portrait of amyloids has led to the recognition that many of the peculiarities of their formation can ultimately be traced back to simple physical principles related to their polymeric nature and the unusual physical properties of the cross-β structure. In addition, while a wide variety of cross-β protein polymers are now described as amyloids, it has become clear that Congo red and ThT are neither completely amyloid-specific, nor sensitive to all cross-β structures [93, 94]. As a result, in the molecular biosciences, the cross-β motif has now become more closely identified with the term 'amyloid', and is often considered their defining feature, rather than their histological characteristics. The aim of this section of this literature review is to describe the basic physical principles that govern formation of the cross-β motif, and the shared structural, morphological, and mechanical characteristics of amyloid fibrils. In the following sections, these properties will then be related to the pathways, intermediates, and kinetics of amyloid self-assembly.

1.3.1 Biophysical and biochemical methods for studying the structure of amyloid fibrils

Amyloids are insoluble, high molecular weight (MDa), fibrous assemblies, making them difficult to study by conventional structural approaches [95]. Nonetheless, recent advances in structural techniques have allowed high-resolution structures to be obtained [77, 96]. Diffraction techniques for investigating amyloid fibrils include: X-ray fibre diffraction [95], which provided the first indications of the cross-β structure [33,86]; X-ray crystallography, which is harder to apply to amyloids due to their fibrous nature and structural heterogeneity [95], but has been used to study amyloid-like peptide micro-crystals [97–99]; and micro-electron diffraction (micro-ED), which can be applied to micro-crystals of smaller sizes [100]. Spectroscopic techniques that provide general indications of secondary structure content include Fourier transform infrared (FTIR) and circular dichroism (CD) spectroscopy, with the former measuring infrared (IR) absorbance peaks corresponding to the vibrational modes of amides and other bonds in the polypeptide chain, and the latter reporting on the chirality of secondary structures by measuring the differential absorption of circularly polarised light [95]. Nuclear magnetic resonance (NMR) spectroscopy techniques offer much more detailed information, providing measurements such as dihedral angles and both intramolecular and intermolecular distance restraints that can be used to construct 3D models of amyloid fibrils [95,96]; due to the insolubility of amyloid fibrils, solid-state NMR (ssNMR) is the dominant NMR technique [28], although solution-state NMR has been applied to unstructured regions of amyloid fibrils, such as the surface domains of some prions [101, 102]. Electron microscopy (EM) techniques are widely used, and include: negative stain electron microscopy (NS-EM), which provides high-contrast mesoscale transmission electron microscopy (TEM) images of amyloids negatively stained with a heavy metal salt such as uranyl formate [95,103]; cryo-electron microscopy (cryo-EM), in which cryogenically frozen samples are imaged with low electron doses, usually without staining, in order to obtain TEM images with high resolution and low contrast [103–105]; and

scanning transmission electron microscopy (STEM), which can be used to obtain mass-per-length (MPL) measurements of amyloid fibrils [95]. Recent advances in sample preparation, detector design, and image processing have led to a revolution in cryo-EM resolution that has provided the first near-atomic-resolution density maps of amyloid fibrils [77, 104, 105]. Besides EM, another commonly used microscopy technique is atomic force microscopy (AFM). In AFM, a sample is deposited on a flat surface such as mica, and raster-scanned with a molecularly sharp cantilever tip. Interactions between the sample and the tip are then detected via a laser beam reflected off the cantilever, resulting in a topographic image of the sample [106]. AFM can be used to obtain high-resolution images of the surface of amyloid fibrils, which can now be further improved using recently developed tip-sample contact point deconvolution techniques [107]. In addition, AFM can be carried out under under native conditions, allows real-time imaging, and provides a means to probe the mechanical properties of the sample and protein-ligand interactions via the use of force-distance curves [108–110]. Lastly, in addition to structural approaches, biochemical experiments such as dye binding, cross-linking, and hydrogen-deuterium exchange (HX) have provided supplementary insights that have often anticipated the conclusions of subsequent high-resolution work [95].

1.3.2 Hierarchical organisation of amyloid fibrils

Amyloids have a hierarchical structural organisation, consisting of symmetric associations of smaller structural units formed at multiple different length scales [77]. Confusingly, the terminology used to describe these components is rather inconsistent across the field; in this thesis, an attempt has been made to use the terms that are the most neutral and least likely to cause confusion, as outlined in this subsection. Plaques or deposits of amyloid are composed of fibrous assemblies termed *fibres* or *fibrils*, although fibres are sometimes treated as a higher level in the organisational hierarchy than fibrils, and fibril is the most common term in *in vitro* contexts. Each fibril consists of one or more laterally associated *protofilaments*, each of which is a long, filamentous assembly with its own continuous cross-β structure. The protofilaments adhere tightly to one another with a well-defined symmetry and set of inter-protofilament packing interactions, and often wrap around one another to form a fibril with an overall twisted ribbon or helical morphology. In turn, each protofilament is a hydrogen-bonded stack of *subunits*, which are usually monomers. While some studies have reported single protofilaments that have multimeric subunits, in most cases these can be re-analysed as tight bundles of separate protofilaments with monomeric subunits. For example, the 2A polymorph of Aβ(1-40), which was originally described as a single protofilament consisting of a stack of quasi-planar dimers that stack on top of one another in a face-to-face manner [111], has also been analysed as an in-register association of two separate protofilaments, each consisting of a stack of monomers [112]; both interpretations are common in the literature. Due to differences in contact area and the nature of the interactions, attractive forces between monomers are usually much stronger in the direction of the protofil-

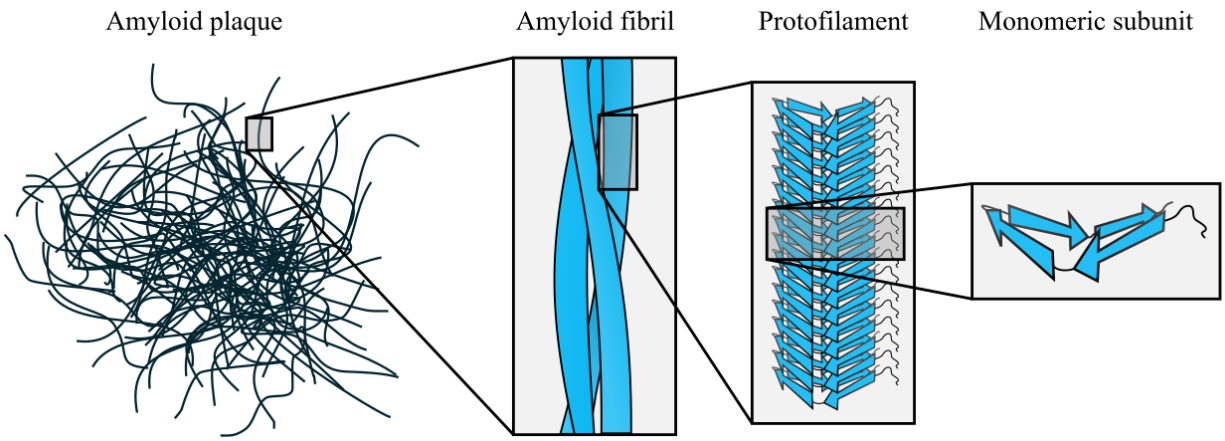

Figure 1.4: Hierarchical organisation of amyloid fibrils. The dominant components of amyloid plaques are amyloid fibrils, which are formed by close lateral association of protofilaments. In turn, protofilaments are stacks of subunits, which are often monomeric [77]. The density map obtained by Mizuno *et al.* [114] was used as a template for the fibril schematic in the centre-left part of the figure.

ament axis than orthogonal to it (see Section 1.3.5), meaning that separate stacks of monomers usually only adhere to one another because their length results in a large number of interactions between stacks. Therefore, if a single dimeric 'subunit' from the 2A polymorph were isolated from the rest of the 'protofilament', it would most likely dissociate into monomers, lacking the specific contacts needed to overcome random thermal motion and the net electrostatic repulsion between monomers. Therefore, in this thesis, the subunits of protofilaments are defined as the smallest asymmetric units capable of stacking to form a cross-β structure, unless there is a clear reason why a lateral pair of asymmetric units should interact more strongly with one another than with their neighbours along the fibril axis. This usually favours the interpretation where each protofilament is a stack of monomers, although heterogeneous or very tightly associated multimers would also satisfy this definition. Assemblies with a level of organisation intermediate between a protofilament and a fibril are here termed *protofilament groups*. In certain studies, the term proto*fibril* is used in place of proto*filament* (eg. [113–115]); however, that particular usage is less common and is avoided in this thesis, as protofibril is also the term used to refer to entire, metastable, fibril-like structures formed by Aβ [116] and some other polypeptides (Section 1.4.3). Lastly, the more neutral term *filament* is used in statements that would be true for protofilaments or fibrils alike. The hierarchical organisation of amyloid fibrils is summarised in Fig. 1.4.

1.3.3 Stacking of subunits to form protofilaments

As outlined above, each protofilament consists of a stack of subunits, usually monomeric, that collectively form a cross-β structure. Although there are notable exceptions [117–120], in pathological amyloids the subunits usually have a flattened, single-layered tertiary structure containing one or more β-strands with

the backbone hydrogen-bonding groups oriented parallel to the protofilament axis. As a result, the protofilament as a whole contains one or more intermolecular β-sheets, with each subunit contributing a single β-strand per β-sheet. Adjacent subunits may have peptide backbones oriented parallel or antiparallel to one another, giving rise to parallel or antiparallel β-sheets (Fig. 1.5), although the former type is more commonly observed [77]. Interactions between monomers along the protofilament axis are clearly dominated by backbone hydrogen-bonding; although the hydrophobic effect and van der Waals (vdW) forces play an important role in inter-protofilament interactions, their role in stack formation is much more limited. This means that the balance of interactions that defines the topology of amyloid fibrils is different from that observed in globular proteins, where the hydrophobic effect plays a more important role in maintaining a globular structure [121]. Accordingly, the anisotropic nature of backbone hydrogen bonding is responsible for the extreme aspect ratio of amyloid fibrils, in contrast to globular proteins whose folding is dominated by more isotropic forces. The significant topological differences between amyloids and globular proteins, particularly the scale, uniformity, anisotropy, and high level of symmetry of the former, affect the nature of supplementary molecular interactions. This is particularly pronounced in parallel in-register cross-β structures, where the alignment of the same amino acids in adjacent subunits induces the formation of massive arrays of polarised amide sidechains and π-stacked aromatics; at the same time, alignment of charged residues results in an unfavourable enthalpic contribution that opposes this alignment [41, 97, 122].

While the high degree of structural order exhibited by amyloids would be expected to result in an unfavourable entropy of formation, amyloid formation is also associated with a favourable desolvation entropy [123], which partly mitigates these losses just as it does for globular proteins. In addition, desolvation creates a less dielectric environment within the fibril, strengthening the hydrogen bonding in the cross-β core [97]. Existing structures suggest at least two stages of assembly at which desolvation is likely to occur: firstly, during folding of the subunits, whether this happens before or during their assembly into a protofilament, and secondly when forming a dry interface between laterally associated protofilaments. It is also worth noting that most amyloids retain large disordered regions around their periphery, and domains that are well-folded in the native state may become less ordered in the amyloid. For example, while the N-terminal domain (NTD) of the yeast prion HET-s is folded in the non-amyloid state, it is a molten globule in the amyloid [118], an effect which may also help to mitigate the loss of chain entropy in the cross-β core. Monomer rigidity also strongly affects amyloid formation. More flexible polypeptides suffer from a greater loss of chain entropy during cross-β structure formation; as a result, under physiological conditions, chains with a low glycine content tend to aggregate to form amyloids, while those with a high glycine content tend to remain as solvated, disordered elastomers, despite being in an aggregated state [124].

As previously discussed, the subunits of a protofilament can assemble to form a parallel or antiparallel cross-β structure [95] (Fig. 1.5). Parallel structures almost always have an in-register alignment between

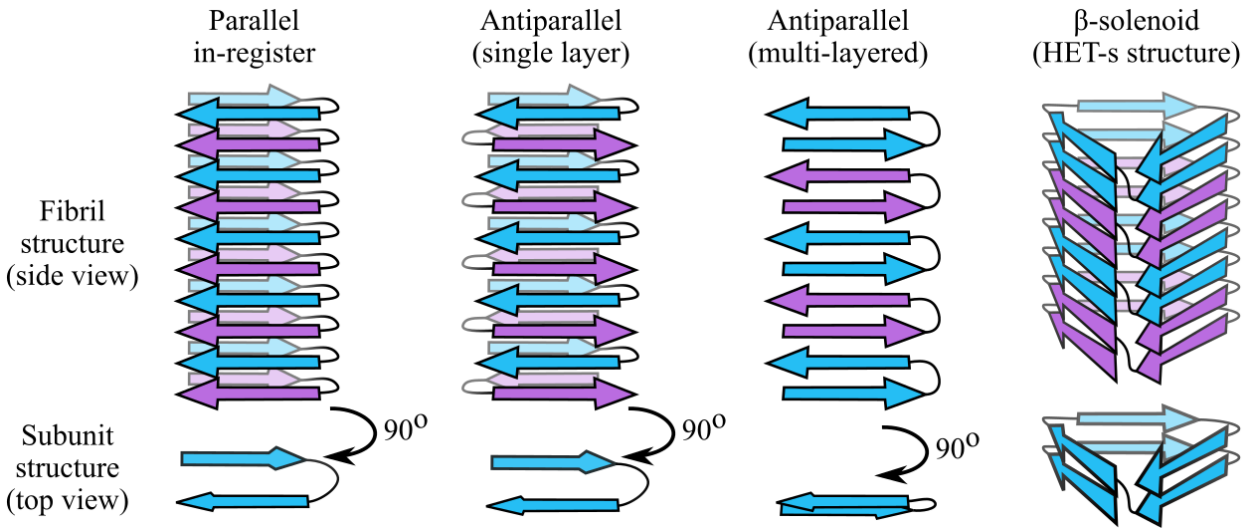

Figure 1.5: Types of cross-β structures. In parallel in-register structures, each subunit contributes a single strand per intermolecular β-sheet, and the strands are oriented parallel and in-register with one another. The hairpin-like structure shown in this figure has two intermolecular β-sheets. In single-layered antiparallel cross-β structures, each subunit contributes a single β-strand per β-sheet, but the strand direction alternates. Multi-layered antiparallel structures are also possible, in which each subunit contributes more than one β-strand per β-sheet. In β-solenoids such as HET-s [117–119], subunits occupy more than one layer by coiling in a solenoidal fashion. To make them easier to distinguish, adjacent subunits are alternately coloured blue and purple in these schematics. To allow comparisons, each monomeric subunit in the parallel in-register and antiparallel structures is a two-strand hairpin, differing only in orientation of the strands; a different monomer structure is used for the β-solenoid, based on the HET-s structure [117–119]. Schematics based on information in Toyama and Weissmann [95] and Tycko [96].

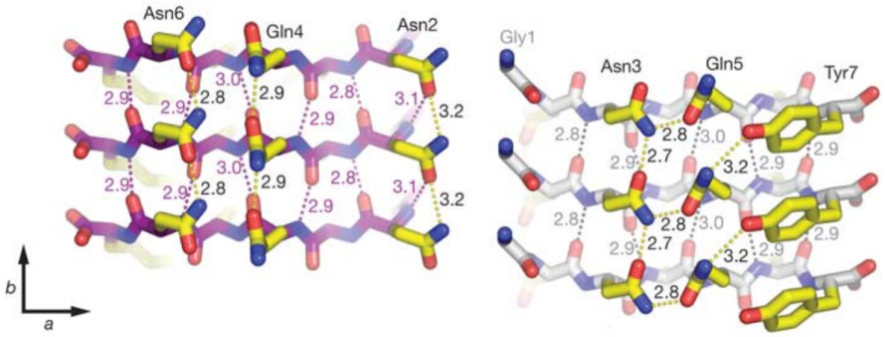

Figure 1.6: Interactions stabilising parallel in-register structures include π-stacking of aromatic residues and formation of hydrogen-bonded ladders by amide sidechains. This figure shows these interactions in amyloid-like microcrystals of the GNNQQNY peptide, which provided early support for their importance in stabilising parallel in-register cross-β structures. Image from Nelson *et al.* [97].

β-strands from adjacent subunits, implying that the forces responsible for stabilising parallel orientations are strongly dependent on the alignment of identical sidechains. An obvious candidate for such an interaction is π-stacking, which would be expected to occur along the extensive ladders of aromatic residues formed both within and on the outside of amyloid fibrils, in a manner similar to the stacking of nucleobases within nucleic acids. The importance of π-stacking is confirmed by existing ssNMR and cryo-EM structures [125–132]. In addition, studies of polyglutamine (poly-Q) revealed the presence of amide ladders caused by polarisation of aligned hydrogen-bonding groups in the sidechain amides of adjacent β-strands [122]. Amide ladders have since been discovered in structures obtained using a wide variety of techniques [97, 117, 128, 133–142], and it is now believed that they often play an important role in stabilising the parallel in-register alignment [77]. Examples of π-stacking and amide ladders in a parallel in-register cross-β structure are shown in Fig. 1.6. It is also now understood that the majority of monomeric subunits have a highly complex tertiary structure often resembling a Greek key motif [128,130,131,135,137–139,142–150], although the backbone hydrogen-bonding groups are oriented orthogonal rather than parallel to the plane of the key-like structure, in order to form hydrogen bonds with adjacent monomers (Fig. 1.7). If the chain direction were to alternate between subunits, the differing distribution of residues such as prolines and glycines, which affect the distribution of turns and β-strands, would make it difficult for layered subunits to have β-strands in the same place. Thus, antiparallel cross-β structures may be entropically disfavoured in long, flexible polypeptides that tend to adopt highly convoluted tertiary structures.

The primary effect that disfavours parallel in-register structures, and favours antiparallel structures, appears to be the electrostatics [151]. Alignment of the termini and charged sidechains of parallel in-register subunits results in an unfavourable enthalpic term, which can be lessened by adopting an antiparallel arrangement [151]. Accordingly, one would expect polypeptides with a higher content of aromatics and sidechain amides to prefer a parallel in-register alignment, while those with more charged sidechains would

prefer an antiparallel alignment. There is also a length effect, since shorter chains are likely to have a higher fraction of charged residues (FCR) due to the length-independent charges at their termini [151]. In most cases, the forces favouring parallel alignment appear to win out, but there are occasional instances of antiparallel cross-β structures; these include the sequence-designed peptide KFFEAAAKKFFE ('AAAK') [90], the small Aβ-derived peptides Aβ(11-25) [152] and Ac-KLVFFAE-NH_2 [153, 154], and a recent structural model of Huntingtin exon 1 (HttEx1) [155].

In the majority of protofilament structures, each subunit consists of a single layer of β-strands and other secondary structural elements [77]. The main reason for this may be the comparative stability of parallel in-register cross-β motifs; these are most easily formed if each subunit contributes only a single β-strand per intermolecular β-sheet, favouring quasi-planar subunits that are flattened along the protofilament axis. The most notable exception to this rule is the existence of amyloids formed by stacked β-solenoid subunits (Fig. 1.5). In these structures, each subunit folds along the protofilament axis to form a multi-layered solenoid; the prototypical example of this is the C-terminal domain (CTD) of the HET-s prion from the fungus *Podospora anserina*, in which the polypeptide chain folds upon itself in a left-handed β-helical manner to form a two-layered structure with three parallel β-sheets, each consisting of a pair of stacked β-strands. Inter-subunit stacking then assembles these sheets into a cross-β protofilament with a β-solenoid structure, in which each subunit contributes two aligned β-strands to each of the structure's three parallel intermolecular β-sheets [117–119]. The HET-s CTD structure is remarkable for the elegant manner in which it overcomes the opposing effects of favourable in-register interactions and electrostatic repulsion to form a stable protofilament structure. As would be expected, the two layers of the β-helix have a high degree of sequence complementarity to achieve this. Although π-stacking interactions are not present in the cross-β core, there are two amide ladders formed by the residue pairs N226-N262 and N243-N279, which run along the protofilament in an alternating fashion. However, by adopting a two-layered pseudo-in-register alignment, the HET-s CTD is also able to avoid unfavourable alignment of like charges between adjacent β-strands; instead, there is a system of complementary alternating charges created by the residue pairs K229-E265, E234-K270, and R236-E272 [117, 118]. Besides the obvious enthalpic advantages of this structure, it is worth noting that folding of the β-solenoidal subunit is based on more local interactions than in most amyloids, where interactions between separate subunits are likely to be required for the final tertiary structure to appear. This may encourage rapid folding and emergence of a mature subunit structure prior to assembly, potentially explaining the apparent lack of evidence for non-fibrillar intermediates formed by HET-s. Given their functional role and the need to avoid toxicity caused by prefibrillar intermediates, there is a clear incentive for yeast prions to form via a predominantly two-state process, and the concentrations of intermediates formed by the Ure2p prion have previously been shown to be low compared to other amyloids [156]. By adopting a β-solenoid subunit structure, HET-s may thus be able to avoid toxic prefibrillar

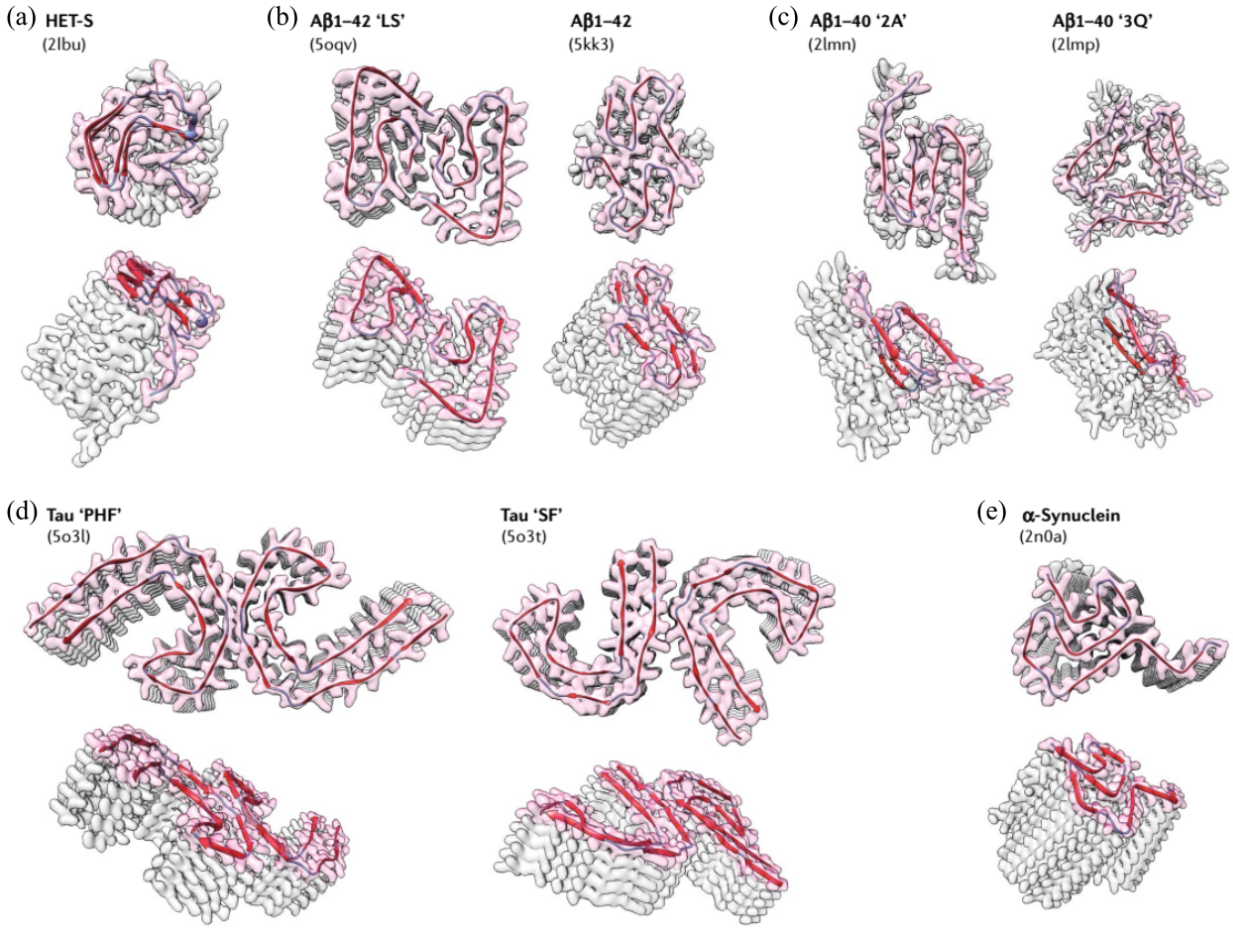

Figure 1.7: Structures of amyloid fibril subunits. Panels show space-filling representations of amyloid fibrils formed by (a) HET-s [117], (b) Aβ(1-42) [144, 159], (c) Aβ(1-40) [111], (d) Tau [128], and (e) α-syn [135]. All models are filtered to 4 Å, and subunits at the top of each protofilament stack are coloured red for contrast, with a cartoon representation of the polypeptide chain superimposed to show the fold. The names of specific polymorphs are shown in quotation marks. Figure from Iadanza *et al.* [77].

intermediates altogether. Besides HET-s, β-solenoids have now been induced in engineered amyloids based on modifications of existing β-solenoid proteins [157, 158], and there are data to suggest that at least one polymorph of the mammalian prion protein may have a four-layered β-solenoid structure [120].

1.3.4 Tertiary structure of protofilament subunits

In the majority of high-resolution cryo-EM structures [115, 129–132, 137–139, 142, 144–150, 160, 161], and many ssNMR structures [117, 135, 136, 143, 162], the subunits are single-layered or rarely multi-layered monomers that fold orthogonally to the protofilament axis to produce convoluted but flattened tertiary structures. While early models of amyloids had relatively simple tertiary structures organised from a small number of secondary structural elements, such as the β-hairpin-like models proposed for Aβ(1-40) [163] and Aβ(1-42) [164], more recent models based on high-resolution cryo-EM density maps and/or large

numbers of ssNMR restraints typically depict monomers containing a large number of separate turns and β-strands, with a complex tertiary organisation (Fig. 1.7). In some cases, the more complex structures have been likened to Greek key motifs [135], although a key distinguishing feature is that the backbone hydrogen-bonding groups in these subunits are oriented orthogonal to the plane of the motif, in order to form inter-subunit β-sheets, rather than parallel to the plane as would be expected in a canonical Greek key. Reports of differing levels of tertiary structural complexity for the same polypeptide are not mutually incompatible, since amyloids are often highly polymorphic; thus, in some cases the formation environment and the natural tendency of amyloids to nucleate a variety of different polymorphs may result in fibrils with a more or less complex tertiary structure. In addition, studies of amyloids such as Aβ [144, 160] and α-syn [135, 137, 138, 145–147, 150] have revealed a high degree of polymorphism resulting from protofilaments having distinct but comparably complex tertiary structures.

Collapse of subunits orthogonal to the protofilament axis is both entropically and enthalpically favoured. An alternation between non-β-strand regions and β-strands is statistically probable for all but the shortest amyloidogenic peptides ($\lessapprox$ 10 residues), and the degeneracy of this form of folding is likely to contribute to the stability of the amyloid state as an ensemble. While the hydrophobic effect and vdW forces play only a minor role in interactions along the protofilament axis, they appear to be the dominant driver for collapse of the subunit orthogonal to this axis. The majority of single-layer subunit structures have a desolvated core containing clusters of hydrophobic residues, while the hydrophilics are typically, but not exclusively, exposed to the solvent [77]. Similarly, in the multi-layered β-solenoid of HET-s, the β-helix of the CTD has a hydrophobic cluster of residues at the centre, with the hydroxyl, amide, and charged sidechains on the outside [117–119]. This orientation effect is usually particularly pronounced for the charged sidechains, as well as the N- and C-termini in relevant cases, as charged groups experience a highly unfavourable free energy change upon transfer from the solvent to the less dielectric interior of the cross-β structure. One of the most common exceptions to this tendency can be attributed to the formation of salt bridges by pairs of charged residues within the cross-β core, since the desolvated environment results in a very negative free energy for this interaction; often, these salt bridges stabilise key turns in the subunit structure, such as the H6-E11 and E11-H13 salt bridges in the LS polymorph of Aβ(1-42) [144]. The structure of this polymorph, which also demonstrates the importance of clusers of hydrophobic residues in stabilising the fold of subunits, is shown in Fig. 1.8. Another interesting exception is a zipper-like interface formed by glutamines from adjacent β-sheets in the memory-associated amyloid Orb2, from *Drosophila* [161]. In this 'Q-zipper' motif, glutamine repeats on either side of a dry intramolecular interface form an interdigitated system of amide ladders. In addition to the backbone and sidechain hydrogen bonds running along the protofilament axis, the -NH_2 groups of the ladder each donate an additional hydrogen bond to the backbone carbonyls on the opposite side of the interface, forming an extended tetragonal network of hydrogen bonds that holds the two

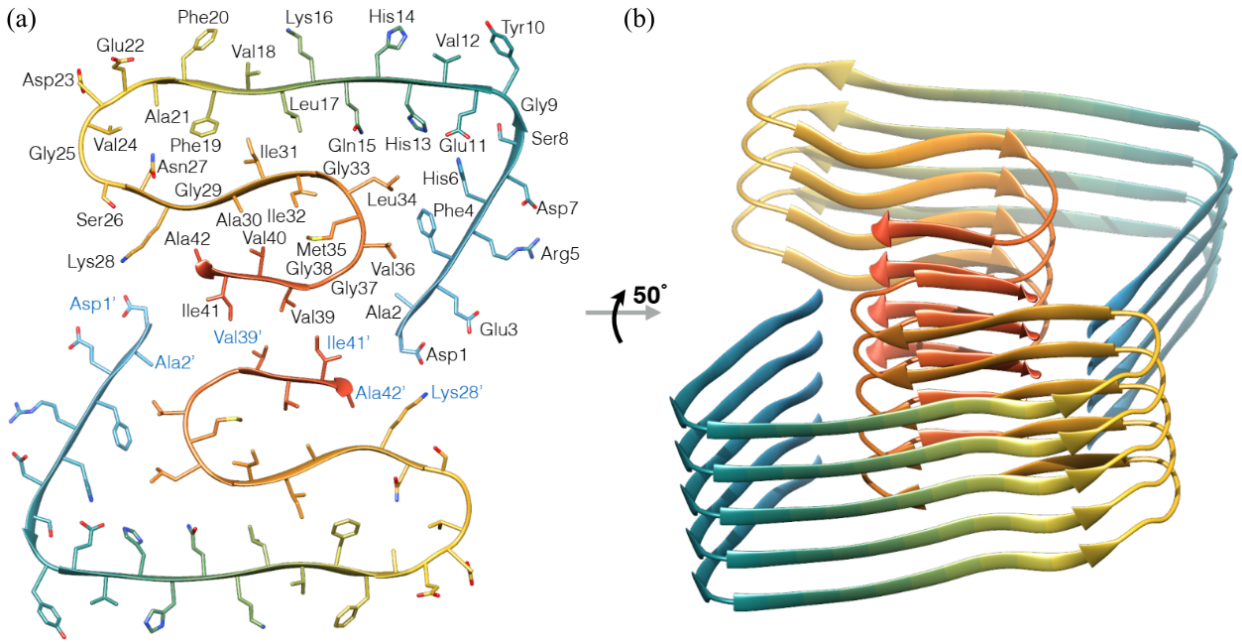

Figure 1.8: Structure of the LS polymorph of Aβ(1-42), showing typical interactions that stabilise the fold of protofilament subunits. The fibril consists of a pair of protofilaments, each of which is a stack of monomers, as shown in this figure. Note the H6-E11-H13 salt bridge, and the formation of clusters of hydrophobic residues on the interior of each protofilament, and at the interface. Figure from Gremer *et al.* [144].

β-sheets together. The authors of the study speculated that similar structures might be observed in amyloids formed by other glutamine-rich proteins, such as Huntingtin (Htt). More generally, it is also worth noting that the formation of a desolvated core strengthens backbone hydrogen-bonding between subunits in a wide variety of amyloids [97], suggesting that desolvation may be coupled to either emergence or consolidation of the cross-β structure.

While subunits are most often single-layered structures, giving them a quasi-planar character, complete (or more accurately near-complete) planarity is actually quite rare; one of the best examples to date is the recent cryo-EM structure of a protease-resistant human prion fragment, PrP^{Sc}(94-178), in which the coordinates of the C_α atoms that are most distant along the protofilament axis differ by only ∼3.6 Å along that axis [141]. Instead, the vast majority of structures have flexed, non-planar subunits, so that β-strands from the same subunit occur in different planes of the stack, and the orientation of the β-strands is only approximately orthogonal to the protofilament axis [128, 129, 131, 137–139, 142, 144–146, 161]. This means that the non-planar subunit conformation contributes to the polar structure of the amyloid protofilament, and ensures that the two ends of the protofilament present distinct interfaces for binding of new subunits. In turn, this explains why association and dissociation of new monomers is often much faster at one end of an amyloid than at the other [165, 166]. Examples of non-planar subunits are shown in Fig. 1.9.

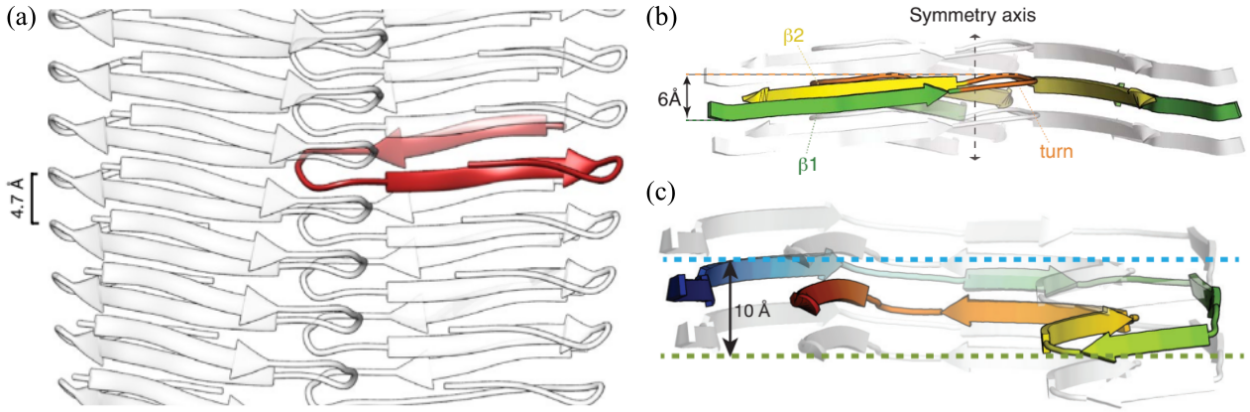

Figure 1.9: The subunits of amyloid fibrils often occupy a single layer of the protofilament stack, but are not truly planar. Panels show side-on views of amyloid fibrils formed by (a) islet amyloid polypeptide (IAPP) [142], (b) Orb2 [161], and (c) phosphatidyl-inositol-3-kinase Src-homology 3 domain (PI3K-SH3) [139], with a single subunit highlighted in each case. All images adapted from their respective sources.

Another important feature of the tertiary structure of subunits, which has been clear since the first ss-NMR and EPR studies [118, 134, 164, 167–171], is that only part of the polypeptide sequence typically contributes to the highly ordered cross-β core. The rest may exist in a disordered state [128–130, 137–140, 142, 144–150, 167, 172–175], or even as a relatively well-ordered surface domain often separated by a flexible linker region [118, 134, 171]. The decoration of the fibril surface with these non-amyloid domains probably strongly affects surface-mediated processes such as inter-protofilament interactions, protofilament-oligomer interactions, and secondary nucleation. In addition, it is possible that interactions between aligned surface domains may contribute to protofilament stability. At present, it is difficult to address these questions as the dynamic nature of the surface domains means that prevailing biophysical techniques often struggle to resolve their structure; for example, while additional density corresponding to these domains is often visible in cryo-EM density maps, resolution is typically far too poor to model a polypeptide backbone [128–130, 137–140, 142, 144–150]. In addition, areas of extra density are sometimes also interpreted as representing heterogeneous fibril constituents that stabilise the protofilament structure, or inter-protofilament interactions; in some cases these species may be metal ions and polyanions that help to balance aligned charges on the protofilament surface [115, 128].

1.3.5 Supra-protofilament assembly

While some amyloid fibrils consist of a single protofilament [114, 119, 131, 132, 135, 147–149] (eg. Fig. 1.10(a)), many contain several protofilaments that closely associate with one another to form the complete structure [111, 112, 120, 128, 130, 135–142, 144–147, 150, 160–162, 164, 172, 173, 175–181]. The most common variation appears to be a pair of protofilaments (eg. Fig. 1.10(b)), but larger numbers are possi-

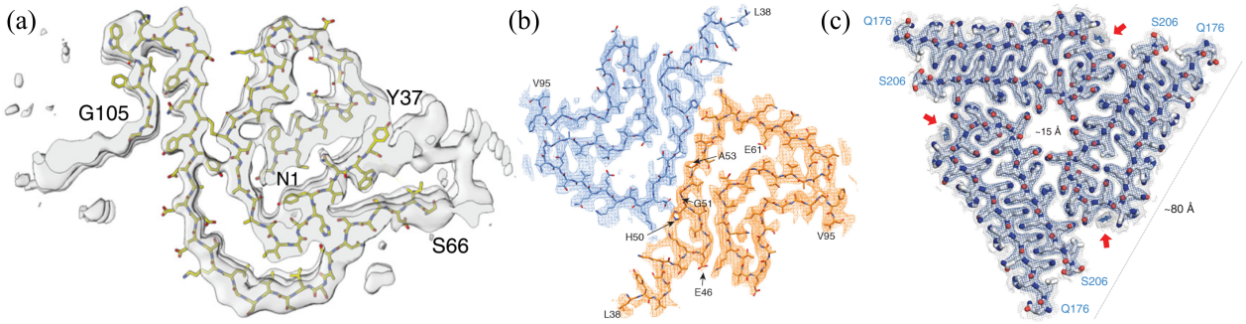

Figure 1.10: Protofilament organisation (part 1). Panels (a-c) show cryo-EM density maps and modelled polypeptide backbones of amyloid fibrils formed by (a) immunoglobulin light chain [149], (b) α-syn [137], and (c) Orb2 [161], which consist of a single protofilament or rotationally symmetric associations of two or three protofilaments, respectively. All images adapted from their respective sources.

ble [111, 150, 161, 172, 173, 176, 182–185] (eg. Fig. 1.10(c)), and in these more complex cases the protofilaments are sometimes further organised into subgroups that occupy an intermediate layer of the structural hierarchy between protofilaments and fibrils [172, 173, 176, 182, 184, 185]. For fibrils without intermediate levels of structural organisation, the constituent protofilaments typically share the same structure and associate with one another in a rotationally symmetric manner about the fibril axis (Fig. 1.10(b-c)), although cases of heterogeneous protofilament structures and rotationally asymmetric orientations have been observed [115,128,182]. In rotationally symmetric fibrils, the associated protofilaments usually twist around one another, giving the fibril an overall twisted ribbon morphology. In other cases, including many fibrils with intermediate layers of hierarchical structural organisation, protofilaments or groups of protofilaments may associate in a row, forming a tape-like structure [164, 178–181, 183–185] (eg. Fig. 1.11); in turn, these often twist to form helices [178, 181], and the grooves of these helices may close up to form a tubular structure with a solvated core [186]. Lastly, side-by-side association of a large number of protofilaments may result in a flattened, sheet-like structure similar to a 2D crystal [179, 180]. Supra-protofilament organisation is a source of considerable polymorphism, with different fibril polymorphs differing not only in the number of protofilaments, but also their arrangement and mode of interaction. For example, there are at least four α-syn polymorphs that have a similar protofilament structure but a completely different set of packing interactions [146, 147], and a similar phenomenon has been reported for Aβ(1-40) [111, 187] and Tau [128].

Protofilaments are polar structures, with the backbone hydrogen-bonding groups oriented in a particular direction along the the protofilament axis, and each end of the protofilament presenting a distinct interface for addition of new subunits. As a result, a pair of associated protofilaments can be oriented either parallel or antiparallel to one another. The parallel orientation is much more common; while antiparallel and mixed pairings have been predicted in coarse-grained simulations [188], they are rather uncommon in experimental structures [77]. The bias towards parallel orientation may be partly driven by the self-assembly mechanism;

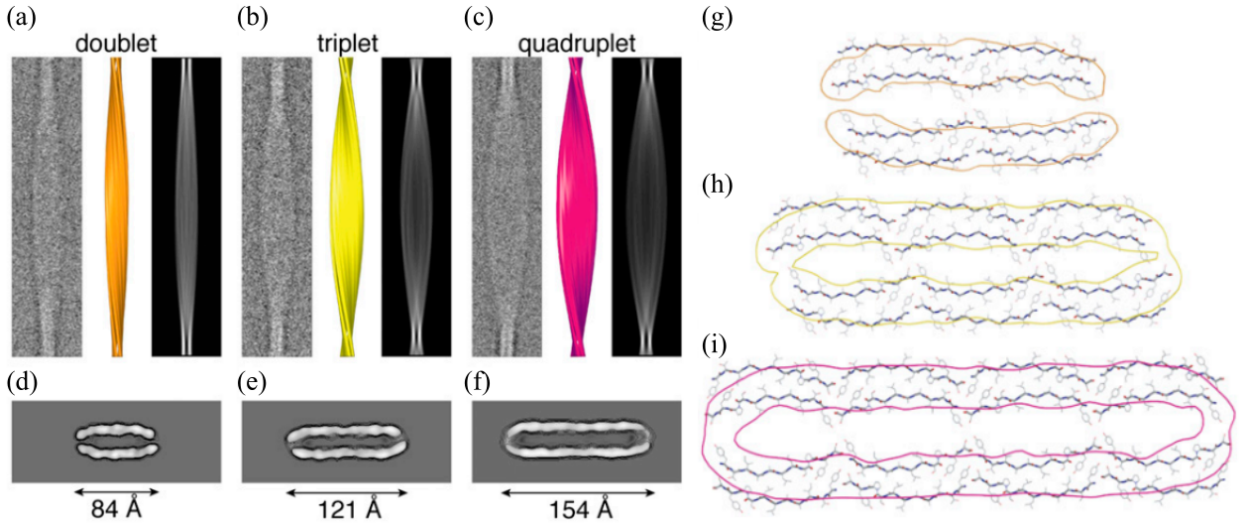

Figure 1.11: Protofilament organisation (part 2). This figure shows the tape-like TTR(105-115) fibrils characterised by Fitzpatrick *et al.* [183]. (a-c) Side views of the cryo-EM 3D class averages of these fibrils, showing width polymorphism. (d-f) Cross-sections of the EM density of the same fibrils, facing down the filament axis. (g-i) Structural models interpreting the fibrils as consisting of 2, 3, or 4 groups of protofilaments aligned in a row, respectively, based on a combination of cryo-EM and MAS-NMR data. The backbones are superimposed on the EM density isosurfaces, with the cut-off at 1σ above the mean density. Panels (a, d, g) show 'doublet' fibrils, panels (b, e, h) show 'triplet' fibrils, and panels (c, f, i) show 'quadruplet' fibrils. Figure adapted from Fitzpatrick *et al.* [183].

as previously mentioned, the polar nature of protofilaments often results in unequal elongation rates at their two ends, with a bias towards elongation in a particular direction [165, 166]. If two nascent protofilaments laterally associate in a parallel orientation, they will exhibit biased elongation in the same direction, allowing cooperative extension of the structure as a whole. On the other hand, if two protofilaments associate in an antiparallel orientation, they will exhibit biased elongation in opposite directions. This will cause one protofilament to tend to elongate faster than the other at each end, reducing the cooperativity of elongation and limiting growth of the interface between the protofilaments. In protofilaments with a low growth polarity, the pressure for parallel orientation is not likely to exist; furthermore, successful association of a pair of protofilaments in this manner will result in an apolar fibril structure, with both ends of the fibril presenting the same pair of interfaces for elongation.

The structure of a fibril is typically maintained by a well-defined set of interactions between its constituent protofilaments. Early structures of amyloid fibrils assumed an in-plane alignment between the subunit stacks of different protofilaments [111, 136, 162]. However, with the advent of high-resolution cryo-EM density maps that give more precise information about the relative orientation of the protofilaments, it has become clear that many fibrils that consist of a pair of protofilaments have an overall 2_1 screw symmetry [128, 130, 137–139, 141, 144–146, 150, 160]. In this arrangement, which is very common, one of the

subunit stacks is ∼2.4 Å further along the fibril axis than the other, half of the ∼4.8 Å separation between β-strands in a single stack. Thus, the complete fibril can be analysed as a 2_1 screw, in which each monomer is separated from the 'last' by a translation of ∼2.4 Å along the fibril axis and a rotation of ∼180° about that axis. Although in-plane alignments also occur for rotationally symmetric 2-fold fibrils [129], 2_1 screws appear to be the most common organisation for this sort of fibril [128,130,137–139,141,144–146,150,160], which is probably due to the enthalpic advantages of improved packing at the inter-protofilament interface. In addition, 2_1 screws may answer the question of how fibrils consisting of a pair of protofilaments can exhibit elongation kinetics that are first-order with respect to the free monomer [144]. For an in-plane 2-fold fibril whose protofilaments both end at the same point, addition of a single monomer to one of those protofilaments will create an overhanging fibril end. However, for a 2_1 screw in which one of the protofilaments ends half a β-sheet spacing further along than the other, addition of a monomer to the non-overhanging protofilament will simply cause a rotation of the binding interface at the fibril end by ∼180°, preserving its symmetry. Since the non-overhanging protofilament has the better interface for monomer addition, monomer addition would usually alternate between protofilaments, causing the entire fibril to grow as a single co-ordinated unit at a rate proportional to the free monomer concentration [144]. Examples of 2_1 screw symmetry can be seen in Fig. 1.12 and Fig. 1.13.

For both in-plane and screw-symmetric fibrils, the high degree of alignment between protofilaments allows a specific set of molecular interactions to occur at their interface. These interactions are typically more similar to those responsible for subunit folding than subunit stacking, although there are some interesting exceptions. Many protofilament interfaces are desolvated; unsurprisingly, the hydrophobic effect and vdW interactions play an important role in this context. A notable feature of many dry interfaces is a 'steric zipper', which was first observed in amyloid-like microcrystals of the GNNQQNY peptide by Nelson *et al.* [97]. In this motif, hydrophobic sidechains pointing into the cleft between protofilaments interdigitate with complementary sidechains from the opposing protofilament, forming a tight, zipper-like interface that optimises vdW interactions. Since their discovery, steric zippers have been observed in many amyloid structures [126,129,130,132,136,137,141,144–146,150,175,184,189], and a similar degree of complementarity is sometimes observed in the hydrophobic core of individual protofilaments. Examples of steric zippers are shown in Fig. 1.8(a), Fig. 1.12(a), and Fig. 1.12(c-e).

Polar zipper-like structures have also been observed. The interfaces of many fibril structures, dry or wet, are stabilised by salt bridges between ladders of charged sidechains [130, 137, 138, 144–146, 150, 160, 162, 184, 185], similar to the ionic 'polar zipper' originally described by Perutz and colleagues [190]. In fibrils with a 2_1 screw symmetry, the alignment of the subunits of one protofilament with the stacking interface between the subunits of the other encourages charged residues in these ionic ladders to form bidentate salt bridges with oppositely charged residues above and below them on the opposing protofilament, creating a

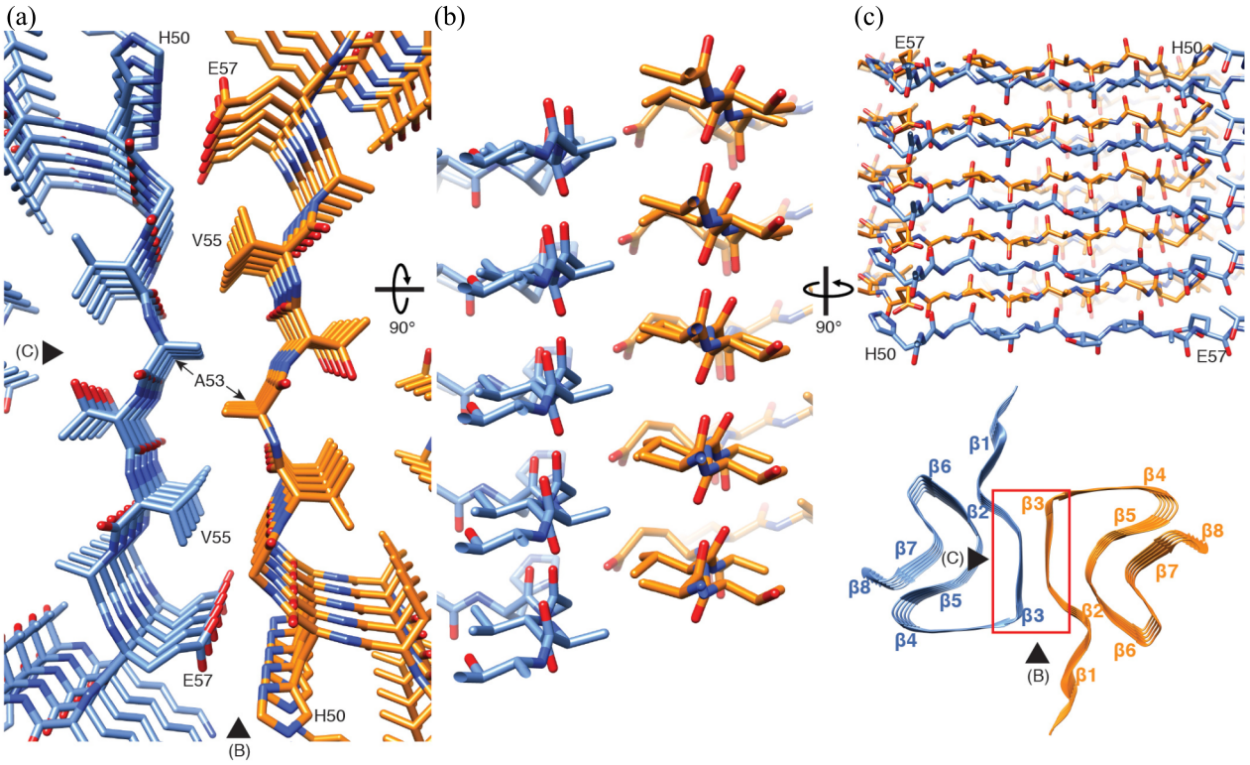

Figure 1.12: Protofilament packing interactions in α-syn fibrils. The structure of the same fibril polymorph is shown in Fig. 1.7(e) and Fig. 1.10(b), as well as the bottom right of this figure. (a) A close-up view of the interface between protofilaments, facing down the fibril axis. (b) A side-on view of the same interface, showing 2_1 screw packing and interdigitation of the subunits of the two protofilament stacks. (c) A face-on view of the interface. The views in panels (a-c) correspond to the red box and black arrows in the ribbon diagram at the bottom right of this figure. Figure from Guerreiro-Ferreira *et al.* [137].

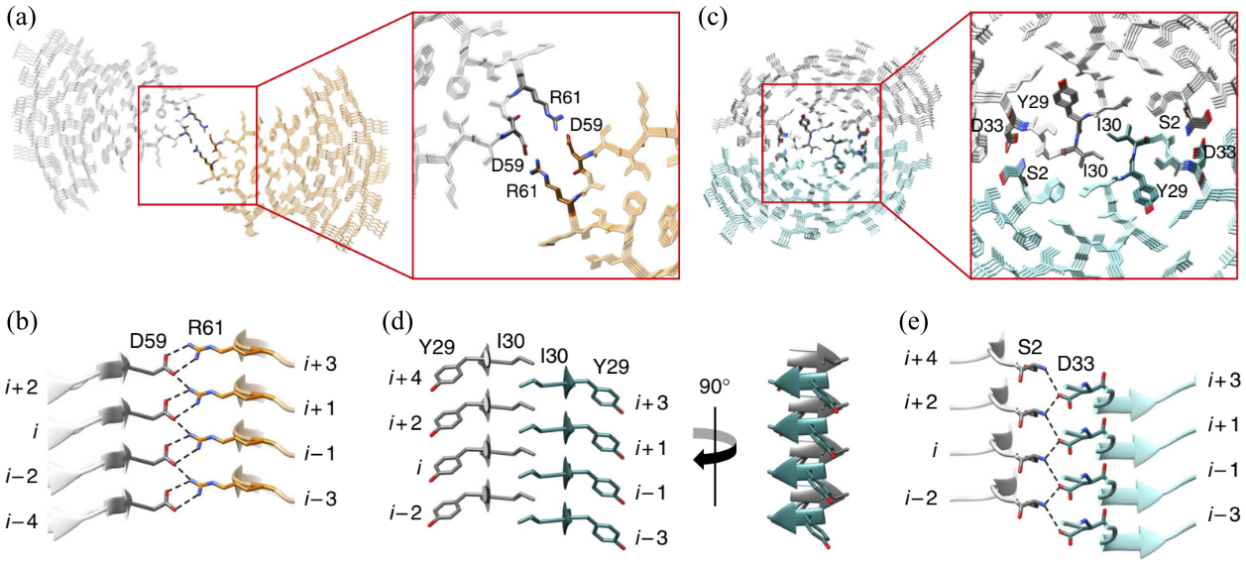

Figure 1.13: Protofilament packing interactions in amyloid A (AA) fibrils. Panels (a-b) show cross-sectional views of the cryo-EM structures of (a) left-handed murine and (b) right-handed human fibrils, highlighting the packing interactions at the interface between protofilaments. (c) A side-on view of the ionic polar zipper at the interface of the murine fibrils. (d) Side-on views of the steric zipper at the interface of human fibrils. (e) A side-on view of a polar zipper at the interface of human fibrils. Figure from Liberta *et al.* [130].

dipolar chain-type arrangement [130]. In addition, in a sub-Ångström micro-ED structure of a mammalian prion fragment, Gallagher-Jones *et al.* [191] observed a 'polar clasp' formed by juxtaposition of a pair of amide ladders at a desolvated interface. In this motif, asparagine sidechains from opposite sides of the cleft formed an extended tetragonal network of hydrogen bonds, with each carbonyl accepting a pair of hydrogen bonds and each -NH_2 donating a pair. This motif was hypothesised to be relevant to the structure of the complete prion fibril [191], and a similar motif involving inter-protofilament backbone hydrogen bonding by glycines has been observed in the paired helical filaments (PHFs) of Tau [128]. Two examples of polar zippers in amyloid A (AA) fibrils are shown in Fig. 1.13.

An unusual and yet informative hydrophobic interface was observed by Iadanza *et al.* [129], who obtained a cryo-EM structure of fibrils formed by β_2-microglobulin (β_2m), an amyloid involved in dialysis-related amyloidosis (DRA). This structure contained a pair of protofilaments whose main interface consisted of a stack of six tyrosine residues for every pair of laterally opposed subunits, three from each protofilament, oriented orthogonal to the protofilament axis. Thus, the interface was stabilised by π-π interactions, and perhaps also π-amide interactions involving the polypeptide backbone. This is a comparatively weak interface, and illustrates the principle that inter-protofilament interfaces do not need to be particularly strong to hold protofilaments together, as they occur in large numbers along the length of the fibril, and are also stabilised by steric constraints resulting from helical twisting of the protofilaments around one another [129]. While

many 2-fold fibrils have a 2_1 screw organisation, the β_2m structure had protofilament subunits aligned in the same plane. This may have been due to the lack of a requirement for interdigitation of the sidechains of laterally interacting subunits, which normally serves to optimise vdW contacts; instead, alignment of subunits in the same plane would have optimised the π-π interaction that held the protofilaments together.

An interesting feature of some amyloid fibrils is the presence of extensive, hydrated channels running along their interior. Although water-filled cavities do sometimes occur within individual protofilaments, such as the case of α-syn [137,138,145–147], these are typically narrow and the water molecules within tend to be relatively ordered. Between protofilaments, however, much larger channels can form. For example, the 3Q polymorph of Aβ(1-40) [111], which is a rotationally symmetric fibril with three protofilaments, has a dry interface between the protofilaments around the outside of the fibril, but a hollow core at the centre [192,193]. A central channel has also been observed in SH3 amyloid fibrils formed by a double helix of protofilament pairs [176], as well as a double-helical Aβ(1-42) structure [177]. Although such channels may be able to transport water and metal ions, their potential role in pathology remains unclear.

1.3.6 Mesoscale structural and mechanical properties

The structure of amyloid fibrils is maintained by highly specific molecular interactions at all levels of their organisational hierarchy, from subunit collapse to protofilament packing. As a result, amyloid fibrils are very regular, and the conformation and orientation of their constituent monomers remain strongly correlated over large length scales (typically several μm). This allows amyloids to exhibit mesoscale (here $\gtrapprox 100$ nm) structural and mechanical properties unlike those of most other protein aggregates, in which the orientation and often also conformation of assembled monomers tend to decorrelate over a matter of nanometres, resulting in an amorphous structure. Three major consequences of the molecular order of amyloids are their mesoscale chirality, rigidity, and considerable tensile strength. Viewed by EM or AFM, amyloids are often visibly chiral, with a helical or twisted ribbon topology, and a strong correlation in their pitch or twist rate along their length [194]. While some amyloids are flexible, meaning that the persistence length l_p over which the direction of the fibril axis decorrelates is significantly less than their typical length ($l_p \ll l$), many are relatively rigid ($l_p \gg l$) [195]; in addition, many amyloids have high tensile strength [109]. The rigidity and tensile strength of amyloids are testament to the stable, extensive network of interactions that maintains their structure, and the low frequency of structural defects. The nanoscale structure of amyloids is inextricably related to their mesoscale properties, meaning that small changes in the former can dramatically affect the latter [41]. This section aims to outline the factors that contribute to these properties, and to discuss the mechanical properties of amyloids in the context of other materials and biomacromolecules.

Amyloids have a tendency towards left-handed helical or twisted ribbbon topologies, although right-handed and achiral topologies are also observed [41]. The molecular-level chirality of the constituent

polypeptide chains is only able to propagate to the mesoscale level because of the stable, uniform, and highly repetitive interactions between stacked subunits, and at the interface between protofilaments. Within a single protofilament, the interactions responsible for chirality can be separated into backbone-backbone, backbone-sidechain, and sidechain-sidechain interactions. Generally speaking, backbone-backbone interactions tend to limit twisting of the protofilaments, while those involving sidechains tend to encourage it [196]. Nonetheless, in parallel cross-β structures, which appear to be the dominant type, there is a close, two-way relationship between the chirality of the protofilament and that of its constituent β-strands, meaning that the chiral preferences of the amino acids can affect the protofilament topology, and *vice versa*. The overall twist of a β-strand can be determined from the average torsion angles of its constituent amino acids, $\langle\phi\rangle$ and $\langle\psi\rangle$, where $\langle\phi\rangle + \langle\psi\rangle > 0$ implies a right-handed twist, and $\langle\phi\rangle + \langle\psi\rangle < 0$ implies a left-handed twist [197]. A β-sheet formed from β-strands with a right-handed twist will tend to twist in a left-handed manner between strands, as the effect of a small right-handed rotation of the backbone hydrogen bonding groups along the length of each β-strand can be partly compensated for by a small left-handed rotation of each β-strand about the axis of the β-sheet. Since the protofilament axis is approximately parallel to the axis of its constituent β-sheets, this will in turn result in a protofilament with a left-handed twist. Conversely, a protofilament consisting of β-strands with a left-handed twist will tend to twist in a right-handed manner, as confirmed by existing amyloid structures [130, 160]. Non-amyloid proteins strongly prefer right-handed β-strands [198], which is caused by unfavourable interactions between the backbone carbonyl and the sidechain in the left-handed orientation [197], and probably explains the tendency of amyloids to form left-handed protofilaments. Nonetheless, right-handed protofilaments are by no means rare, and the same polypeptides can often form left- or right-handed protofilaments depending on their formation conditions [144, 160]. Thus, while the twisting of protofilaments is coupled to that of their constituent β-strands, neither is solely determined by the primary sequence, and extrinsic factors can affect both.

Experiments and simulations have demonstrated that the sidechains play an important role in inducing torsion of amyloid protofilaments [181, 196, 199–201]. While interactions that stabilise parallel in-register cross-β structures would be expected to favour straighter protofilaments, those that oppose this alignment would be expected to favour more twisted protofilaments. Accordingly, electrostatics appear to be one of the key drivers for protofilament twisting [181, 199–201], meaning that factors such as pH and ionic strength can alter fibril morphology; for example, fibrils of β-lactoglobulin and β-endorphin have a twisted appearance when grown at low ionic strength, and a flat, ribbon-like appearance at high ionic strength [181, 200, 201]. Interactions between protofilaments are also important, as their free energy depends on the alignment of steric zippers, charged residues, and other functional groups; therefore, higher-order assembly of protofilaments is usually associated with a change in pitch or the rate of twist [142, 146, 147, 173, 187, 199], and occasionally even handedness [202]. In addition, the balance of forces that induce and oppose torsion is

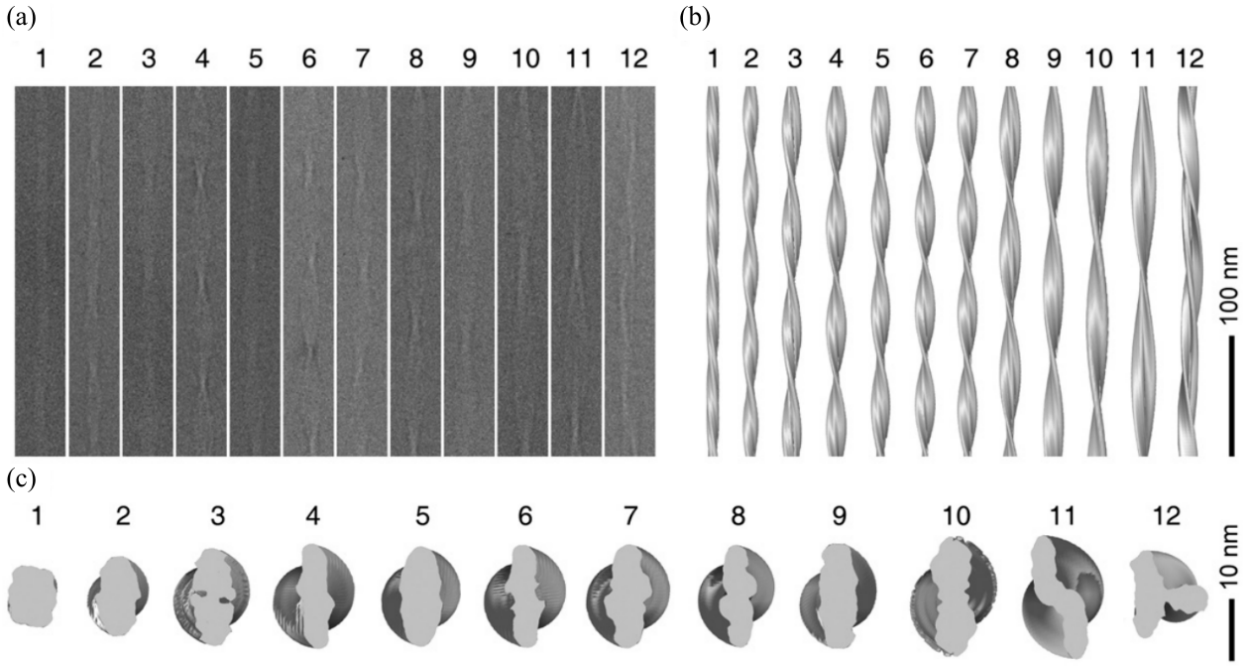

Figure 1.14: Cross-sectional polymorphism and pitch polymorphism of Aβ(1-40) fibrils. (a) Cryo-EM images of 12 fibril polymorphs identified by Meinhardt *et al.* [187]. (b) Side views of the density reconstructions of the same fibrils. (c) Cross-sections of the EM density of those fibrils. The numbering of fibrils corresponds across panels and refers to different polymorphs from the same sample. Note that fibrils with a wider or less compact cross-section have a lower twist rate and longer pitch; the authors established that this variation correlated well with differences in the polar moment of area I_z. Figure from Meinhardt *et al.* [187].

also affected by the number and relative orientation of the protofilaments [187]. While a fibril with a single protofilament or a more compact association of protofilaments can maintain a high rate of twist, a fibril with a greater number of protofilaments, or protofilaments that are distributed further from the central axis, will have disproportionately greater resistance to torque, and thus a lower twist rate and longer pitch. It has been demonstrated that the pitch of fibril polymorphs formed from the same primary sequence is positively correlated with the polar moment of area I_z, which describes the extent to which the volume of fibrils is distributed away from their central axis [187]. A variety of Aβ(1-40) polymorphs from the same sample are shown in Fig. 1.14, demonstrating the principle that wider fibrils formed from the same primary sequence tend to have a lower rate of twist [187]. For particularly wide fibrils, the shear stress on the outer β-strands makes a twisted ribbon topology unsustainable; in these instances, protofilaments are more likely to arrange into helically coiled, tape-like structures, as the shear stress in these structures is not closely related to the number of protofilaments [186].

In a similar manner, the same structural properties affect the bending stiffness of fibrils. When a fibril is bent in a particular direction, its bending stiffness is proportional to the planar moment of area in that axis, I, which also strongly depends on the width of the fibril [203]. Thus, thinner fibrils will bend more easily in

response to thermal fluctuations, and will have a more coil-like appearance when viewed by EM or AFM, whereas thicker fibrils will tend to have a more rod-like appearance. The persistence length of a fibril is determined from its bending stiffness and the scale of thermal fluctuations [204],

$$l_p = \frac{EI}{k_B T}, \tag{1.1}$$

where E is the Young's modulus of the fibril, I is the planar moment of area in the relevant axis, k_B is Boltzmann's constant, and T is the temperature. For bending of a fibril with a highly non-circular cross-section, I will mostly reflect the lowest-energy bending mode. In general, the dependence of I on the width of fibrils is approximately $I \sim w^4$, meaning that even small variations in width can strongly affect l_p; coupled with significant variation in total length, from tens of nm to tens of μm, this means that the morphology of amyloid fibrils can vary from flexible ($l_p \ll l$) to rod-like ($l_p \gg l$) [195] (Fig. 1.15). These differences are mainly attributable to variations in the size, number, and packing of protofilaments, and comparisons of the second planar moment of area and bending stiffness of a wide variety of fibrils have revealed that the majority have a Young's modulus in the 2-14 GPa range. This is a relatively narrow range, implying underlying structural commonalities, and is comparable to that of silk or collagen [109, 195]. In addition to bending rigidity, the tensile strength of fibrils has also been measured. The tensile strength is strongly dependent on the stability of inter-subunit interactions along each protofilament, and requires a relatively uniform structure with a low defect rate. Amyloids have tensile strength in the 0.1-1 GPa range, in the same region as steel, which is a testament to the uniformity of the fibril structure, and the strong network of interactions that maintains it [109]. The Young's modulus and tensile strength of amyloid fibrils are compared to a variety of other materials in Fig. 1.16. Overall, the mechanical properties of amyloids make them highly attractive for materials science applications, as they provide a means to rapidly assemble strong, flexible, highly regular polymers [109].

1.3.7 Structure of Aβ fibrils

Aβ is one of the most extensively studied amyloidogenic polypeptides, and many structural models of its fibrils have been proposed. As with other amyloids, ssNMR has historically been the dominant structural technique [96], although the recent cryo-EM 'resolution revolution' [105] has now allowed high-resolution density maps of Aβ fibrils to be obtained [144, 160]. The wealth of structural models has revealed an impressive level of polymorphism involving diverse tertiary structures and forms of protofilament packing. This polymorphism results from a high degree of sensitivity of Aβ fibril structures to their self-assembly conditions [187, 205–208], and the natural tendency of Aβ to self-assemble polymorphically *in vitro* [187, 209] and *in vivo* [160, 208]. Nonetheless, there are features that are common to all or al-

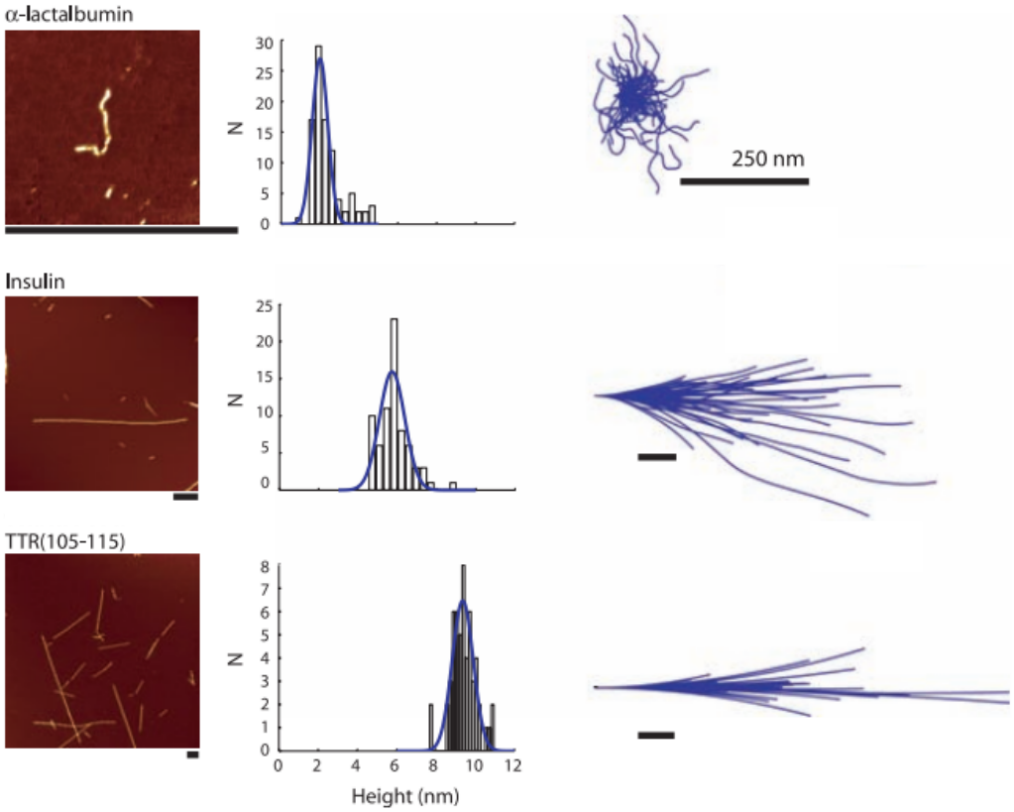

Figure 1.15: Effect of thickness on the bending stiffness of amyloid fibrils. Representative AFM images (left) of fibrils formed by α-lactalbumin, insulin, and TTR(105-115) are aligned against their AFM height histograms (centre) and traces of the AFM images, whose initial tangents were aligned to allow comparison (right). Thinner fibrils are more flexible, whereas thicker fibrils are rigid and rod-like. The scale bar is 250 nm. Figure adapted from Knowles *et al.* [195].

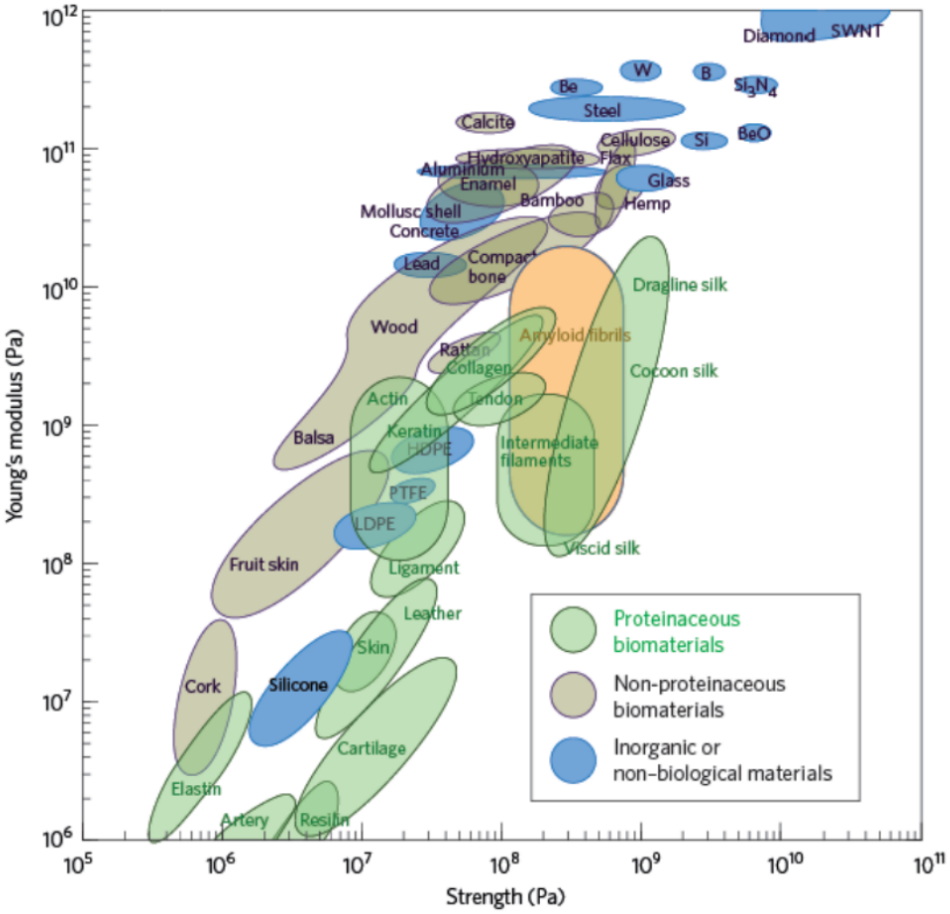

Figure 1.16: Tensile strength and Young's modulus of amyloid fibrils, compared to a variety of other materials. Figure from Sweers *et al.* [109].

most all Aβ fibrils, and in many respects Aβ can be considered quite a typical amyloid, with most of the common features discussed in preceding subsections often observed among Aβ polymorphs. While some studies have favoured an antiparallel cross-β structure [210–213], ssNMR and cryo-EM studies in the last 20 years have mostly supported a parallel in-register alignment resulting from stacking of single-layered subunits [111, 112, 136, 143, 144, 153, 160, 162–164, 172, 173, 214, 215], with the central and C-terminal regions of the peptide typically involved in the core, and the N-terminal region exhibiting a varying degree of order. The tertiary structure of Aβ fibrils, examples of which are shown in Fig. 1.7(b-c), Fig. 1.8, and Fig. 1.17, in addition to the low-resolution density maps in Fig. 1.14, is highly variable and one of the main sources of polymorphism, but there are several broad classes. One class that was revealed by early ssNMR studies has a subunit consisting of a planar, hairpin-like monomer, with a dynamic N-terminus and a turn stabilised by the D23-K28 salt bridge [111, 163, 164]; examples of this class include the 3Q and 2A polymorphs of Aβ(1-40) [111, 207] (Fig. 1.7(c)), and a similar polymorph formed by Aβ(1-42) [164]. A second class has a more kinked, S-shaped or LS-shaped cross-β core, with the N-terminus either dynamic or also part of the core (Fig. 1.7(b), Fig. 1.8); examples of this class are mainly restricted to fibrils formed by Aβ(1-42) [136, 143, 144]. A third class, which has been observed for fibrils formed by both Aβ(1-40) and Aβ(1-42), appears to consist of a J-shaped monomer with straight central and C-terminal regions, and a bent or dynamic N-terminus [172, 173]. In addition, there are a variety of other polymorphs that do not fit into these classes, including a recent high-resolution *ex vivo* structure [160] (Fig. 1.17). Despite this diversity, the interactions that maintain these structures are broadly similar to those seen in other amyloid fibrils; in addition to hydrogen bonding and hydrophobic interactions, amide ladders and steric zippers have both been identified in Aβ fibril structures [136, 144, 175], and the parallel in-register structures also have aligned aromatics, making π-π interactions likely. As with other amyloids, many Aβ fibrils have twofold symmetry and are formed from paired stacks of monomers [111, 112, 144, 160, 162, 173, 175, 187], with examples including the 2A fibrils of Aβ(1-40) [111] and the LS fibrils of Aβ(1-42) [144], the latter of which was revealed by high-resolution EM density maps to have an overall 2_1 screw symmetry. However, threefold fibrils have also been observed, such as the 3Q polymorph of Aβ(1-40) [111]; in addition, helical tubes and hierarchically organised fibrils have also been described [164, 177]. Lastly, while the majority of Aβ fibrils have a left-handed twist [144, 172, 173, 175, 177, 187], a recent structure of patient-derived amyloid fibrils had a right-handed twist [160] (Fig. 1.17). Although amyloid fibrils formed by Aβ are structurally polymorphic, they have many features in common with amyloids formed by other polypeptides. Thus, general insights into the structure and self-assembly mechanisms of Aβ fibrils are likely to be transferrable to other amyloids, particularly those formed by peptides and small disordered proteins such as islet amyloid polypeptide (IAPP) and α-syn, and insights from studies of those systems are likely to be relevant to Aβ.

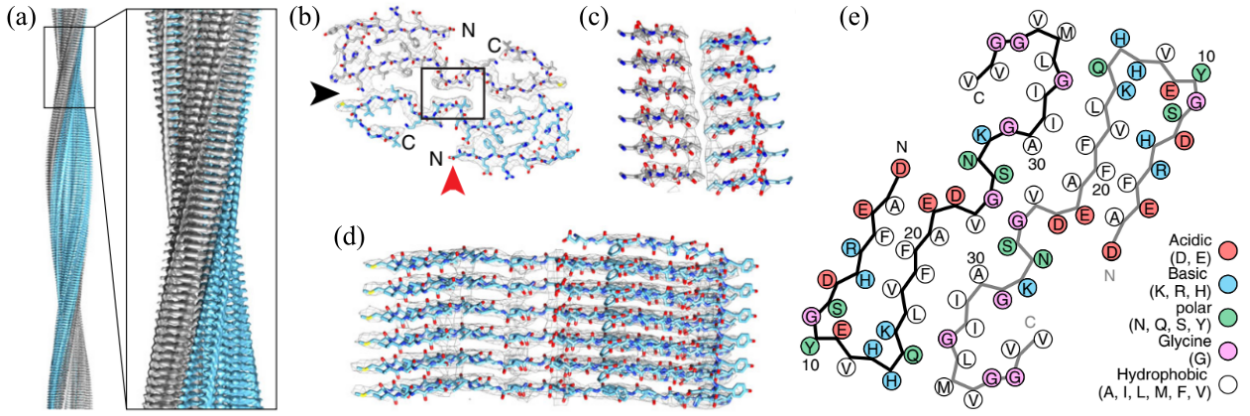

Figure 1.17: Cryo-EM structure of *ex vivo* Aβ fibrils. (a) A side-on view of the fibril structure, showing a right-handed twisted ribbon formed from a pair of protofilaments. (b) A cross-sectional view of the fibril structure. (c) A side-on view of the protofilament packing interface, corresponding to the region enclosed in a box in panel (b). The two subunit stacks are staggered to form a fibril with an overall 2_1 screw symmetry. (d) A side-on view of a stack of six monomeric subunits; as with many other amyloids, the subunits are single-layered but non-planar. (e) The distribution of hydrophilic and hydrophobic residues in the fibril structure. Figure adapted from Kollmer *et al.* [160].

1.3.8 Summary

Although the structure and biophysical properties of amyloids are highly varied, there are common features. The dominant interactions responsible for amyloid formation are markedly different from those responsible for collapse of globular proteins; as a result, amyloids have repetitive, hierarchically organised structures with a high degree of symmetry. This organisation causes unusual interaction motifs such as amide ladders and steric zippers to play an important role in the structure of amyloids, so that there are further structural commonalities despite extensive polymorphism. The highly ordered structure of the cross-β core, and the well-defined, specific set of interactions it entails, leads to unusual morphological and mechanical properties at the mesoscale level, which are closely linked to both the role of amyloids in pathology and their potential applications in materials science. Nonetheless, in many pathological contexts, the metastable species that occur during amyloid formation that are the primary species responsible for toxicity [49]. Thus, in order to understand disease mechanisms, it is important not only to understand the structure and biophysics of mature amyloids, but also the species populated along their formation pathways, and the kinetics by which these species are formed. The kinetics and intermediates of amyloid self-assembly pathways are the focus of the following sections of this literature review.

1.4 Metastable states populated during amyloid formation

In addition to mature amyloid fibrils, proteins and peptides populate a diverse range of non-amyloid conformational states *en route* to amyloid formation. These include misfolded monomer conformers, globular oligomers with varying degrees of structural order, and filamentous assemblies such as protofibrils. An overview of these species is provided in Fig. 1.18, the details of which will be elaborated on in the following subsections. In most cases, non-amyloid states that form during amyloid formation are metastable with respect to mature amyloid fibrils, and they often occur transiently. These metastable states can be studied using a similar range of structural, biophysical, and biochemical techniques to amyloid fibrils, although many of them are relatively unstructured, meaning that cryo-EM has less potential to yield high-resolution density maps, and solution-state spectroscopic techniques such as NMR and fluorescence spectroscopy have a greater role (eg. [216, 217]). In addition, while computational approaches such as atomistic or coarse-grained molecular dynamics (MD) and Monte Carlo simulations have occasionally been used in structural studies of amyloid fibrils [218], and more so in the study of fibril-dependent self-assembly kinetics (Section 1.5), they have also proved extremely informative in the study of many of the highly dynamic, structurally heterogeneous metastable states formed during amyloid self-assembly (eg. [219–224]). The aim of this section is to discuss the structure, morphology, and toxicity of these metastable species. Their role in the nucleation and growth of amyloids will be discussed in the next section.

1.4.1 Structure and physicochemical properties of amyloidogenic monomers

Amyloid formation does not typically proceed directly from a fully folded native state [225]. In most cases, the native and amyloidogenic folding pathways diverge at some point outside of the native basin of attraction (NBA), defined as the basin in the folding free energy surface that contains the global non-amyloid thermodynamic minimum [226]. Thus, in order to form amyloids, proteins with a well-defined native state must typically unfold to some extent. This requirement stems from the substantial conformational differences between the native and amyloid states of proteins; as outlined in Section 1.3.3, the structure and topology of the two are governed by a different balance of molecular interactions [121], and they differ fundamentally in their symmetry and their propensity for particular structural motifs. As a result, it is difficult to envisage how the transition between the two could occur directly, without involving intermediates with a greater degree of conformational flexibility. This explains why peptides such as Aβ and IAPP, and intrinsically disordered proteins (IDPs) and domains (IDDs) such as α-syn, Tau, and poly-Q, which have large disordered regions and in many cases lack a folded 'native' state, are particularly prone to amyloid formation [225]. At the same time, it has been noted that the amyloidogenic pathways of folded proteins, larger peptides and IDPs often branch off at a collapsed or partly ordered monomer, rather than a true random

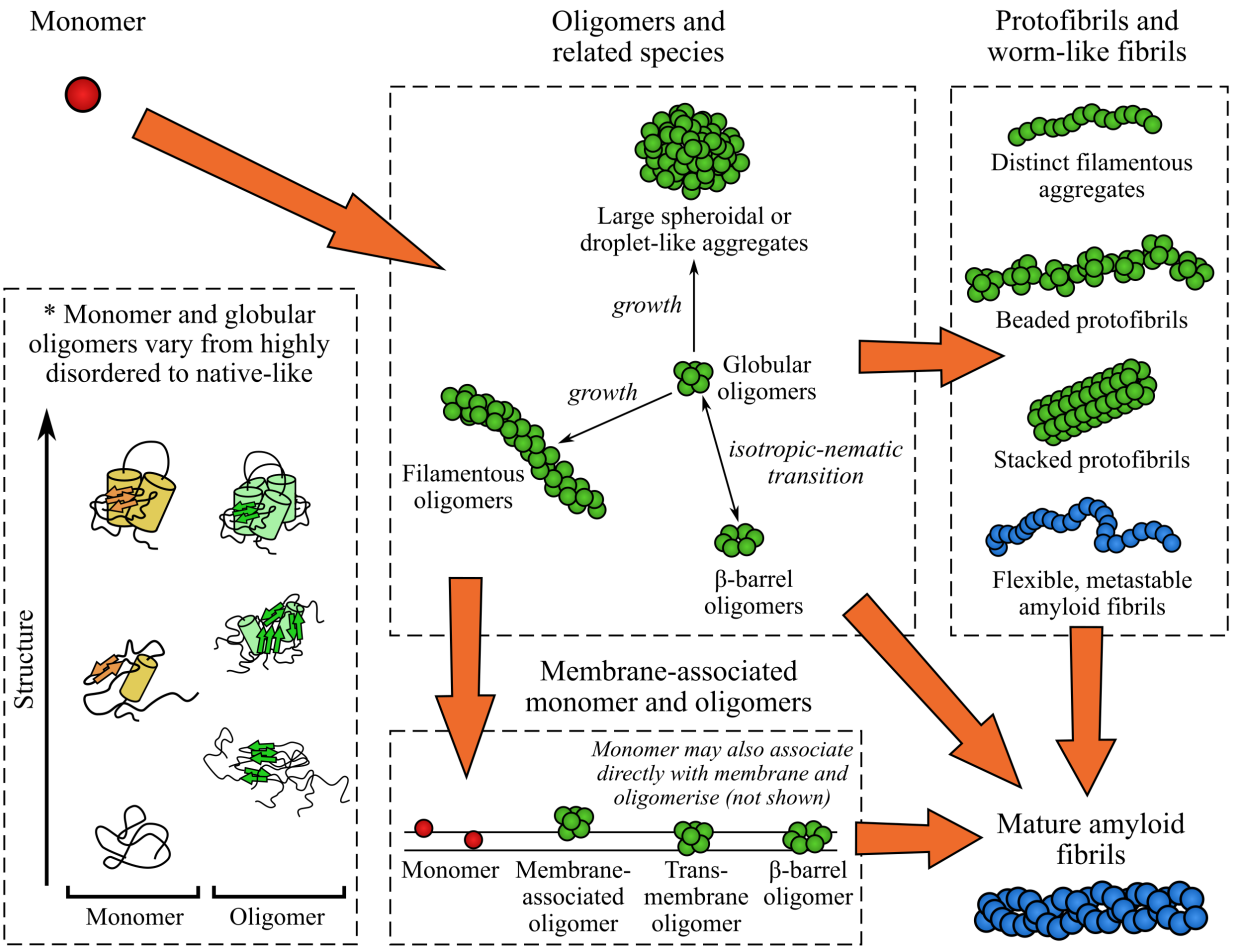

Figure 1.18: An overview of metastable states populated during amyloid formation. Coloured circles represent separate or assembled monomers, with the colour broadly representing the conformational state: red or gold, monomeric conformational ensemble; green, non-amyloid aggregates; blue, amyloid. Metastable or unstable states occurring in amyloid formation include: amyloidogenic monomer conformers (top, left; see Section 1.4.1); oligomers, which may acquire filamentous or droplet-like morphologies as they grow (top, centre; see Section 1.4.2, Section 1.4.4, and Section 1.4.5); protofibrils and worm-like fibrils, a heterogeneous class of filamentous species that are structurally distinct from oligomers and mature amyloid fibrils (top, right; see Section 1.4.3); and species associated with membranes or other surfaces (bottom, centre; for simplicity only membranes are shown here; see Section 1.4.6). Amyloidogenic monomers and oligomers have variable structure content, ranging from negligible to native-like (bottom, left; see Section 1.4.1 and Section 1.4.2). Arrows show the most common structural transitions that occur during amyloid fibril formation, but do not represent all possible pathways; in addition, many polypeptides can only form a subset of the species depicted in this diagram, and may not be able to undergo all structural transitions. For more information on the species and processes represented in this figure, see the corresponding sections indicated above. Figure based on the sources cited in the indicated sections.

coil [225]. The aim of this subsection is to discuss the nature of amyloidogenic monomers in the context of the conformational state of protein folding intermediates and IDPs, in order to examine the requirements for initial assembly and the extent to which the structural features of amyloids may originate in the monomer.

A wide variety of distinct conformational states have been identified along protein folding pathways, and in IDPs and IDDs. The states that are most commonly observed in amyloidogenic monomer conformers are summarised in Fig. 1.19. Besides random coils, collapsed disordered states are also observed, as well as more ordered states such as molten globules (MGs), which have native-like secondary structure but relatively ill-defined tertiary contacts, and folding intermediates with a non-native tertiary structure [227–229]. Although amyloidogenic 'unfolded' states are often assumed to be random coils, unambiguous examples of direct, untemplated amyloid formation by a random coil monomer are rare. Small amyloidogenic peptides ($\lessapprox$ 10 residues) such as KLVFF and GNNQQNY, which lack persistent secondary structure, do not have a well-defined distinction between coil and globular states, as they are too short and inflexible to exhibit random coil statistics or undergo collapse. While the full-length Aβ peptides (39-43 residues) are sometimes proposed to exist in a random coil state, data from CD, NMR, and molecular dynamics (MD) simulations often reveal a significant, fluctuating secondary structure content [4, 219, 221, 230–234]. For example, the simulated free energy surface of the Aβ(1-42) monomer [219] shown in Fig. 1.20 has numerous local minima corresponding to distinct, rapidly interconverting conformational states, and many of these contain a substantial amount of secondary structure. In addition, experiments and simulations have shown that Aβ(1-40) and Aβ(1-42) have a radius of gyration in the 1.0-1.6 nm range, depending on the conditions [235–238], which indicates a partial degree of collapse between a coil ($\sim$1.8 nm) and a dense globule ($\sim$1 nm) [226]. Analyses of the radial distribution of C_α atoms within the partly collapsed monomer have revealed a 'micelle-like' arrangement, with the hydrophobic residues more often occurring at the centre of the globule and the hydrophilic residues closer to the exterior, although the average solvent-accessibility of all residues is still higher than in a folded protein [221]. MD simulations have also predicted a *negative* coefficient of thermal expansion under certain conditions, reflecting the formation of extended secondary structure at lower temperatures ($\leq$ 320 K) [237]. Similarly, α-syn (140 residues), which is highly unstructured and often assumed to be a random coil, has long-range interactions [239] and a radius of gyration of $\sim$2.7 nm [240], which is again intermediate between a true coil in neutral solvent ($\sim$3.7 nm) and a dense globule ($\sim$1.1 nm) [226]. Thus, Aβ, α-syn, and other unstructured amyloidogenic peptides often exist in partly collapsed disordered states, rather than as true random coils. There is also evidence from NMR, MD, and Raman optical activity (ROA) data that many unfolded and denatured polypeptides that were previously interpreted as random coils, including Aβ, α-syn, and Tau, may in fact contain significant quantities of fluctuating polyproline-II (PPII) helices [230, 241–251]. PPII helices are not restricted to polyproline and can be formed by a wide variety of primary sequences, but can be difficult to distinguish from coils by CD; it

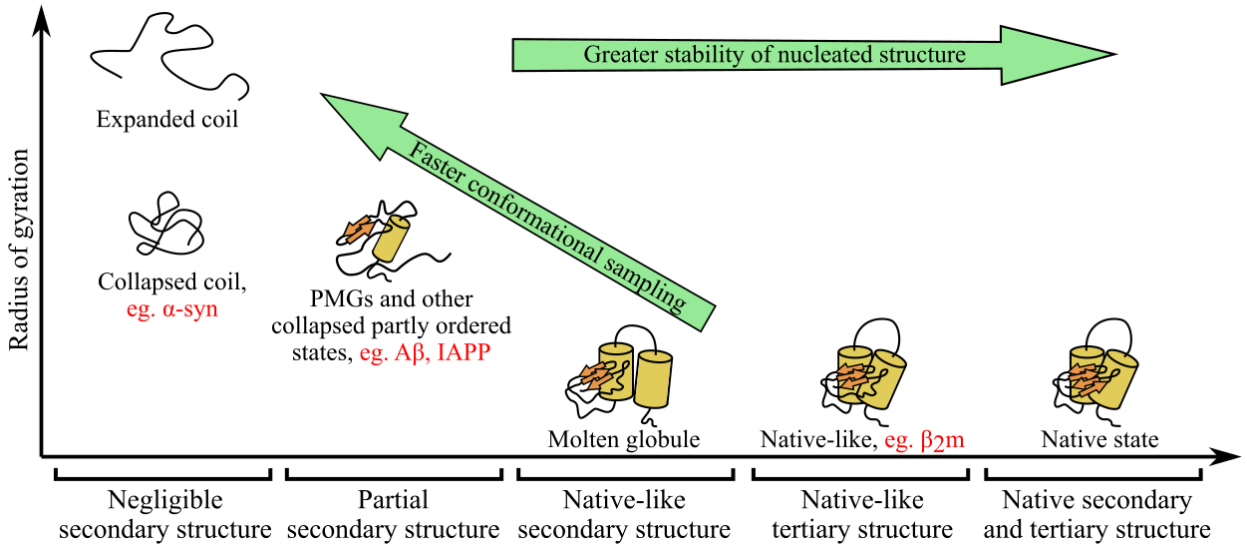

Figure 1.19: An overview of amyloidogenic monomer conformers. Schematic representations of the species often associated with amyloid formation are organised by structure content and radius of gyration, which can be used to measure the degree of hydrophobic collapse of the polypeptide chain. Although there is often a correlation between the degree of collapse and the structure content, there are exceptions [229], and some amyloidogenic polypeptides such as α-syn have a low structure content despite exhibiting a relatively high degree of collapse [253]. Nonetheless, many amyloidogenic monomers exhibit an intermediate degree of collapse and are partly ordered, such as Aβ [221, 232] and IAPP [254, 255]. Other amyloidogenic conformers are native-like, such as β_2m [256]. Green arrows indicate the trade-off between rapid conformational sampling and stability of nucleated cross-β structure, which is often greater in chains that favour a more folded state. Figure based on the aforementioned sources, as well as other sources cited in Section 1.4.1.

has been proposed that PPII helices may be suitable precursors for cross-β structure as they are extended, flexible, and have (ϕ, ψ) angles close to those of β-strands [252].

At the other end of the spectrum, some amyloids have been observed to form from highly structured monomers that are close to the native state (Fig. 1.19). For example, β_2m enters the amyloidogenic pathway via dimerisation of a native-like folding intermediate with a *trans*-proline in place of a native *cis*-proline, and a destabilised β-strand that participates in oligomerisation. These dimers then further assemble to form hexamers, which progress to amyloids via a thus far undetermined mechanism [256, 257]. In a similar manner, amyloid formation by the cystatins proceeds via domain-swapped dimers that can be composed of the native or MG states, although it is implied that the dimerisation of both these species involves a significantly more unfolded transition state [258]. In general, for assembly pathways whose intermediates have a native-like structure, formation of amyloids is likely to require transient sampling of more unfolded states. Therefore, amyloids such as β_2m and the cystatins do not completely circumvent the requirement to unfold, although β_2m may be able to delay major unfolding until the hexamer [256]. Most other amyloids,

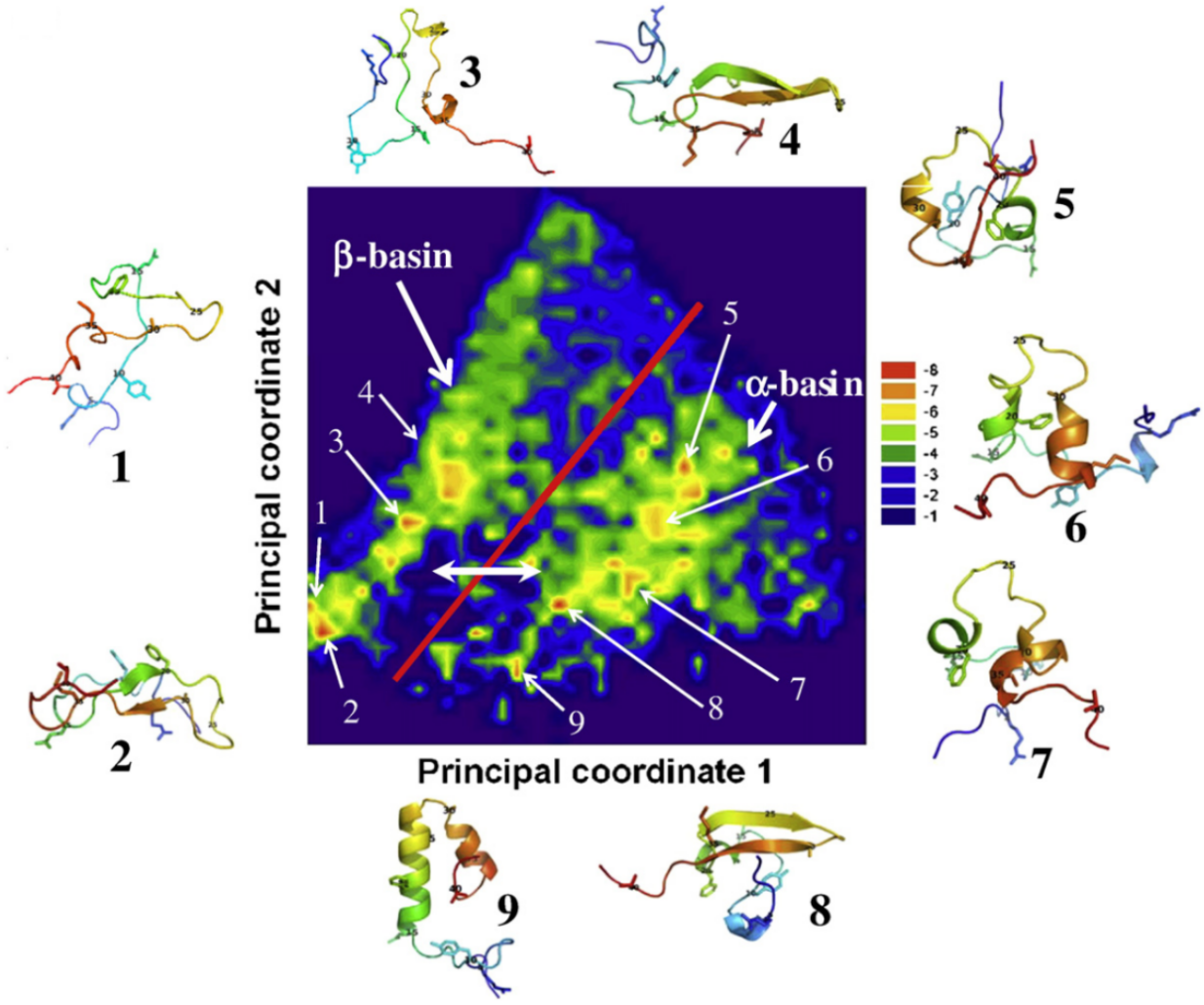

Figure 1.20: Free energy surface of Aβ(1-42) monomer, from MD simulations by Yang and Teplow [219]. The axes are the two main principal coordinates of the peptide's conformational free energy surface. These do not formally relate to any single variable, but are derived from the first two eigenvectors of the distance matrix between sampled conformations; thus, conformations that appear close to one another on this plot are typically conformationally similar. While principal coordinate 1 is the main correlate of whether the peptide's secondary structure is predominantly α-helix or β-sheet, principal coordinate 2 correlates better with conformational conversion within the α- and β-basins. The colour of the free energy surface represents the free energy of conformers (kcal.mol^{-1}; key to right of plot), and the red line is a separatrix highlighting the free energy barrier between the α- and β-basins, with interconversion between these basins depicted by the white double-headed arrow. Representative conformations corresponding to prominent local minima are shown arround the edges of the plot, with their position on the free energy surface indicated by numbered arrows. The structural models are coloured spectrally from the N-terminus (indigo) to C-terminus (red). Figure adapted from Yang and Teplow [219].

perhaps including the cystatins, appear to require a more dynamic monomer.

Many authors have argued that amyloidogenic monomers are dynamic species with an intermediate level of secondary structure, which can be transient or persistent [34, 225, 255, 259–263]. In contrast, aggregation pathways that begin with more structured, native-like monomers have been proposed to result in aggregates that are trapped in a globular state, and undergo amorphous rather than fibrillar assembly [259]. Uversky and Fink [225] have proposed that the amyloidogenic monomer is a pre-molten globule (PMG; see Fig. 1.19). The PMG, which is proposed to be a distinct state of polypeptide chains, is characterised by an intermediate level of secondary structure and lacks a native-like tertiary organisation. In double-angle plots derived from CD data, in which the molar ellipticities at 200 nm and 222 nm are plotted against one another, PMGs form a discrete cluster situated between those corresponding to coils and globules. PMGs have a partial affinity for 8-anilinonaphthalene-1-sulfonic acid (ANS), a fluorescent dye that detects accessible hydrophobic regions and is often used as probe for MG states, have a radius of gyration intermediate between a coil and a MG, and are relatively dynamic [225, 227]. The more structured Aβ conformers are consistent with this description [4, 230–234]; in addition, the monomers of IAPP, poly-Q, and a number of other amyloid-forming proteins are similar to PMGs [225, 254, 255, 264], and α-syn is able to undergo a transition to a PMG-like state when interacting with certain metal ions [265]. PMGs are proposed to be well-suited for amyloid nucleation as they are more dynamic than folded states, but have an appreciable secondary structure content, allowing them to transiently sample a diverse ensemble of amyloid-like conformations until a cross-β structure forms [225].

If the advantage of PMGs lies in their secondary structure content, then structured conformers occurring in more expanded monomers are also likely to be suitable for amyloid formation, meaning that PMGs are not the only suitable precursors. The importance of pre-existing secondary structure is supported by the observation that many amyloidogenic polypeptides transiently form fibril-like structural motifs in their disordered monomeric state; for example, both Aβ and IAPP form β-hairpins that have been suggested to be amyloidogenic [255, 260, 261]. In addition, these amyloids appear to exhibit second-order nucleation kinetics, which has been interpreted as resulting from stabilisation of an unstable β-hairpin conformer by binding of an additional monomer, forming a stable dimer on-pathway to amyloid formation [263, 266]. Although this mechanism is debated [267–269], even if lasting secondary structure does not originate in the monomer, the presence of a significant amount of fluctuating secondary structure could increase the success rate of molecular collisions, enhancing the formation of prefibrillar oligomers.

An alternative interpretation is that it is the poor solubility of the polypeptide backbone that drives aggregation, rather than specific interactions between transiently formed secondary structure elements. A high secondary structure propensity is not a universal characteristic of amyloidogenic monomers; for example, α-syn only becomes a PMG under highly specific conditions, and assembly usually proceeds from a

monomer with a very low secondary structure content [253]. In addition, mutations or modifications could independently destabilise particular secondary structure elements in the monomer and the fibril structure, without requiring a causal relationship between the two. In the alternative interpretation, the correlation between secondary structure content and aggregation propensity exists because both are caused by the same physicochemical properties of the polypeptide chain [268]. Although collapse is not always required for structure formation [229], in general a collapsed or partly collapsed state has greater proximity between polypeptide chains, increasing the probability of forming non-local interactions and thus secondary or tertiary structure. Thus, factors that encourage collapse may indirectly encourage structure formation, and if these factors independently encourage aggregation, a correlation between secondary structure content and aggregation propensity will emerge. As with other peptides and proteins, collapse of amyloidogenic monomers is driven by a complex interplay of backbone-backbone interactions and sidechain-dependent effects [229]. The polypeptide backbone itself has poor solubility, so that both polyglutamine (poly-Q) and polyglycine undergo collapse transitions driven by the tendency of the backbone amides to preferentially solvate one another, rather than forming hydrogen bonds with the solvent [270, 271]. At the same time, the sidechains modulate this tendency; for example, while the burial of hydrophobic sidechains encourages collapse [221], the unfavourable desolvation enthalpy of charged sidechains opposes collapse [229]. MD simulations have shown that aggregation of small oligomers of Aβ(10-40) [272] and poly-Q [268] is driven by the same set of physical principles as collapse; just as the polypeptide backbone of a single monomer prefers to solvate itself, the backbones of monomers within an oligomer can mutually solvate one another [268], and hydrophobic interactions that encourage collapse also encourage oligomerisation in a similarly nonspecific manner [220, 223, 273–275]. In agreement with this, small oligomers formed by these peptides have similar secondary structure content and radial density profiles to the monomers [268, 272]. Thus, monomer collapse, secondary structure formation, and globular oligomer formation may be correlated simply because they all depend on the poor solubility of the expanded monomer [268].

The prevalence of collapse among amyloidogenic monomers also presents a challenge for hypotheses that cross-β structure originates in the monomer [268]. Although collapse often results in an increase in secondary structure content, it also has detrimental effects on the monomer's ability to sample amyloidogenic conformers, without first self-assembling to form oligomers. While collapsed disordered states are much more dynamic than folded states, they are denser than random coils, often contain restrained water, and have large numbers of non-amyloid-like interactions that create a frustrated free energy surface with numerous local minima [219, 268, 270, 276], similar to that shown in Fig. 1.20. As a result, PMGs and other collapsed disordered states have slower conformational sampling than random coils, and can exhibit broken ergodicity [229], which means that monomers may be individually unlikely to 'find' amyloidogenic conformers on timescales relevant to nucleation. This is problematic for theories of monomeric 'nuclei', since notions

of nucleation resulting from conformational fluctuations in the monomer are often predicated on the idea that the monomer is ergodic and exhibits coil-like statistics [263, 266]. As a solution, Vitalis *et al.* [268] proposed that the cross-β structure could arise in collapsed disordered *oligomers*; in this context, the authors found that intermolecular interfaces were able to promote β-sheet formation, suggesting that nucleation of the cross-β structure is likely to be enhanced as the size of oligomers increases. Similarly, more recent work has shown that the apparent second-order nucleation kinetics could be ascribed to a dimer being the smallest species in which the cross-β structure can nucleate, rather than 'nucleation' in a monomer and stabilisation by dimer formation [224].

Nonetheless, it should be noted that the disordered monomers of different amyloidogenic proteins present a spectrum of conformational states, with varying degrees of collapse and secondary structure. Thus, an expanded state with a high secondary structure content may favour nucleation in the monomer, while a collapsed disordered state may delay nucleation until oligomers are formed. The fact that many polypeptides exhibit a positive correlation between the degree of collapse and the secondary structure content may create a trade-off that typically results in an intermediate propensity for these two pathways, as represented in Fig. 1.19. Based on the available evidence, it is not possible to settle the question of when different amyloids nucleate by only examining the monomer. Therefore, the structural and physicochemical characteristics of oligomers are investigated in greater detail in the following subsections.

1.4.2 Globular oligomers and micelles

Oligomers are often observed during amyloid self-assembly, and the oligomers formed by many polypeptides, such as Aβ, α-syn, and IAPP, have been proposed to be the primary species responsible for toxicity [49]. Species described as oligomers typically have a spheroidal, ellipsoidal, or irregular appearance when imaged by AFM and EM (Fig. 1.21(a-b)), with a diameter from 2 nm [277] to several tens of nm (eg. [278, 279]), and range from dimers to large assemblies containing thousands of monomers. Arguably such large aggregates are not true oligomers, but due to the broad size distribution of many oligomer populations there is often no clear structural distinction between small oligomers and large multimeric aggregates (eg. [278]); the morphologies of large oligomer-derived aggregates, which are typically filamentous or droplet-like, are discussed in greater detail in Sections 1.4.4 and 1.4.5. The structural and mechanical properties of oligomers are varied (Fig. 1.21(c-f)); some bind ThT, implying the presence of amyloid-like structural motifs [278], while others do not [280], and some have well-defined tertiary structures [256, 258, 281, 282], while others are liquid-like and deformable [283, 284]. In general, oligomers tend to be less structured and more dynamic than the amyloid and the native state, if present. This section provides an introduction to globular oligomers that form in solution; elongated prefibrillar assemblies such as protofibrils and filamentous oligomers are discussed in the next two sections, followed by

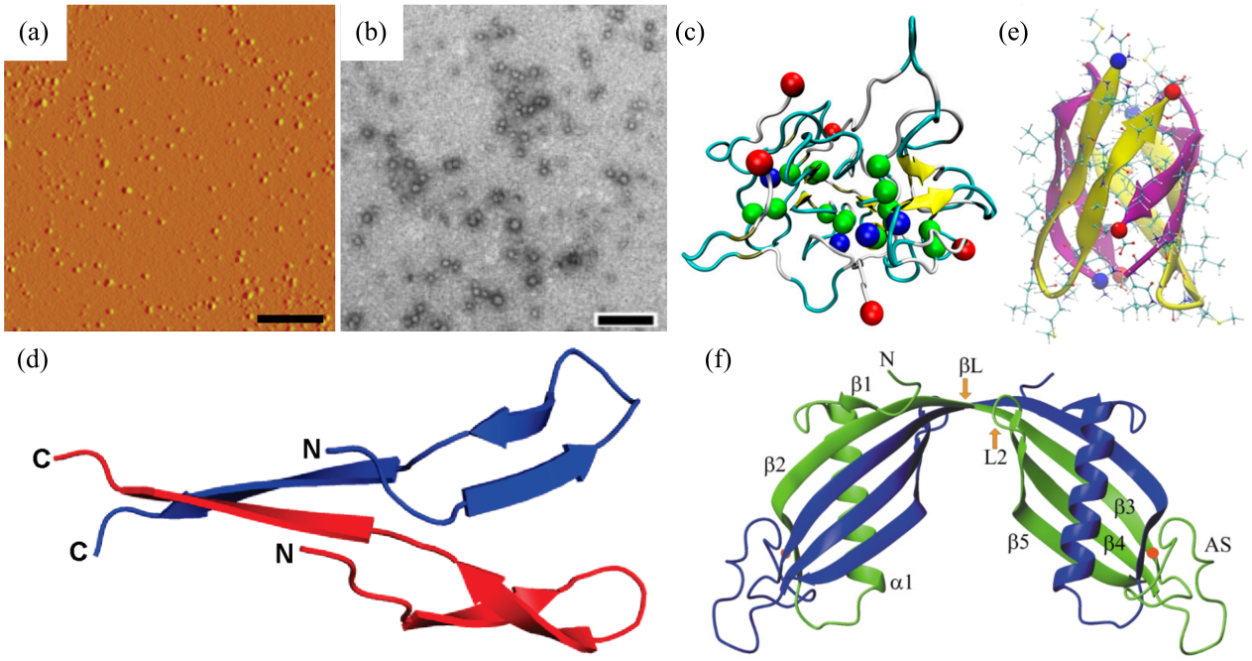

Figure 1.21: Morphology and structure of globular oligomers. Panels (a-b) show the typical appearance of globular oligomers by (a) AFM (Aβ(M1-42), ie. N-terminally methionylated Aβ(1-42), scale bar 200 nm) [303] and (b) NS-EM (Aβ(1-42), scale bar 100 nm) [304]. Panel (c) shows a representative conformation of a relatively disordered Aβ(1-42) pentamer, from MD simulations [273]. Coloured spheres represent residues of interest: red, N-terminal D1; green, selected hydrophobic residues (I31, I32, I41); blue, C-terminal A42. Panel (d) (bottom left) shows the ssNMR-derived structure of an ordered subdomain of a globular oligomer formed by Aβ(M1-42) [303], comprising residues 17-42. Ordered regions appeared after assembly following a delay, and the N-terminal region remained disordered (not shown). Similarly, panel (e) (top right) shows a representative conformation of the ordered core of a simulated Aβ(1-42) β-barrel tetramer [305], comprising the C-terminal regions of the peptides (residues 27-43). The remainder is mostly disordered (not shown). Panel (f) shows the X-ray crystal structure of a domain-swapped dimer of human cystatin C (hCC) [281]. In panels (d-f), different polypeptide chains are represented in different colours. All images adapted from their respective sources.

large spheroidal aggregates, and the various assemblies formed at surfaces and in contact with membranes. Soluble globular oligomers have been described in most amyloid proteins, with examples including the Aβ peptides [51, 54, 71, 216, 278, 280, 285–296], α-syn [51, 297–299], β_2m [256], IAPP [51, 99, 300, 301], PrP [51], poly-Q [51], Htt [251, 302], and Sup35p [283], and can be divided into several broad classes: disordered or partly ordered globular oligomers (Fig. 1.21(c-d)), β-barrels (Fig. 1.21(e)), and native-like oligomers (Fig. 1.21(f)).

Many oligomers formed in experimental contexts are characterised by a low or intermediate level of secondary structure, a globular appearance, broad size distribution, and in some cases clear evidence of deformability when interacting with surfaces and amyloid fibrils. Examples include the majority of

Aβ oligomers that have been analysed at the structural level [216, 286, 287, 290, 296, 303], as well as oligomers formed by IAPP [99, 300, 301, 306], Sup35p [283, 284], and various Htt constructs and poly-Q fusion proteins [251, 307, 308]. In addition, these characteristics are likely to extend to many other amyloid oligomers whose structural properties have been studied in less detail. The morphology and mechanical properties of these species strongly imply that their poorly developed secondary structure results in a lack of long-range higher-order structure throughout the assembly, although there is good evidence for short-range tertiary and quaternary contacts within subdomains of co-assembled monomers in some cases [216, 255, 278, 290, 296, 303, 306]. The lack of long-range structure gives these species a 'molten' character [268,283,284]; in agreement with this, the majority of oligomers that are spontaneously formed in molecular simulations have a low or intermediate level of secondary structure, and a fluid or irregular tertiary and quaternary structure [220, 222, 223, 268, 272–275, 309–314]. Due to the lack of a fixed structure, MD simulations are often the only means to obtain conformational ensembles for disordered or partly ordered oligomers, meaning it can be difficult to validate these structures experimentally. Nonetheless, the ensemble predictions of MD simulations, such as the R_g, structure propensity, and oligomer size distributions, typically agree with experimental measurements from techniques such as CD and NMR [220,223,268,272–274,314], validating their use to examine the structural characteristics of these oligomers. Fig. 1.21(c) shows a representative conformation of a relatively disordered Aβ(1-42) pentamer from an MD trajectory [273], typical of the simulated and experimentally supported characteristics of partly ordered oligomers.

Disordered and partly ordered oligomers are a relatively broad class, with considerable variation between the assemblies formed by different polypeptides, and even by the same polypeptide. For example, experimental estimates of β-strand content in Aβ(1-40) oligomers range from ∼10% [304] to ∼40% [290], and poly-Q dimers are predicted to have a β-strand content of ∼30% [268]. It is important to note that the secondary structure contents of amyloidogenic monomers and early disordered oligomers are not particularly different; CD and MD data suggest that the Aβ(1-40) monomer has a β-strand content in the 10-30% range [4, 219, 221, 230–232], and Vitalis *et al.* [268] observed only a small difference in the stability of β-strands between poly-Q monomers and dimers. Thus, the principles that are responsible for collapse and structure formation of the monomer are also likely to be important early in the oligomerisation process. Some oligomers with a higher secondary structure content have a number of well-defined tertiary and quaternary contacts [216, 255, 278, 290, 296, 303, 306]; these oligomers often dissociate into stable dimers and trimers when treated with sodium dodecyl-sulfate (SDS), indicating that they are organised into 'subdomains' containing intermolecular β-sheets [216, 290]. An example of such a motif is shown in Fig. 1.21(d). When observed, tertiary and quaternary structure usually consists of a mixture of amyloid-like and non-amyloid elements [216,255,290,296,303,306]. Moreover, while the majority of amyloid fibrils have a parallel cross-β structure, small antiparallel and mixed β-sheets are common in oligomers [290, 291, 301, 303, 305, 315];

similarly, NMR and MD data suggest that oligomers are enriched in intramolecular β-sheets compared to fibrils [220, 273, 274, 290, 301, 303, 305, 315]. Nonetheless, the presence of some amyloid-like contacts suggests that small oligomers and the subdomains present in larger oligomers may act as precursors for the subsequent development of a mature cross-β structure [220, 278, 290, 305, 306, 315].

Some authors have described 'molten' oligomers as micelles [285, 309, 316–318]. Much of the experimental evidence for micellar oligomers comes from Aβ(1-40), but this is simply a result of particularly intense research into Aβ oligomers [285, 316, 317]; oligomers formed by Sup35p [283], κ-casein [318], and Htt [251] have also been described as micelles, and both the generality of the underlying physical principles and the results of molecular simulations suggest that a micellar organisation is likely to occur in oligomers formed by other amphiphilic polypeptides [222, 309]. The main experimental evidence for the micellar nature of Aβ(1-40) oligomers comes from the fact that the monomers have a surfactant-like ability to lower the surface tension of the solution, but above a critical concentration oligomers form from the excess peptide, and the surface tension stabilises in a manner similar to micelle formation. At the same time, pyrene segregates into these oligomers and exhibits a drop in the fluorescence intensity ratio of its first and third vibrational peaks, indicating formation of a hydrophobic environment [317]. These results indicate that monomers within the oligomers are organised so that their hydrophilic sidechains interact with the solvent, and their hydrophobics are buried. In addition, Aβ oligomers often exhibit a preference for a particular size at local equilibrium, which may indicate a micellar arrangement. In some cases, this has been found to be 5-6 monomers [304], whereas in others a size of 25-50 monomers appears to be preferred [316, 317]. Either way, the presence of a discrete peak in the oligomer size distribution could be explained by the geometric constraints imposed on micelles, as hydrophobic burial is optimised at a particular diameter and curvature [319]. It is worth noting that Aβ(1-40) micelles are not necessarily spherical; in one study, small angle neutron scattering (SANS) data suggested a spherocylindrical morphology, with an average length of 11 nm and width of 2.4 nm [316]. Besides experimental studies on Aβ(1-40), micelle-like organisation occurs spontaneously in many molecular simulations of oligomers [220, 222, 223, 273–275], which also suggest that micellar oligomers can have elongated, non-spherical morphologies [220, 222, 274, 275].

At the same time, describing prefibrillar oligomers as micelles overlooks the other complexities of their formation and structural organisation. For a relatively disordered oligomer, a micellar organisation is unsurprising given that the hydrophobic effect, which is one of the main drivers for oligomerisation [220, 223, 273–275], favours burial of hydrophobic sidechains and *vice versa*, exactly the same as in folded proteins and amyloids. The fact that oligomers form above a critical concentration similar to a critical micellar concentration (CMC) is also unsurprising; all large aggregates are likely to do the same, including amyloid fibrils. In addition, the fact that monomers with a low level of amphiphilicity such as poly-Q are able to form oligomers [51] indicates that the hydrophobic effect is not the only factor that drives oligomeri-

sation; others, such as mutual solvation of polypeptide backbones, sidechain-sidechain interactions, and intermolecular β-sheet formation are also likely to be important. Lastly, the fact that some studies have attributed the toxicity of amyloid oligomers to the presence of exposed hydrophobics [320–322] implies that they are *less* micellar than amyloids and folded proteins. Thus, while all oligomers may have a varying degree of micellar organisation, there are other effects that drive their formation.

Analyses from the perspective of polymer physics have emphasised the similarity of prefibrillar oligomers to collapsed polymer globules in poor solvent. In poly-Q, the formation of disordered oligomers is favourable for the same reason that collapse of the monomer is favourable; water is a poor solvent for the polypeptide backbone, and the backbone amides preferentially solvate one another, whether intramolecularly or intermolecularly [268]. Similarly, simulations of Aβ(10-40) dimers and tetramers predicted features typical of collapsed polymer globules [272]. The dimers and tetramers were both relatively unstructured, with similar radial density profiles that revealed a dense core surrounded by a surface layer through which the density decreased continuously towards the solvent; at lower temperatures, more atoms where incorporated into the core, whereas temperature-induced melting of the oligomers was associated with expansion of the surface layer. The authors concluded that collapse of the oligomers was a continuous structural transition similar to the collapse of other polymer globules. These conclusions are less likely to apply to oligomers with a high degree of structural order, or short, relatively inflexible peptides such as KLVFF and GNNQQNY; however, for the majority of prefibrillar oligomers, which appear to have a low or intermediate secondary structure content and are formed by polypeptides that are long enough to undergo a collapse transition, it is likely that many aspects of oligomerisation can be explained by more general principles from polymer theory.

At a more intermediate level of molecular order, it is possible that some soluble oligomers may have a β-barrel structure. β-barrels are a commonly proposed structure for prefibrillar membrane pores, which will be discussed in Section 1.4.6, but soluble, relatively dynamic β-barrels have also been predicted by MD simulations of Aβ(1-40) [305, 315], and coarse-grained Langevin dynamics (LD) simulations of generic polypeptide chains [310]; an example of a simulated β-barrel structure from MD is shown in Fig. 1.21(e). β-barrels have also been observed in larger assemblies, such as crystal structures of KVKVLGDVIEV, an amyloidogenic peptide derived from αB-crystallin [323], and metastable, rod-like protofibrils formed by Aβcc(1-42), a double-cysteine mutant of Aβ(1-42) in which disulfide bond formation prevents the transition to fibrils [324]. In both of these examples, the β-barrels have been proposed to form independently as soluble oligomers, which then assemble to form the final structure. While the crystals and protofibrils are highly structured, the β-barrels predicted by molecular simulations are typically more dynamic. However, it is likely that the interactions that occur during higher-order assembly, as well as the engineered disulfide bond in Aβcc(1-42), would favour greater ordering; thus, if β-barrel oligomers are able to exist independently in solution, they may exhibit a more intermediate level of structural order. The 6-fold stoichiometry

of Aβcc(1-42) β-barrels has been proposed [324] as an explanation for why cross-linking and ion mobility mass spectrometry (IM-MS) data show a peak in the Aβ(1-42) oligomer size distribution around the pentamer and hexamer [304, 325]; however, it should be noted that MD simulations predicting comparatively disordered oligomers are also able to replicate this peak, casting doubt on the need for a β-barrel to explain this observation [220, 275]. Although direct experimental evidence for soluble β-barrel oligomers appears to be relatively scarce, the oligomers formed by KVKVLGDVIEV were found to bind the A11 antibody [323], a 'conformational' antibody [326] that has also been shown to recognise α-hemolysin, a soluble β-barrel protein, and a variety of toxic prefibrillar oligomers [327, 328]. Thus, it is possible that many toxic oligomers with a higher β-sheet content may have a β-barrel structure. If this is the case, then it appears that many amyloidogenic proteins can alternately form either disordered or β-barrel oligomers under different conditions. A transition between relatively isotropic, disordered oligomers and β-barrels has been predicted in coarse-grained LD simulations, with the β-barrels occurring at lower temperatures or higher chain stiffness; in addition, the authors noted a quantitative similarity to the isotropic-nematic transition of liquid crystals, which involves a similar change from spherical to uniaxial symmetry [310]. Thus, β-barrel formation may be a common property of all amyloidogenic oligomers under appropriate conditions.

At the more structured end of the spectrum, some prefibrillar oligomers are relatively well-folded and native-like. Examples include the dimers and hexamers formed by β_2m [256], and domain-swapped dimers (see Fig. 1.21(f)) and tetramers formed by the cystatins [258, 281, 282], both of which are able to enter the amyloidogenic pathway from a relatively well-folded monomer. Despite being comparatively well-folded, the tetramers and hexamers formed by these proteins are more dynamic than dimers or the native state, exhibiting features such as enhanced ANS fluorescence and a loss of resonance dispersion in their NMR spectra [256, 282]. This implies that more structured oligomers have an inverse relationship between aggregate size and structure content compared to that observed in relatively disordered oligomers, such as those formed by Aβ or poly-Q, with successive aggregation steps destabilising the native fold and reducing the free energy barrier for the major structural rearrangement needed to form an amyloid fibril.

Although there are clear exceptions, most prefibrillar oligomers appear to exist in an unfolded or partly folded state. In these cases, early oligomers typically contain less secondary structure than those occurring later during aggregation [216, 220, 290, 306, 315], and tertiary and quaternary contacts are observed rather infrequently [216, 255, 278, 290, 296, 303, 306]. This indicates that oligomerisation is initially driven by general principles such as the hydrophobic effect and the poor solubility of the polypeptide backbone, with higher-order structure developing later on. The counterexample to the progressive increase in structure during oligomerisation is given by proteins such as β_2m and the cystatins, which enter the amyloidogenic pathway from a well-folded precursor and become progressively more dynamic as they assemble [256, 258, 281, 282]. Provided both types of oligomers are situated *en route* to fibril formation, this implies that there

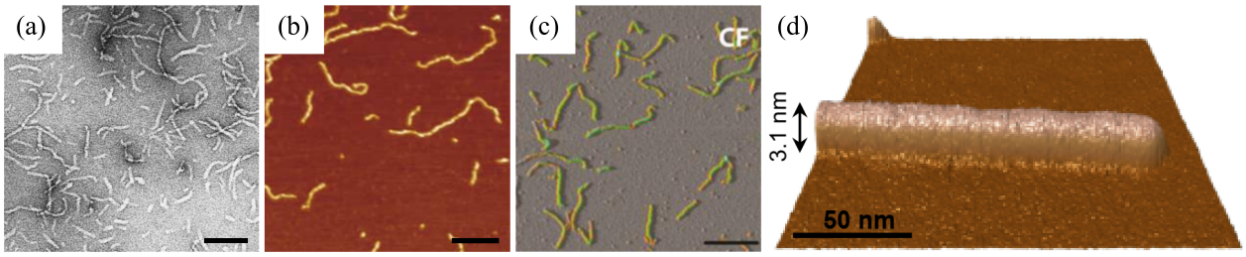

Figure 1.22: Morphology of protofibrils and worm-like fibrils. (a) A NS-EM image of protofibrils formed by Aβ(1-40) [116] (scale bar 100 nm). (b) An AFM image of worm-like fibrils formed by β_2m [329] (scale bar 200 nm). (c) An AFM image of metastable, curvilinear fibrils formed by lysozyme [339] (scale bar 300 nm). (d) A 3D represention of an AFM image of rod-like Aβcc(1-42) protofibrils [324]. All images adapted from their respective sources.

is an approximate level of structure that is optimal for formation of the cross-β structure: the immediate precursors may be dynamic species that are rich in secondary, tertiary, and quaternary contacts but have the flexibility needed to undergo the final conformational rearrangement to form a cross-β structure.

1.4.3 Protofibrils and worm-like fibrils

In addition to oligomers and mature amyloid fibrils, many amyloidogenic polypeptides assemble to form metastable, filamentous species such as protofibrils and worm-like fibrils; as will be discussed in the next section, the basic physical principles that drive globular oligomer formation can also cause globular or micellar oligomers to acquire a filamentous morphology, creating an additional class of metastable filamentous species. In general, protofibrils and worm-like fibrils can be regarded as short, metastable, filamentous aggregates with an atypical structure or morphology; an overview of these assemblies is provided in Fig. 1.18 and Fig. 1.22. There is not always a well-defined distinction between amyloid fibrils, worm-like fibrils, and protofibrils. The description of 'worm-like' fibrils is the more specific, as it usually refers to amyloid fibrils with a cross-β structure that are highly flexible, ie. $l_p \ll l$ [329, 330] (see Section 1.3.6). In contrast, the term 'protofibril' was originally applied to metastable, curvilinear, non-amyloid filaments formed by Aβ [116, 331], but has since been applied to metastable amyloid fibrils formed by other polypeptides [332–335], as well as other metastable filamentous species with a rod-like or beaded morphology [324, 336–339]. Protofibrils and worm-like fibrils have been observed in Aβ [116, 324, 331], α-syn [332, 335], β_2m [329], and a wide variety of other amyloids [330, 333, 334, 337–340]; as with oligomers, some have been proposed to cause toxicity *in vivo* [72, 341].

Metastable filamentous species have a wide variety of structural features, and have been proposed to assemble by either monomer addition or coalescence of oligomers. The three most common models for these species are: (i) amyloid fibrils with an atypical morphology [209, 329, 330, 333–335, 340, 342]; (ii) a distinct,

non-amyloid state [291]; or (iii) stacks or beaded chains of globular oligomers [324, 336–339]. Schematic representations of these three models are shown in Fig. 1.18. In all three cases, the atypical morphology of these species is probably connected to their metastability, since both imply that the network of molecular interactions that stabilise their structure is weaker or less extensive than in mature amyloid fibrils. Worm-like fibrils and curvilinear cross-β protofibrils, which both fall into the first class, have been observed in α-syn [335], β_2m [329], and various other proteins [330, 333, 340]. In some instances, the curvilinear morphology of these species may be explained by a reduced number of protofilaments, which leads to a fibril with a lower second moment of area and a shorter persistence length as a result [195, 333, 340]. In others, the greater flexibility may result from polymorphism of the cross-β core, as protofilaments with less extensive cross-β structure and fewer stabilising interactions will have a less negative free energy of polymerisation and a lower Young's modulus, resulting in flexible assemblies that are metastable with respect to more structured amyloid fibrils [329, 330, 335, 342]. Similarly, the metastability of non-amyloid filamentous species can be attributed to the lack of a cross-β structure, and protofibrils that are formed by beading of globular oligomers are likely to be flexible and metastable due to the poorly folded nature of their subunits, and the weak interactions between them. While some protofibrils and worm-like fibrils have been proposed to be on-pathway to formation of mature amyloid fibrils [116, 331, 334–337, 340, 342], others are suggested to be off-pathway [329, 339], particularly if there is a well-folded tertiary and quaternary structure that is markedly different from that of stable fibrils.

1.4.4 Filamentous oligomers

Metastable filamentous assemblies can also arise as a natural consequence of the growth of globular oligomers without requiring dramatic structural changes or a different mode of supramolecular assembly (Fig. 1.18), a possibility that is sometimes overlooked. The tendency of large oligomers to acquire an elongated and even filamentous morphology is supported by the majority of sufficiently large molecular simulations [220, 222, 223, 275, 343] and several experimental studies [251, 290, 296, 304, 307, 344, 345], and can be explained in terms of simple physical constraints on the dimensions of oligomers. For example, both NS-EM and AFM have revealed irregular, thread-like oligomers formed during aggregation of Aβ(1-40) [290, 296, 304, 344, 345], Aβ(1-42) [290, 344], and some poly-Q-containing proteins, including Htt [251, 307]; these appear to develop from smaller globular oligomers, are relatively unstructured (∼80% coil for Aβ), and seem to be on pathway to fibril formation; in addition, SANS data indicate that 'micelles' formed by Aβ(1-40) have an elongated morphology, with a length almost five times their width [316]. Atomistic simulations also predict that globular oligomers formed by a wide variety of Aβ peptides, including Aβ(1-40) and Aβ(1-42) as well as N-terminally truncated variants, will undergo a transition from spheroidal to protofibril-like growth around the size of approximately a pentamer or hexamer [220, 223, 275]; a similar

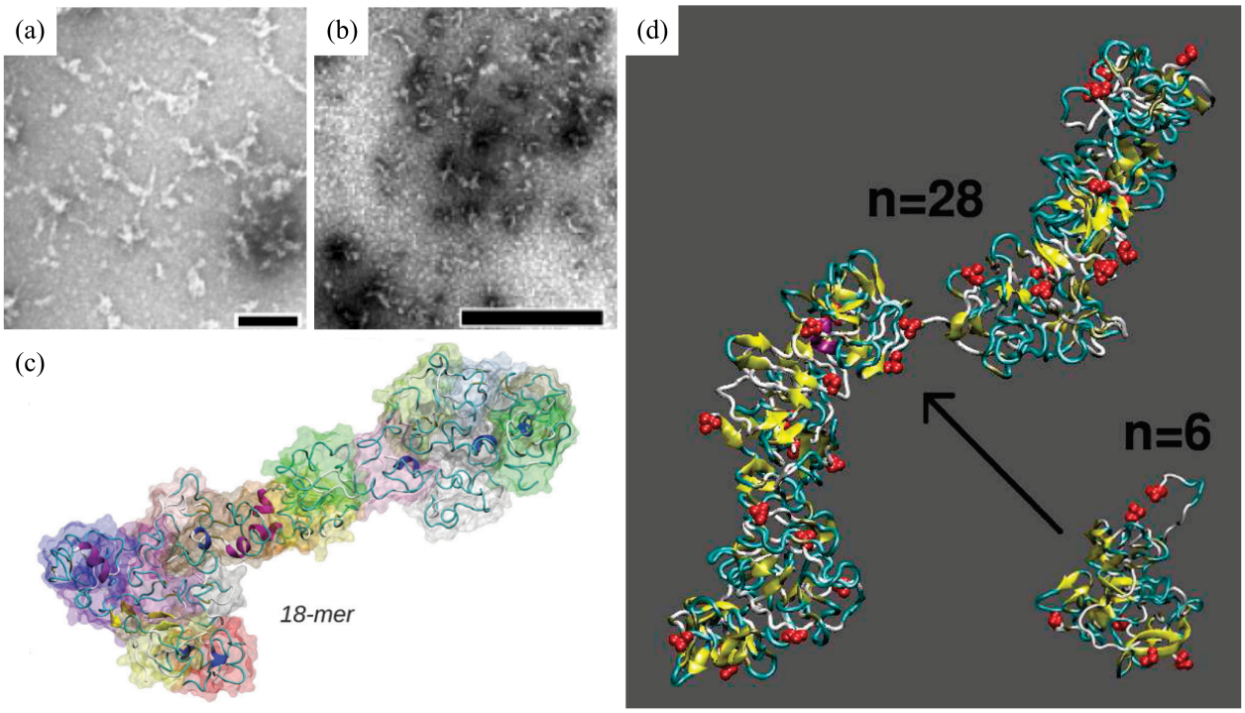

Figure 1.23: Oligomers may acquire a filamentous morphology as a consequence of continued growth. Panels (a-b) show NS-EM images of oligomers with a filamentous or elongated morphology formed by (a) Aβ(1-40) [304] (scale bar 100 nm) and (b) Met(O_2)35 Aβ(1-40) [344] (scale bar 100 nm). Panels (c-d) show representative conformations of large Aβ(1-42) oligomers from MD simulations: (c) shows a disordered 18-mer with an elongated morphology [223]; and (d) compares the morphology of hexamers and 28-mers with a higher β-sheet content than the oligomers in the previous panel [220]. The red spheres mark the N-termini (D1) of each assembled peptide. Note that the width of the 28-mer is approximately the same as that of the 6-mer. All images adapted from their respective sources.

morphology has been predicted for oligomers of the KLVFFAE peptide [343]. Lastly, the self-assembly kinetics of α-syn oligomers have also been shown to be consistent with a pseudo-1D mechanism of growth [346]. Filamentous oligomers contrast with protofibrils as they are small, appear to lack a recurring tertiary or quaternary structure, and have a highly irregular morphology; moreover, they are structurally continuous with smaller globular oligomers, and their formation is a natural consequence of the growth of such species, rather than resulting from a change in structure or growth mechanism. Examples of the morphology and simulated structures of filamentous oligomers are shown in Fig. 1.23.

The possibility of filamentous, disordered oligomers is often overlooked because it is assumed that a filamentous morphology requires a specific quaternary structure, such as a cross-β structure or the stacking of relatively folded globular subunits. Relatively disordered oligomers are often assumed to be either completely lacking in any type of internal organisation, which would result in isotropic growth [347], or being typical micelles, which often have ellipsoidal or spherocylindrical structures, but are often restricted

in size and curvature [319]. However, as discussed previously, globular oligomers are neither completely unstructured, nor simple micelles; they are more complex. Similar to micelles, the requirement to solvate the charged groups and other hydrophilic moieties means that the maximum width of a globular oligomer is restricted under many conditions; an oligomer that is too wide must contain desolvated polar groups, which is unfavourable in the absence of compensating interactions. However, oligomers differ from non-polypeptide micelles in their complexity; in addition to the poor solubility of the backbone and hydrophobic sidechains [220, 223, 268, 273–275], globular oligomers are held together by more specific interactions, whether transient or persistent; these include the formation of small β-sheets and various sidechain-sidechain and sidechain-backbone interactions [268, 272, 276, 290, 301, 303, 315]. Even if these interactions are too irregular to result in long-range order, they can contribute to the overall stability of oligomers. In addition, most amyloidogenic monomers are flexible, deformable, and have alternating hydrophobic and hydrophilic regions. The presence of additional stabilising interactions and the flexibility and sequence complexity of polypeptide chains may allow globular oligomers to tolerate larger structural deviations than the smaller or more rigid molecules found in many 'typical' micelles, allowing them to adopt a more elongated morphology.

The micellar origin of the transition from spheroidal to filamentous growth is supported by the fact that this transition happens around the pentamer or hexamer for Aβ [220, 275], when the width of an oligomer is slightly more than twice that of a pseudo-spherical monomer of the same density, and there is a peak in the oligomer size distribution. More direct evidence for a micellar explanation is also provided by the coarse-grained MD simulations of Barz *et al.* [222], who considered the self-assembly of coarse-grained amphiphilic monomers with a variable energy term disfavouring desolvation of the hydrophilic groups. Completely 'hydrophobic' monomers, for which there was no penalty for desolvating those groups, underwent amorphous assembly to form large spheroidal structures. Progressively increasing the penalty caused the simulations to produce increasingly filamentous structures with a smaller width and a more micellar cross-section, without need for specific features to mimic intermolecular β-sheets. Another important feature of this study was the fact that they modelled each monomer as a deformable entity, rather than a hard spherocylinder as in many other coarse-grained simulations [224, 319, 348]. While hard spherocylinder models have computational advantages, they do not form elongated structures under a micelle-like interaction potential. This indicates that coarse-grained models must incorporate some degree of flexibility or deformability in order to replicate the filamentous oligomers seen in atomistic simulations and experiments, supporting the hypothesis that the deformability of polypeptide chains allows oligomers to tolerate more filamentous arrangements.

1.4.5 Large spheroidal and droplet-like aggregates

Past a certain point, continued growth of oligomers usually requires a transition to a structurally distinct protofibrillar or fibrillar state (see Section 1.4.3), or a gradual shift to an elongated morphology due to the micellar constraints on oligomer size (see Section 1.4.4). However, in some cases, continued isotropic growth may occur, resulting in large, spheroidal aggregates consisting of thousands of monomers, without an obvious micellar architecture (Fig. 1.18, Fig. 1.24). This is a rather uncommon occurrence, but has been observed in Aβ(1-40), where spheroidal aggregates can grow to widths as great as several microns [278, 292, 295]. The morphology of these species indicates that favourable energetic terms resulting from desolvation of the backbone and hydrophobic sidechains, and in at least one case β-sheet formation [278], outweigh unfavourable terms resulting from desolvation of charged sidechains and other hydrophilic moieties, allowing non-micellar assembly. Although there does not appear to be a single environmental factor that induces this mode of assembly, there may be individual explanations. In one study, the Aβ(1-40) monomers within the aggregates were found to be relatively structured, with tertiary and quaternary contacts reminiscent of cross-β structure [278]; in this case, it is possible that the structured nature of the constituent monomers may have prevented them from adopting a micellar arrangement, with assembly driven instead by high peptide concentration (100 μM). In the other studies, the peptide concentration was lower, so the cause of the phenomenon remains unclear. In some instances, the formation of these large, droplet-like species may be similar to liquid-liquid phase separation (LLPS), in which interactions with electrolytes often provide the charge neutralisation required for the protein to condense. LLPS has been observed in many IDPs and has been proposed to play a role in the nucleation of amyloid fibrils by Tau [349].

While one study suggested that spheroidal and droplet-like Aβ(1-40) aggregates were off-pathway from amyloid formation [292], others have suggested that that they provide a favourable environment for fibril nucleation. In the studies by Chimon *et al.* [278] and Luo *et al.* [295], spheroidal aggregates were metastable and ultimately replaced by amyloid fibrils, and both studies presented evidence to suggest that the aggregates acted as nucleation sites for amyloid fibrils. Chimon *et al.* [278] (Fig. 1.24(a-b)) observed the formation of β-sheets and amyloid-like tertiary and quaternary contacts in spheroidal aggregates, similar to the subdomains described in smaller oligomers [216, 255, 290, 296, 303, 306]. In addition, immediately before the appearance of amyloid fibrils, elongated aggregates were observed, with an apparently spherocylindrical morphology intermediate between spheroids and fibrils [278] (Fig. 1.24(b)); it is possible that these may have represented an intermediate state in the transition to amyloid fibrils, or spheroids undergoing structural distortions due to the growth of amyloid fibrils in their interior. Similarly, Luo *et al.* [295] presented AFM images showing the emergence of amyloid fibrils from within droplet-like aggregates of Aβ(1-40)

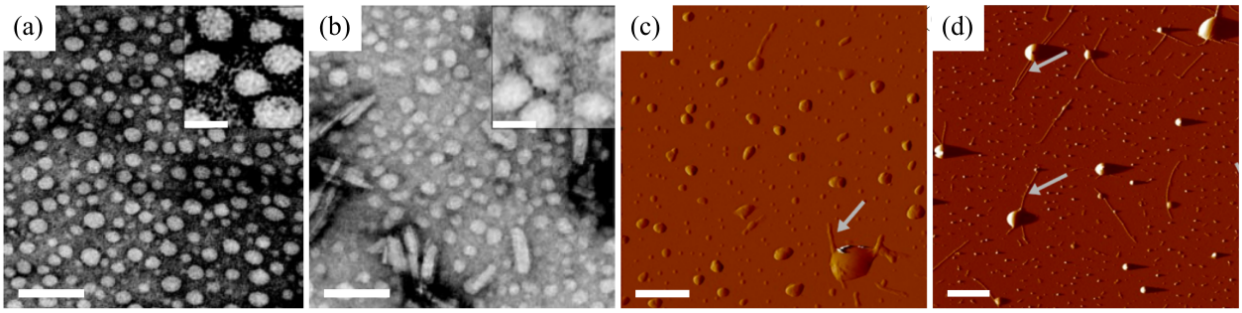

Figure 1.24: Metastable spheroidal aggregates formed by Aβ(1-40). Panels (a-b) show NS-EM images of spheroidal aggregates (a) 52 h and (b) 55 h after the start of assembly [278], with elongated morphologies beginning to appear in the second image. The scale bar is 100 nm, or 25 nm in the inset panels. Amyloid fibrils appeared shortly after the appearance of elongated assemblies [278]. Panels (c-d) show AFM images of spheroidal aggregates and amyloid fibrils (c) 57 h (scale bar 500 nm) and (d) 71 h (scale bar 2 μm) after the start of assembly [295]. Note that fibrils often appear to pierce or emerge from the spheroids, as indicated by the white arrows. All images adapted from their respective sources.

(Fig. 1.24(c-d)), sometimes accompanied by structural distortions of the droplets. Thus, even if the crowded interior of spheroidal or droplet-like aggregates slows the conformational sampling of individual constituent monomers, the total fibril nucleation rate in these aggregates may be high simply due to the large number of monomers incorporated into them, and the resulting degeneracy of possible nucleation sites.

1.4.6 Surface and membrane-bound aggregates

Many surfaces stabilise oligomers and other nonfibrillar assemblies, or catalyse their formation. Common experimental surfaces that cause this effect include polystyrene [350, 351], mica [352] and the air-water interface (AWI) [353], and lipid membranes have received considerable attention as physiological surfaces [51, 63–68, 313, 354–358]. There are a number of reasons why surfaces may induce aggregation: firstly, attractive surfaces create a concentration effect that encourages aggregation [359, 360]; secondly, surfaces typically present a less dielectric environment than the solvent, which strengthens intermolecular interactions and encourages structure formation [359, 361]; and thirdly, interactions with the surface may induce orientation preferences in the polypeptide chains, which increase the probability of forming parallel in-register β-sheets [350, 352, 362, 363]. In addition to stabilising and catalysing formation of prefibrillar assemblies, surfaces may also bind to species formed in solution, and this interaction may alter their structural properties in a way that promotes the transition to fibrils [357, 364]. The species observed either assembling on or binding to surfaces are morphologically diverse. In addition to species similar to those formed in solution, such as globular oligomers and protofibrils [334,352], structurally distinct species can occur on surfaces; Aβ has been observed to form both thin films [350–353, 365] and pseudo-crystalline sheets [352] on

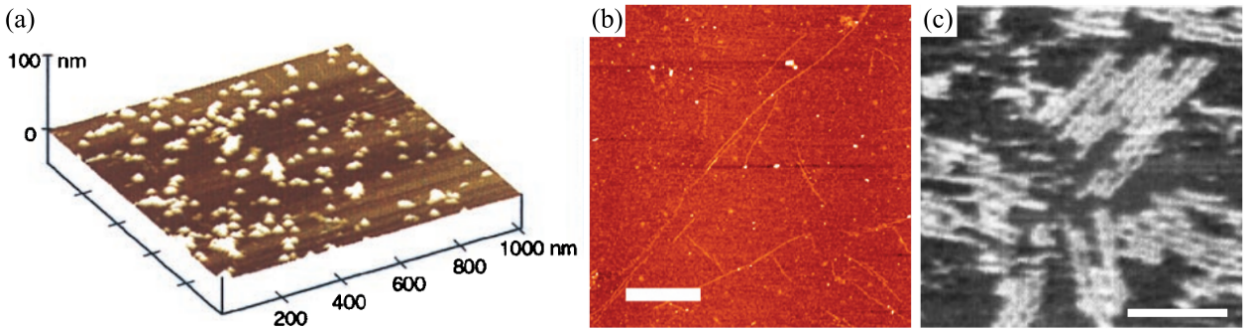

Figure 1.25: Metastable assemblies formed on non-membrane surfaces. (a) A 3D representation of an AFM image of Aβ(1-42) oligomers formed on mica [352]. (b) An AFM image of amyloid fibrils and protofibrils formed by IAPP on a hydrocarbon-coated mica surface [334] (scale bar 660 nm). (c) An AFM image of pseudo-crystalline sheets of Aβ(1-42) formed on graphite [352] (scale bar 200 nm). All images adapted from their respective sources.

experimental surfaces, and many polypeptides are able to form transmembrane oligomers [63–66, 355, 356] (see Fig. 1.18 for a summary). Examples of aggregates formed on non-membrane surfaces are shown in Fig. 1.25, and examples of membrane pores formed by N-terminally truncated Aβ isoforms are shown in Fig. 1.26.

Membrane-induced aggregation is of particular interest due to its physiological relevance. Lipid membranes are the most abundant physiological surface for which there are well-established interactions with a variety of amyloidogenic polypeptides [63–68, 355, 357]. There is evidence that membranes both induce the formation of on-pathway oligomers [357], and catalyse the conformational conversion of pre-existing assemblies [313]; in addition, many oligomers have been shown to cause membrane permeabilisation or other forms of membrane damage, with toxic consequences [63–66, 68, 355, 356]. Transmembrane pores appear to be the most common class of membrane-active prefibrillar assemblies. AFM images have revealed that many of these species are small, annular oligomers with a similar appearance to those formed by bacterial pore-forming toxins [64, 66, 355, 356]. While these oligomers are likely to be structurally diverse, AFM-validated MD simulations have predicted that pores formed by N-terminally truncated Aβ(1-42) variants (see Fig. 1.26) and several other polypeptides have a β-barrel structure [66, 354–356], and this model is supported by the observation that many toxic oligomers bind to the A11 antibody [65, 323, 328], a 'conformational' antibody that also recognises β-barrel pores formed by α-hemolysin [327]. As previously discussed in Section 1.4.2, the transition from disordered, globular oligomers to soluble β-barrel oligomers has similarities to the isotropic-nematic transition occurring in liquid crystals [310]. The soluble β-barrel oligomers predicted by molecular simulations are relatively dynamic, and are physically similar to liquid crystals; therefore, this transition may be underpinned by similar physical principles [310]. However, while soluble β-barrel oligomers appear to be relatively uncommon, there is considerably more evidence for the existence

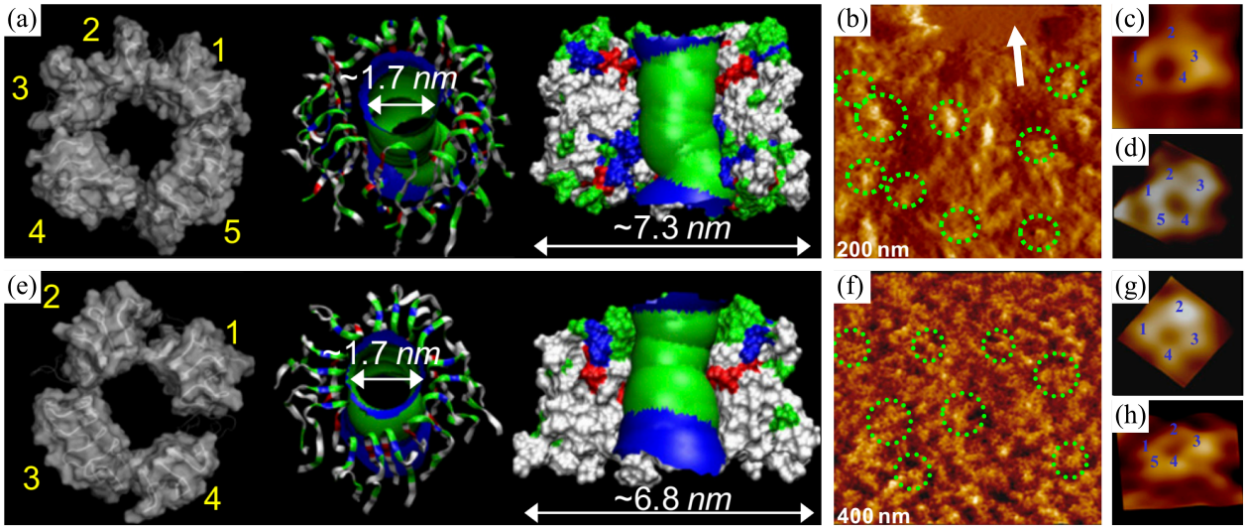

Figure 1.26: Membrane pores formed by N-terminally truncated Aβ isoforms. Panels (a-d) show MD simulations and AFM images of pores formed by Aβ(9-42), and panels (e-h) show simulations and images of pores formed by Aβ(17-42) [66]. Panels (a) and (e) show the average pore structures predicted by MD simulations, consisting of 16 Aβ monomers each: left, surface representation with subunits highlighted; centre, ribbon representation with the solvent-accessible pore predicted by the HOLE program embedded in the channel; right, side-on cut-through view of a surface representation, showing the predicted pore. In the protein structures, the colour corresponds to the hydropathy and charge of exposed residues: white, hydrophobic; green, neutral hydrophilic; blue, positively charged; red, negatively charged. In the calculated pore, the colour qualitatively corresponds to the diameter: red, constrictions; green, intermediate; blue, wider regions. Panels (b) and (f) show error-mode AFM images of reconstituted lipid bilayers containing membrane pores formed by the same peptides, with the pores enclosed in dotted circles. The white arrow indicates an area of mica without lipid bilayer. Panels (c-d) and (g-h) show high-resolution AFM images of individual channels, with image sizes: (c) 22 nm; (d) 19 nm; (g) 15 nm; and (h) 23 nm. Channel subunits are numbered, and the typical inner pore diameter is 1-2 nm. Figure adapted from Jang *et al.* [66].

of these species in membranes. This is unsurprising, as the uniaxial symmetry of the monomers within these oligomers allows each monomer to span the membrane in a way that is not possible for oligomers with a spherical symmetry. It is interesting to note that both AFM images and MD simulations suggest that transmembrane β-barrel oligomers are relatively fluid, and are organised into loosely associated oligomeric subunits that cluster together to form a single channel (see Fig. 1.26). This organisation allows channels to have a range of different sizes, and suggests that they may grow by insertion of subunits; thus, membrane pores may form by the stepwise assembly of smaller oligomers [66, 355]. In addition to channel formation, some oligomers disrupt membranes by other mechanisms; for example, globular oligomers formed by Aβ(1-42), α-syn, and poly-Q induce membrane permeabilisation without containing an obvious pore [51], and oligomers formed by IAPP have been shown to more generally disrupt the structure and integrity of membranes [366].

1.4.7 Summary

Metastable, non-amyloid self-assembly states associated with amyloid formation are highly diverse, but can be split into several broad classes on the basis of their morphology. Because the morphology of these species can often be attributed to general physical principles that drive their formation, members of the same class often have similar physical, structural, and functional properties. For example, many amyloidogenic peptides are able to form remarkably similar ion channels in lipid membranes, with shared structural features such as parallel β-hairpins and organisation into smaller domains, and a shared mechanism of toxicity [64–66, 355, 356, 367]. Similarly, polypeptides with little to no sequence identity are able to form disordered, globular oligomers simply as a result of the poor solubility of all or part of the polypeptide chain [283, 301, 304, 308]. Although their aggregation is initially driven by poor solubility, these oligomers often have shared structural and functional characteristics, such as the progressive development of amyloid-like tertiary and quaternary contacts [220, 278, 306], a transition to a filamentous morphology with increasing size [220, 304, 307, 343], and exposed hydrophobics with the potential to cause toxicity [320–322]. Although there are recurring structural features such as β-hairpins [255, 290], there do not appear to be any universal structural motifs, and there is certainly no 'fold' shared by all amyloid-related oligomers and protofibrils. Nonetheless, many characteristics of the aggregation, amyloidogenicity, and toxicity of these species can be explained in terms of general physical, structural, and biological principles, so that polypeptides with similar amino acid composition, such as Aβ and IAPP, form similar oligomers and amyloid fibrils [142, 144, 301, 304], and may have similar mechanisms of toxicity [51]. As with mature amyloids, where there is also considerable polymorphism (see Section 1.3), this means that insights into oligomers formed by one polypeptide are transferrable to similar polypeptides. Moreover, small molecules or proteins that target diverse oligomers from the same class, such as the A11 antibody, which appears to generally bind β-barrel oligomers [323,

326–328], may have general therapeutic potential.

1.5 Mechanisms and kinetics of amyloid fibril formation

In order to limit or control the self-assembly of amyloids and metastable aggregates, it is necessary to understand not only the structure of these species, but also the mechanisms by which they form. While the structural approaches detailed in Section 1.3.1 give snapshots of the self-assembly process that can be used to suggest mechanisms, a purely structural approach is ill-suited to test these mechanisms. Moreover, the dynamic, partly ordered nature of many of the species formed during amyloid self-assembly means that high-resolution structures can often be difficult to obtain, and the rapidity of many processes and transience of conformational transition states and short-lived intermediates leaves little time for structural investigation. Thus, while more detailed mechanistic information can be acquired via structural means, especially with measures to arrest the self-assembly process, kinetic data are needed to fully understand the self-assembly process. These can be obtained through spectroscopic techniques, such as solution-state NMR or CD spectroscopy, as well as real-time imaging techniques such as HS-AFM [368] or high-resolution fluorescence microscopy (Section 1.3.1). In addition, fluorimetry using ThT or other dyes has become a workhorse technique to assay the concentration of fibril-like species as an ensemble, subject to the caveats that these dyes are not ideal probes for amyloid, and do not detect many non-amyloid species [93, 94]. Light-scattering techniques such as dynamic light-scattering (DLS) or multi-angle light-scattering (MALS) also provide information about the size and hydrodynamic properties of species that can be used to further characterise the self-assembly process [292, 369, 370]. Similarly, imaging techniques such as NS-EM and AFM can be used to obtain size distributions of fibrils and self-assembly intermediates, which are specific predictions made by most kinetic models and can thus be used to constrain model fitting [371, 372]. Lastly, theoretical approaches such as molecular simulations and kinetic modelling provide highly complementary approaches in this field, and the workflow of proposing mechanistic models and testing their mathematical predictions against the available kinetic data has proved highly productive [9, 373]. In this section, kinetic and structural insights into amyloid self-assembly are discussed, as well as mathematical models and general analytical theories of the self-assembly process.

1.5.1 Nucleated polymerisation

Kinetic studies of amyloid self-assembly often reveal a sigmoidal progress curve, with the accumulation of amyloid mass beginning at a low rate, gathering speed, and then slowing down again due to the depletion of soluble precursors. As a result, these progress curves are often conveniently divided into three phases of self-assembly: the lag phase, the 'growth' phase, and the plateau phase (Fig. 1.27(a)), although

this is usually an artificial distinction that is not underpinned by a fundamental change in the self-assembly mechanism [374]. Amyloid formation is typically considered to be a nucleated polymerisation (NP), meaning that amyloids are initially formed by a nucleation event, generally defined as the crossing of a size or conformation-dependent free energy barrier to form a minimally sized self-assembling species, and then subsequently grow by polymerisation (Fig. 1.27(b)) [375]. Nucleation that occurs independently of pre-existing fibrils is termed primary nucleation, and will later be contrasted with secondary nucleation, in which pre-existing fibrils provide a surface that catalyses further nucleation events [376]. While variant models such as nucleated conformational conversion (NCC) are often described as an alternative to NP models [283, 345, 377–379], they still involve nucleation and polymerisation, regardless of whether polymerisation proceeds via addition of monomers or oligomers to growing aggregates; as such, while models involving conversion of intermediates are referred to as NCC by some authors [345, 378, 379], they are referred to as NP by other authors [224, 380], and the latter convention is followed here. Therefore, the discussion of multi-step nucleation models provided in much of this section contains arguments that are also applicable to scenarios previously described as NCC, since there is often no formal distinction between the two. In addition to the basic processes of primary nucleation and polymerisation, other processes may occur. These often include secondary (ie. fibril-dependent) processes such as fragmentation, where fibrils break in two, and secondary nucleation, where existing fibrils provide a surface that catalyses further nucleation events (Fig. 1.27(c)) [381].

In vivo, and in ensemble *in vitro* experiments, the processes of nucleation and polymerisation occur progressively and affect different fibrils at the same time. Early studies proposed that the lag phase represented the time required for nucleation to occur, while the 'growth' phase constituted the period of time in which monomer was incorporated into the newly nucleated fibrils [382, 383], and many authors persist in this interpretation. However, this is usually only the case in small volumes, where a limited number of nucleation events are expected to occur (Fig. 1.27(d)). In a typical experiment containing approximately $10^9 - 10^{16}$ monomers, one would expect large numbers of individual nucleation events to occur (perhaps $10^4 - 10^{13}$ events, if fibrils have a typical size of $10^3 - 10^5$ monomers and the rate of fragmentation is low); thus, the timescale for the first nucleation event is much less than the timescale for monomer depletion, so that nucleation occurs continuously throughout the lag phase (Fig. 1.27(e)), rather than as a single event [374]. Moreover, the specific growth rate of fibrils is usually expected to be highest when the free monomer concentration is highest, which occurs at the start of the lag phase. Thus, the distinction between 'lag' and 'growth' phase in most experiments is not because nucleation and elongation of the entire ensemble occur at different times, but because progressive nucleation causes the accumulation of elongating filaments, with the increasing number of filaments causing a continuous increase in the total fibrillisation rate and thus the slope of the self-assembly curve. In addition, secondary (ie. fibril-dependent) processes such as fragmenta-

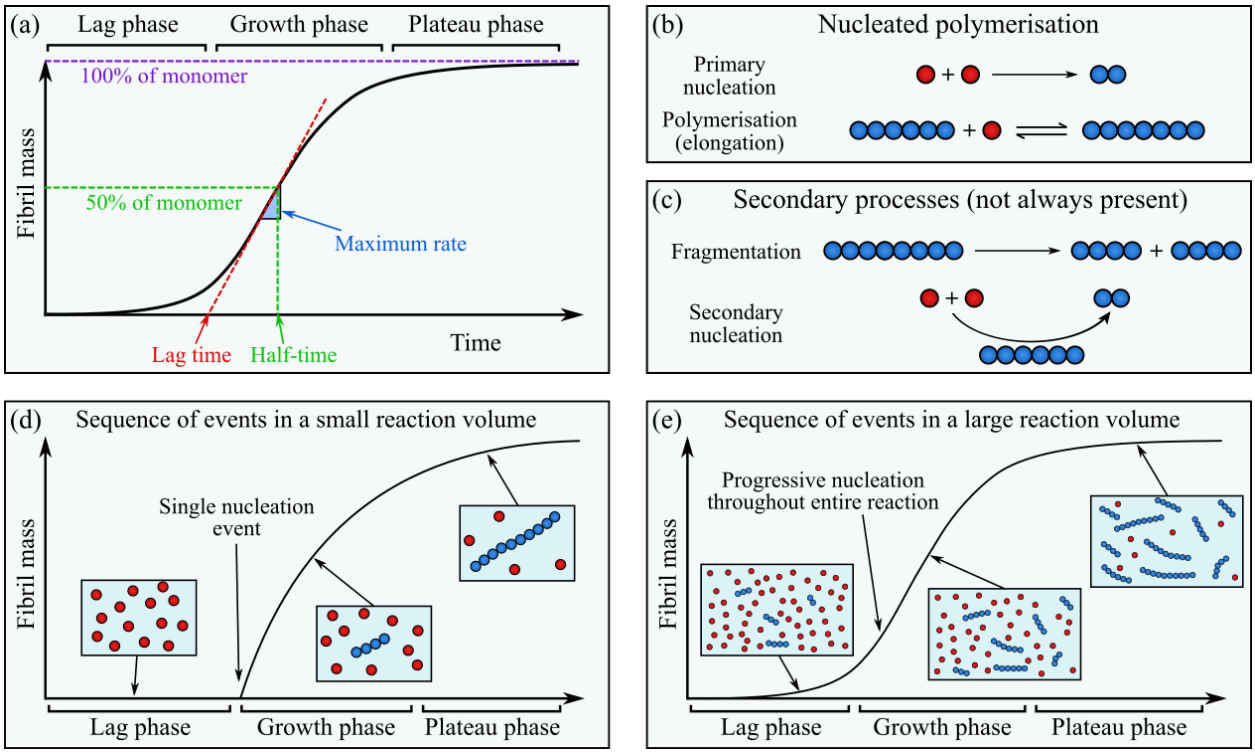

Figure 1.27: Nucleated polymerisation of amyloids. (a) Amyloid formation often has a sigmoidal progress curve. The half-time τ_{50} is defined as the time at which half of the monomer has been converted to an amyloid state, and according to one definition [374] the lag time τ_{lag} is found by extrapolating a tangent to the curve from the inflection point back to the time axis. (b) Nucleated polymerisation is characterised by two basic processes, primary nucleation and polymerisation (elongation). Simplified schematics of these processes are provided in this panel, with non-fibrillar monomers represented as red spheres, and monomers incorporated into fibrils shown as blue spheres. In primary nucleation, n_c monomers assemble to form a minimally-sized fibril; in this instance $n_c = 2$. In polymerisation, a fibril grows by incorporation of monomers or other precursors. (c) In addition to primary nucleation and polymerisation, other processes may occur. These include secondary (fibril-dependent) processes such as fragmentation, where a fibril breaks in two, and secondary nucleation, where a fibril provides a surface that catalyses further nucleation events. Same colouring as previous panel. (d) In a small reaction volume (typically fl-pl), polymerisation depends on a single nucleation event; thus, the lag time is the time required for this event to occur, and polymerisation only begins once the first fibril nucleates. (e) In a larger reaction volume (including most experimental contexts), total polymerisation results from the cumulative growth of many thousands or millions of fibrils. These fibrils are nucleated progressively throughout the time course, and the accumulation of greater numbers of fibrils results in a progressive increase in total fibrillisation rate, which is responsible for the smooth, sigmoidal kinetics. Figure based on information from the sources cited in Section 1.5.1.

tion and secondary nucleation can create positive feedback, enhancing the distinction between the lag and growth phases [374].

1.5.2 Primary nucleation

Primary nucleation is the process by which amyloid fibrils first form, without need for pre-existing amyloid fibrils (Fig. 1.27(b)). Broadly speaking, nucleation is the emergence of a new thermodynamic phase by crossing a free energy barrier, and is the mechanism by which first-order phase transitions usually occur. In classical nucleation theory, which was originally developed for non-amyloid systems such as nucleation of liquid droplets from vapour or solution, this barrier results from the fact that the free energy of the system initially increases as the new phase grows, before reaching a maximum, and then beginning to decrease with continued growth. The maximally unstable species is termed the critical nucleus, and the nucleation rate is defined as the rate at which nuclei proceed to form larger species for which growth is stable, rather than disassembling or otherwise returning to the old phase [384]. In the context of amyloid, this implies that growth of the amyloid is initially unfavourable, but becomes favourable past a certain point, so that the nucleation rate is given by the rate at which critical nuclei proceed to form larger species rather than reverting to soluble monomer. This sort of nucleation can be termed one-step nucleation. However, it is now clear that first-order phase transitions can often have two-step or multi-step nucleation mechanisms, proceeding via metastable intermediates that are distinct from the old phase, and separated from the new phase by an additional free energy barrier [385]. Multi-step nucleation was first identified in the context of protein crystallisation [386, 387], but has since been described in non-biological contexts such as AgBr and acetic acid crystallisation [388, 389], as well as polymerisation of Boc-diphenylalanine [390], sickle-cell haemoglobin (HbS) [391], and now many amyloids [217, 251, 278, 283, 287, 335, 345, 346, 370, 392, 393]. The presence of additional free energy barriers is often the result of a more complex free energy landscape with multiple degrees of freedom, rather than a simple size-dependence of the free energy of newly formed clusters; these can include differences in supramolecular organisation and the conformation of the assembled monomers. In the context of amyloid formation, commonly proposed causes of free energy barriers include nucleation of prefibrillar intermediates [347, 394], expulsion of ordered water [395, 396], and reorganisation of the polypeptide chains to form a cross-β structure [315, 335, 394, 397–401]. In non-amyloid systems, intermediates are often distinct solid phases [390] or liquid-like droplets [386–388, 391]; in amyloid formation, proposed nucleation intermediates include partly ordered [251, 283, 287, 345, 346] or native-like [256, 281, 282] globular oligomers, droplet-like spheroidal aggregates [295], and protofibrils [331, 335]. The aim of this subsection is to review the various underlying mechanisms of one-step and multi-step primary nucleation of amyloids, and the role of intermediates in this process.

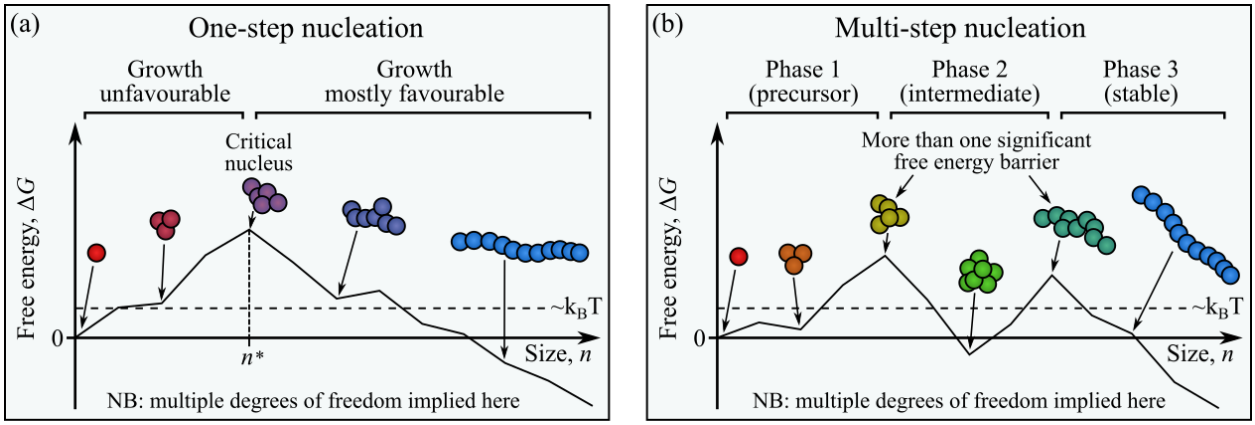

Figure 1.28: Thermodynamics of nucleation (part 1). (a) In one-step nucleation, a new thermodynamic phase emerges by crossing a free energy barrier that is often, but not always, associated with a change in the size of the nucleating phase. This panel shows a plausible nucleation mechanism of an amyloid fibril, with multiple degrees of freedom (size, arrangement of constituent monomers, and monomer conformation). For visual simplicity, it is assumed that size is the only slowly equilibrating degree of freedom, so that oligomers of a particular size rapidly assume a particular arrangement and conformational state. This linearises the free energy profile, allowing the free energy ΔG to be plotted as a function of size n. In the annotated schematics, spheres represent individual self-assembling monomers, and the colour of the spheres represents the conformational state, ranging continuously from red (monomer-like) to blue (fibril-like). The least stable species, the critical nucleus, is shown in the centre in purple, and has size n^*. Successive growth steps are mostly unfavourable for oligomers smaller than the critical nucleus, and mostly favourable for those that are larger. In order for nucleation to occur, the critical nucleus must first form as a fluctuation, and then be stabilised by further growth, conformational change, or some other variation with respect to a slow degree of freedom. (b) Multi-step nucleation has more than one significant free energy barrier, when compared to k_BT. In this schematic, there are two significant free energy barriers, with an intermediate phase (green) in between. As with the previous panel, changes in colour of the oligomers represent continuous variation in the conformational state. Figure based on information from the sources cited in Section 1.5.2.

1.5.2.1 Phenomenological kinetics

The rate of primary nucleation is often described by a phenomenological rate law of the form [2, 375],

$$\Phi_n(t) = k_n m(t)^{n_c}, \tag{1.2}$$

where $\Phi_n(t)$ is the molar rate of formation of new fibrils by primary nucleation, k_n is the effective n_c^{th}-order nucleation rate parameter, $m(t)$ is the free monomer concentration, and n_c is the effective reaction order. In one-step nucleation, the nucleation theorem [402] allows the effective reaction order n_c to be directly related to the size of the critical nucleus n^*; the exact relationship between the two depends on the mechanism by which the nucleation barrier is crossed [224, 384], and is discussed in greater detail in the following subsections. In multi-step nucleation, the same rate law is still valid if all intermediate populations are at a steady state, and it is still possible to relate n_c to n^* with the aid of analytical theory [224, 380]. However, if intermediate populations are not at a steady state, then it is necessary to describe nucleation as a cascade of sequential assembly or conversion processes [380], in which case Eq. (1.2) alone is not sufficient.

1.5.2.2 Classical nucleation theory

Classical nucleation theory, which was originally developed for non-amyloid systems such as condensation of liquid droplets [384], provides a starting point for theories of the thermodynamics and kinetics of amyloid nucleation. In classical nucleation theory, the free energy profile of nucleation has only a single degree of freedom, the size of the nucleating phase, and the free energy of this phase results from the balance of volume and interfacial terms. While the former becomes more favourable with increasing size of the nucleating phase, the latter becomes less favourable, and the balance of the two results in a peak in the free energy profile that must be crossed for nucleation to occur, resulting in one-step nucleation [384]. For example, during nucleation of condensed spherical droplets (Fig. 1.29(a)), the free energy ΔG is expressed as

$$\Delta G = -\frac{4}{3}\pi r^3 \rho_n \Delta\mu + 4\pi r^2 \sigma, \tag{1.3}$$

where r is the droplet radius, $\rho_n = 1/v_{\text{eff}}$ is the density of molecules in the nucleating phase, inversely proportional to the effective volume v_{eff} of those molecules, $\Delta\mu$ is the chemical potential of the pre-existing phase minus that of the nucleating phase, and σ is the droplet surface tension [384, 403]. Nucleation occurs under conditions where $\Delta\mu > 0$, in which case the first term accounts for favourable contributions due to increasing volume of the stable phase, and the second term accounts for the unfavourable contribution of

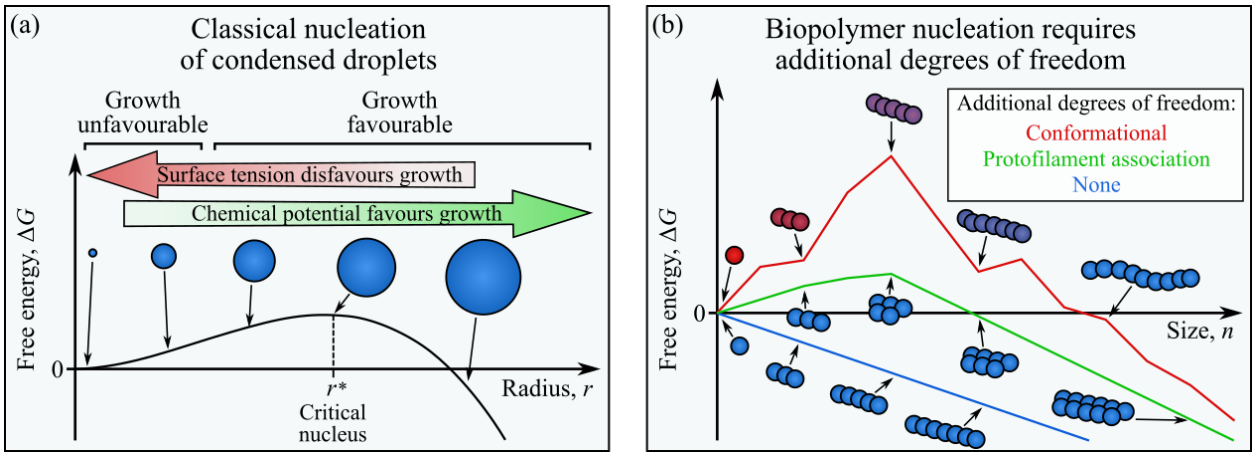

Figure 1.29: Thermodynamics of nucleation (part 2). (a) Classical nucleation of condensed spherical droplets, showing a plot of the free energy ΔG against the droplet radius r, annotated with representations of droplets of different sizes. The droplet radius is the only degree of freedom, and the free energy ΔG is the sum of unfavourable surface tension ($\propto r^2$) and favourable bulk ($\propto r^3$) terms. For small droplets, the surface tension term dominates, making growth unfavourable. For larger droplets, the favourable bulk term dominates, so that growth is favourable. The critical nucleus occurs when ΔG reaches a maximum. (b) The same balance between bulk and interfacial terms does not exist for truly one-dimensional biopolymers without additional degrees of freedom, as their bulk and interfacial terms are both grow linearly with size. In this panel, three plausible free energy profiles are plotted for nucleation of amyloid fibrils, with free energy ΔG shown as a function of size n. The colour of the linearised free energy profiles corresponds to whether there are any additional degrees of freedom: blue, none (ie. size only); green, supramolecular arrangement of monomers; red, conformational. For convenience, any additional degrees of freedom are assumed to equilibrate rapidly compared to changes in size, so that they can be assumed to reach a local minimum and the free energy can be plotted as a linearised function of the size. For a more realistic representation of a free energy surface with more than one slow degree of freedom, see Fig. 1.30. The curves are annotated with schematics representing possible oligomer structures; constituent monomers are represented as spheres, and the colour of the spheres represents the conformational state, varying continuously from red (monomer-like) to blue (fibril-like). For nucleation of one-dimensional polymers without additional degrees of freedom, free energy is a linear function of size, so there is no critical nucleus. Introducing additional degrees of freedom can lead to a peak in the free energy profile, which is the critical nucleus. Figure based on information from the sources cited in Section 1.5.2.2.

surface tension between the old and new phases. In a dilute solution,

$$\Delta\mu = k_B T \ln\left(\frac{c}{c_{\text{sat}}}\right), \tag{1.4}$$

where c the concentration of molecules of the old phase, and c_{sat} is the critical concentration above which the new phase nucleates. For spherical droplets, the free energy has a maximum when

$$\frac{\partial \Delta G}{\partial r} = -4\pi r^2 \rho_n \Delta\mu + 8\pi r\sigma = 0, \tag{1.5}$$

which is the condition for the critical nucleus [403]. Thus, the critical nucleus has radius

$$r^* = \frac{2\sigma}{\rho_n \Delta\mu}, \tag{1.6}$$

and free energy

$$\Delta G^* = \frac{16\pi\sigma^3}{3(\rho_n\Delta\mu)^2} = \frac{2}{3}\rho_n \Delta\mu (r^*)^3. \tag{1.7}$$

In other systems, there will be a different relationship between the size and free energy of the nucleating phase, which will give rise to a different definition of the size and free energy of the critical nucleus. In general, at a non-equilibrium steady state where species no larger than the critical nucleus are in local thermodynamic equilibrium with one another, the homogeneous nucleation rate has the expression [384]

$$\Phi_n = A(c) \exp\left(-\frac{\Delta G^*}{k_B T}\right), \tag{1.8}$$

where $A(c)$ is a pre-exponential factor that accounts for the concentration of precursors and the rate of successful barrier crossing, and is approximately proportional to c for nucleation of a condensed phase ($A(c) \sim c$) [384]. For diverse geometries, including cases where the critical nucleus is small so that discrete size effects are important, as is the case with amyloid fibrils [404], nucleation theorem states that [402]

$$\frac{\partial \Delta G^*}{\partial \Delta\mu} = -n^*, \tag{1.9}$$

where n^* is the number of molecules in the critical nucleus. Thus, taking the logarithmic derivative of Eq. (1.8) with respect to $\Delta\mu$,

$$\frac{\partial \ln \Phi_n}{\partial \Delta\mu} \approx \frac{\partial \ln A(c)}{\partial \Delta\mu} + \frac{n^*}{k_B T}. \tag{1.10}$$

Multiplying both sides by $\partial\Delta\mu/\partial \ln c$, which can be obtained by differentiating Eq. (1.4), and applying $\partial \ln A(c)/\partial \ln c \approx 1$,

$$\frac{\partial \ln \Phi_n}{\partial \ln c} \approx 1 + n^*. \tag{1.11}$$

Noting from Eq. (1.2) that $\partial \ln \Phi_n / \partial \ln c = n_c$, and exchanging the order of terms,

$$n_c \approx n^* + 1. \tag{1.12}$$

This relationship is often applied to nucleation of amyloids, in which the critical nucleus is considered to be a fibrillar or non-fibrillar oligomer of size n^* [375]. However, this relationship is not necessarily correct, as classical nucleation theory and its extensions do not necessarily apply to amyloids, and the identity $n_c \approx n^*$ is expected in many non-classical cases where it is conformational change, rather than growth, that stabilises the critical nucleus [224, 380].

An important consequence of the insights of classical nucleation theory and statistical physics is that, regardless of whether nucleation is classical or non-classical, amyloid formation can only occur as a nucleated phase transition if each assembled monomer interacts with more than two other monomers in the fibril, or has additional degrees of freedom such as conformational heterogeneity. In the context of classical nucleation theory, this is because the bulk and interfacial free energy terms of a one-dimensional polymer with only nearest-neighbour interactions between subunits and no additional degrees of freedom are linear functions of its size. Thus, the free energy profile has no maximum except for the soluble monomer, meaning that there is no free energy barrier and a nucleated phase transition cannot occur (Fig. 1.29(b)) [384]. However, there is also a more general principle from statistical physics, that equilibrium phase transitions do not occur in 1D systems without non-nearest-neighbour interactions [405, 406], meaning that the requirement for additional interactions or degrees of freedom is more general than classical nucleation theory alone would suggest. In reality, of course, amyloids usually have multiple protofilaments, non-nearest-neighbour interactions between monomers, and additional conformational, structural, and motional degrees of freedom; theoretical treatments have shown that these factors allow nucleation to occur [404, 407]. For example, interactions between laterally associated protofilaments can give amyloids a quasi-2D character, resulting in a nucleated phase transition [404]. Due to the small, discrete number of protofilaments in amyloid fibrils, theories of this sort predict sharp jumps in n_c as c varies, resulting from changes in the number of protofilaments in the critical nucleus [404]. However, these models only produce nucleated assembly when the interaction free energy between laterally associated monomers in different protofilaments is comparable to or greater than $\Delta\mu$. As discussed in Section 1.3.3 and Section 1.3.5, lateral interactions between monomers in different protofilaments are typically weak compared to interactions between hydrogen-bonded monomers in the same cross-β protofilament; thus, many amyloids consist of single protofilaments [114, 119, 131, 132, 135, 148, 149], and others exist polymorphically as either a single protofilament or several [136, 143, 144, 147], despite the fact that the highly cumulative nature of inter-protofilament interactions would usually be expected to stabilise the latter. In these systems, as well as others at sufficiently high supersaturation, conformational degrees of

freedom are likely to be required for nucleation.

1.5.2.3 The importance of non-fibrillar assembly states in amyloid nucleation

As discussed in Section 1.4, amyloidogenic polypeptides often form metastable assemblies such as oligomers and protofibrils, which are structurally distinct from amyloid fibrils. Many studies have proposed that these species are involved in nucleation, with representatives from Aβ [216,278,285,287,295,331,345], α-syn [335, 346], Tau [392, 393], β_2m [256], poly-Q [251, 268], and many other amyloidogenic polypeptides [217, 258, 283, 306, 318, 370, 408] all proposed to act as precursors for amyloid fibrils. In some cases, there is direct evidence to support this role, such as images revealing the emergence of amyloid fibres from condensed droplets of Aβ(1-40) [295], or the observation that kinetically trapped α-syn protofibrils undergo a direct conversion to amyloid fibrils following a temperature change [335]. In other cases, the evidence is less direct, but not necessarily weaker; for example, studies of Tau [401] and Ure2p [217] have shown that the simplest model that explains the kinetics of oligomer and fibril formation is one where the oligomers are structurally distinct from fibrils, but situated on-pathway. The additional conformational degrees of freedom associated with the transition from a non-amyloid aggregate to an amyloid state provide one possible justification for why amyloid formation is a nucleated process [407]. Nucleation of intermediates or structural conversions between sequential intermediates can also introduce extra free energy barriers, resulting in a multi-step nucleation mechanism in which the intermediate and amyloid are distinct phases. Likely examples of this include oligomer and protofibril-dependent nucleation of Aβ(1-40) [278, 295, 345], Aβ(1-42) [216], Sup35p [283], and α-syn [335], under appropriate conditions. In other cases, the distinction between non-fibrillar precursors and amyloid fibrils is less clear, with a smooth structural transition from a non-amyloid to an amyloid state occurring after nucleation, as a result of coupling between size and structure [409]; these cases are arguably one-step nucleation, as the precursor and amyloid are not truly distinct phases. An example of a simulated free energy surface for fibril nucleation is shown in Fig. 1.30. In this instance, which comes from coarse-grained simulations of Aβ(1-40), the transition from a pre-fibrillar state dominated by β-barrel conformers to a fibrillar state occurs between the tetramer (IV) and the pentamer (V), and manifests as a saddle point in the free energy surface [315]. It should be noted that, although the single free energy barrier in this figure suggests a one-step nucleation mechanism, the authors do not make this claim, and there are additional degrees of freedom that are not represented on this free energy surface. Simulations on polyvaline have shown that multi-step nucleation processes may appear single-step or barrierless when viewed in lower dimensional spaces [397].

Regardless of whether the mechanism is one-step or multi-step, nucleation of the majority of amyloids initially involves oligomers that are structurally distinct from mature fibrils, and in many cases these oligomers lack cross-β structure altogether [216, 251, 256, 281, 283, 287, 299, 318, 345]. There are several

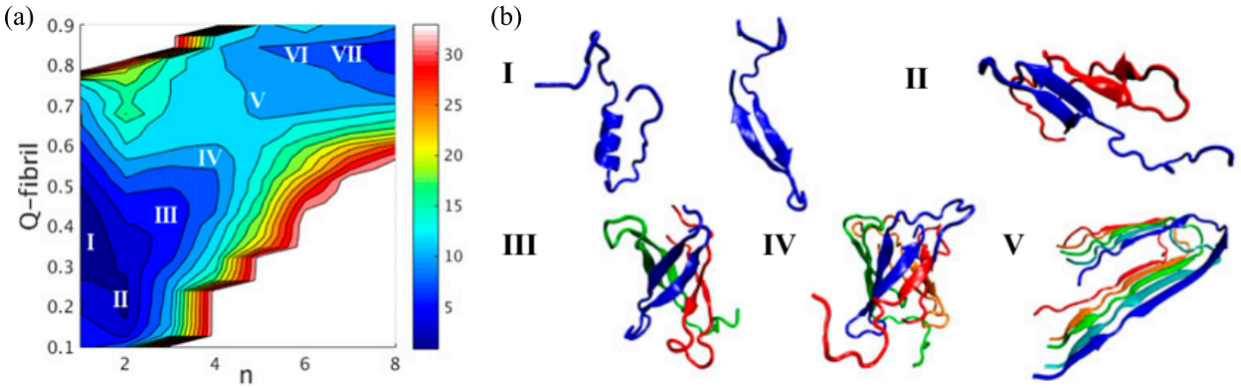

Figure 1.30: A simulated free energy surface for nucleation of Aβ(1-40) fibrils, from coarse-grained MD simulations by Zheng *et al.* [315]. (a) The free energy surface. The axes are *n*, the effective oligomer size, and *Q-fibril*, a numerical measure of the structure's similarity to the fibril structure published by Petkova *et al.* [218]; the colour corresponds to the free energy in the Grand canonical ensemble (kcal.mol^{-1}; key to right of plot). The simulation was performed at a concentration of 1 mM, and a correction was implemented to reduce the effective concentration to 40 μM. (b) Representative conformations corresponding to the most populated clusters in the simulations. The Roman numerals correspond to the size of the oligomers, and are marked on the free energy surface in panel (a). Both helical and hairpin-like conformations were observed for the monomer. Note that the authors used umbrella sampling to selectively sample regions of conformational space containing structures similar to that published by Petkova *et al.* [218]. This does not affect the reported free energies, as a correction is made as part of the umbrella sampling procedure. Nonetheless, since conformational sampling was slow without this procedure, other areas of conformational space may be unexplored, including those close to other fibril polymorphs. It should also be noted that the transition from a pre-fibrillar β-barrel state (eg. panel (b), IV) to a fibril-like state (eg. panel (b), V) is not necessarily direct, and the authors proposed that a significant amount of backtracking was likely to have to occur. Figure adapted from Zheng *et al.* [315].

lines of evidence to support both the broader and narrower points. Firstly, on-pathway oligomers formed by polypeptides such as α-syn, Tau, and Ure2p all have distinct self-assembly kinetics compared to fibrils, with greater accumulation of these oligomers implying slower elongation, and thus less efficient templating of the conformation of new monomers; in turn, this indicates that there are underlying structural differences [156, 217, 346, 401]. Fig. 1.31 shows an example of these measurements for Tau, from Shammas *et al.* [393]. Secondly, while amyloidogenic monomers are often assumed to be random coils that are able to rapidly sample conformational space, both experimental and computational evidence suggests that the density, structure content, and conformational dynamics of many amyloidogenic monomers are not dissimilar from small, disordered, globular oligomers [268, 272]. In this case, globular oligomers have the advantage as environments for cross-β structure formation, as monomers do not benefit from significantly enhanced conformational sampling [268], experimental and computational results show that progressive growth of oligomers promotes secondary and higher-order structure formation [220,278,290,296], including amyloid-like structural motifs [216,255,278,290,296,303,306], and amyloid-like conformers that arise in condensed phases can be rapidly stabilised by intermolecular β-sheet formation without need for further molecular collisions [268]. This may also explain the observation that the amyloidogenicity of small peptides correlates with their propensity to form globular oligomers [287], although this correlation could exist because both depend on another factor, such as poor solubility. Thirdly, while small non-amyloid oligomers are commonly observed in experiments and simulations [216,220,223,256,268,272–275,287,289,290,293,294,298,299], and there is strong evidence that many of these are involved in nucleation, evidence for small amyloid-like oligomers [301,306,410,411] is comparatively rare. This agrees with the suggestion of multiple authors that cross-β structure is stabilised by progressive increases in oligomer size, and is not stable in small oligomers formed by many polypeptides [268,410–412]. Aβ, whose oligomers have been extensively studied by computational techniques on account of their small number of atoms and pathogenic role, has been shown to be incapable of maintaining a fibrillar structure in the dimer [315, 410, 411], relaxing from an initially fibrillar conformation to a disordered, non-amyloid state on a timescale of $\lessapprox 50$ ns [410]. Thus, while it has been proposed that the rate-determining step in Aβ self-assembly is formation of structurally committed on-pathway dimers from an amyloid-like monomer conformer [263], explaining why $n_c \approx 2$ [54], the fact that Aβ dimers relax to a non-fibrillar state on a timescale several orders of magnitude less than the typical timescale for addition of monomers to fibril ends ($\sim$10 s, at a typical concentration of 2 μM Aβ(1-42) [54]) indicates that the fate of an Aβ aggregate cannot be determined at the dimer. Otherwise, on-pathway dimers would be much more likely to relax to off-pathway dimers than proceed to on-pathway trimers, and the concentration-dependence of the ratio of these rates would entail $n_c = 3$. In other words, $n_c = 2$ is only possible if the majority of accessible dimer conformations are on-pathway, meaning that Aβ self-assembly initially proceeds via disordered dimers, with cross-β structure arising in larger oligomers. This is likely to

be the case with other disordered peptides and IDPs that have low-order nucleation kinetics, such as α-syn, Tau, and poly-Q, which have low-order primary nucleation [346, 393, 413] and for all of which there is evidence to support an initial non-amyloid assembly step [251, 346, 393].

Thus, nucleation of amyloids by many polypeptides initially involves non-amyloid self-assembly states prior to the emergence of cross-β structure. In addition, in systems where direct evidence is not available, it is not necessarily the most probable *a priori* hypothesis that nucleation should proceed without non-amyloid precursors. While the multi-layered subunit structure of some amyloids [117, 118, 157, 158] suggests that cross-β structure may be stable in assemblies as small as the dimer, many amyloids arise from highly disordered monomers that are unable to form long-lasting tertiary structure, and similar structure propensities are often observed in small oligomers [216, 268, 280, 290, 304]. In these cases, nucleation may prefer non-amyloid precursors until aggregates have reached sufficient size for cross-β structure to be stable. Although this argument does not apply to oligomers formed by more structured proteins, native-like β_2m oligomers have also been demonstrated to have non-amyloid structures [129, 256]. Thus, there may be distinct reasons why both disordered and native-like monomers typically form non-amyloid oligomers before proceeding to amyloid fibrils. Lastly, it should be noted that some polypeptides may initially aggregate via amyloid-like or non-amyloid pathways depending on the conditions; high supersaturation, molecular crowding, high sidechain hydrophobicity, and low β-propensity are predicted to favour an initially unstructured aggregation pathway, followed by conversion to amyloid, while marginal supersaturation, low sidechain hydrophobicity, and high β-propensity are predicted to favour early cross-β structure formation [309, 347, 394, 414–418].

1.5.2.4 Structural and morphological differences between on-pathway and off-pathway aggregates

Although many amyloidogenic polypeptides form oligomers that are distinct from mature amyloids *en route* to amyloid formation, this does not mean that the majority of non-fibrillar assemblies are on-pathway, and many have been shown to be off-pathway. This raises the questions: what characteristics make an aggregate a suitable precursor for cross-β structure formation, and at what point do the amyloidogenic and non-amyloidogenic pathways diverge?

As discussed in Section 1.4.2, progressive increases in the size of globular oligomers from either an unstructured or native-like starting point are often coupled to structural changes that make the transition to fibrils more likely to occur. Globular oligomers formed by disordered polypeptides typically have an intermediate level of secondary structure [99, 216, 251, 284, 286, 287, 290, 296, 300, 301, 303, 306–308], and often contain subdomains that have amyloid-like tertiary and quaternary contacts [216, 255, 278, 290, 296, 303, 306]. In addition, there is a progressive increase in structure content with increasing oligomer size [220, 290]. Although globular oligomers often develop non-amyloid structural motifs [220, 273, 274, 290, 301, 303, 305, 315], amyloid-like contacts also develop [220, 278, 290, 296, 305, 306, 315], and partly

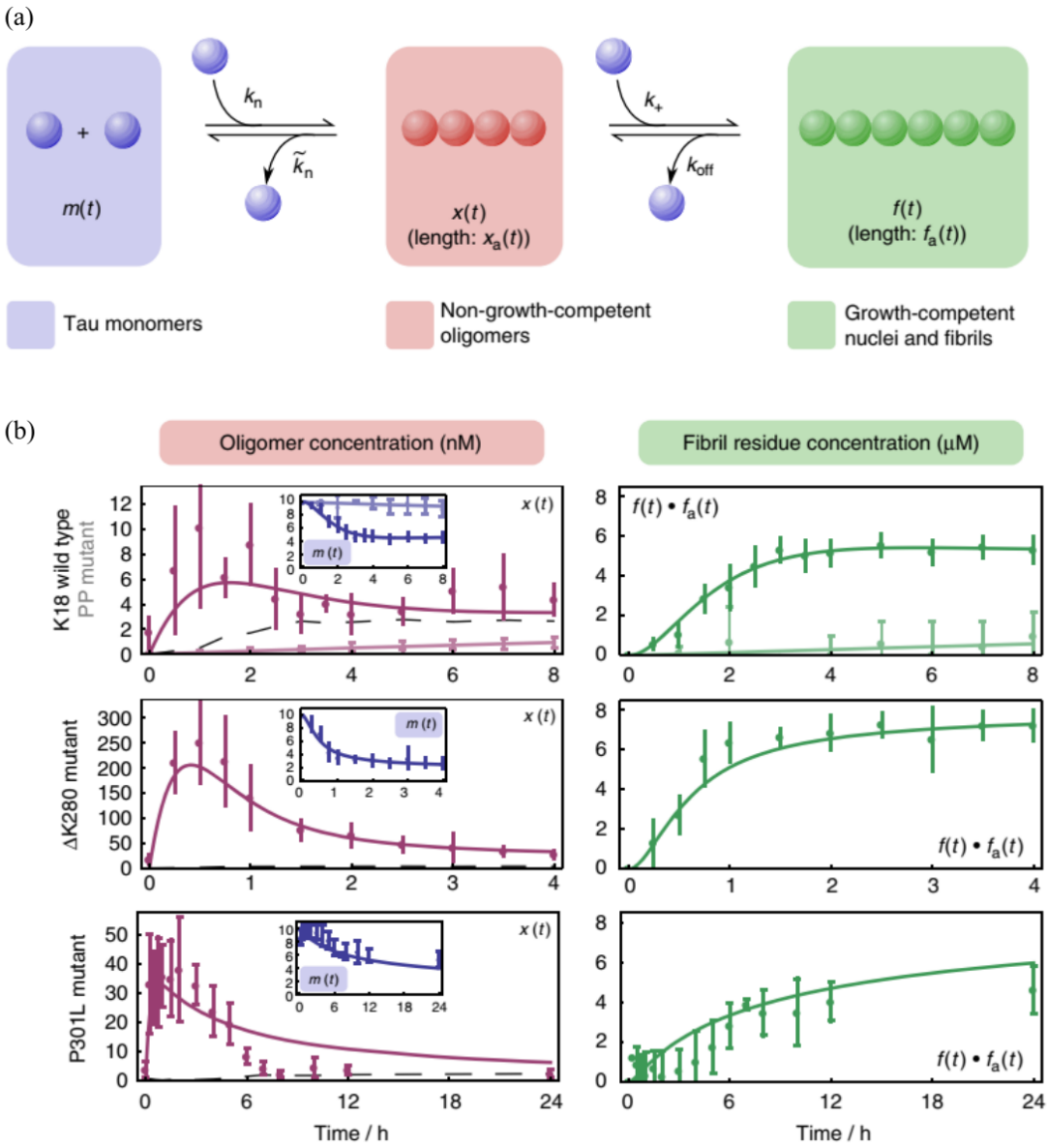

Figure 1.31: Primary nucleation of Tau involves oligomers that are structurally and kinetically distinct from mature amyloid fibrils. (a) The model of Tau nucleation proposed by Shammas *et al.* [393]. Non-growing oligomers form by an n_c^{th}-order nucleation process, followed by monomer-dependent conversion to growing amyloid fibrils. The rate constants are annotated on the diagram. (b) Fits of the above model to the oligomer and fibrillar monomer concentrations for wild-type K18 Tau and three different mutants (K18-PP, K18-ΔK280, K18-P301L), from the same paper [393]. Note that the data and fits for the PP mutant are shown on the same row as the wild-type, in a lighter shade. On the plots of oligomer concentration, the dashed lines represent the predicted upper bounds for the oligomer concentration if the oligomers were structurally indistinct from small fibrils, and there were no rate-determining conversion. Comparison of the fits obtained for the two alternative scenarios strongly favours structurally distinct oligomers. The on-pathway nature of the oligomers was established elsewhere in the paper. Figure from Shammas *et al.* [393].

ordered globular oligomers with amyloid-like intermolecular β-sheets are commonly suggested precursors for amyloid formation [220,278,290,305,306,315]. At the same time, proteins that enter the amyloidogenic pathway from a more structured precursor form oligomers that are more structured and native-like, but are progressively destabilised as they grow [256, 282], meaning that the initially disordered and initially native-like self-assembly pathways may converge to some extent. This suggests that the most favourable intermediates for amyloid nucleation may be oligomers or protofibrils with a moderate to high β-strand content, but a relatively unstable tertiary and quaternary structure.

While initial increases in oligomer size usually increase the likelihood of converting to a fibrillar state, one might expect the more constrained environment of larger oligomers to slow conformational sampling of the constituent monomers. In some cases, this may well be true; for example, structures of Aβcc(1-42) protofibrils suggest that stacking of globular Aβ(1-42) oligomers might stabilise a non-amyloid β-barrel conformation [324], which could prevent the transition to fibrils. In addition, the large spheroidal oligomers formed by Aβ(1-40) [278, 292, 295] may create an environment that retards conformational diffusion, meaning that fibril nucleation is restricted to their more dynamic surface. However, size does not always strongly affect the conformational dynamics of constituent monomers, particularly in the case of filamentous oligomers and thin protofibrils, where most polypeptide chains have regions in contact with the solvent; in these aggregates, an assembled monomer is unlikely to behave in a markedly different way depending on whether it is part of a 20-mer or a 50-mer. In addition, although the conversion rate of individual monomers may be reduced within large aggregates, the total rate at which conversion occurs may still be higher than in a small aggregate, as larger oligomers contain more sites where cross-β structure can originate; thus, computational simulations have predicted a positive correlation between the size and total nucleation rate in oligomers, partly owing to the degeneracy of the sites where cross-β structure can emerge [224]. Instead of excessive size, development of non-amyloid structural motifs is perhaps more likely to commit a particular aggregate to non-amyloidogenic self-assembly. While the comparatively ordered oligomers formed by β_2m [256] demonstrate that non-amyloid structure is not always a barrier to cross-β structure formation, in general it certainly seems plausible that the suitability of oligomers as precursors would correlate with the presence of amyloid-like structural motifs, as has been suggested by several authors [220, 278, 290, 301]. This means that some oligomers with particularly unfavourable, non-amyloid structures may be more likely to 'backtrack' to a less ordered state than convert directly to amyloid, or may be more likely still to simply disassemble once amyloids formed from more suitable precursors begin to grow and thus deplete the soluble monomer [315, 400, 419]. Nonetheless, in general there is strong experimental evidence for nucleation of cross-β structure in diverse classes of aggregates, including partly ordered globular oligomers [216, 251, 304, 306, 318, 392], native-like oligomers [256], large, droplet-like 'oligomers' [295], and protofibrils [335]. Thus, although individual aggregates may have particular struc-

tural features that promote or prevent cross-β structure formation, the diversity of nucleation intermediates across different systems suggests that amyloid formation does not require a single specific pathway, and instead supports the proposal that amyloid formation is a general behaviour of condensed, poorly folded phases [268, 287].

1.5.2.5 Summary

Nucleation of amyloids can probably proceed via a range of different mechanisms depending on the primary sequence and the conditions under which aggregation occurs. However, amyloids that form from larger peptides, intrinsically disordered proteins, and misfolded globular proteins are likely to first aggregate via non-fibrillar states, due to the complexity of the required conformational rearrangements and the fact that they are unlikely to be coupled to or precede dimerisation. In itself, this does not guarantee that nucleation will have a multi-step mechanism, and many experimentally observed non-fibrillar aggregates are also likely to be off-pathway. Nonetheless, more recent structures of many amyloids have complex subunit folds with large numbers of mutually supporting interactions [77], suggesting that the transition from the intermediate to the amyloid state is likely to be cooperative, and involve a significant free energy barrier. Thus, multi-step nucleation mechanisms may be relatively widespread among amyloids, in agreement with the conclusions of an increasing number of experimental studies [217, 251, 278, 283, 287, 335, 345, 346, 370, 392, 393].

1.5.3 Polymerisation and depolymerisation

After nucleation, amyloids grow by adding subunits to their ends, a process that is variably termed either elongation or polymerisation, and whose reverse process is termed depolymerisation or disassembly. During this process, a precursor binds to the end of an amyloid fibril and undergoes a templated conformational change, becoming part of the fibril structure; thus, the precursors themselves are often non-amyloid, although in some cases they may contain amyloid-like structural elements [420] (Fig. 1.32(a)). Although various studies have proposed that these precursors are either monomeric [166, 421–424] or oligomeric [283, 369], in the majority of cases the specific elongation rate of amyloid fibrils is linearly proportional to the free monomer concentration, supporting the addition of monomers rather than oligomers [166,421–424]. In addition, in some cases, closer analysis of the polymerisation kinetics has caused mechanisms of oligomer addition to be re-evaluated as monomer addition [421,424]; thus, monomer addition appears to be by far the most common polymerisation mechanism across systems (Fig. 1.32(a)). Polymerisation and depolymerisation by addition or removal of monomers have the rate laws [425, 426]

$$\nu_e^+(t) = 2k_e^+ m(t), \tag{1.13}$$

$$\nu_e^-(t) = 2k_e^-, \tag{1.14}$$

where $\nu_e^+(t)$ and $\nu_e^-(t)$ are the frequencies with which monomers are added to and removed from the ends of a single fibril, and the factor of 2 can be omitted if the processes only occur at a single end. For fibrils that have multiple protofilaments, growth of these protofilaments is typically co-ordinated [165], which is probably due to the stabilising effect of inter-protofilament interactions and the fact that many fibrils have an overall 2_1 screw symmetry, so that successive monomer additions simply result in rotation of the binding interface for new monomers at the fibril end (Fig. 1.32(a)) [144]. It has been suggested that amyloid fibril elongation may be driven by desolvation entropy of the incorporated monomer [427], and both entropic effects and the thermodynamic contributions of π-π interactions have been implicated in stabilising the conformational transition state [428, 429]. Nonetheless, elongation often proceeds at a rate well below that expected for diffusion-limited bimolecular collisions, which has been interpreted as evidence that this transition state is highly unstable [422]. Alternatively, other causes have been suggested; in particular, it has been found that the success rate of collisions between monomers and the fibril end is reduced by the high frequency with which monomers bind in incorrect orientations, and have to dissociate in order for further attempts at binding to occur (Fig. 1.32(b)) [430, 431]. This may also be the cause of commonly observed 'stop-start' kinetics, where single-molecule measurements reveal that growth sometimes periodically stalls, perhaps reflecting the binding of monomers in long-lived, growth-incompetent states (Fig. 1.32(b, c)) [166, 429, 432]. Several studies have also supported a 'dock-lock' mechanism of growth, where the monomer initially weakly binds to the fibril end, and must cross a free energy barrier in order to adopt the final fibrillar conformation, resulting in Michaelis-Menten-like saturation of the growth kinetics (Fig. 1.32(b, d)) [6, 420, 427, 429, 433–436]. Lastly, as previously discussed in Section 1.3.4, polar growth is sometimes observed, with elongation occurring at a higher rate at one end of the fibril than at the other (Fig. 1.32(e)) [165, 166]. This behaviour has also been predicted by MD simulations [420], and results from the fact that amyloid fibrils have distinct interfaces for growth at each end (Section 1.3.4).

1.5.4 The Oosawa model

Models of amyloid formation can be tested by obtaining mathematical predictions for experimental variables such as the concentration of fibrils, the total fibril mass, and the fibril length distribution, and comparing these predictions to the experimental data [9, 373, 437]. To convert a model into a set of mathematical predictions, the rate laws for the underlying microscopic self-assembly processes are integrated either analytically or numerically to obtain predictions based on particular values of the rate constants and other kinetic parameters. These parameters can be constrained based on known or likely parameters, or varied in order to determine the values that best fit the experimental data. The ability of different models to

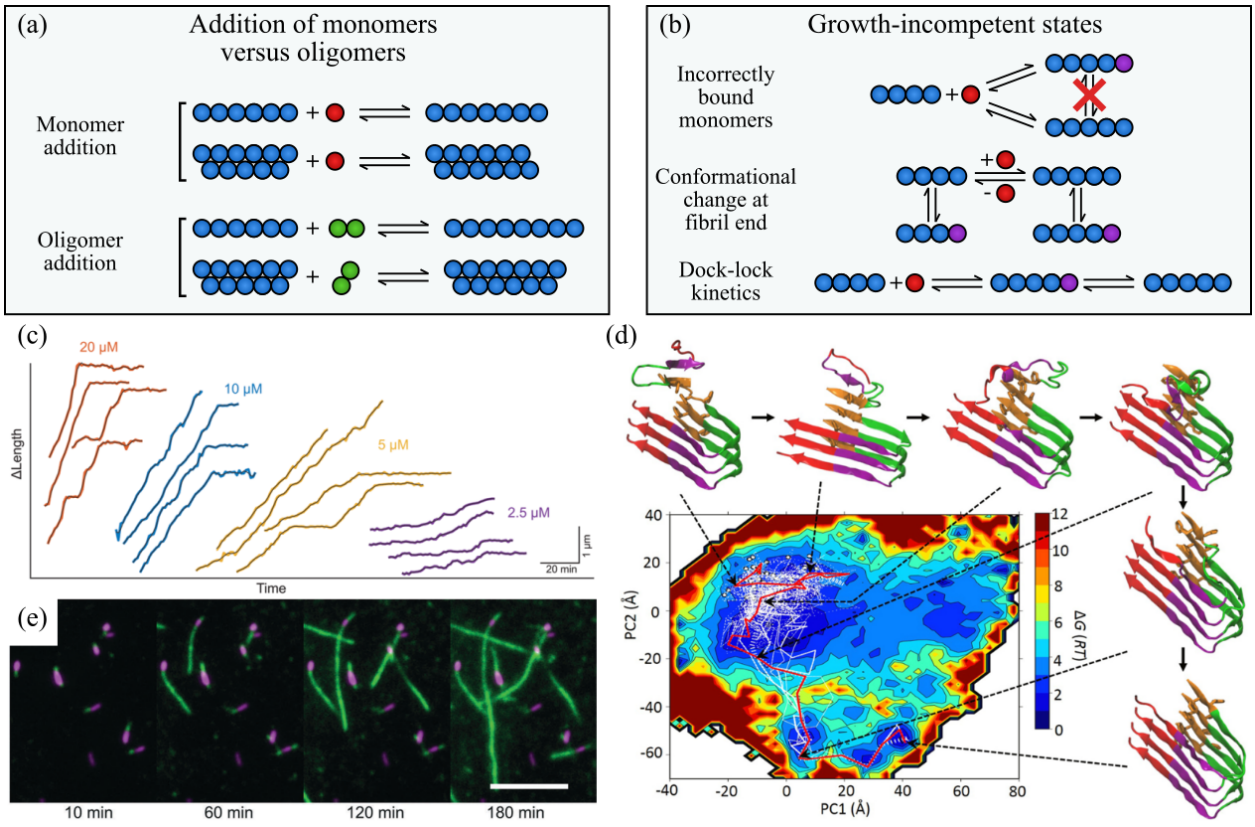

Figure 1.32: Elongation of amyloid fibrils. (a) Elongation has been suggested to involve addition of either monomers or oligomers. Spheres represent individual assembled monomers, with the colour corresponding to the conformational state: red, monomeric; green, part of an oligomer; blue, fibrillar. (b) Polymerisation and depolymerisation often involve growth-incompetent states. Same colour scheme as the previous panel, but with purple spheres representing fibrillar monomers in a state incapable of further monomer addition. Both incorrect binding and conformational change at the fibril end are plausible explanations for stop-start kinetics; the dock-lock mechanism is more likely to result in Michaelis-Menten kinetics. (c) Examples of growth traces of Aβ(1-42) fibrils, from Young *et al.* [166]. The change in fibril length is plotted against time; the colour corresponds to the free monomer concentration, as indicated on the plot. Note that growth sometimes stalls; this is termed 'stop-start kinetics'. (d) A free energy surface for elongation of Aβ(17-42) fibrils, from MD simulations by Han *et al.* [420]. The simulations involve the addition of a monomer onto a pre-formed fibril fragment, converting from a largely disordered to a fibrillar state. The axes are the two main principle coordinates of the conformational free energy surface, derived from the first two eigenvectors of the distance matrix between sampled conformations. The colour represents the free energy (units of RT, key to right of plot), and the most common sampled trajectories have been superimposed on the free energy surface as as white lines, or red for the pathway that was most populated overall. Selected conformations are shown around the outside of the plot, with arrows indicating their location on the free energy surface. The free energy barriers on this surface are the cause of dock-lock kinetics. (e) *In situ* growth of Aβ(1-42) amyloid fibrils viewed by TIRFM, from Young *et al.* [166]. Two different fluorophores were used, allowing discrimination between fibril seeds (violet) and material added by subsequent elongation (green). Scale bar 5 μm. Note that seeds exhibit polarised growth, with faster monomer addition at one end. Panels (a-b) based on information in Section 1.5.3, and panels (c-e) adapted from their respective cited sources.

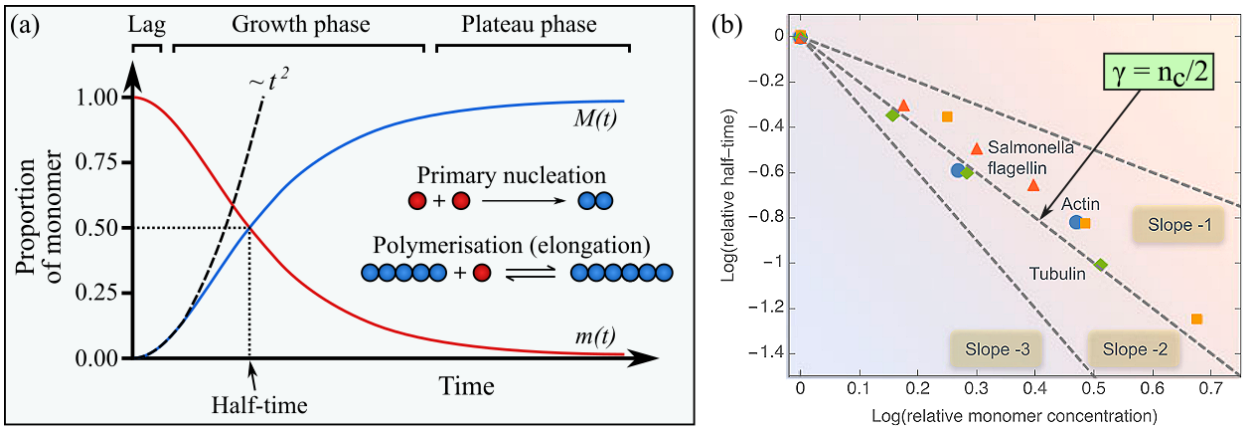

Figure 1.33: The Oosawa model. (a) The curve shape predicted by the Oosawa model, with the free monomer concentration $m(t)$ shown in red and the fibrillar monomer concentration $M(t)$ in blue (from Eq. 1.20). The lag phase is brief and fibril mass accumulation is quadratic in the early time, ie. $\sim t^2$. The Oosawa model only accounts for primary nucleation and polymerisation, as shown in the schematic (here $n_c = 2$). (b) The Oosawa model predicts a power law relationship between the initial monomer concentration $m(0)$ and the half-time τ_{50}, which appears linear when plotted on double-logarithmic axes. The scaling exponent, which can be obtained from the slope on this plot, is equal to $\gamma = n_c/2$. The data for *Salmonella* flagellin (red) [439], tubulin (green) [440] and actin (orange and blue) [441] all have $\gamma \approx 2$, indicating $n_c \approx 4$. Panel (a) is based on the information in Section 1.5.4; panel (b) is adapted from the review by Michaels *et al.* [442], with the original data from the sources indicated above.

fit the data can then be used to determine which candidate model is most likely to be correct [9, 373, 437].

Primary nucleation and elongation form a minimal self-assembly pathway, and the vast majority of mathematical models of amyloid formation are based on extensions to this basic scenario [438]. Thus, this basic form of nucleated polymerisation provides an introduction to the more complex pathways discussed in the remainder of this literature review. Nucleated polymerisation involving n_c^{th}-order primary nucleation and monomer-dependent elongation can be described by Eq. (1.2, 1.13, 1.14). This type of self-assembly is not unique to amyloids, and global solutions for the concentration of polymers $P(t)$ and polymerised monomers $M(t)$ were first obtained by Oosawa and colleagues, who studied actin polymerisation [425, 426]. The rates of change of $P(t)$ and $M(t)$ are [375, 425, 426]

$$\frac{dP(t)}{dt} = k_n m(t)^{n_c}, \tag{1.15}$$

$$\frac{dM(t)}{dt} = n_c k_n m(t)^{n_c} + 2k_e^+ m(t)P(t) - 2k_e^- P(t), \tag{1.16}$$

where the terms proportional to k_n account for the change in polymer number and mass due to primary nucleation, and the subsequent terms in Eq. (1.16) account for the change in mass due to reversible poly-

merisation of the existing fibrils. The total number of monomers is conserved, so that

$$\frac{dm(t)}{dt} = -\frac{dM(t)}{dt}. \tag{1.17}$$

Initial insights into the accumulation of polymer number and mass can be gained by examining the early time limit ($t \to 0$), in which the free monomer concentration can be treated as approximately constant ($m(t) \approx m(0)$). Experimentally, these solutions are valid for timescales on which significant monomer depletion does not occur, ie. during the lag and early growth phase. In this limit, assuming that aggregation is unseeded ($P(0) = 0$ and $M(0) = 0$) and the solution is sufficiently supersaturated ($m(0) \gg k_e^-/k_e^+$), Eq. (1.15-1.16) can be linearised and integrated to give the results [375, 426]

$$\lim_{t\to 0} P(t) = k_n m(0)^{n_c} t, \tag{1.18}$$

$$\lim_{t\to 0} M(t) = n_c k_n m(0)^{n_c} t + k_n k_e^+ m(0)^{n_c+1} t^2. \tag{1.19}$$

The linear terms in these equations come from direct contributions to $P(t)$ and $M(t)$ due to nucleation of fibrils with initial size n_c, and the quadratic term in $M(t)$ accounts for elongation of these fibrils at a linearly increasing rate, and is usually the dominant term on experimental timescales. Models involving intermediates whose concentrations have not reached a steady state are predicted to have higher-order scaling in the early time, due to the greater number of sequential processes occurring at non-steady rates [380]. Oosawa's exact solution for Eq. (1.15-1.16), which is valid throughout the entire time course so long as aggregation is unseeded and $m(0) \gg k_e^-/k_e^+$, is [2, 443]

$$M(t) = m(0)\left[1 - \operatorname{sech}^{2/n_c}\left(\sqrt{\frac{n_c}{2}}\lambda t\right)\right], \tag{1.20}$$

where λ is the 'macroscopic' or effective rate constant for the combined pathway of primary nucleation and polymerisation [2],

$$\lambda = \sqrt{2k_n k_e^+ m(0)^{n_c}}. \tag{1.21}$$

Eq. (1.20) predicts a sigmoidal progress curve, and recovers Eq. (1.19) as $t \to 0$ (Fig. 1.33(a)). The Oosawa model also predicts a power-law relationship between the initial monomer concentration $m(0)$ and either the lag time τ_{lag} or the half-time τ_{50} [425, 426, 444], where the former is defined as the time at which a tangent from the steepest part of the curve intercepts the $m(0)$ axis, and the latter is the time taken for half of the monomer to have been polymerised ($M(t) = m(0)/2$) (Fig. 1.33(b)). This power law relationship can be written

$$\tau_{\text{lag}} \sim \tau_{50} \sim m(0)^{-n_c/2}. \tag{1.22}$$

Alternatively, one can express the scaling law in the form of the scaling exponents γ_{lag} and γ_{50}

$$\gamma_{\text{lag}} = -\frac{\partial \log \tau_{\text{lag}}}{\partial \log m(0)}, \tag{1.23}$$

$$\gamma_{50} = -\frac{\partial \log \tau_{50}}{\partial \log m(0)}, \tag{1.24}$$

where $\gamma_{\text{lag}} \approx \gamma_{50} \approx n_c/2$. Thus,

$$\tau_{\text{lag}} \sim m(0)^{-\gamma_{\text{lag}}}, \tag{1.25}$$

$$\tau_{50} \sim m(0)^{-\gamma_{50}}. \tag{1.26}$$

Note that, in the above formulae, the binary operator '$\sim$' denotes that two quantities are approximately or asymptotically proportional to one another. As per the convention in Gillam *et al.* [438], a factor of -1 has been introduced before the derivative in Eq. (1.23-1.24), and into the exponent in Eq. (1.25-1.26), as the relationship between $m(0)$ and the characteristic times is usually inverse; however, there is an alternative convention that does not include this factor of -1, in which case the sign is flipped [2].

Although the Oosawa model predicts a sigmoidal progress curve, the quadratic scaling of $M(t)$ in the early-time is comparatively low-order, and does not produce a particularly pronounced lag phase (Fig. 1.33(a)). However, experimental data often show well-defined lag phases, indicating that $M(t)$ exhibits higher-order scaling in the early time than the Oosawa model is able to produce [9]. Although one possible cause of this scaling is a cascade of multiple sequential nucleation intermediates [380], this would typically require a large number of sequential intermediates, and closer analysis of the kinetic data often reveals that the scaling behaviour is exponential, indicating that positive feedback is the cause of high-order early-time kinetics [9, 381]. The most common processes that result in positive feedback are fibril fragmentation, in which a fibril breaks in two (Section 1.5.5), and secondary nucleation, in which the surface of existing fibrils catalyses additional nucleation events (Section 1.5.6). Both cause a fibril mass-dependent increase in the concentration of growing fibril ends, which in turn increases the rate of mass accumulation, resulting in positive feedback. Schematics of these processes are shown in Fig. 1.34(a-b), and their mechanisms and effects on the macroscopic self-assembly kinetics are discussed in greater detail in the following subsections.

1.5.5 Fragmentation and end-to-end annealing

Amyloids can fragment due to thermal fluctuations under quiescent conditions, or in response to shear forces caused by factors such as stirring or agitation of the reaction mixture. When a fibril breaks, the total fibril mass is usually unchanged, but the number of growing fibril ends doubles; thus, the cycle of successive growth and breakage can create a positive feedback loop that causes exponential accumulation

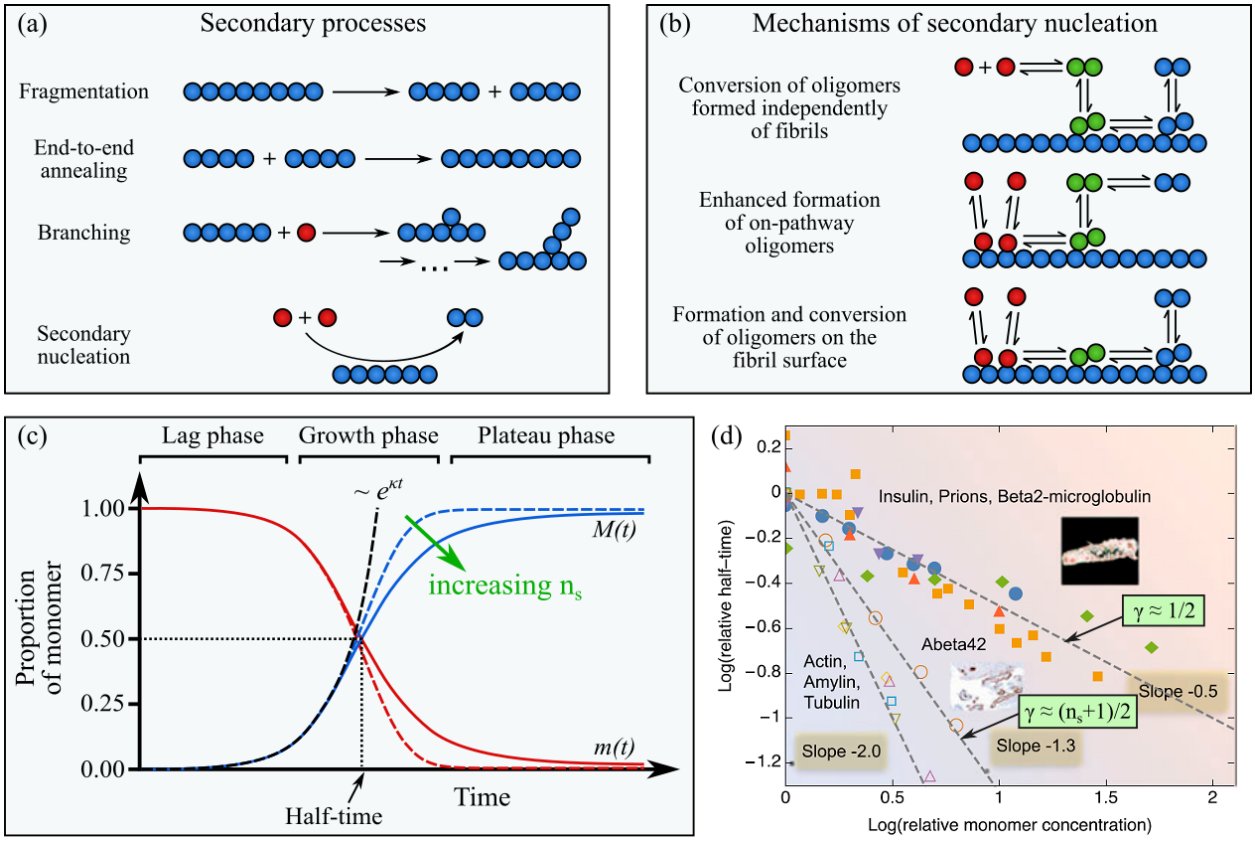

Figure 1.34: Secondary processes. (a) A schematic of commonly discussed secondary processes. The spheres represent self-assembling monomers, with the colour corresponding to the conformational/assembly state: red, monomeric; blue, fibrillar. The ellipsis in the schematic for branching represents intervening elongation steps affecting the newly formed branch. Secondary nucleation encompasses a wide range of processes that produce new, independent fibrils in a manner dependent on both the pre-existing fibrils, and soluble species such as monomers or oligomers. In this panel, a simple version of secondary nucleation has been shown, with intermediates omitted and $n_s = 2$. (b) Schematics of possible mechanisms of secondary nucleation, based on speculative proposals by Törnquist *et al.* [445]. Same colour scheme as the previous panel, but with green spheres corresponding to monomers that have been incorporated into non-fibrillar oligomers. (c) The curve shape observed for pathways dominated by secondary processes, with the free monomer concentration $m(t)$ shown in red and the fibrillar monomer concentration $M(t)$ in blue (from Eq. 1.20). The dashed blue and red curves are for $n_s = 0$ (fragmentation), and the solid curves are for $n_s = 2$ (secondary nucleation operating as an apparent dimerisation). Increasing n_s causes progressive levelling of the approach to maximum fibril yield, as indicated by the green arrow. Unlike the Oosawa model (Fig. 1.33(a)), models with secondary processes often have pronounced lag phases and exponential early-time scaling ($\sim e^{\kappa t}$). (d) Like the Oosawa model, models with secondary processes usually exhibit a power law relationship between the initial monomer concentration $m(0)$ and the half-time τ_{50}, which appears linear when plotted on double-logarithmic axes. The scaling exponent is equal to $\gamma = (n_s+1)/2$, becoming $\gamma = 1/2$ in the case of unbiased fragmentation. Panels (a-c) are based on the information in Sections 1.5.5-1.5.7; panel (d) is adapted from the review by Michaels *et al.* [442], with the original data from earlier studies [54, 74, 439–441, 446–450].

of fibril mass [381]. The simplest models of fibril fragmentation involve a fragmentation rate proportional to the aggregate mass, leading to the rate law [1]

$$\frac{dP(t)}{dt} = k_n m(t)^{n_c} + k_f \big[M(t) - (2n_c - 1)P(t)\big], \tag{1.27}$$

where k_f is the fragmentation rate constant, and the term proportional to $2n_cP(t)$ accounts for the possibility that fragmentation may produce a fragment that is too small to be stable. The rate law for the fibrillar monomer concentration is mostly unchanged from the Oosawa model, but has a small term to account for the formation of unstable fragments [1],

$$\frac{dM(t)}{dt} = n_c k_n m(t)^{n_c} + 2k_e^+ m(t)P(t) - 2k_e^- P(t) - k_f n_c (n_c - 1)P(t), \tag{1.28}$$

and the conservation of mass condition described by Eq. (1.17) is still valid. For unseeded aggregation ($P(0) = 0$ and $M(0) = 0$) at sufficient supersaturation ($m(0) \gg k_e^-/k_e^+$), Eq. (1.27-1.28) predict approximately exponential accumulation of aggregate mass in the early time [1, 9],

$$\lim_{t\to 0} M(t) = m(0)\left\{ \frac{\lambda^2}{2\kappa^2} e^{\kappa t} + \frac{\lambda^2}{2\kappa^2} e^{-\kappa t} - \frac{\lambda^2}{\kappa^2} \right\}, \tag{1.29}$$

where κ is the 'macroscopic' or effective rate constant for secondary pathways, and has the form [1]

$$\kappa = \sqrt{2k_f k_e^+ m(0)}. \tag{1.30}$$

From a single fixed-point iteration, Knowles and colleagues obtained an approximate solution for the whole time course [1, 9]

$$M(t) \approx m(0)\left\{ 1 - \exp\left(-\frac{\lambda^2}{2\kappa^2} e^{\kappa t} - \frac{\lambda^2}{2\kappa^2} e^{-\kappa t} + \frac{\lambda^2}{\kappa^2} \right) \right\}. \tag{1.31}$$

Similar solutions have also been obtained for seeded aggregation [2], and an example of this curve shape is shown in Fig. 1.34(c). If most new fibrils are produced by fragmentation of existing fibrils, the above model predicts $\gamma_{\text{lag}} \approx \gamma_{50} \approx 1/2$ (Fig. 1.34(d)) [1, 2], in contrast to $\gamma_{\text{lag}} \approx \gamma_{50} \approx n_c/2$ as predicted by the Oosawa model [425, 426]. Although the Knowles model assumes that fragmentation occurs at all locations in the fibril with equal probability, in reality the fragmentation rate is likely to depend on the position where the break occurs, as well as the fibril length. While thermally induced fragmentation is predicted to occur more often at the ends, agitation-induced fragmentation is more likely to occur at the centre of fibrils [451, 452]. In addition, some authors have used length and position-dependent fragmentation kernels based on polymer statistics [7, 378, 450], as the rotational and translational degrees of freedom of suspended polymers mean

that even in the absence of factors such as protofilament pairing or conformational differences, the free energy of amyloid fibrils is not a linear function of length; this introduces a length and position-dependence of the free energy change associated with fragmentation, and thus the free energy barrier, affecting the rate of the process [453]. As a result, fragmentation is typically expected to occur disproportionately more often in longer fibrils. In cases where fragmentation is the dominant secondary process, such as assembly of β_2m [450] or Ure2p [454] fibrils, a detailed characterisation of the length and position-dependence of fragmentation is likely to be needed to accurately describe the macroscopic self-assembly kinetics.

The reverse process, end-to-end annealing, is sometimes also discussed. A proper description of this process is attractive from a physical standpoint, as it provides a reverse process for thermally induced fragmentation, allowing the system to reach equilibrium under quiescent conditions. However, practically speaking, for long amyloid fibrils the end-to-end annealing rate is probably very low, as the rate of this process is heavily penalised by slow diffusion of the merging fibrils [378,453]. In addition, while annealing can allow the fibril length distribution to reach an equilibrium on long timescales, it does not significantly affect the kinetics during assembly [455]. Nonetheless, there are cases where annealing may be more common, including: non-fibrillar oligomers, which diffuse more rapidly and are sometimes proposed to join together [220,275,339]; Tau, in which end-to-end annealing of separate fibrils has been observed [392,456]; and apoC-II, where annulation can occur due to annealing of the ends of the same fibril [457].

Not only is an accurate description of fragmentation needed to describe fibril self-assembly, but also prion-like spreading and toxicity. Fragmentation is more effective than secondary nucleation in preserving the conformational state of the seed fibril [454, 458–460], meaning it is probably the basis of prion strain propagation [454,461]. In addition, the infectivity of PrP fibrils and toxicity of β_2m fibrils are both correlated with the number of fibril ends, and thus sensitive to the effects of fragmentation on the average fibril size [461, 462]. In the former case, this is probably because shorter fibrils have more ends at which templated assembly can occur [454], whereas in the latter it is because exposed hydrophobics at the fibril ends can disrupt lipid membranes [462]. In both cases, fragmentation increases the number of fibril ends, resulting in a more biologically 'active' fibril population that is either indirectly or directly more toxic.

1.5.6 Secondary nucleation and branching

Secondary nucleation is a common phenomenon in crystallisation processes in which new crystals nucleate on the surface of pre-existing crystals [445, 463]. Secondary nucleation has also been observed in non-crystalline phases such as biopolymers, where it was first described in sickle cell haemoglobin (HbS) gelation by Ferrone and colleagues [376, 381]. Like fragmentation, secondary nucleation results in positive feedback, causing approximately exponential accumulation of fibril mass in the early time (Fig. 1.34(c)). However, unlike fragmentation, which occurs at a rate independent of the free monomer concentration, sec-

ondary nucleation involves the assembly of soluble monomers to form an entirely new fibril, rather than breakage of a pre-existing fibril; thus, self-assembly reactions with secondary nucleation as the dominant secondary process are more concentration-dependent, and have a less abrupt approach to the plateau as the rate of secondary nucleation begins to decrease earlier in the growth phase [2, 376, 381, 464, 465] (Fig. 1.34). Since its identification in HbS, secondary nucleation and similar processes have been identified in a number of amyloids, such as IAPP [74], glucagon [466], HET-s [114], Aβ [4, 54], and α-syn [56]. Usually, new fibrils detach after nucleating on the sides of pre-existing fibrils, but in some cases this does not occur, resulting in branched structures as seen in glucagon [466]. There are diverse forms of evidence to support secondary nucleation in certain amyloids. Besides the diagnostic self-assembly kinetics, imaging data have allowed direct visualisation of secondary nucleation of Aβ(1-42) [460], α-syn [56], and glucagon [466] fibrils, and a growing number of molecular simulations have also predicted behaviours similar to secondary nucleation [348, 467]. Secondary nucleation of Aβ fibrils has recently been demonstrated to occur in the cerebrospinal fluid (CSF), supporting its relevance under physiological conditions [75].

Usually, secondary nucleation is proposed to occur at sites distributed along the sides of fibrils, rather than at the ends [3, 56, 376, 460, 466, 468]. In this case, the secondary nucleation rate is proportional to the fibril mass,

$$\Phi_s(t) = k_s m(t)^{n_s} M(t), \tag{1.32}$$

where k_s is the rate parameter for secondary nucleation, and n_s is the effective number of monomers involved in the process. The rate of accumulation of aggregate number and mass are [3, 376]

$$\frac{dP(t)}{dt} = k_n m(t)^{n_c} + k_s m(t)^{n_s} M(t), \tag{1.33}$$

and

$$\frac{dM(t)}{dt} = n_c k_n m(t)^{n_c} + n_s k_s m(t)^{n_s} M(t) + 2k_e^+ m(t) P(t) - 2k_e^- P(t). \tag{1.34}$$

The early time behaviour is still approximately described by Eq. (1.29), but the value of κ is different [3],

$$\kappa = \sqrt{2k_s k_e^+ m(0)^{n_s+1}}. \tag{1.35}$$

Although Eq. 1.31 provides an approximate solution for self-assembly with dominant secondary nucleation, provided the correct value of κ is used, it has low accuracy as the free monomer is depleted. Knowles and colleagues [3] obtained a more accurate solution through several iterations of fixed point analysis,

$$M(t) = m(0)\left\{1 - \left(\frac{B_+ + C_+}{B_+ + C_+ e^{\kappa t}} \frac{B_- + C_+ e^{\kappa t}}{B_- + C_+}\right)^{\frac{k_\infty^2}{\kappa k_\infty}} e^{-k_\infty t}\right\}, \tag{1.36}$$

where

$$B_{\pm} = \frac{k_{\infty} \pm \tilde{k}_{\infty}}{2\kappa}, \tag{1.37}$$

$$C_{\pm} = \pm \frac{\lambda^2}{2\kappa^2}, \tag{1.38}$$

$$k_{\infty} = \sqrt{\frac{2\kappa^2}{n_s(n_s+1)} + \frac{2\lambda^2}{n_c}}, \tag{1.39}$$

$$\tilde{k}_{\infty} = \sqrt{k_{\infty}^2 - 4C_{+}C_{-}\kappa^2}. \tag{1.40}$$

Similar solutions have also been obtained for seeded aggregation [3], and it is worth noting that Eq. (1.36) is also an accurate solution for fragmentation in the limit $n_s \to 0$ [3]. While the Oosawa model predicts $\gamma_{\text{lag}} \approx \gamma_{50} \approx n_c/2$, and the fragmentation-dominated Knowles model predicts $\gamma_{\text{lag}} \approx \gamma_{50} \approx 1/2$, the secondary nucleation-dominated Knowles model predicts $\gamma_{\text{lag}} \approx \gamma_{50} \approx (n_s+1)/2$, with the extra factor of $1/2$ compared to primary nucleation accounting for the effect of $M(t)$ on the secondary nucleation rate [3]. Secondary nucleation can be distinguished from fragmentation as it results in a stronger concentration-dependence, and a more gentle approach to the plateau [2, 381, 465] (Fig. 1.34(c-d)).

Until recently, mechanistic information on secondary nucleation was limited; however, details have now begun to emerge. Coarse-grained simulations have suggested that secondary nucleation is likely to proceed via enhanced formation of on-pathway pre-fibrillar oligomers (Fig. 1.34(b), middle schematic), some of which then go on to convert to fibrils [348]. This is effectively surface-catalysed two-step nucleation, and is consistent with the observation that the concentrations of oligomeric species observed during Aβ fibrillisation peak during the 'growth' phase, when the rate of secondary nucleation is highest [469]. In addition, secondary oligomers have been shown to correlate with toxicity in cell and lipid-based assays, indicating that secondary nucleation plays an important role in Aβ neurotoxicity [54, 55, 68]. While the coarse-grained simulations do not give precise information about the regions of Aβ involved in secondary nucleation, more detailed simulations have shown that Aβ(1-42) monomers and oligomers interact with the hydrophobic C-termini of the corresponding amyloid fibrils [467]. In addition, the same simulations predicted enhanced assembly and β-structure content of Aβ(1-42) oligomers in this environment, lending credence to the hypothesis that secondary nucleation results from enhanced formation of on-pathway oligomers [348, 467]. The importance of exposed hydrophobics in stimulating secondary nucleation is also supported by studies of HET-s, where the packing interfaces of unpaired protofilaments provide sites for secondary nucleation, but lateral association of those protofilaments to form a fibril occludes those interfaces, and prevents secondary nucleation from occurring [114].

Secondary nucleation has been shown to be relatively sequence-specific, with Aβ(1-42) and Aβ(1-40) unable to cross-seed via this mechanism [458–460]. This suggests a more structured route for secondary

nucleation than simple non-specific aggregation. In addition, near-neutral pH has been shown to stabilise relatively ordered protofibrillar aggregates on the surface of Aβ(1-42) fibres, which were suggested to be on-pathway [460]. At the same time, secondary nucleation does not propagate strain polymorphism of Aβ [459] or α-syn [470], meaning that pre-fibrillar secondary oligomers typically lose 'memory' of their seed fibril prior to the conversion to an amyloid state. In this sense, secondary nucleation contrasts with fragmentation, which conserves strain polymorphism [454]. Thus, while fragmentation is likely to be the basis of prion-like propagation behaviours [454, 461], secondary nucleation may play more of a role in generating heterogeneous populations of partly folded oligomers that can be responsible for direct toxicity [54, 55, 68]. Nonetheless, it is not yet clear whether these are general trends, as fragmentation can also directly produce toxic species [462], and it has been speculated that forms of secondary nucleation that conserve polymorphism may yet be identified [471].

1.5.7 Self-similarity and the effects of changes in the microscopic kinetic parameters

As previously discussed, Eq. (1.36) is valid for cases of both secondary nucleation and fragmentation, with the latter described by the equation in the $n_s \to 0$ limit [3]. More recently, it has been shown that a simpler approximation provides a good fit for the experimental data [465],

$$M(t) \approx m(0)\left\{1 - \left[1 + \frac{C_+ e^{\kappa t}}{\sqrt{2/[n_s(n_s+1)]}}\right]^{-\sqrt{2/[n_s(n_s+1)]}}\right\}, \tag{1.41}$$

which is essentially a generalised logistic function, or Richards' function [472]. While κ is the main determinant of the maximum rate, both κ and C_+ affect the lag time, and the main effect of n_s is on the approach to the plateau. When n_s is large, there is a smooth approach to plateau; when n_s is small (ie. the fragmentation limit), there is a sharper approach to plateau. In the special case where $n_s = 1$, a logistic function is obtained [465]

$$M(t) \approx m(0)\left\{\frac{C_+ e^{\kappa t}}{1 + C_+ e^{\kappa t}}\right\}, \tag{1.42}$$

which is symmetric on either side of the half-time. In the fragmentation limit ($n_s \to 0$), a Gompertz function is obtained [465, 473],

$$M(t) \approx m(0)\Big\{1 - \exp\big(-C_+ e^{\kappa t}\big)\Big\}, \tag{1.43}$$

which can be seen to be similar to Eq. (1.31). Thus, curves with different microscopic rate constants but similar n_s can often be rescaled onto one another by compressing or expanding the time axis to correct for differences in κ, although small adjustments to the length of the lag phase may sometimes be needed to account for changing κ/λ [442, 465]. More generally, these universal scaling behaviours lead to the following conclusions regarding the effect of various microscopic processes on curve shape: primary nucleation

mainly affects the length of the lag time and half-time; secondary nucleation mainly affects the lag time, half-time, and maximum rate; elongation generally stretches or compresses the curve shape, affecting all the characteristic times and rates; and the order of the dominant nucleation process affects how sharply the curve approaches a plateau [374, 465, 471]. The self-similarity of biopolymer self-assembly kinetics is shown in Fig. 1.35, and the effects of variations in the microscopic rate constants on the macroscopic self-assembly kinetics are shown in Fig. 1.36.

1.5.8 Saturable microscopic processes

While the following subsections have dealt with non-saturable microscopic processes, in reality many microscopic processes are likely to be saturable [6]. This is because, as discussed in the preceding sections, the microscopic processes are usually multi-step processes with rate-determining conformational conversion steps; in addition, these processes often occur in restricted environments, which can be saturated. For example, in some cases primary nucleation has been shown to be surface-catalysed [6, 350–352, 357, 359, 361–363, 474, 475], so that saturation of catalytic sites can cause Michaelis-Menten-like kinetics [6]. In addition, secondary nucleation is by definition a surface-catalysed process, and has been shown to be saturable in the case of Aβ(1-40) and Aβ(1-42) [4–6]. Lastly, as discussed in Section 1.5.3, elongation often proceeds via a dock-lock mechanism in which the monomer binds to the fibril end and converts to an amyloid state in distinct steps [6, 420, 427, 429, 433–436]. Michaelis-Menten-style rate laws have been proposed for all three processes [4–6],

$$\Phi_n(t) = k_n m(t)^{n_c} \frac{K_{M,n}}{K_{M,n} + m(t)^{n_c}}, \tag{1.44}$$

$$\Phi_s(t) = k_s m(t)^{n_s} M(t) \frac{K_{M,s}}{K_{M,s} + m(t)^{n_s}}, \tag{1.45}$$

$$\nu_e^+(t) = 2k_e^+ m(t) \frac{K_{M,e}}{K_{M,e} + m(t)}, \tag{1.46}$$

where $K_{M,n}$, $K_{M,s}$, and $K_{M,e}$ are the n_c^{th}-order, n_s^{th}-order, and first-order effective Michaelis constants for the process. These can be accounted for in the macroscopic rate constants by using the more general definitions

$$\lambda = \sqrt{2k_n k_e^+ m(0)^{n_c} \frac{K_{M,n}}{K_{M,n} + m(t)^{n_c}} \frac{K_{M,e}}{K_{M,e} + m(t)}}, \tag{1.47}$$

$$\kappa = \sqrt{2k_s k_e^+ m(0)^{n_s+1} \frac{K_{M,s}}{K_{M,s} + m(t)^{n_s}} \frac{K_{M,e}}{K_{M,e} + m(t)}}, \tag{1.48}$$

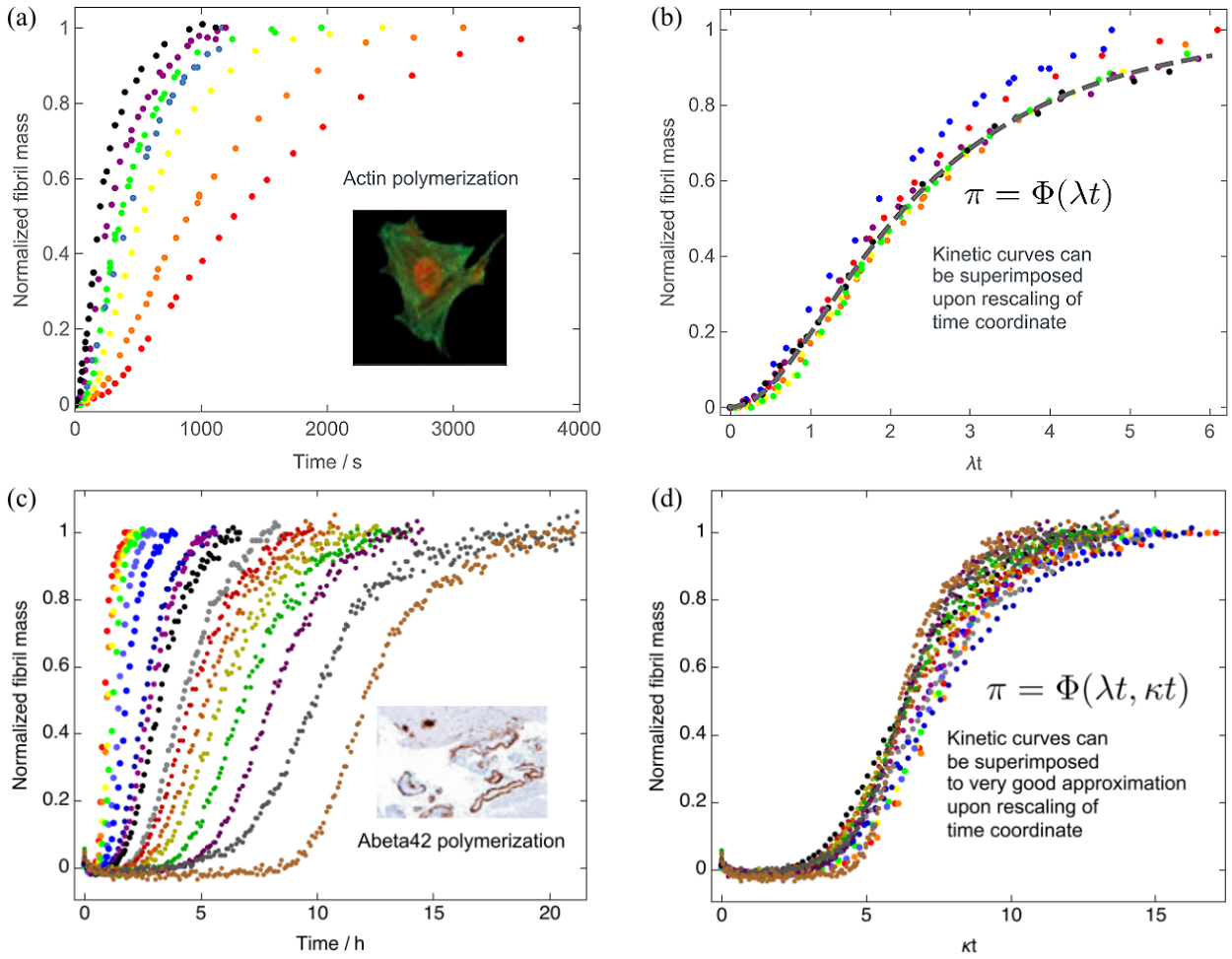

Figure 1.35: The self-assembly kinetics of amyloid fibrils and other biopolymers are either exactly or approximately self-similar, so that curves that are dominated by the same pathway and have the same reaction order of microscopic processes can thus be rescaled onto one another. Panels (a-b) show the normalised mass accumulation of actin filaments at different monomer concentrations and under a variety of conditions [441], and panels (c-d) show mass accumulation by Aβ(1-42) at a range of monomer concentrations [54]. The panels on the left (a, c) show the data in absolute time units, and the panels on the right (b, d) show the data rescaled according to the macroscopic rate constant of the dominant self-assembly pathway. Rescaling causes the actin kinetics, which are described by the Oosawa model (Section 1.5.4), to overlay exactly. The Aβ(1-42) kinetics, which are described by the Knowles model (Section 1.5.6), overlay approximately but have the small discrepancies due to changes in λ/κ across the concentration range. Figure adapted from Michaels *et al.* [442], with the original data from the sources cited above.

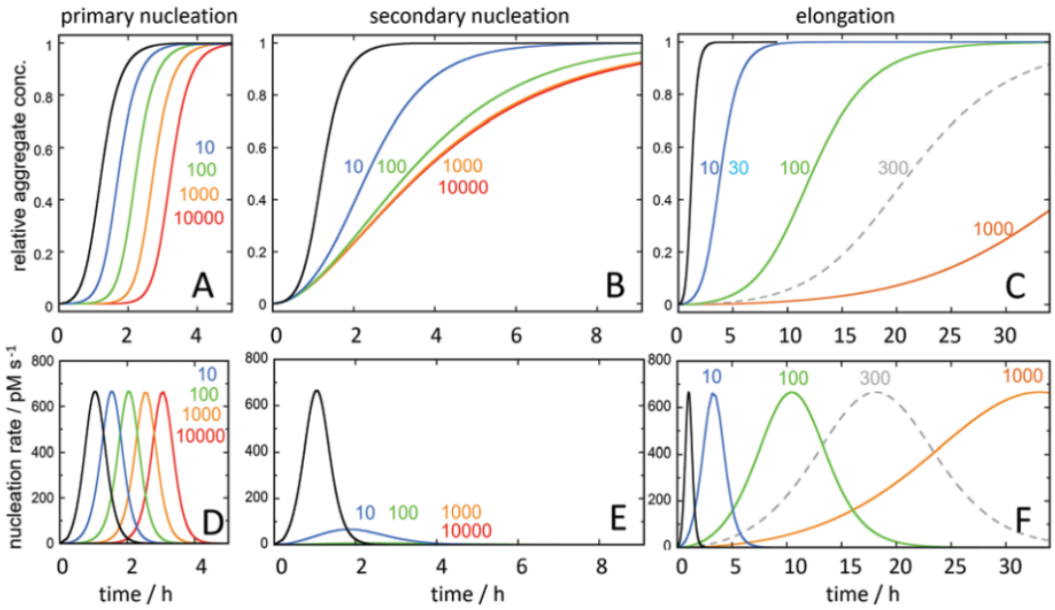

Figure 1.36: The effects of variations in the microscopic rate constants on the macroscopic self-assembly kinetics. Panels in the upper row show the effect of varying (a) k_n, (b) k_s, or (c) k_e^+ on the normalised accumulation of fibril mass. Panels in the lower row show the effects of varying (d) k_n, (e) k_s, or (f) k_e^+ on the absolute nucleation rate. In each panel, the black curve corresponds to the expected self-assembly kinetics for 3 μM Aβ(1-42), predicted by the Knowles model with dominant secondary nucleation (Eq. (1.36), using the best-fit parameters from Cohen *et al.* [54]). The coloured curves indicate the effects of various fold-reductions in those rate constants, as indicated on the panels. Note that reducing k_n only delays the peak in nucleation, as the dominant nucleation process is secondary. A sufficient reduction in k_s results in primary-dominated Oosawa kinetics. Figure from Törnquist *et al.* [445].

or for the case where only the nucleation processes are saturable,

$$\lambda = \sqrt{2k_n k_e^+ m(0)^{n_c} \frac{K_{M,n}}{K_{M,n} + m(t)^{n_c}}}, \tag{1.49}$$

$$\kappa = \sqrt{2k_s k_e^+ m(0)^{n_s+1} \frac{K_{M,s}}{K_{M,s} + m(t)^{n_s}}}. \tag{1.50}$$

Meisl *et al.* [4] showed that Eq. (1.36) can be adapted to account for the case where only secondary nucleation is saturable by using the value of κ given by Eq. (1.50), and a modified expression for k_∞,

$$k_\infty = \sqrt{A(\infty) - A(0)}, \tag{1.51}$$

where

$$\begin{aligned} A(t) = &- \frac{\lambda^2}{n_c} - 2k_s k_e^+ K_{M,s} m(0) \frac{\log\left[K_{M,s} + m(t)^{n_s}\right]}{n_s} \\ &- 2k_s k_e^+ K_{M,s} m(t) \left({}_2F_1\left[\frac{1}{n_s}, 1, 1 + \frac{1}{n_s}, -\frac{m(t)^{n_s}}{K_{M,s}}\right] - 1 \right), \end{aligned}$$

and ${}_2F_1$ is a hypergeometric function. More recently, Dear *et al.* [6] presented an approximate solution similar to Eq. (1.41) that accounts for saturation of all microscopic processes,

$$M(t) \approx m(0) \left\{ 1 - \left[1 + \frac{C_+ (e^{\kappa t} + e^{-\kappa t} - 2)}{3/(2n_s' + 1)} \right]^{-3/(2n_s'+1)} \right\}, \tag{1.52}$$

where the appropriate definition of κ is given by Eq. (1.48), the definitions of λ and κ used to calculate C_+ are given by Eq. (1.47) and Eq. (1.48), respectively, and

$$n_s' = n_s \frac{K_{M,s}}{K_{M,s} + m(t)^{n_s}} - 2\frac{K_{M,e}}{K_{M,e} + m(t)}. \tag{1.53}$$

By applying Eq. (1.52) to Aβ(1-40) self-assembly kinetics, the authors showed that the best fit for the kinetics was obtained in the scenario where all three processes saturated [6], although saturation of elongation only occurred at high concentrations ($K_{M,e} \approx 130\,\mu$M). By reducing the apparent order of microscopic processes, saturation causes weaker concentration scaling of the macroscopic self-assembly kinetics. For example, self-assembly with saturated secondary nucleation as the dominant nucleation process, and unsaturated elongation, is expected to give $\gamma = 1/2$, similar to fragmentation, although it is still possible to distinguish the processes based on the curve shape and fibril length distributions [4, 5]. In addition, in cases where elongation also saturates, an even lower concentration-dependence is expected [4, 6]. Thus, in or-

der to test whether saturation of microscopic processes is occurring, it is preferable to acquire kinetic data over a broad concentration range, allowing identification of any saturation-induced variation in the scaling exponents of the characteristic times or the macroscopic rate constants.

1.6 Overview of this thesis

The aim of this study was to use a combination of macroscopic self-assembly kinetics from ThT assays, complementary measurements from other biochemical and biophysical techniques, and theoretical approaches to investigate outstanding questions regarding Aβ(1-42) self-assembly mechanisms. In particular, three major areas of uncertainty were investigated. Firstly, while there is evidence to suggest that surfaces can sometimes catalyse primary nucleation (see Section 1.4.6, Section 1.5.2, and Section 1.5.8), the extent to which primary nucleation depends on a surface at physiological peptide concentrations remains unclear. Secondly, this thesis aims to address some of the continuing uncertainty regarding the mechanisms of primary and secondary nucleation, in particular the extent to which these processes have multi-step mechanisms involving pre-fibrillar intermediates, and the possible identity and conformational characteristics of those intermediates. Thirdly, this thesis aims to investigate the cause of kinetic behaviours that are not explained by existing models, but have been observed in experiments, such as weak monomer-dependence of the half-time and lag-time. While Chapter 2 contains a general description of the methods used throughout the other chapters in this thesis, Chapter 3 describes the development and validation of an improved protocol for solubilisation of Aβ, which establishes the validity of the kinetic results obtained in the rest of this thesis. Chapter 4 presents an investigation of the role of heterogeneous surfaces in the self-assembly process, leading to the conclusion that primary nucleation is usually dependent on surfaces at physiological peptide concentrations, and a diverse range of surfaces are likely to stimulate the process *in vivo*. Lastly, Chapter 5 presents the results of investigations of the effects of ionic strength on Aβ(1-42) self-assembly, which led to the finding that previously inexplicable features of the self-assembly kinetics that occur at physiological ionic strength can be ascribed to the accumulation of on-pathway oligomers produced by secondary nucleation. Altogether, the results presented in this thesis suggest that both primary and secondary Aβ nucleation are surface-catalysed multi-step processes at physiological concentrations.

Chapter 2

Materials and Methods

The details of materials and methods that are common throughout this thesis are described below, while details that are specific to individual chapters are provided in the methods sections of those chapters.

2.1 Materials

Ultra-pure recombinant Aβ(1-42) was purchased from rPeptide (Watkinsville, GA) in glass vials containing 0.5 mg (catalogue number A-1163-1) or 1.0 mg (catalogue number A-1163-2) lyophilised peptide, from HFIP. All other materials were analytical grade and were purchased from Fisher Scientific (UK) or Sigma-Aldrich (UK). Buffers and solvents were prepared with deionised water (dH_2O) and passed through a 0.2 μm filter, except where otherwise stated, and were checked frequently for the presence of dust, microbial growth, or other contaminants. Buffers and solvents for SEC and AF4 were passed through a 0.1 μm filter, degassed, and prepared no more than 3 days before use. To prevent microbial growth, sodium azide (NaN_3) was added to buffers whenever experimental constraints would allow, and its use is indicated wherever relevant in the remainder of this thesis.

2.2 Preparation and handling of Aβ(1-42)

Aβ is notoriously sensitive to preparative and experimental conditions [476]. The high aggregation rate and extreme sensitivity of this peptide to contaminants such as dust, metal ions, and chemical modifications mean that Aβ must be handled carefully to avoid seeding or otherwise altering the aggregation process, or allowing uncontrolled aggregation to occur prior to experimentation. Thus, it is essential to take appropriate precautions when handling Aβ in order to limit these effects. In addition, Aβ preparations or solubilisations must attain a high level of reproducibility, and sufficiently sensitive quality control procedures must be applied to identify any issues with Aβ samples. The protocols described here, which were used for the work

in Chapters 4 and 5, were based on the optimisation described in Chapter 3.

2.2.1 Precautions when handling Aβ(1-42)

In all preparative and experimental work, it was essential to avoid exposing Aβ(1-42) to contaminants such as dust, bubbles, and chemical residues that might affect the aggregation process. This meant that extra precautions had to be taken when handling the peptide, in addition to those described in Section 2.1. Pipetting of Aβ(1-42) solutions was performed gently, to avoid introducing bubbles that might affect aggregation. Aβ(1-42) solutions were mixed gently before extraction from tubes or microplates, as larger aggregates have a tendency to sediment. Wherever possible, Aβ(1-42) was handled in low-binding Eppendorf tubes (Hamburg, Germany), to reduce adhesion of the peptide to the interior of the tubes and the presence of dust or other contaminants. Similarly, buffers and solvents used in Aβ(1-42) preparation and self-assembly experiments were only prepared and handled in labware that was supplied at a high degree of cleanliness, or had been thoroughly cleaned before use. Other precautions are mentioned where relevant in the rest of this methods section, and subsequent chapters of this thesis.

2.2.2 Solubilisation of Aβ(1-42)

As described in Section 2.1, recombinant Aβ(1-42) was supplied in glass vials containing 0.5 mg or 1.0 mg of lyophilised peptide, from HFIP. Vials were thawed on the benchtop for 5 min, and 50 mM NaOH was injected into them with a Hamilton syringe (Reno, NV) to a peptide concentration of 1 mg/ml. Vials were manually rotated for 10 s to ensure that any material on the sides came into contact with solvent, and sonicated for 5 min using a DECON Ultrasonics sonicator bath (Sussex, UK). Dissolved peptide was extracted using a Hamilton syringe, split into 50 µl aliquots in Eppendorf tubes (Hamburg, Germany), and flash-frozen by immersion in liquid N_2. The syringe was kept clean by repeated washing in dH_2O and 50 mM NaOH between uses. The pH of the 50 mM NaOH was tested with pH indicator strips before injection into vials, and after extraction from vials, to check for pH changes. Prior to use in experiments, peptide aliquots were thawed at 37°C and triturated to ensure that they were well-mixed. As described in Chapter 4, it was found that samples could be successfully re-frozen and re-thawed between uses, without affecting the quality of the peptide; wherever possible, samples were re-frozen with liquid N_2.

2.2.3 Quality control

Aβ(1-42) samples were routinely tested for pre-aggregation by ThT assays and AF4-MALS, according to the procedures described in Chapter 3.

2.3 Determination of peptide concentration

The concentration of peptide was determined from either the UV absorbance at 280 nm (UV_{280}) or the refractive index (RI). UV_{280} measurements were obtained using either a NanoDrop One (Thermo Scientific, UK) or the in-line UV detector of the AF4/SEC-MALS system (Shimadzu, UK). RI measurements were obtained using the inline RI detector of the AF4/SEC-MALS system (Postnova Analytics, Germany). Molar concentration was calculated from UV_{280} measurements according to the Beer-Lambert law,

$$A = \varepsilon l c, \tag{2.1}$$

where A is the absorbance, ε is the extinction coefficient, l is the path length, and c is the concentration. The extinction coefficient of Aβ(1-42) was calculated from the primary sequence using the ProtParam tool provided by ExPASy [477]. At pH well below the pK_a (≈ 10.5) of the tyrosine hydroxyl, the predicted extinction coefficient at 280 nm was 1490 $M^{-1}.cm^{-1}$ ($= 0.330$ $ml.mg^{-1}.cm^{-1}$), which was confirmed empirically. At pH 11, the extinction coefficient of the same samples increased to an empirically determined value of 1860 $M^{-1}.cm^{-1}$ ($= 0.412$ $ml.mg^{-1}.cm^{-1}$) as the tyrosine hydroxyl was mostly deprotonated. Concentration was calculated from the RI according to the relation

$$\Delta n = c\frac{\partial n}{\partial c}, \tag{2.2}$$

where Δn is the change in refractive index of the solution, c is the concentration, and $\partial n/\partial c$ is the refractive index increment of the peptide. A refractive index of $\partial n/\partial c = 0.871$ M^{-1} ($= 0.193$ $ml.g^{-1}$) was calculated from the primary sequence based on the per-residue $\partial n/\partial c$ values in Zhao *et al.* [478]. Concentrations determined by UV_{280} and RI were compared, and the two were found to be self-consistent.

2.4 Fibrillisation buffers

The fibrillisation buffers used in this thesis are similar to those used in other studies in the literature [5, 479], but were pre-adjusted to correct for pH changes occurring after the addition of Aβ dissolved in 50 mM NaOH, as the addition of NaOH raises the pH of the final buffer. Adjustment had to be carried out before the addition of Aβ, rather than afterwards, as Aβ typically aggregates rapidly once the pH drops below ~10 [294]. This required preparation of buffer stocks that were more acidic than desired, but would reproducibly reach the intended pH after addition of a known quantity of 50 mM NaOH. In order for the strategy to work, the quantity of NaOH added to the buffer had to be constant, so the Aβ concentration was varied by adding complementary volumes of 50 mM NaOH with and without dissolved peptide. The theoretical basis of

the preparation of these buffers is described in the following subsection, and the application of the process to produce pre-adjusted 20 mM and 10 mM sodium phosphate buffers with varying salt concentrations is described in the subsequent subsections. In addition to sodium phosphate, all fibrillisation buffers contained various concentrations of NaN_3 to limit microbial growth, 200 μM EDTA to sequester transition metal ions, and 20 μM ThT, to allow their use in ThT assays. ThT was included in all fibrillisation buffers regardless of whether they were used in ThT assays, in order to ensure that results were comparable, and ThT has previously been shown not to affect the aggregation process at these concentrations and under these conditions [4]. Buffers often also contained variable quantities of the halide salts NaF, NaCl, and NaI, which were used to investigate screening, Hofmeister, and electroselective effects on Aβ(1-42) self-assembly.

2.4.1 Preparation of pH-corrected buffers

The pH of the buffer solution is given by the Henderson-Hasselbalch equation [480],

$$\mathrm{pH} = \mathrm{p}K_{a,\mathrm{app}} + \log_{10}\left(\frac{[\mathrm{A}^-]}{[\mathrm{AH}]}\right), \tag{2.3}$$

where $\mathrm{p}K_{a,\mathrm{app}}$ is the apparent $\mathrm{p}K_a$ of the acid, correcting for the effects of factors such as ionic strength on the activity of the solutes, $[\mathrm{AH}]$ is the concentration of the acid, and $[\mathrm{A}^-]$ is the concentration of its conjugate base; for phosphate buffers at pH ≈ 8, the acid and base are $H_2PO_4^-$ and HPO_4^{2-}, respectively. Let us distinguish between the initial composition of the buffer stock before addition of a known quantity of NaOH, which has concentrations $[\mathrm{AH}] = [\mathrm{AH}]_{\mathrm{initial}}$ and $[\mathrm{A}^-] = [\mathrm{A}^-]_{\mathrm{initial}}$, and the final composition after addition of the NaOH, which has the concentrations $[\mathrm{AH}] = [\mathrm{AH}]_{\mathrm{final}}$ and $[\mathrm{A}^-] = [\mathrm{A}^-]_{\mathrm{final}}$. Thus,

$$\mathrm{pH}_{\mathrm{initial}} = \mathrm{p}K_{a,\mathrm{initial}} + \log_{10}\left(\frac{[\mathrm{A}^-]_{\mathrm{initial}}}{[\mathrm{AH}]_{\mathrm{initial}}}\right), \tag{2.4}$$

$$\mathrm{pH}_{\mathrm{final}} = \mathrm{p}K_{a,\mathrm{final}} + \log_{10}\left(\frac{[\mathrm{A}^-]_{\mathrm{final}}}{[\mathrm{AH}]_{\mathrm{final}}}\right), \tag{2.5}$$

where $\mathrm{p}K_{a,\mathrm{initial}}$ and $\mathrm{p}K_{a,\mathrm{final}}$ are apparent $\mathrm{p}K_a$ values that account for the changing activities of the solutes between the initial and final solutions. When NaOH is added, most of the hydroxide is consumed in the reaction

$$\mathrm{OH}^- + \mathrm{AH} \rightarrow \mathrm{H_2O} + \mathrm{A}^-, \tag{2.6}$$

and only a small quantity is neutralised,

$$\mathrm{OH}^- + \mathrm{H}^+ \rightarrow \mathrm{H_2O}. \tag{2.7}$$

Thus, if NaOH is added from a separate stock with concentration $[\mathrm{NaOH}]_{\mathrm{stock}}$, and the added volume of NaOH stock is V_{NaOH},

$$[\mathrm{AH}]_{\mathrm{final}} V_{\mathrm{final}} \approx [\mathrm{AH}]_{\mathrm{initial}} V_{\mathrm{initial}} - [\mathrm{NaOH}]_{\mathrm{stock}} V_{\mathrm{NaOH}}, \tag{2.8}$$

$$[\mathrm{A}^-]_{\mathrm{final}} V_{\mathrm{final}} \approx [\mathrm{A}^-]_{\mathrm{initial}} V_{\mathrm{initial}} + [\mathrm{NaOH}]_{\mathrm{stock}} V_{\mathrm{NaOH}}, \tag{2.9}$$

where V_{initial} is the initial volume of the buffer stock before addition of the NaOH, and V_{final} is the final volume of the buffer after this addition. Let us now consider the case where the NaOH is added from two sources: a stock containing only NaOH, with concentration $[\mathrm{NaOH}]_{\mathrm{stock}}$ ($= 50$ mM) and volume V_{NaOH}; and a stock containing NaOH with 1 mg/ml dissolved Aβ, which also has an NaOH concentration of $[\mathrm{NaOH}]_{\mathrm{stock}}$ and has volume $V_{\mathrm{NaOH+A}\beta}$. The final concentration of Aβ is comparatively small (< 20 μM), so that it does not significantly affect [AH] and $[\mathrm{A}^-]$. Thus,

$$[\mathrm{AH}]_{\mathrm{final}} V_{\mathrm{final}} \approx [\mathrm{AH}]_{\mathrm{initial}} V_{\mathrm{initial}} - [\mathrm{NaOH}]_{\mathrm{stock}} (V_{\mathrm{NaOH}} + V_{\mathrm{NaOH+A}\beta}), \tag{2.10}$$

$$[\mathrm{A}^-]_{\mathrm{final}} V_{\mathrm{final}} \approx [\mathrm{A}^-]_{\mathrm{initial}} V_{\mathrm{initial}} + [\mathrm{NaOH}]_{\mathrm{stock}} (V_{\mathrm{NaOH}} + V_{\mathrm{NaOH+A}\beta}). \tag{2.11}$$

By varying V_{NaOH} and $V_{\mathrm{NaOH+A}\beta}$ while keeping $V_{\mathrm{NaOH}} + V_{\mathrm{NaOH+A}\beta}$ the same, one can prepare solutions with different Aβ concentrations, but a constant final pH. If only NaOH $\pm$ Aβ were added at this point, one would expect $V_{\mathrm{final}} = V_{\mathrm{initial}} + V_{\mathrm{NaOH}} + V_{\mathrm{NaOH+A}\beta}$. However, at this point one also has to add ThT, and it is convenient to make the solution up to a greater volume with $\mathrm{dH_2O}$, as this provides the flexibility to add other solutes for specific experiments. Thus,

$$V_{\mathrm{final}} = V_{\mathrm{initial}} + V_{\mathrm{NaOH}} + V_{\mathrm{NaOH+A}\beta} + V_{\mathrm{ThT}} + V_{\mathrm{dH_2O}}, \tag{2.12}$$

where part of $V_{\mathrm{dH_2O}}$ can be replaced with stocks of salts, proteins, or other constituents as required, although it is sometimes more convenient to incorporate those constituents into V_{initial}. Rearranging Eq. (2.10-2.11) yields theoretical expressions for the concentrations of AH and A^- in the buffer stock,

$$[\mathrm{AH}]_{\mathrm{initial}} = \frac{[\mathrm{AH}]_{\mathrm{final}} V_{\mathrm{final}} + [\mathrm{NaOH}]_{\mathrm{stock}} (V_{\mathrm{NaOH}} + V_{\mathrm{NaOH+A}\beta})}{V_{\mathrm{initial}}}, \tag{2.13}$$

$$[\mathrm{A}^-]_{\mathrm{initial}} = \frac{[\mathrm{A}^-]_{\mathrm{final}} V_{\mathrm{final}} - [\mathrm{NaOH}]_{\mathrm{stock}} (V_{\mathrm{NaOH}} + V_{\mathrm{NaOH+A}\beta})}{V_{\mathrm{initial}}}, \tag{2.14}$$

where $[\mathrm{AH}]_{\mathrm{final}}$ and $[\mathrm{A}^-]_{\mathrm{final}}$ are determined from Eq. (2.5) as one normally would for a buffer, V_{final} is determined from Eq. (2.12), and the volumes of the individual buffer constituents are chosen as part of the experimental design.

When estimating $[\mathrm{AH}]_{\mathrm{final}}$ and $[\mathrm{A}^-]_{\mathrm{final}}$, it is important to be mindful that the $\mathrm{p}K_{a,\mathrm{app}}$ of the acid con-

stituent of the buffer varies with its concentration; for example, while the $pK_{2,app}$ of phosphate (ie. the $pK_{a,app}$ for the equilibrium between $H_2PO_4^-$ and HPO_4^{2-}) is 7.2 at an ionic strength close to 0 mM, it decreases to around 6.8 at an ionic strength of 300 mM, due to the changing activity coefficients of H^+, HPO_4^{2-}, and $H_2PO_4^-$ [481]. Thus, the final total concentration of phosphate affects the ratios of A^- and AH in the initial buffer stock. In addition, apparently innocuous solutes such as NaCl can affect the pH by altering the ionic strength of the solution, and can also be accompanied by small quantities of free acid that complicate the results. Therefore, in practice, it is essential to empirically confirm that the buffer stock produces the correct final pH over the full range of Aβ concentrations. If a buffer stock does not produce the correct final pH, its pH must be adjusted, and the test repeated. Because the buffers used in this thesis had a constant concentration of phosphate and variable (ie. pH-dependent) concentration of Na^+, this could not be performed by adding acid; therefore, stocks had to be prepared to a pH that was slightly too low, and adjusted upwards. This optimisation process requires a repeated cycle of testing the stock by making up a reaction mixture containing added NaOH and other buffer constituents, measuring the pH of the mixture, and then incrementally adjusting the pH of the stock. These tests were performed in small volumes in Eppendorf tubes (Hamburg, Germany), and the amount of NaOH that had to be added was recorded and used to adjust the ratios of $[HPO_4^{2-}]$, and $[H_2PO_4^-]$ used to produce a larger volume of stock. The pH of a solution prepared from this larger volume of stock was then confirmed empirically, and the stock was stored for use. The application of this procedure to produce pre-adjusted 20 mM and 10 mM sodium phosphate buffers is described in the following subsections.

2.4.2 Preparation of 20 mM sodium phosphate buffers without halide salts

The procedures used to carry out the pH correction in this protocol were also applied to the protocols described in the following subsections; therefore, this protocol is given in greater detail, and the subsequent protocols refer back to this one. The buffer has the following constituents:

- 20 mM sodium phosphate (pH 8),
- 1 mM NaN_3,
- 200 μM EDTA,
- 20 μM ThT,

and is designed to be made up immediately prior to use from:

- a pre-adjusted buffer stock, described below (20% of final volume),
- 1 mg/ml Aβ dissolved in 50 mM NaOH (x% of final volume, where $x \leq 10$),

- 50 mM NaOH stock ($(10-x)\%$ of final volume),
- 2 mM ThT stock (1% of final volume),
- dH_2O (69% of final volume),

where the volumes of Aβ + NaOH and NaOH stock are complementary so that the same quantity of NaOH is added despite varying the Aβ concentration. Thus, to make 1 ml of fibrillisation buffer, the volumes are as follows,

- $V_{\text{initial}} = (20\%/100\%) \times 1 \text{ ml} = 200 \text{ µl}$,
- $V_{\text{NaOH+A}\beta} = (x\%/100\%) \times 1 \text{ ml} = 10x \text{ µl}$,
- $V_{\text{NaOH}} = ((10-x)\%/100\%) \times 1 \text{ ml} = (100-10x) \text{ µl}$,
- $V_{\text{ThT}} = (1\%/100\%) \times 1 \text{ ml} = 10 \text{ µl}$,
- $V_{\text{dH}_2\text{O}} = (69\%/100\%) \times 1 \text{ ml} = 690 \text{ µl}$.

The concentration of Aβ in the final mixture will be $1 \text{ mg.ml}^{-1} \times (x\%/100\%) = 2.22x$ µM (for Aβ(1-42). Therefore, for 1 µM Aβ(1-42), $x\% = 0.451\%$, for 2 µM Aβ(1-42), $x\% = 0.902\%$, and so on. The pre-adjusted buffer stock contains:

- 100 mM sodium phosphate (ratios of NaH_2PO_4 to Na_2HPO_4 depend on pH pre-adjustment, as described below),
- 5 mM NaN_3,
- 1 mM EDTA.

Theoretically, given $pK_{2,\text{app}} \approx 6.9$ at ionic strength $I \approx 60$ mM [481], one would expect $[H_2PO_4^-]_{\text{final}} \approx 1.5$ mM and $[H_2PO_4^-]_{\text{final}} = 18.5$ mM; applying Eq. (2.13-2.14), $[H_2PO_4^-]_{\text{initial}} \approx 32.5$ mM and $[H_2PO_4^-]_{\text{initial}} \approx 67.5$ mM, which would give $pH_{\text{initial}} \approx 7.1$, accounting for the change in $pK_{2,\text{app}}$ due to the higher ionic strength of the stock. However, the buffer stock is first produced as a test solution so that its pH can be checked and adjusted with NaOH if necessary, recording the final amount of NaOH added in order to determine the precise NaH_2PO_4:Na_2HPO_4 ratio needed to attain the correct pH. As the pH can only be adjusted upwards, this test solution is initially produced to yield a lower final pH than ultimately intended ($pH_{\text{final}} \approx 7.8$). In the test solution, $[H_2PO_4^-]_{\text{final}} \approx 2.2$ mM and $[H_2PO_4^-]_{\text{final}} \approx 17.8$ mM; applying Eq. (2.13-2.14), $[H_2PO_4^-]_{\text{initial}} \approx 36$ mM and $[H_2PO_4^-]_{\text{initial}} \approx 64$ mM, which would give $pH_{\text{initial}} \approx 7.0$. Therefore, a small volume (typically 5-10 ml) of a test stock was prepared, containing the following:

- 36 mM NaH_2PO_4, from 500 mM stock,
- 64 mM Na_2HPO_4, from 500 mM stock,
- 5 mM NaN_3, from 1 M stock,
- 1 mM EDTA, from 200 mM stock.

After preparing the test stock, 200 µl was mixed with 100 µl of 50 mM NaOH, 10 µl of 2 mM ThT, and 690 µl of dH_2O to produce 1 ml of 'final' test buffer with an expected $pH_{final} \approx 7.8$. The pH of this test buffer was measured empirically, and the quantity of concentrated NaOH that had to be added to raise the pH to 8.0 was recorded. The corresponding concentration (ie. concentrated $5\times$ due to the concentration difference between test stock and test buffer) of NaOH was then added to another aliquot of the test *stock*; this was added from a concentrated NaOH stock to avoid significantly diluting the other constituents of the test stock. The adjusted test stock was used to produce another 'final' test buffer with an expected $pH_{final} \approx 8.0$. If the pH was too high (> 8.02), the process was repeated with a smaller quantity of NaOH; if the pH was too low (< 7.98), more NaOH was added, the required amount was recorded, and a new test buffer was produced. Once a test stock had been produced that would produce a test buffer at pH 8.0 when mixed with the other ingredients, the quantity of NaOH that had been added to this test buffer was then used to inform a change in the NaH_2PO_4:Na_2HPO_4 ratio; for example, if 25 mM NaOH had to be added to the test stock to produce a 'final' test buffer with pH 8.0, 25 mM of NaH_2PO_4 was replaced with Na_2HPO_4 in the new test stock. This was then tested again to check that the strategy had worked. If the new test stock produced a test buffer with pH 8.0 (or in the pH 7.98-8.02 range) when 200 µl of test stock was mixed with 100 µl of 50 mM NaOH, 10 µl of 2 mM ThT, and 690 µl of dH_2O, a larger quantity of stock was made with the same NaH_2PO_4:Na_2HPO_4 ratio, for use in experiments. Before use, the pH of fibrillisation buffers prepared with this larger stock was checked again, and this time the pH was also checked with variable quantities of Aβ(1-42). Buffers were only tested with variable quantities of Aβ(1-42) at the end as, in practice, they never failed this test, so they never had to be re-made because of it; nonetheless, in order to be certain that varying the Aβ(1-42) concentration did not affect the pH, this test was regularly performed. The final NaH_2PO_4:Na_2HPO_4 ratios of buffer stocks were usually close to the theoretical predictions, but differed enough to require empirical determination as described above.

2.4.3 Preparation of 20 mM sodium phosphate buffers with variable NaCl

These buffers were prepared in a similar manner to 20 mM sodium phosphate buffer without halide salts, except that NaCl was incorporated into the buffer stocks. The buffers had the following constituents:

- 20 mM sodium phosphate (pH 8),

- 1 mM NaN_3,
- 200 μM EDTA,
- 20 μM ThT,
- y mM NaCl,

where the concentration of NaCl was variable. Due to the effect of ionic strength on the $pK_{2,app}$ of phosphate, a separate buffer stock had to be prepared for each NaCl concentration; therefore, it was most convenient to incorporate the NaCl into the stock itself, rather than adding it separately. The buffer was made up immediately prior to use from:

- a pre-adjusted buffer stock, described below (20% of final volume),
- 1 mg/ml Aβ dissolved in 50 mM NaOH (x% of final volume, where $x \leq 10$),
- 50 mM NaOH stock ($(10-x)$% of final volume),
- 2 mM ThT stock (1% of final volume),
- dH_2O (69% of final volume).

The pre-adjusted buffer stock contained:

- 100 mM sodium phosphate (ratios of NaH_2PO_4 to Na_2HPO_4 depend on pH pre-adjustment, as described below),
- 5 mM NaN_3, from 1 M stock,
- 1 mM EDTA, from 200 mM stock,
- $5y$ mM NaCl, from 1 M stock.

The correct NaH_2PO_4:Na_2HPO_4 ratio was determined by the same process that was described for 20 mM sodium phosphate buffers in Section 2.4.2, and the final pH of all buffers was checked prior to use.

2.4.4 Preparation of 20 mM sodium phosphate buffers with 300 mM NaF

This buffer was prepared in a similar manner to 20 mM sodium phosphate buffer with 300 mM NaCl, but with a more dilute buffer stock, as the solubility of NaF at room temperature is around 1 M. The buffer had the following constituents:

- 20 mM sodium phosphate (pH 8),

- 1 mM NaN_3,
- 200 μM EDTA,
- 20 μM ThT,
- 300 mM NaF,

and was made immediately prior to use from the following ratios:

- a pre-adjusted buffer stock, described below (50% of final volume),
- 1 mg/ml Aβ dissolved in 50 mM NaOH (x% of final volume, where $x \leq 10$),
- 50 mM NaOH stock ($(10-x)$% of final volume),
- 2 mM ThT stock (1% of final volume),
- dH_2O (39% of final volume),

with the pre-adjusted buffer stock containing:

- 40 mM sodium phosphate (ratios of NaH_2PO_4 to Na_2HPO_4 depend on pH pre-adjustment, as discussed below),
- 2 mM NaN_3, from 1 M stock,
- 400 μM EDTA, from 200 mM stock,
- 600 mM NaF, from 750 mM stock.

The correct NaH_2PO_4:Na_2HPO_4 ratio was determined as described for 20 mM sodium phosphate buffers without NaF in Section 2.4.4, accounting for the difference in dilution factor (here 2×) between test stocks and the test buffers prepared from them.

2.4.5 Preparation of 10 mM sodium phosphate buffers with variable NaCl or NaI

This buffer was prepared in a similar manner to 20 mM sodium phosphate buffer with variable concentrations of NaCl, except that the salts were added separately from the stock (although a separate buffer stock still had to be produced for each intended salt concentration). The buffer had the following constituents:

- 10 mM sodium phosphate (pH 8),
- 200 μM NaN_3,

- 200 μM EDTA,
- 20 μM ThT,
- y mM NaCl or NaI,

where the concentration of NaCl or NaI was variable. NaF was also used, but required slight modifications to the protocol in order to achieve the high concentrations used in the buffer, and is discussed separately in the following subsection. The buffer was made immediately prior to use from the following ratios:

- a pre-adjusted buffer stock, described below (10% of final volume),
- 1 mg/ml Aβ dissolved in 50 mM NaOH (x% of final volume, where $x \leq 7$),
- 50 mM NaOH stock ($(7-x)$% of final volume),
- 2 mM ThT stock (1% of final volume),
- 1 M NaCl or NaI stock ($0.1y$ % of final volume),
- dH_2O ($(82-0.1y)$% of final volume),

with the pre-adjusted buffer stock containing:

- 100 mM sodium phosphate (ratios of NaH_2PO_4 to Na_2HPO_4 depend on pH pre-adjustment, as discussed below),
- 2 mM NaN_3, from 1 M stock,
- 2 mM EDTA, from 200 mM stock.

The correct NaH_2PO_4:Na_2HPO_4 ratio was determined as described for 20 mM sodium phosphate buffers in Section 2.4.4, accounting for the difference in dilution factor (here 10×) between test stocks and the test buffers prepared from them.

2.4.6 Preparation of 10 mM sodium phosphate buffers with variable NaF

This buffer was prepared in a similar manner to 10 mM sodium phosphate buffer with variable concentrations of NaCl or NaI, but a more dilute NaF stock had to be used as the solubility of NaF is ∼1 M at room temperature. The buffer had the following constituents:

- 10 mM sodium phosphate (pH 8),
- 200 μM NaN_3,

- 200 μM EDTA,
- 20 μM ThT,
- y mM NaF,

where the concentration of NaF was variable. The buffer was made immediately prior to use from the following ratios:

- a pre-adjusted buffer stock, described below (10% of final volume),
- 1 mg/ml Aβ dissolved in 50 mM NaOH (x% of final volume, where $x \leq 7$),
- 50 mM NaOH stock ($(7-x)$% of final volume),
- 2 mM ThT stock (1% of final volume),
- 750 mM NaCl or NaI stock ($0.133y$ % of final volume),
- dH_2O ($(82-0.133y)$% of final volume),

with the pre-adjusted buffer stock containing:

- 100 mM sodium phosphate (ratios of NaH_2PO_4 to Na_2HPO_4 depend on pH pre-adjustment, as discussed below),
- 2 mM NaN_3, from 1 M stock,
- 2 mM EDTA, from 200 mM stock.

The correct NaH_2PO_4:Na_2HPO_4 ratio was determined as described for 20 mM sodium phosphate buffers in Section 2.4.4, accounting for the difference in dilution factor (here 10×) between test stocks and the test buffers prepared from them.

2.4.7 Preparation and handling of stocks and salt solutions

Stocks of NaH_2PO_4 and Na_2HPO_4 were prepared to 500 mM, stocks of EDTA were prepared to 200 mM, and stocks of ThT were prepared to 2 mM. To prevent bleaching, ThT stocks were covered in foil and stored in the fridge; to avoid over-exposure of the main stock from repeated use, small aliquots of ThT were periodically separated into Eppendorf tubes for use in experiments. Stocks of NaCl and NaI were prepared to 1 M, while stocks of NaF were prepared to 750 mM, as the solubility of NaF is ∼1 M at room temperature. NaI was wrapped in foil and stored in the dark to prevent photo-oxidation, and was checked frequently for brown discolouration caused by oxidation ($2I^- \rightarrow I_2 + 2e^-$); if oxidation was observed, the

stock was replaced. NaF stocks were stored in Falcon tubes rather than glass, as NaF slowly reacts with glass. In addition, NaF stocks could not be vacuum-filtered as the NaF reacted with the filters; nonetheless, there was no detectable seeding in buffers prepared with NaF, and the results of experiments carried out with NaF always agreed closely with the results of those carried out with NaCl. Larger quantities of NaF were handled in the fume hood due to the risk of producing HF gas.

2.5 Thioflavin T (ThT) assays

ThT is a fluorescent dye that non-covalently binds to amyloid fibrils, as well as some other proteins, and exhibits enhanced fluorescence (excitation at 440 nm, emission at 485 nm) when bound [92]. ThT has previously been shown not to affect the self-assembly process under the conditions used in this thesis [4]. In addition, ThT binding is weak at these concentrations, so that an excess of ThT is not strictly required to ensure linearity between the fibril mass and the ThT signal [5, 54]. Nonetheless, other phenomena such as polymorphism and fibril-fibril interactions may still affect the linearity of the ThT response. It should also be noted that ThT is neither a completely sensitive nor a completely specific probe for amyloid fibrils [93, 94], and non-fibrillar oligomers have been observed to bind ThT [278].

2.5.1 Setup of fibrillisation experiments

ThT assays were initiated by dilution of Aβ(1-42) dissolved in 50 mM NaOH into fibrillisation buffer, whose pH had been pre-adjusted so that it would reach the intended value after mixing with the Aβ(1-42) stock. The preparation of pre-adjusted buffers is discussed in Section 2.4, and the success of this strategy was confirmed by pH measurements. Before thawing the Aβ(1-42), all constituents of fibrillisation buffers apart from the Aβ(1-42) stock were pre-mixed in low-bind Eppendorf tubes (Hamburg, Germany), in the ratios described in Section 2.4. Aβ(1-42) stocks, which had been prepared in 50 mM NaOH and stored at -80^{o}C as described in Section 2.2, were thawed and added to the pre-mixed fibrillisation buffers. If added Aβ(1-42) volumes were small, the Aβ(1-42) was diluted in 50 mM NaOH beforehand, correcting the compensatory volume of 50 mM NaOH that was added to the pre-mixed buffer accordingly. Buffers were mixed thoroughly after addition of Aβ(1-42), taking care not to introduce bubbles, and then pipetted into the wells of 96-well microplates, with 100 μl per well. Unless otherwise specified, ThT assays were carried out in 96-well microplates treated with a PEG-like low-binding surface (Corning 3881, NY). For each buffer composition in a single plate, there was a control containing the same buffer without any Aβ(1-42), which was also used as a blank. Experiments were typically performed with 5 replicate wells per set of conditions, although a smaller number of replicates was used in some instances. Each plate was sealed with a qPCR seal (4titude, UK) to restrict evaporation, and incubated in a FLUOstar Omega plate reader

(BMG Labtech, UK). The scale of experiments was always planned so that the dead time would be small (typically < 300 s) compared to the self-assembly timescale. Most time courses were collected with reading every 2 min, and 4 s double-orbital shaking (100 rpm) before reading to dislodge any aggregates weakly associated with the sides or bottom of the plate wells; as shown in Section 3.3.9 and Section 5.3.2, shaking did not cause significant fibril fragmentation. Due to limitations on the number of reads the plate reader could perform in a single program, some of the longer experiments were carried out with reading every 5 min, and 10 s double-orbital shaking (100 rpm) before reading. ThT fluorescence was measured with an excitation wavelength of 440 nm and emission wavelength of 485 nm. Except where otherwise stated, ThT experiments were carried out at 37^{o}C. At all stages of the experiment, pipetting had to be fast in order to reduce the dead time, but also accurate, and care had to be taken to ensure that solutions were mixed well without introducing bubbles.

2.5.2 Processing of kinetic data

Initial data processing was carried out in Microsoft Excel (2010/2013/365), with final processing in GraphPad Prism 8. As discussed in Section 2.5.1, each experiment typically had a set of blank wells containing the same buffer as other wells in the plate, but without any Aβ(1-42). In these experiments, the fluorescence intensities were baselined by subtracting the average fluorescence intensity of all comparable blanks, without smoothing. For older data and data collected by some other lab members, blanks were not always available. In these cases, the baseline was determined wherever possible by linear extrapolation of the minimum fluorescence intensity of wells containing different Aβ(1-42) concentrations to $m(0) = 0$, with averaging across replicate wells and smoothing of the averaged fluorescence intensities (Savitzky-Golay, 2nd order) to eliminate noise from the minimum intensities. Comparisons using data for which blanks were available showed that this approach yielded very similar results to blank subtraction, as the ThT signal of the blanks was typically flat throughout the entire experimental time course, and the blank-subtracted minimum fluorescence intensities were linearly proportional to the Aβ(1-42) concentration. In cases where blanks were not available and an extrapolated baseline could not be determined, the baseline was simply set as the minimum average fluorescence intensity across all replicates, with smoothing (Savitzky-Golay, 2nd order) to eliminate noise. Yield analyses were only performed on data for which blanks were available. After subtracting the baseline, ThT data were often normalised relative to the maximum fluorescence intensity, as indicated where relevant in the remainder of the thesis. This was defined as the maximum average fluorescence intensity of all comparable replicate wells, with smoothing of the average intensities (Savitzky-Golay, 2nd order) to eliminate noise. This caused the average fluorescence intensity of all replicates to range between 0 and 1, without eliminating variation between replicates. Although smoothing was used when determining maximum and minimum intensities for the purpose of normalisation, it was not applied to the

raw, blank/baseline-subtracted, or normalised fluorescence intensities; therefore, the ThT data presented in this thesis are all affine functions of the raw intensities, ie. $I = aI_{\text{raw}} + b$, where I is the presented intensity, I_{raw} is the raw intensity, a is the normalisation, and b is the baseline. The half-time τ_{50} was defined as the time at which the baseline-subtracted fluorescence reached 50% of its maximal value. The maximum relative rate ν_{max} was defined as the maximum normalised rate of fluorescence intensity gain, and the lag time was determined by extrapolation of a tangent from the inflection point of the curve back to the x-axis, as described in Arosio *et al.* [374].

2.6 Circular dichroism (CD) spectroscopy

CD spectroscopy was performed on a JASCO J-810 (JASCO, UK) spectropolarimeter, in a quartz cuvette with a 1 mm path length (Hellma, UK) at 37°C. Spectra were acquired over the 190 nm $\leq \lambda \leq$ 250 nm range, with a bandwidth of 1 nm and scan speed of 20 nm.min^{-1}. All spectra were blank-subtracted; the samples and their corresponding blanks are described in the methods sections of subsequent chapters. Three replicates were acquired for each spectrum (3 min apart), and the replicates were compared to ascertain whether the sample changed between replicates. In all experiments, no significant change was observed, so the replicates were averaged to improve the signal-to-noise. Spectra were often truncated at the shorter wavelengths, as the HT increased and the signal-to-noise became too poor; due to the low signal-to-noise of many of the spectra in this thesis, this often occurred at HT $\approx$ 500, but occasionally higher. Due to the requirement to use low concentrations and the peptide's mixed conformational state, low signal-to-noise was unavoidable for some experiments in this thesis. Measured ellipticities were converted to mean residue ellipticities according to the equation

$$[\Theta]_{\text{MR}} = \frac{\Theta}{10ncl}, \tag{2.15}$$

where $[\Theta]_{\text{MR}}$ is the molar residue ellipticity in deg.cm^2.dmol^{-1}, Θ is the measured ellipticity in mdeg, n is the number of amino acids in the polypeptide, c is the molar concentration of the sample in M, and l is the path length in cm.

2.7 Negative stain electron microscopy (NS-EM)

Samples for NS-EM were prepared and incubated in the same manner as samples for ThT assays (Section 2.5), but were aspirated and pipetted onto pre-prepared carbon-coated grids after allowing fibrillisation for a set amount of time, as described in the following subsections. Carbon coating and preparation of stain were performed by myself and Dr. Svetomir Tzokov; negative staining and imaging were carried out by myself and other experimentalists mentioned where relevant in this thesis.

2.7.1 Carbon coating of grids

Carbon film was deposited on freshly cleaved mica using a TEM Turbo Carbon Coater (Agar Scientific), and then transferred to Cu-Pd grids (Agar Scientific). To transfer the carbon film, grids were arranged on a piece of filter paper that had been immersed in a tank of Milli-Q water and weighted down. After cleaning the water surface, the carbon film was transferred to the surface from the mica and the water was siphoned out of the tank to float the carbon film onto the the grids, which were then covered and left to dry overnight.

2.7.2 Preparation of uranyl formate stain

Uranyl formate was prepared to a concentration of 0.75% (w/v). To prepare the stain, 5 ml of dH_2O was boiled in a glass test tube over a bunsen and poured into a foil-wrapped beaker containing 0.0375 g uranyl formate. The beaker was covered and left to stir for 5 min, then 5 M NaOH was added dropwise until a small colour change was observed ($\sim$8 µl required), and the solution was covered and stirred for another 5 min. The uranyl formate solution was then passed through a 0.2 µm filter, made up to 5 ml with dH_2O, and stored in the fridge in a foil-wrapped falcon tube. Stain was discarded once a precipitate formed at the bottom of the tube.

2.7.3 Sample deposition and negative staining

Carbon-coated grids were glow-discharged at low pressure in the glow discharge unit of a Cressington 208 carbon coater (Ted Pella Inc., CA). The usual glow discharging time was 20 s, but was increased to 40 s when grids were not expected to be used immediately, which was often the case when samples were extracted from fibrillisation experiments at specific time points, as time constraints required the grids to be glow-discharged in batches before the start of the experiment. Samples were prepared according to one of two methods: dilution into fibrillisation buffer followed by immediate staining, or incubation in fibrillisation buffer in a 96-well microplate at 37°C. Further details of sample preparation are experiment-specific, and are described in the relevant methods sections of the following chapters. Samples were mixed gently and 7 µl was pipetted onto a glow-discharged grid and left to adsorb for 1 min. Grids were blotted edge-on with filter paper and briefly washed twice in dH_2O and once in 0.75% uranyl formate stain, blotting after each wash. Grids were then immersed in 0.75% uranyl formate stain for 20 s, blotted again, and dried with a vacuum pump. For long-term storage, grids were covered with foil to prevent damage to the stain.

2.7.4 Imaging and analysis

Grids were imaged on a Philips CM100 TEM at 100 kV, with either a LaB_6 cathode or tungsten filament and spot size 2. Micrographs were recorded with a 1024×1024 px Gatan CCD camera, typically at 8900-

28500× magnification. Images were analysed using FIJI [482, 483].

2.8 Size Exclusion Chromatography (SEC)

Samples were analysed and purified using an analytical Superdex 75 column (GE healthcare), with in-line UV (280 nm; Shimadzu, UK), MALS (Postnova Analytics, Germany), and RI (Postnova Analytics, Germany) detectors. The details of specific experiments are described in the methods sections of the following chapters. Data processing and analysis were carried out in the AF2000 Control software (Postnova Analytics, Germany), with final data processing in GraphPad Prism version 8.3.0. For analysis of elution volumes, K_{av} values were calculated for each peak. These describe the extent to which the molecules partition into the beads, and were determined according to the relation

$$K_{av} = \frac{V_e - V_0}{V_t - V_0}, \tag{2.16}$$

where V_e is the elution volume of the peak, V_0 is the void volume, and V_t is the total column volume. The K_{av} values are expected to be proportional to the logarithm of the molecular weight, and so were plotted against M_w and fitted to the equation

$$K_{av} = a \log M_w + b, \tag{2.17}$$

where a and b are unconstrained parameters.

Chapter 3

Optimisation of the Aβ Preparation Protocol

3.1 Introduction

Biophysical investigation of Aβ self-assembly requires reproducible, controlled experiments with a well-defined starting point. For this reason, it is essential that Aβ preparation protocols produce highly monomeric, unseeded solutions with minimal chemical modification or pre-aggregation. Moreover, any such protocol must eliminate other common sources of error, such as contamination, pH variation, and inconsistent yields. Obtaining such a high level of reproducibility has been a significant challenge in the study of Aβ, and despite more than 50 years of intense experimental research, there is still no single preferred protocol. While many groups use synthetic peptide (eg. [51,163,214,233,278,280,285,286,289,383,484–486]), others use recombinant peptide, which may be prepared in-house [303, 487–496] or obtained commercially [144,277,295,365,497,498]. A wide variety of solvents may be used to monomerise the peptide before addition to the reaction buffer, including urea [369], hexafluoroisopropanol (HFIP) [116, 216, 233, 277, 279, 289, 296, 498–500], NaOH [72, 216, 234, 279, 296, 466, 497–499], and NH_4OH [116, 165, 280, 286, 500]; in addition, solvent treatment is often supplemented by steps such as sonication [116, 289, 484] or additional rounds of size exclusion chromatography (SEC) [116,231,286,485,494,501,502] to remove high molecular weight species. These options allow for considerable diversity of possible preparation protocols, and the methods used vary almost from one research group to the next. Given the lack of consensus and the extreme sensitivity of Aβ to its self-assembly conditions, it is unsurprising that the consistency of the experimental literature remains poor. For example, different groups using apparently similar conditions have reported fibrillisation half-times spanning several orders of magnitude [234, 383, 479, 486]. Furthermore, many have reported considerable variation between replicate experiments [486, 487, 503]. While this variability has

sometimes been attributed to stochasticity of the underlying aggregation process [487], careful experimental work has shown that recombinant preparations can yield highly reproducible kinetics, so long as steps are taken to ensure sufficient sample quality and reproducible self-assembly conditions [479].

Previous work in this lab has used recombinant Aβ [504, 505], as synthetic preparations are highly prone to truncation, racemisation, and other chemical modifications, and are thus considered less reliable and physiologically relevant [495]. Dr. Abigail Williams, a past member of the lab, was able to express and purify sufficient quantities of Aβ(1-40) for NMR; however, the aggregation-prone nature of Aβ required the peptide to be expressed with a ubiquitin tag, and the peptide's tendency to aggregate following cleavage of this tag meant that purification was both complex and time-consuming [504]. More generally, many research groups have found that the time and loss of peptide required to purify Aβ prohibit the use of in-house preparations in high-frequency experiments, such as ThT or CD assays screening a broad range of conditions. Because commercial preparations require fewer monomerisation and purification steps prior to use, they provide an attractive alternative. However, while highly consistent kinetics have been attained with in-house preparations [479], the same level of consistency has not been observed from commercial sources. To some extent, development of a reproducible protocol is hindered by a lack of transparency regarding commercial preparation procedures and the identity of possible contaminants; any protocol aiming to use commercial peptide must account for this uncertainty. In addition, experimentalists have differed over the preferred protocol for solubilising commercial peptide, which is typically supplied in a lyophilised form to prevent self-assembly during storage. A variety of solvents are used for this purpose, including bases such as NaOH [72, 216, 234, 279, 296, 466, 497–499] and NH_4OH [116, 165, 280, 286, 500], and denaturants such as urea [369] and HFIP [116, 216, 233, 277, 279, 289, 296, 498–500]; research groups also use a wide range of solvent concentrations, balancing the need to avoid chemical modification against the risk of using overly 'gentle' conditions that allow pre-aggregation.

This chapter describes the development of a simple, reproducible protocol for solubilisation of commercial Aβ(1-42), capable of yielding highly consistent self-assembly kinetics suitable for biophysical study. This protocol was validated using a variety of biophysical techniques, including a novel fractionation technique, asymmetric flow field-flow fractionation (AF4) [506], which was coupled with multi-angle light scattering (MALS) to fractionate samples and determine their molecular weight in the liquid phase. To assist with discussion of the AF4-MALS results, a brief overview of these techniques is given in the following two subsections of this introduction. The data presented in this chapter show that the dilute base (often 1-10 mM NaOH or 0.02-1% NH_4OH (v/v)) used in many existing protocols [72, 165, 234, 280, 497–499] is insufficient to prevent pre-aggregation; however, a high level of sample monomerisation can be attained by using more concentrated base, coupled with cryogenic storage and careful batch control. Samples prepared in this way are stable, not chemically modified, and do not contain detectable seed. In addition, self-assembly assays

reveal an extremely high level of experimental reproducibility, and additional purification measures simply result in loss of peptide, without significantly altering the kinetics. Thus, this preparation protocol is simple, convenient and economical, and allows commercial Aβ(1-42) to be used to obtain high-quality biophysical data.

3.1.1 Principles of AF4

Asymmetric flow field-flow fractionation (AF4) [506] is a powerful analytical and preparative technique for liquid-phase fractionation of samples with a broad range of particle sizes, from 1 nm to 50 μm [507]. AF4 is a member of the broader field-flow fractionation (FFF) family of techniques, which rely on a separation field to sort the constituents of a heterogeneous sample to different positions within a channel, and laminar flow within the channel to translate that separation into different elution times [508]. While a variety of separation fields are used in FFF techniques – electrophoresis, thermophoresis, and sedimentation can all generate the initial separation – AF4 is uniquely characterised by the use of asymmetric flow orthogonal to the main flow of material through the channel, fractionating the sample by translational diffusion coefficient [506]. A schematic of the 'normal' mode of AF4 separation is provided in Fig. 3.1(a). With the frit inlet channel, which was used in the experiments described in this chapter, the sample enters the channel via the TIP flow, passing through a frit inlet which prevents over-concentration during injection. The TIP flow entering the channel is matched by the detector flow leaving the channel, causing an overall flow of material through the channel towards the detector outlet. Solvent also enters the channel via the focus flow, which has a variable rate that is matched by the cross-flow. The cross-flow draws solvent out of the channel through a semi-permeable membrane at the channel bottom, creating an additional asymmetric flow orthogonal to the flow along the channel. This cross-flow exerts force on the sample and causes it to accumulate next to the membrane, through which it is unable to pass. The flux density J_x of a solute particle in the direction of the cross-flow depends on the distance x from the membrane,

$$J_x = Uc(x) - D\frac{dc(x)}{dx}, \tag{3.1}$$

where U is the drift velocity of the solute particle, $c(x)$ is its concentration, and D its translational diffusion coefficient. In Eq. (3.1), the first term accounts for advection of the particle towards the membrane due to the cross-flow, and the second accounts for diffusion along the established concentration gradient, according to Fick's law. At a steady-state, $J_x = 0$, such that

$$c(x) = c_0 e^{-\frac{Ux}{D}}, \tag{3.2}$$

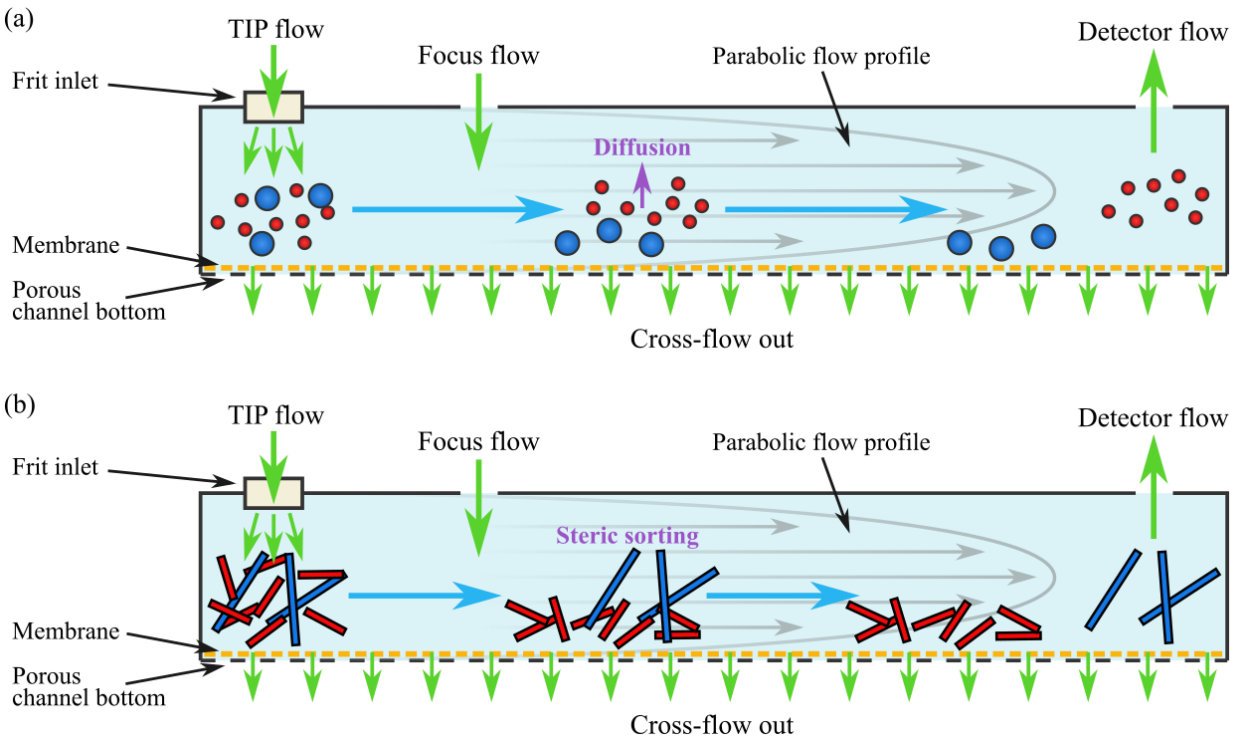

Figure 3.1: Schematic of sample separation by AF4 with a frit inlet channel. (a) Operation in normal mode. (b) Operation in steric mode. In both schematics, green arrows indicate flows in and out of the channel, blue arrows indicate the general direction of flow within the channel, and the gray arrows represent the parabolic flow profile, with flow faster towards the centre of the channel and slower towards the edges. See text for full description of elution behaviour in both modes. Figure based on information in Cölfen and Antonietti [507] and training material provided by Postnova Analytics (Landsberg am Lech, Germany).

where c_0 is the sample concentration at the membrane. Thus, after the sample enters the channel its distance from the membrane reaches a steady-state distribution according to U and D; greater U will cause the sample to be concentrated close to the membrane, while greater D will cause the sample to spread out through the channel. For AF4, the former is expressed as

$$U = \frac{\dot{V}_c w}{V_0}, \tag{3.3}$$

where $\dot{V}_c$ is the cross-flow rate, V_0 the channel volume, and w the channel thickness along the axis of cross-flow. Thus,

$$c(x) = c_0 e^{-\frac{\dot{V}_c w x}{V_0 D}}. \tag{3.4}$$

At this point, it is useful to introduce a dimensionless parameter $\lambda_r = \langle x \rangle / w$, which is the average distance of the sample from the membrane as a proportion of the channel thickness. From the mean of the exponential distribution described by Eq. (3.4),

$$\lambda_r = \frac{V_0 D}{\dot{V}_c w^2}. \tag{3.5}$$

For sufficiently small particles undergoing rapid rotational diffusion, the translational diffusion coefficient D is connected to the hydrodynamic (Stokes) radius R_H by the Stokes-Einstein relation,

$$D = \frac{k_B T}{6\pi\eta R_H}, \tag{3.6}$$

where k_B is the Boltzmann constant, T the temperature, and η the dynamic viscosity of the carrier fluid. Thus, particles with smaller R_H will have greater D, resulting in greater λ_r due to Eq. (3.5). In other words, smaller particles are more able to diffuse against the cross-flow, meaning they are distributed further from the membrane, as shown in Fig. 3.1(a). Flow along the channel has a low Reynold's number Re, meaning that it is laminar and not turbulent. Under these conditions, friction with the channel walls causes the carrier fluid to exhibit a parabolic flow profile, faster towards the centre of the channel and slower towards the edges, including the membrane. Because smaller particles occupy a position more distant from the membrane, they will experience faster flow towards the detector outlet, and will thus elute first, as shown in Fig. 3.1(a). For small λ_r, theoretical work has shown that the sample retention time t_r is given by the relation

$$t_r \approx \frac{t_0}{6\lambda_r} = \frac{t_0 \dot{V}_c w^2}{6 V_0 D} = \frac{t_0 \dot{V}_c w^2}{V_0} \frac{\pi\eta R_H}{k_B T}, \tag{3.7}$$

where t_0 is the elution time of an unretained solute. Thus, the retention time is inversely proportional to the diffusion coefficient D, or simply proportional to the hydrodynamic radius R_H [507]. In addition, sample retention may be improved by increasing the cross-flow rate $\dot{V}_c$ or channel thickness w. The former of

these may be actively controlled throughout a sample run in order to give fine control over the elution of the sample. A typical AF4 run will begin with high cross-flow for maximum retention, and then slowly ease the cross-flow to allow increasingly large particles to elute. This level of fine control and the lack of a solid phase allow AF4 to fractionate samples across a broad range of sizes. The channel thickness w can be controlled via a spacer, which separates the top of the channel from the membrane. Although changing w also affects V_0, the quadratic dependence of Eq. (3.5) on w^2 ensures that this still results in a change in λ_r. The ability to recover larger species and exert fine control over the fractionation process gives AF4 a significant advantage over SEC. In addition, the column matrix used in SEC provides a large surface area with the potential to bind to Aβ, potentially affecting the aggregation process; by separating particles in the liquid phase, AF4 is therefore a less perturbative technique for analysis of aggregation-prone samples.

In addition to the 'normal' elution mode, AF4 exhibits an alternative form of elution for particularly large samples, such as amyloid fibrils. Steric elution occurs when a particle's hydrodynamic radius is large compared to its mean distance from the membrane, with the transition zone typically occurring around $R_H \approx 500$ nm [507, 509]. As shown in Fig. 3.1(b), the large size of the particle limits its proximity to the membrane, so that larger particles have a centre of mass further from the membrane, rather than closer to it as in normal mode. As a result, larger species flow faster through the channel, and elute first. The expression for λ_r is thus proportional to R_H,

$$\lambda_r = \frac{R_H}{w}, \tag{3.8}$$

and the retention time is inversely proportional to R_H,

$$t_r \approx \frac{t_0}{6\lambda_r} = \frac{t_0 w}{6R_H}, \tag{3.9}$$

This reversal of the elution order can present a challenge to fractionation of particularly polydisperse samples in which both normal and steric elution occur, although careful optimisation of the flow profile will usually allow adequate resolution to be attained. In addition to normal mode and steric mode, samples may sometimes be compressed against the membrane, in which case they will usually only be released after cross-flow has ceased. For small, soluble molecules, this is rare; however, particularly large particles may sometimes adhere, and poor choice of membrane chemistry can also encourage attraction between the sample and the membrane.

Fig. 3.2(a) shows an example of the detector output from a typical AF4 run, demonstrating the three main types of peak that can occur during elution. The first is the 'system' peak ($t_r \approx 2$ min), which contains a mixture of (i) the smallest constituents of the sample that did not pass through the membrane, and (ii) some of the largest constituents of the sample, undergoing steric elution. In this case, the system peak has a strong light scattering (LS) signal, indicating an abundance of high molecular weight species; the relationship

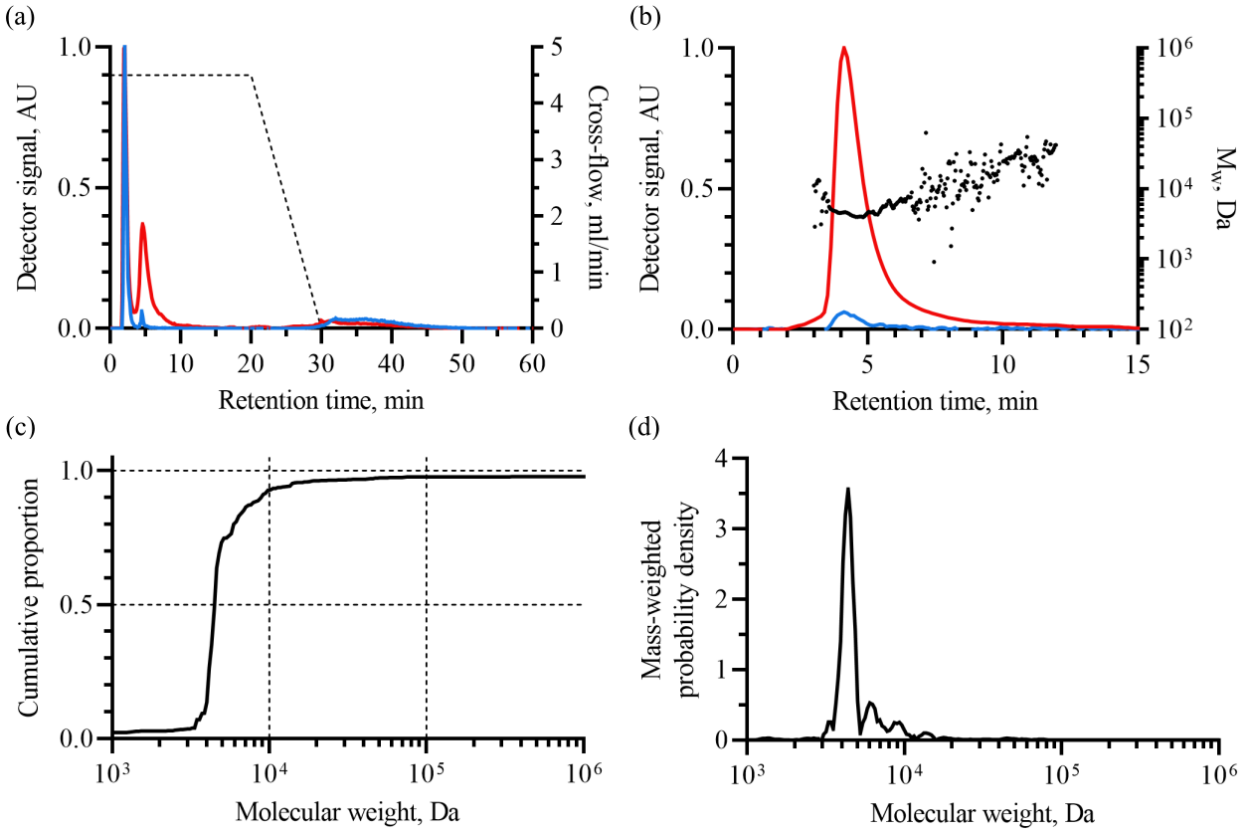

Figure 3.2: Analysis of AF4-MALS data. (a) Detector output from a typical AF4-MALS run, in this case a sample of 1 mg/ml Aβ(1-42) solubilised by 30 min sonication in 10 mM NaOH, with a 1 mM NaOH mobile phase. Colour scheme: red, UV_{280} signal; blue, LS at 90°, with the other angles omitted for clarity; black dashed, cross-flow rate. (b) Analysis of an AF4 peak, in this case a sample of 1 mg/ml Aβ(1-42) solubilised by 5 min sonication in 50 mM NaOH, with a 1 mM NaOH mobile phase. Colour scheme: red, UV_{280} signal; blue, LS at 90°; black, estimated M_w. (c) Cumulative molecular weight distribution $P(M)$ of the peak in panel (b). (d) Mass-weighted molecular weight distribution $Mp(M)$ of the peak in panel (b), derived by differentiation and transformation of panel (c) as described in Section 3.1.2

between molecular weight and LS intensity is discussed in the following subsection. The second peak ($t_r \approx 5$ min) consists of properly separated sample eluting in normal mode, mainly Aβ(1-42) monomer with some oligomer forming a tail on the right-hand side. If the oligomer size distribution were bimodal or multimodal, this would be revealed by additional peaks after this point. The third peak ($t_r > 30$ min) consists of very high-molecular-weight species that were compressed against the membrane when cross-flow was high, and were released at after the end of cross-flow.

3.1.2 Analysis of AF4-MALS data

After eluting from the channel, the sample passes through the detectors. In the work described in this chapter, the primary concentration detector was UV absorbance at 280 nm (UV_{280}), although a refractive

index (RI) detector was also used for the SEC-MALS data. In addition, MALS was used to determine the sample's molecular weight (working range from ∼200 Da to ∼10^9 Da) and radius of gyration (R_g; working range from ∼8 nm to ∼500 nm). The two most commonly used molecular weight averages in AF4-MALS data analysis are the number-averaged molecular weight M_n and the weight-averaged molecular weight M_w [510]. The former is defined as

$$M_n = \frac{\sum_i n_i m_i}{\sum_i n_i}, \tag{3.10}$$

where n_i represents the number and m_i the molecular weight of each particle i in the sample mixture. The mass-averaged molecular weight is defined as

$$M_w = \frac{\sum_i n_i m_i^2}{\sum_i n_i m_i}. \tag{3.11}$$

While M_n gives the expected molecular weight of a randomly chosen particle in the sample, M_w gives the expected molecular weight of a particle containing a randomly chosen *unit of mass*; since larger particles have greater mass, more of the mass of the sample will be contained within these species. For example, for a sample consisting only of different Aβ self-assembly species, M_n will give the expected molecular weight of a randomly chosen species, while M_w will give the expected molecular weight of a species that a randomly chosen Aβ molecule is part of. For a monodisperse sample containing species of only a single size, M_n and M_w will be the same; however, for any other sample, M_w will exceed M_n due to the greater contribution of larger species. The ratio of these masses gives the polydispersity index (PDI) [510],

$$\mathrm{PDI} = \frac{M_w}{M_n} \geq 1. \tag{3.12}$$

A PDI of 1 indicates that the sample is completely monodisperse; a PDI greater than 1 indicates a heterogeneous size distribution, or the presence of experimental noise artificially broadening the apparent size distribution. The PDI can be related to the variance of the MW distribution σ^2 according to the relation

$$\mathrm{PDI} = 1 + \frac{\sigma^2}{M_n^2}, \tag{3.13}$$

which confirms that PDI $= 1$ when $\sigma = 0$. Practically speaking, it is M_w rather than M_n that is determined from the MALS data [511]. However, provided separation is good, the polydispersity of the sample passing through the detector at any given time is small, so that $M_w \approx M_n$. In these cases, the calculated M_w values can be used to construct a molecular weight distribution for the entire region of interest, which has its own M_n and M_w values.

As the sample passes through the MALS detector, it is irradiated with laser light at wavelength λ. The

light interacts with the sample, is scattered, and the angular dependence of the scattered light is measured at discrete angles θ. Small particles ($R_g \lessapprox \lambda/20$) scatter isotropically, while larger particles scatter with an angular dependence. This results from interference between photons scattered by different mass centres within the same particle. At each angle, the Rayleigh ratio R_θ gives the normalised ratio of the scattered light intensity to the incident light intensity. For a homogeneous sample, R_θ depends on the mass concentration ρ and average molecular weight M_w according to the relation

$$R_\theta = \frac{K\rho M_w P_\theta}{1 + 2A_2\rho M_w}, \tag{3.14}$$

where K is the optical constant, P_θ is a form factor that accounts for the angular dependence, and A_2 is the second virial coefficient. The form factor P_θ, which satisfies the boundary condition $P_{\theta=0} = 1$ and has $P_\theta < 1$ for $\theta > 0$, depends on the R_g and shape of the particles in the sample; thus, by using known values of K, A_2, and ρ, with the latter supplied by the concentration detector, it is possible to fit a model assuming a particular shape to the angular dependence, and thus estimate M_w and R_g. Comparison of fits can then inform which model describes the data best, and thus provides the best estimate of these parameters. Alternatively, in the absence of specific information about the geometry of particles, one can still obtain the M_w from the value of R_θ when $\theta = 0$, since $P_\theta = 1$ at this point. Although the high intensity of unscattered light at $\theta = 0$ makes direct measurement of $R_{\theta=0}$ impossible, an extrapolated $R_{\theta=0}$ value can be obtained by polynomial fitting of R_θ across a range of angles. The form factor is a polynomial of $\sin^2(\theta/2)$ of the form [511]

$$P_\theta = 1 - \frac{2}{3!}\langle R_g^2\rangle \left[\frac{4\pi}{\lambda}\sin\left(\frac{\theta}{2}\right)\right]^2 + \ldots \ , \tag{3.15}$$

so that for $2A_2\rho M_w \ll 1$,

$$\frac{R_\theta}{K\rho} = M_w\left\{1 - \frac{2}{3!}\langle R_g^2\rangle \left[\frac{4\pi}{\lambda}\sin\left(\frac{\theta}{2}\right)\right]^2 + \ldots\right\}. \tag{3.16}$$

In the Debye fitting method [512], $R_\theta/K\rho$ values are plotted against $\sin^2(\theta/2)$ and polynomially fitted. The M_w value can then be obtained from the extrapolated $R_\theta/K\rho$ value at $\theta = 0$, and $\langle R_g^2\rangle$ from the gradient at this point. In the Zimm fitting method [513], the reciprocal quantity $K\rho/R_\theta$ is plotted against $\sin^2(\theta/2)$, which extends the region close to $\theta = 0$ in which the curve is approximately linear. Thus, one can make the approximation,

$$\frac{K\rho}{R_\theta} \approx \frac{1}{M_w}\left\{1 + \frac{2}{3!}\langle R_g^2\rangle \left[\frac{4\pi}{\lambda}\sin\left(\frac{\theta}{2}\right)\right]^2\right\}, \tag{3.17}$$

which allows M_w and $\langle R_g^2\rangle^{1/2}$ to be obtained from linear fitting. In order for this approach to work across

the range of $\sin^2(\theta/2)$ values, R_g must be sufficiently small compared to λ. In the Berry method [514], the square root reciprocal intensity $(K\rho/R_\theta)^{1/2}$ is plotted against $\sin^2(\theta/2)$, and polynomially fitted. While the Debye method is typically superior for spherical particles, the Berry plot is favoured for random coils. For large particles, the Zimm plot is inferior, but it is appropriate for small particles for which one does not expect a highly non-linear angular dependence [511].

An example of the analysis of an AF4 peak is given in Fig. 3.2(b), with M_w values determined from the Zimm plot. In practice, most well-separated peaks in the samples investigated in this chapter consisted of small species with a low angular dependence, making fitting of R_g unreliable; however, this did not affect fitting of M_w. As can be seen in the figure, the calculated M_w is initially around 4500 Da, indicating that the peak corresponds to Aβ(1-42) monomer. Towards the right-hand side, the M_w begins to increase, reflecting an increasing concentration of oligomers. The cumulative mass proportion $P(M)$ of sample that eluted in fractions with M_w up to a certain value M can be calculated from the relation

$$P(M) = \frac{\int_{t_{r,1}}^{t_{r,2}} H[M - M_w(t_r)]\dot{V}_d(t_r)\rho(t_r)dt_r}{\int_{t_{r,1}}^{t_{r,2}} \dot{V}_d(t_r)\rho(t_r)dt_r}, \tag{3.18}$$

where the limits of the integral can correspond to the entire experimental timescale, or a particular region of interest (ROI). Here, $H(x)$ is a Heaviside step function such that $H(x) = 1$ for $x \geq 0$, and $H(x) = 0$ for $x < 0$. In addition, $M_w(t_r)$ is the M_w value calculated from the concentration detector and MALS, $\dot{V}_d(t_r)$ is the detector flow rate, and $\rho(t_r)$ is the sample mass concentration, where all are functions of retention time t_r. The denominator in Eq. (3.18) is equal to the total recovery of sample. An example of a plot of $P(M)$ is shown in Fig. 3.2(c). The corresponding probability density function $p(M)$ can then be obtained by differentiating $P(M)$,

$$p(M) = \frac{dP(M)}{dM} = \frac{\int_{t_{r,1}}^{t_{r,2}} \delta[M - M_w(t_r)]\dot{V}_d(t_r)\rho(t_r)dt_r}{\int_{t_{r,1}}^{t_{r,2}} \dot{V}_d(t_r)\rho(t_r)dt_r}, \tag{3.19}$$

where $\delta(x)$ is a Dirac delta function. In practice, of course, measured t_r values are discrete, so discrete approximations must be used for Eq. (3.18, 3.19) (see Section 3.2.4) [515]. Although $p(M)$ is important for further calculations, it has a significant drawback for data representation as it is typically most convenient to use a logarithmic M axis. This causes peaks occurring at lower M to be laterally stretched, and those occurring at higher M to be compressed. When presenting data, this can cause the area under peaks situated at lower M to appear overly large, and *vice versa*. Therefore, for presenting data it is often preferable to use a mass-weighted probability density function $Mp(M)$,

$$Mp(M) = M\frac{dP(M)}{dM} \equiv \frac{dP(M)}{d\log M}, \tag{3.20}$$

which corrects for the distortion occurring when a logarithmic M axis is used. Thus, the apparent area under peaks in $Mp(M)$ when using logarithmic M will be proportional to the actual area under the corresponding peak in $p(M)$ obtained via linear integration, and thus the corresponding $\Delta P(M)$. An example of a plot of $Mp(M)$ is shown in Fig. 3.2(d).

Technically, the distributions $P(M)$, $p(M)$, and $Mp(M)$ represent the quantities of sample eluting in fractions with $M_w(t_r)$ at or below a certain value. As previously discussed, if the separation is good, the polydispersity of the sample at each t_r will be relatively low so that $M_w(t_r) \approx M_n(t_r)$. In these instances, the $M_w(t_r)$ value during elution is close to the molecular weight of a single eluting species, so that $P(M)$, $p(M)$, and $Mp(M)$ closely approximate the underlying mass distribution of the entire ROI. If this is the case, then it is appropriate to use $p(M)$ to calculate molecular weight averages for the ROI as a whole, according to the relations [510]

$$M_n^{\mathrm{ROI}} = \left[\int_0^\infty M^{-1} p(M) dt_r \right]^{-1}, \tag{3.21}$$

$$M_w^{\mathrm{ROI}} = \int_0^\infty M p(M) dt_r. \tag{3.22}$$

Similarly, the corresponding PDI can then be calculated from these averages using Eq. (3.12). If separation is poor, the eluting sample will be polydisperse, so that $P(M)$, $p(M)$, and $Mp(M)$ will be poor approximations for the underlying molecular weight distributions. In practice, this is likely to cause unresolved peaks in $p(M)$ to 'merge' into a single peak occurring at an intermediate M value, with corresponding changes in $P(M)$ and $Mp(M)$. If separation is poor but experimental noise is low, this can even give the appearance of a narrow molecular weight distribution and a low PDI; however, such a result is misleading as proper estimation of the PDI across an ROI requires good separation of the sample.

It is also important to remember that experimental noise has a strong effect on the breadth of peaks in the apparent molecular weight distribution. The sample itself has a discrete distribution of molecular weights. However, error in $\rho(t_r)$ and $R_\theta(t_r)$ is propagated in $M_w(t_r)$, and results in broadening of the peaks in $p(M)$. In addition, random clustering of $M_w(t_r)$ values at points away from the mean can result in artificial peaks in $p(M)$; this effect is responsible for much of the fine detail in Fig. 3.2(c-d), such as the organisation of the right-hand tail of the peak in Fig. 3.2(d) into a succession of small peaks. The solution to this problem is simply to eliminate the noise; this can be achieved by only investigating the regions of the elugram where the signal-to-noise is good, carrying out data processing to remove the noise, or accumulating the results of replicate experiments. The latter option has the advantage of allowing investigation of a broad region of the elugram with a low risk of creating artifacts due to data processing.

3.2 Materials and methods

3.2.1 Materials

For a description of the materials used in this chapter, see Section 2.1.

3.2.2 Aβ(1-42) preparation and handling

When preparing Aβ(1-42), it was important to avoid introducing contaminants such as dust and bubbles that might affect self-assembly; readers are referred to Section 2.2.1 for details of the general precautions taken. In this chapter, three different dissolution protocols were used. In protocol 1, Aβ(1-42) was dissolved in HFIP to a concentration of 1 mg/ml peptide. Solvent was injected into the vials in which the peptide was supplied using a Hamilton syringe (Reno, NV), which was kept clean by frequent washing. After addition of solvent, vials were manually rotated for 10 s to ensure that any material on the sides came into contact with solvent, and then sonicated for 30 min using a DECON Ultrasonics sonicator bath (Sussex, UK). Peptide was extracted from the vials using a Hamilton syringe and split into 100 μl aliquots. The HFIP was evaporated off under a stream of N_2 gas and the peptide was re-lyophilised and stored at -20^{o}C. Prior to the start of experiments, each aliquot was solubilised in 10 mM NaOH to a peptide concentration of 1 mg/ml, with trituration to ensure adequate mixing. In protocol 2, the HFIP treatment step was omitted. Each peptide sample was directly dissolved in 10 mM NaOH to a concentration of 1 mg/ml peptide, again injected using a Hamilton syringe. The vial was manually rotated for 10 s after addition of solvent, and sonicated for 30 min using a DECON Ultrasonics sonicator bath (Sussex, UK). Peptide was extracted using a Hamilton syringe, split into 50 μl aliquots in Eppendorf tubes, and flash-frozen by immersion in liquid N_2. Protocol 3 was the same as protocol 2, except that the solvent was 50 mM NaOH and the sonication time was 0 min (ie. directly flash-frozen), 5 min (the default for this protocol), or 30 min. Prior to use in experiments, peptide aliquots prepared according to protocol 2 or 3 were thawed at 37^{o}C; thawing on ice was not attempted as it would prolong the time spent in the liquid phase at high pH. Samples were then triturated to ensure that they were well-mixed. As described in the Section 3.3.8, it was found that peptide samples prepared according to protocol 3 could be successfully re-frozen and re-thawed between uses, without affecting the quality of the peptide. Three re-freezing protocols were attempted: flash-freezing in liquid N_2 (freezing time < 1 s); freezing in contact with pre-cooled metal at -80^{o}C (< 1 min); and simply placing the sample in a rack in the -80^{o}C freezer (< 5 min). All re-freezing protocols had identical results.

3.2.3 ThT assays

ThT assays were carried out as described in Section 2.5, with a fibrillisation buffer containing 20 mM sodium phosphate (pH 8), 200 μM EDTA, 1 mM NaN_3, and 20 μM ThT.

3.2.4 Asymmetric flow field-flow fractionation (AF4)

Samples were analysed using an AF4 frit inlet (FI) channel equilibrated in 1 mM NaOH, with a 250 μm spacer and a 1 kDa PES membrane, and in-line UV (280 nm; Shimadzu, UK), MALS, and RI detectors. Except where otherwise stated, the channel, associated pumps, autosampler, and detectors were purchased or loaned from Postnova Analytics (Landsberg am Lech, Germany). The RI detector was purged following equilibration, and the UV and RI detectors were then zeroed. The sample injection volume was 20 μl, except where otherwise stated. The sample was run with 0.2 ml/min TIP and detector flow; the focus and cross-flow rates were also matched to one another, and varied throughout the run. To ensure that results were comparable, the same flow profile was used for all runs after initial optimisation: cross-flow began at 4.5 ml/min for 20 min, followed by a linear decay to 0 ml/min over the course of 10 min, followed by a period with constant cross-flow of 0 ml/min for at least 30 min. Blanks consisting of the same solvent without the Aβ(1-42) were run before and after samples, to ensure that the channel was clean and to allow blank subtraction of the UV and RI detector signals. For AF4-MALS, UV_{280} was found to be preferable to RI for concentration determination, as the latter is highly sensitive to changes in flows, and given the relatively small quantities of sample injected gave poor signal-to-noise as a result. Data processing and estimation of sample concentration, molecular weight, and recovery were carried out in the AF2000 Control software (Postnova Analytics, Landsberg am Lech, Germany), with additional data processing in GraphPad Prism version 8.3.0. The M_w values were calculated using a variety of different fitting methods for each ROI, and the method that gave the best fit without over-fitting the data was used wherever possible. Collated M_w estimates were converted to the cumulative density function $P(M)$ using a discrete approximation of Eq. (3.18),

$$P(M) \approx \frac{\sum_{t_r|M>M_w(t_r)} \dot{V}_d(t_r)\rho(t_r)\Delta t_r}{\sum_{t_r} \dot{V}_d(t_r)\rho(t_r)\Delta t_r}, \tag{3.23}$$

where Δt_r is the time interval between reading, which was sufficiently small ($\sim$0.12 min) for the approximation to be reasonably accurate. The probability density functions $p(M)$ and $Mp(M)$ were then calculated from $P(M)$ according to Eq. (3.19) and Eq. (3.20), respectively.

3.2.5 Circular dichroism (CD) spectroscopy

CD spectroscopy was carried out as described in Section 2.6. The sample contained 0.1 mg/ml Aβ(1-42) in 5 mM NaOH, prepared by 10x dilution of an aliquot of Aβ(1-42) prepared according to protocol 3. The blank was simply 5 mM NaOH.

3.2.6 Negative stain electron microscopy (NS-EM)

NS-EM was carried out as described in Section 2.7. Prior to staining, Aβ(1-42) was diluted to a concentration of 4 μM peptide in a pre-adjusted fibrillisation buffer containing 20 mM sodium phosphate (pH 8.0), 200 μM EDTA, 1 mM NaN_3, and 20 μM ThT. The sample was stained either immediately, or after incubation for ∼1 h in a 96-well plate treated with a PEG-like low-binding surface (Corning 3881, NY), at 37°C.

3.2.7 Ultracentrifugation

Ultracentrifugation was carried out at 436,000 g and 21°C for 60 min. In order to obtain a sufficiently large volume, a 70 μl sample of 1 mg/ml Aβ(1-42) in 50 mM NaOH was diluted 10x in dH_2O, to give 700 μl of 0.1 mg/ml Aβ(1-42) in 5 mM NaOH, at pH 11.6. The control was similarly treated, but was simply incubated at 21°C in a centrifuge tube without ultracentrifugation, for the same amount of time. For AF4-MALS, a larger-than-usual injection volume of 200 μl was used to ensure the same mass injection as other experiments with undiluted Aβ(1-42). For ThT assays, the buffer was pre-adjusted to account for the increased volume of the Aβ(1-42) as described in Section 2.4, and the pH of the dissolved solution was checked.

3.2.8 Size exclusion chromatography (SEC)

Samples were analysed and purified in small batches using an analytical Superdex 75 column (GE healthcare) equilibrated in 20 mM sodium phosphate buffer (pH 8) with 200 μM EDTA and 1 mM NaN_3. The column was run with the TIP pump from the AF4 system (Postnova Analytics, Landsberg am Lech, Germany), and in-line UV (280 nm; Shimadzu, UK), MALS (Postnova Analytics, Landsberg am Lech, Germany), and RI (Postnova Analytics, Landsberg am Lech, Germany) detectors. The RI detector was purged following equilibration, and the UV and RI detectors were then zeroed. The sample injection volume was 50 μl, and the sample was run at 1.0 ml/min for 35 min. Between sample runs, blanks consisting of the same solvent without the Aβ(1-42) were loaded to ensure that the column was clean and to allow blank subtraction of the detector signals. As molecular weight standards, lysozyme (14.3 kDa), β-phosphoglucomutase (βPGM; monomer, 24.2 kDa), insulin (hexamer, 34.4 kDa), bovine serum albumin (BSA; monomer, 66.5 kDa; dimer, 133.0 kDa), and blue dextran (∼2000 kDa) were used. Although MALS confirmed the expected molecular weight of all standards, lysozyme and insulin interacted with the column due to the low ionic strength and the former's high pI, and had to be excluded. Data processing and estimation of sample concentration, molecular weight, and recovery were carried out in the AF2000 Control software (Postnova Analytics, Landsberg am Lech, Germany), with final data processing in GraphPad Prism version 8.3.0. For

preparative runs, the protocol was the same except that the sample was collected at the end. Purified Aβ(1-42) was collected on ice between 15.3 min and 16.3 min after injection, corresponding to an elution time of 13.6 min to 14.6 min; the detector volume (1.7 ml) was determined by flowing blue dextran through the detectors. Eluted Aβ was mixed and split into three aliquots; these were then diluted to 60%, 80%, or 100% (ie. undiluted) their concentration in the same elution buffer and supplemented with 20 μM ThT from a 2 mM stock, as described in Hellstrand *et al.* [479]. This yielded final solutions containing approximately 3.8 μM, 5.0 μM, or 6.3 μM Aβ(1-42) as determined by RI, in almost exactly 20 mM sodium phosphate (pH 8), 200 μM EDTA, and 1 mM NaN_3 (99.0% nominal concentration), with exactly 20 μM ThT. The pH of these samples was confirmed experimentally. Due to the potential for ThT to interact with the column, ThT had to be added from a concentrated stock after purification; the slight dilution of the buffer due to addition of 1% ThT is too small to significantly affect the kinetics, and cannot explain any significant differences between these experiments and corresponding experiments performed with exactly 20 mM sodium phosphate, 200 μm EDTA, and 1 mM NaN_3. Purified Aβ(1-42) was then used immediately in ThT assays, as described in Section 2.5; exact Aβ(1-42) concentrations accounting for all dilutions were calculated retrospectively from the RI quantitation data, after the start of the ThT experiment. All SEC and SEC-ThT methods are based on the protocol described by Hellstrand *et al.* [479]. The K_{av} values, which describe the extent to which molecules partition into the beads of the column matrix, were calculated according to Eq. 2.16 and fitted to 2.17, as described in Section 2.8.

3.2.9 Liquid chromatography mass spectrometry (LC-MS)

LC-MS was performed by the staff at the Department of Chemistry's mass spectrometry facility. Each sample was loaded onto an Agilent Zorbax Extend-C18 reverse-phase column with a 1.8 μm particle size, equilibrated with 0.1% formic acid and 5% acetonitrile. The injection volume was 1 μl, and the sample was eluted at 0.4 ml/min, with a linear acetonitrile gradient from 5% to 95% over 15 min. Masses were detected using an Agilent 6530 Q-ToF (Agilent Technologies, Santa Clara, CA) in ESI positive ion mode.

3.2.10 Nonlinear regression

Wherever possible, analytical models were fitted in GraphPad Prism 8 using Levenberg-Marquardt least squares fitting. Due to its complexity, Eq. (1.36) could not be fitted in GraphPad Prism; therefore, initial parameter estimates were found by fitting Eq. (1.41) in GraphPad Prism, and then refined by fitting to Eq. (1.36) using the solver add-in in Microsoft Excel (365). When fitting τ_{50}, whose error is expected to scale with the mean, residuals were weighted relative to the square of the mean. Akaike's corrected information criterion (AICc) values were calculated from the residual sum of squares (RSS) according to

the relation [516]

$$\mathrm{AICc} = N \ln\left(\frac{\mathrm{RSS}}{N}\right) + 2K + \frac{2K^2 + 2K}{N - K - 1}, \tag{3.24}$$

where N is the number of data points and K is the number of fitted parameters. The likelihood of each model was proportional to $\exp(-\mathrm{AICc}/2)$, so that the relative likelihood between two models was $\exp(-\Delta\mathrm{AICc}/2)$.

3.3 Results and discussion

3.3.1 Irreproducible kinetics of Aβ(1-42) prepared using existing protocols

Prior to the work described in this chapter, members of the lab had used 10 mM NaOH to solubilise commercial Aβ(1-42) samples. Two main protocols were used, the full details of which are given in Section 3.2.2. In protocol 1, which was based on Sato *et al.* [499], lyophilised peptide was first dissolved in HFIP by sonication for 30 min, then aliquoted, re-lyophilised, and stored at -20°C. Aliquots were then thawed and re-solubilised in 10 mM NaOH. In protocol 2, which is close to several protocols in the literature [72,234,497], Aβ(1-42) was directly dissolved in 10 mM NaOH by sonication for 30 min, flash-frozen in liquid N_2, and then stored at -80°C. Protocol 2 was originally introduced by Dr. Liam Aubrey as a simplification of protocol 1, and was also motivated by concerns that HFIP treatment might induce pre-aggregation [231, 517, 518]. Several members of the lab prepared Aβ(1-42) according to both these protocols, and the self-assembly kinetics of the solubilised Aβ(1-42) were investigated by ThT assays. These kinetics are highly sensitive to the peptide's composition and chemical environment, and so provide a quick and informative initial experiment to assess the quality of different preparations. ThT assays were carried out in low-binding plates (Section 3.2.6) with a 20 mM sodium phosphate buffer (pH 8.0) containing 200 μM EDTA, 1 mM NaN_3, and 20 μM ThT; in-house recombinant preparations have previously been shown to produce highly reproducible kinetics under these conditions [479, 519]. Fig. 3.3(a) shows a representative example of a ThT assay of Aβ(1-42) prepared according to protocol 2, with peptide concentrations ranging from 1-5 μM. The concentration-dependence γ_{50} of the fibrillisation half-time is significantly lower than expected, with $\gamma_{50} = 0.88$ for Aβ(1-42) concentrations in the 1-4 μM range, compared to the value of $\gamma_{50} = 1.33$ previously reported for the same concentration range with in-house recombinant peptide [54]. In addition, curves have a significant, non-zero initial fluorescence indicating that some aggregation had occurred before the start of the experiment.

In addition, a low level of consistency was observed between the self-assembly kinetics of different Aβ(1-42) preparations. Fig. 3.3(b) provides a comparison of the fibrillisation half-times of ThT experiments in which the Aβ(1-42) concentration was varied. Each data point corresponds to the accumulated results of several replicate fibrillisations, carried out with Aβ(1-42) from a single solubilisation. The green and cyan

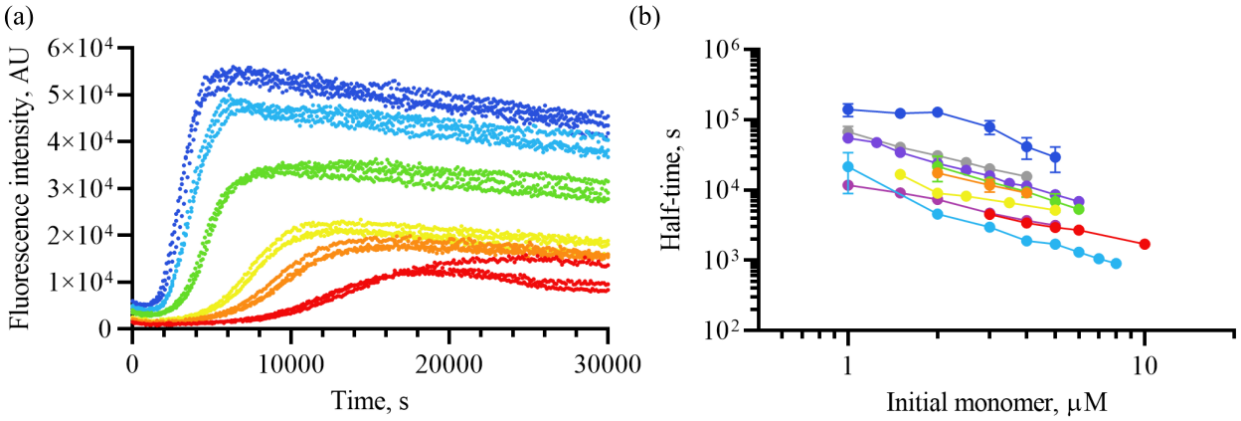

Figure 3.3: Self-assembly kinetics of Aβ(1-42) solubilised with 10 mM NaOH. (a) Representative fibrillisation kinetics of Aβ(1-42) prepared according to protocol 2, viewed by ThT assay. Colour scheme encodes Aβ(1-42) concentration: red, 1 μM; orange, 1.5 μM; yellow, 2 μM; green, 3 μM; cyan, 4 μM; blue, 5 μM. Three replicate curves are shown for each Aβ(1-42) concentration. (b) Comparison of the concentration-dependence of the fibrillisation half-times of 9 different Aβ(1-42) samples prepared in 10 mM NaOH. The colour scheme indicates individual preparations of Aβ(1-42). The datasets coloured red, orange, yellow, green, and cyan were prepared using protocol 1; those coloured blue, indigo, violet, and gray were prepared according to protocol 2. Error bars, which for most datasets are too small to show, indicate the standard deviation of several replicate fibrillisations with the same Aβ(1-42) sample.

datasets are from Aβ(1-42) that was solubilised by Miss Zoe Parton and Mr. Joshua White, respectively, who also acquired those datasets. In addition, the blue dataset is from Aβ(1-42) that was solubilised by Mr. Joshua White, which I later examined by ThT assay. Concordancy between replicate experiments was typically good; thus, Fig. 3.3(b) shows variability between Aβ(1-42) preparations, rather than replicate experiments. Both the absolute rate and concentration-dependence can be seen to vary significantly between different Aβ(1-42) samples. For kinetics at single peptide concentrations acquired by other members of the lab (data not shown), a similar degree of inconsistency was also observed. This variation persisted despite standardisation of the protocol for ThT assays, and did not correlate with the experimentalist preparing the sample or carrying out the experiment. Thus, comparison of these data indicated that flaws in the existing protocols resulted in poor control of one or more experimental variables during solubilisation, and that this was responsible for the observed variation. The high initial ThT fluorescence suggested that significant pre-aggregation was one of the likely causes of the poor reproducibility.

3.3.2 Kinetic variability results from incomplete monomerisation

In order to diagnose the cause of the irreproducible self-assembly kinetics, Aβ(1-42) samples prepared using protocol 2 were analysed by AF4-MALS, in a 1 mM NaOH mobile phase. The sample composition was then correlated with the final pH at the end of solubilisation, and the self-assembly kinetics observed in

ThT assays. Fig. 3.4(a-b) shows the UV_{280} and MALS elugrams from a representative selection of experiments; for two of these datasets, the corresponding M_w elugrams are shown in Fig. 3.4(c), and representative ThT kinetics acquired with the same Aβ(1-42) are shown in Fig. 3.4(d). The fitting methods used for the MALS analysis depended on the sample, and are described in greater detail in the following paragraphs. The UV_{280} and MALS elugrams revealed three different peaks in varying quantities: the system peak at 2.0 min, containing varying quantities of sterically eluting material; the main peak from normal elution, with a maximum at 4.2-5.0 min; and a broad peak after 30 min, corresponding to large material that accumulated close to the membrane and was only released after cross-flow. The high degree of variation in the UV_{280} and MALS signals of these peaks supported the hypothesis that poor sample consistency was responsible for the irreproducible kinetics. By correlating the pH of preparations following dissolution with the extent of pre-aggregation revealed by AF4 and the ThT assembly kinetics, it was possible to classify the preparations into two distinct groups. Only protocol 2 was used here, so the differences between these groups result from the inability of the protocol to result in consistent Aβ(1-42) samples, rather than differences in methodology. In both sets of preparations, it is important to note that the pH (6.5-10.5) was well below the expected pH (12.0) of 10 mM NaOH. The pH of the solvent was checked immediately prior to use and a substantial reduction was always observed following dissolution of the peptide, indicating that a constituent of the vials was neutralising the NaOH to a varying extent. Since the concentration of Aβ(1-42) (222 μM) was not high enough to neutralise a sufficient proportion of the solvent, variable quantities of residual counterions were most likely to be responsible.

The first set of preparations solubilised to a moderately high pH (10.0-10.5). Representative examples are provided by the datasets coloured red and amber in Fig. 3.4(a-d), which are from different preparations that both had a final pH of 10.0. These samples usually had little to no steric elution and mostly eluted in normal mode, although some larger species were also detected after cross-flow (Fig. 3.4(a-b)). The UV_{280} and MALS data were used to obtain a M_w elugram (Fig. 3.4(c)), with the linear Zimm fit used from 3.3-12.0 min and the 4^{th} degree Berry fit from 30.0-45.0 min. Examination of this elugram revealed that the peak at ∼4.2 min had $M_w \approx 4500$ Da, consistent with Aβ(1-42) monomer; after ∼6 min, the M_w began to increase, indicating that the tail of the peak contained Aβ(1-42) oligomers. It was not possible to exactly quantify the monomer content, as the data were too noisy to obtain a reliable molecular weight distribution. Nonetheless, it was possible to estimate the proportion of low molecular weight (LMW) and high molecular weight (HMW) species by integrating the UV_{280} signal from 3.3-30.0 min and 30.0-60.0 min, respectively. In this chapter, LMW fractions are defined as those that elute in normal mode during crossflow, while HMW fractions are defined as those that elute in the system peak or after cross-flow, as this is a convenient and informative distinction to make based on the experimental data. While monomers, oligomers, and small fibrillar species would be expected to elute in the LMW fraction, larger aggregates such as mature fibrils

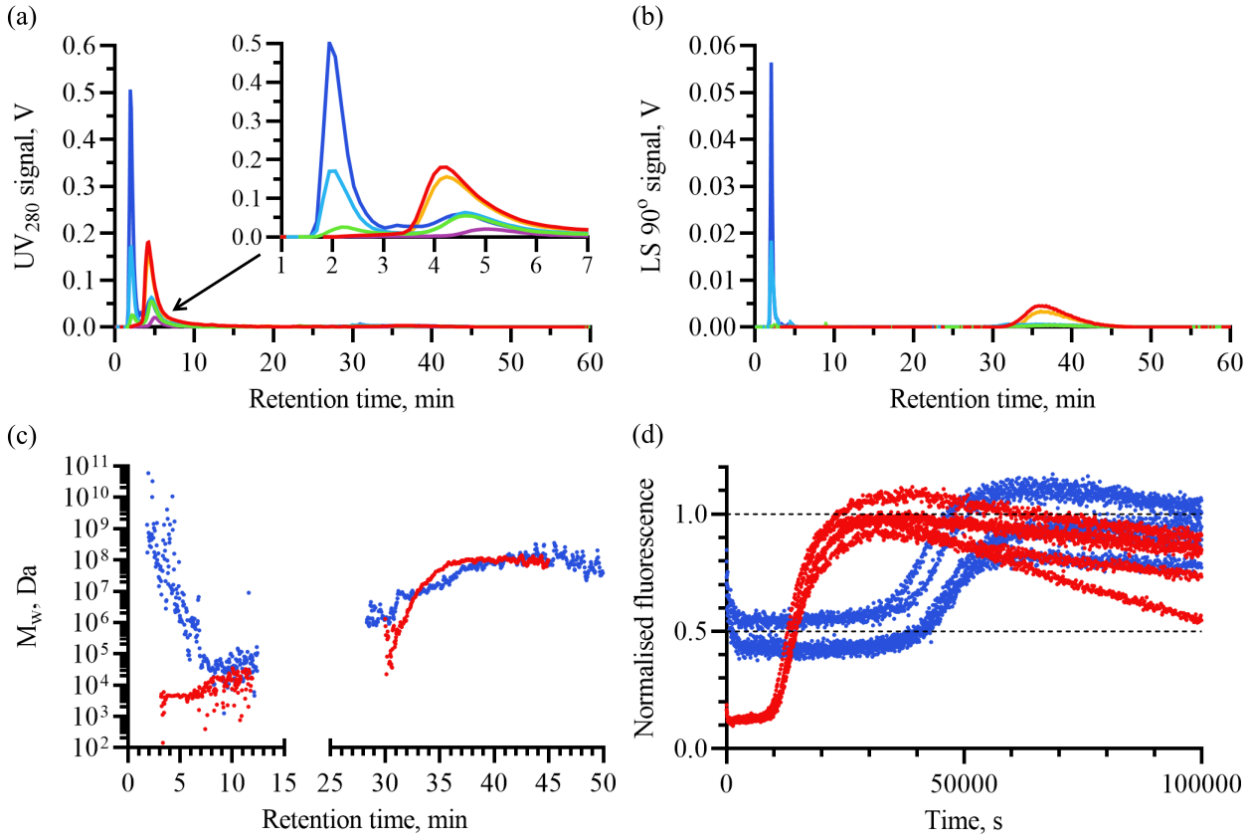

Figure 3.4: AF4-MALS analysis of Aβ(1-42) samples previously solubilised with 10 mM NaOH (protocol 2). (a) Blank-subtracted UV_{280} elugrams from the AF4-MALS analyses, with each curve corresponding to the results of a single experiment. For clarity, data were selected from a broader body of experiments (6/13) to represent the full range of results. (b) The corresponding LS 90° elugrams, with the same colour scheme. (c) The M_w elugrams corresponding to the red and blue curves in panels (a) and (b), with the same colouring. For clarity, only these two datasets are shown in this panel. (d) Representative ThT self-assembly kinetics obtained with the same Aβ(1-42) samples as the red and blue curves in panels (a) and (b). The ThT experiments were conducted at different times and with different gain settings; to allow comparison, each ThT curve has been normalised relative to the maximum mean fluorescence of its own set of replicates. The colour scheme corresponds across all panels, and identifies different Aβ(1-42) samples. After solubilisation, the final pH values of the samples were: red and amber, 10.0; green, cyan and blue, 7.4; violet, 7.0.

would be expected to elute in the HMW fraction. Empirically, the transition between these two fractions appeared to occur at molecular weights of 10^5-10^7 Da, although the high level of noise and poor separation at $t_r = 30$ min mean this is a very approximate figure. Averaged across all AF4-MALS analyses of Aβ(1-42) samples in this group, around 18.4 ± 0.144 μg eluted in the LMW fractions and 2.35 ± 1.65 μg in the HMW fraction, where the error margins represent one standard deviation. Given that a nominal 20 μg of peptide was injected in each case, this indicates that approximately 10% of the injected Aβ(1-42) was in too aggregated a state to be recovered in the LMW fraction. Similarly, the blank-subtracted initial fluorescence in ThT assays was typically around 10% of the final fluorescence (Fig. 3.4(d)), suggesting that a significant proportion of these HMW species were able to bind ThT. Although ThT-positive aggregates are often suggested to seed fibrillisation, a clear relationship between the size of the HMW fraction and the fibrillisation rate was not observed. Furthermore, the fact that the ThT kinetics had a well-defined lag phase despite such large quantities of aggregate indicated that the majority of aggregates did not seed fibrillisation. Nonetheless, results presented later in this chapter show that elimination of the HMW species results in a reduced initial ThT fluorescence and highly consistent kinetics, indicating that they are responsible for the reproducibility issues. Instead, they may exert a more complex effect on the self-assembly process, with some species seeding fibrillisation and others inhibiting it. Although some studies have proposed that pH >10.0 is sufficient to prevent aggregation [233, 486, 520, 521], others have observed limited self-assembly behaviour in the pH 10.0-11.0 range [294]. The AF4-MALS data presented here clearly show significant levels of aggregation in this range, indicating that the moderate pH either allowed aggregation to occur, or was unable to disassemble pre-formed aggregates.

While one set of preparations reached a moderately high pH (10.0-10.5) after dissolution, the other had a more neutral pH (6.5-8.7). Representative examples are provided by the remaining datasets in Fig. 3.4(a-d). The data coloured green, cyan, and blue are all replicate experiments from a single Aβ(1-42) preparation (pH 7.4), demonstrating the poor concordancy of experiments carried out with this sample; the dataset coloured violet is from a separate Aβ(1-42) preparation (pH 7.0). The lower pH of these preparations suggested that the 10 mM NaOH had been more extensively neutralised by counterions, and was well within the established aggregating range [294, 421]. Unsurprisingly, these samples had strong UV_{280} (Fig. 3.4(a)) and MALS (Fig. 3.4(b)) signals at $t_r \approx 2$ min, indicating that large species ($R_H \gtrapprox 500$ nm) were sterically eluting in the system peak. The UV_{280} and MALS signals were used to obtain a M_w elugram (Fig. 3.4(c)); the angular dependence was analysed using the 4th degree Berry fit from 2.0-7.0 min, the linear Zimm fit from 7.0-12.5 min, and the 3rd degree Berry fit from 28.0-50.0 min. Analysis of the M_w elugram revealed high molecular weights and a reversal of separation order early during elution, as would be expected for steric elution, although for these particular experiments the system peak and monomer peak were not fully resolved. The quantity of material in the system peak (Fig. 3.4(a)) varied considerably; in some cases, as

much as half of the sample eluted in this peak, whereas in others this portion of the sample appeared to be missing. Samples were mixed before injection, but were often very viscous, and had a strong tendency to foam when pipetted; therefore, insoluble aggregates may still have been inhomogeneously distributed in the vials. Alternatively, other protein aggregates have been observed to adhere irreversibly to the membrane when injected at high concentrations, and this may have contributed to the observed variation. On average, out of the 20 μg of sample injected, 6.36 ± 6.75 μg eluted in the system peak (0.0-3.3 min), 6.62 ± 2.07 μg eluted in normal mode (3.3-30.0 min), and 2.52 ± 1.51 μg after cross-flow (30.0-60.0 min), confirming that the sample was in a highly aggregated state. In some cases, ThT experiments with these samples simply resulted in a high fluorescence with no observable kinetics; in other cases, kinetics were observed (Fig. 3.4(d)), but the blank-subtracted initial fluorescence was large compared to the final fluorescence, and the kinetics were delayed. The fact that the kinetics were delayed despite the high initial fluorescence further supports the conclusion that the aggregates contaminating these samples are predominantly off-pathway.

3.3.3 High-pH solubilisation yields highly reproducible Aβ(1-42) preparations

The above data indicate that preparations with a final pH in the 10.0-10.5 range do not contain large quantities of seed material, but the pH must be raised higher still to remove the confounding influence of non-fibrillar aggregates. Furthermore, overly dilute base can be neutralised even by small quantities of residual counterions in the vial; this causes pH inconsistency, and risks total failure of the preparation. Therefore, in order to improve both the quality and the reliability of preparations, the issue of pH neutralisation had to be addressed. One possible approach was to purify solubilised samples by SEC, removing the counterions. However, SEC of Aβ(1-42) typically results in significant loss of peptide and dilution of the eluted sample, limiting the concentrations that can be used in experiments down the line. This negates one of the main advantages of commercial preparations, which are already supplied at at high level of purity. Furthermore, given the substantial cost of commercial peptide, the losses incurred in purification are more of an issue than they are for in-house preparations. This approach also fails to address the sub-optimal yields and high failure rate of dilute base treatments, since SEC cannot recover Aβ(1-42) that has already aggregated. Lastly, in order to use Aβ(1-42) at even moderate concentrations (1-6 μM) it is typically necessary to purify the peptide in the buffer that will be used for subsequent experiments [479]. This is inconvenient, limiting the lifespan of the purified samples to a few minutes, and risking further pre-aggregation during elution and sample collection. For these reasons, the decision was made to address the issue of partial neutralisation at the point of dissolution, before attempting any additional purification procedures.

The simplest means to achieve a higher and more reliable pH was to increase the concentration of NaOH. This would ensure that there was an excess of strong base, preventing formation of a buffered solution with any residual acids in the vials. In addition, the greater the concentration of base, the smaller

the proportional variation of the concentration that would be neutralised, resulting in a more consistent pH. The main disadvantages of this approach were (i) uncertainty over whether the higher pH would cause modification of the peptide, and (ii) the increased care required to properly control the pH of experiments carried out using such samples. Nonetheless, since the current pH was clearly not high enough to prevent pre-aggregation, and proper pH control was still completely possible so long as experimental buffers were pre-adjusted and the pH was regularly checked (Section 2.4), higher pH solubilisation was attempted.

In protocol 3, Aβ(1-42) was directly dissolved in 50 mM NaOH by sonication for 5 min, flash-frozen in liquid N_2, and then stored at -80°C; more complete details are provided in Section 3.2.2. The sonication time was reduced as a precaution to limit the exposure of the peptide to high pH while in the liquid phase; as will be shown in Section 3.3.8, flash-freezing and cryogenic storage then reduce the rate of any potential chemical modifications and allow long-term storage. In most cases (92%), peptide samples solubilised in this manner had a final pH above 12.0, and the final pH was typically around 12.5, which is close to the expected value (12.7) for 50 mM NaOH. Initial investigation by AF4-MALS, using the same method that was applied to samples prepared by other methods (1 mM NaOH mobile phase, pH 11), showed that these samples were highly consistent and had negligible steric elution. These data are presented in Fig. 3.5. On average, 20.1 $\pm$ 1.11 μg of material eluted from 3.3-30.0 min, and a nominal 0.777 $\pm$ 0.380 μg eluted from 30.0-60.0 min, where the error margins represent a single standard deviation. It is worth noting that the sum of these values is slightly larger than the injected mass of 20 μg Aβ(1-42), whereas the mean recovery between 3.3 and 30.0 min is remarkably close to the expected value. This suggests that close to 100% of peptide may have been recovered in the LMW fraction, and the material eluting after cross-flow may instead have been other contaminants, such as dust. This assessment is supported by analyses presented later in this chapter, which show that removal of the material eluting after cross-flow in high-pH preparations did not affect the self-assembly kinetics.

Initial comparison of the collated UV_{280} elugrams suggested that samples prepared in 50 mM NaOH exhibited a greater degree of monomerisation and overall solubilisation than those prepared in 10 mM NaOH. Fig. 3.6(a) compares the average UV_{280} elugrams of these samples. The use of 50 mM NaOH resulted in a more intense monomer peak with a shorter tail, indicating that the sample contained more monomer and a smaller proportion of oligomers. In addition, the quantity of sample eluting after cross-flow was significantly reduced, in line with the previously stated recovery figures and a lower level of pre-formed aggregates. As can be seen in Fig. 3.6(b), the final preparation pH strongly affects the degree of solubilisation, confirming the importance of using sufficiently concentrated base to achieve full peptide recovery.

The abundance of AF4-MALS data enabled a detailed analysis of the molecular weight distribution of the 50 mM NaOH Aβ(1-42) samples. Fig. 3.7(a) contains an overlay of M_w elugrams obtained from 11 closely concordant experiments, and Fig. 3.7(b) shows the geometric average of those results. For self-

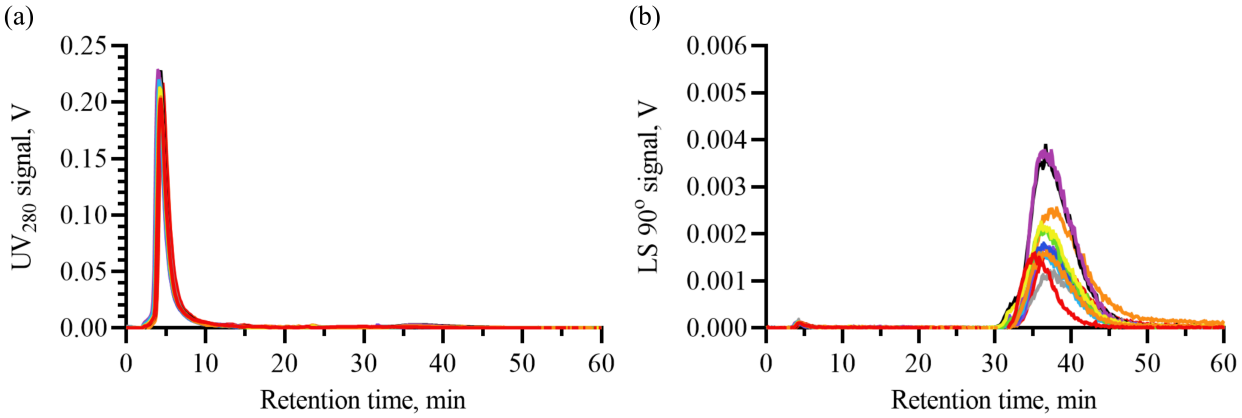

Figure 3.5: AF4-MALS analysis of Aβ(1-42) samples previously solubilised with 50 mM NaOH (part 1). (a) Blank-subtracted UV_{280} elugrams from the AF4-MALS analyses, with each curve corresponding to the results of a single experiment ($n = 13$). (b) The corresponding LS 90° elugrams, with the same colour scheme. Further analysis of the data in this figure is shown in Fig. 3.7.

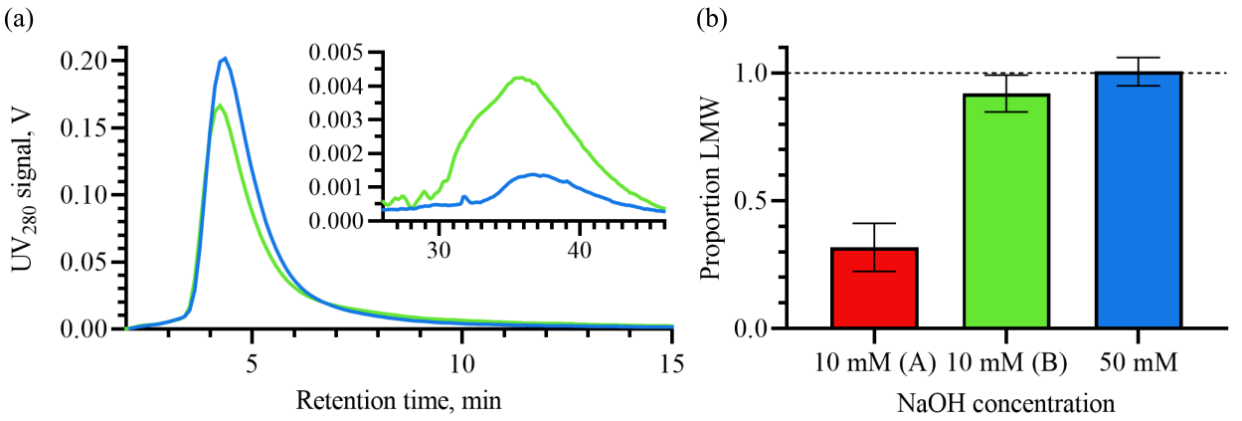

Figure 3.6: AF4 comparison of Aβ(1-42) samples previously solubilised with 10 mM NaOH (protocol 2) and 50 mM NaOH (protocol 3). (a) Average blank-subtracted UV_{280} elugrams of Aβ(1-42) samples prepared with 10 mM NaOH ($n = 5$) and 50 mM NaOH ($n = 11$). Due to consistency issues with low-pH samples, only those that had final pH $\geq$10.0 are included in this panel. Two experiments with 50 mM NaOH samples were excluded, as a difference in the volume of the detector tubing caused a small peak shift that would have artificially broadened the average UV_{280} peak. The inset panel shows the average signal after cross-flow. (b) Proportion of injected sample eluting in LMW fractions (3.3-30.0 min). Colour scheme for both panels: red, Aβ(1-42) prepared with 10 mM NaOH, with final pH in the 6.5-8.7 range ($n = 8$); green, Aβ(1-42) prepared with 10 mM NaOH, with final pH in the 10.0-10.5 range ($n = 5$); blue, Aβ(1-42) prepared with 50 mM NaOH, with final pH in the 11.0-12.7 range ($n = 13$). One of the Aβ(1-42) samples included in this analysis was prepared by Dr. Liam Aubrey (10 mM NaOH, final pH 10.5).

consistency, the linear Zimm fit was used throughout this ROI, from 0.0-20.0 min; this provided a good fit for all retention times. Applying Eq. (3.22) gave the molecular weight average $M_w^{\mathrm{ROI}} = 4380$ Da for the fractions eluting from 4.0-5.0 min (with PDI = 1.00046), within an expected level of systematic error of the value of 4513 Da expected for a monomeric self-assembly state. As in the 10 mM NaOH samples (Fig. 3.4(c)), the M_w began to increase towards the tail of the peak, suggesting that some oligomeric species were present. Although distinct peaks were not observed for the oligomers, meaning that the particle size distribution was approximately unimodal, the low dM_w/dt_r indicated that separation was of sufficient quality to produce a molecular weight distribution. Due to the noise present in individual M_w elugrams, it was preferable to first sum or average the data before calculating the distributions, as this is theoretically predicted to improve the signal-to-noise in proportion to the square root of the number of concordant replicates. Initial attempts to do this involved separate summations of the UV_{280} and MALS signals; these were then combined to produce a M_w elugram with a lower level of noise. In practice, this approach did not work well, as small variations in the volume of the detector tubing meant that it was difficult to properly align data from different experiments. In the end, an alternative approach was adopted. The M_w elugrams (Fig. 3.7(a)) exhibited a high degree of concordancy, meaning that the average of those elugrams (Fig 3.7(b)) could be used to obtain molecular weight distributions. Since the $\log M_w$ values varied more slowly than the MALS signals, the difficulties with alignment affected the outcome less. Using Eq. (3.23), with $M_w(t_r)$ supplied by the geometric mean M_w across samples and $\rho(t_r)$ obtained from the arithmetic mean of the UV_{280} signal, a cumulative density function (CDF) was obtained for the molecular weight of an ROI lasting from 3.3-20.0 min (Fig. 3.7(c)). Fractions eluting before 3.3 min were not analysed as they contained too much material undergoing steric elution, biasing the MALS signal, and fractions eluting after 20.0 min were excluded due to excessive noise. Strictly speaking, this CDF gives the proportion of sample that eluted in fractions with M_w below a particular value; however, due to the low dM_w/dt_r, it is likely to be a reasonable approximation of the underlying molecular weight distribution. Around 88% of sample eluted in fractions whose M_w was closest to monomer, and 12% of sample eluted in higher M_w fractions, mostly consistent with small oligomers. This probably somewhat underestimates the monomer content, as: (i) the excluded material eluting before 3.3 min was probably monomer contaminated with trace amounts of sterically eluting material; (ii) the averaging process did not fully eliminate the noise from the M_w elugram, which will have exaggerated the oligomer content; and (iii) samples with M_w closer to dimer or larger may still have been predominantly monomer, with small quantities of particularly large species biasing the results. Nonetheless, although this analysis suggests that the LMW fraction consisted predominantly of monomer, it is clear that small quantities of oligomeric species were present.

The cumulative molecular weight distribution was then used to obtain a mass-weighted probability density function (PDF) of the sample (Fig. 3.7(c)), according to Eq. (3.19, 3.20). As described in Section 3.1.2,

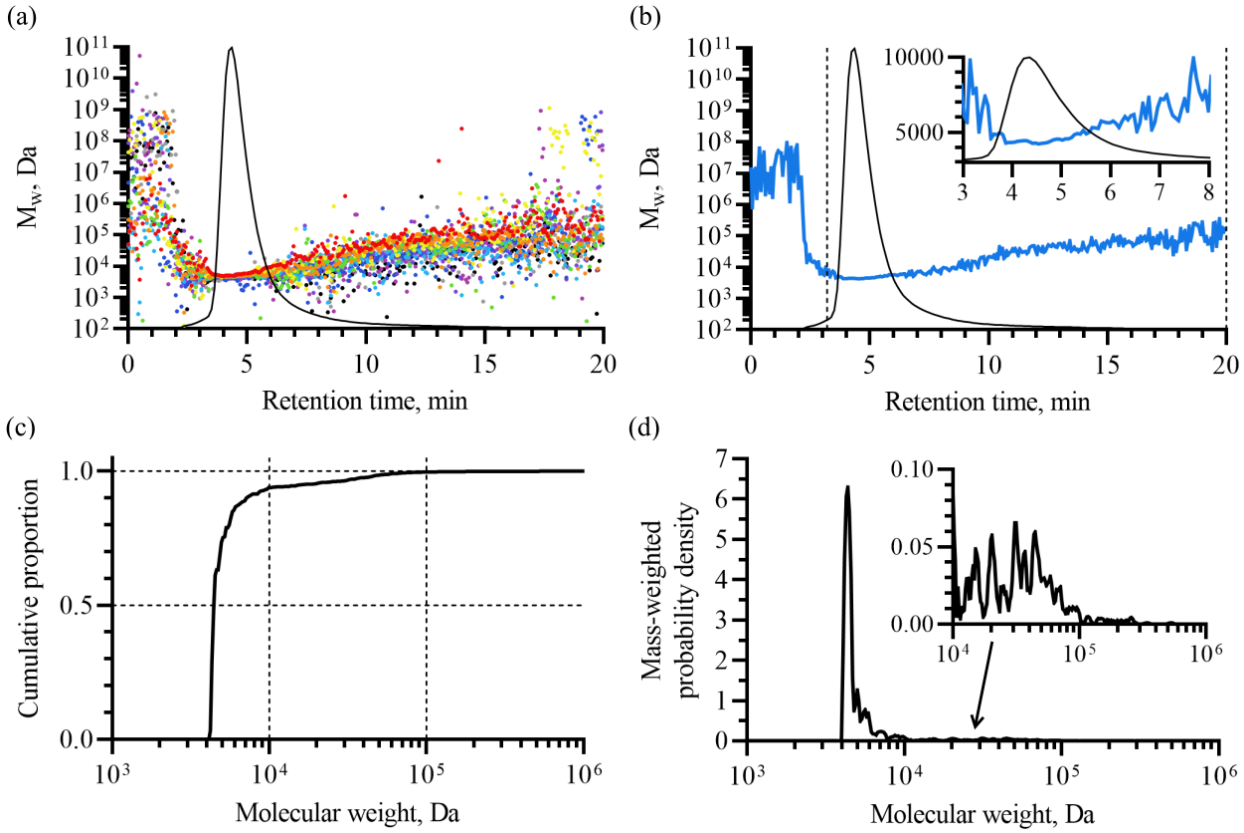

Figure 3.7: AF4-MALS analysis of Aβ(1-42) samples previously solubilised with 50 mM NaOH (part 2). (a) Overlay of M_w elugrams obtained from 11 concordant experiments. Calculated M_w values are represented as points on a logarithmic axis, with the colour representing different experiments. The average UV_{280} signal has been included for reference (black line, linear scale, relative units). (b) Average of the M_w values presented in panel (a) (blue line, logarithmic axis), with the average UV_{280} signal included for reference (black solid line, linear scale, relative units). The inset panel shows a close-up of the monomer peak, with the M_w represented on a linear axis. The dashed vertical lines represent the boundaries of the ROI used to construct molecular weight distributions. (c) Cumulative density function $P(M)$ of the ROI in panel (b). (d) Mass-weighted probability density function $Mp(M)$ of the ROI in panel (b).

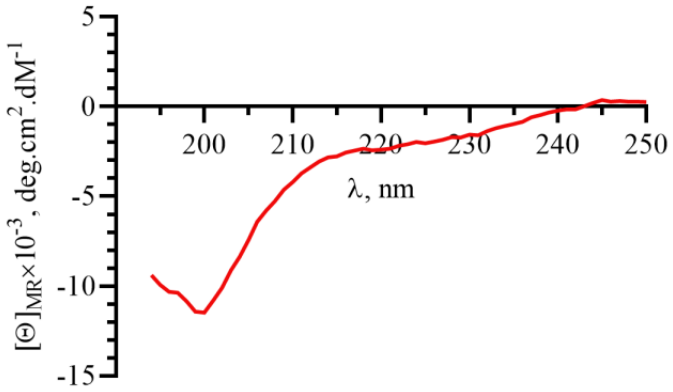

Figure 3.8: CD spectrum of an Aβ(1-42) sample solubilised with 50 mM NaOH, showing molar residue ellipticity Θ as a function of wavelength λ. The spectrum is an average of 3 concordant replicates; ellipticities below 195 nm were excluded due to a poor signal-to-noise ratio. The sample was diluted 10× in dH_2O before measurement, resulting in a concentration of 0.1 mg/ml Aβ(1-42) in 5 mM NaOH.

the mass weighting corrects for the distortions caused by using a logarithmic molecular weight axis, so that the area under the peaks is proportional to the area under the corresponding unweighted peaks on a linear axis. Consistent with the lack of additional peaks in the UV_{280} elugrams, the molecular weight distribution had a single major peak at ∼4500 Da corresponding to the Aβ(1-42) monomer. The tail to the right-hand-side of this peak reflects the presence of fractions containing a mixture of monomer and oligomers, and the small peak from 10^4-10^5 Da may reflect the presence of fractions containing mainly 2-20mers, or alternatively a mixture of retarded monomer and larger species. The finer peaks in the PDF are the result of noise, and should not be interpreted.

The predominantly LMW composition of the high-pH Aβ(1-42) samples was also indirectly supported by CD spectroscopy. An Aβ(1-42) sample that had been prepared in 50 mM NaOH was diluted 10x in dH_2O, and then a CD spectrum was immediately acquired (Fig. 3.8). The spectrum had a strongly negative signal at 199 nm, indicating a high level of disorder consistent with Aβ(1-42) monomer, or certain non-fibrillar oligomers, and was quantitatively similar to monomer spectra previously reported in the literature [4, 230, 231, 233, 234].

Altogether, the AF4-MALS data indicate that high-pH treatment causes almost complete dissolution of the Aβ(1-42), and that the dissolved peptide is predominantly monomeric, with small but significant quantities of oligomers detected during elution. It is unclear whether these oligomers existed in the initial preparations, or were induced by pH changes occurring in the channel, since the dilution would have brought the pH to the edge of the aggregating range. If they were present in the preparations themselves, their formation was probably induced by the high Aβ(1-42) concentrations, as Aβ(1-42) monomers would otherwise be expected to repel one another strongly at pH 12.5. Small oligomers are inevitable in all Aβ(1-

42) preparations, due to the peptide's high aggregation propensity and the requirement to prepare samples at high concentrations. There do not appear to be any equivalent analyses of the oligomer content of Aβ(1-42) preparations in the literature, as most protocols use more qualitative approaches to check for oligomers, such as NS-EM and gel electrophoresis. In addition, it should be noted that these techniques lack the sensitivity to identify oligomers of the size and quantities identified here: NS-EM struggles to identify aggregates with diameter <5 nm (∼200 kDa), and electrophoretic techniques are unlikely to detect oligomers that have a very broad size distribution and consequently a low individual abundance. Nonetheless, since the conditions used here are more denaturing than those used to monomerise Aβ(1-42) in most other studies, and the methods such as filtration [216, 234, 278, 287, 336, 466, 522, 523] and centrifugation [51, 165, 357] that are commonly used to 'monomerise' the protein would be unable to remove most of the species observed here (see Section 3.3.3 and 3.3.5 for comments and data regarding the effectiveness of SEC in native buffers), it seems likely that other preparations would give similar results if subjected to the same analysis. Furthermore, it is shown in Section 3.3.5 that isolation of the monomer peak by SEC does not affect the self-assembly kinetics, despite purportedly increasing the monomer content of the purified sample. The simplest interpretation of this result is that any oligomers formed at high pH and peptide concentration rapidly equilibrate with the monomer upon dilution into the fibrillisation buffer, so that the free monomer content of untreated and 'monomerised' samples are ultimately the same. This argument does not negate the possible role of SEC in removing persistent oligomers or on-pathway species such as fibril seeds, which is evaluated in the next section.

3.3.4 Aβ(1-42) samples solubilised at high pH exhibit highly reproducible, unseeded self-assembly kinetics

In order to determine whether Aβ(1-42) samples prepared in 50 mM NaOH exhibited controlled, unseeded fibrillisation, ThT assays were carried out under the same conditions previously used for 10 mM NaOH Aβ(1-42) (Section 3.3.1). The higher pH of the Aβ(1-42) preparations meant that the fibrillisation buffer had to be pre-adjusted so that it would reach the correct pH when the Aβ(1-42) was added (Section 2.4); the success of this strategy was confirmed by pH measurements, and further adjustments were never needed after adding the peptide. The results of these ThT assays are shown in Fig. 3.9. Consistent with their predominantly monomeric composition and lack of large populations of HMW species, Aβ(1-42) samples prepared in 50 mM NaOH had a low initial ThT fluorescence, typically $< 6\%$ of the final value (mean 2.2%), and exhibited classically unseeded sigmoidal fibrillisation kinetics with a distinct lag phase. Moreover, unlike Aβ(1-42) prepared in 10 mM NaOH, the Aβ(1-42) samples prepared in 50 mM NaOH produced highly consistent self-assembly kinetics, with the concentration-dependences from different samples aligning almost exactly. Since the main differences between these samples and the 10 mM NaOH data shown in Fig.

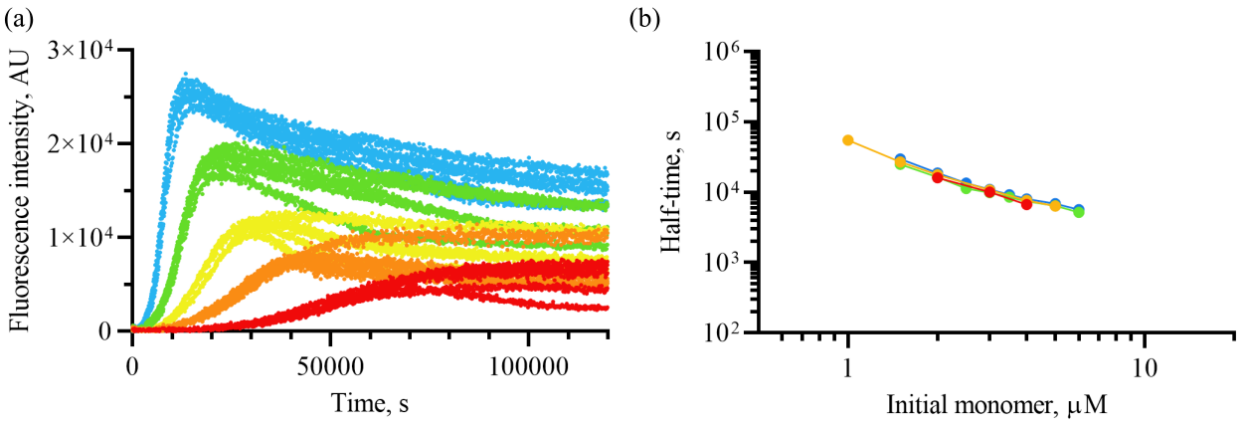

Figure 3.9: Self-assembly kinetics of Aβ(1-42) solubilised with 50 mM NaOH prior to use in ThT assays. Self-assembly was induced by dilution of the high-pH Aβ(1-42) sample into a pH-corrected 20 mM sodium phosphate buffer (pH 8) containing 200 μM EDTA, 1 mM NaN_3, and 20 μM ThT, at 37°C. (a) Representative fibrillisation kinetics of Aβ(1-42) prepared according to protocol 3, viewed by ThT assay. Colour scheme encodes Aβ(1-42) concentration: red, 1 μM; orange, 1.5 μM; yellow, 2 μM; green, 3 μM; cyan, 4 μM. Five replicates are shown for each Aβ(1-42) concentration. (b) Comparison of the concentration-dependence of the fibrillisation half-times of four Aβ(1-42) samples prepared according to protocol 3. The colour scheme indicates individual preparations of Aβ(1-42). For all datasets, the standard deviation between replicate experiments is too small to represent in this panel.

3.3 are the full solubilisation of Aβ(1-42) and reduced levels of HMW material, this result confirms that those two factors were responsible for the majority of variation between preparations.

To examine the kinetic consistency of 50 mM NaOH preparations in greater detail, the ThT curves of 4 μM Aβ(1-42) were collated from experiments involving 8 different preparations, with a total of 88 curves collated. These data, summarised in Fig. 3.10, show a high level of reproducibility across preparations. The fibrillisation half-times of these samples ranged from around 6900-8620 s, with a mean of 7700 s and a standard deviation of 380 s (4.9%). To investigate whether the variation in initial ThT fluorescence accounted for the half-time variation, the two were plotted against one another. As can be seen in Fig. 3.11, they do not correlate, indicating that the low level of initial ThT fluorescence seen in these samples is not caused by seed material. In agreement with this, negative stain electron microscopy (NS-EM) did not reveal any fibrillar species present in 4 μM Aβ(1-42) samples immediately after dilution into pre-adjusted fibrillisation buffer; after incubation for ∼1 h under fibrillisation conditions, equivalent to the early growth phase in ThT assays, amyloid fibrils were observed (Fig. 3.12).

3.3.5 Aβ(1-42) samples solubilised at high pH do not contain detectable fibril seeds

The very low initial fluorescence and high level of reproducibility of the kinetic data strongly indicated that the assembly kinetics were not confounded by seeding or off-pathway aggregation, which would be

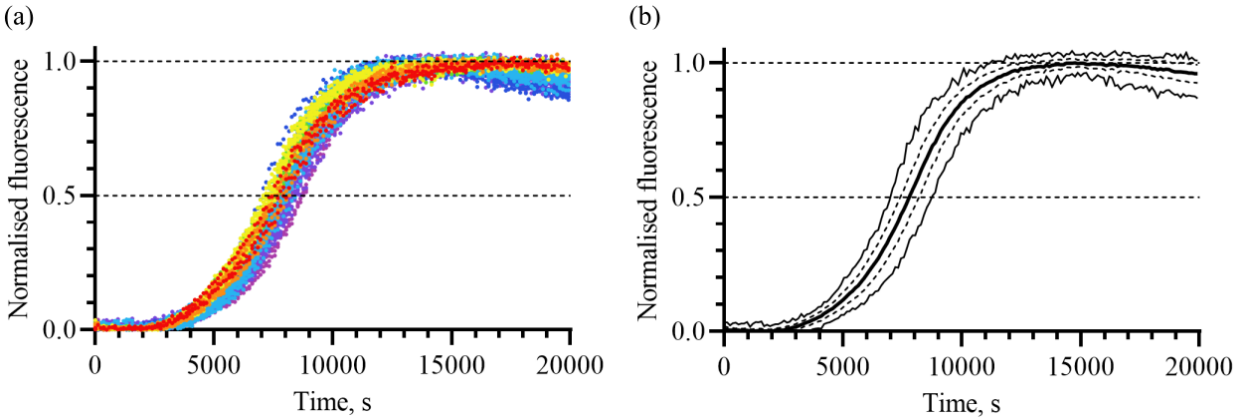

Figure 3.10: Kinetic consistency of 4 μM Aβ(1-42) solubilised with 50 mM NaOH prior to use in ThT assays. Self-assembly was induced by dilution of the high-pH Aβ(1-42) sample into a pH-corrected 20 mM sodium phosphate buffer (pH 8) containing 200 μM EDTA, 1 mM NaN_3, and 20 μM ThT, at 37°C. (a) An overlay of the ThT self-assembly kinetics of 8 different Aβ(1-42) preparations, normalised relative to their maximum fluorescence to correct for varying gain between experiments. The colour scheme indicates individual preparations of Aβ(1-42). For each preparation, 3-25 self-assembly curves are shown, from 1-5 experiments with 3-5 replicate wells. A total of 88 self-assembly curves are shown. (b) Consistency of the self-assembly data shown in panel (a). The black central curve is the mean, while the dashed curves represent the mean plus or minus a single standard deviation, and the thin black curves at the edges show the range.

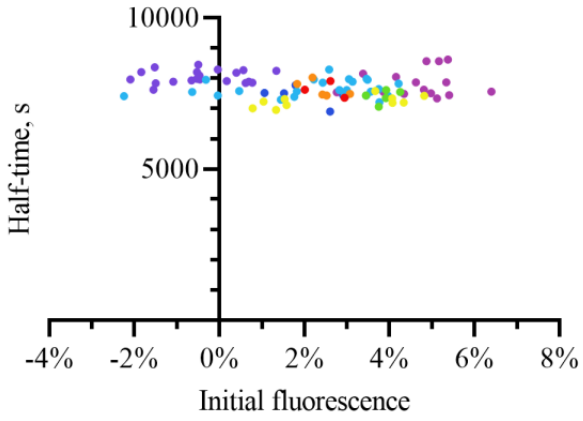

Figure 3.11: The initial ThT fluorescence of Aβ(1-42) solubilised in 50 mM NaOH does not correlate with the fibrillisation half-time. Self-assembly was induced by dilution of the high-pH Aβ(1-42) sample into a pH-corrected 20 mM sodium phosphate buffer (pH 8) containing 200 μM EDTA, 1 mM NaN_3, and 20 μM ThT, at 37°C. Each data point corresponds to the interpolated half-time and initial fluorescence of a ThT curve shown in Fig. 3.10, with the same colour scheme.

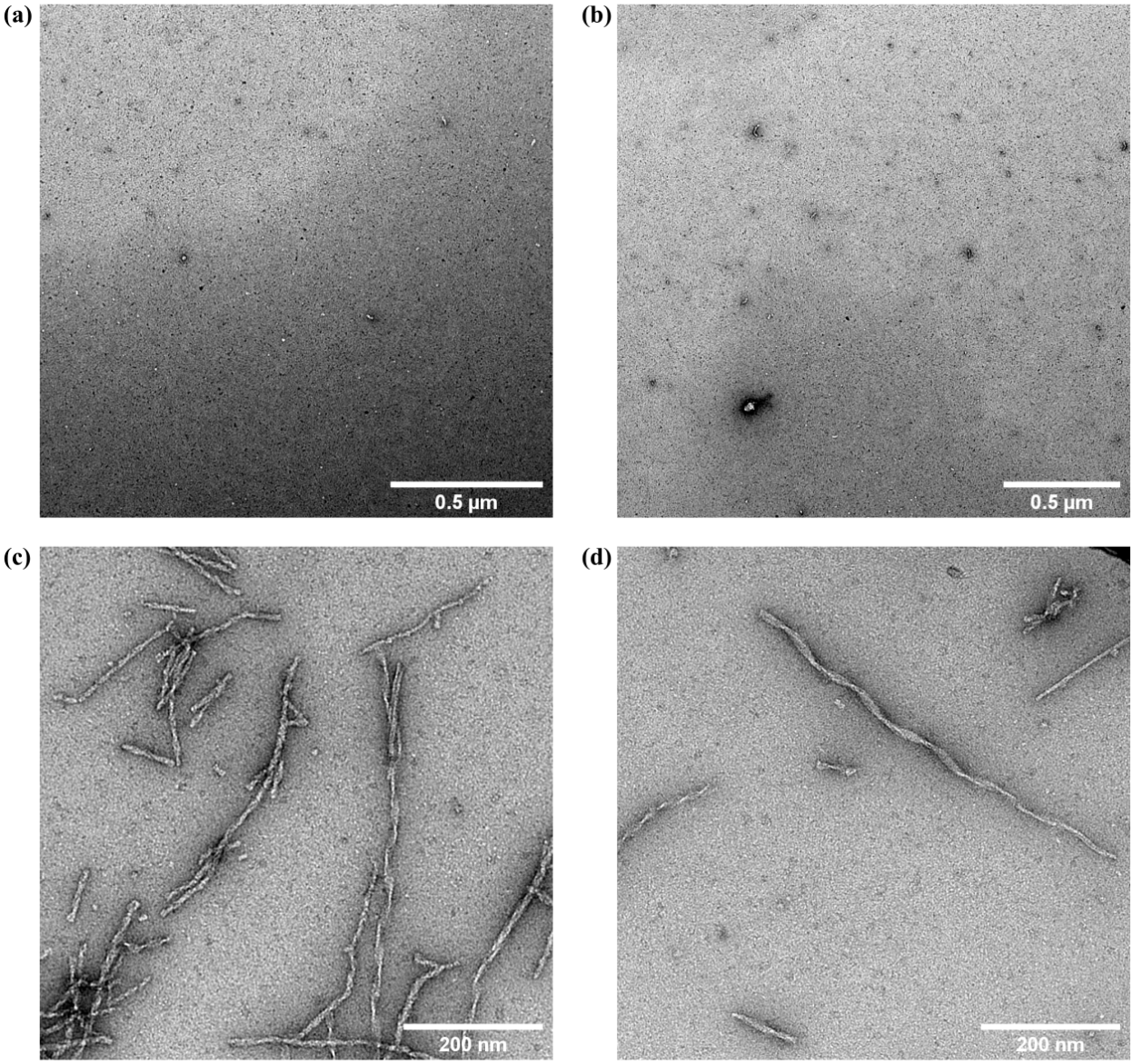

Figure 3.12: Negative stain electron microscopy of 4 µM Aβ(1-42) solubilised with 50 mM NaOH, and then diluted into pH-corrected fibrillisation buffer containing 20 mM sodium phosphate (pH 8), 200 µM EDTA, 1 mM NaN_3, and 20 µM ThT. Panels (a) and (b) are representative images of Aβ(1-42) samples immediately after the dilution. Panels (c) and (d) show early growth phase samples from the same experiment, after incubation for ∼1 h in a 96-well microplate at 37°C.

expected to vary between preparations. In order to test this, HMW material was removed from Aβ(1-42) samples using either ultracentrifugation or SEC, and the self-assembly kinetics of the purified peptide were compared to those of an untreated control. For the ultracentrifugation experiment, a 1 mg/ml Aβ(1-42) sample solubilised according to protocol 3 was diluted 10× in dH_2O to give 0.1 mg/ml Aβ(1-42) in 5 mM NaOH. This sample was then centrifuged at 436,000g for 1 h, and examined by AF4 and ThT assays. As a control, another aliquot from the same Aβ(1-42) preparation was diluted in the same manner, and incubated in a centrifuge tube for the same period of time without ultracentrifugation. As shown in Fig. 3.13, ultracentrifugation resulted in an approximately 3× reduction in the integral of the UV signal after cross-flow; in the control, the integrated signal was equivalent to 1.004 μg Aβ(1-42) (although it is not certain that this material was Aβ(1-42), so the true mass is unknown), whereas in the centrifuged sample the integral was equivalent to 0.365 μg Aβ(1-42). Similarly, ultracentrifugation caused an approximately 4× reduction in the integral of the LS 90° signal. Although the composition and degree of homogeneity of the HMW material is not known, making exact quantitation difficult, the AF4 data indicate that the majority of this material was removed. Despite removal of this material, the treated and untreated samples exhibited almost identical ThT kinetics, indicating that the HMW material did not cause a significant level of seeding.

To analyse this result more quantitatively, one can calculate the expected fibrillisation half-time if the HMW material consisted of homogeneous fibril seed. In the EM data acquired throughout this PhD, Aβ(1-42) fibrils have been observed to have a typical length of 100-2000 nm. Mass-per-unit-length measurements were not acquired, but literature values typically range from 2 to 4 monomers per β-sheet spacing of 0.48 nm [136, 164], meaning that a typical Aβ(1-42) fibril may contain approximately 400 to 20,000 monomers (to 1 s.f.). If all of the 1.004 μg of HMW material in the uncentrifuged sample had been fibril seed, then approximately 95% of the sample would have been in LMW state, giving an approximate free monomer concentration of $m(0) \approx 3.8\ \mu$M and a fibrillar monomer concentration of $M(0) \approx 0.2\ \mu$M. In the corresponding ultracentrifuged sample, $m(0)$ would have been the same but the fibrillar monomer concentration would have been reduced to $M(0) \approx 0.073\ \mu$M, with a fibril number concentration in the range 3.65 pM $\lessapprox P(0) \lessapprox$ 183 pM, depending on the mean fibril length. Regardless of nucleation, based on the elongation rate constant $k_e^+ \approx 3 \times 10^6$ M^{-1}.s^{-1} [54], and assuming symmetric elongation at both fibril ends, one would expect an initial polymerisation rate of 83.2 pM.s^{-1} $\lessapprox -dm(0)/dt \lessapprox$ 4.16 nM.s^{-1}; this would result in exponential disappearance of the monomer with a half-time in the 630-32000 s range. Even the slower bound would have resulted in a significant linear gradient in the 0-3000 s region of Fig. 3.13, which was clearly not observed; this suggests that, at the very least, the 0.365 μg of HMW material that remained in the ultracentrifuged sample did not contain a large quantity of seed.

Let us now consider the case where the 0.365 μg of HMW material in the ultracentrifuged sample was non-seed material, but rest of the material that was removed by ultracentrifugation was fibril seed.

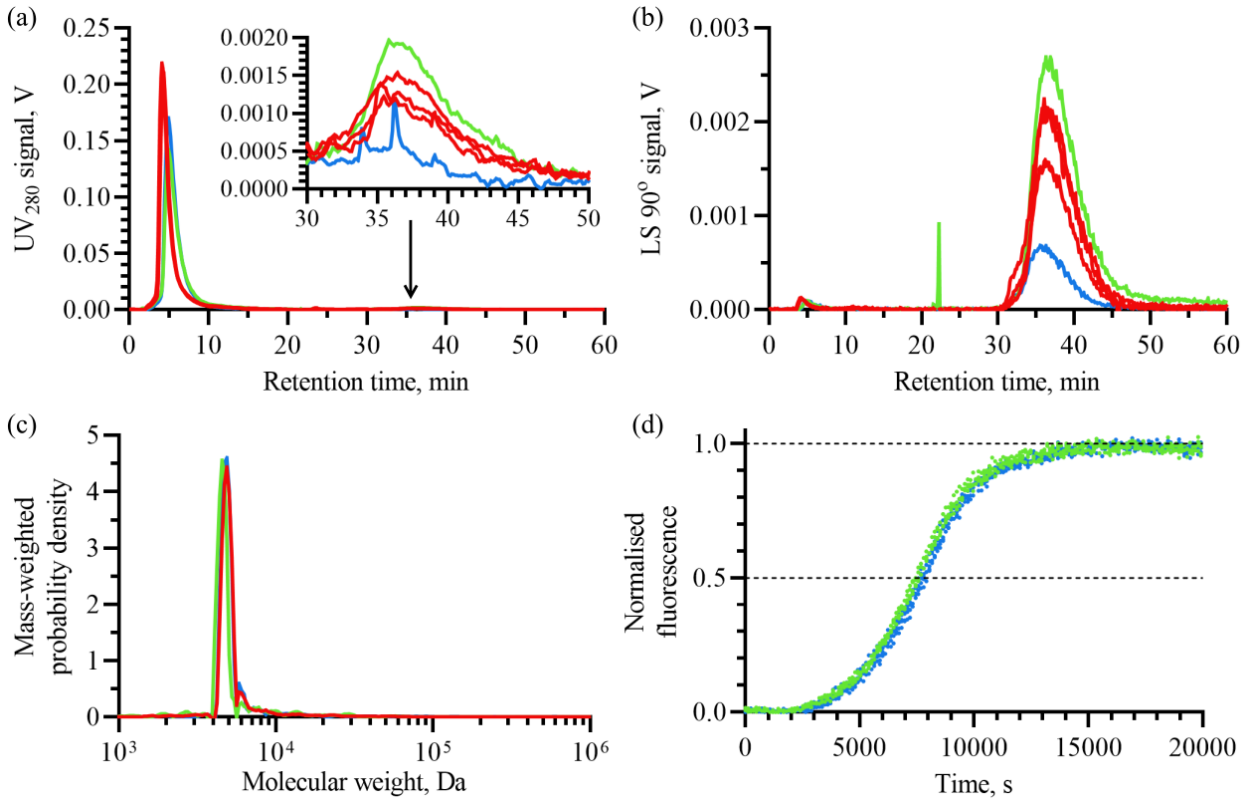

Figure 3.13: Removal of HMW material from high-pH Aβ(1-42) preparations does not affect the self-assembly kinetics. Panels show (a) the UV_{280} signal, (b) the LS 90° signal, (c) the approximate M_w distribution, derived from MALS analysis of the ROI from 3.3-12.0 min using the linear Zimm fit, and (d) the corresponding ThT self-assembly kinetics of an Aβ(1-42) sample prepared in 50 mM NaOH. Colour scheme: red, 1 mg/ml sample before dilution (not included in ThT assay); green, 10× diluted 0.1 mg/ml sample, incubated for 1 h before use in experiments; blue, 10× diluted 0.1 mg/ml sample, centrifuged at 436,000*g* for 1 h and then used in experiments.

Therefore, the quantity of seed was $1.004 - 0.365 \approx 0.639$ μg, equivalent to 3.2% of the Aβ(1-42) in the sample. Thus, in the ThT experiment shown in Fig. 3.13(d), the untreated sample would have had a free monomer concentration of $m(0) \approx 3.87$ μM, and a seed concentration of $M(0) \approx 0.13$ μM. Given the estimated range of fibril lengths, the fibril number concentration would have been in the range 6.5 pM $\lessapprox$ $P(0)$ $\lessapprox$ 325 pM. In the treated sample, $m(0)$ would have been the same, but with $M(0) = P(0) = 0$. Fitting the self-assembly kinetics of the treated sample with Eq. (1.36) gave an estimated primary nucleation rate constant $k_n \approx 3.06 \times 10^{-5}$ $M^{-1}.s^{-1}$ and secondary nucleation rate constant $k_s \approx 2.15 \times 10^{3}$ $M^{-1}.s^{-2}$; for the other constants, the literature values of $k_e^+ \approx 3 \times 10^6$ $M^{-1}.s^{-1}$, $k_e^- \approx 0.01$ s^{-1}, and $n_c = n_s = 2$ were used [54], with $k_f = 0$ to reflect negligible fragmentation as supported by Cohen *et al.* [54]. For the fitted k_n and k_s values, adding fibrillar seed with the $M(0)$ and $P(0)$ values estimated above would cause a pronounced loss of the lag phase, reducing the half-time from around 7600 s to between 650 s (for 400 monomers/fibril) and 4000 s (for 20,000 monomers/fibril). Clearly, this effect was not observed, since the kinetics of the untreated sample are almost identical to those of the treated sample; thus, the HMW material does not engage in secondary nucleation or elongation at an appreciable rate. One possibility is that the HMW fraction consists of off-pathway Aβ(1-42) species. However, the fact that the full expected 20 μg of Aβ(1-42) was recovered in the LMW fraction favours the alternative possibility, that the HMW material is not actually Aβ(1-42). Instead, it may consist of small quantities of dust, microorganisms, or pre-existing contaminants in the vials, which were resistant to 50 mM NaOH but had no observable seeding potential.

Although ultracentrifugation removed the majority of the HMW material, it did not remove all of it, and was also unable to remove oligomers. A more common approach in the literature is SEC [116, 231, 286, 485, 494, 501, 502], which has the advantage of allowing the monomer peak to be selectively purified, with the disadvantages of loss of peptide and possible aggregation in the column. To test whether column purification altered the self-assembly kinetics of high-pH Aβ(1-42) preparations, a 50 mM NaOH-treated Aβ(1-42) sample was purified according to the SEC protocol previously described by Hellstrand *et al.* [479]. In summary, 50 μl of Aβ(1-42) was loaded onto a Superdex-75 column in a 20 mM sodium phosphate (pH 8) mobile phase, with 200 μM EDTA and 1 mM NaN_3. The fraction eluting from 13.6-14.6 min (at 1 ml/min) was collected on ice, diluted variably (60%, 80%, or 100%, ie. undiluted) in the elution buffer to give a range of concentrations, supplemented with 20 μM ThT from a concentrated stock, and used in ThT assays. Because the peptide was diluted considerably during purification, the elution buffer had to be almost the same as the fibrillisation buffer in the subsequent ThT experiments, as Aβ(1-42) is too aggregation-prone for a slow buffer-exchange process and the desired concentration range was close to the concentration of the eluent. This purification was carried out several times, with reproducible results; a representative elugram is shown in Fig. 3.14(a). The UV_{280} and RI elugrams are very similar to those previously reported for in-house recombinant peptide purified according to the same protocol [479], and the

peak at ∼14 min has already been identified as the monomer. MALS analysis of the ROI from 13.6-14.6 min was challenging, as the very weak LS signal meant that the M_w estimates were particularly sensitive to LS baseline subtraction errors. Nonetheless, the average M_w^{ROI} value of three concordant replicates was 6460 ± 712 Da, where the error margins represent one standard deviation; this was calculated using the linear Zimm fit. This M_w^{ROI} is consistent with the peak containing mostly monomer, with a small but significant amount of contaminating oligomer. It is interesting to observe that, despite claims in the literature [479, 494, 496], this SEC protocol does not yield particularly monomeric Aβ(1-42) solutions. As discussed previously, some oligomeric species are inevitable in any Aβ(1-42) preparation, and in this case the purification protocol was either unable to completely separate pre-formed oligomers, or actively encouraged re-formation of oligomers during elution, since purification was carried out under aggregation conditions. In addition to the MALS analysis, comparison of the K_{av} value of the peak at ∼14 min with those of other molecular weight standards also confirmed the predominantly monomeric nature of the peptide. Due to time constraints and issues with some of the standards, a full set of molecular weight standards was not obtained. Nonetheless, Fig. 3.14(b) clearly shows that Aβ(1-42) monomer, βPGM, BSA monomer, and BSA dimer all exhibited the expected logarithmic dependence of elution volume on molecular weight, further supporting the monomeric nature of the material eluting at ∼14 min.

The total mass of Aβ(1-42) recovered from SEC was calculated by integrating the UV_{280} and RI signals from 8.0-16.3 min; data acquired after this time could not be used due to elution of NaOH and salts. While the UV_{280} signal gave an estimate of 55.4 ± 1.84 μg peptide, the RI gave an estimate of 47.2 ± 0.945 μg peptide, out of a nominal 50 μg injected. The RI estimate was unsurprising since some Aβ(1-42) would be expected to elute outside of the ROI or become trapped in the column; however, the UV_{280} estimate was somewhat higher than expected. This discrepancy was not caused by an error in the extinction coefficient of the monomer, which was determined theoretically and empirically for both the AF4 and SEC mobile phases. However, closer inspection of the UV_{280} and RI elugrams revealed that the signals from the two detectors were not always proportional (Fig. 3.14(a)); this was reproducible across replicates, and the signal from both detectors had a sufficiently flat baseline at early and late elution times that baselining error could not explain this effect. If the composition of the eluting material remained the same from 8.0-16.3 min, then the UV_{280} and RI signals would be expected to remain approximately proportional. However, the shoulder to the left of the monomer peak appeared to have an excess of UV_{280} signal, indicating that it had a higher extinction coefficient than would otherwise be expected, and this was responsible for the apparent increase in recovery. One explanation would be that a larger, non-Aβ(1-42) contaminant was eluting before the Aβ(1-42) monomer. However, this was unlikely to be the case as: (i) the RI signal gave far too low a recovery when this shoulder was excluded; (ii) this shoulder is commonly seen in purification of Aβ(1-42) samples, and is already established to contain Aβ(1-42) oligomers [479]; and (iii) no such contaminant was

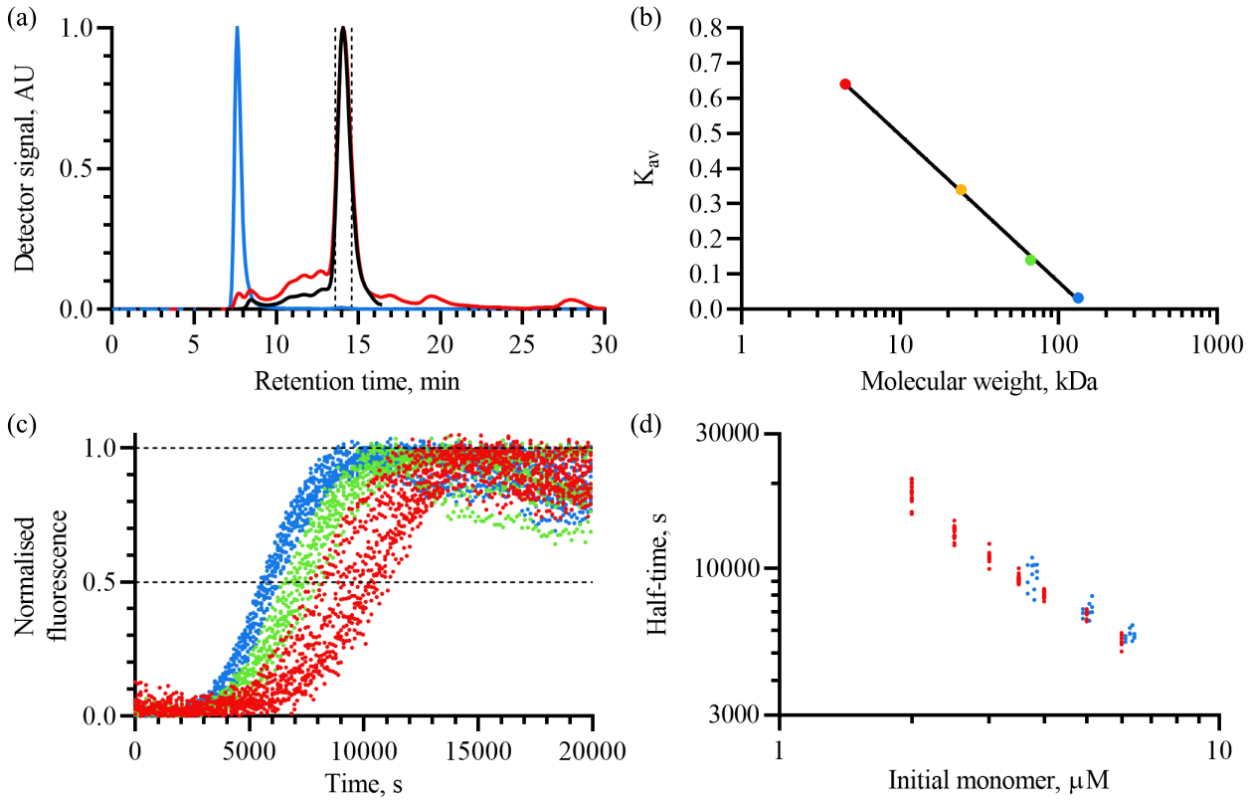

Figure 3.14: SEC purification of high-pH Aβ(1-42) preparations does not affect the self-assembly kinetics. Aβ(1-42) that had been solubilised in 50 mM NaOH was purified using a Superdex-75 column and then used in ThT assays at 37°C. The buffer used for elution and ThT assays was sodium phosphate (pH 8) containing 200 μM EDTA and 1 mM NaN_3, and the sample was eluted at 1 ml/min. (a) Detector outputs from a typical SEC-MALS run of Aβ(1-42) prepared in 50 mM NaOH. Colour scheme: black, RI; red, UV_{280}; blue, LS 90°. Dashed vertical lines demarcate the fraction (13.6-14.6 min) that was collected for ThT assays. (b) K_{av} values versus molecular weight of Aβ(1-42) and standards. Colour scheme: red, Aβ(1-42) monomer (4.5 kDa); amber, βPGM (24.2 kDa); green, BSA monomer (66.5 kDa); blue, BSA dimer (133 kDa). (c) Normalised ThT curves of purified Aβ(1-42). Colour scheme indicates Aβ(1-42) concentration as a percentage of the eluent concentration: red, 60% (∼3.8 μM); green, 80% (∼5.0 μM); blue, 100% (∼6.3 μM). (d) Similarity between the fibrillisation half-times of unpurified (red) and purified (blue) Aβ(1-42).

observed by AF4, for which the UV_{280} signal gave the correct extinction coefficient. An alternative and more likely possibility was that the shoulder consisted of Aβ(1-42) oligomers binding to a small molecule or peptide contaminant ($\lessapprox$ 1000 Da) with a stronger UV_{280} signal. This explanation is compatible with the fact that excess UV_{280} signal was not observed in AF4 experiments; in the higher-pH AF4 mobile phase (1 mM NaOH), deprotonation and reduced Aβ(1-42) oligomerisation would abolish this interaction, allowing the contaminant to independently pass through the membrane ($\sim$1000 Da MWCO) instead of eluting.

Due to the issues with the UV_{280} signal, the RI detector was used for quantitation of Aβ(1-42) in the fraction collected from 13.6-14.6 min, although both detectors provided very similar estimates for this narrower ROI. On average, 28.4 $\pm$ 7.13 μg of peptide was collected in this fraction, equivalent to 56.8% of the nominal injected mass at a concentration of 0.0284 mg/ml (6.29 μM), approximately 35$\times$ more dilute than the concentration at which the sample was injected. For each purification, the Aβ(1-42) was then diluted in the same buffer to 60%, 80%, or 100% (undiluted) of that concentration, supplemented with ThT, and used in a ThT assay (see Section 3.2.8 for more details). Exact concentrations of Aβ(1-42) in individual experiments were then calculated retrospectively for use in further analyses. An overlay of all concordant ThT self-assembly curves is shown in Fig. 3.14(c), in which the kinetics can be seen to have broadly the same rate and characteristics as the untreated peptide. Because the Aβ(1-42) eluted at a variable concentration, an exact overlay of the self-assembly kinetics of SEC-treated samples with those of untreated samples was not possible. However, the relative rates can still be compared by overlaying the concentration-dependences of the fibrillisation half-times. As shown in Fig. 3.14(d), the fibrillisation half-times of the SEC-treated and untreated Aβ(1-42) samples overlay almost exactly. While it is possible that the SEC-treated samples may be slightly slower, the difference between the two is very minor and well within experimental variation. Even a small quantity of seed would be expected to strongly affect the fibrillisation rate; however, SEC has little if any effect on the half-time, indicating that the untreated samples did not contain a significant level of seed. If an effect does exist, it is very small and more consistent with the removal of very low quantities of heterogeneous contaminants such as dust or microorganisms, which may weakly stimulate heterogeneous primary nucleation. Thus, SEC results in a substantial loss of peptide and places considerable constraints on the way the Aβ(1-42) can be used in subsequent experiments, without effectively removing oligomeric species or significantly affecting the self-assembly kinetics. The only obvious advantage of the SEC step is removal of the UV-absorbing contaminant; however, this is a very minor advantage given that the presence of this species does not seem to alter the self-assembly kinetics. Thus, it was decided that column purification was not necessary for the majority of Aβ(1-42) samples, and was best restricted to control experiments in cases where it was particularly important to eliminate seeding, heterogeneous primary nucleation, or small molecule contaminants.

3.3.6 LC-MS to assess the purity of Aβ(1-42) preparations

Although the AF4-MALS analysis showed that Aβ(1-42) prepared according to protocol 3 was predominantly monomeric and lacked detectable seed, MALS did not provide sufficient M_w resolution and accuracy to identify chemical modifications, truncated Aβ variants, and contaminants with a similar molecular weight. To address this issue, Aβ prepared according to protocol 3 was examined by LC-MS. Fig. 3.15(a) shows the reverse-phase HPLC elugram of an Aβ sample, with a monomer peak at ∼5.9 min, and Fig. 3.15(b) shows the ESI-MS spectrum of the fraction collected from 5.84-6.04 min. The mass spectrum contained a strong peak at 4513 Da, corresponding to monomeric Aβ(1-42), as well as a number of smaller peaks in the 2500-5000 Da range, which likely corresponded to contaminants and truncated variants. The only other species that could be identified from its molecular weight alone was the secondary peak at 3895 Da, whose molecular weight was consistent with the N-terminally truncated Aβ(6-42) variant. Thus, the mass spectrum indicates that the peptide samples consist predominantly of Aβ(1-42), with a small but significant quantity of Aβ(6-42), and smaller amounts of chemically modified, truncated, or non-Aβ species. As shown in the next section, this heterogeneity appears to have been present in the vials prior to solubilisation, as it is not caused by the high pH treatment. The loss of the 5 N-terminal residues (DAEFR) in the Aβ(6-42) variant is unlikely to strongly affect the self-assembly process as the central and C-terminal regions of the peptide are believed to be more important in initiating and stabilising fibril structures [136, 143, 164, 219, 273, 324, 383, 524]. Nonetheless, some studies have supported a supplementary role for the N-terminus in modulating the aggregation rate, toxicity, and mechanical properties of fibrils [275, 525–527], so the presence of a small quantity of Aβ(6-42) may explain some kinetic differences between this peptide and Aβ from other sources. Overall, the degree of heterogeneity in the commercial peptide is similar to that observed for in-house recombinant preparations, which also contain contaminants and truncated variants [494]. As with oligomerisation, some level of contamination and truncation is impossible to eliminate, and does not necessarily affect the validity or reliability of experimental results.

3.3.7 Effect of sonication time on preparation quality and kinetics

The 50 mM NaOH solubilisations discussed above had all been carried out with 5 min sonication, due to concerns that the 30 min sonication previously used for 10 mM NaOH preparations might cause chemical modification at higher pH. However, experiments had not yet been carried out to establish whether this was actually the case, and whether sonication was even necessary in 50 mM NaOH. In order to determine the optimum sonication time, AF4-MALS experiments and ThT assays were used to compare the composition and self-assembly kinetics of Aβ(1-42) samples that had been sonicated for different amounts of time during preparation. These data, presented in Fig. 3.16, did not show a significant difference between the AF4-

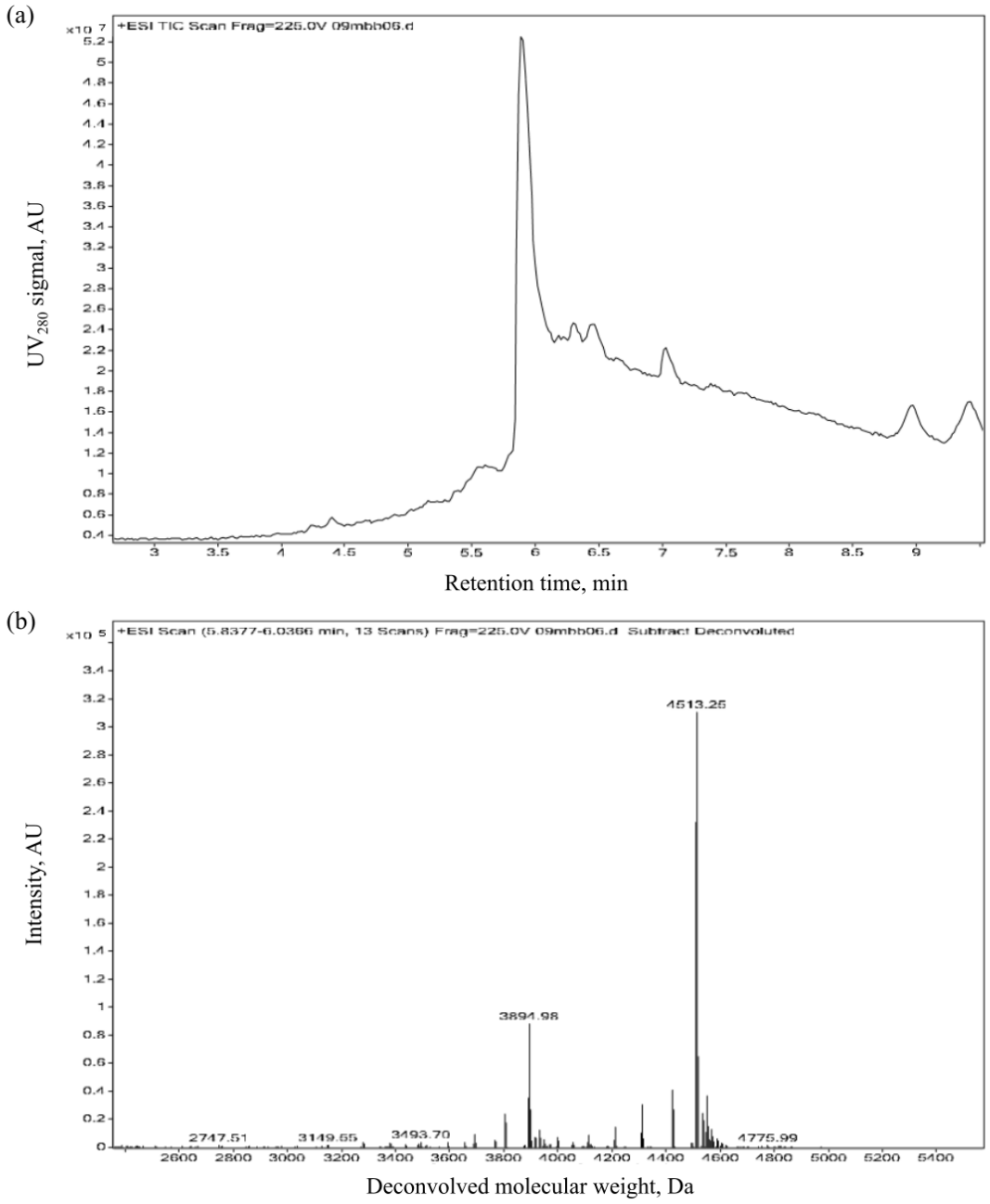

Figure 3.15: LC-MS of Aβ(1-42) prepared by 5 min sonication in 50 mM NaOH (protocol 3). (a) Reverse-phase HPLC elugram. (b) Deconvolved mass spectrum of the fraction collected from 5.84-6.04 min.

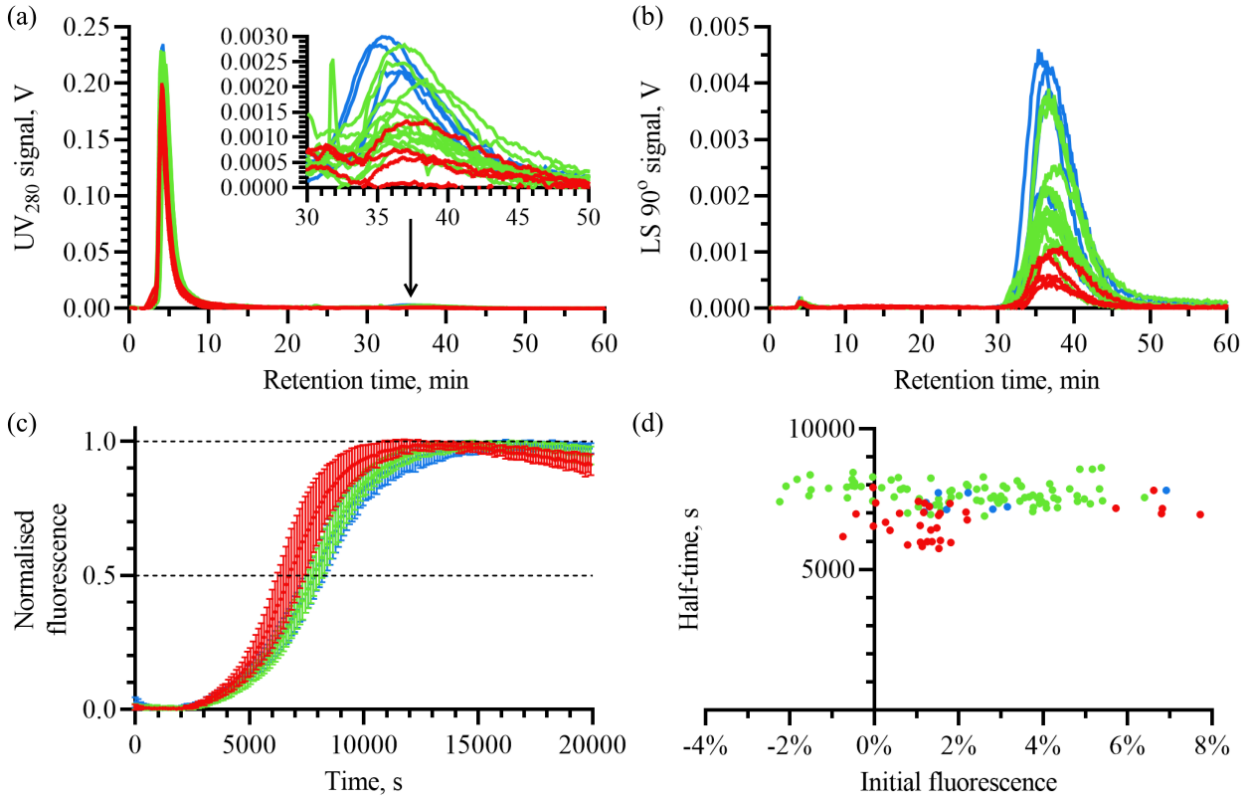

Figure 3.16: Effect of sonication time on Aβ(1-42) preparations. (a) The UV_{280} signal from AF4-MALS separation of 50 mM NaOH Aβ(1-42) preparations. (b) The corresponding LS 90° signal. (c) The normalised ThT self-assembly kinetics, where error margins represent a single standard deviation. ThT data are normalised as described in Section 2.5.2, as they were acquired in different experiments with different gain values. (d) The proportional initial fluorescence plotted against the interpolated fibrillisation half-time, for the ThT assays shown in panel (c). All panels use the same colour scheme: red, no sonication; green, 5 min sonication, same data as presented in previous figures; blue, 30 min sonication.

MALS elugrams and self-assembly kinetics of samples that were sonicated for 5 min and 30 min. The stability of the Aβ(1-42) over this timescale was further corroborated by LC-MS. Fig. 3.17(a) shows the reverse-phase HPLC elugram of a sample, and Fig. 3.17(b) shows the ESI-MS spectrum of the fraction collected from 5.81-6.11 min; both are almost identical to the corresponding data for Aβ sonicated for 5 min, shown in Fig. 3.15. Thus, significant degradation does not appear to have occurred on this timescale. Furthermore, AF4-MALS and ThT analysis of samples that were flash-frozen immediately after injection of 50 mM NaOH into the vials, without sonication, provided very similar results (Fig. 3.16), indicating that the sample did not change significantly during the first 5 min of sonication. The samples that were not sonicated had a very similar yield and initial fluorescence, but did fibrillise slightly faster; this may indicate that some seed was initially present, and was removed by sonication. For this reason, to minimise the risk of chemical modification while allowing complete removal of any pre-formed seed, 5 min appears to be the optimum sonication time for Aβ(1-42) solubilisation.

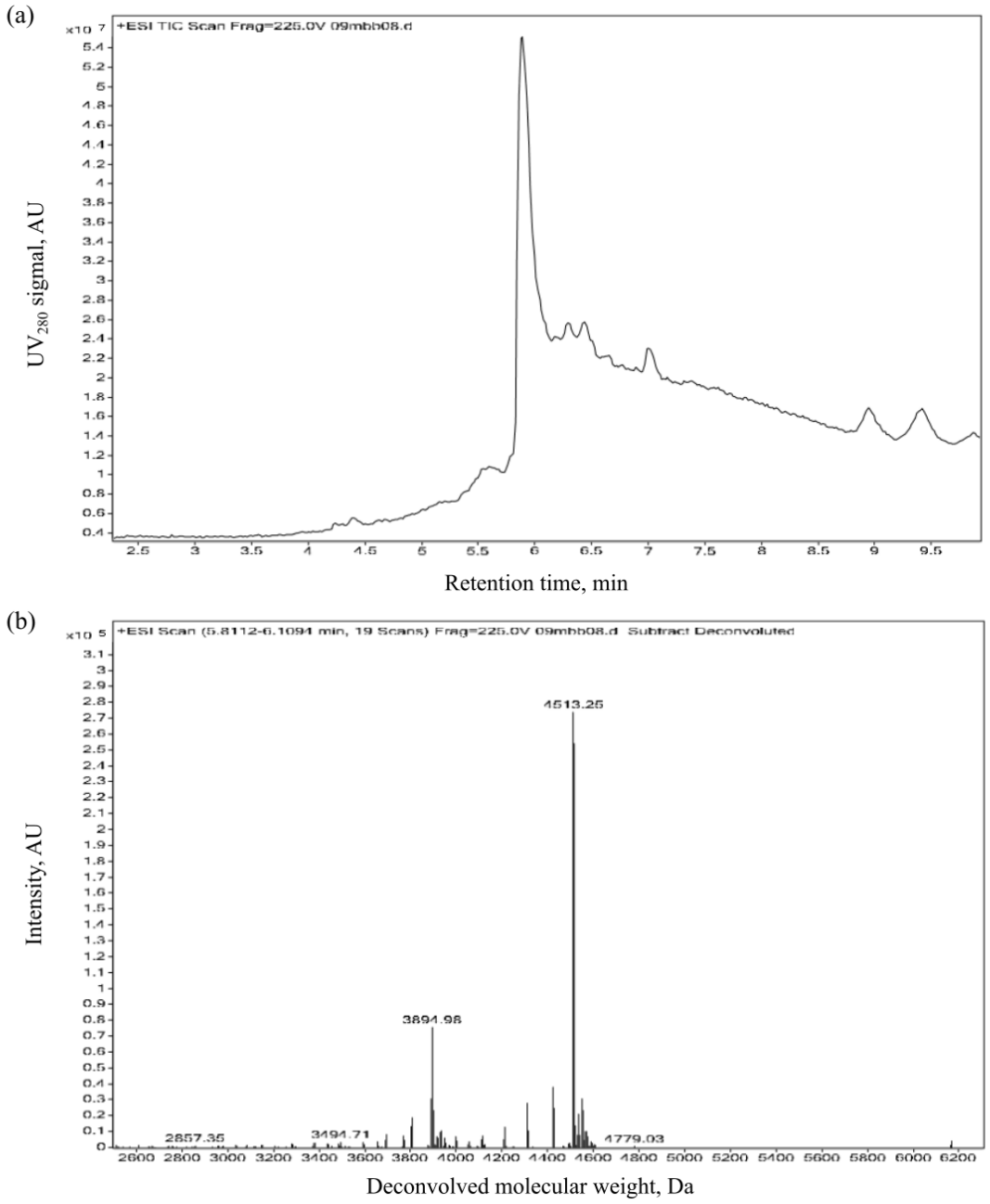

Figure 3.17: LC-MS of Aβ(1-42) prepared by 30 min sonication in 50 mM NaOH. (a) Reverse-phase HPLC elugram. (b) Deconvolved mass spectrum of the fraction collected from 5.81-6.11 min.

3.3.8 Long-term stability of high-pH Aβ(1-42) preparations

The data presented in Fig. 3.15-3.17 indicate that Aβ did not undergo major chemical modifications, such as alkaline hydrolysis of the peptide backbone, on timescales of up to 30 min in 50 mM NaOH. The LC-MS data do not rule out deamidation of sidechains, as this modification only has a small impact on the molecular weight (+1 Da). However, sidechain amides play a prominent role in stabilising the Aβ(1-42) fibril structure [136, 144], and the corresponding carboxylic acids formed by deamidation would repel one another in a parallel cross-β structure, further destabilising monomer-monomer interactions. Therefore, deamidation would be expected to strongly delay or even abolish fibrillisation at the concentrations used in the ThT assays. Aβ(1-42) samples have indistinguishable fibrillisation half-times regardless of whether they were sonicated for 5 min or 30 min, indicating that deamidation did not occur on this timescale. Moreover, these kinetics are similar to those of other samples reported in the literature [479], low-pH preparations with the same peptide (Fig. 3.3), and un-sonicated samples that were kept in the liquid phase for only a very short time period (< 30 s; Fig. 3.16), indicating that deamidation did not occur in the first 5 min.

Although these data indicate that Aβ(1-42) was not chemically modified by spending short periods of time in 50 mM NaOH, it was useful to determine whether longer timescales or harsher treatments could result in modification. To test this, Aβ(1-42) aliquots from a single sample prepared by 5 min sonication in 50 mM NaOH were thawed and incubated at 21°C, for times up to 20 h. In addition, one aliquot was thawed and incubated at 37°C for 100 h, to further stress the peptide. As shown in Fig. 3.18, incubation at 21°C did not significantly affect the AF4-MALS or ThT data, indicating that chemical modification and degradation were not significant on these timescales. This shows that, while it is still best practice to minimise the amount of time spent at high pH in the liquid phase, the peptide is relatively stable under these conditions and attempts to minimise this time should not be made at the expense of other experimental precautions.

While the 37°C aliquot also did not show a significant change in the AF4-MALS elugrams, it failed to produce ThT kinetics, indicating that the severe treatment of this sample had resulted in chemical modification. LC-MS revealed a second peak at ∼5.1 min in the reverse-phase HPLC elugram (Fig. 3.19(a)), which was not present in the corresponding untreated sample (Fig. 3.15(a)). While the existing peak at ∼5.9 min (Fig. 3.19(b)) appeared similar to the untreated sample by ESI-MS (Fig. 3.15(b)), the peak at ∼5.1 min appeared to consist mainly of truncated variants (Fig. 3.20), which were probably formed by alkaline hydrolysis of Aβ. The formation of these species and/or the effects of possible deamidation are likely to be responsible for the lack of self-assembly of this peptide sample. Thus, while storage at 21°C is possible for moderate timescales, longer timescales or higher temperature may increase the risk of chemical modification. As a result, time spent in the liquid phase should be minimised and the peptide stored at -80°C wherever possible.

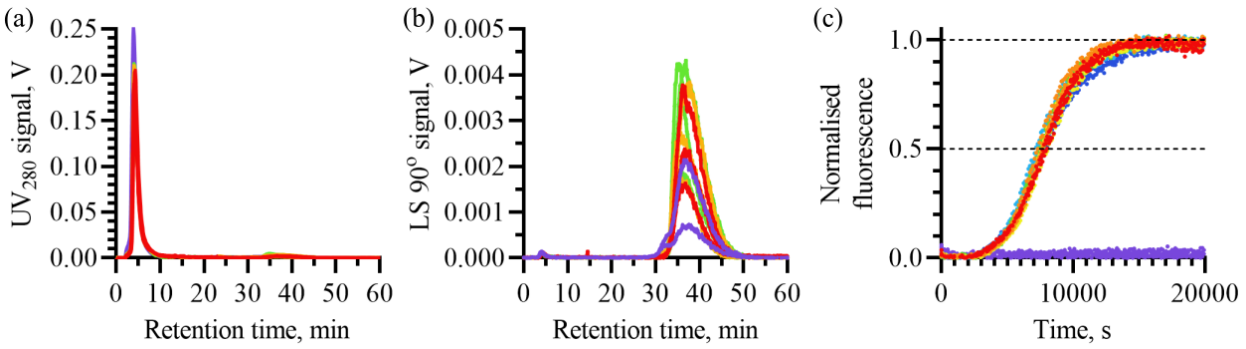

Figure 3.18: Stability of high-pH Aβ(1-42) preparations in the liquid phase. (a) UV_{280} signal from AF4-MALS separation of Aβ(1-42) preparations incubated for different amounts of time in the liquid phase. Colour scheme represents the incubation time and temperature: red, 10 min at 21°C; amber, 140 min at 21°C; green, 270 min at 21°C; purple, 6000 min (100 h) at 37°C. (b) The corresponding LS 90° signal, with the same colour scheme as panel (a). (c) The normalised ThT self-assembly kinetics of Aβ(1-42) preparations incubated for different amounts of time in the liquid phase. The colour scheme is different from panels (a) and (b): red, 15 min at 21°C; orange, 60 min at 21°C; yellow, 120 min at 21°C; green, 300 min at 21°C; cyan, 600 min at 21°C; blue, 1200 min at 21°C; purple, 6000 min (100 h) at 37°C.

The Aβ(1-42) used in the experiments shown in Fig. 3.10 was stored at -80°C for a range of different times before use, ranging from 1-39 days. Despite this, the data shown in that figure are highly consistent, indicating that the peptide was stable at -80°C and did not undergo significant modification during storage. To more quantitatively determine whether this was the case, the mean fibrillisation half-time τ_{50} of each ThT experiment was plotted against the storage time t_{storage} of the corresponding aliquot. As shown in Fig. 3.21, there is little to no relationship between the two. If such a change did occur, one of the most likely empirical relationships between τ_{50} and t_{storage} would be an exponential curve,

$$\tau_{50} = \tau_{50,0} e^{k_{\text{mod}} t_{\text{storage}}}, \tag{3.25}$$

where $\tau_{50,0}$ is the τ_{50} value prior to chemical modification, and k_{mod} is the rate of change of the fibrillisation half-time due to chemical modification such that the characteristic timescale is $|1/k_{\text{mod}}|$. Fitting this equation to the data in Fig. 3.21 gave an exponential decay with fitted values $\tau_{50,0} = 7760$ s and $k_{\text{mod}} = -6.53 \times 10^{-4}$ d^{-1}, indicating a very slow decrease in half-time. To determine whether this fit suggested a significant level of degradation, the fitted k_{mod} value was then compared to a hypothetical value of $k_{\text{mod}} = 0$ using the extra-sum-of-squares F-test. This gave a P-value of 0.3011, too high to reject the null hypothesis that $k_{\text{mod}} = 0$, and thus indicating that a significant level of degradation was not observed for this dataset. Therefore, Aβ(1-42) samples prepared according to protocol 3 and stored at -80°C remain stable for well over 39 days, and possibly a matter of years (note that $|1/k_{\text{mod}}| = 1530$ d ≈ 4 yr). Since this analysis, different members of the lab have obtained identical results with Aβ(1-42) samples stored for considerably longer periods of

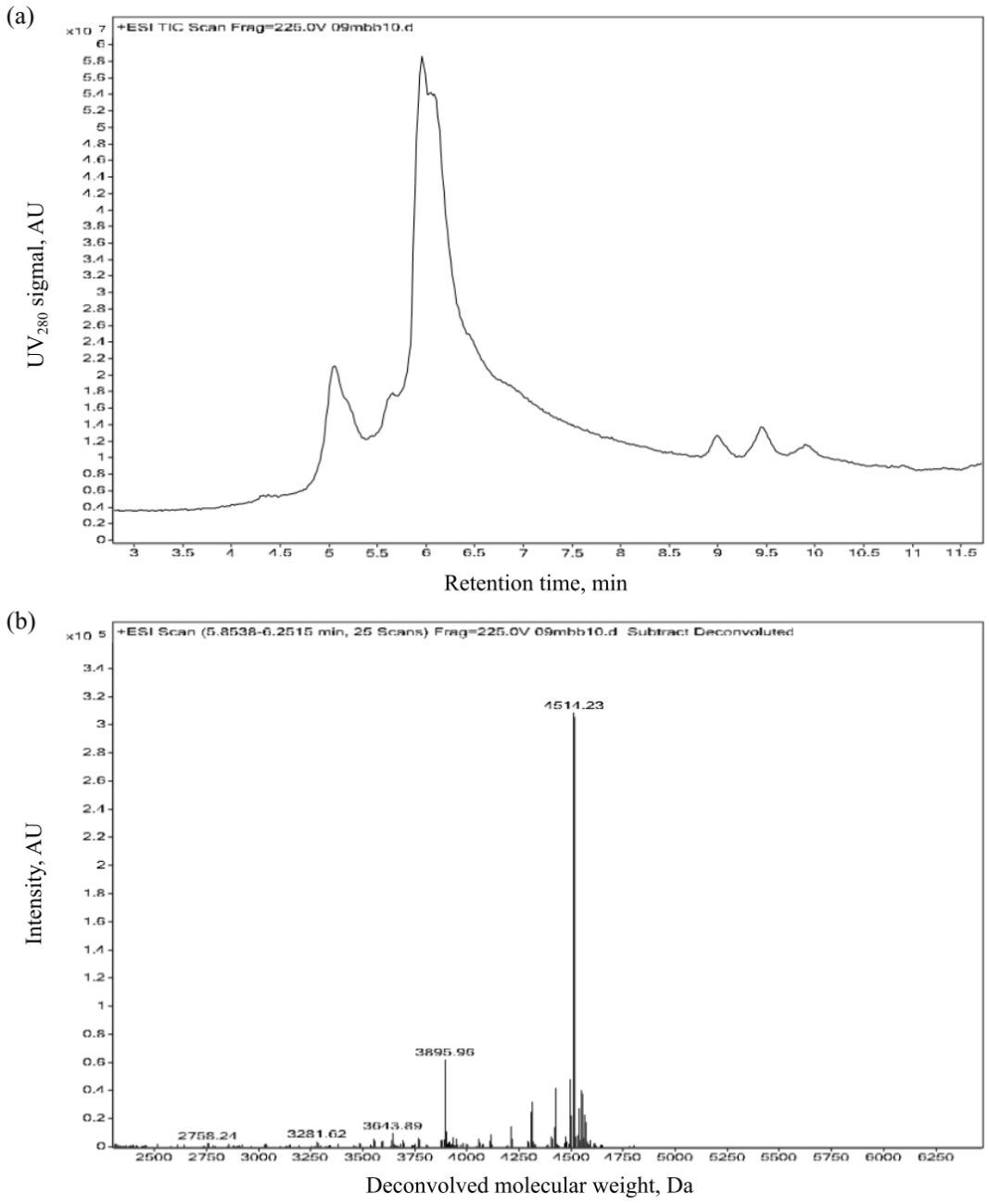

Figure 3.19: LC-MS of Aβ(1-42) prepared by 5 min sonication in 50 mM NaOH and subsequently stressed by incubation at 37°C for 100 h. (a) Reverse-phase HPLC elugram. (b) Deconvolved mass spectrum of the fraction collected from 5.85-6.25 min.

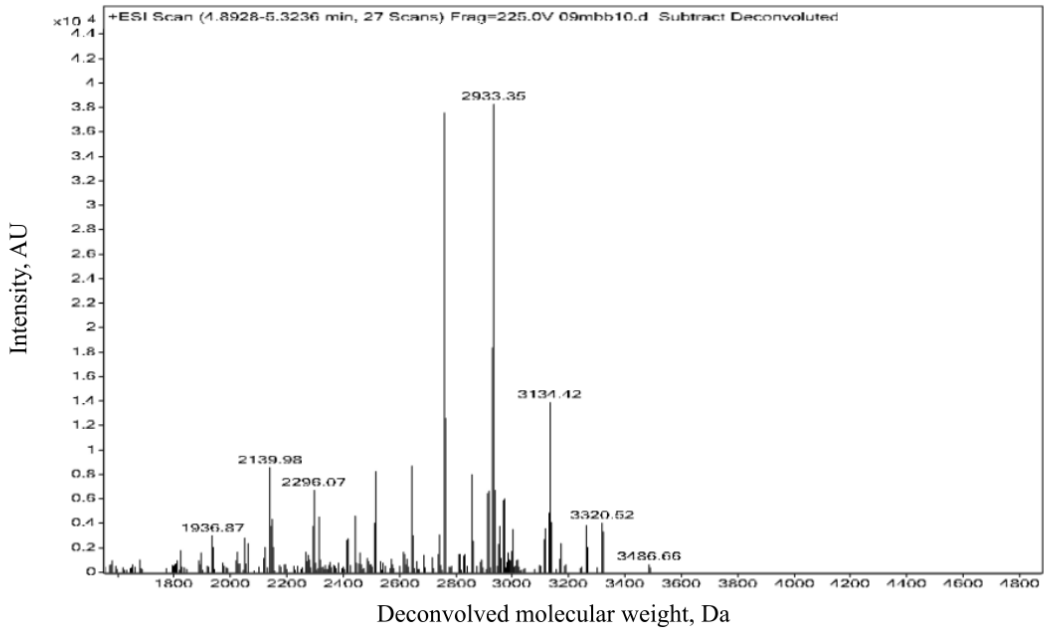

Figure 3.20: Deconvolved mass spectrum of the fraction collected from 4.89-5.32 min in the reverse-phase HPLC purification shown in Fig. 3.19(a).

time (up to 1 year, although exact storage times were not recorded), further supporting this conclusion.

Lastly, it was useful to determine whether the remainder of Aβ(1-42) aliquots that had been thawed for use could be re-frozen, allowing Aβ(1-42) from a single aliquot to be used on multiple separate occasions. To test this, aliquots were thawed and then re-frozen according to one of three methods: flash-freezing by immersion in liquid N_2 (freezing time < 1 s); freezing by placing the Eppendorf tube in contact with pre-cooled metal at -80^{o}C (< 1 min); and simply placing the sample in a rack in the -80^{o}C freezer (< 5 min). While the former was obviously preferable, the other two methods were tested due to their convenience, and to ascertain whether improper freezing protocols could affect the quality of Aβ(1-42) aliquots. The AF4-MALS elugrams and ThT self-assembly kinetics obtained with re-frozen peptide, shown in Fig. 3.22, are identical to the results obtained with first-use aliquots (Fig. 3.5, Fig. 3.10), and did not depend significantly on the re-freezing method. Therefore, Aβ(1-42) aliquots solubilised according to protocol 3 can be re-frozen for multiple uses, which is highly convenient when performing a range of experiments requiring different quantities of peptide. Although the re-freezing protocol does not appear to make a difference, so long as the final temperature is -80^{o}C, liquid N_2 is still recommended whenever possible.

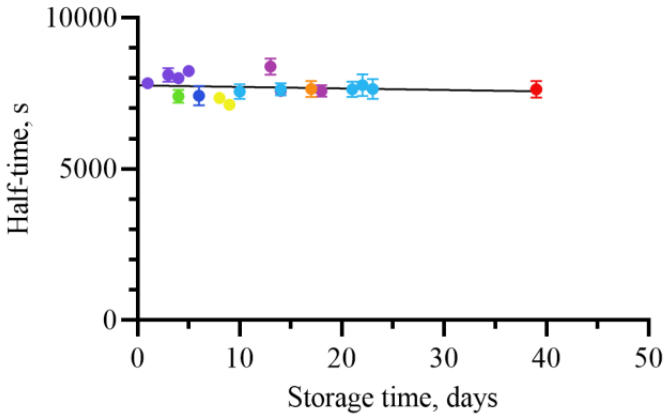

Figure 3.21: Effect of storage time on the fibrillisation half-time of Aβ(1-42) samples solubilised by 5 min sonication on 50 mM NaOH (protocol 3). Each point corresponds to the average fibrillisation half-time of a single ThT experiment; the error bars, which in some cases are too small to show, represent a single standard deviation. The colour scheme indicates individual Aβ(1-42) preparations, and corresponds to the experiments shown in Fig. 3.10. The fitted curve is Eq. 3.25; see text for values of the fitted parameters.

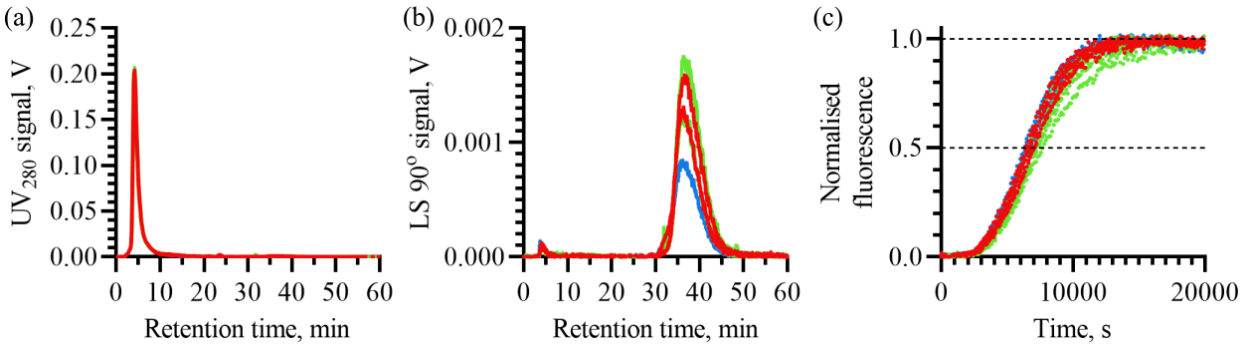

Figure 3.22: Effect of re-freezing on Aβ(1-42) solubilised by 5 min sonication in 50 mM NaOH. (a) UV_{280} signal from AF4-MALS separation of re-frozen Aβ(1-42) preparations. (b) The corresponding LS 90° signal. (c) The normalised ThT self-assembly kinetics. All panels use the same colour scheme, which encodes re-freezing method: red, placement in a rack in the -80°C freezer; green, freezing in contact with pre-cooled metal at -80°C; blue, flash-freezing by immersion in liquid N_2.

3.3.9 Identical self-assembly pathway of commercial and in-house recombinant Aβ(1-42) preparations

The experimental results presented in Sections 3.3.3-3.3.8 show that protocol 3 provides a reliable means to obtain highly monomeric Aβ(1-42) samples from a pre-purified commercial recombinant source. Peptide samples solubilised and stored in this way are stable for long time periods, convenient for use in high-throughput experimental assays, and produce highly reliable self-assembly kinetics that are not complicated by detectable seeding, chemical modification, or the effects of contaminants. As a result, these peptide samples satisfy all the criteria for use in highly sensitive biophysical assays. To test whether the self-assembly kinetics of these samples were similar to those obtained using in-house recombinant peptide, the four concentration-dependent kinetic datasets summarised in Fig. 3.9(b), each of which corresponds to a single Aβ(1-42) sample, were compared to results in the literature [54, 519]. An analysis of a representative dataset, corresponding to the curve shown in blue in Fig. 3.9(b), is presented in Fig. 3.23-3.25.

Firstly, the initial monomer concentration was plotted against the fluorescence intensity change in the corresponding ThT assays, which is expected to be proportional to the fibril yield under these experimental conditions [54]. Because experiments were carried out on different occasions with minor variations in experimental parameters, the fluorescence intensities of different experiments were not exactly equivalent. Therefore, a normalisation procedure was needed before collation could occur. In brief, each experiment featured a range of Aβ(1-42) concentrations with a large number of data points in the 1.5-4.0 μM range, across which an approximately linear relationship between the initial monomer concentration and fluorescence intensity change was observed. Data from different experiments were linearly fitted in this range, with a shared x-intercept and different gradients to account for small variations in the gain or the activity of the ThT. Data were then divided by the fitted gradient to obtain normalised intensities ΔI_{norm} that could then be collated. For a full justification of this procedure and the corresponding equations see Section 4.3.2. As shown in Fig. 3.23(a), the collated data exhibit an approximately linear relationship between the initial monomer concentration and the fluorescence intensity change, as would be expected and has previously been observed for in-house recombinant preparations [54]. Data points at 5.0 μM and 6.0 μM, which were not included in the fitting, can be seen to deviate somewhat from this relationship. This deviation was observed across preparations, and was confirmed by the more detailed characterisation of the initial intensities presented in Section 4.3.2, which extended to lower Aβ(1-42) concentrations. Since the normalisation is a linear transformation, the deviation is not caused by the normalisation process, and the slightly superlinear appearance of data in Fig. 3.23(a) would persist regardless of the fitting range used in the normalisation process. Instead, the excess intensity at high concentrations may reflect a change in fibril polymorphism, since different polymorphs would be expected to bind ThT with different affinities. A more detailed charac-

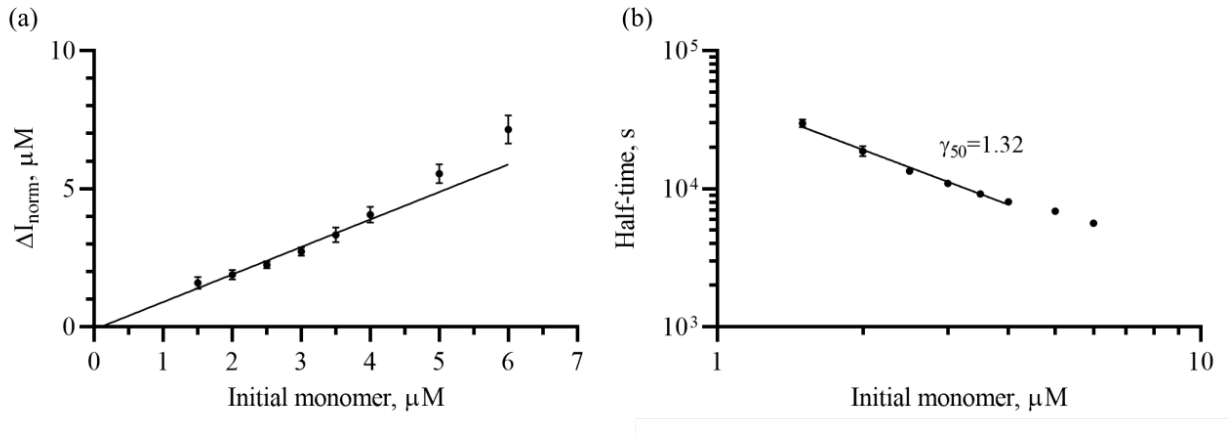

Figure 3.23: Kinetic analysis of commercial Aβ(1-42) preparations solubilised according to protocol 3 (part 1). (a) The relationship between the initial monomer concentration and the normalised fluorescence intensity change in ThT assays. The normalisation allows collation of data from multiple experiments and is described in greater detail in Section 4.3.2. Error bars represent a single standard deviation. The black line is a linear fit from 1.5-4.0 μM. (b) Concentration-dependence of the mean fibrillisation half-time. Error bars represent a single standard deviation. Data from 1.5-4.0 μM have been fitted to the equation $\tau_{50} = \alpha m(0)^{-\gamma_{50}}$. All data in this figure are from repeat experiments using a single Aβ(1-42) sample.

terisation of the initial intensities that is better suited to calculation of an x-intercept is provided in Section 4.3.2.

An important indicator of the underlying mechanism of biopolymer self-assembly is the scaling exponent $\gamma_{50} = -\partial \log \tau_{50} / \partial \log m(0)$, which relates the polymerisation half-time τ_{50} to the initial monomer concentration $m(0)$, and is described in more detail in Section 1.5. In Cohen *et al.* [54], the fitted γ_{50} value was 1.33±0.03, which is consistent with a self-assembly pathway dominated by secondary nucleation ($\gamma_{50} = (n_s + 1)/2$, where $n_s \approx 2$) with a minor contribution from primary nucleation ($\gamma_{50} = n_c/2$, where $n_c \approx 2$). In that study, a fragmentation-dominated model was unable to fit the data, as it had too low a scaling exponent ($\gamma_{50} = 1/2$). Fig. 3.23(b) shows the relationship between $m(0)$ and τ_{50} for a representative sample of commercial recombinant peptide, from the same dataset that was shown in blue in Fig. 3.9(b), and also in Fig. 3.23(a). Nonlinear regression with the scaling law $\tau_{50} \propto m(0)^{-\gamma_{50}}$ gave the fitted value $\gamma_{50} = 1.32 \pm 0.02$, which is almost identical to the value reported in Cohen *et al.* [54]. Fitting was only carried out in the 1.5-4.0 μM range, as the higher concentrations were not present in the equivalent data in Cohen *et al.* [54]. Similarly, the other Aβ(1-42) samples prepared according to protocol 3 had $\gamma_{50} = 1.26 \pm 0.04$, $\gamma_{50} = 1.26 \pm 0.03$, and $\gamma_{50} = 1.26 \pm 0.05$ in the same concentration range. It should be noted that the dataset shown in Fig. 3.23, which equates to the blue curve in Fig. 3.9(b), is not an outlier in having a slightly higher concentration-dependence than the others in the 1.5-4.0 μM range. Not only is the difference small, but this dataset is the most complete in the 1.5-4.0 μM range and has the greatest number

of repeats. Thus, the estimate of $\gamma_{50} = 1.32 \pm 0.02$ is probably the most accurate, as reflected by its smaller error margins.

The similarity of the concentration-dependences indicates that commercial recombinant Aβ(1-42) fibrillises according to the same microscopic processes as in-house recombinant peptide, and with a similar balance of primary versus secondary pathways. In Cohen *et al.* [54], nonlinear regression of Aβ(1-42) self-assembly curves supported a nucleated polymerisation model with autocatalytic secondary nucleation (Knowles model with secondary nucleation, see Eq. (1.36, 1.35)). Models without secondary nucleation (Oosawa model, see Eq. (1.20)), or where fragmentation was the dominant secondary process (Knowles model with fragmentation, see Eq. (1.36, 1.30)), were discounted by comparison of fits. Since then, data obtained using Aβ(1-40) and higher concentrations of Aβ(1-42) have suggested a modified secondary nucleation mechanism in which the process is saturable, proceeding via Michaelis-Menten-like kinetics (see Eq. (1.36, 1.50, 1.51)); this modification extends the model's range to include higher Aβ(1-42) concentrations [4, 5].

To test whether the kinetics of commercial recombinant peptide are also consistent with secondary nucleation, a similar comparison was made for each of the Aβ(1-42) samples prepared according to protocol 3, with representative examples for a single dataset shown in Fig. 3.24. Four models were tested: the Oosawa model, which includes primary nucleation and elongation but lacks secondary processes (Fig. 3.24(a)); the Knowles model with fragmentation as the dominant secondary process (Fig. 3.24(b)); the Knowles model with non-saturable secondary nucleation (Fig. 3.24(c)); and the Knowles model with saturable secondary nucleation (Fig. 3.24(b)). The fitted parameters, which were shared across all Aβ(1-42) concentrations and whose significance is discussed in Section 1.5, are summarised in Table 3.1. Although n_c and n_s are often assumed to take integer values, they are effective reaction orders and can thus take non-integer values; therefore, for these four fits, non-integer values were allowed. Another common convention is to set $n_c = n_s$, which reduces the size of parameter space and is mechanistically justified, since secondary nucleation is currently believed to involve a similar mechanism to primary nucleation [74, 348]; this constraint was used here. Lastly, when fitting the Knowles model with fragmentation as the dominant secondary process, the value of k_f was constrained such that $k_f k_e^+ = k_n k_e^+ \times (10^{-5.5}\ \mathrm{M})^{n_c}/(10^{-8}\ \mathrm{M})$, a constraint that was also applied in [54]. This ensures that fragmentation becomes dominant when the fibril mass concentration $M(t) \approx 10$ nM for a reaction with initial monomer concentration $m(0) = \sqrt{10}\,\mu$M, forcing the fitting algorithm to maintain an appreciable level of fragmentation. Without this constraint, k_f is simply minimised in order to attain a high concentration-dependence, resulting in a fit very similar to that obtained for the Oosawa model.

As shown in Fig. 3.24(a-d), saturable secondary nucleation provides the best fit, followed closely by non-saturable secondary nucleation. A poor fit is obtained for the other two models. The main cause of fail-

Parameter	Global fits in this chapter					Ref. [519]
	Fig. 3.24(a)	**Fig. 3.24(b)**	**Fig. 3.24(c)**	**Fig. 3.24(d)**	**Fig. 3.25**	
	Eq. (1.20)	**Eq. (1.36), Eq. (1.30)**	**Eq. (1.36), Eq. (1.35)**	**Eq. (1.36), Eq. (1.50), Eq. (1.51)**	**Eq. (1.36), Eq. (1.35)**	**Eq. (1.36), Eq. (1.35)**
n_c	2.37	5.23	1.68	2.37	2	2
n_s	—		1.68	2.37	2	2
$k_n k_e^+$, $\mathrm{M}^{-n_c}.\mathrm{s}^{-2}$	9.72×10^4	2.43×10^{19}	1.75×10^1	1.19×10^4	1.00×10^2	9×10^2
$k_s k_e^+$, $\mathrm{M}^{-(n_s+1)}.\mathrm{s}^{-2}$	—		8.10×10^7	1.29×10^{12}	5.52×10^9	1×10^{11}
$k_f k_e^+$, $\mathrm{M}^{-1}.\mathrm{s}^{-2}$	—	*see text*	—			
$K_{M,s}^{1/n_s}$, μM	—			2.74	—	
AICc	-125352	-126594	-166419	-181155	-134338	—
R^2	0.888	0.892	0.970	0.982	0.965	—

Table 3.1: Globally fitted parameters and diagnostic statistics for the data fitting in this chapter and Ref. [519]. In cases where an n_s value was present, the fit was constrained such that $n_c = n_s$, as in Refs. [54, 519]. As described in the text, the value of k_f was constrained to ensure that $k_f k_e^+ = k_n k_e^+ \times (10^{-5.5}\ \mathrm{M})^{n_c}/(10^{-8}\ \mathrm{M})$, as previously performed in Ref. [54]. Diagnostic statistics for the data fitting in this chapter are the AICc and R^2 values. Note that AICc values are only meaningful in a comparative sense, with lower AICc indicating a higher probability, and the fact that the AICc values are negative is simply a reflection of the fact that the fitted data had been normalised (ie. RSS $< N$).

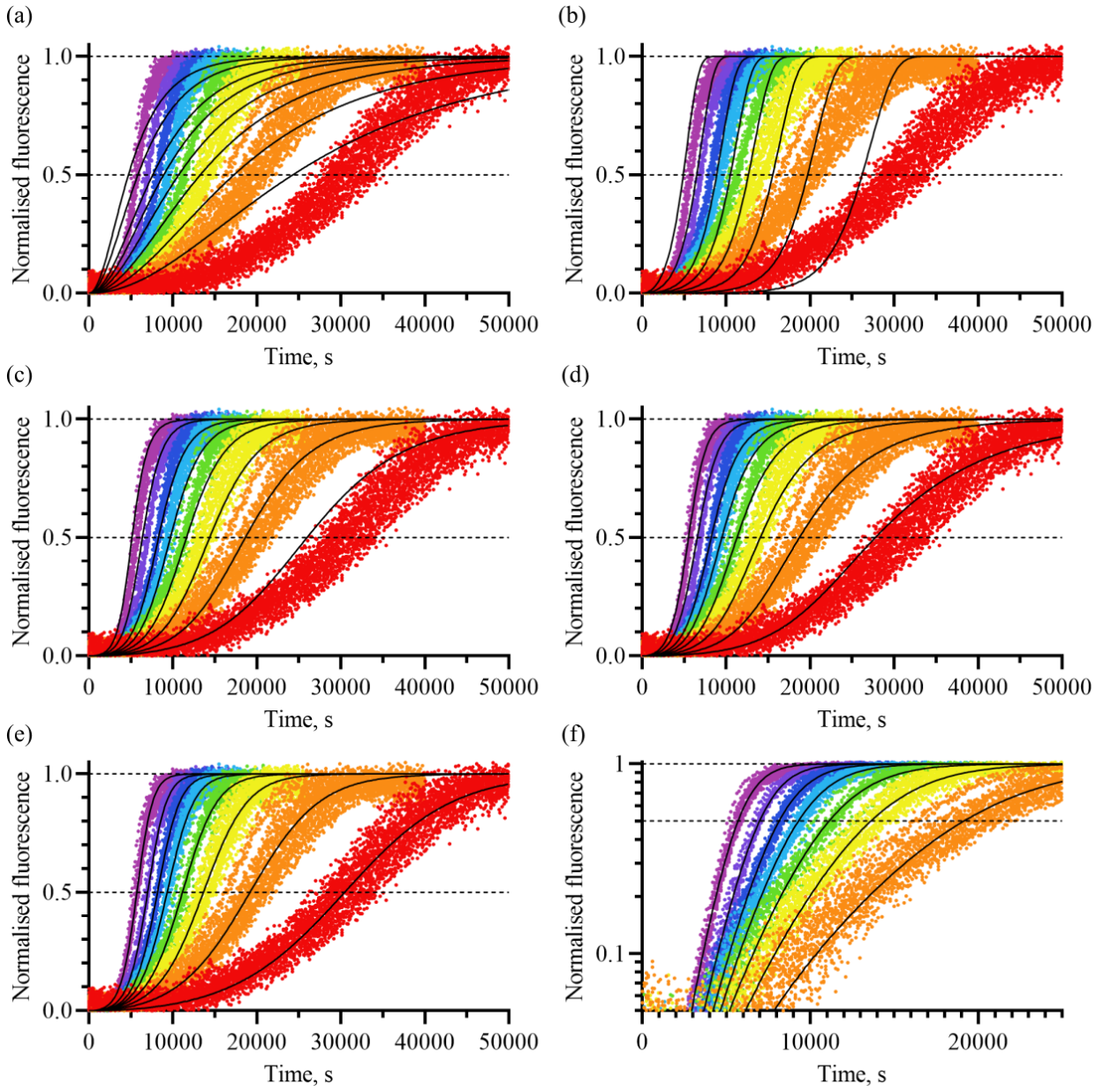

Figure 3.24: Kinetic analysis of commercial Aβ(1-42) preparations solubilised according to protocol 3 (part 2). This figure shows various fits of nucleated polymerisation models to the ThT kinetics of the dataset summarised in Fig. 3.23. Panels (a-d) show global fits of (a) the Oosawa model (Eq. (1.20)) [425, 426], (b) the Knowles model with fragmentation as the secondary process (Eq. (1.36, 1.30)) [1–3], (c) the Knowles model with non-saturable secondary nucleation (Eq. (1.36, 1.35)) [3], and (d) the Knowles model with saturable secondary nucleation (Eq. (1.36, 1.50, 1.51)) [4], with all fitted parameters shared across Aβ(1-42) concentrations. Panels (e-f) show fitting of the Knowles model (Eq. (1.36, 1.35)) [3] to the same data on linear and semi-logarithmic axes, with only $n_c = n_s$ shared across Aβ(1-42) concentrations. The colour scheme is the same across all panels, and indicates the initial Aβ(1-42) concentration: red, 1.5 μM; orange, 2.0 μM; yellow, 2.5 μM; green, 3.0 μM; cyan, 3.5 μM; blue, 4.0 μM; indigo, 5.0 μM; violet, 6.0 μM. The fitted curves shown as black lines. The 1.5 μM dataset was omitted from panel (f) for clarity, as it otherwise obscured the other data points.

ure of the Oosawa model (Fig. 3.24(a)) is its inability to produce exponential scaling in the early time, which means it lacks a pronounced lag phase. The fragmentation-dominated Knowles model (Fig. 3.24(b)) fails for a number of reasons. While fragmentation causes exponential early-time scaling, the rate of fragmentation is insensitive to monomer depletion, causing an overly sharp approach to maximum fluorescence. Furthermore, the fragmentation-dominated secondary pathway has a low concentration-dependence ($\gamma_{50} = 1/2$), so the fit tries to compensate by increasing the order of primary nucleation to a high value ($n_c = 5.23$). Had the value of k_f been left unconstrained, the fit would instead have done this by minimising the role of secondary pathways, producing an Oosawa-like fit similar to Fig. 3.24(a). Non-saturable secondary nucleation (Fig. 3.24(c)) provides a significantly better fit, as it is able to simultaneously produce exponential early-time scaling, the correct concentration-dependence at intermediate $m(0)$, and a less abrupt approach to maximum fluorescence caused by greater sensitivity to monomer depletion. Nonetheless, the fit is not perfect, since the concentration-dependence is not constant across the 1.5-6.0 μM range (Fig. 3.23(b)). Saturable secondary nucleation (Fig. 3.24(d)) addresses this issue by allowing γ_{50} to vary with $m(0)$, and so further improves the fit. Although the difference between non-saturable and saturable secondary nucleation visually appears to be small, it is significant; comparison of the two using using the AICc favoured the latter (ΔAICc = 14736, equivalent to >99.99% probability).

Although saturable secondary nucleation provides the best fit for the data, it should still be noted that this fit is not perfect, with some difference between the data and the fitted curves in the early growth phase, particularly at lower $m(0)$. To test whether this was caused by insufficiently exponential early-time scaling in the experimental data, the Knowles model was individually fitted to each Aβ(1-42) concentration, with only the $n_c = n_s$ values shared (Fig. 3.24(e-f)). This significantly improved the quality of the fits, and both the data and the fitted curve exhibit a pronounced straightening at higher concentrations when viewed on semi-logarithmic axes, which is indicative of exponential scaling caused by secondary processes. Thus, the discrepancies in Fig. 3.24(d), which are comparable to those seen in other papers using the Knowles model [4, 5, 464, 468, 519, 528, 529], do not mean that the wrong type of scaling is present in the early time. Instead, they indicate that the fitting algorithm is sacrificing fit quality in the early time for other regions of the curve. This may indicate that other processes are also present that still have not been accounted for, such as lag-phase oligomerisation. However, the main conclusions are not affected: (i) the exponential early-time scaling supports the existence of a secondary process; (ii) the overall curve shape and concentration-dependence suggest a higher-order secondary process such as secondary nucleation, rather than a lower-order process such as fragmentation; and (iii) the concentration-dependence shows some evidence of variation with $m(0)$, which may be explained by saturation of secondary nucleation, or another process along the secondary pathway. Thus, the same conclusions can be drawn from this comparison of fits as were drawn in Cohen *et al.* [54].

One significant difference between commercial and in-house recombinant Aβ(1-42) is the overall fibrillisation rate. For example, while the τ_{50} of 4 μM commercial peptide was shown to be 7700 ± 380 s in Section 3.3.4, the τ_{50} of 4 μM in-house peptide appears to be around 2000 s, based on interpolation of the data presented in [519], which is almost 4× faster. This is actually a rather small difference in the context of the Aβ(1-42) literature [234, 383, 479, 486], but is still worthy of attention. To investigate the cause of slower fibrillisation in the commercial preparations, a comparison was made between the fitted microscopic rate parameters of the commercial and in-house recombinant peptide. To make an exact comparison with Silvers *et al.* [519], which provides the most exactly equivalent set of fitted rate parameters in the literature, the same fitting procedure was used: non-saturable secondary nucleation, $n_c = n_s = 2$, and a range of initial monomer concentrations across which γ_{50} was approximately constant (here 1.5-4.0 μM). The fitted curves are shown in Fig. 3.25 and the kinetic parameters of both this fit and the one in Silvers *et al.* [519] are included in Table 3.1. As would be expected from the difference in rate, the commercial peptide has fitted rate parameters ($k_n k_e^+ = 1.00 \times 10^2$ M$^{-n_c}$.s^{-2} and $k_s k_e^+ = 5.52 \times 10^9$ M$^{-(n_s+1)}$.s^{-2}) around an order of magnitude lower than those obtained for the in-house preparations ($k_n k_e^+ = 9 \times 10^2$ M$^{-n_c}$.s^{-2} and $k_s k_e^+ = 1 \times 10^{11}$ M$^{-(n_s+1)}$.s^{-2}) [519]. One possible explanation for this is a reduction in the elongation rate constant k_e^+; alternatively, since primary and secondary nucleation are believed to have very similar mechanisms [74,348], both k_n and k_s may differ in a similar way between the two preparations. The data presented in Section 3.3.3-3.3.8 show that Aβ(1-42) solubilised according to protocol 3 is seedless, lacks off-pathway aggregates, and does not acquire chemical modifications during solubilisation; Silvers *et al.* [519] have also shown that their peptide is seedless and mostly monomeric [479, 494]. Therefore, changes occurring between preparation and experimentation are unlikely to explain this effect. Instead, small differences in the abundance and variety of truncated species, post-translationally modified peptides and other contaminants are much more likely to be responsible. Even a small change in the primary sequence of Aβ(1-42) can strongly affect self-assembly behaviour: for example, in the 1.5-4.0 μM concentration range, removal of residues 1-4 causes a 2-5× increase in the fibrillisation rate [530], and the absence of residues 41-42 (ie. Aβ(1-40)) causes a 15-20× reduction in the fibrillisation rate [4]. While the mass spectra in both Fig. 3.15 and Walsh *et al.* [494] have major peaks that appear to be unmodified monomer, both reveal an abundance of smaller peaks that most likely correspond to other Aβ(1-42) variants. Even small quantities of slowly aggregating variants could 'poison' elongation or nucleation, and rapidly aggregating variants could template the self-assembly of other peptides in solution. Therefore, co-aggregation of the unmodified peptide with small quantities of truncated or post-translationally modified variants appears to be the most plausible explanation for the difference in rate. Since both preparations appear to be equally monomeric and these contaminating species could either accelerate or retard fibrillisation, it is impossible to say with any confidence which of the two is closer in behaviour to pure Aβ(1-42). However, since completely pure Aβ(1-42) does not exist

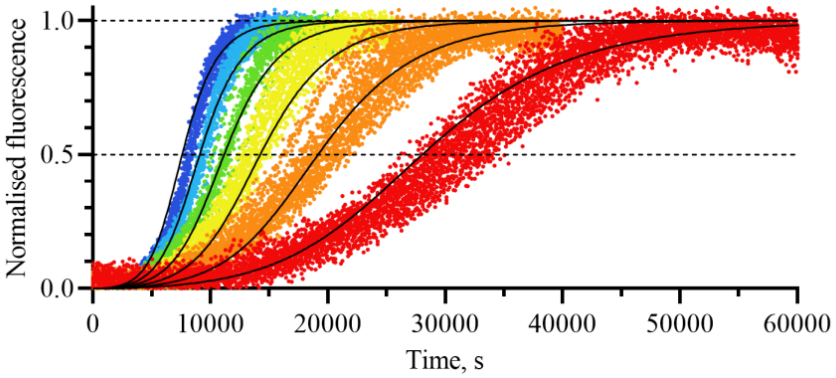

Figure 3.25: Kinetic analysis of commercial Aβ(1-42) preparations solubilised according to protocol 3 (part 3). This figure shows a global fit of the Knowles model with non-saturable secondary nucleation (Eq. (1.36, 1.35)) [3] to the ThT kinetics of the dataset summarised in Fig. 3.23. Fitting was carried out for ThT curves with an initial monomer concentration of 1.5-4.0 μM, with $n_c = n_s = 2$. The colour scheme indicates the initial Aβ(1-42) concentration and is the same as Fig. 3.24: red, 1.5 μM; orange, 2.0 μM; yellow, 2.5 μM; green, 3.0 μM; cyan, 3.5 μM; blue, 4.0 μM. The fitted curves shown as black lines.

in vivo, and both preparations produce highly reproducible kinetics suitable for the same kinds of analyses, this question is of limited value anyway.

3.4 Conclusions

The results presented in this chapter show that commercial recombinant Aβ(1-42) can be used to obtain reproducible, high-quality self-assembly kinetics, consistent with the same underlying mechanism that was previously characterised for in-house preparations [54,519]. Until now, the poor consistency of peptide from commercial sources has presented a barrier to its use in quantitative biophysical analyses, a major problem for smaller research groups that lack the resources to prepare peptide in-house on a large scale. Although some of the kinetic inconsistency in the literature may be due to contamination with different truncated or post-translationally modified variants, and such variation is probably unavoidable due to the requirement for different groups to use peptide from different sources, much of the observed variation between experiments, solubilised samples, and batches prepared according to the same protocol appears to result from improper dissolution and storage techniques. In particular, for the large number of studies that use basic solvents to monomerise Aβ [72, 116, 165, 216, 234, 279, 280, 286, 296, 466, 497–500], the use of insufficiently concentrated base is an issue. While pH 10-11 is often assumed to monomerise Aβ [233, 486, 520, 521], there is evidence against this in the literature [294], and the data presented in this chapter show that higher pH is required to completely eliminate pre-formed aggregates, and minimise the risk of preparation failure. By addressing this issue, the protocol developed in this chapter allows highly monomeric Aβ(1-42) samples to

be reproducibly obtained from a pre-purified commercial recombinant source, and is expected to be equally applicable to other Aβ isoforms. Peptide prepared in this way exhibits a remarkable level of consistency, lacks detectable seed, and is easy to store and use. Although small quantities of LMW oligomers and pre-existing modified variants were detected, their levels are maintained at a minimum by the solubilisation protocol, and are comparable to those seen in in-house recombinant preparations [116]. Furthermore, while many groups rely on additional purification steps such as SEC to remove pre-formed aggregates immediately prior to use, the results in this chapter show that high-pH sonication and proper storage eliminate the need for this, except in control experiments where appropriate. Since these steps result in considerable loss of Aβ and limit its manner and timescale of use in subsequent assays, this finding will allow users of both commercial and in-house preparations to acquire biophysical data in greater quantities, and under a wider variety of conditions. Thus, the results presented in this chapter are expected to make it easier for experimentalists to acquire high-quality biophysical data, and provide insights important to improving the reproducibility of the Aβ literature.

3.5 Acknowledgments

Fig. 3.3 and Fig. 3.6 include data from Aβ(1-42) aliquots that were prepared and in some cases experimented on by Mr. Joshua White, Miss Zoe Parton, and Dr. Liam Aubrey, as indicated in the text. The ultracentrifugation experiment was carried out with the assistance of Dr. Peter Davis, and the LC-MS by members of the University of Sheffield Chemistry department's mass spectrometry service. Many thanks to all lab members for useful conversations regarding the work in this chapter; in particular, thanks to Dr. Peter Davis for technical expertise concerning AF4-MALS and SEC-MALS. Thanks also to Dr. Barbara Ciani for loan of a Superdex 75 column, Dr. Henry Wood for providing the β-PGM, and Postnova Analytics (Landsberg am Lech, Germany) for loan of an in-line MALS detector.

Chapter 4

Surface-Catalysed Primary Nucleation of Aβ(1-42) Fibrils

4.1 Introduction

Interactions between Aβ and a variety of physiologically and experimentally relevant surfaces are well-supported by the literature. In a physiological context, Aβ oligomers are able to permeate or otherwise damage lipid membranes [51, 63–68], and membranes have also been proposed to catalyse the assembly and conformational conversion of on-pathway oligomers, enhancing the rate of primary nucleation and thus accelerating fibril formation [313, 357, 531]. The effect of non-physiological surfaces on Aβ self-assembly is less well-characterised; however, there is evidence that Aβ adsorbs tightly to many common experimental surfaces, such as polystyrene [350,351], mica [352], graphite [352], and the air-water interface (AWI) [353], forming assemblies such as films, sheets, oligomers, and protofibrils. Thus, the surfaces present *in vitro* may strongly affect the Aβ self-assembly pathway.

Although recent progress in the mathematical theory of protein polymerisation has led to major advances in our understanding of Aβ self-assembly mechanisms [1–5, 54, 68], the majority of studies that have successfully applied these models have used a restricted range of experimental surfaces. In particular, regardless of the presence or absence of additional physiological surfaces such as vesicles, most studies that produce ensemble kinetic data suitable for the application of these mathematical models use polystyrene microplates coated with a polyethylene glycol (PEG) low-binding surface, which reduces adsorption of the peptide. While the use of a low-binding surface substantially improves the consistency, reproducibility, and interpretability of the experimental data, the role of other experimental surfaces remains poorly understood. In many experiments, it is not possible to use PEG-treated surfaces, and the majority of published studies use other experimental surfaces, many of which interact strongly with Aβ and may thus alter the peptide's

self-assembly pathway [317, 350–353, 365]. The lack of data on the aggregation mechanisms that occur in the presence of these surfaces means that it is difficult to apply the mechanistic insights of recent mathematical modelling studies to much of the literature. In addition, while PEG-treated surfaces reduce adsorption of Aβ, even infrequent interactions have the potential to influence processes that occur at low baseline rates, such as primary nucleation, and there is evidence in the literature to support an interaction between PEG and Aβ(1-42) [532]. Therefore, it is unclear to what extent the primary nucleation process occurring in PEG-treated microplates represents a truly homogeneous nucleation process, as opposed to a distinct form of heterogeneous nucleation occurring at either the plate surface or the AWI. Moreover, it has been shown that nucleation of fibrils by 5 μM Aβ(1-40) can be prevented by removing the AWI and potentially interacting surfaces [353]; although the situation may be different for Aβ(1-42), due the isoform's higher aggregation propensity, the possibility remains that the Aβ peptides may, in general, be entirely dependent on heterogeneous nucleation to form amyloid at physiologically relevant concentrations.

In this chapter, the self-assembly mechanism of Aβ(1-42) was investigated in the presence of four common experimental surfaces: PEG, polystyrene, glass, and quartz. The results of ThT assays, AFM, NS-EM, and mathematical modelling indicate that each surface results in a distinct self-assembly mechanism, and that primary nucleation is catalysed by all surfaces apart from quartz. While the interactions between Aβ(1-42) and PEG are comparatively weak, they result in a high rate of primary nucleation that is responsible for the deterministic macroscopic self-assembly kinetics observed in PEG-treated plates. In the presence of exposed polystyrene surfaces, deposition of multilayer films of Aβ(1-42) results in a complex self-assembly pathway where the surface both promotes and inhibits aggregation, explaining the slower, biphasic kinetics observed in untreated polystyrene plates. The fibrillisation mechanism in glass plates is less clear, but may be mediated by surface defects, whereas fibrillisation in quartz plates is consistent with a very low nucleation rate, with primary nucleation occurring either homogeneously or at the AWI. The difference between polystyrene, PEG, and quartz demonstrates how strongly, weakly, and non-interacting surfaces can result in dramatically different self-assembly behaviours; since these differences result from general kinetic principles rather than specific structural mechanisms, they are also likely to apply to physiological surfaces such as membranes. Although the data do not completely eliminate the possibility of homogeneous primary Aβ(1-42) nucleation, they indicate that the dominant primary nucleation pathway is heterogeneous at physiological concentrations, in both experimental and physiological contexts; in addition, they add to a growing body of evidence that Aβ aggregation is a multi-step process involving on-pathway prefibrillar intermediates under many experimental conditions. These conclusions provide a more detailed understanding of the primary nucleation process that will assist with interpretation of *in vitro* fibrillisation experiments, and underline the crucial importance of surfaces in the nucleation of Aβ fibrils *in vivo*.

4.2 Materials and methods

4.2.1 Materials

Four types of 96-well plate were used for ThT and NS-EM experiments in this chapter: low-binding microplates treated with a PEG surface layer (Corning 3686/3881, NY), untreated polystyrene microplates (Corning 3694, NY), glass-coated polystyrene microplates (Thermo Scientific, UK), and a quartz plate (Hellma Analytics, UK). For a full description of the other materials used in this chapter, see Section 2.1.

4.2.2 ThT assays

ThT assays were carried out as described in Section 2.5, with a fibrillisation buffer containing 20 mM sodium phosphate (pH 8), 200 μM EDTA, 1 mM NaN_3, and 20 μM ThT. The area of the well in contact with the plate surface was calculated as previously described in [533], with the same parameters. Each plate well is the frustrum of a cone, so that the volume V and depth h_S of the solvent are related by the equation [534]

$$V = \frac{1}{3}\pi h_S(r_B^2 + r_B r_S + r_S^2), \tag{4.1}$$

where r_B is the radius at the base of the well and r_S is the radius at the AWI. The latter can be determined from the radius r_T at the top of the well from the relation

$$r_S = r_B + (r_T - r_B)\frac{h_S}{h_T}, \tag{4.2}$$

where h_T is the total well depth. Given that $r_B = 0.225$ cm, $r_T = 0.250$ cm, $h_T = 1.054$ cm, and $V = 100$ μl, it is calculated that $r_S = 0.239$ cm and $h_s = 0.591$ cm, to 3 significant figures. The area of the well surface in contact with the solvent is given by the area of the well base plus that of the sides of the frustrum [534],

$$A = \pi r_B^2 + \pi(r_B + r_S)\sqrt{h_S^2 + (r_S - r_B)^2}, \tag{4.3}$$

which gives the estimate $A = 1.02\ \text{cm}^2$.

4.2.3 Atomic force microscopy (AFM)

AFM was performed by Dr. Liam Aubrey and analysed by both of us. Two substrates were used: polystyrene and quartz. To prepare the polystyrene surface, a silicon wafer was cleaned with N_2 gas and spin-coated with 2% polystyrene (MW 200 MDa, in toluene). To prevent movement, this was then fixed to a glass microscope slide with green glue (JPK BioAFM, Berlin, Germany). Substrates were positioned on an MFP-3D microscope stage (Asylum Research, UK) and incubated in a solution of 20 mM sodium

phosphate buffer (pH 8) containing 2 mM NaN_3. The surface was imaged in contact mode (set point 0) using tip E from a Bruker MLCT AFM chip (Bruker, Billerica, MA). The spring constant was typically in the 150-200 $nN.m^{-1}$ range. Images were recorded every 255 s for > 6 h; after at least one image had been obtained in the absence of Aβ(1-42), monomeric peptide was injected to final concentration of 11 μM, while imaging was ongoing. To ensure comparable timescales, $t = 0$ has been set to the last time point before Aβ(1-42) was injected. AFM data were previously presented in a PhD thesis by Dr. Liam Aubrey [505]; all analyses presented in this chapter were carried out by myself in Gwyddion [535], including the R_a measurements which had previously been obtained, but were independently verified during preparation of this thesis. Manual calculation of the area of Aβ(1-42) films observed in AFM images was carried out by measuring the semi-major and semi-minor axes of the films in Gwyddion, and applying the formula for the area of an ellipse [534],

$$A = \pi ab, \tag{4.4}$$

where a is the semi-major axis and b is the semi-minor axis. The correction to z values in extracted height profiles was applied by fitting a straight line through the linear regions on either side of films, and subtracting this line from the z values across the entire height profile.

4.2.4 Negative stain electron microscopy (NS-EM)

NS-EM was carried out as described in Section 2.7. Prior to staining, Aβ(1-42) was diluted to a concentration of 4 μM peptide in a pre-adjusted fibrillisation buffer containing 20 mM sodium phosphate (pH 8.0), 200 μM EDTA, 1 mM NaN_3, and 20 μM ThT. The sample was stained either immediately, or after incubation for 1 h or 5 h in a 96-well untreated polystyrene plate (Corning 3694, NY), at 37°C.

4.2.5 Nonlinear regression

Wherever possible, analytical models were fitted in GraphPad Prism 8 using Levenberg-Marquardt least squares fitting. The models shown in Fig. 4.16(e-f) had to be numerically modelled, and were integrated using Euler's method (making sure that the timestep was small enough that resulting error in the fitted parameters was less than the precision) and fitted to the averaged normalised fluorescence intensities using the generalised reduced gradient method, weighting the residuals relative to the standard error of the mean. Regression was carried out from a wide range of intitial parameter sets, to check that the fits had converged to the global minimum. When fitting τ_{50}, whose error is expected to scale with the mean, residuals were weighted relative to the square of the mean. AICc values were calculated using Eq. (3.24), and the likelihood of each model was proportional to $\exp(-\mathrm{AICc}/2)$.

4.3 Results and discussion

4.3.1 The assembly kinetics of Aβ(1-42) are surface-dependent

In order to investigate the effects of common experimental surfaces on Aβ(1-42) self-assembly kinetics, ThT assays were carried out in four different types of 96-well microplate: PEG-treated low-binding microplates, untreated polystyrene plates, glass-coated plates, and quartz plates. All four surfaces are frequently used in experimental studies of amyloid formation. Apart from the differing surfaces, all experiments were carried out under the same conditions, in a 20 mM sodium phosphate (pH 8) buffer containing 200 μM EDTA, 1 mM NaN_3, and 20 μM ThT, at 37°C; these conditions have previously been shown to result in highly reproducible kinetics [479], and were used for validation of preparation quality in Chapter 3. Several repeats of each experiment were carried out, and microplate wells in each experiment contained a range of Aβ(1-42) concentrations in order to evaluate the concentration-dependence of fibrillisation. The blank-subtracted fluorescence intensities from representative experiments are presented in Fig. 4.1, while Fig. 4.2(a) compares the curve shape of the 4 μM data shown in Fig. 4.1, and Fig. 4.2(b) shows the dependence of the ThT half-time on the initial monomer concentration across all repeat experiments.

As shown in Fig. 4.1, the Aβ(1-42) self-assembly kinetics are strongly dependent on the plate surface. The PEG-treated plate produces kinetics that are very similar to those previously published [5,54,479], with a sigmoidal curve shape, a high level of concordancy between replicate wells, and a strong concentration-dependence of the fibrillisation half-time. The kinetics of a separate Aβ(1-42) sample self-assembling in a PEG-treated plate were analysed in Section 3.3.9, and were found to be consistent with the findings of existing mathematical modelling studies [5,54]; the kinetics of the sample used in Fig. 4.1(a) are very similar, and lead to the same mechanistic conclusions. Specifically, the experiments in PEG plates all support the conclusion that Aβ(1-42) self-assembly is a two-state nucleated polymerisation involving distinct primary and secondary pathways, with both primary and secondary nucleation having an approximate reaction order of $n_c \approx n_s \approx 2$ and elongation proceeding via addition of monomers onto the fibril end.

The self-assembly kinetics in other plate types do not support such a simple self-assembly mechanism (Fig. 4.1-4.2). In untreated polystyrene, glass, and quartz plates, the self-assembly kinetics have a lower degree of concordancy between replicate wells and a weaker concentration-dependence; in addition, they often appear to have a biphasic character. The ThT self-assembly kinetics in polystyrene plates have a higher initial fluorescence and are clearly biphasic, as shown in Fig. 4.2(a), although it is not clear whether the first phase represents formation of fibrils or a weakly ThT-binding prefibrillar assembly from the ThT data alone. As shown in Fig. 4.2(b), while the kinetics are highly concentration-dependent in PEG-treated plates, in untreated polystyrene plates the concentration-dependence is very weak, and appears to reverse above an initial peptide concentration of 1-2 μM, meaning that more concentrated samples have longer half-

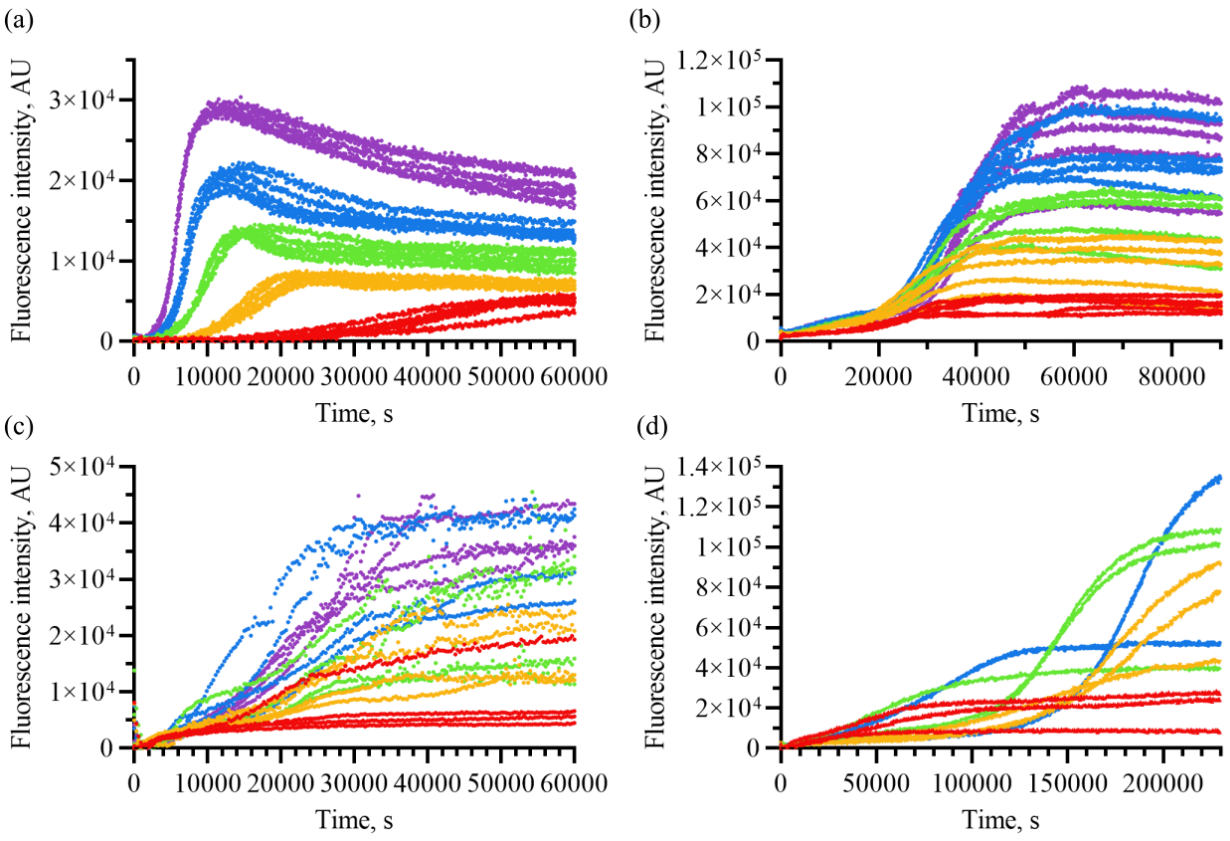

Figure 4.1: Aβ(1-42) self-assembly kinetics are affected by experimental surfaces (part 1). Panels show fluorescence intensities from representative ThT assays, reporting on Aβ(1-42) self-assembly in the presence of different surfaces: (a) PEG-treated low-binding surface, (b) untreated polystyrene, (c) glass, and (d) quartz. The colour scheme corresponds to the initial concentration of Aβ(1-42) monomer: red, 1 μM; amber, 2 μM; green, 3 μM; blue, 4 μM; indigo, 5 μM. Identically coloured curves in the same panel show individual replicates from the same experiment. The absolute fluorescence intensities are not comparable between panels due to differences in gain of the instrument.

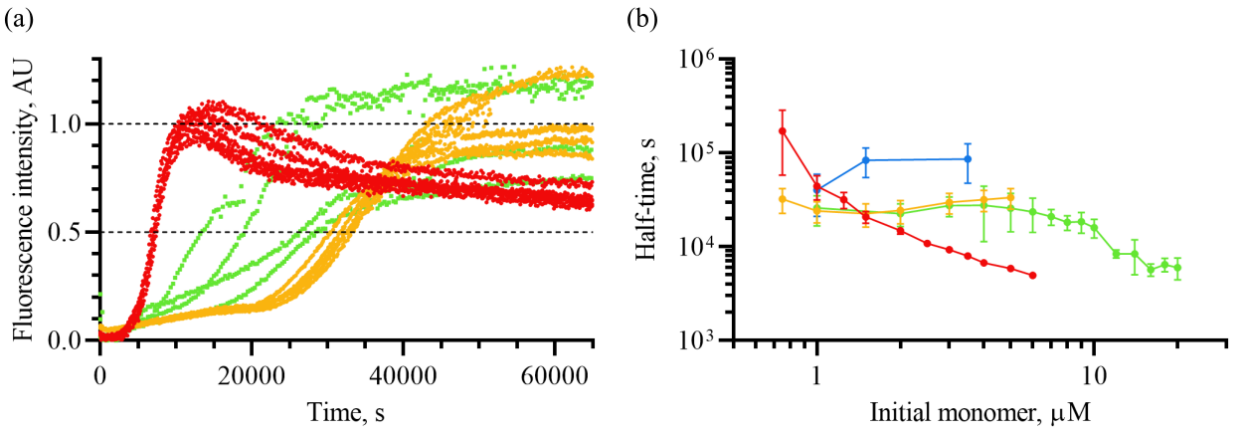

Figure 4.2: Aβ(1-42) self-assembly kinetics are affected by experimental surfaces (part 2). (a) Normalised fluorescence intensities from representative ThT assays with 4 μM Aβ(1-42). (b) Fibrillisation half-times of the normalised ThT curves, averaged across all repeat experiments and with error bars showing a single standard deviation. The colour scheme in both panels corresponds to the type of surface: red, PEG; amber, untreated polystyrene; green, glass; blue, quartz. Normalisation of the quartz data was not possible at 4 μM, but the corresponding un-normalised curves can be seen in Fig. 4.1(d). Apart from the surfaces, all experiments were carried out under the same conditions.

times. The half-times shown in Fig. 4.2(b) were obtained as averages across three repeat experiments with a single Aβ(1-42) preparation. The kinetics were highly concordant, and were reproducible both between repeats and between different Aβ(1-42) preparations; therefore, they do not reflect anomalous behaviour of a single experiment.

Fibrillisation in glass plates has a similar rate and concentration-dependence to untreated polystyrene, and often also appears to have a biphasic curve shape; however, concordancy is much lower. One possible explanation is that fibrillisation is more dependent on a small number of random events that result in the production of primary nuclei. Alternatively, the kinetics may be more sensitive to random variation between the plate wells, such as the presence of surface defects that catalyse primary nucleation.

In quartz plates, fibrillisation is both slow and stochastic, which are hallmarks of a low nucleation rate [536,537]. While the kinetics in PEG-treated and untreated polystyrene plates are consistent, indicating that they result from a large number of primary nucleation events, those occurring in glass plates appear to result from fewer such events, and those in quartz from the least. Across the different plate types, the degree of consistency of the half-time also appears to correlate with that of the final fluorescence intensity; this is interesting as it indicates that different primary nucleation events result in distinct fibril polymorphs that result in different specific ThT intensities. The variable final intensities are unlikely to be due to inconsistent fibril yields, as the Aβ(1-42) concentrations used in these experiments are all well above the typical critical concentrations for fibril stability ($m_0 \gg k_e^- / k_e^+$); with the exception of polystyrene, where tight adsorption of

the peptide to the surface may occur [350,351] (see Section 4.3.3 for confirmation of this hypothesis), close to 100% fibril yield is expected in all cases. It is worth noting that it was not always possible to calculate the half-time and yield in quartz plates, as the extremely low rate of the reaction meant that reactions could not always be followed to the end. Therefore, these quantities were only calculated for initial monomer concentrations at which *all* replicates reached a plateau, to avoid introducing bias into the results. However, the data for which these quantities could be calculated clearly show a low rate and concentration-dependence of fibrillisation, and a variable half-time and yield.

4.3.2 Analysis of fibril yields in polystyrene plates

The cause of biphasic kinetics in untreated polystyrene plates was of particular interest due to the large body of experimental evidence previously accumulated using these plates in this research group, as well as in the wider literature [233,487,523,538–540]. AFM and neutron scattering studies have previously suggested that Aβ adsorbs to polystyrene and forms tightly bound films [350,351]; therefore, it was hypothesised that the biphasic kinetics resulted from film deposition, with the first phase reflecting either film deposition or a process occurring in a deposited film, and the second representing fibril formation. Depletion of monomer from solution could also explain the low, slightly reversed concentration-dependence of fibrillisation. Even if the Aβ(1-42) deposited in films were able to result in a ThT signal, previous studies have suggested that Aβ(1-42) remains relatively non-fibrillar and diffusible in this environment [351], meaning it would probably result in a lower ThT fluorescence than mature amyloid fibrils. Thus, if some quantity of Aβ(1-42) were retained in the films at the end of the experiment, this would be reflected in a lower final fluorescence intensity. The highly consistent self-assembly kinetics in both PEG-treated and untreated polystyrene plates meant that it was possible to perform an analysis of the final fluorescence intensities, and estimate the final fibril yield as a function of the initial monomer concentration. In a two-state system containing only monomer and fibrils, in which the peptide is initially entirely monomeric, the final fibril yield $M(\infty)$ is given by the relation

$$M(\infty) = m(0) - m(\infty), \tag{4.5}$$

where $m(0)$ is the initial free monomer concentration, and $m(\infty)$ is the final free monomer concentration,

$$m(\infty) \approx \frac{k_e^-}{k_e^+}, \tag{4.6}$$

where k_e^+ and k_e^- are the forward and reverse elongation rate constants, respectively. Previous estimates have $k_e^+ \approx 3 \times 10^6$ M^{-1}.s^{-1} and $k_e^- \approx 1 \times 10^{-2}$ s^{-1}, giving $m(\infty) \approx 3.3$ nM. Therefore, $m(0) \gg m(\infty)$, such

that

$$M(\infty) \approx m(0). \tag{4.7}$$

The blank-subtracted ThT fluorescence intensity $\Delta I(t)$ is usually proportional to the fibrillar monomer concentration $M(t)$ [54],

$$\Delta I(t) = f_M M(t), \tag{4.8}$$

where f_M is the specific fluorescence of the fibrillar monomer. Thus,

$$\Delta I(\infty) \approx f_M m(0). \tag{4.9}$$

However, in a three-state system where a population of nonfibrillar aggregated monomer $N(\infty)$ is stable at $m(t) = k_e^- / k_e^+$,

$$M(\infty) \approx m(0) - N(\infty). \tag{4.10}$$

Thus, if the nonfibrillar aggregated population has a specific fluorescence intensity f_N,

$$\Delta I(\infty) \approx f_M \big[m(0) - N(\infty)\big] + f_N N(\infty). \tag{4.11}$$

This can be expressed as a straight line equation with gradient $\partial \Delta I(\infty)/\partial m(0) = f_M$, and a zero $\Delta I(\infty) = 0$ occurring when $m_0 = (1 - f_N/f_M)N(\infty)$,

$$\Delta I(\infty) \approx f_M m(0) + (f_N - f_M)N(\infty). \tag{4.12}$$

As previously discussed, the specific ThT fluorescence of a nonfibrillar species is likely to be much smaller than that of amyloid fibrils; this is supported by the low fluorescence intensity of the first phase, which is likely to represent a greater extent of nonfibrillar aggregation than $N(\infty)$. Thus, $f_N/f_M \approx 0$, so that

$$\Delta I(\infty) \approx f_M \big[m(0) - N(\infty)\big], \tag{4.13}$$

which has a zero at $m(0) \approx N(\infty)$, when almost all the initial monomer is contained in nonfibrillar aggregate. This means that $N(\infty)$ can be obtained from linear regression of $\Delta I(\infty)$ versus $m(0)$, and comparison of the $N(\infty)$ values obtained in PEG-treated and untreated polystyrene plates would provide a lower bound for the extent of any possible films formed on exposed polystyrene surfaces in the latter. It is worth noting that, in order to be observed, the species responsible for $N(\infty)$ need not be stable indefinitely (ie. *thermodynamically* stable) at $m(t) = k_e^- / k_e^+$; it simply needs to persist on the experimental timescale. In order to obtain accurate estimates of $N(\infty)$, it was desirable to collate data from multiple repeat experiments. However,

small differences in the instrument gain reference and activity of the ThT meant that the f_M values differed somewhat between experiments. This did not present a barrier to determination of $N(\infty)$, as these variations in f_M would not be expected to affect $N(\infty)$; therefore, f_M could be individually fitted for each repeat, while $N(\infty)$ could be fitted as a single value shared across all repeats. However, in order to aid data presentation, it was desirable to normalise the data so that all would have the same gradient. This was achieved by carrying out the aforementioned fit, with individual f_M values and a shared $N(\infty)$, and then dividing the intensities of each dataset by its respective fitted f_M value. Thus,

$$\Delta I_{\text{norm}}(\infty) = \frac{\Delta I(\infty)}{f_M} \approx m(0) - N(\infty) = M(\infty). \tag{4.14}$$

It is worth noting that $\Delta I_{\text{norm}}(\infty)$ has dimensions of molar concentration, and is equal to $M(\infty)$ under the assumptions used to derive Eq. (4.14), although in practice $N(\infty)$, f_M, and f_N are likely to vary with $m(0)$ in a way that may cause concentration-dependent deviations from this predicted relationship. The normalisation procedure does not affect the x-intercept, meaning the normalised data give approximately the same estimate of $N(\infty)$ as the un-normalised data, and are suitable for presentation and determination of $N(\infty)$. The normalisation process also ensures the same gradient $\partial \Delta I_{\text{norm}}(\infty)/\partial m(0) = 1$, facilitating comparison between data acquired under different conditions such as PEG-treated versus untreated polystyrene plates. The normalised intensities, obtained using f_N values fitted for $m(0)$ in the 0-4 μM range, are shown in Fig. 4.3. As previously discussed in Section 3.3.9, higher concentrations are excluded from fitting of final fluorescence intensities in this thesis, as they often exhibit enhanced fluorescence indicative of a change in fibril polymorphism. Although the relationship between $\Delta I_{\text{norm}}(\infty)$ and $m(0)$ does exhibit some deviations from linearity (Fig. 4.3(a)), indicating that $N(\infty)$, f_M, or f_N exhibits some dependence on $m(0)$, the overall trend is approximately linear. The $\Delta I_{\text{norm}}(\infty)$ values in PEG-treated plates are consistently above those obtained for untreated polystyrene plates; because the gradients of the two normalised datasets are identical, this indicates that $N(\infty)$ is greater in the latter. Consistent with this, linear regression (Fig. 4.3(b)) gave fitted $N(\infty)$ values of 0.165 μM in PEG-treated plates (asymmetric 95% CI 0.121-0.208 μM) and 0.518 μM in untreated polystyrene plates (asymmetric 95% CI 0.431-0.604 μM), which was determined to be statistically significant by an F-test ($p < 0.0001$). In addition, the normalised final fluorescence intensity in PEG at $m(0) = 0.5$ μM was $\Delta I_{\text{norm}}(\infty) = 0.731 \pm 0.156$ μM, while fibrillisation was never observed at that concentration in untreated polystyrene plates, on timescales in excess of 120000 s (approximately 4× the expected half-time for that concentration); this supports the conclusion from the linear fitting that the $N(\infty)$ value was typically below 0.5 μM in PEG-treated plates, and above that value in untreated polystyrene plates.

Altogether, analysis of the final fluorescence intensities indicates that the fibril yields exhibit a small but statistically significant reduction in untreated polystyrene plates compared to PEG plates. This is likely

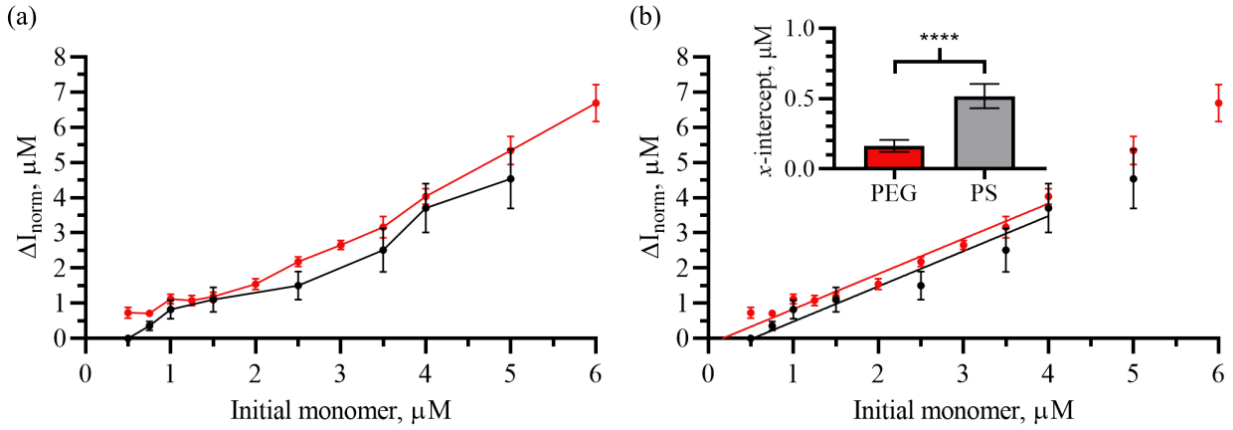

Figure 4.3: Fibril yields are reduced in untreated polystyrene plates. (a) The normalised final fluorescence intensities are lower in polystyrene than in PEG. Colour scheme: red, PEG-treated plates; black, untreated polystyrene plates. (b) The same data linearly fitted in the 0-4 μM range, with the same colour scheme. The inset panel compares the x-intercepts ($N(\infty)$ values) of the two fits, showing a significant ($p < 0.0001$) difference between the two. The normalisation process affects the gradient of the fitted curves, but not the x-intercepts; for more details, see text. The error bars of the normalised intensities show a single standard deviation; the error bars in the inset panel show asymmetric 95% CIs of the fitted x-intercepts.

to be due to adhesion of Aβ(1-42) to the plate surface to form a tightly adsorbed film that is stable, or at least metastable and long-lived, at $m(t) = k_e^-/k_e^+$. The size of this film is likely to vary somewhat with $m(0)$, but an approximate estimate can be obtained from the difference in $N(\infty)$ between the two plate types, $\Delta N(\infty) = 0.353$ μM. Although this estimate is probably only accurate to a low level of precision (perhaps 1 s.f.) due to the probable $m(0)$-dependence of $N(\infty)$, calculations in the remainder of this section are performed to a higher precision to avoid excessive propagation of errors. It should also be noted that although PEG-treated plates are used as a baseline due to the probability that any Aβ(1-42):PEG interaction is weak, low-affinity binding of Aβ(1-42) to PEG has still been observed [532] and still has the potential to affect the self-assembly kinetics, even though it is unlikely to strongly affect the final fibril yields. As will be shown in Section 4.3.7, the differing behaviour of PEG-treated and quartz plates indicates that this interaction also has a catalytic effect on primary nucleation.

Based on an adsorption of 0.353 μM Aβ(1-42) from a 100 μL volume, with 1.02 cm^2 of the plate in contact with the solvent (see Section 4.2.2), the estimated surface density of adsorbed monomers is 0.208 nm^{-2}. This is close to the previously reported value of 0.32 nm^{-2}, which was also for Aβ(1-42) films deposited on polystyrene [351]. If the residual film is a monolayer, this indicates that each monomer occupies an area of around 4.80 nm^2, assuming 100% surface coverage; in an idealised square lattice model of packing within the monolayer, this would equate to an inter-monomer spacing of 2.19 nm, which is plausible given that the R_g of soluble, unfolded Aβ(1-42) monomer is typically in the 1.0-1.6 nm range

[235–238]. As a further test of the plausibility of this figure, one can calculate the likely thickness of such a monolayer for a variety of possible densities of the adsorbed monomer, and compare this to the value previously determined for Aβ(1-40) films by neutron scattering [350]. In its most expanded state, the disordered Aβ(1-42) monomer has $R_g = 1.6$ nm, which would give an average polypeptide chain density of 0.203 g.cm^{-3} in an idealised spherical model of the unfolded peptide's density distribution. This gives 7.68 nm as an extreme upper bound for the film thickness, although such a value is very unlikely as monomer-surface and monomer-monomer interactions would be expected to cause collapse of the adsorbed peptide. For a lower bound on the film thickness, the density of folded protein is typically around 1.35 g.cm^{-3}, which gives a film thickness of 1.16 nm. Again, this is an extreme value, and it is doubtful that an adsorbed monolayer of Aβ(1-42) would be sufficiently dense to achieve this thickness; however, one would expect the thickness of a monolayer film to be closer to the lower bound of 1.16 nm than the upper bound of 7.68 nm. For an example of an intermediate case, experimental and computational studies have often suggested $R_g \approx$ 1.1 nm for the monomer [235, 236, 238], which reflects a relatively collapsed state. Applying an idealised spherical model of the peptide's density distribution, this would give an average polypeptide density of 0.625 g.cm^{-3} and a thickness estimate of 2.50 nm. This is closer to the lower bound than to the upper bound, and is close to the value of $\sim$2 nm previously determined for Aβ(1-40) films by neutron scattering [350]. It is worth noting that all these estimates require a non-planar conformation of the adsorbed monomer; in their study of Aβ(1-40) on hydrophobic surfaces, Rocha *et al.* [350] proposed that the central hydrophobic cluster (CHC, with the sequence LVFFA) and the C-terminal region (CTR) would interact with the surface, while the other regions of the peptide would be oriented towards the solvent, and a similar orientation seems likely for Aβ(1-42).

Despite small variations at specific concentrations, the data in Fig. 4.3 suggest that, on average, there is no trend between $m(0)$ and the amount of peptide adsorbed to the surface at the end of the experiment. However, the low concentration-dependence of the fibrillisation rate indicates that it is the free monomer concentration, rather than the adsorbed monomer concentration, that is constant during the growth phase. This may indicate that a greater quantity of peptide initially adsorbs to the surface, but the formation of amyloid fibrils causes depletion of the free monomer reservoir, resulting in the disassembly of all but the most stable species. Thus, the kinetic data suggest that larger aggregates may initially form on the polystyrene surface, but only a residual monolayer persists at the end of the growth phase.

4.3.3 Deposition of films of Aβ(1-42) on polystyrene surfaces

To test the hypotheses proposed in the previous section, AFM was used to image the surface topography of a spin-coated polystyrene surface in the presence of 11 μM Aβ(1-42), in a 20 mM sodium phosphate buffer (pH 8). Topography images of a representative experiment are shown in Fig. 4.4-4.7. Due to the

large changes in topography in these images, the 2D and 3D representations give complementary views of the processes occurring at the surface; therefore, both have been provided, with the 3D representations shown in Fig. 4.4-4.6 and the corresponding 2D representations in Fig. 4.7. Initially, the surface was flat and showed no sign of any large films or Aβ(1-42) deposits (Fig. 4.4(a), Fig. 4.7(a)). By ∼1 h, several small areas of raised topography had appeared (Fig. 4.4(b), Fig. 4.7(b)), which increased in number, area, and height until ∼3 h after the start of the experiment (Fig. 4.4(c), Fig. 4.5(a), Fig. 4.7(c-d)). From ∼4 h onwards, the assemblies began to disassemble (Fig. 4.5(b-c), Fig. 4.7(e-f)); late in the time course, they acquired a flattened morphology, although small areas of raised topology remained (Fig. 4.6, Fig. 4.7(g-h)). The assemblies were observed consistently on polystyrene, were not observed on other surfaces (see Section 4.3.7), and could only have been Aβ(1-42), as there was no other species present in solution that could have adsorbed to the polystyrene in such quantities. Although the 3D representations in Fig. 4.4-4.7 appear almost hemispherical at their maximum, the chosen z-scale is enhanced in order to clearly show the surface topography. In reality, the assemblies are thin and 'pancake-like', with an approximate depth of ∼0.1 μm and width of up to ∼10 μm at their maximum extent; thus, they are films, and their maximum depth is consistent with a multi-layered composition.

To gain a deeper insight into the deposition and disassembly kinetics of these films, the number of films, surface roughness R_a, and maximum z-height $z_{\max}$ were calculated for each image and plotted against time (Fig. 4.8). The surface roughness is calculated as an average of the unsigned deviation in the z-height over the entire image

$$R_a = \frac{1}{A}\iint |z| dxdy. \tag{4.15}$$

It is worth noting that the sharp changes in topography across the image resulted in artifactual changes in the z-height of the surface itself, as is clearly visible in 4.4(c); this confounded measurements of R_a and $z_{\max}$ by (i) reducing the apparent z-height of the films, and (ii) introducing additional contributions to the integral in Eq. (4.15) that are not due to the film surface. Nonetheless, since these errors are systematic and approximately proportional to the height of the films, they do not strongly affect the overall trend of the data in Fig. 4.8(b-c).

As shown in Fig. 4.8(a-b), the increase in R_a, which is approximately proportional to the volume of the deposited films, is preceded by an initial increase in the number of films. This supports a nucleated deposition mechanism of film growth, in which small films nucleate on the polystyrene, and then grow by incorporation of additional monomers from solution. At $t \approx 5000$ s, nucleation of new films ceases and the growth of the existing films slows, as revealed by the levelling of R_a and $z_{\max}$. The fact that the drop in nucleation and the growth of separate films occur approximately simultaneously indicates that they are both caused by global depletion of the soluble monomer due to extensive deposition on the surface. After

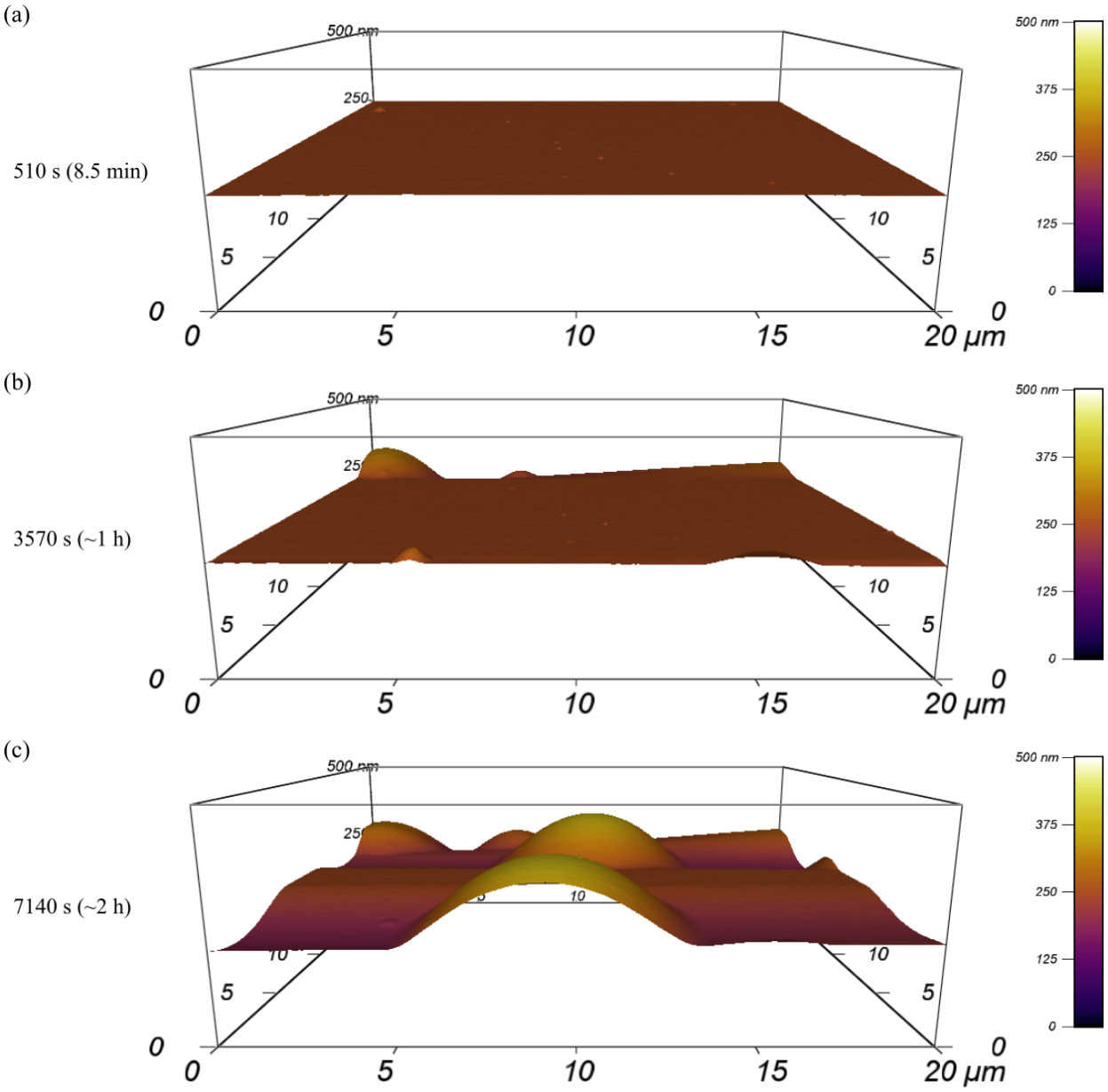

Figure 4.4: Deposition of thick films of Aβ(1-42) on polystyrene, imaged by AFM (part 1). Panels show 3D topography images of different time points in the same AFM experiment. See Fig. 4.5 and Fig. 4.6 for later time points, and Fig. 4.7(a-c) for the 2D representation of the same time points.

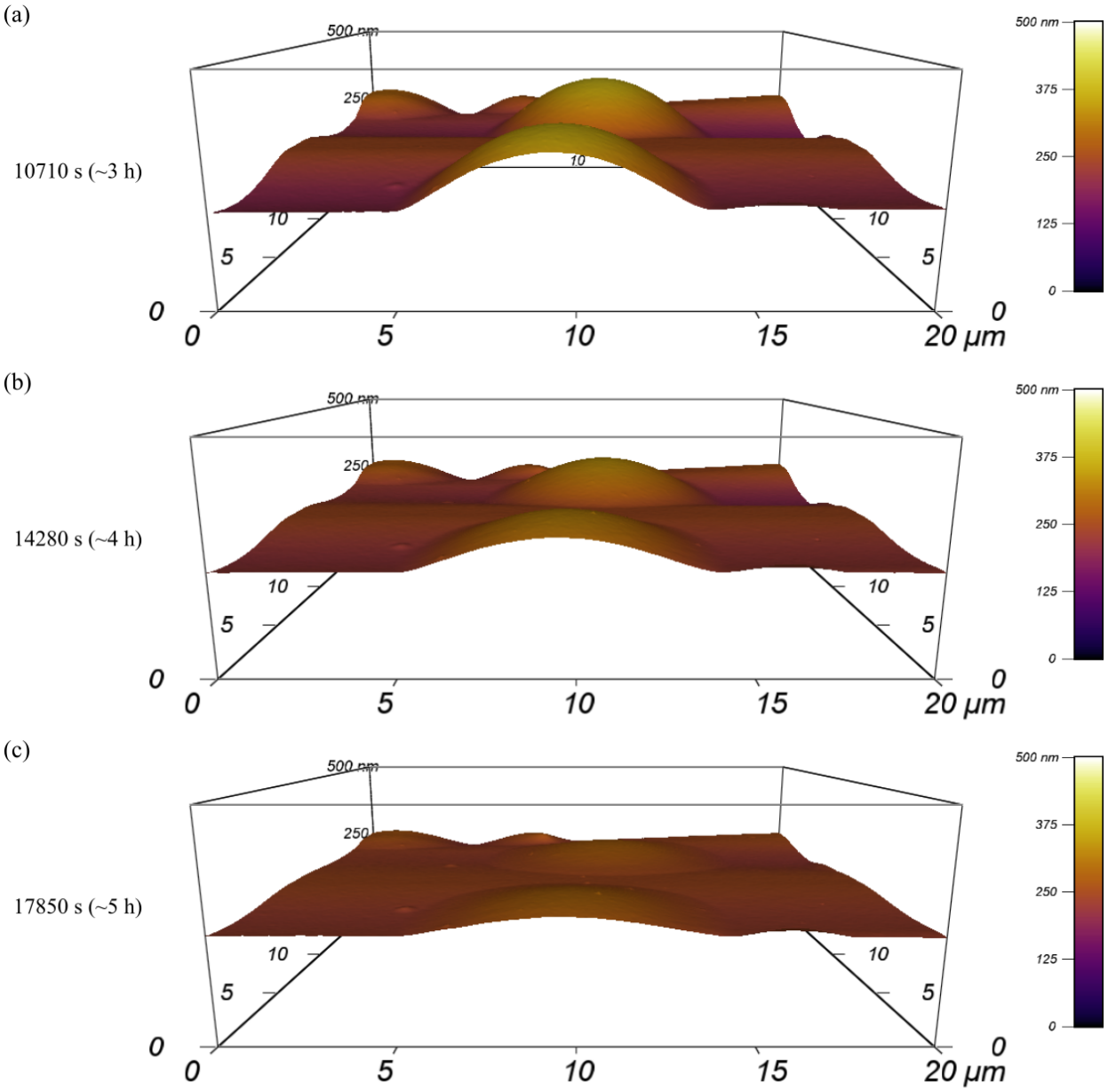

Figure 4.5: Deposition of thick films of Aβ(1-42) on polystyrene, imaged by AFM (part 2). Panels show 3D topography images of different time points in the same AFM experiment. See Fig. 4.4 and Fig. 4.6 for earlier and later time points, and Fig. 4.7(d-f) for the 2D representation of the same time points.

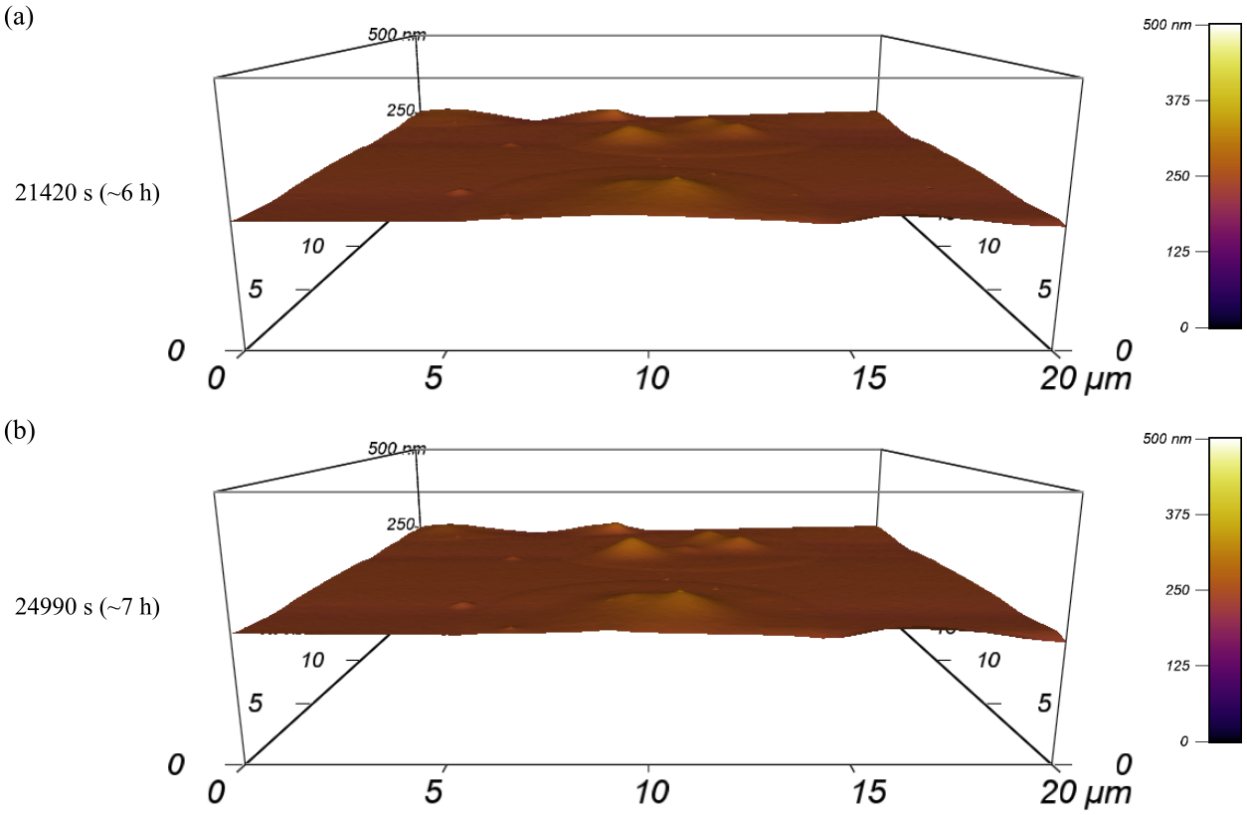

Figure 4.6: Deposition of thick films of Aβ(1-42) on polystyrene, imaged by AFM (part 3). Panels show 3D topography images of different time points in the same AFM experiment. See Fig. 4.4 and Fig. 4.5 for earlier time points, and Fig. 4.7(g-h) for the 2D representation of the same time points.

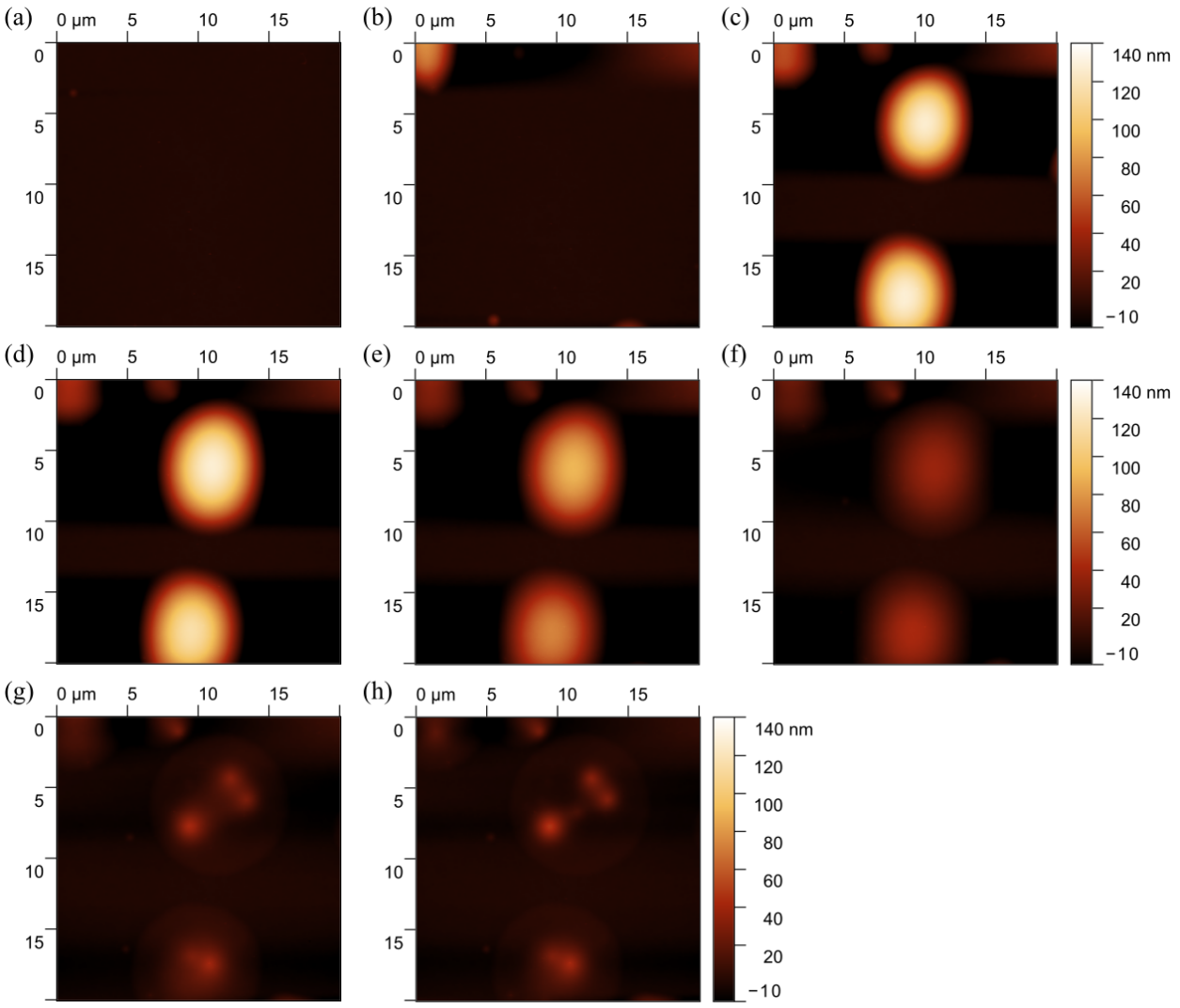

Figure 4.7: Deposition of thick films of Aβ(1-42) on polystyrene, imaged by AFM (part 4). Panels show different time points in the same AFM experiment: (a), 510 s (8.5 min); (b), 3570 s (∼1 h); (c), 7140 s (∼2 h); (d), 10710 s (∼3 h); (e), 14280 s (∼4 h); (f), 17850 s (∼5 h); (g), 21420 s (∼6 h); (h), 24990 s (∼7 h). All images are shown on the same colour scale. See Fig. 4.4-4.6 for 3D topography images of the same time points.

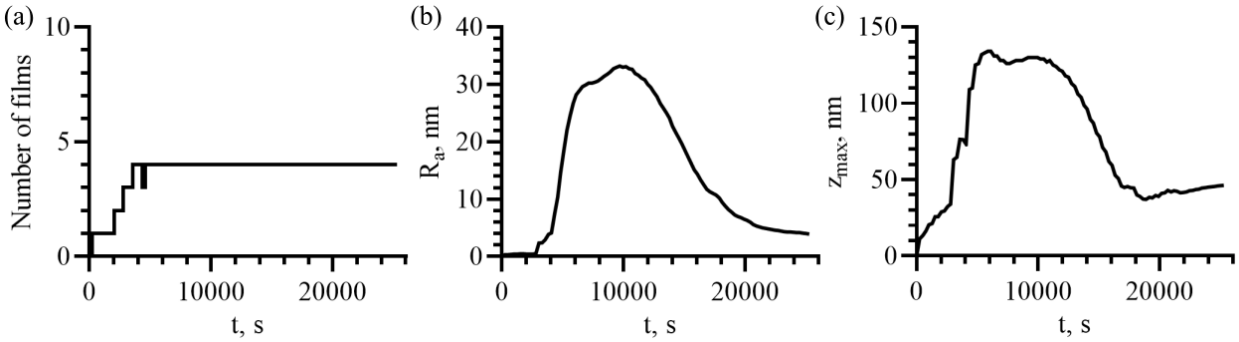

Figure 4.8: Global analysis of Aβ(1-42) films formed on polystyrene. Panels show statistics pertaining to the entire area that was imaged, as a function of time: (a) the number of films whose centre appeared within the imaging area; (b) the surface roughness R_a of the entire area; and (c) the maximum z-height.

an experimental time of $t \approx 10000$ s, both R_a and $z_{\max}$ begin to decrease, indicating that the multilayers have been destabilised; this is likely to require the free monomer concentration to drop below the critical concentration for multilayer stability, which would be caused by the ongoing formation of a more stable species. Since the decrease in R_a implies an approximately proportional decrease in the volume of the films, it is unlikely that the multilayers are simply being replaced with a more widespread, tightly adsorbed monolayer with the same volume. Instead, the continued decrease in free monomer concentration may be caused by the formation of suspended amyloid fibrils, as fibrils do not associate with the surface under these conditions and so would not be visible by AFM. This conclusion is also supported by local analysis of height profiles, as shown in Fig. 4.9(a-f). While the height of the background remains consistent from before Aβ(1-42) is added until the end of the experiment, indicating that formation of a blanket monolayer does not occur, the height of the films changes dramatically during this time, reaching a maximum at ∼10000 s and decreasing after that point.

At the same time as the decrease in the volume and height of the films, their area continues to grow. Automated calculation of the area of the films was confounded by their effects on the z-heights of the surrounding surface; however, a manual calculation was carried out to determine the projected area of the single film centred at coordinates $(x,y) \approx (11\ \mu\text{m}, 6\ \mu\text{m})$, as described in Section 4.2.3 and shown in Fig. 4.9(b, c, g). This film nucleated comparatively late (∼4000 s), and its area growth rate decreased approximately in line with the R_a and $z_{\max}$ of the image as a whole. However, while R_a decreased monotonically after $t \approx 10000$ s, the area continued to increase at a very low rate. This indicated that the lower layers of the film, or perhaps just the single layer in contact with the polystyrene, remained stable despite depletion of the soluble monomer. At the same time, late in the time course, the maximum height of the films began to increase. This was not an artifact of systematic errors in the baseline z-height, as manual measurements of the difference in height between the centre of the film situated at $(x,y) \approx (11\ \mu\text{m}, 6\ \mu\text{m})$ and the adjacent

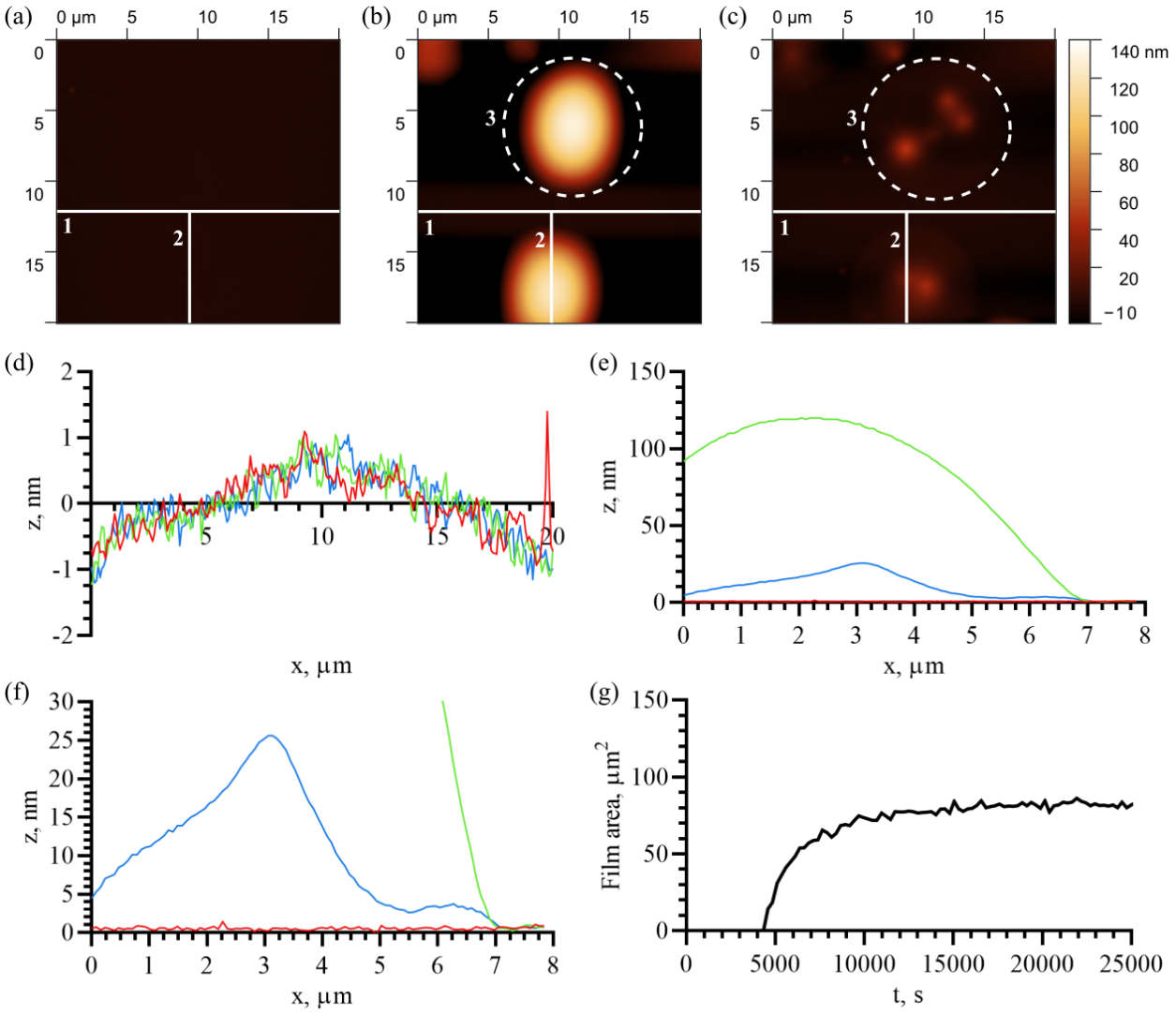

Figure 4.9: Local analysis of Aβ(1-42) films formed on polystyrene. Panels (a-c) show 2D topography images of the films during assembly and disassembly, on the same z-scale: (a), 0 s; (b), 9945 s (∼3 h); (c), 24490 s (∼7 h). The horizontal line ('1'), vertical line ('2'), and ellipse ('3') mark features of interest that are analysed in panels (d-g). Panel (d) shows superimposed height profiles corresponding to the horizontal line marked '1' in panels (a-c), coloured according to time point: red, 0 s, panel (a); green, 9945 s, panel (b); blue, 24490 s, panel (c). Panel (e) shows superimposed height profiles corresponding to the vertical line marked '2' in panels (a-c), using the same colour scheme as panel (d). Panel (f) shows a close-up view of the profiles in panel (e), with an expanded z-scale. Panel (g) shows the time-dependence of the estimated projected area of a single film that nucleated at ∼4000 s, situated at $(x, y) \approx (11\ \mu\text{m}, 6\ \mu\text{m})$ and marked '3' in panels (b-c). Note that, although the margins of the film appear unclear in panels (b-c) due to the use of a broad z-scale, they were unambiguously determined for this analysis by using a narrower z-scale. This film is examined in greater detail in Fig. 4.10.

surface confirmed that Δz increased from $\sim$47 nm to $\sim$50 nm between 21420 s and 24990 s. Examination of the topography images shown in Fig. 4.6(a-b) and Fig. 4.7(g-h) revealed that the increase in z_{max} was caused by the slow continued growth of small 'sub-films' which had similar morphology to the original films, but apparently increased stability. These films may have been formed by nucleated conformational changes within the self-assembled monomers to form a more stable polymorph.

To gain a closer view of the changing topography of the films, height profiles were obtained. 2D images of the films at various stages of their disassembly are shown on an expanded z-scale in Fig. 4.10(a-c), with the corresponding height profiles for the start of the process in Fig. 4.10(d-e), and the height profiles for the end of the process in Fig. 4.10(f-g). To eliminate systematic error in the baseline z-height, a linear correction was applied, as described in Section 4.2.3. Fig. 4.10(a-c) shows that a thin residual film is left behind after disassembly of the bulk of the film, containing several small sub-films. Prior to disassembly, the depth of the film increases continuously towards its centre (Fig. 4.10(d-e)); towards the end of the process, the film is flat (Fig. 4.10(f-g)), apart from the areas that are part of the stable sub-films. The flat topography of the film indicates that it consists of a constant number of layers of Aβ(1-42) monomers, and it is most likely to be a monolayer. The lowest layer of monomers is in direct contact with the polystyrene surface, and so forms a distinct set of molecular interactions compared to the layers deposited on top; accordingly, theories of film deposition typically allow for distinct kinetics and thermodynamics for assembly of the lowest layer [384]. In the case of Aβ(1-42), a monolayer would have distinct thermodynamic advantages, as it would allow the CHC and CTR to interact with the polystyrene, while the hydrophilic N-terminal region (NTR) and turn region (TR) could interact with the bulk solvent. To test whether the dimensions of the residual film are consistent with a monolayer, the thickness was compared to the range of values previously estimated based on the data in Fig. 4.3 (see Section 4.3.2). The inset panel in Fig. 4.10(g) shows that the residual film has a thickness of $\sim$3 nm, which is within the predicted range for a monolayer film (1.2-7.7 nm) capable of explaining the observed loss of fibril yield, and close to the 'intermediate' estimate of 2.5 nm, which was obtained for a partly collapsed state, as well as the estimate of $\sim$2 nm previously obtained by Rocha *et al.* [350]. If the per-area density of the film is approximately the same as that suggested by the yield analysis and previously published data [351], a bilayer film would require an unusually high density of the adsorbed monomers, close to that of a folded state, in addition to lacking the thermodynamic advantages afforded to a monolayer; a film thicker than a bilayer would have to be impossibly dense. Therefore, the available AFM and ThT data, as well as previously published data [350, 351] and basic physical considerations, all point to the residual film being a monolayer.

A schematic of the self-assembly behaviours evident from the AFM data, encompassing film nucleation, growth, maturation, and disassembly, is provided in Fig. 4.11. At the start of the experiment, the vast majority of the peptide is monomeric, as determined in Chapter 3. Early on, films nucleate on the polystyrene,

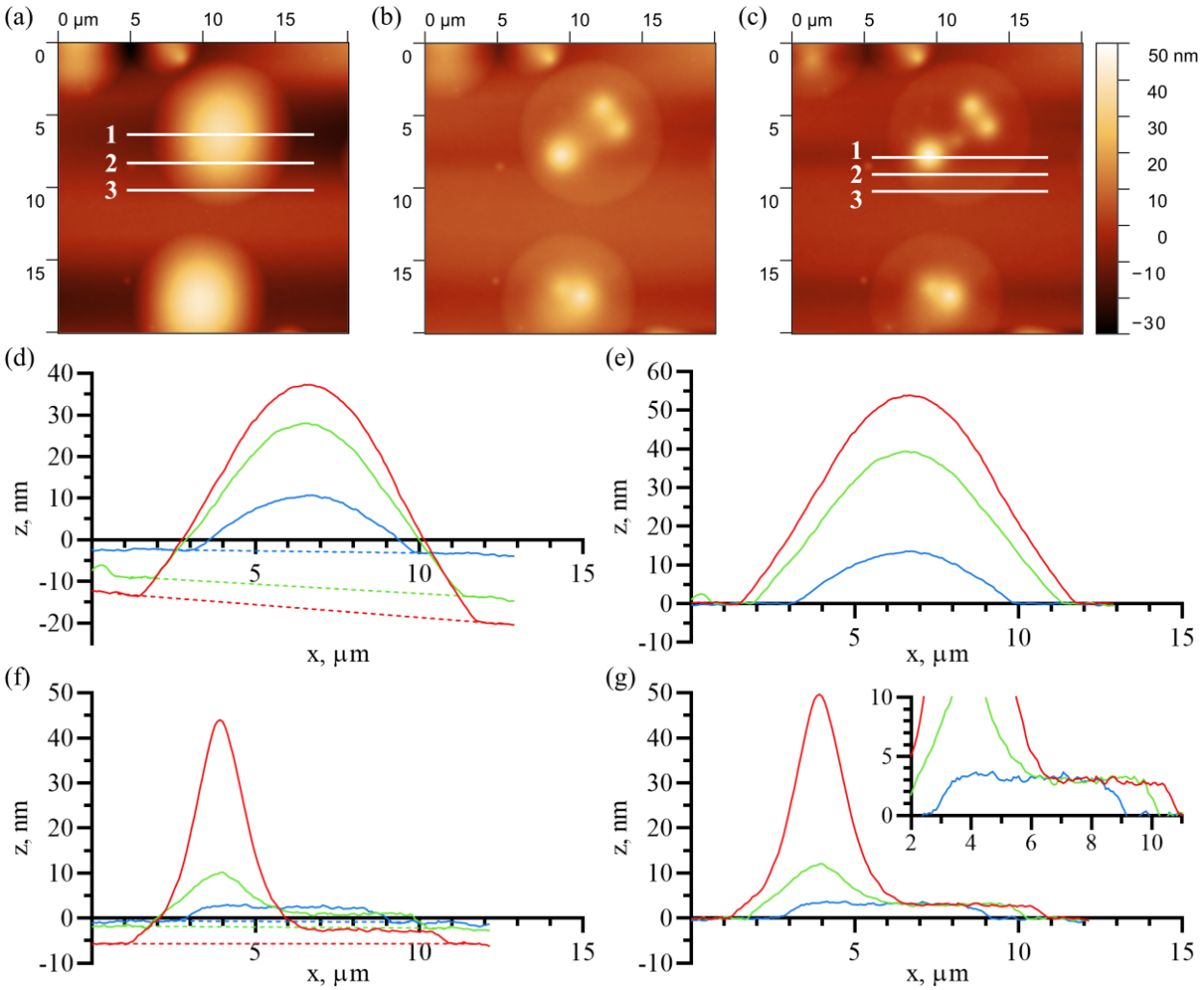

Figure 4.10: Thickness of Aβ(1-42) films formed on polystyrene. Panels (a-c) show 2D topography images of the films during the disassembly process, with an expanded z-scale to more clearly show the height differences: (a), 17850 s (∼5 h); (b), 21420 s (∼6 h); (c), 24990 s (∼7 h). Panels (d-e) show height profiles corresponding to the horizontal lines in panel (a), and panels (f-g) show height profiles corresponding to the lines in panel (c). Raw profiles are shown in panels (d) and (f), and profiles with a linear baseline correction are shown in panels (e) and (g). Colour scheme for panels (d-g): red, line 1 in the corresponding image; green, line 2; blue, line 3. The inset in panel (g) shows a close-up view of same set of profiles with an expanded z-scale.

and amyloid fibrils may also begin to appear in solution at this point. The films and amyloid fibrils grow, depleting the soluble monomer until dissociation of the monomer from the films exceeds association, causing the reversal of film growth. As a result, films begin to disassemble, sustaining the monomer reservoir for elongation of amyloid fibrils. Towards the end of the experiment, the only residual films are a thin monolayer tightly adsorbed to the polystyrene surface, as well as thicker multilayer films, which may arise from a structural phase transition in the films prior to disassembly (phase 1 $\rightarrow$ phase 2).

4.3.4 Initial analysis of Aβ(1-42) self-assembly kinetics in polystyrene plates

The insights gained from the AFM experiments were used to inform further analysis of the ThT data presented in Fig. 4.1-4.2. In the context of these data, the changes in ThT fluorescence intensity occurring from approximately 0-20000 s are referred to as the first phase, and those occurring from approximately 20000 s onwards are referred to as the second phase. Fig. 4.12(a) provides a closer view of the first phase and the early part of the second phase, and Fig. 4.12(b) specifically focuses on the early part of the first phase. While the majority of film growth occurred at times from 4000-6000 s in the AFM experiment, no change in signal occurs specifically within that time frame in the ThT experiment, and the general increase in ThT fluorescence from 0-20000 s is unlikely to represent film deposition as its kinetics are much slower than those of film deposition observed by AFM. However, rapid changes in fluorescence do occur very early in the ThT data ($<$2000 s), and appear to result from a combination of two conflicting effects: an initial drop in the specific ThT fluorescence intensity, which is commonly seen in ThT experiments and is caused by equilibration to the experimental temperature of 37^{o}C; and an initial increase in the quantity of ThT-positive species, which is easily visible at 0.5 μM Aβ(1-42), partly masked by the decrease in fluorescence at 1 μM Aβ(1-42), and not visible at higher concentrations. Although this initial increase is only visible at the lower peptide concentrations, the ThT fluorescence appears to start at an elevated level at the higher concentrations; this indicates that an initial increase in the abundance of ThT-positive species occurs at all peptide concentrations, but is sometimes too fast to observe, or is obscured by the effects of temperature equilibration. In the discussion of the kinetics in this section, both the fast initial increase in fluorescence and the subsequent slower increase until $\sim$20000 s are treated as separate parts of the first phase, termed the 'fast' and 'slow' processes. Both were reproducibly observed in repeat experiments.

The initial increase in ThT fluorescence is probably the best candidate for film deposition, as it has a low amplitude and a similar timescale to deposition of films in the AFM experiment after nucleation. In support of this conclusion, the timescale for multilayer formation in the AFM experiment following deposition of a monolayer can be estimated from the maximum rate of increase of R_a in the analysis shown in Fig. 4.8(b), which is ~ 0.017 nm.s^{-1} at a time between 4590 s and 4845 s. Let us make the following assumptions and approximations: (i) the surface coverage is half-maximal ($\sim$15% of total area) in the AFM experiment

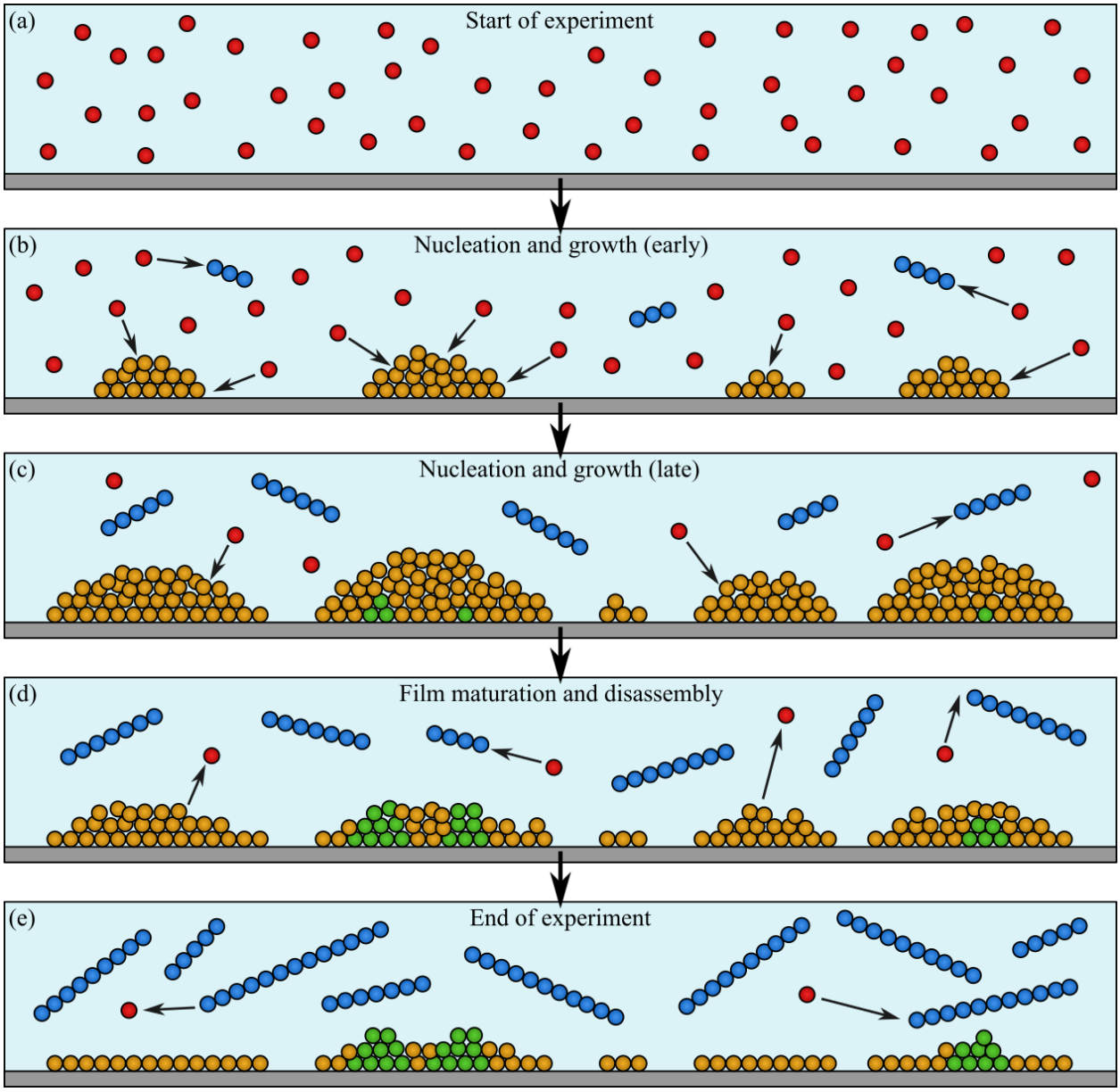

Figure 4.11: Schematic of Aβ(1-42) self-assembly in the presence of polystyrene (AFM experiments). Panels show snapshots of different time points in the experiment. Circles represent Aβ(1-42) monomers, with the colour scheme representing the conformational state: red, soluble; gold, films (phase 1); green, films (phase 2); blue, fibrillar. The gray surface represents the polystyrene, and the smaller arrows represent the association with or dissociation of the monomer from the films and the fibril ends.

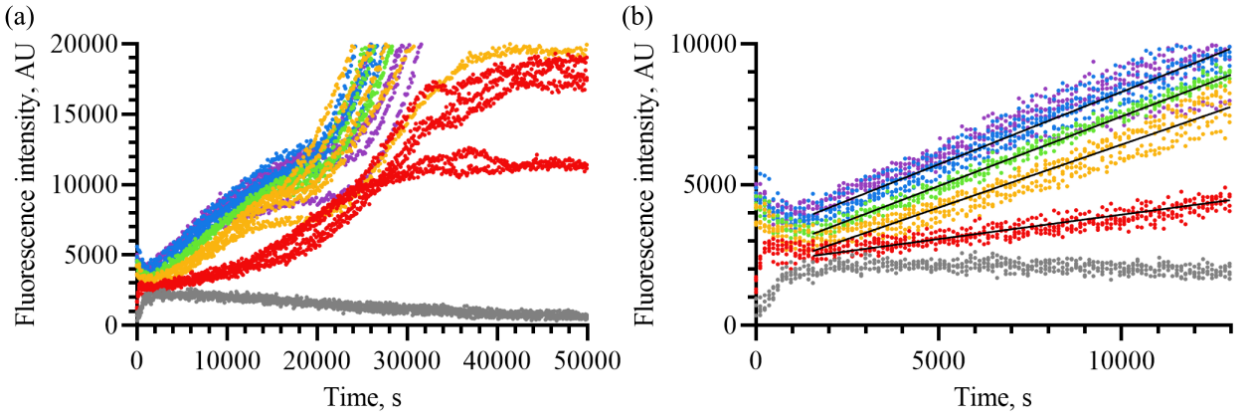

Figure 4.12: Analysis of the first phase of ThT fluorescence gain in untreated polystyrene plates (part 1). (a) A close-up view of the ThT data originally presented in Fig. 4.1(b), focusing on the first phase. The 0.5 μM curves from the same experiment have been added to show the ThT kinetics at concentrations where fibrillisation is not observed. The colour scheme corresponds to the initial monomer concentration: gray, 0.5 μM; red, 1 μM; amber, 2 μM; green, 3 μM; blue, 4 μM; indigo, 5 μM. (b) A closer view of the ThT fluorescence in the early time, using the same colour scheme. The data from wells containing 1-4 μM Aβ(1-42) have been linearly fitted over the range of times from 1500-15000 s, as described in the main text.

at this point in time; (ii) the loss of z-height of the films due to systematic baseline error is approximately cancelled by additional contributions to the integral in Eq. (4.15) made by artifactually negative z values; and (iii) the other causes of negative z values are negligible. Although these assumptions are unlikely to be exactly correct, they allow a very approximate estimate of the growth rate to be obtained. Correcting for ∼15% surface coverage, it follows that the maximum rate of vertical film growth is ~ 0.12 nm.s^{-1}, which is close to the maximum rate of increase of $z_{\max}$ (~ 0.14 nm.s^{-1}), indicating that the assumption of ∼15% surface coverage is approximately correct. This growth rate is attained at a time when R_a is at ∼40% of its maximum value, indicating that ∼60% of the initial 11 μM of Aβ(1-42) is still in solution; thus, if the rate of film deposition is proportional to the free monomer concentration, the growth rate per monomer concentration is $\sim 1.7 \times 10^4$ nm.M^{-1}.s^{-1}. Assuming that the density of the film remains approximately constant between successive layers, so that the vertical density of monomers is ∼1/3 nm^{-1}, this implies that layers are deposited at a rate of $\sim 5.8 \times 10^3$ M^{-1}.s^{-1}. If a single layer with the maximum level of coverage contains ~ 0.35 μM of peptide in the ThT experiments, then once this level of coverage is reached the excess free monomer should disappear from solution with a pseudo-first-order rate constant of $\sim 2.0 \times 10^{-3}$ s^{-1}, not accounting for dissociation or the temperature difference between the AFM and ThT experiments. This would result in exponential kinetics with a half-time of ~ 340 s, which is close to the rate of the fast process, and also close to the experimental dead time of 200-300 s, explaining why an initial increase in ThT fluorescence is sometimes not observed.

Although the calculated timescale is very approximate, it is much closer to the fast process (<1000 s)

than the slow process (1000-20000 s). If film nucleation occurred more rapidly in the ThT experiments than in the AFM experiments, the fast process could easily correspond to multilayer deposition; in contrast, the rate of the slow process is two orders of magnitude too low. A difference in nucleation rate between the ThT and AFM experiments would not be surprising, as the surfaces used in these experiments were produced by different methods, meaning they would have different nanoscale structures. While it is possible that film deposition could proceed on a slower timescale, but not cause any change in ThT fluorescence, there is no other obvious explanation for the initial increase in ThT fluorescence, which is not observed in PEG-treated polystyrene plates. The ability of film deposition to result in a very small increase in ThT fluorescence would also not be surprising; ThT is not strictly specific to amyloid fibrils [93, 94], and has been observed to bind oligomers [278], as well as films of Aβ(1-42) formed at the air-water interface [353].

A consequence of the implied increase in the film nucleation rate is that the films formed in the ThT experiment are likely to have greater surface coverage than those formed in the AFM experiment. Under conditions where the film nucleation rate is low, the films will be fewer in number and grow over a longer period of time. This will result in a small number of films that individually cover a larger area, and the extended growth period means these films will be relatively thick. In contrast, if the nucleation rate is high, the films will be more numerous but will have less time to grow, meaning they will individually cover less area, and will be thinner. Therefore, the mean thickness of films at their maximum extent is likely to be negatively correlated with the number of nucleation events. Since the total volume of the films is limited when they reach their maximum extent, thinner films are likely to cover more area, meaning they will be more likely to merge into a single multilayer. Therefore, while the surface coverage in the AFM experiment was around 30%, the surface coverage in the ThT experiment is likely to be higher, and may approach 100%, a figure which would explain the fact that there was no apparent overall trend between $m(0)$ and the loss of final fibril yield in the ThT experiments.

While the fast process is most likely to correspond to film deposition, the cause of the slow process is less clear; however, its shape and concentration-dependence provide clues about the underlying mechanism. As shown by the linear fitting in Fig. 4.12(b), the rate of fluorescence gain is approximately constant from 1500-15000 s, implying that the slow process occurs in a single rate-determining step, rather than a sequence of steps occurring at a non-steady rate, which would result in polynomial kinetics. The fitted parameters from the linear regression are $\Delta I(t = 1500\ \mathrm{s})$, which is the fluorescence intensity at 1500 s, and $\partial \Delta I(t)/\partial t$, which is the rate of increase of the ThT fluorescence; both are summarised in Table 4.1. The $\Delta I(t = 1500\ \mathrm{s})$ values, which are approximately equal to the amplitude of the fast process, are nonlinearly correlated with the initial monomer concentration; for example, the $\Delta I(t = 1500\ \mathrm{s})$ value of the well containing 0.5 μM Aβ(1-42) is approximately 40% that of the well containing 5 μM Aβ(1-42). This does not imply that there is a particularly nonlinear relationship between the initial monomer concentration and the extent of the

Parameter	Initial monomer concentration					
	0.5 μM	1 μM	2 μM	3 μM	4 μM	5 μM
$\Delta I(t = 1500\,\mathrm{s})$, AU	(1910)	2460	2620	3220	3900	4440
$\partial \Delta I(t)/\partial t$, AU.s^{-1}	—	0.173	0.447	0.494	0.514	0.453

Table 4.1: Fitted parameters from linear fitting of the first phase of ThT fluorescence intensity gain in polystyrene plates. The $\Delta I(t = 1500\,\mathrm{s})$ for $m(0) = 0.5$ μM is obtained as an average of the raw data at that time point, rather than linear fitting, but is included for reference.

film, as ThT is usually proposed to bind to the surface of aggregates [93, 94], meaning that an increase in film thickness may have only a weak effect on the ThT signal. The $\partial \Delta I(t)/\partial t$ values, which report on the rate of the slow process, also depend nonlinearly on the initial monomer concentration; while an increase in fluorescence is not observed for 0.5 μM peptide, and the rate is reduced at 1 μM, approximately the same rate is observed at 2, 3, 4, and 5 μM. The exact mechanism of the slow process is not clear from these data; however, the fact that the slow process is not observed in PEG-treated plates indicates that it is film-dependent, and the fact that it has a concentration-independent rate at $m(0) \gtrapprox 2$ μM indicates that the process occurs at the film surface, as existing theories of film deposition predict that the kinetics of processes occurring at the surface of multilayer films are likely to become independent of film thickness past a certain point [384]. Therefore, the slow process involves a single rate-determining step and probably occurs at the surface of the films.

A further clue was provided by examination of ThT data obtained with an initial peptide concentration of 11 μM, at a temperature of 25°C (Fig. 4.13). These are the conditions under which the AFM experiments were conducted, and the original aims of this experiment were (i) to test whether biphasic ThT kinetics were also observed under those conditions, and (ii) to ascertain whether film deposition had a more pronounced lag phase, as observed in the AFM experiments. Although the experiment confirmed that the ThT kinetics remained biphasic under the conditions used for the AFM experiment, film deposition still occurred without an observable lag phase, indicating that differences in the surface structure of the polystyrene were the primary cause of rapid film deposition. However, the lower temperature resulted in a much better separation between the first and second phases of ThT fluorescence intensity change, exposing more of the first phase. As shown in Fig. 4.13(b), the slow process of the first phase fits well to an exponential curve of the form

$$\Delta I(t) = \Delta I(0) + [\Delta I(\infty) - \Delta I(0)][1 - \exp(-kt)], \tag{4.16}$$

where $\Delta I(0)$ and $\Delta I(\infty)$ are the fluorescence intensities at $t = 0$ and $t = \infty$, and k is a first-order rate constant. For the data shown in Fig. 4.13, the fitted parameters are $\Delta I(0) = 4500$ AU, $\Delta I(\infty) = 11600$ AU, and

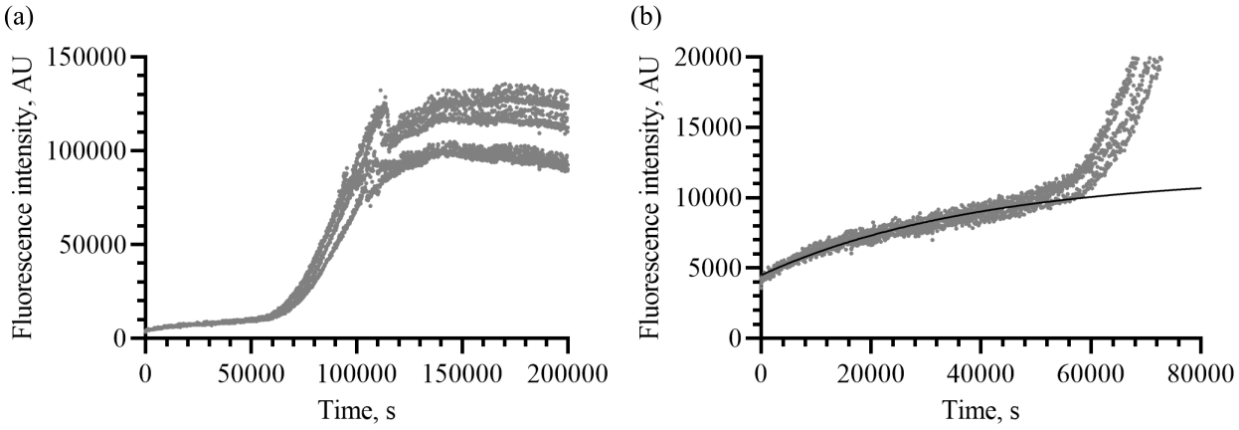

Figure 4.13: Self-assembly kinetics of 11 μM Aβ(1-42) in untreated polystyrene plates at 25°C. (a) Full view of the ThT curves. (b) A close-up view of the first phase of fluorescence increase, nonlinearly fitted with an exponential approach over the range of times from 0-50000 s, as described in the main text.

$k = 2.51 \times 10^{-5}$ s^{-1}, corresponding to a half-time of 27600 s. Eq. (4.16) is the solution for a first-order irreversible process, agreeing with the previous assessment that the slow process has a single rate-determining step, and indicating this process involves a limited supply of precursors undergoing a structural conversion at a rate that is not limited by intermolecular collisions; this could mean that collisions are not required for the slow process, or it could mean that they occur in a condensed environment where collisions are rapid.

Following this observation, the data shown in Fig. 4.12 were re-fitted with Eq. (4.16); these fits are shown in Fig. 4.14, and the values of the fitted parameters are provided in Table 4.2. For initial Aβ(1-42) concentrations in the 2-5 μM range, a good fit was obtained by globally fitting the fluorescence intensities from 1500-20000 s with a shared rate constant $k = 3.85 \times 10^{-5}$ s^{-1}, corresponding to a half-time of 18000 s, and different $\Delta I(0)$ and $\Delta I(\infty)$ values. This approach did not provide a satisfactory fit for the 1 μM data, in agreement with previous analyses that had suggested that the rate of the process responsible for the first phase was reduced at Aβ(1-42) concentrations below 2 μM. Therefore, the 1 μM data were fitted separately with an unconstrained k value, over times ranging from 1500-12000 s. Because the curve is approximately linear in this range, a large number of combinations of k and $\Delta I(\infty)$ were able to fit the data similarly well; therefore, the fit was constrained by setting $\Delta I(\infty) = 17100$ AU, a value that was obtained by linear extrapolation of the $\Delta I(\infty)$ fitted for curves in the 2-5 μM range. Although the fitted values for the 1 μM dataset are unlikely to be numerically correct, they prove the principle that an exponential fit is still appropriate for those data.

The amplitude of the slow process, which is given by $\Delta I(\infty) - \Delta I(0)$, was approximately the same across the 2-5 μM concentration range (Table 4.2), indicating that a similar quantity of material was involved across this range. This is consistent with a process occurring in a limited environment such as the film surface, rather than the film interior or the bulk solvent, where the soluble monomer can be replenished

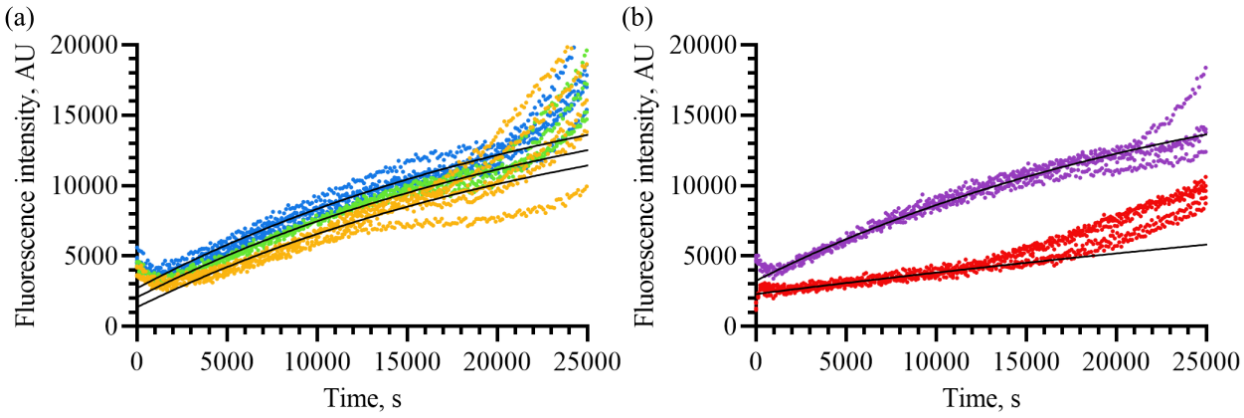

Figure 4.14: Analysis of the first phase of ThT fluorescence gain in untreated polystyrene plates (part 2). Curves have been split across two panels to make presentation clearer; both show a close-up view of the ThT data originally presented in Fig. 4.1-4.2, focusing on the first phase. The colour scheme corresponds to the initial monomer concentration: red, 1 μM; amber, 2 μM; green, 3 μM; blue, 4 μM; indigo, 5 μM. The data from wells containing 1-5 μM Aβ(1-42) have been nonlinearly fitted with an exponential approach, as described in the main text.

Parameter	**Initial monomer concentration**					
	0.5 μM	1 μM	2 μM	3 μM	4 μM	5 μM
$\Delta I(0)$, AU	—	(2310)	1370	2070	2720	3250
$\Delta I(t = 1500\,\mathrm{s})$, AU	(1910)	(2550)	2280	3020	3710	4190
$\Delta I(\infty)$, AU	—	(= 17100)	17640	19000	20300	20100
$\Delta I(\infty) - \Delta I(0)$, AU	—	(14800)	16300	16900	17600	16800
k, 10^{-5} s^{-1}	—	(1.08)	3.85	3.85	3.85	3.85

Table 4.2: Fitted parameters from exponential fitting of the first phase of ThT fluorescence intensity gain in polystyrene plates, using Eq. (4.16). Data obtained with 2-5 μM Aβ(1-42) were globally fitted, with a shared rate constant k and different $\Delta I(0)$ and $\Delta I(\infty)$ values. A satisfactory fit could not be obtained for 1 μM Aβ(1-42) by global fitting, and previous analyses had suggested that the mechanism responsible for the first phase differed at lower concentrations, so these data were fitted separately as described in the text. The $\Delta I(t = 1500\,\mathrm{s})$ and $\Delta I(\infty) - \Delta I(0)$ values were calculated from the other fitted parameters; the $\Delta I(t = 1500\,\mathrm{s})$ value for 0.5 μM Aβ(1-42) was simply obtained as an average of the raw data at that time point, rather than nonlinear fitting, and has been included for reference.

by disassembly of the films. Therefore, the kinetics of the slow process point to a first-order or pseudo-first-order structural change occurring at the film surface or in the uppermost layers of the film, resulting in enhanced ThT fluorescence. This change must be film-dependent as it is not observed in PEG-treated plates, and its precursor is unlikely to be the soluble monomer, as replenishment of the soluble monomer due to dissociation of the film would cause the amplitude of the slow process to scale approximately linearly with the initial monomer concentration. While processes involving the entirety of the film could produce the correct amplitude if ThT only reported on the process when it occurred in the upper layers of the film, the fact that the rate differs significantly between initial peptide concentrations of 1 μM and 2 μM implies that the upper layer or upper few layers of the film are more likely to be involved than the lower layers, as this is where the structure of the film is expected to change the most between 1 μM and 2 μM.

The exact nature of the transition responsible for the slow process is unclear, and it could be as simple as slow penetration of ThT into the uppermost layers of the film; however, the large amplitude of this phase, equivalent to the ThT fluorescence of $\sim$ 1 μM of amyloid fibrils, indicates that it may reflect the formation of more ordered metastable species that are capable of binding ThT and inducing a change in fluorescence with a similar intensity to amyloid fibrils. Thus, the slow process could represent the formation of an on-pathway species, although it is not possible to assess this hypothesis based on the available data. The slow process is unlikely to reflect the formation of the 'sub-films' previously observed in the AFM images (Fig. 4.6-4.10), as they appear to form via a nucleated process that is not consistent with the kinetics of the slow process. There is no evidence for the formation of 'sub-films' from the kinetic data, so whether they occur in polystyrene plates or were specific to the films formed in the AFM experiments remains uncertain.

4.3.5 Heterogeneous nucleation of Aβ(1-42) in films deposited on polystyrene surfaces

The observation that fibrillisation is significantly faster in untreated polystyrene plates than in quartz plates indicates that the interactions between Aβ(1-42) molecules and the surface either directly or indirectly catalyse the formation of amyloid fibrils. The counter-hypothesis, that quartz surfaces somehow inhibit fibrillisation, can be discounted on the basis of the fact that quartz is a much more weakly interacting surface than polystyrene, and is very unlikely to interact with Aβ(1-42) monomer or aggregates with sufficient frequency to inhibit fibrillisation. The weakness of interactions between proteins and quartz surfaces is the reason why quartz is commonly used in experiments where there is a need to eliminate surface effects, and the lack of interactions between Aβ(1-42) and quartz is confirmed by the AFM data subsequently presented in Section 4.3.7. Heterogeneous nucleation is the most commonly reported mechanism by which surfaces can accelerate amyloid fibril formation, and the increase in the consistency of the ThT curves from quartz to polystyrene plates (Fig. 4.1-4.2) indicates that heterogeneous nucleation is reponsible for the enhanced fibrillisation kinetics observed in polystyrene plates, as a greater nucleation rate results in a larger

concentration of individual amyloid fibrils, with a more deterministic total elongation rate.

To test this, the ThT curves were globally fitted with a variety of kinetic models with different homogeneous and heterogenous primary nucleation mechanisms. While models that accounted for all processes would have been preferable, it was not possible to treat the product of the slow process of the first phase as a distinct species in these models, as the size, concentration, precursor, specific ThT response, and disassembly mechanism of this species were all unknown, so that its inclusion resulted in far too many unconstrained variables to perform data fitting. Therefore, in order to carry out fitting, simplifying assumptions had to be made that reduced the complexity of the model and allowed fitting of the fibril mass concentration, for which there were a sufficient number of parameters that had already been constrained. Specifically, it was assumed that the species formed by the slow process was metastable and off-pathway, and that its disassembly rate was approximately proportional to the rate of fibrillar mass gain. Similar models where this species was on-pathway were tested, but did not improve upon the best fits obtained with the off-pathway models. The specific assumptions regarding the disassembly of this species entailed that the excess ThT fluorescence above that predicted by Eq. 4.16 should be proportional to the fibrillar mass concentration, allowing normalised estimates of the fibrillar mass concentration to be obtained by subtracting the fitted exponential kinetics of the first phase and then normalising the data, as shown in Fig. 4.15(a).

In reality, the disassembly kinetics of the species formed by the slow process are likely to be more complex; however, since there are no data available to provide a description of them, and there are too many possibilities and unconstrained parameters to examine the disassembly of this species by data fitting, a simplifying assumption is unavoidable. Although the subtraction procedure is likely to introduce some numerical inaccuracies, the comparatively low amplitude of the slow process at sufficiently high $m(0)$ (3-5 μM) means that these inaccuracies are likely to be too small to explain most instances where candidate models do not fit the data, especially given the large discrepancy between the predictions of most models and the experimental data; thus, fitting to the subtracted data still provides a means to eliminate ineffective models. Therefore, while subtraction of the slow process is not ideal, it is necessary in order to obtain a fit, and despite inevitable errors due to an incomplete understanding of the species formed by this process, it is still possible to draw definite conclusions from fitting to the second phase alone.

The models examined in this section are based on modifications of the Knowles model [1–3], which has been shown in both the literature [54, 519] and Chapter 3 to accurately describe Aβ(1-42) self-assembly in PEG-treated plates. In the Knowles model, fibrils are first formed by primary nucleation, whose rate is given by Eq. (1.2), and then grow by elongation, which is described by Eq. (1.13); the rate of dissociation of Aβ(1-42) monomers from fibril ends has previously been shown to be negligible at the concentrations used in this experiment [54], and so this process was not included. In addition to primary nucleation, fibrils are also able to form by secondary nucleation, in which the surface of pre-existing fibrils catalyses

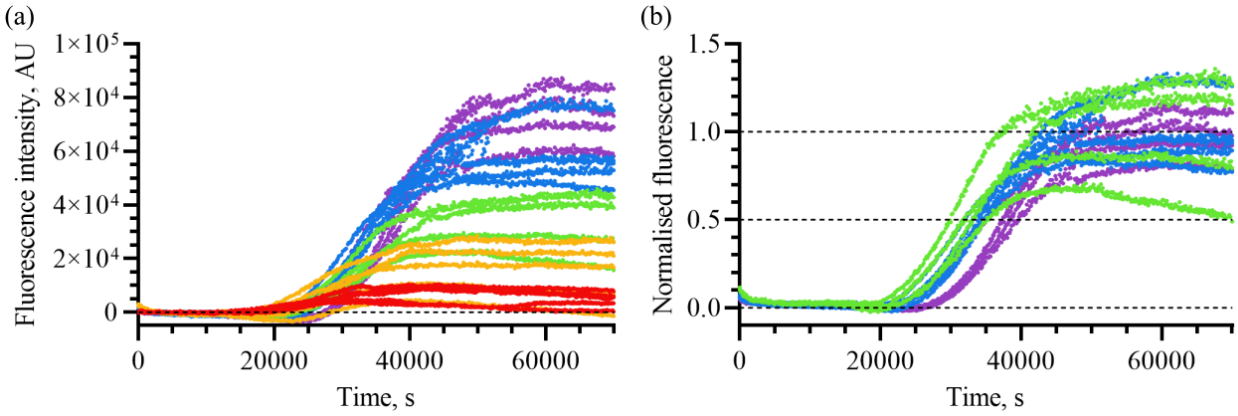

Figure 4.15: ThT fluorescence intensities of the second phase observed in untreated polystyrene plates. (a) The approximate ThT fluorescence intensities of the second phase, obtained by subtracting the fitted intensities of the first phase from the raw data as described in the main text. (b) The normalised fluorescence intensities of the second phase, obtained by normalisation of the data presented in panel (a). Only the data from wells containing 3 μM, 4 μM, or 5 μM Aβ(1-42) are shown, as the normalisation was carried out for the purpose of data fitting, and the stochasticity, differing concentration-dependence, and probably distinct film structure of the lower concentrations made them unsuitable for fitting with the same model. The colour scheme is shared across panels, and represents the initial free monomer concentration: red, 1 μM; amber, 2 μM; green, 3 μM; blue, 4 μM; indigo, 5 μM.

heterogeneous nucleation of new fibrils as described by Eq. (1.32), completing a positive feedback loop. This basic model is shown in Fig. 4.16(a). Since there is no evidence from the literature or the AFM data analysed in this chapter to support the existence of interactions between fibrils and polystyrene surfaces, it was assumed that the rate of the fibril-dependent processes was not affected by polystyrene. Therefore, the elongation rate parameter was set to the literature value of $k_e^+ = 3 \times 10^6$ M^{-1}.s^{-1} [54], with the assumption that elongation occurs equally at both ends of the fibril, and the secondary nucleation rate parameter was set to $k_s = 1.84 \times 10^3$ M^{-2}.s^{-1}, which is based on the value $k_s k_e^+ = 5.52 \times 10^9$ M^{-3}.s^{-2} determined by data fitting in Chapter 3 (see Table 3.1). The order of homogeneous primary nucleation and secondary nucleation was set to $n_c = n_s = 2$, a value that is supported by the literature [54,519] and the data fitting in Chapter 3, and the contribution of primary and secondary nucleation to fibril mass was assumed to be negligible compared to that of elongation, a common approximation [2, 3] that is supported by the large size difference between amyloid fibrils and most on-pathway oligomers (Section 1.4). With the elongation and secondary nucleation processes kept the same, modifications to the model to account for the effects of surface interactions involved changes to the primary nucleation mechanism, and the introduction of monolayer or multilayer films. In total, five models were tested; schematics of these models are presented in Fig. 4.16, the rate laws, boundary conditions, and model parameters are summarised in Table 4.3, the fitted curves are shown in Fig. 4.17, and the values of the fitted and constrained parameters are presented in Table 4.4.

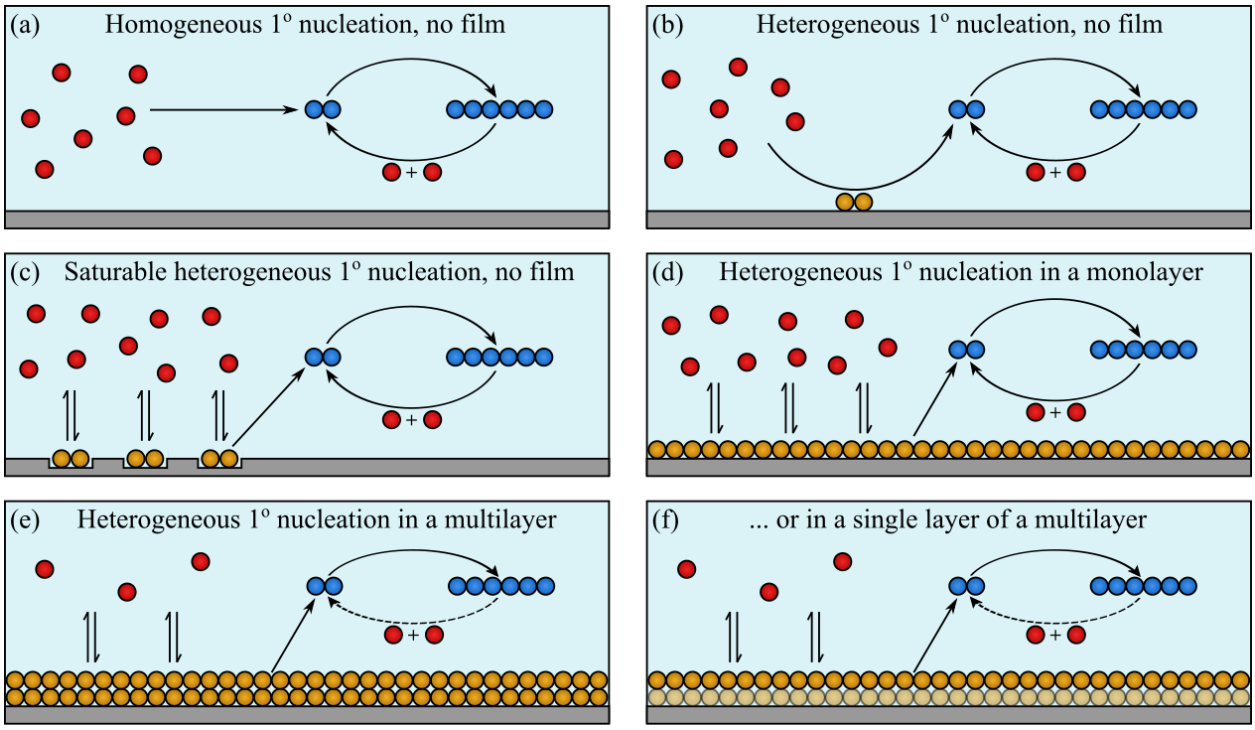

Figure 4.16: Schematics of the tested models of Aβ(1-42) fibrillisation in polystyrene plates. Panels represent different mechanistic models; (a) and (b) both result in the same macroscopic kinetics and so correspond to the same model at the mathematical level. The five models are: (a-b), model 1, concentration-dependent homogeneous or heterogeneous primary nucleation; (c), model 2, concentration-independent heterogeneous primary nucleation, no film deposition; (d), model 3, heterogeneous primary nucleation in a monolayer film; (e), model 4, heterogeneous primary nucleation in a multilayer film; (f), model 5, heterogeneous primary nucleation in a single layer of a multilayer film. The associated rate equations, formulae for determining the concentrations of free and deposited monomer, boundary conditions, and model parameters are summarised in Table 4.3, the fitted curves are shown in Fig. 4.17, and the values of the fitted and constrained parameters are presented in Table 4.4. Circles represent Aβ(1-42) monomers, with the colour scheme representing the conformational state: red, soluble; gold, surface-associated; blue, fibrillar. The gray surface represents the polystyrene. The arrows represent the microscopic molecular processes, which are: adsorption to form films or other surface-associated intermediates; primary nucleation to form a minimally sized elongating species (shown here as a fibrillar dimer); elongation, which increases the size of fibrils; and secondary nucleation, which produces new fibrils in a fibril-and-monomer-dependent manner. Elongation and secondary nucleation form a positive feedback loop, which is represented by the pair of arrows forming a cycle in the right of each panel. All models have the same microscopic elongation and secondary nucleation mechanisms, but differ in their mechanisms of surface-association and primary nucleation. In panels (e) and (f), the arrow for secondary nucleation is represented as a dashed line to reflect a reduction in rate, due to the depletion of soluble monomer caused by multilayer formation.

Quantity		Model number				
		1	**2**	**3**	**4**	**5**
Primary nucleation rate	$\Phi_n(t) =$	$k_n m(t)^{n_c}$	k_n	$k_n L_1(t)$	$k_n L_{\text{tot}}(t)$	$k_n L_1(t)$
Secondary nucleation rate	$\Phi_s(t) =$	$k_s m(t)^{n_s} M(t)$				
Specific elongation rate	$\nu_e^+(t) =$	$2k_e^+ m(t)$				
Rate of fibril formation	$\partial_t P(t) =$	$\Phi_n(t) + \Phi_s(t)$				
Rate of fibril mass gain	$\partial_t M(t) \approx$	$P(t)\nu_e^+(t)$				
Forming first layer of film	$\partial_t L_1(t) \approx$	0		$\delta(t)\min(m(t),\, L_{1,\max})$		
Rate of monomer use	$\partial_t[m(t) + L_+(t)] =$	$-\partial_t M(t) - \partial_t L_1(t)$				
Free monomer concentration	$m(t) =$	$m(t)$			$\min(m(t) + L_+(t),\, c^*)$	
Dissociable monomer in film	$L_+(t) =$	0			$[m(t) + L_+(t)] - m(t)$	
Non-dissociable monomer in film	$L_1(t) =$	0		$H(t)\min(m(0),\, L_{1,\max})$		
Total monomer in film	$L_{\text{tot}}(t) =$	$L_1(t) + L_+(t)$				
Boundary conditions	—	$m(0) \neq 0, \quad P(0) = M(0) = L_1(0) = L_+(0) = 0$				
Model parameters	—	k_n, k_s, k_e^+, n_c, n_s	k_n, k_s, k_e^+, n_s	k_n, k_s, k_e^+, n_s, $L_{1,\max}$	k_n, k_s, k_e^+, n_s, $L_{1,\max}$, c^*	

Table 4.3: Summary of the tested models of Aβ(1-42) fibrillisation. Five models were tested: model 1, Fig. 4.16(a-b) and Fig. 4.17(a-c), concentration-dependent homogeneous or heterogeneous primary nucleation; model 2, Fig. 4.16(c) and Fig. 4.17(d-f), concentration-independent heterogeneous primary nucleation, no film deposition; model 3, Fig. 4.16(d) and Fig. 4.17(g-i), heterogeneous primary nucleation in a monolayer film; model 4, Fig. 4.16(e) and Fig. 4.17(j-l), heterogeneous primary nucleation in a multilayer film; and model 5, Fig. 4.16(f) and Fig. 4.17(m-o), heterogeneous primary nucleation in a single layer of a multilayer film. This table presents the rate laws, formulae for determining the concentrations of free and deposited monomer, boundary conditions, and parameters of these models. Model development is described in greater detail in the text, and the fitted and constrained values of the above parameters are presented in Table 4.4.

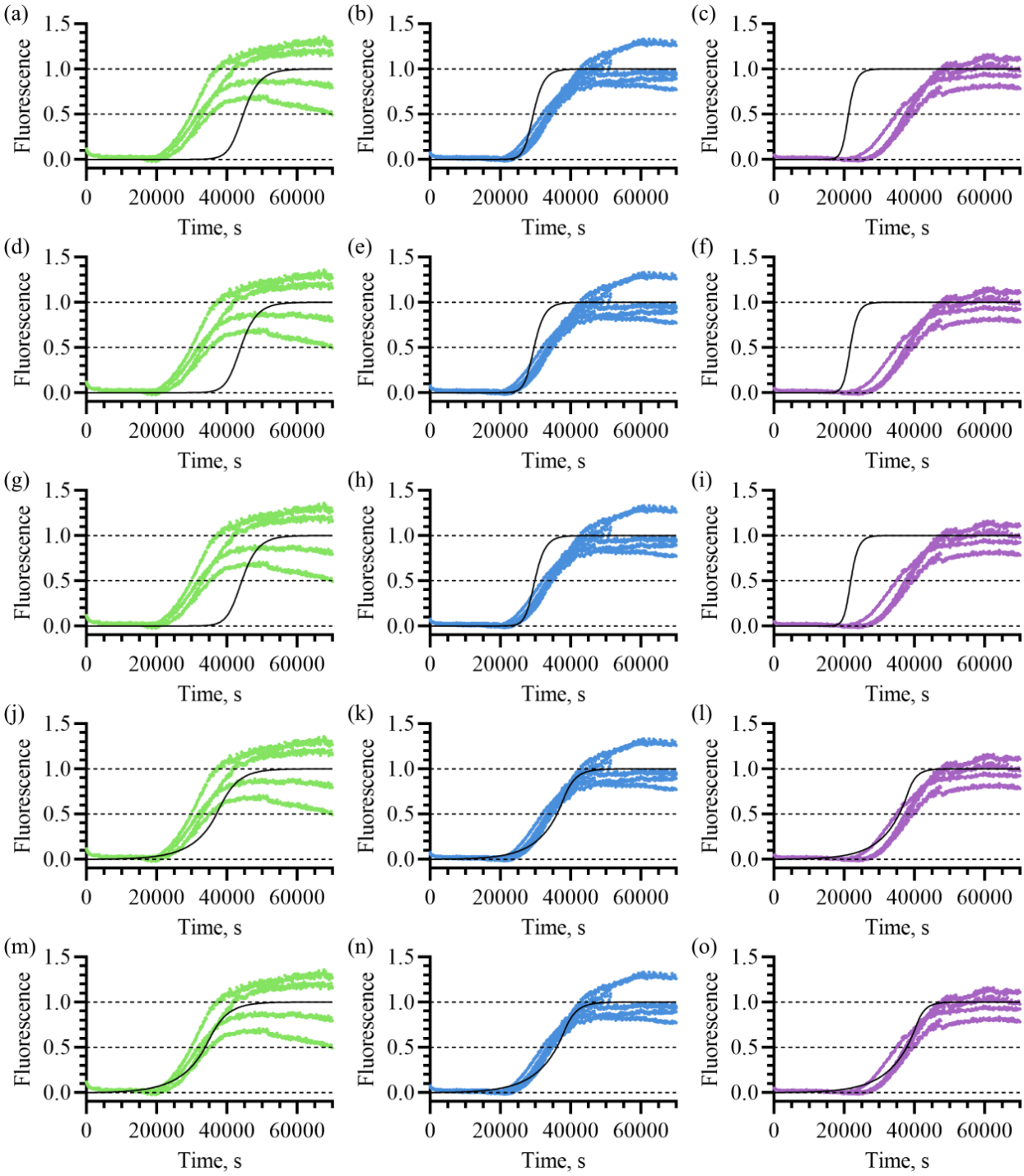

Figure 4.17: Global fitting of the second phase observed in untreated polystyrene plates. ThT curves are normalised approximate intensities of the second phase of ThT fluorescence gain, as originally presented in Fig. 4.15(b). Models were globally fitted across all initial monomer concentrations, but different concentrations are shown in different columns for clarity. Five fits are shown, organised by row: (a-c), model 1, concentration-dependent homogeneous or heterogeneous primary nucleation, no film deposition; (d-f), model 2, concentration-independent heterogeneous primary nucleation, no film deposition; (g-i), model 3, heterogeneous primary nucleation in a monolayer film; (j-l), model 4, heterogeneous primary nucleation in a multilayer film; (m-o), model 5, heterogeneous primary nucleation in a single layer of a multilayer film. The colour scheme represents the initial monomer concentration: green, 3 μM; blue, 4 μM; indigo, 5 μM.

Parameter	Model number				
	1	**2**	**3**	**4**	**5**
k_n	3.87×10^{-13} $M^{-1}.s^{-1}$	5.20×10^{-24} $M.s^{-1}$	1.25×10^{-17} s^{-1}	1.96×10^{-11} s^{-1}	1.84×10^{-10} s^{-1}
c^*	—			1.25 μM	1.22 μM
k_s	$= 1.84 \times 10^3$ $M^{-2}.s^{-1}$				
k_e^+	$= 3 \times 10^6$ $M^{-1}.s^{-1}$				
n_c	$= 2$	—			
n_s	$= 2$				
$L_{1,\max}$	—		$= 0.35$ μM		
AICc	-31154	-31619	-31617	-40115	-40948
R^2	0.477	0.496	0.496	0.866	0.874

Table 4.4: Fitted parameters, constrained parameters, and diagnostic statistics from global fitting of the second phase of ThT fluorescence intensity gain in polystyrene plates. Five models were tested: model 1, Fig. 4.16(a-b) and Fig. 4.17(a-c), concentration-dependent homogeneous or heterogeneous primary nucleation; model 2, Fig. 4.16(c) and Fig. 4.17(d-f), concentration-independent heterogeneous primary nucleation, no film deposition; model 3, Fig. 4.16(d) and Fig. 4.17(g-i), heterogeneous primary nucleation in a monolayer film; model 4, Fig. 4.16(e) and Fig. 4.17(j-l), heterogeneous primary nucleation in a multilayer film; and model 5, Fig. 4.16(f) and Fig. 4.17(m-o), heterogeneous primary nucleation in a single layer of a multilayer film. Parameter values and diagnostic statistics are presented in this table. The fitted parameters were k_n and c^*, the constrained parameters were k_s, k_e^+, n_c, n_s, and $L_{1,\max}$, and the diagnostic statistics were the AICc and R^2 values. Note that AICc values are only meaningful in a comparative sense, with lower AICc indicating a higher probability, and the fact that the AICc values are negative is simply a reflection of the fact that the fitted data had been normalised (ie. RSS $< N$). From the above AICc values, model 5 is favoured over models 1-4 with $> 99.99\%$ probability.

Model 1 was the unmodified Knowles model, in which the concentration of surface-associated species is negligible and primary nucleation occurs as a simple multimerisation of monomers to form a minimally sized fibril, the rate of which is given by Eq. (1.2). Schematics of two possible versions of this model are shown in Fig. 4.16(a-b), a summary of the mathematics is given in Table 4.3, the fitted curves are shown in Fig. 4.17(a-c), and the parameter values are presented in Table 4.4. Since k_s, n_c, and n_s were constrained as described in the previous paragraph, the only free parameter was the primary nucleation rate constant k_n, which was shared across all fitted Aβ(1-42) concentrations. Besides the original formulation of the model, in which primary nucleation occurs in the absence of a catalytic surface (Fig. 4.16(a)), the Knowles model is also valid in the case where the multimerisation occurs on a catalytic surface (Fig. 4.16(b)), so long as binding between the nucleating monomers and the surface is sufficiently weak that saturation does not occur. Thus, globally fitting the Knowles model does not directly test whether nucleation is heterogeneous, but does test the other assumptions of the model, such as whether the same microscopic processes occur, and whether the concentration of non-fibrillar aggregates is negligible. As shown in Fig. 4.17(a-c), the unmodified Knowles model is unable to globally fit the kinetics of the second phase. The main reason for this is that the model predicts the wrong concentration-dependence, given by the scaling exponent $\gamma_{50} = -\partial \log \tau_{50} / \partial \log m(0)$. While the predicted exponent is in the $1 < \gamma_{50} < 1.5$ range when $n_c = n_s = 2$, the value observed in polystyrene plates is $\gamma_{50} \approx -0.3$ for initial monomer concentrations in the 3 μM to 5 μM range, a very low concentration-dependence that is also slightly reversed compared to the trend predicted by most models. Therefore, when the model is globally fitted across all the data, the fitted curves are too slow when $m(0) = 3$ μM, and too fast when $m(0) = 5$ μM. In addition, the maximum fibrillisation rate of the fitted curves is too high; since secondary nucleation is the dominant mechanism by which new fibrils are formed by this point, this indicates that the number of fibrils formed by secondary nucleation is too great. The cause of this issue will be discussed later.

Models 2 and 3 attempted to improve fit quality by incorporating a concentration-independent heterogeneous primary nucleation mechanism. As discussed in the previous paragraph, model 1 fails becase it predicts too high a concentration-dependence. This indicates that the dominant nucleation process has a low concentration-dependence in the experiments; thus, one might suspect that saturation of the primary nucleation process would significantly reduce the γ_{50} value. There are two main ways that this might occur, corresponding to models 2 and 3; schematics of these models are shown in Fig. 4.16(c-d), a summary of the mathematics is given in Table 4.3, the fitted curves are shown in Fig. 4.17(d-i), and the parameter values are presented in Table 4.4. Firstly, as described by model 2, primary nucleation might occur at discrete, tightly binding sites on the plate surface such as cracks or defects, which could be saturated without significantly reducing the free monomer concentration. In the tight binding limit, this would result in a modified rate law

for primary nucleation,

$$\Phi_n(t) = k_n, \tag{4.17}$$

where k_n is now an effective zeroth-order rate parameter. The alternative possibility, which corresponds to model 3 and is better supported by the experimental data, is that Aβ(1-42) might form a monolayer film and nucleate in that environment, causing saturation accompanied by a partial loss of free monomer at the start of the experiment. Since formation of the monolayer is very rapid and seems to be effectively irreversible on the experimental timescale, the rate of monolayer formation can be approximated by a delta distribution,

$$\frac{dL_1(t)}{dt} = \begin{cases} \delta(t)m(0), & \text{if } m(0) < L_{1,\max}, \\ \delta(t)L_{1,\max}, & \text{if } m(0) \geq L_{1,\max}, \end{cases} \tag{4.18}$$

where $\delta(t)$ is a Dirac delta and $L_{1,\max}$ is the maximum occupancy of a monolayer, previously estimated as ~ 0.35 μM based on analysis of apparent fibril yields. Thus,

$$L_1(t) = \begin{cases} H(t)m(0), & \text{if } m(0) < L_{1,\max}, \\ H(t)L_{1,\max}, & \text{if } m(0) \geq L_{1,\max}, \end{cases} \tag{4.19}$$

where $H(t)$ is a Heaviside step function, such that $H(t) = 1$ when $t \geq 0$ and $H(t) = 0$ when $t < 0$. An additional mass conservation term must also be incorporated into $dm(t)/dt$,

$$\frac{dm(t)}{dt} = -\frac{dM(t)}{dt} - \frac{dL_1(t)}{dt}. \tag{4.20}$$

so monolayer formation results in the loss of an equal amount of monomer. Primary nucleation occurring in the monolayer has the rate law

$$\Phi_n(t) = k_n L_1(t), \tag{4.21}$$

where k_n is an effective first-order rate parameter. Thus, Eq. (4.17) and Eq. (4.18-4.21) describe two separate modifications to the Knowles model that result in a concentration-independent nucleation rate for sufficiently high $m(0)$. Although these models are both physically plausible, neither model is able to fit the data, as shown in Fig. 4.17(d-i), and the concentration-dependence of the fitted curves remains high. Closer examination shows that the predicted γ_{50} value is still approximately 1.5, indicating that the fitted curves represent scenarios where secondary nucleation predominates. The predominance of secondary nucleation is caused by the fact that the models presented in Fig. 4.16(a-d) have the same nucleation rate parameter as PEG plates, but a much lower primary nucleation rate, and it is this predominance of secondary nucleation that explains why saturating the primary process does not cause a noticeable reduction in the concentration-

dependence. The conclusion that the fitting of these models fails due to a high secondary nucleation rate is also supported by the curve shape; as discussed previously, the high maximum fibrillisation rate indicates that too many secondary nuclei are being formed.

The low rate of secondary nucleation in the experimental data implies a reduction in either k_s or $m(t \approx \tau_{50})$ due to the effects of the surface. In addition, the maximum fibrillisation rate has a low concentration-dependence (Fig. 4.15(b)), which indicates that the secondary nucleation rate around this time scales weakly with $m(0)$. While surface-induced changes in fibril polymorphism could result in a reduction in k_s, they would not explain the weak concentration scaling of the secondary nucleation rate; in addition, it is worth noting that the NS-EM data later presented in Fig. 4.20-4.21 show no obvious difference in polymorphism compared to the equivalent data from PEG plates in Fig. 3.12. An alternative hypothesis, which would explain both the rate and concentration-dependence of the secondary nucleation rate, is that $m(t \approx \tau_{50})$ is restricted by the formation of aggregated species above a critical concentration c^*, and scales weakly with $m(0)$ as a result. The prime candidate for such an aggregated state is a multilayer, as multilayer formation has already been demonstrated to occur under the same conditions by AFM, and the 3D structure and large number of monomer-monomer interactions within a multilayer would make its formation highly cooperative, and thus likely to occur above a critical concentration.

Thus, the fits in Fig. 4.17(d-i) suggest that multilayer formation must be incorporated into the model in order to fit the experimental data. This is the basis of models 4 and 5; schematics of these models are shown in Fig. 4.16(e-f), a summary of the mathematics is given in Table 4.3, the fitted curves are shown in Fig. 4.17(j-o), and the parameter values are presented in Table 4.4. While models 4 and 5 have different nucleation mechanisms, they have the same mechanism of multilayer formation. If $L_1(t)$ represents the concentration of monomer incorporated into the first layer of the film, as described by Eq. (4.18), then let $L_+(t)$ represent the concentration of monomer incorporated into additional layers of the film. Thus, the total concentration $L_{\text{tot}}(t)$ of deposited monomer is expressed as

$$L_{\text{tot}}(t) = L_1(t) + L_+(t). \tag{4.22}$$

As with the monolayer in model 3, the reduced fluorescence yield in untreated polystyrene plates means that the first layer must be tightly bound; however, the AFM data presented in Section 4.3.3 indicate that additional layers of the film are more weakly bound, meaning they can dissociate to maintain a supply of free monomer for secondary nucleation and elongation. Analysis of the fast process of the first phase previously suggested that multilayer formation occurs rapidly once a monolayer is established (typically $\ll 1000$ s); thus, the simplifying assumption can be made that multilayer formation is a dynamic process, with additional layers of film rapidly assembling or disassembling to maintain $m(t) = c^*$, until there is no

remaining dissociable monomer. This means that depletion of the available monomer due to fibril formation results in changes in $m(t)+L_+(t)$ as a collective quantity, rather than $m(t)$ alone. In other words,

$$\frac{d}{dt}\left[m(t)+L_+(t)\right] = -\frac{dM(t)}{dt} - \frac{dL_1(t)}{dt}. \tag{4.23}$$

At any given instant, the quantities of free monomer $m(t)$ and dissociable deposited monomer $L_+(t)$ can then be calculated from $m(t)+L_+(t)$ according to the relations

$$m(t) = \begin{cases} m(t)+L_+(t), & \text{if } m(t)+L_+(t) < c^*, \\ c^*, & \text{if } m(t)+L_+(t) \geq c^*, \end{cases} \tag{4.24}$$

and

$$L_+(t) = \begin{cases} 0, & \text{if } m(t)+L_+(t) < c^*, \\ m(t)+L_+(t)-c^*, & \text{if } m(t)+L_+(t) \geq c^*. \end{cases} \tag{4.25}$$

Thus, as the available monomer is consumed by fibril formation, there will first be a decrease in $L_+(t)$ reflecting dynamic disassembly of the multilayer to maintain $m(t) = c^*$, and $m(t)$ will only start to decrease once $L_+(t)$ is fully depleted. The difference between models 4 and 5 is the manner in which primary nucleation occurs. In model 4, which is depicted in Fig. 4.16(e), primary nucleation occurs at an approximately even rate throughout the film, so that the total nucleation rate is simply proportional to the concentration of monomer incorporated into the film. Thus, the rate law will be

$$\Phi_n(t) = k_n L_{\text{tot}}(t). \tag{4.26}$$

In model 5, which is perhaps more likely *a priori*, primary nucleation occurs in a single layer of the film with favourable physicochemical properties, as depicted in Fig. 4.16(f), so that the nucleation rate will be proportional to the coverage of that layer. It is most likely that primary nucleation would be biased towards either the lowest or the uppermost layer of the film; in particular, the latter would help to explain the reversal of concentration-dependence between 1 μM and 2 μM Aβ(1-42), as the structure of the upper layers of the film is likely to change in this concentration range. If most of the film has more than one layer, the quantity of peptide in the layer in contact with the bulk solvent is likely to be approximately proportional to the quantity in contact with the polystyrene surface, since the AFM data show that the films are relatively flat, and both layers will cover approximately the same projected area. Thus, one can use the same rate law for both cases,

$$\Phi_n(t) \approx k_n L_1(t), \tag{4.27}$$

with the caveat that the dependence on $L_1(t)$ merely reflects a dependence on the film area, rather than necessarily implying that the lowest layer is the precursor; thus, in this particular usage, k_n is an effective rate constant. In the special case where nucleation occurs in the layer in contact with the solvent *unless* that layer is part of the lowest layer, which may be too stable to produce fibril nuclei, the rate law is slightly more complex,

$$\Phi_n(t) \approx \begin{cases} k_n L_+(t), & \text{if } L_+(t) < L_1(t) \\ k_n L_1(t), & \text{if } L_+(t) \geq L_1(t). \end{cases} \tag{4.28}$$

In practice, however, $L_+(t) \gg L_1(t)$ for almost all of the growth phase at the concentrations used in fitting, so both models gave almost identical results when tested, even towards the end of the growth phase; thus, only fits with the former are shown in this section.

As shown in Fig. 4.17(j-l), model 4, in which nucleation occurs at an equal rate in all layers of the film, offers a significant improvement on the fits obtained by models lacking a multilayer. However, there are still some issues with the fit; most importantly, although the γ_{50} value is low, it is still too high. Unlike previous instances, where the issue was caused by secondary pathways, in this case the issue with the concentration-dependence is caused by primary nucleation, which plays a greater role due to the reduced rate of secondary nucleation. Since the excess monomer above a concentration of $L_{1,\max} + c^*$ is converted to additional layers of the film, the extent of the film changes between 3 μM and 5 μM. Thus, if the primary nucleation rate is proportional to the quantity of monomer incorporated into the film, it will also change across this range, which is the origin of the excess γ_{50} of the predicted curves.

Thus, the slightly reversed concentration-dependence of the experimental data implies that not only does the excess monomer assemble to form multilayer films, but primary nucleation is only able to occur in specific layers within these films, so that its rate does not depend on the quantity of deposited monomer. In agreement with this, the fits shown in Fig. 4.17(m-o), which correspond to model 5, have the correct concentration-dependence and are relatively close to the experimental curves. It is not surprising that primary nucleation should predominantly occur in a particular layer of the film, as different layers present different molecular environments. On the one hand, fibril seeds might be more likely to form in the lower layers of the film, as these are more likely to be desolvated, have a less dielectric environment that may encourage structure formation, and have the potential for specific interactions between the surface and the monomers that could stimulate nucleation. On the other hand, if fibril nucleation requires rapid conformational sampling, this is more likely to occur in the upper layers of the film, which are likely to be more solvated and less dense; in addition, fibrils seeds formed in the upper layers may be more able to diffuse or otherwise propagate to the surface, which is likely to be required for the release and subsequent elongation of newly formed fibrils.

Thus, model 5 provides the best fit for the data and is as well-supported by the available experimental evidence as possible, given that the nucleation events themselves are still expected to be rare and unfortunately unlikely to be observed by AFM (the fitted rate parameter implies a nucleation rate per film area of 3.8×10^{-5} $\mu m^{-2}.s^{-1}$ at 37°C, and the value is likely to even lower at 25°C). The multilayer films on which the model is based have been observed under equivalent experimental conditions, and there are solid physical reasons why the deposition of additional film layers should occur above a critical concentration, and fibril nucleation should be biased to occur in a particular layer within such a film. The ability of the model to accurately reproduce the concentration-dependendence is also notable, as in general only a small subset of possible nucleated polymerisation models are able to produce inverse concentration-dependences, and this is the only such model that is supported by the experimental evidence. The fit obtained at 3 μM Aβ(1-42) (Fig. 4.17(m)) is particularly good, with only a small discrepancy close to the start of the second phase that may well be an artifact caused by subtraction of the first phase, if the mathematical behaviour of that phase was not quite exponential around the time when the second phase began.

Nonetheless, there are still some issues with the fits obtained for 4 μM and 5 μM Aβ(1-42) (Fig. 4.17(n-o)) that are worthy of attention. As with the 3 μM curves, the fits have a small discrepancy at the start of the second phase, which may be due to subtraction errors. However, these two curves also suffer from excessive $d^2M(t)/dt^2$ close to the half-time, and an overly sharp approach to their maximum fluorescence intensity. These are both caused by the fact that, in the model, the free monomer concentration does not begin to deplete until relatively late in the self-assembly time course, as it is continuously replenished by the remaining layers of the film until $m(t) + L_+(t) < c^*$. Monomer depletion limits the $d^2M(t)/dt^2$ value in the original Knowles model, causing the inflection point to occur before the half-time as in the experimental data, rather than after it as in the fitted curves. This does not necessarily indicate that the multilayer model is incorrect, as the other aspects of the kinetics strongly support a model where the availability of free monomer is limited in the early-to-mid growth phase, and primary nucleation is surface-dependent and scales weakly with $m(0)$. Instead, the issue is most likely the rather artificial treatment of the equilibrium between $m(t)$ and $L_+(t)$, and perhaps also small errors introduced by the subtraction process. According to Eq. (4.24-4.25), the free monomer concentration should be constant until $m(t) + L_+(t)$ is depleted to a level below c^*, at which point there should be no remaining layers apart from the residual monolayer, and $m(t)$ should begin to drop. Fig. 4.3-4.10 show that this is not the case; while the majority of the film disassembles relatively fast (perhaps ~ 0.005 layers.s^{-1}), small areas of multilayer persist for long periods of time, and are still observed 10000 s after the onset of disassembly. In addition, the fact that a slow process is not observed in the first phase when $m(0) = 0.5$ μM, but such a phase does occur at a reduced rate when $m(0) = 1$ μM, indicates that a partial multilayer may be able to form in the latter case, despite $m(0)$ being below the required value of $L_{1,\max} + c^* = 1.57$ μM predicted by fitted parameters. Thus, while c^* may function as

an effective parameter at high $m(t) + L_+(t)$ values, a smoother transition from film disassembly to loss of free monomer may occur close to this concentration, so that the actual value of $m(t)$ is below the predicted value when $m(t) + L_+(t) \approx c^*$. In addition, the slow disassembly of some parts of the film indicates that the kinetics of film disassembly may limit the fibrillisation rate towards the end of the growth phase.

At present, it is not possible to further improve fitting of the ThT curves until a better description of the structure, equilibrium thermodynamics, and disassembly kinetics of films formed in untreated polystyrene plates can be obtained. Such a description would also allow better fitting of the first phase, so that both phases could be fitted simultaneously without need for subtraction. Nonetheless, these issues are not likely to strongly affect the slightly reversed concentration-dependence of the second phase, which is present in both the subtracted and un-subtracted data, and is diagnostic of weak scaling between $m(0)$ and both the free monomer concentration and the nucleation rate. In addition, the comparatively low amplitude of the first phase means that possible subtraction errors alone cannot explain the low maximum rate of the second phase; thus, depletion of the soluble monomer is the most likely explanation. Therefore, despite the challenges faced due to the large number of unknowns concerning the structure, disassembly dynamics, and ThT fluorescence contributions of the multilayer films and the product of the slow process, the results of the fitting allow several definite conclusions to be obtained: (i) models without film deposition cannot explain the experimental data; (ii) secondary pathways remain important, but have a reduced rate and monomer-dependence in polystyrene plates; (iii) the weak scaling of elongation and secondary nucleation is most likely caused by multilayer formation; and (iv) primary nucleation occurs in a specific environment in the films, most likely the upper or lower layer.

4.3.6 Distinct oligomer populations in untreated polystyrene plates

While the AFM images provide information about the processes occuring at the surface of polystyrene plates, and this information is sufficient to develop a model that approximately fits the kinetic data, they do not provide information about the fibrillar and non-fibrillar species present in solution. In order to determine whether the distinct nucleation mechanism resulted in different populations of oligomers and fibril polymorphs, and whether the inclusion of these species in a mechanistic model could result in a better fit for the kinetic data, NS-EM images were obtained of 4 μM Aβ(1-42) samples that had been incubated for 0 s (ie. before incubation), 3600 s (1 h), or 18000 s (5 h) in untreated polystyrene plates, under the conditions previously used for ThT assays. As shown in Fig. 4.18, and consistent with the images previously presented in Fig. 3.12, Aβ(1-42) samples did not contain large aggregates prior to incubation, although some small globular or filamentous oligomers were observed, which may have formed dynamically after dilution into the aggregation buffer, or as a consequence of the pH changes occurring during staining.

However, as shown in Fig. 4.19, large quantities of spheroidal oligomers were observed after incuba-

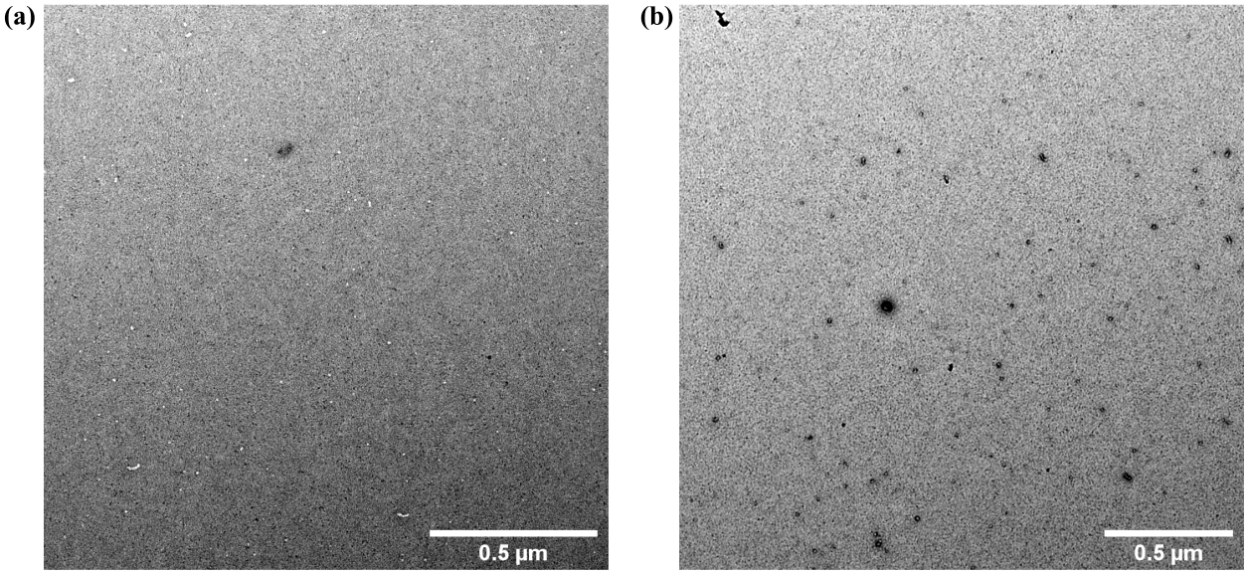

Figure 4.18: Large aggregates are not present in 4 µM Aβ(1-42) samples prior to incubation in untreated polystyrene plates. Both panels show representative images of Aβ(1-42) samples immediately after dilution into pre-adjusted fibrillisation buffer.

tion in polystyrene plates for 3600 s, equivalent to the start of the slow process of the first phase in ThT experiments. These oligomers had a typical diameter of 5-30 nm, although they were occasionally larger, and the possibility of smaller oligomers cannot be ruled out due to the limited resolution of the technique. Because these oligomers were not observed before incubation in untreated polystyrene plates, or after incubation for a similar amount of time in PEG-treated plates (Fig. 3.12), it appears that their formation was induced by interactions between Aβ(1-42) and the polystyrene surface. Since film deposition occurs rapidly in polystyrene plates, these oligomers probably formed at a time when a multilayer film was already present, and probably covered much of the surface; thus, they may have formed directly from the film, by a process such as budding or shear-induced fragmentation of the film. No such process was observed in the AFM experiments, but the samples that were negatively stained for TEM were given the same treatment as the ThT experiment, which included periodic agitation (double-orbital, 4 s every 2 min) to prevent fibril sedimentation. While the data fitting in Section 3.3.9 indicates that this level of shaking does not induce a significant amount of fibril fragmentation, the multilayer films may have been more fragile structures than fibrils, making fragments more likely to break off under shear forces. Another possibility that was examined was that the oligomers might correspond to the sub-films identified by AFM. However, there is a major size difference between the two, as the sub-films are typically 1-3 µm across and up to 50 nm thick; in addition, the sub-films appear to be more stable and to adhere more tightly to the monolayer than the rest of the multilayer. Therefore, it seems most likely that the oligomers were derived from other regions of the multilayer.

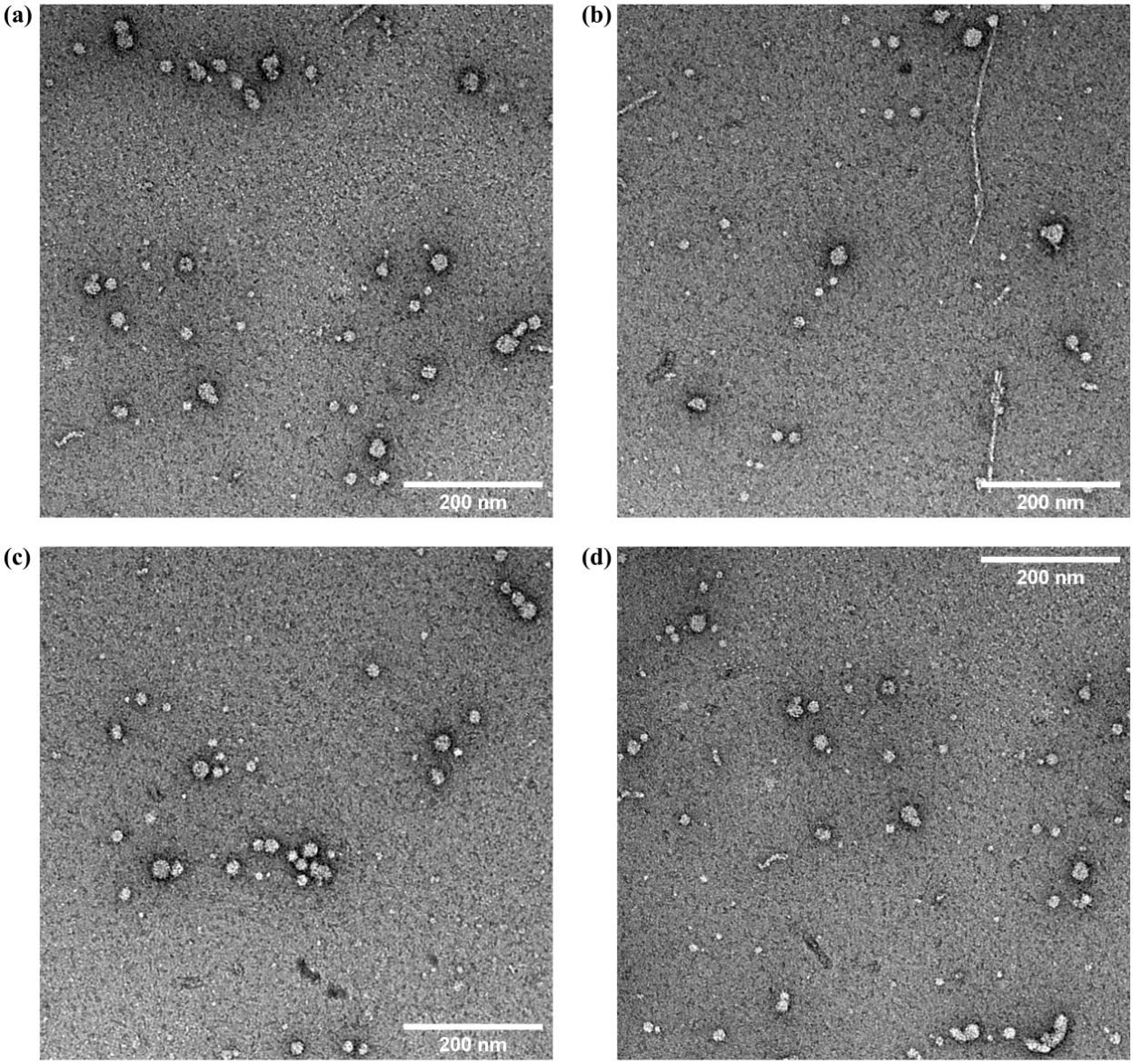

Figure 4.19: Oligomers are formed after incubation of 4 μM Aβ(1-42) in untreated polystyrene plates for 3600 s (1 h). All panels show representative images of Aβ(1-42) incubated in polystyrene plates in a 20 mM sodium phosphate buffer (pH 8) containing 200 μM EDTA, 1 mM NaN_3, and 20 μM ThT at 37°C. This figure focuses on the oligomeric species observed at this time point; images of fibrils are provided in Fig. 4.20.

In addition to spheroidal oligomers, short fibrils were also observed after incubation in polystyrene plates for 3600 s, with a typical length from 50 nm to over 1 μm. The observation of fibrils at this time is not particularly surprising, as primary nucleation is an ongoing process throughout the lag phase, and both the model favoured in Section 4.3.5 and other mechanistic models in the literature [1–3] predict small but significant quantities of fibrils well before the 'growth phase'. Interestingly, as shown in Fig. 4.20, there often appear to be interactions between the fibrils and oligomers, and more diverse oligomer morphologies are also observed in the vicinity of fibrils. Not only do spheroidal oligomers often appear to interact with fibrils, but fibril-associated oligomers with an irregular or filamentous morphology are also observed, and these species seem to occur more specifically in the presence of fibrils. Although apparent interactions between the spheroidal oligomers and the fibrils could be an artifact of the staining process, the fact that the irregular and filamentous oligomers in particular are rarely observed in the absence of fibrils indicates that they either bind to fibrils, or are formed as a result of interactions between monomers or spheroidal oligomers and the fibril surface. Thus, these fibril-oligomer interactions could be evidence for a form of secondary nucleation, and the images in Fig. 4.20 bear a resemblance to the images of secondary nucleation recently obtained by Törnquist *et al.* [460]. However, while secondary nuclei are often proposed to form directly from monomeric precursors [4, 5, 54], the fibril-associated oligomers shown in Fig. 4.20 are only observed under conditions where monomer concentrations are low, and spheroidal oligomers are present; thus, these particular species might instead be formed by templated conversion of oligomeric precursors.

Spheroidal oligomers are not observed after a longer incubation period of 18000 s (5 h), as shown in Fig. 4.21. At this time, which is close to the start of the second growth phase, only fibrils and occasional small oligomers are observed. Consistent with the predictions of the mechanistic model in Fig. 4.16(f) and Fig. 4.17(m-o), there is an increase in the average length of fibrils from 3600 s to 18000 s, indicating that primary nucleation remains the predominant nucleation mechanism in this time interval. The fact that oligomer populations decrease from the start to the end of the lag phase, but before significant depletion of the soluble monomer is likely to have occurred, suggests that the oligomers are formed rapidly from an unstable species present only at the start of the lag phase, such as weakly associated portions of the multilayer, and subsequently convert to something more stable, such as fibrils, larger aggregates, or more stable regions of the multilayer. Alternatively, the drop in oligomer concentrations could be caused by enhanced templated conversion of on-pathway oligomers due to a higher fibril concentration. Thus, there are several possibilities for the role of spheroidal and fibril-associated oligomers in the self-assembly pathway; however, in all scenarios the oligomers are formed by a surface-dependent, and probably film-dependent process, and it is possible that they may be on-pathway to fibril formation.

Although the NS-EM images suggest that spheroidal oligomers might act as nucleation intermediates, the ThT data do not provide enough information to test this hypothesis, and the oligomers do not have

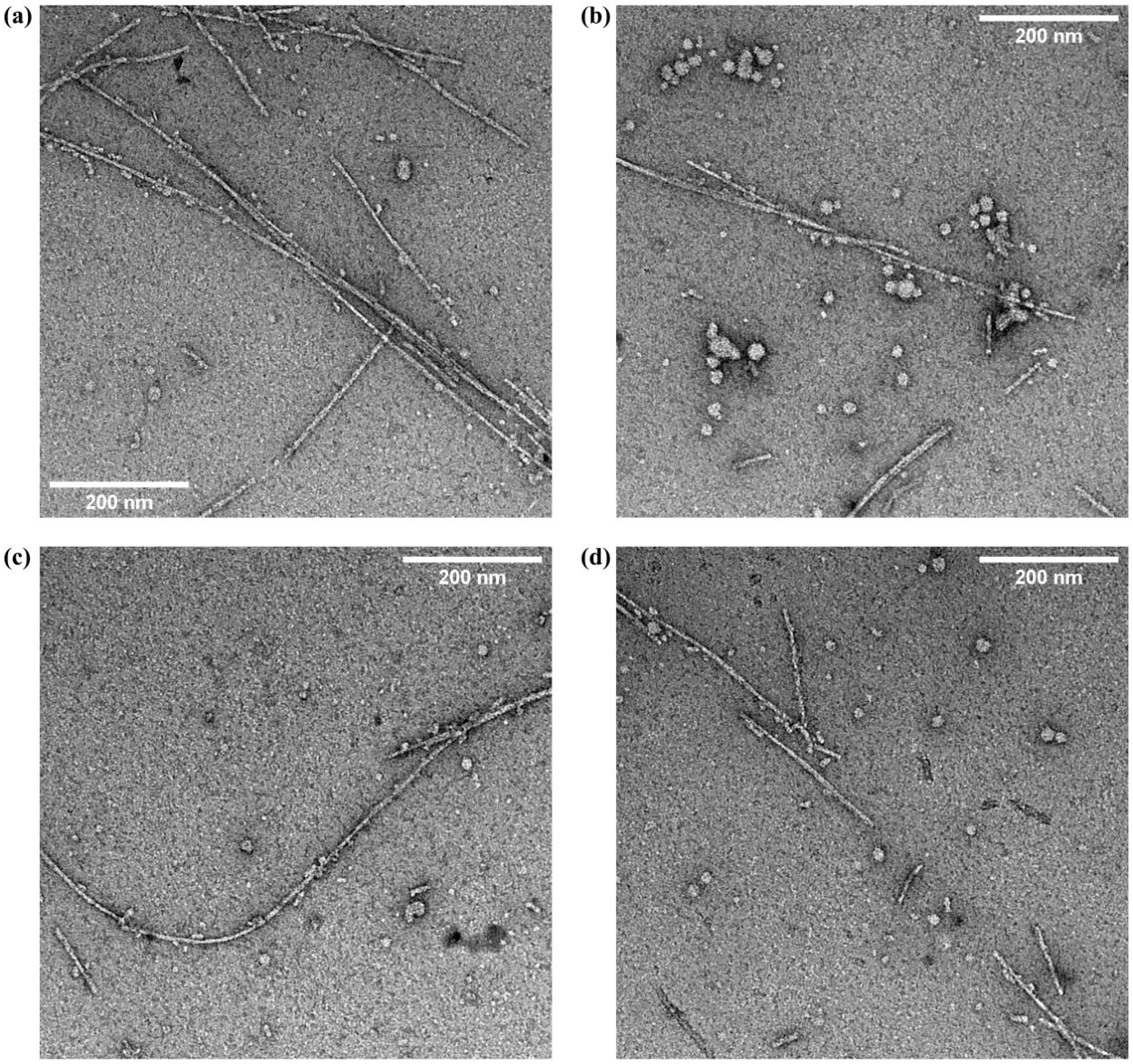

Figure 4.20: Interactions between oligomers and fibrils formed in untreated polystyrene plates. All panels show representative images of Aβ(1-42) incubated in polystyrene plates for 3600 s (1 h), in a 20 mM sodium phosphate buffer (pH 8) containing 200 μM EDTA, 1 mM NaN_3, and 20 μM ThT at 37^{o}C.

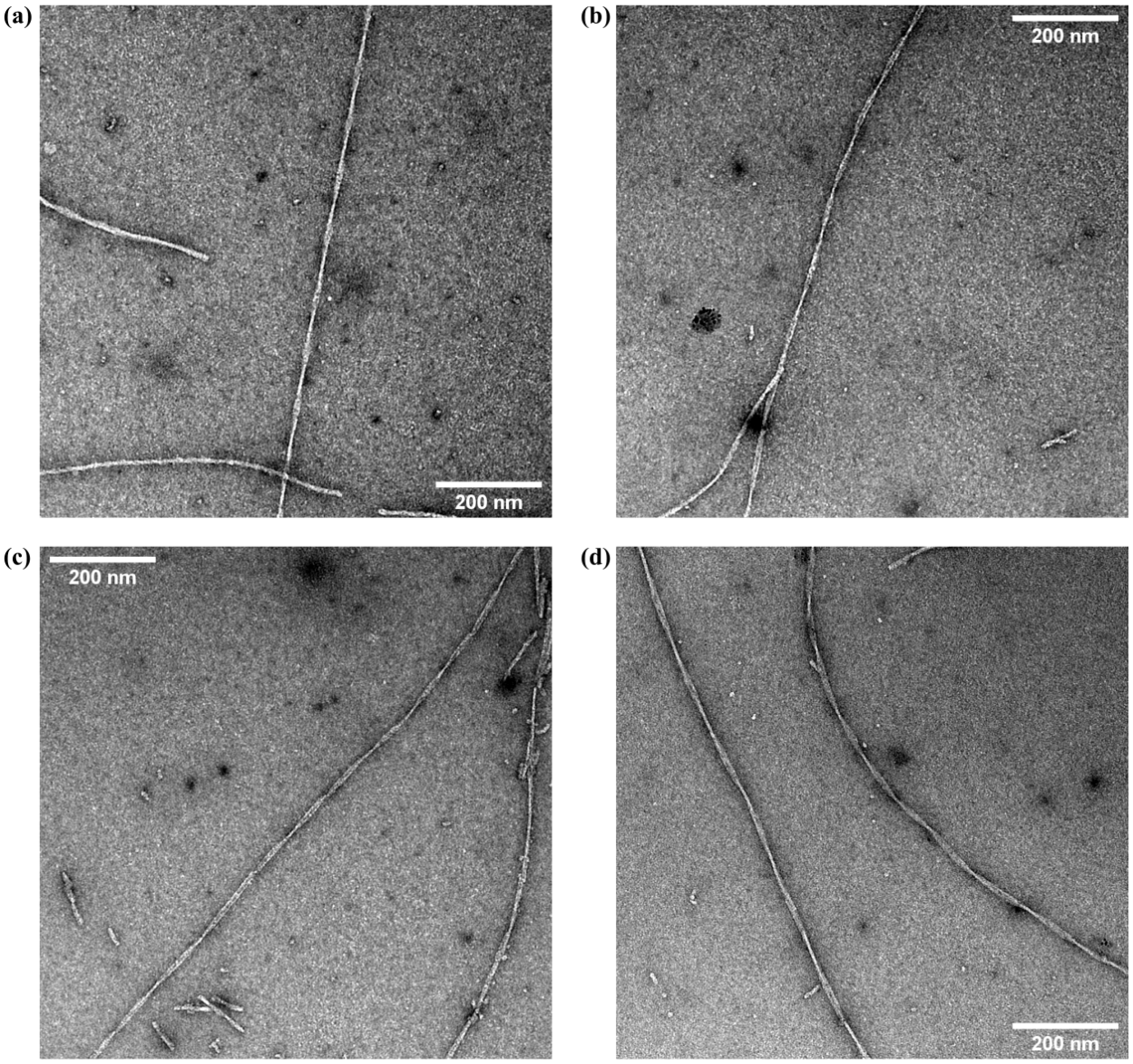

Figure 4.21: Aβ(1-42) is mostly fibrillar after incubation in polystyrene plates for 18000 s (5 h). All panels show representative images of Aβ(1-42) incubated in polystyrene plates in a 20 mM sodium phosphate buffer (pH 8) containing 200 μM EDTA, 1 mM NaN_3, and 20 μM ThT at 37°C.

the prerequisite features to address the remaining issues with the fits presented in Fig. 4.17(n-o). If the spheroidal oligomers *are* on-pathway, the fact that they are depleted by 18000 s indicates that they are formed at a limited rate; this will restrict the rate of any downstream secondary processes involving such oligomers, preventing the formation of a positive feedback loop. Thus, conversion of the spheroidal oligomers is not able to result in high-order kinetics in the early second growth phase. In addition, the fact that both the spheroidal and fibril-associated oligomers are absent by 18000 s indicates that the dominant nucleation mechanism in the growth phase is still monomer-dependent secondary nucleation, rather than an oligomer-dependent process. Thus, while conversion of spheroidal oligomers may affect the early fibril formation kinetics, it does so at a time when the fibril population is too low to detect by ThT anyway. Lastly, as previously discussed, the main issue with the fits in Fig. 4.17(n-o) is a poor description of $m(t)$ towards the end of the growth phase, and mis-fitting in the middle of the growth phase is largely a collateral result of this, as the fitting algorithm sacrifices fit quality in the early growth phase compensate for poor fitting later on. The inclusion of spheroidal oligomers does not address this issue.

Thus, while the EM data suggest that spheroidal oligomers could have an on-pathway role early in the experimental timecourse, an off-pathway role cannot be ruled out. In addition, monomer-dependent secondary nucleation is still likely to be dominant in the fittable parts of the ThT curves, and the poor fitting towards the end of the growth phase is due to an incomplete description of the film disassembly kinetics, rather than a lack of intermediates. Thus, data fitting does not benefit from the inclusion of spheroidal oligomers, and cannot satisfactorily test whether they have an on-pathway role. Nonetheless, even if spheroidal oligomers are not likely to affect the macroscopic fibril self-assembly kinetics, they still highlight the ability of strongly binding non-physiological surfaces to affect oligomer populations, an important consideration in experimental studies of oligomer structure and morphology.

Although the EM data show that surfaces strongly affect the oligomer populations, it is important to stress that these data provide no evidence for changes in fibril morphology. Although it has been suggested that distinct nucleation intermediates might correspond to different fibril polymorphs [206, 209], in studies supporting this idea it is often hard to extricate the conditions under which nucleation originally occurs from the wider solution conditions, which can also strongly and dynamically alter fibril morphology after fibril formation [181, 200, 201]. Fibrils with morphologies similar to those shown in Fig. 4.21 have also been observed in PEG-treated plates (Section 5.3.2); although the quantity of images of fibrils obtained in untreated polystyrene plates is not enough to perform a proper statistical analysis, fibrils formed in both plate types are highly polymorphic and there is no clear evidence for a significant difference in the variety of polymorphs observed. Thus, while the data do not exclude the possibility that different surfaces may result in different frequencies of particular fibril polymorphs, they also fail to suggest any specificity between the type of non-physiological surfaces used in an *in vitro* experiment and the fibril polymorphism. This indicates

that, in these experiments, the specific fold of protofilament subunits and the packing between protofilaments are predominantly determined after fibril nucleation, during maturation of on-pathway oligomers that have already overcome the free energy barrier for continued assembly. As a result, polymorphism may depend more on the environment in which these oligomers and early fibrils mature than the one in which they originate, a hypothesis that is supported by coarse-grained simulations [188] and the observation that polymorphism is more clearly dependent on the ionic strength than on surfaces (Section 5.3.2).

4.3.7 Catalytic interaction between Aβ(1-42) and hydrophilic surfaces

Comparison of the self-assembly kinetics occurring in the presence of different surfaces (Fig. 4.1-4.2) leads to another conclusion regarding the nucleation mechanism, which has been alluded to earlier in this chapter. Fibrillisation is slowest in quartz plates, fastest in PEG-treated plates, and occurs at an intermediate rate in untreated polystyrene plates. At the same time, the fibrillisation half-times are also most variable in quartz plates, relatively consistent in PEG-treated plates, and intermediate in untreated polystyrene plates; thus, the fibrillisation rate and variability of the kinetics are inversely correlated. Glass plates also approximately fit into the same pattern, although they have greater half-time variability than untreated polystyrene plates despite having a similar aggregation rate, the likely reasons for which are discussed later. The correlation between the rate and variability of the fibrillisation kinetics indicates that the differences in nucleation account for differences in the rate, as a lower nucleation rate means there will be fewer individual fibrils, resulting in slower, more stochastic kinetics. Moreover, out of the key processes of primary nucleation, secondary nucleation, and elongation, the former is the most likely to be affected by the plate surface, as secondary nucleation and elongation are fibril-dependent processes, there is no interaction between fibrils and polystyrene under these conditions (Fig. 4.3-4.5, Fig. 4.22), and there appears to be no evidence for specific interactions between fibrils and polystyrene or PEG-coated surfaces in the literature. Analysis of the kinetic data already supports the hypothesis that untreated polystyrene plates catalyse Aβ(1-42) fibril nucleation; however, the fact that fibrillisation is faster in all other plate types than in quartz plates indicates that PEG, polystyrene, and glass all catalyse primary nucleation to differing extents. The alternative hypothesis, that primary nucleation is a homogeneous process that is inhibited by quartz, would require significant interactions between quartz and Aβ(1-42); however, as shown in Fig. 4.22, no such interactions were observed by AFM on timescales of over 6 h. In addition, while quartz is typically believed to be a weakly interacting surface, and is often used in biophysical studies to reduce surface adsorption, interactions between Aβ(1-42) and PEG have been observed [532]. Thus, the effect of different surfaces on Aβ(1-42) fibrillisation indicates that PEG, polystyrene, and glass all catalyse heterogeneous primary nucleation.

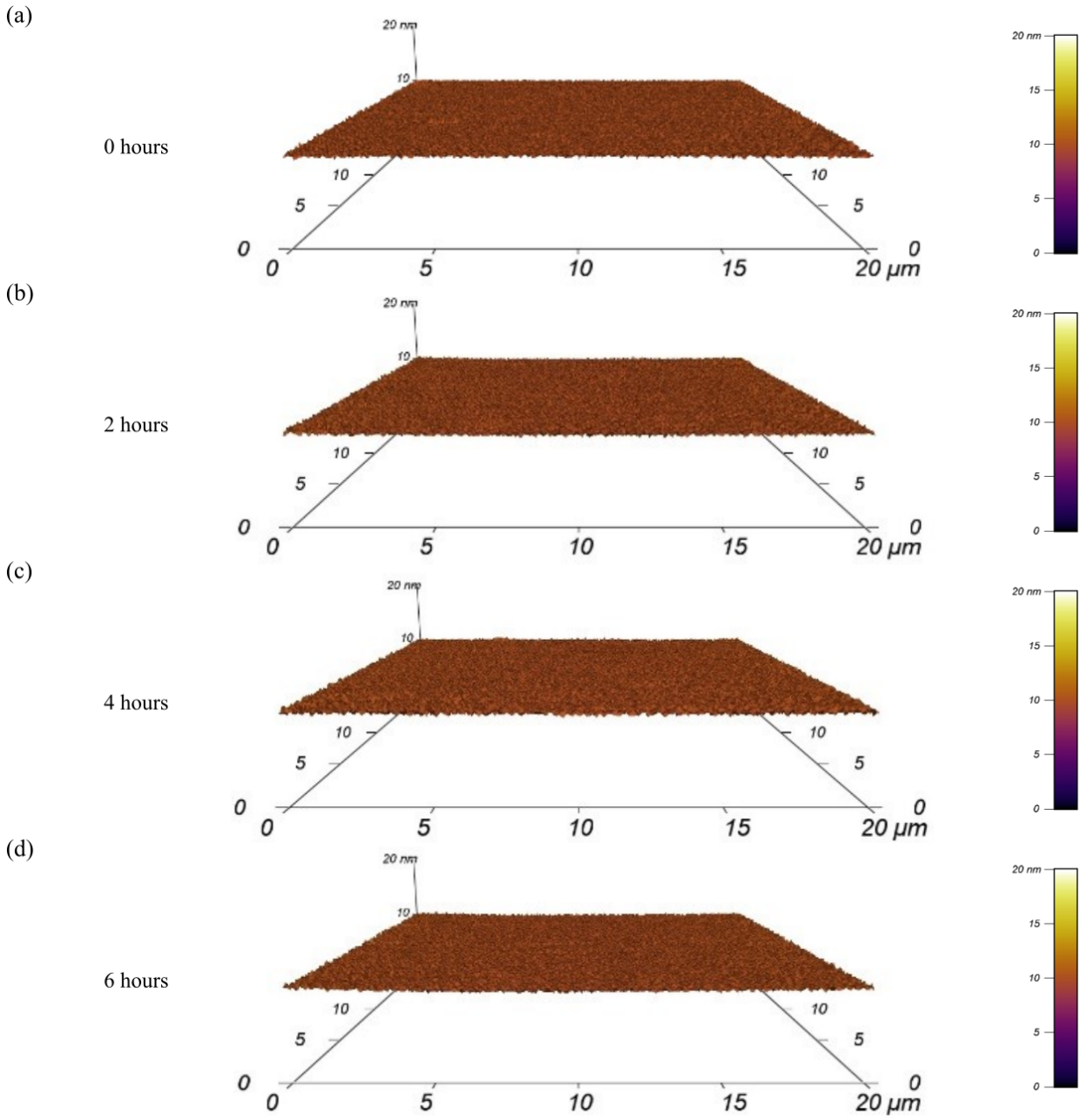

Figure 4.22: Aβ(1-42) does not interact with quartz surfaces. Panels show 3D topography images of different time points in the same AFM experiment.

4.3.7.1 PEG-treated plates

To enhance the nucleation rate, PEG would have to reduce the free energy of the critical nucleus, or provide an alternative pathway with a more favourable critical nucleus. Even weak interactions between PEG and Aβ(1-42) could significantly increase the local monomer concentration, stabilising an oligomeric critical nucleus in that environment; this form of heterogeneous primary nucleation has previously been supported by molecular modelling studies [360, 475]. Alternatively, specific interactions between PEG and Aβ(1-42) could alter the conformational state of the adsorbed peptide, as supported by previous work on the interactions between PEG and Aβ(1-42) [532], and this change in conformational preferences could increase the probability of on-pathway oligomer formation. The fact that fibrillisation is faster in PEG-treated plates than in untreated polystyrene plates appears paradoxical, as the latter is the more strongly binding surface. For example, at 4 μM peptide, the mean ThT half-time is 7700 s in PEG-treated plates (across all preparations), and 31800 s in untreated polystyrene plates, around 4× slower. However, fibrillisation in untreated polystyrene plates is complicated by the fact that large quantities of monomer are incorporated into multilayer films, reducing the rates of secondary nucleation and elongation. To specifically compare the primary nucleation rate between the two surfaces, one can calculate the nucleation rate J_n per plate surface area from the relation

$$J_n = \frac{\Phi_n N_A V}{A}, \tag{4.29}$$

where N_A is the Avogadro constant, $V = 100\ \mu\text{L}$ is the reaction volume, and $A = 1.02\ \text{cm}^2$ is the plate area in contact with the solvent. This is the rate at which individual fibrils are produced per unit area of the catalytic surface. In PEG-treated plates, J_n is a function of the free monomer concentration,

$$J_n = \frac{k_n N_A V m(t)^{n_c}}{A}, \tag{4.30}$$

When $k_n k_e^+ = 100\ \text{M}^{-2}.\text{s}^{-2}$ (see the fitted parameters in Table 3.1) and one uses the literature values of $k_e^+ = 3 \times 10^6\ \text{M}^{-1}.\text{s}^{-1}$ and $n_c = 2$ [54],

$$J_n = \begin{cases} 2.0 \times 10^7\ \text{M}^{-2}.\mu\text{m}^{-2}.\text{s}^{-1}\ \times\ m(t)^2, & \text{generally,} \\ 2.0 \times 10^{-5}\ \mu\text{m}^{-2}.\text{s}^{-1}, & \text{when } m(t) = 1\ \mu\text{M,} \\ 3.1 \times 10^{-4}\ \mu\text{m}^{-2}.\text{s}^{-1}, & \text{when } m(t) = 4\ \mu\text{M,} \end{cases} \tag{4.31}$$

where each rate is given to 2 significant figures. In untreated polystyrene plates, J_n is independent of the free monomer concentration,

$$J_n = \frac{k_n N_A V L_1(t)}{A}. \tag{4.32}$$

Using the kinetic parameters for model 5 in Table 4.4, when $m(0) \geq L_{1,\max}$ and $m(0) - L_{1,\max} \gg c^*$ so that $L_1(t) = L_{1,\max}$,

$$J_n = 3.8 \times 10^{-5}\ \mu\text{m}^{-2}.\text{s}^{-1}, \tag{4.33}$$

which equal to the rate expected for $\sim$1.4 μM Aβ(1-42) in PEG-treated plates. This means that the primary nucleation rate per surface area is similar in PEG-treated and untreated polystyrene plates at the Aβ(1-42) concentrations used in the ThT experiments, although the nucleation rate is much more concentration-dependent in the former case than the latter. Thus, although differences in primary nucleation can partly explain the differing rate and concentration-dependence of overall fibrillisation, depletion of the soluble monomer also has a major impact. In agreement with this, if polystyrene surfaces resulted in the same nucleation rate as calculated above, but the quantity of peptide removed from solution were negligible, the expected fibrillisation half-time of 4 μM Aβ(1-42) would be 10500 s, which is much closer to the half-time of 7700 s observed in PEG-treated plates.

Nonetheless, even though the two surfaces result in similar primary nucleation rates at the experimental concentrations, nucleation occurs in very different environments, with different implied efficiencies. In PEG-treated plates, there is no evidence of saturation of primary nucleation between the initial peptide concentrations of 1 μM and 4 μM, indicating that only a small quantity of peptide is adsorbed to the plate surface. In contrast, in untreated polystyrene plates, primary nucleation occurs in a highly saturated environment containing a large quantity of aggregated peptide. This means that individual adsorbed monomers are much more likely to be engaged in successful nucleation events in PEG-treated plates than in untreated polystyrene plates. Thus, nucleation is much more efficient in PEG plates, indicating that the relatively dynamic, solvated environment of the PEG-like surface layer is favourable for the formation of on-pathway oligomers, whereas the crowded, probably less solvated environment of the films is less so. The importance of dynamics in heterogeneous Aβ(1-42) nucleation was previously supported by Shen *et al.* [351], who found that polystyrene surfaces retard self-diffusion of monomers compared to less strongly attractive surfaces, with a detrimental effect on the nucleation rate. In addition, the tight interactions between Aβ(1-42) monomers and either the surface or other monomers within the film could prevent the release of fibril precursors, in a manner similar to a poor chemical reaction catalyst that binds too strongly to the product.

The surface of PEG-treated plates catalyses primary Aβ(1-42) nucleation without causing significant depletion of the soluble monomer. As a result, fibrillisation in PEG-treated plates has a high nucleation rate, resulting in consistent kinetics, but is not complicated by the formation of large quantities of off-pathway or low-productivity aggregates, as in polystyrene. This means that fibrillisation in PEG-treated plates has a relatively simple mechanism under the experimental conditions, and is well-suited for kinetic analysis.

4.3.7.2 Glass-coated plates

In glass-coated plates, the underlying mechanism appears to be more complex and unpredictable. While glass would be expected to be a relatively weakly interacting surface, fibrillisation in glass plates is often multiphasic (Fig. 4.1-4.2), and has a similar rate and concentration-dependence to polystyrene plates. However, half-times are much more variable in glass plates than in polystyrene plates, and after an initial increase in ThT fluorescence the subsequent phases appear to be more randomly distributed. The observation that the fibrillisation rate exhibits multiple randomly distributed peaks throughout the time course indicates that infrequent, highly productive events produce large numbers of fibril nuclei, so that each causes a rapid increase in the fibrillisation rate. One possible mechanism could be the adhesion of fibrils to defects in the glass, and the formation of large clusters of secondary fibrils on the surface of those fibrils; a process of this sort has previously been reported for adsorbed Aβ(1-40) fibril seeds, based on TIRFM images [206]. In these images, large numbers of secondary fibrils initially formed around each seed, but these did not engage in further secondary nucleation events, indicating that their polymorphism or environment restricted the formation of further secondary fibrils. If the surface-dependent nature of the process resulted in weak scaling of the nucleation processes with the free monomer concentration, then these combined effects could result in a very low monomer concentration. However, at present there are no imaging data to confirm this mechanism. In addition, it is important to bear in mind that the 'glass' plates are actually glass-coated polystyrene plates, and during data acquisition there were concerns that overly harsh cleaning treatments could etch the glass, exposing the underlying polystyrene. Thus, it is possible that the glass plates might result in a similar mechanism to polystyrene plates, complicated by the effect of residual layers of glass coating. Lastly, both acidic and basic peptides have been shown to adsorb to glass surfaces [541], indicating that interactions between Aβ(1-42) and glass could be stronger than previously suspected. Thus, glass-coated plates could result in depletion of the soluble peptide and saturated heterogeneous nucleation similar to polystyrene plates, explaining the multiphasic kinetics and similar concentration-dependence.

4.3.7.3 Quartz plates

As previously discussed, the low fibrillisation rate and inconsistent half-times in quartz plates suggest that primary nucleation events are rare (Fig. 4.1-4.2); in addition, the variable fluorescence intensities indicate that fibril polymorphism may differ significantly between replicate wells, as a result of the small number of primary nucleation events. Nonetheless, the smooth, sigmoidal curve shape suggests that in addition to the small number of primary nucleation events, a large number of ensuing secondary nucleation events occur. In addition, the maximum fibrillisation rate is typically lower in quartz plates than in PEG-treated plates, indicating that the secondary process occurring in the former has a lower rate. This could be

due to polymorph-dependent differences in the secondary nucleation mechanism, or partial depletion of soluble monomer due to off-pathway processes occurring in the extended lag phase. Unfortunately, due to the variable rate and final fluorescence intensities, and the fact that many of the curves were too slow to follow to completion, it was not possible to carry out global fitting to test this hypothesis. In addition, although attempts were made to eliminate the AWI in order to determine whether primary nucleation occurred at the AWI in quartz plates, these experiments were challenging due to the presence of air bubbles and issues with the seal, and did not yield consistent results. Thus, it remains an open question whether primary nucleation in quartz plates occurs homogeneously, at the plate surface, or at the AWI.

4.4 Conclusions

The results of this chapter indicate that the majority of experimental surfaces are likely to interact with Aβ(1-42) in a way that alters the fibril self-assembly pathway. In addition, there is substantial evidence in the literature for the importance of physiological surfaces, especially membranes, in Aβ(1-42) aggregation [313, 352, 357, 531]. While the surfaces used in this chapter are non-physiological, they are commonly used in *in vitro* studies; thus, the conclusions of such studies are likely to be highly dependent on the type of surface used, perhaps explaining many of the inconsistencies in the literature. For example, the oligomer populations observed in PEG-treated and untreated polystyrene plates differ in size, abundance, and morphology, and further investigation would likely reveal that these morphological differences reflected underlying differences in their structure. The surface-dependence of oligomer populations could explain why different research groups observe such a vast range of Aβ oligomer morphologies, despite the lack of obvious differences in the temperature or solvent.

In addition to its direct relevance for *in vitro* studies, the work in this chapter demonstrates that there are general principles governing the effects of surfaces on protein aggregation, which are also likely to apply to physiological surfaces. These principles are best illustrated by comparing the fibrillisation pathways in quartz, PEG-treated, and untreated polystyrene plates, which are summarised in Fig. 4.23. In quartz plates, interactions with the surface are very weak; therefore, primary nucleation occurs at a low rate, resulting in slow, stochastic kinetics, and perhaps competing processes. In PEG-treated plates, interactions between Aβ(1-42) and the plate surface are somewhat stronger, although they are still relatively weak; a K_D of 160 μM has previously been suggested [532], and would be consistent with the results in this chapter. As a result, the primary nucleation rate is higher, but interactions are still too weak to sequester large quantities of the soluble monomer, resulting in rapid, highly reproducible self-assembly kinetics with only small quantities of non-fibrillar aggregates. In untreated polystyrene plates, interactions between Aβ(1-42) and the surface are strong, resulting in the deposition of large, multi-layered films of peptide. After

film deposition, complex maturation processes occur, such as the formation of spheroidal oligomers, the unidentified 'slow process' (Section 4.3.4), and the formation of stable 'sub-films' (Section 4.3.3); only the former of these is represented in Fig. 4.23, as the mechanism of the slow process is unclear and it is uncertain whether sub-films are general to films formed on all polystyrene surfaces, or specific to those formed on surfaces with a particular structure. While fibrils are able to nucleate in these films, nucleation is less efficient than on weakly binding surfaces such as PEG, as tightly binding surfaces trap Aβ(1-42) and restrict translational and conformational diffusion, hindering the release of fibril seeds. In addition, film deposition sequesters Aβ(1-42) and limits the concentration of soluble peptide, reducing the role of secondary nucleation and further slowing fibrillisation. Thus, while only weak surface interactions are required to stimulate primary nucleation, stronger interactions are required to inhibit nucleation and overall fibrillisation, as inhibition is achieved by forming strongly bound states with slow dynamics, or sequestering large quantities of monomer in metastable, non-fibrillar aggregates.

These conclusions are likely to apply to other surfaces that are relevant *in vivo*, such as membranes, extracellular matrix (ECM) components, oligosaccharides, and the fibril surface (ie. secondary nucleation), whose catalytic effect has recently been confirmed in cerebrospinal fluid (CSF) [75]. Even weak interactions between Aβ and other surfaces and biomolecules may increase the local peptide concentration sufficiently to stimulate primary nucleation; thus, primary nucleation pathways may be exceptionally diverse *in vivo*, corresponding to the diversity of possible binding partners. While it is already well-established that strongly binding surfaces stimulate oligomer formation and complicate the self-assembly pathway [51, 63–68, 352, 357, 531], the ability of such surfaces to limit Aβ(1-42) monomer concentrations, and thus reduce the rate of secondary nucleation and elongation, must be borne in mind when translating the insights of *in vitro* studies to a physiological context. The finding that there is an optimum level of surface binding for primary nucleation also has implications for our understanding of secondary nucleation. An efficient secondary nucleation process does not necessarily require strong, highly complementary interactions between the fibril surface and the developing seed; instead, weak, transient interactions may be most effective at generating secondary nuclei, while strong lateral binding is likely to result in expansion of the existing fibril, without creating secondary nuclei. This may favour a nonspecific mechanism of secondary nucleation in which monomer-fibril interactions stimulate the formation of globular oligomers that subsequently convert to fibrils, as suggested by recent theoretical work [348], rather than a structure-driven pathway in which the mature protofilament structure is stabilised by binding of monomers or oligomers to the surface of pre-existing fibrils, although the data presented in Section 4.3.5-4.3.6 suggest that both mechanisms may occur under appropriate conditions.

The complex self-assembly mechanism of Aβ(1-42) in the presence of polystyrene surfaces, and perhaps also glass, means that great care must be taken when interpreting the results of *in vitro* studies carried

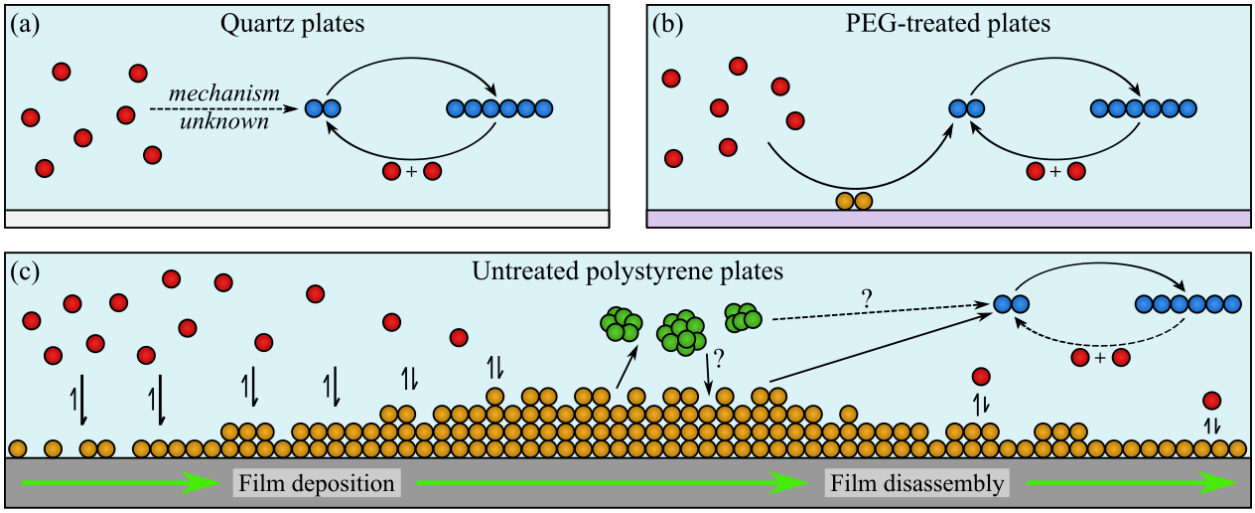

Figure 4.23: Schematics of Aβ(1-42) fibrillisation in quartz, PEG-treated, and polystyrene plates. Panels represent different plate types: (a), quartz; (b), PEG-treated; (c) untreated polystyrene. Circles represent Aβ(1-42) monomers, with the colour scheme representing the conformational state: red, soluble; gold, surface-associated; green, non-fibrillar oligomers; blue, fibrillar. The colour of the surfaces represents the surface type: light gray, quartz; violet, PEG-treated low-binding surface; dark gray, polystyrene. The black arrows represent the microscopic molecular processes, which are: adsorption to form films or other surface-associated intermediates; primary nucleation to form a minimally sized elongating species (shown here as a fibrillar dimer); elongation, which increases the size of fibrils; and secondary nucleation, which produces new fibrils in a fibril-and-monomer-dependent manner. Elongation and secondary nucleation form a positive feedback loop, which is represented by the pair of arrows forming a cycle in the right of each panel. All models have similar microscopic elongation and secondary nucleation mechanisms, but differ in their mechanisms of surface-association and primary nucleation. Dashed arrows represent processes occurring at a low rate, and arrows with question marks represent processes that are suggested by the data, but not confirmed. The green arrows in panel (c) represent the general evolution of film structure; note that while fibril nucleation and elongation are represented to the right of this panel due to space constraints, they are active throughout the entire span of time that films are present.

out without paying attention to the role of surfaces. The majority of experimental studies do not refer to the type of surface used in *in vitro* fibrillisation assays; however, from the few that do, it is clear that Aβ(1-42) is often exposed to polystyrene surfaces [233, 487, 523, 538–540]. Furthermore, the kinetics in glass plates are similar to those in polystyrene, and a wide variety of other plastics are used in other common items of labware, so the issue is likely to be widespread. As shown in this chapter, strongly binding surfaces profoundly alter the self-assembly pathway; while fibrillisation in the presence of weakly binding surfaces such as PEG can be explained by simple mechanistic models, the kinetics in polystyrene plates are complex, challenging to interpret, and involve a large number of microscopic processes and unconstrained parameters that makes global fitting difficult. In addition, the mechanistic complexity, depletion of the soluble monomer, and saturation of primary nucleation all weaken the relationship between alterations to the underlying microscopic processes and their signatures in the macroscopic kinetics. For example, in PEG-treated plates, an inhibitor that tightly bound a proportion of the soluble monomer would increase the half-time and reduce the maximal fibrillisation rate, as well as reducing the final fluorescence intensity; in untreated polystyrene plates, only the latter effect would be observed, which indicates a loss of fibril yield but provides no clues as to the nature of the species bound. Lastly, it should be noted that the same untreated polystyrene plates that are often used in *in vitro* self-assembly assays are also used in cell culture [489]. Since oligomers are proposed to be the more toxic species in Aβ(1-42) self-assembly [73], and polystyrene has a pronounced effect on oligomer populations, the use of untreated polystyrene plates or other strongly binding surfaces may affect the outcome of toxicity assays. Thus, while studies of the self-assembly mechanisms occurring in the presence of polystyrene and other strongly binding surfaces are needed to interpret the results of past work using such surfaces, wherever possible, future experiments should be designed to minimise strong interactions between Aβ and non-physiological surfaces.

In summary, while primary nucleation of Aβ(1-42) is often assumed to occur homogeneously, the results presented in this chapter show that homogeneous nucleation is at best very slow at physiological Aβ(1-42) concentrations, and primary nucleation is predominantly surface-dependent in most experimental contexts. Heterogeneous, surface-dependent primary nucleation is unavoidable if reproducible fibrillisation is to occur, and can even improve the interpretability of experimental results by ensuring more deterministic self-assembly kinetics, as in the case of PEG-treated surfaces. However, greater care must be taken to avoid strong interactions between Aβ(1-42) and non-physiological surfaces, which can complicate the self-assembly pathway and confound interpretation of the results. In addition, the observation that even weak interactions can stimulate primary nucleation indicates that a more diverse range of physiological surfaces may be involved in this process than previously suspected; thus, a broader survey of the effects of such surfaces is needed. While further investigation of the effects of non-physiological surfaces may allow better interpretation of existing self-assembly data, *in vitro* studies should increasingly attempt to incorporate

biological surfaces in order to replicate physiological primary nucleation mechanisms, which may result in very different self-assembly behaviours both at the surface and in the bulk solvent.

4.5 Acknowledgments

The data presented in this chapter were collected jointly by myself and Dr. Liam Aubrey, in a project supervised by Dr. Rosemary Staniforth and Prof. Jamie Hobbs. I made the initial observation that surfaces affected the self-assembly kinetics, collected the ThT data in PEG-treated and untreated polystyrene plates, and obtained the NS-EM images. Dr. Aubrey collected the ThT data in glass and quartz plates, and the AFM images. All analyses presented in this chapter, including the analyses of the ThT data, the analyses of the AFM data, and the mathematical modelling, were carried out by myself. Dr. Aubrey had previously obtained R_a measurements, but the measurements presented here were obtained independently by myself; to my knowledge, all other analyses of the AFM data are new. Many thanks to Dr. Aubrey and other lab members for useful discussions regarding the work in this chapter.

Chapter 5

Salt-Induced Accumulation of On-Pathway Aβ(1-42) Oligomers

5.1 Introduction

A realistic, physiologically relevant description of Aβ self-assembly requires a thorough understanding of the effects of ionic cosolutes on aggregation. At present, the majority of detailed kinetic studies have been carried out in relatively dilute buffers with low salt concentrations and ionic strengths ($\sim$ 60 mM) [54, 519]. However, the low salt concentration of these buffers contrasts with the physiological situation, where the cerebrospinal fluid (CSF) contains around 140 mM NaCl, in addition to several other salts, and has a higher ionic strength as a result ($\sim$ 160 mM) [75, 542]. At physiological pH ($\sim$ 7.3), as well as the near-physiological pH often used for *in vitro* work ($=$ 8) [54, 519], Aβ has a net charge that results in an electrostatic repulsion between monomers, creating a free energy barrier to aggregation. In addition, electrostatic interactions play both destabilising and stabilising roles in the mature fibril structure (see Section 1.3), determine the morphology of globular oligomers (see Sections 1.4.2 and 1.4.4), and facilitate the higher-order assembly of oligomers to form filamentous structures that may be on-pathway to fibril formation [220]. By screening electrostatic interactions, salts can thus be expected to affect all stages of Aβ self-assembly. In addition, many salts may have effects beyond charge screening alone; for example, Hofmeister effects have been reported at low salt concentrations for α-syn [543], and certain anions exhibit electroselective binding to aggregates formed by glucagon and PrP, altering the aggregation process [544, 545]. Thus, a detailed understanding of the effects of salts on Aβ self-assembly is needed to properly predict and control aggregation.

Work conducted early in this PhD showed that salts accelerate Aβ(1-42) self-assembly. At the same time, it was shown by others that the same mechanistic framework that was developed for low ionic strengths

can be applied to ThT kinetics obtained at intermediate ionic strengths ($\lessapprox$ 310 mM) [5]. More recently, it has been shown that the same basic processes that dominate Aβ(1-42) self-assembly at low ionic strength, namely primary nucleation, elongation, and secondary nucleation, are active in both artificial and patient-derived CSF [75]. Nonetheless, there are several major unanswered questions. Firstly, these studies did not explore the possibility of low-concentration Hofmeister or electroselective effects on Aβ self-assembly. If identified, such effects could have physiological relevance, and might also provide insights into the underlying self-assembly mechanisms. Secondly, while it has been assumed that a two-state model of self-assembly is valid at physiological ionic strengths, with significant concentrations of monomer and fibrils but negligible concentrations of intermediates, there are only bulk ThT fluorescence measurements and low-contrast EM images to support this [5,75]. A proper test of this assumption would require the use of complementary spectrometric or spectroscopic techniques, higher-contrast imaging that actually permits the identification of any oligomers, or analytical fractionation techniques such as SEC-MALS or AF4-MALS. Thirdly, and lastly, high ionic strengths often result in low concentration-dependences of the self-assembly half-time and lag time ($\gamma < 0.5$); since it has been clearly shown that elongation exhibits negligible saturation under the conditions in question [5], this weak scaling is inconsistent with existing models of self-assembly. These issues point to gaps in our understanding of Aβ(1-42) self-assembly at physiological ionic strength that must be filled in order to accurately describe aggregation and toxicity *in vivo*.

In the work described in this chapter, these questions were addressed by performing a scan of the Aβ(1-42) self-assembly kinetics across a broader range of initial monomer and salt concentrations than previous investigations conducted at this level of detail. Kinetics were recorded by ThT assays, NS-EM imaging, and CD spectroscopy. In addition, fractionation has been attempted by SEC-MALS and AF4-MALS, but continues to face technical challenges due to the labile nature of the species of interest. Nonetheless, by combining the aforementioned measurements with data fitting and analytical modelling, conclusions can be drawn regarding all three issues discussed above. Firstly, the primary effect of salts on Aβ(1-42) self-assembly is one of ionic strength, although electroselective effects also appear to be present. This means that buffers of different compositions are usually equivalent if they share the same ionic strength, simplifying comparison of the diverse experimental conditions present in the literature. Secondly, it is shown that Aβ(1-42) self-assembly at physiological ionic strength and moderate peptide concentration cannot be described by a simple two-state model, requiring the addition of at least one oligomeric species. From the kinetics of accumulation of this species, it is determined that the oligomer, which is highly unstructured but appears to contain ThT-binding motifs, is an on-pathway intermediate produced by secondary nucleation. Thirdly, it is shown that the transition to a regime where this oligomer accumulates is the cause of the weak monomer-dependence of the self-assembly kinetics. On the basis of these observations, a non-equilibrium phase diagram of Aβ(1-42) self-assembly regimes is proposed, containing a region of secondary oligomer

accumulation that overlaps with the physiological range of conditions. Since secondary oligomers have previously been shown to be toxic [54, 55, 68], the existence of a regime where these oligomers undergo unbounded accumulation has important consequences for our understanding of the mechanisms of toxicity *in vivo*.

5.2 Materials and methods

5.2.1 Materials

For a description of the materials used in this chapter, see Section 2.1.

5.2.2 ThT assays

ThT assays were carried out as described in Section 2.5, with two types of fibrillisation buffers: 20 mM sodium phosphate (pH 8) containing 1 mM NaN_3, 200 μM EDTA, 20 μM ThT, and variable quantities of NaF or NaCl; and 10 mM sodium phosphate (pH 8) containing 200 μM NaN_3, 200 μM EDTA, 20 μM ThT, and variable quantities of NaF, NaCl, or NaI. Buffers were prepared as described in 2.4.

5.2.3 Negative stain electron microscopy and analysis of fibril length distributions

NS-EM was carried out as described in Section 2.7. Prior to staining, Aβ(1-42) was diluted to the required concentration in the appropriate fibrillisation buffer, as indicated where relevant in the results section. The sample was stained either immediately, or after incubation for a specified amount of time in a 96-well plate treated with a PEG-like low-binding surface (Corning 3881, NY), at 37°C. When analysing the NS-EM data, the standard error of the mean (SEM) of binomially distributed variables was estimated as [546],

$$\text{SEM} \approx \sqrt{\frac{\hat{p}(1-\hat{p})}{N}} \tag{5.1}$$

where $\hat{p}$ is the proportion of positive results in N observations. Violin plots of fibril length distributions were produced in GraphPad Prism 8, using the 'high' smoothing option when calculating the kernel density estimation (KDE) to avoid over-interpretation of noise. To calculate the relative rate parameters $R'_n(I) = k'_n(I)/k'_n(30\,\text{mM})$, $R'_s(I) = k'_s(I)/k'_s(30\,\text{mM})$, and $R^+_e(I) = k^+_e(I)/k^+_e(30\,\text{mM})$ from the ThT-derived λ and κ values and the EM-derived mean fibril lengths $\langle l \rangle$, the variation in the effective microscopic rate parameters was calculated first. The macroscopic rate parameters are functions of the microscopic rate parameters [3,6],

$$\lambda = \sqrt{2k'_n k^+_e m(0)^{n_c}}, \tag{5.2}$$

$$\kappa = \sqrt{2k_s' k_e^+ m(0)^{n_s+1}}, \tag{5.3}$$

and in the absence of seed material, k_e^+ can be expressed as a function of the average fibril size $L_{\text{end}} = M_{\text{end}}/P_{\text{end}}$ at the end of the growth phase,

$$k_e^+ = \frac{L_{\text{end}}\sqrt{\frac{2\lambda^2}{n_c} + \frac{2\kappa^2}{n_s(n_s+1)}}}{2m(0)}, \tag{5.4}$$

where the above equation is derived from the results in Appendix C of Cohen *et al.* [3]. The average number of monomers in a fibril can be expressed in terms of the frequency δ^{-1} of monomeric subunits along the fibril length, and the average fibril length $\langle l \rangle$,

$$L_{\text{end}} = \delta^{-1}\langle l \rangle. \tag{5.5}$$

While δ^{-1} is unknown, $\langle l \rangle$ is provided by the NS-EM measurements. Thus,

$$k_e^+ \delta = \frac{\langle l \rangle\sqrt{\frac{2\lambda^2}{n_c} + \frac{2\kappa^2}{n_s(n_s+1)}}}{2m(0)}, \tag{5.6}$$

For each trio of λ, κ, and $\langle l \rangle$ values corresponding to self-assembly of 2 μM Aβ(1-42) at a single ionic strength, it was possible to calculate $k_e^+\delta$ using Eq. (5.6). For the purpose of this analysis, it was assumed that $n_c = n_s = 2$, a value from the literature [54, 519]; however, since only a single term ($\propto \kappa^2$) dominates in Eq. (5.6), use of incorrect n_c and n_s values is not expected to strongly affect the relative variation in estimated $k_e^+\delta$, only the absolute values. Although it is possible that δ may vary with ionic strength, in the absence of further information it was assumed that any variation was not significant. Therefore,

$$R_e^+(I) = \frac{\delta k_e^+(I)}{\delta k_e^+(30\text{ mM})}, \tag{5.7}$$

allowing the relative variation in k_e^+ to be calculated. From Eq. (5.2-5.3), it follows that

$$R_n'(I)R_e^+(I) = \frac{\lambda^2(I)}{\lambda^2(30\text{ mM})}, \tag{5.8}$$

$$R_s'(I)R_e^+(I) = \frac{\kappa^2(I)}{\kappa^2(30\text{ mM})}, \tag{5.9}$$

allowing the $R_n'(I)$ and $R_s'(I)$ values to be calculated from the fitted macroscopic rate parameters and $R_e^+(I)$. It should be noted that estimation of the absolute values of k_e^+ using plausible values of δ suggested that k_e^+ may be somewhat lower than the rate observed by Cohen *et al.* [54], perhaps explaining the difference

in half-time commented on in Chapter 3. For example, if a fibril consists of two protofilaments and the β-sheet spacing is 4.75 Å, then $\delta = 0.238$ nm, which yields estimates of $k_e^+(30\,\text{mM}) = 1.1 \times 10^5\,\text{M}^{-1}.\text{s}^{-1}$ and $k_e^+(80\,\text{mM}) = 1.3 \times 10^5\,\text{M}^{-1}.\text{s}^{-1}$, compared to $k_e^+(60\,\text{mM}) = 3 \times 10^6\,\text{M}^{-1}.\text{s}^{-1}$ reported by Cohen *et al.* [54]. This could explain the approximately 10× difference in $k_n k_e^+$ and $k_s k_e^+$ reported in Section 3.3.9, suggesting that the commercial recombinant peptide has a lower elongation rate than the in-house preparations. At the same time, this suggests that the nucleation processes are only weakly affected by the source of the peptide.

5.2.4 Analytical size exclusion chromatography (SEC)

The protocol for these experiments was similar to the protocol for SEC experiments in Chapter 3. Samples were purified in small batches using an analytical Superdex 75 column (GE healthcare) equilibrated in 20 mM sodium phosphate buffer (pH 8) with 1 mM NaN_3, 200 μM EDTA, and 300 mM NaCl. The column was run with the TIP pump from the AF4 system (Postnova Analytics, Landsberg am Lech, Germany), and in-line UV (280 nm; Shimadzu, UK), MALS (Postnova Analytics, Landsberg am Lech, Germany), and RI (Postnova Analytics, Landsberg am Lech, Germany) detectors. The RI detector was purged after equilibration, and the UV and RI detectors were then zeroed. The sample injection volume was 50 μl, and the sample was run at 1.0 ml/min for 35 min. Between sample runs, blanks consisting of the same solvent without the Aβ(1-42) were loaded to ensure that the column was clean and to allow blank subtraction of the detector signals. As molecular weight standards, βPGM (monomer, 24.2 kDa), BSA (monomer, 66.5 kDa; dimer, 133.0 kDa), and blue dextran (∼2000 kDa) were used, with the molecular weight of βPGM and BSA confirmed by MALS. Data processing and estimation of sample concentration, molecular weight, and recovery were carried out in the AF2000 Control software (Postnova Analytics, Landsberg am Lech, Germany), with final data processing in GraphPad Prism version 8.3.0. Purified Aβ(1-42) was collected on ice between 15.7 min and 16.7 min after injection, corresponding to an elution time of 14.0 min to 15.0 min; the detector volume (1.7 ml) was determined by flowing blue dextran through the detectors. Eluted Aβ was mixed and split into three aliquots; these were then diluted to 60%, 80%, or 100% (ie. undiluted) their concentration in the same elution buffer and supplemented with 20 μM ThT from a 2 mM stock, as described in Hellstrand *et al.* [479]. This yielded final solutions containing approximately 3.5 μM, 4.6 μM, or 5.8 μM Aβ(1-42) as determined by RI, in almost exactly 20 mM sodium phosphate (pH 8), 1 mM NaN_3, 200 μM EDTA, and 300 mM NaCl (99.0% nominal concentration), with exactly 20 μM ThT. The pH of these samples was confirmed experimentally. Due to the potential for ThT to interact with the column, ThT had to be added from a concentrated stock after purification; the slight dilution of the buffer due to addition of 1% ThT is too small to significantly affect the kinetics. Purified Aβ(1-42) was then used immediately in ThT assays, as described in Section 2.5; exact Aβ(1-42) concentrations accounting for all dilutions were calculated retrospectively from the RI quantitation data, after the start of the ThT experiment. All SEC and SEC-ThT methods are based on

the protocol described by Hellstrand *et al.* [479]. The identity of the monomer peak was verified by MALS and comparison of its K_{av} value with that of the standards, with K_{av} values calculated as described in Section 2.8.

5.2.5 Circular dichroism (CD) spectroscopy

CD spectroscopy was coupled to ThT assays; except where otherwise specified, ThT assays were carried out as described in Section 2.5 and CD was carried out as described in Section 2.6, with full details of the experimental parameters given in those sections. Moderate-sized ThT assays were set up, with up to 20 replicate wells each containing 100 μl of the same reaction mixture, which was 10 μM Aβ(1-42) in a 20 mM sodium phosphate buffer with 1 mM NaN_3, 200 μM EDTA, 20 μM ThT, and either 0 mM NaF ($I = 59$ mM) or 300 mM NaF ($I = 360$ mM). Periodically, the plate reader was opened between reads and the contents of 2-3 wells were quickly extracted, taking care not to allow significant cooling of the plate or otherwise disrupt the experiment. The contents of the wells were mixed gently before aspiration, and were combined in an Eppendorf tube after extraction, where they were again mixed gently. The combined mixture was pipetted into a freshly cleaned quartz cuvette and CD spectra were recorded at 37°C in a JASCO J-810 (JASCO, UK) spectropolarimeter, as described in Section 2.6. For each experiment, the blank was exactly the same as the fibrillisation buffer, but without Aβ(1-42). Control experiments without ThT were performed, both with and without 10 μM Aβ(1-42), and confirmed that ThT did not affect the peptide's secondary structure. The ThT curves shown in Fig. 5.24(c-d) include the replicate wells from which samples were extracted for CD, with the fluorescence intensities of those wells truncated after the extraction time; therefore, the data in Fig. 5.24 show the CD spectra and ThT fluorescence intensities of the exact same fibrillisation reactions. The secondary structure content of CD spectra was estimated using the CAPITO web server [547]. For the time points for which secondary structure content was discussed (0 s, 280 s, or 1600 s, in the presence of 300 mM NaF), the estimated helical content ranged from 0-4%, and the estimated β-strand content ranged from 35-42%. This variation appeared to be more due to experimental noise in the spectra than an actual trend in secondary structure development, with the spectra remaining approximately the same throughout this time range; therefore, a single approximate value was reported.

5.2.6 Calculation of ionic strengths

Ionic strengths were calculated from the expression

$$I = \frac{1}{2}\sum_i c_i z_i^2, \tag{5.10}$$

where the summation is performed over all ions present in solution, c_i is the molar concentration of each ion, and z_i is the charge number of the ion. Sodium phosphate, NaN_3, EDTA salts, ThT:Cl, and halide salts were assumed to dissociate completely. The relative quantities of EDTA and phosphate anions were modelled using the Henderson-Hasselbalch equation [480]. EDTA was modelled as a ternary mixture of Na_2H_2EDTA, Na_3HEDTA, and Na_4EDTA, with $pK_3 = 6.16$ and $pK_4 = 10.26$ [548], with the effect of ionic strength on the protonation of EDTA neglected for simplicity. Sodium phosphate was modelled as a binary mixture of NaH_2PO_4 and Na_2HPO_4, with an ionic strength-dependent $pK_{2,app}$ given by the semi-empirical relation [481]

$$pK_{2,app} = pK_2 - \frac{1.5\sqrt{I}}{1+1.5\sqrt{I}} + K_s I, \tag{5.11}$$

where $pK_2 = 7.20$, the first term in the correction accounts for the changing activity of the anions according to Debye-Hückel theory [549], and the second term is an empirical correction valid for ionic strengths up to at least ~ 4 M, with the linear coefficient $K_s = 0.1\ \mathrm{M}^{-1}$ [481]. Since $pK_{2,app}$ depends non-linearly on I, and *vice versa*, both values were solved iteratively to fifth order. For presentation in the text, ionic strengths were rounded to the nearest 1 mM; for data analysis, they were rounded to the nearest 10 μM.

5.2.7 Mathematical analysis of secondary oligomer concentrations

For more details of the models considered here, see Section 5.3.5. It is recommended that the working in this section be read after Sections 5.3.3-5.3.5, as it builds on the analysis presented in those sections. The solutions presented here are based on early-time kinetics, obtained by making the approximation $m(t) \approx m(0)$. This means that the scaling exponent γ of a generalised progress-based characteristic time τ, which is described in greater detail below, is used as a proxy for γ_{50} and γ_{inf}, which are the scaling exponents of the half-time τ_{50} and inflection time τ_{inf}, respectively. It was not possible to obtain exact solutions for τ_{50} and τ_{inf} without obtaining approximate solutions for aggregate mass accumulation throughout the entire self-assembly time course. However, this is highly involved and entails an unnecessary level of detail for this analysis, particularly in the case of the fourth model, where the larger system of differential equations would require an unusually large number of rounds of fixed-point analysis to obtain an approximation that works well over the entire time course. Instead, both γ_{50} and γ_{inf} can be approximated by the scaling exponent of the characteristic time required for the early-time asymptote of the aggregate mass to reach some fixed proportion of $m(0)$, defined as the time τ such that

$$M_T(\tau) = \alpha m(0), \tag{5.12}$$

where $M_T(t)$ is the early-time approximation of the total aggregate mass, whether fibril or oligomer, and α is an arbitrary proportion of $m(0)$. For example, setting $\alpha = 0.5$ gives an approximation of the half-time, and setting $\alpha = 0.1$ gives an approximation of the tenth-time. The generalised concentration-dependence is

$$\gamma = -\frac{\partial \ln \tau}{\partial \ln m(0)}, \tag{5.13}$$

and is usually similar over a broad range of values of α. While progressively increasing α causes approximations of the characteristic times to become less accurate, as the effects of monomer depletion become more relevant, estimates of γ remain close to those obtained from the exact solutions, even for the half-time [3]. There are two main reasons for this. Firstly, the early-time asymptote provides an upper bound for the exact solution, so that both must exhibit identical scaling in at least one of the limits. Secondly, biopolymer self-assembly curves that differ only in $m(0)$ are generally highly self-similar, having a similar or in some cases identical curve shape when re-scaled along the time axis [442, 465]. This means that the ratio of an actual progress-based characteristic time to that calculated from the early-time asymptote remains constant or relatively unchanged over a range of $m(0)$ values; as a result, the scaling exponent is either the same or very close. Although τ_{inf} is not calculated as a progress-based characteristic time like τ_{50}, it has been shown repeatedly across numerous different models of nucleated polymerisation [1, 3, 4, 381, 425, 465, 550] that τ_{inf} exhibits the same basic scaling behaviour as the corresponding progress-based characteristic times, subject to minor (usually logarithmic) corrections that disappear in the limits [1, 3, 381]. As before, this is partly because the exact solution is bounded by the early-time asymptote, which also restricts the points at which inflection can occur, and partly a result of the inherent self-similarity of biopolymer self-assembly curves [442, 465]. In addition, it is interesting to note that for most models τ_{inf} is either exactly or almost equal to τ determined from the early-time asymptote, for some value of α. For example, for the Oosawa model $\tau_{\text{inf}} \equiv \tau|_{\alpha=1/2}$ [3, 425], and for models dominated by fragmentation $\tau_{\text{inf}} \approx \tau_{\alpha=1}$ [1, 3, 381, 550]. The above findings are applicable to the models presented in this section, as all four models predict a monomer depletion curve that is functionally either identical or asymptotically the same as that predicted by existing models in the lag and early growth phase, differing only in the definitions of the macroscopic rate constants. In some cases (models one and three), the models discussed can be mapped exactly onto existing models, and in all cases the same arguments regarding boundedness and self-similarity also apply. The experimental data also exhibit a close similarity between γ_{50} and γ_{inf} in all cases (see Section 5.3.5).

5.2.7.1 Off-pathway oligomers with a short lifetime

In this model, oligomers are off-pathway, are produced by a fibril-dependent process with pseudo-first-order rate constant k'_g, and disassemble with the effective first-order rate constant k'_d. Oligomer generation

is treated as first-order as it is proposed to operate a mechanism that is the same as or similar to secondary nucleation, and we are interested in conditions where secondary nucleation is saturated with respect to the monomer. Oligomer disassembly is probably a complex process, but at present is treated as a simple first-order unimolecular process, for lack of a more detailed description. The rate law is

$$\frac{dG(t)}{dt} = k'_g M(t) - k'_d G(t), \tag{5.14}$$

where $G(t)$ is the oligomer concentration. For this specific model, it is assumed that $k'_d \gg [d\ln G(t)/dt]^{-1}$, such that

$$k'_d G(t) = k'_g M(t), \tag{5.15}$$

so that

$$\frac{G(t)}{M(t)} = \frac{k'_g}{k'_d}, \tag{5.16}$$

and the oligomer mass is

$$\frac{\langle N\rangle G(t)}{M(t)} = \frac{\langle N\rangle k'_g}{k'_d}, \tag{5.17}$$

where $\langle N\rangle$ is the average size of oligomers, and is assumed to be invariant. From Eq. (1.29),

$$M(t) \sim \frac{\lambda^2 m(0)}{2\kappa^2} e^{\kappa t}, \tag{5.18}$$

so that

$$G(t) \sim \frac{\lambda^2 k'_g m(0)}{2\kappa^2 k'_d} e^{\kappa t}. \tag{5.19}$$

Given that $M_T(t) = M(t) + \langle N\rangle G(t)$,

$$M_T(t) \sim \left(1 + \frac{\langle N\rangle k'_g}{k'_d}\right) \frac{\lambda^2 m(0)}{2\kappa^2} e^{\kappa t}, \tag{5.20}$$

so that

$$\tau = \kappa^{-1}\left[\ln\frac{2\alpha\kappa^2}{\lambda^2} - \ln\left(1 + \frac{\langle N\rangle k'_g}{k'_d}\right)\right]. \tag{5.21}$$

Thus,

$$\gamma = \frac{\partial \ln\kappa}{\partial \ln m(0)} - \frac{\partial}{\partial \ln m(0)} \ln\left[\ln\frac{2\alpha\kappa^2}{\lambda^2} - \ln\left(1 + \frac{\langle N\rangle k'_g}{k'_d}\right)\right]. \tag{5.22}$$

The second term is typically small, and it is assumed that $m(0) \gg K_{M,s}$, so

$$\gamma \approx \frac{1}{2}. \tag{5.23}$$

In practice, the concentration-dependence is expected to be slightly higher than this value, due to the neglected term in Eq. (5.22). If $\alpha = 1/2$, $\kappa \approx 20\lambda$, $\langle N \rangle G(t) \approx 2M(t)$, and $\partial \log[\kappa^2/\lambda^2]/\partial \log m(0) = 1 - \varepsilon_c \approx 0.35$, as predicted for maximally saturated nucleation based on the analysis in Section 5.3.3, then a more precise prediction would be $\gamma \approx 0.57$.

5.2.7.2 Off-pathway oligomers with a long lifetime

This model is the same as the preceding model, except that $k'_d \ll [d \ln G(t)/dt]^{-1}$. Thus, from Eq. 5.14, it follows that

$$G(t) = k'_g \int_0^t M(t')dt'. \tag{5.24}$$

Integrating Eq. (5.18),

$$G(t) \sim \frac{\lambda^2 k'_g m(0)}{2\kappa^3} e^{\kappa t} \tag{5.25}$$

so that

$$\frac{G(t)}{M(t)} = \frac{k'_g}{\kappa}, \tag{5.26}$$

and

$$\frac{\langle N \rangle G(t)}{M(t)} = \frac{\langle N \rangle k'_g}{\kappa}, \tag{5.27}$$

Given that $M_T(t) = M(t) + \langle N \rangle G(t)$,

$$M_T(t) \sim \left(1 + \frac{\langle N \rangle k'_g}{\kappa}\right) \frac{\lambda^2 m(0)}{2\kappa^2} e^{\kappa t}, \tag{5.28}$$

so that

$$\tau = \kappa^{-1} \left[\ln \frac{2\alpha\kappa^2}{\lambda^2} - \ln \left(1 + \frac{\langle N \rangle k'_g}{\kappa}\right) \right]. \tag{5.29}$$

Thus,

$$\gamma = \frac{\partial \ln \kappa}{\partial \ln m(0)} - \frac{\partial}{\partial \ln m(0)} \ln \left[\ln \frac{2\alpha\kappa^2}{\lambda^2} - \ln \left(1 + \frac{\langle N \rangle k'_g}{\kappa}\right) \right]. \tag{5.30}$$

Neglecting the second term, which is likely to be small,

$$\gamma \approx \frac{1}{2}. \tag{5.31}$$

As before, the concentration-dependence is actually expected to be slightly higher than this value, due to the neglected term in Eq. (5.30). If $\alpha = 1/2$, $\kappa \approx 20\lambda$, $\langle N \rangle G(t) \approx 2M(t)$, and $\partial \log[\kappa^2/\lambda^2]/\partial \log m(0) = 1 - \varepsilon_c \approx 0.35$, as predicted for maximally saturated nucleation based on the analysis in Section 5.3.3, then a more precise prediction would be $\gamma \approx 0.64$.

5.2.7.3 On-pathway oligomers with a short lifetime

In this model, oligomers are on-pathway, are produced by a fibril-dependent process with pseudo-first-order rate constant k'_g, disassemble with the effective first-order rate constant k'_d, and convert to fibrils with the effective first-order rate constant k'_c. The rate law is

$$\frac{dG(t)}{dt} = k'_0 m(t)^{\varepsilon_c} + k'_g M(t) - (k'_d + k'_c)G(t), \tag{5.32}$$

where k'_0 is the effective $\varepsilon_c^{\text{th}}$-order rate constant for primary oligomer generation, and ε_c is the effective rate order of primary oligomer generation under conditions of maximal saturation, as determined in Section 5.3.3. By the growth phase, $k'_g M(t) \gg k'_0 m(t)^{\varepsilon_c}$, and it is assumed that $k'_d \gg [d\ln G(t)/dt]^{-1}$ and $k'_d \gg k'_c$, so Eq. (5.15) still applies, as do the results that come with it. As discussed in Section 5.3.5, k_n and k_s can be re-expressed in terms of k'_0 and k'_g. Since $G(t)$ varies rapidly with $k'_0 m(t)^{\varepsilon_c}$ and $k'_g M(t)$, a steady-state approximation can be made for the nucleation rates,

$$\Phi_n(t) = \frac{k'_0 k'_c m(t)^{\varepsilon_c}}{k'_c + k'_d}, \tag{5.33}$$

$$\Phi_s(t) = \frac{k'_g k'_c M(t)}{k'_c + k'_d}. \tag{5.34}$$

Equating these expressions with Eq. (5.56) and Eq. (1.45), the rate laws ultimately favoured in Section 5.3.3, gives Eq. (5.65-5.66) in the saturating limit. This does not affect the results of the analysis.

5.2.7.4 On-pathway oligomers with a long lifetime

This model is the same as the preceding model, except that $k'_d \ll [d\ln G(t)/dt]^{-1}$. This means that $G(t)$ does not vary rapidly with $k'_0 m(t)^{\varepsilon_c}$ and $k'_g M(t)$, so a steady-state approximation cannot be made for primary and secondary nucleation. Instead,

$$\frac{dG(t)}{dt} = k'_0 m(t)^{\varepsilon_c} + k'_g M(t) - k'_c G(t), \tag{5.35}$$

$$\frac{dP(t)}{dt} = k'_c G(t), \tag{5.36}$$

$$\frac{dM(t)}{dt} = \langle N \rangle k'_c G(t) + 2k_e^+ m(t) P(t), \tag{5.37}$$

where dissociation of monomers from fibril ends is neglected. Conversion is usually a slow process, so it is reasonable to assume that $k'_c \ll [d\ln G(t)/dt]^{-1}$. In addition, the NS-EM data indicate that elongation is the main mechanism of fibril mass gain, so $\langle N \rangle k'_c G(t) \ll 2k_e^+ m(t) P(t)$. Thus, in the early time such that

$m(t) \approx m(0)$,

$$\frac{dG(t)}{dt} \approx k_0' m(0)^{\varepsilon_c} + k_g' M(t), \tag{5.38}$$

$$\frac{dM(t)}{dt} \approx 2k_e^+ m(0) P(t), \tag{5.39}$$

so that

$$\frac{d^3 G(t)}{dt^3} \approx \kappa^3 G(t), \tag{5.40}$$

where $\kappa = \left[2k_g' k_c' k_e^+ m(0)\right]^{1/3}$, and the boundary conditions are

$$G(0) = 0, \tag{5.41}$$

$$\frac{dG(t)}{dt}|_{t=0} = k_0' m(0)^{\varepsilon_c}, \tag{5.42}$$

$$\frac{d^2 G(t)}{dt^2}|_{t=0} = 0. \tag{5.43}$$

Solving Eq. (5.40) for the boundary conditions gives the result

$$G(t) = \sum_{n=0}^{\infty} \frac{k_0' m(0)^{\varepsilon_c} \kappa^{3n} t^{3n+1}}{(3n+1)!}. \tag{5.44}$$

Applying Eq. (5.36),

$$P(t) = \sum_{n=0}^{\infty} \frac{k_0' k_c' m(0)^{\varepsilon_c} \kappa^{3n} t^{3n+2}}{(3n+2)!}. \tag{5.45}$$

and applying Eq. (5.39),

$$M(t) = \sum_{n=0}^{\infty} \frac{2k_0' k_c' k_e^+ m(0)^{\varepsilon_c+1} \kappa^{3n} t^{3n+3}}{(3n+3)!}. \tag{5.46}$$

Asymptotically,

$$G(t) \sim \frac{k_0' m(0)^{\varepsilon_c}}{3\kappa} e^{\kappa t}, \tag{5.47}$$

$$P(t) \sim \frac{k_0' k_c' m(0)^{\varepsilon_c}}{3\kappa^2} e^{\kappa t}, \tag{5.48}$$

$$M(t) \sim \frac{2k_0' k_c' k_e^+ m(0)^{\varepsilon_c+1}}{3\kappa^3} e^{\kappa t}. \tag{5.49}$$

Thus,

$$\frac{\langle N \rangle G(t)}{M(t)} \approx \frac{\langle N \rangle \kappa^2}{2k_c' k_e^+ m(0)} = \langle N \rangle \left[\frac{(k_g')^2}{2k_c' k_e^+ m(0)}\right]^{1/3}, \tag{5.50}$$

and

$$M_T(t) \sim \left(\frac{2k_c' k_e^+ m(0)}{\kappa^2} + \langle N \rangle\right) \frac{k_0' m(0)^{\varepsilon_c}}{3\kappa} e^{\kappa t}. \tag{5.51}$$

Applying Eq. (5.12),

$$\tau = \kappa^{-1}\left[\ln\frac{3\alpha\kappa m(0)}{k_0' m(0)^{\varepsilon_c}} - \ln\left(\frac{2k_c' k_e^+ m(0)}{\kappa^2} + \langle N\rangle\right)\right]. \tag{5.52}$$

Thus,

$$\gamma = \frac{\partial \ln\kappa}{\partial \ln m(0)} - \frac{\partial}{\partial \ln m(0)}\ln\left[\ln\frac{3\alpha\kappa m(0)}{k_0' m(0)^{\varepsilon_c}} - \ln\left(\frac{2k_c' k_e^+ m(0)}{\kappa^2} + \langle N\rangle\right)\right]. \tag{5.53}$$

Neglecting the second term, which is likely to be small,

$$\gamma \approx \frac{1}{3}. \tag{5.54}$$

As before, the concentration-dependence is actually expected to be slightly higher than this value, due to the neglected term in Eq. (5.53). It is hard to estimate the scale of this correction without precise measurements of k_0' and k_c'; however, it is likely to similar to that required for the other models examined in this section. It is noted that Miclaels *et al.* [469] recently, independently, proposed a similar mathematical model to the above. However, the precise details of the model differ, and the reaction orders and rate constants fitted by Michaels *et al.* [469] would not fit the data presented in this chapter, or produce the appropriate scaling behaviours in the limits.

5.2.8 Nonlinear regression and numerical modelling

Analytical models were fitted in GraphPad Prism 8 using Levenberg-Marquardt least squares fitting. When fitting τ_{50}, τ_{lag}, τ_{inf}, and $\nu_{\max}$, whose error is expected to scale with the mean, residuals were weighted relative to the square of the mean. AICc values were calculated using Eq. (3.24), and the likelihood of each model was proportional to $\exp(-\text{AICc}/2)$.

5.3 Results and discussion

5.3.1 Aβ(1-42) self-assembly depends on the ionic strength

Investigation of the salt-dependence of Aβ(1-42) self-assembly was stimulated by the observation that higher salt concentrations result in more rapid assembly kinetics. For example, Fig. 5.1 shows representative self-assembly kinetics of 4 μM Aβ(1-42) in a 20 mM sodium phosphate buffer (pH 8) containing varying concentrations of NaCl. While the half-time is around 7500 s in the absence of NaCl (ionic strength $I = 59$ mM), the addition of 50 mM NaCl ($I = 109$ mM) causes an almost twofold reduction in half-time to around 4500 s, and the half-time is reduced almost twofold again in the presence of 300 mM NaCl ($I = 360$ mM). Since the ionic strengths of CSF (at least 160 mM) and most common experimental buffers (up to 300 mM in this lab) are above the range at which Aβ(1-42) fibrillisation is best characterised

($I \approx 60$ mM), and existing studies provide an incomplete understanding of the manner in which salts affect Aβ(1-42) fibrillisation (see Section 5.1), this effect was investigated in greater detail. Although previous studies have investigated the effect of ionic strength alone on Aβ(1-42) fibrillisation [5, 428], electroselectivity and Hofmeister effects have also been reported in the self-assembly of other amyloids, even at low concentrations (10 mM; [543]). Therefore, to determine whether the main cause of the observed phenomenon was ionic strength, Hofmeister effects, or specific interactions, fibrillisation experiments were carried out with 2 μM Aβ(1-42) in a 10 mM sodium phosphate buffer (pH 8) containing varying concentrations of the halide salts NaF, NaCl, and NaI; the lower sodium phosphate concentration was used to allow examination of a broader range of ionic strengths. These three halide salts make the same contribution to the ionic strength, but lie in different positions in the Hofmeister and electroselectivity series, meaning that equivalent concentrations of the salts would be expected to have distinct effects on the self-assembly process if either of these series were important at the concentrations investigated. According to the Hofmeister series, F^- ions should be most kosmotropic, reducing the solubility of Aβ(1-42) and promoting order, while I^- ions should be most chaotropic, solubilising the peptide and promoting disorder, and Cl^- ions should occupy an intermediate position [551, 552]. Alternatively, the same ions have approximately the same sequence in the electroselectivity series, which describes the strength of anion binding to ion exchange resins [553,554], and has been shown to describe the effects of various salts on glucagon and PrP fibrillisation [544, 545]. If the effect of salts is electroselective, I^- would be expected to bind most tightly and would either accelerate or retard fibrillisation at the lowest concentrations, while Cl^- would bind at intermediate concentrations, and F^- would bind most weakly. While a simple ionic strength effect would implicate electrostatic screening as the mechanism by which salts alter fibrillisation, a Hofmeister effect would implicate a variety of salt-peptide-water interactions, and an electroselective effect would point to specific interactions between anions and positively charged sidechains or the N-terminus.

The self-assembly kinetics of Aβ(1-42) in the presence of varying concentrations of halide salts are presented in Fig. 5.2. Up to a concentration of $\sim$80 mM, NaF, NaCl, and NaI all have approximately the same effect. Despite a systematic variation in the fibrillisation rate between the three datasets, due to the fact that the three datasets were acquired separately over the course of several months, with different Aβ(1-42) preparations, buffer stocks, and batches of microplates, the relative decrease in fibrillisation half-time shows the same pattern for all three salts. At higher salt concentrations, NaF and NaCl continue to produce the same effect, with the fibrillisation half-time decreasing monotonically with the salt concentration. NaI produces a distinct effect; the half-time remains approximately constant above $\sim$150 mM NaI, and the self-assembly kinetics become much more variable than at lower concentrations. This result indicates that the halide salts all cause a general enhancement of the fibrillisation rate via charge screening, but there is a competing inhibitory effect at $[I^-] \gtrapprox 100$ mM, which is more stochastic or more sensitive to variation in

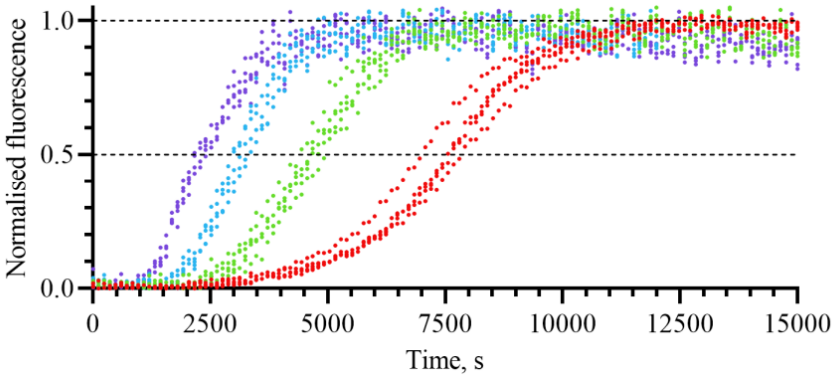

Figure 5.1: Salt accelerates Aβ(1-42) self-assembly. Data points show the normalised fluorescence intensities from representative ThT experiments performed at different concentrations of NaCl. All experiments had 4 μM Aβ(1-42) in a 20 mM sodium phosphate buffer (pH 8) with 1 mM NaN_3, 200 μM EDTA, and 20 μM ThT, at 37°C. The colour corresponds to the NaCl concentration and ionic strength: red, 0 mM NaCl ($I = 59$ mM); green, 50 mM NaCl ($I = 109$ mM); cyan, 100 mM NaCl ($I = 160$ mM); indigo, 300 mM NaCl ($I = 360$ mM).

experimental conditions. While it is possible that oxidation of I^- could result in small quantities of I_2 and I_3^-, precautions were taken to avoid this (Section 2.4.7), and visible browning of the solutions was not observed; therefore, the inhibitory effect is most likely due to I^- itself. The lack of a difference between NaF and NaCl suggests that the inhibitory effect is due to specific I^-:Aβ(1-42) binding rather than a Hofmeister effect, as I^- is typically the most electroselective of the three halide anions that were tested, while F^- and Cl^- might not interact to a significant extent over the concentration range used in these experiments. Nonetheless, since inhibition of fibrillisation is consistent with the expected behaviour of a chaotrope, a Hofmeister effect cannot be ruled out based on the present data, and might be further investigated by the use of a discriminatory anion such as SO_4^{2-}, which is both kosmotropic and highly electroselective [544, 552, 554].

Despite the inhibitory effect observed for NaI, the fact that NaF and NaCl affect the self-assembly kinetics in almost exactly the same way indicates that screening is the general cause of the increase in assembly rate, rather than changes in solvation. In support of this, the 10 mM and 20 mM sodium phosphate buffers produce almost exactly the same kinetics when one corrects for the difference in ionic strength due to the differing concentrations of phosphate and azide (Fig. 5.3). Thus, at sufficiently low concentrations, the effects of $H_2PO_4^-$, HPO_4^{2-}, N_3^-, F^-, and Cl^- are approximately interchangeable so long as the ionic strength remains constant, allowing the buffer composition to be modified to suit the experimental requirements without altering the underlying aggregation mechanism. This is useful as different buffers and salts are suitable for different experiments. For example, while 10 mM sodium phosphate allows investigation of self-assembly at low ionic strengths (and concentrations as low as 4 mM have been used in other studies [5]), and is also preferable for NS-EM as sodium phosphate reacts with uranyl formate stain, its poor buffering

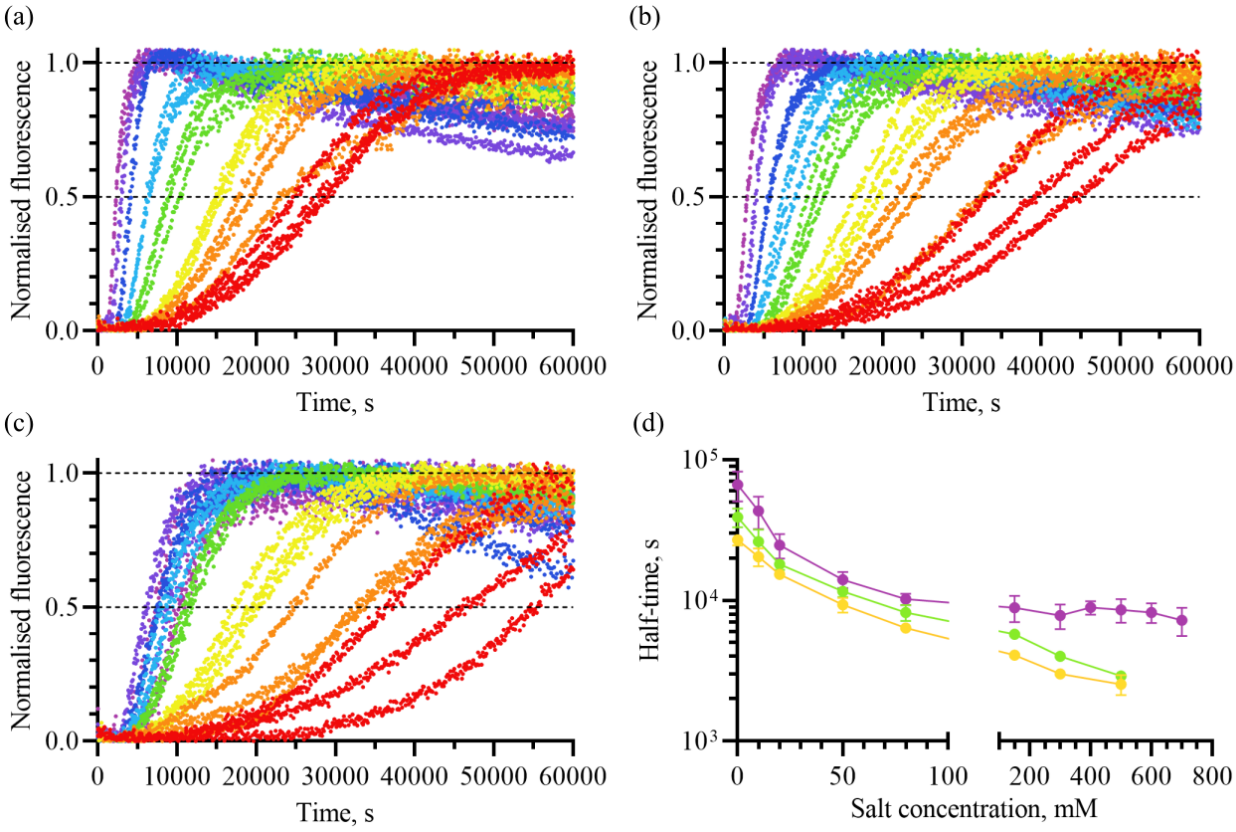

Figure 5.2: Ionic strength, Hofmeister, and electroselectivity effects on Aβ(1-42) self-assembly. Panels (a-c) show representative experiments investigating the effects of varying concentrations of (a) NaF, (b) NaCl, and (c) NaI on the self-assembly kinetics of 2 μM Aβ(1-42), in a 10 mM sodium phosphate buffer (pH 8) with 200 μM NaN_3, 200 μM EDTA, and 20 μM ThT, at 37°C. The colour in panels (a-c) corresponds to the halide salt concentration and ionic strength: red, 0 mM salt ($I = 30$ mM); orange, 10 mM salt ($I = 40$ mM); yellow, 20 mM salt ($I = 50$ mM); green, 50 mM salt ($I = 80$ mM); cyan, 80 mM salt ($I = 110$ mM); blue, 150 mM salt ($I = 180$ mM); indigo, 300 mM salt ($I = 330$ mM); violet, 500 mM salt ($I = 530$ mM). Panel (d) shows the relationship between salt concentration and the mean ThT half-time across all such experiments, with the colour corresponding to the salt whose concentration is being varied: yellow, NaF; green, NaCl; purple, NaI. As discussed in the text, the variation in the 0 mM data points is due to systematic experimental variation independent of salt concentration. Error bars represent a single standard deviation.

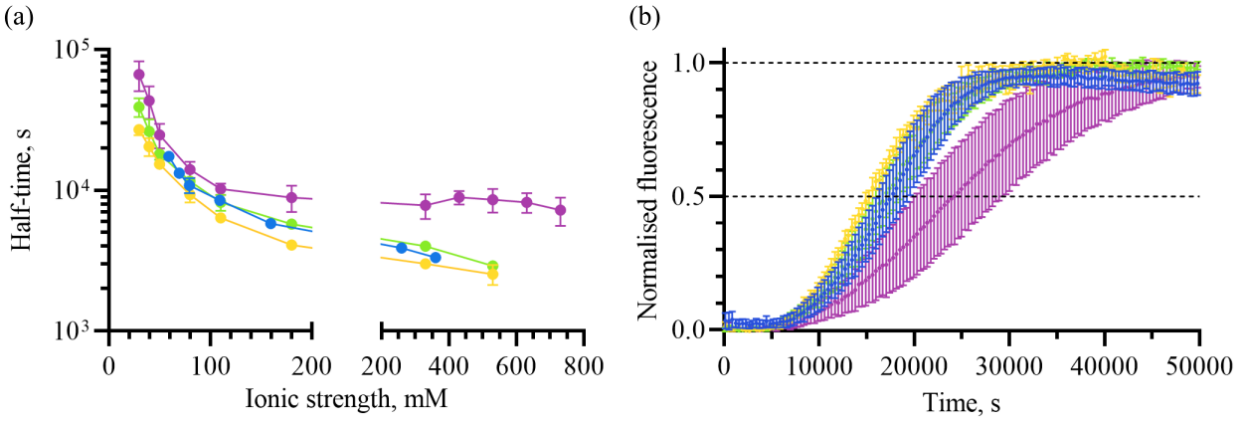

Figure 5.3: Ionic strength is the main determinant of salt-dependent Aβ(1-42) self-assembly kinetics. (a) The relationship between ionic strength and the mean self-assembly half-time of 2 μM Aβ(1-42) at 37°C, from all relevant ThT experiments. The colour scheme corresponds to the buffer used to obtain the data series: yellow, 10 mM sodium phosphate (pH 8) with varying NaF; green, 10 mM sodium phosphate (pH 8) with varying NaCl; purple, 10 mM sodium phosphate (pH 8) with varying NaI; blue, 20 mM sodium phosphate (pH 8) with varying NaCl. (b) The average fluorescence intensity of all relevant ThT curves at ionic strength $I \approx 50$ mM. The colour scheme corresponds to specific salt concentrations from the data series in panel (a): yellow, 10 mM sodium phosphate (pH 8) with 20 mM NaF ($I = 50$ mM); green, 10 mM sodium phosphate (pH 8) with 20 mM NaCl ($I = 50$ mM); purple, 10 mM sodium phosphate (pH 8) with 20 mM NaI ($I = 50$ mM); blue, 20 mM sodium phosphate with no additional salt ($I = 59$ mM). Note that the green and blue curves overlap almost exactly, so that the former are mostly obscured by the latter. All experimental buffers contained 1 mM NaN_3 (or 200 μM in 10 mM sodium phosphate buffers), 200 μM EDTA, and 20 μM ThT, which made a small additional contribution to the ionic strength that has been accounted for in the calculations. Error bars represent a single standard deviation.

capacity at pH 8 makes it difficult to work with, so higher phosphate concentrations are preferable for more regular use. Similarly, while NaF is usually more restrictive due to the reactivity of the F^- ion, it is preferable for CD experiments as the Cl^- ion absorbs in the far UV region.

5.3.2 Ionic strength affects Aβ(1-42) fibril polymorphism

In order to characterise the effect of ionic strength on the polymorphism and length distribution of amyloid fibrils, samples were collected from ThT experiments with 2 μM Aβ(1-42) in a buffer containing 10 mM sodium phosphate (pH 8), 200 μM NaN_3, 200 μM EDTA, 20 μM ThT, and varying concentrations of NaCl, and imaged by NS-EM. Representative NS-EM images from experiments with 0 mM NaCl ($I =$ 30 mM), 50 mM NaCl ($I = 80$ mM), and 500 mM NaCl ($I = 530$ mM) are shown in Fig. 5.4-5.5, Fig. 5.6-5.7, and Fig. 5.8-5.9, respectively. While the first of each of these pairs of figures shows samples taken at the ThT half-time, the second shows samples taken at the end of the ThT growth phase. In addition, images were collected for experiments with 10 mM NaCl ($I = 40$ mM), but are not shown as they were broadly

similar to experiments with 0 mM NaCl ($I = 30$ mM), with minor exceptions that will be discussed in the next paragraph.

At 0 mM NaCl ($I = 30$ mM), fibrils were by far the most common form of aggregate, and there was little evidence of oligomers or other prefibrillar aggregates. The majority of fibrils had either a twisted ribbon (Fig. 5.4(a), Fig. 5.5(a)) or tubular appearance (Fig. 5.4(b), Fig. 5.5(b)); due to the limitations of the imaging method, it is unclear whether the latter reflected truly untwisted fibrils, or simply twisted ribbons with a circular cross-section. In addition, helical species were also occasionally observed (Fig. 5.5(c)). While the polymorphism observed at this salt concentration was mostly similar to polymorphism at 10 mM NaCl ($I = 40$ mM), an occasional feature that appeared to be specific to the lower ionic strength was weakened protofilament pairing and even unwinding of the protofilaments of twisted ribbon fibrils. A partial example of this phenomenon can be seen in Fig. 5.4(c), and a more extreme case in Fig. 5.4(d); a possible case of protofilament unpairing is also shown in Fig. 5.5(d). The most likely cause of this phenomenon was electrostatic repulsion between protofilaments, as the interactions that cause protofilament pairing are typically relatively weak compared to those that stabilise subunit stacking (Section 1.3.5), and might easily be destabilised by electrostatic repulsion at low ionic strengths. Since protofilaments carry a high charge per unit length, even a small decrease in ionic strength (eg. 40 mM to 30 mM) could significantly increase this repulsion.

At 50 mM NaCl ($I = 80$ mM; Fig. 5.6-5.7), a similar variety of polymorphs was observed, although twisted ribbon fibrils appeared to be less dominant at this ionic strength. In addition, while globular oligomers were exceedingly rare at 0 mM NaCl ($I = 30$ mM), they were usually visible in well-stained areas of the grids at 50 mM NaCl ($I = 80$ mM). At 500 mM NaCl ($I = 530$ mM; Fig. 5.8-5.9), these changes in polymorphism were much more pronounced. Although there were occasional suggestions of a twisted ribbon morphology upon closer inspection of images, unambiguous twisted ribbons were rarely observed, and the majority of fibrils were shorter and less regular in appearance than those observed at lower salt concentrations. In some cases, these morphological differences may result from fibrils having a less ordered structure, or a more circular cross-section; however, the loss of obvious twist may also reflect the importance of electrostatics in inducing torsion of the protofilaments, as previously suggested by studies of β-lactoglobulin and β-endorphin [181, 200, 201]. Globular oligomers were also very abundant at this ionic strength, and they appeared to increase, rather than decrease, in abundance towards the end of the growth phase (Fig. 5.9(c-d)), suggesting that fibrillisation and oligomerisation compete with one another throughout the growth phase. Thus, there appears to be a continuous trend in the self-assembly behaviour between 0 and 500 mM NaCl, with increasing salt concentration causing less regular fibril morphologies and greater concentrations of oligomers.

To obtain a more quantitative picture of the effect of ionic strength on fibril morphology, the frequencies

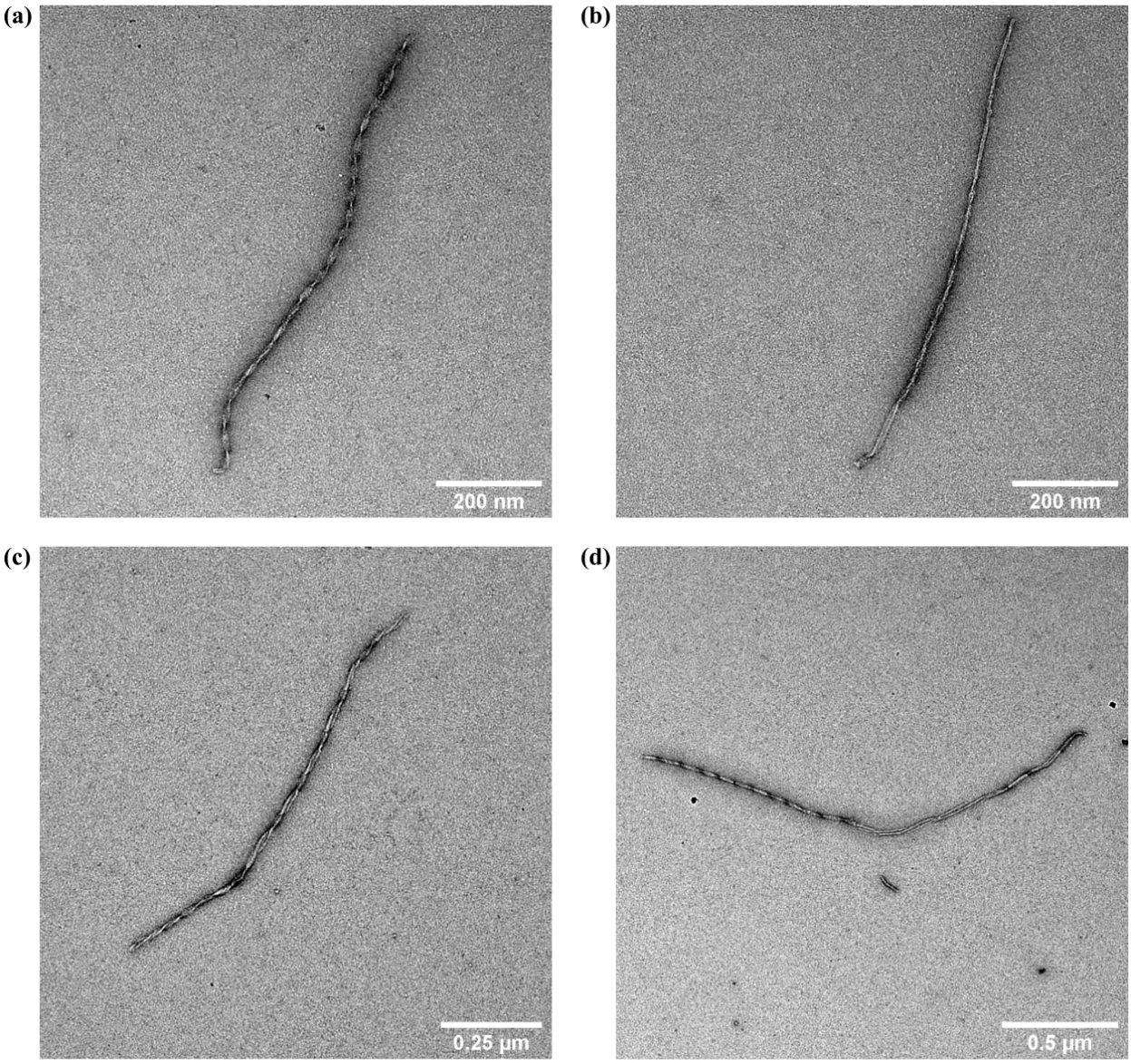

Figure 5.4: NS-EM of 2 μM Aβ(1-42) fibrillisation at an ionic strength of 30 mM (part 1). Panels (a-d) show representative images of Aβ(1-42) fibrils formed in a 10 mM sodium phosphate buffer (pH 8) containing 200 μM NaN_3, 200 μM EDTA, and 20 μM ThT, sampled at the ThT half-time.

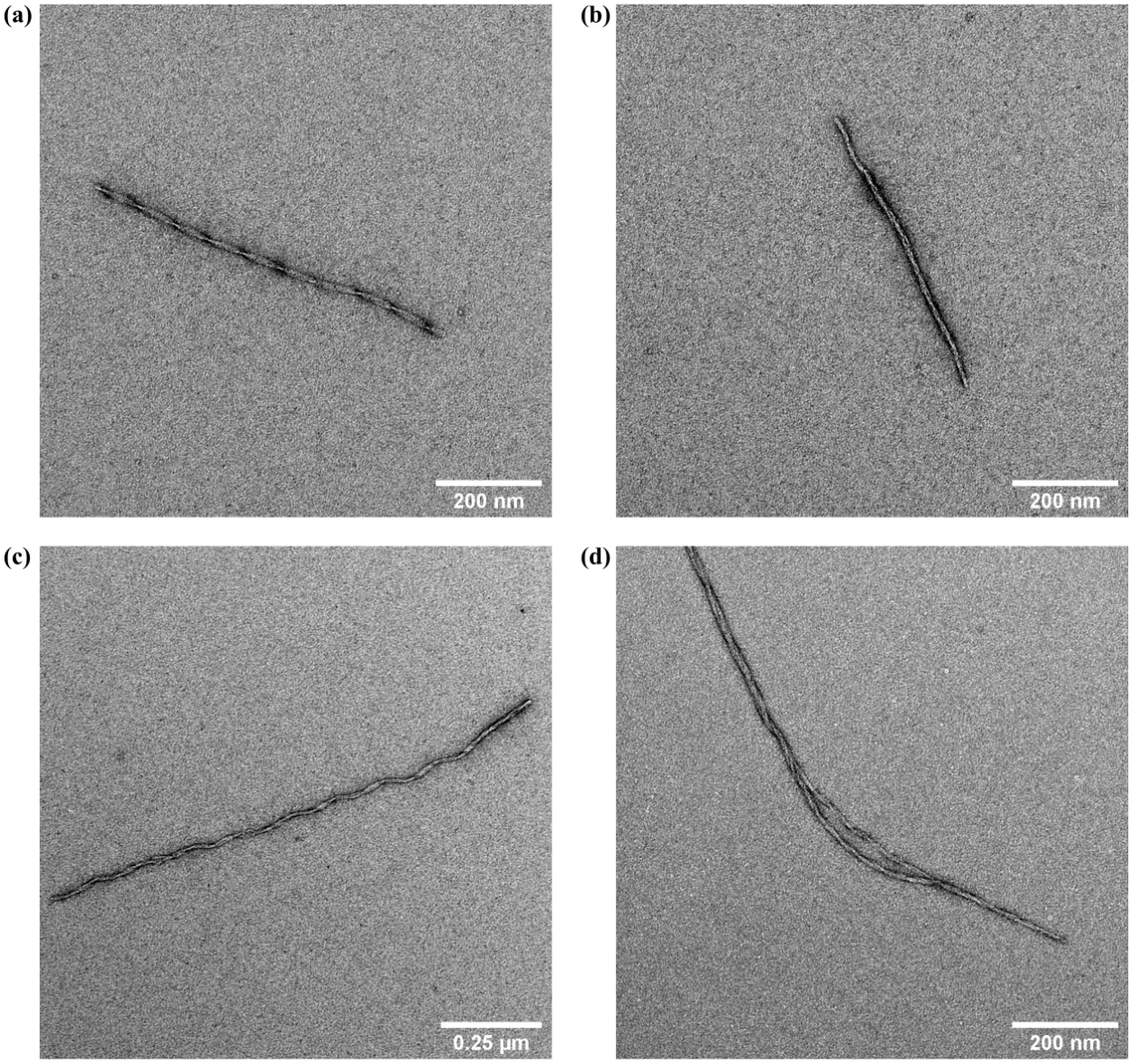

Figure 5.5: NS-EM of 2 μM Aβ(1-42) fibrillisation at an ionic strength of 30 mM (part 2). Panels (a-d) show representative images of Aβ(1-42) fibrils formed in a 10 mM sodium phosphate buffer (pH 8) containing 200 μM NaN_3, 200 μM EDTA, and 20 μM ThT, sampled at the end of the growth phase as determined by ThT fluorescence.

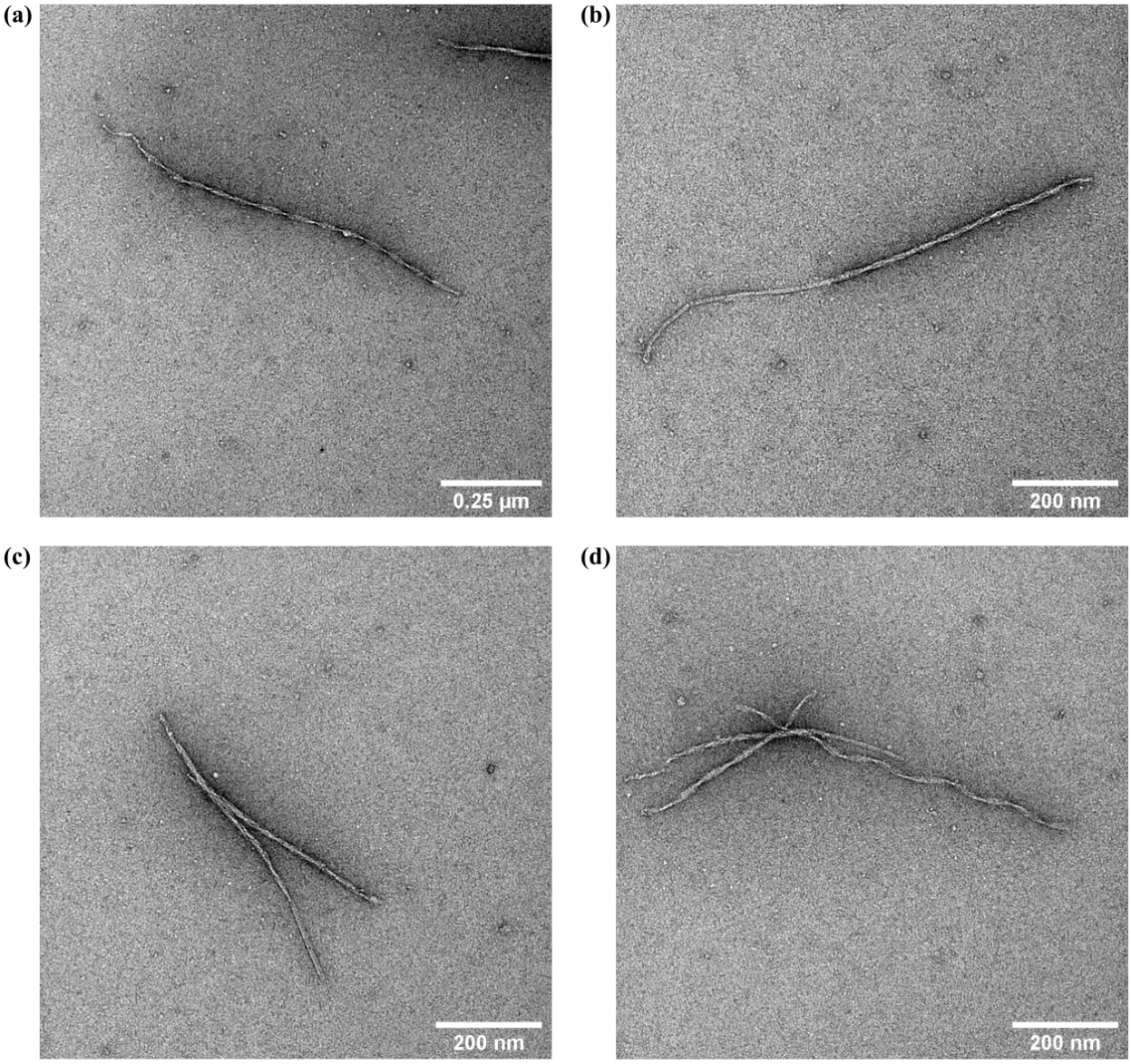

Figure 5.6: NS-EM of 2 μM Aβ(1-42) fibrillisation at an ionic strength of 80 mM (part 1). Panels (a-d) show representative images of Aβ(1-42) fibrils and oligomers formed in a 10 mM sodium phosphate buffer (pH 8) containing 200 μM NaN_3, 200 μM EDTA, 20 μM ThT, and 50 mM NaCl, sampled at the ThT half-time.

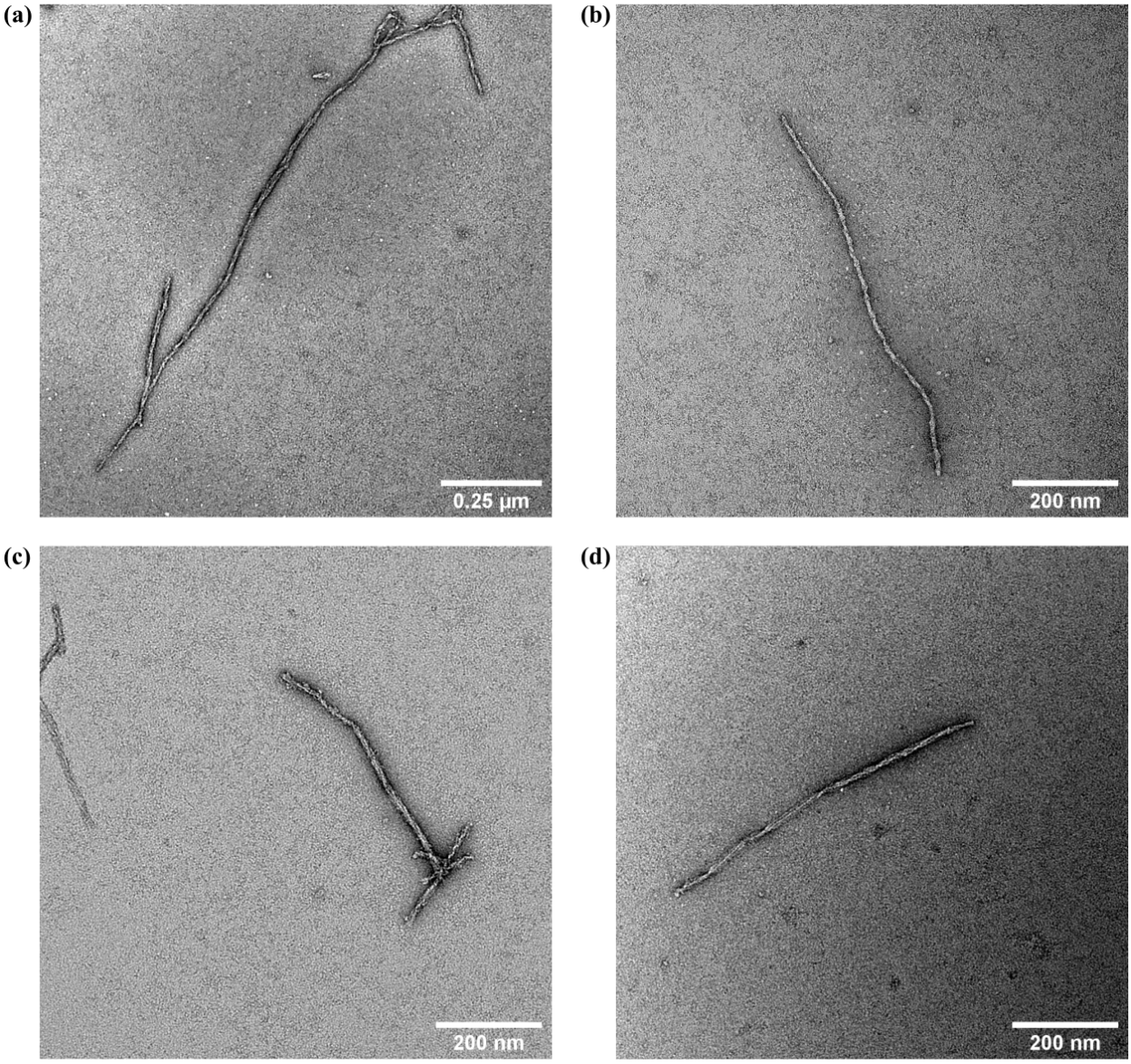

Figure 5.7: NS-EM of 2 μM Aβ(1-42) fibrillisation at an ionic strength of 80 mM (part 2). Panels (a-d) show representative images of Aβ(1-42) fibrils and oligomers formed in a 10 mM sodium phosphate buffer (pH 8) containing 200 μM NaN_3, 200 μM EDTA, 20 μM ThT, and 50 mM NaCl, sampled at the end of the growth phase as determined by ThT fluorescence.

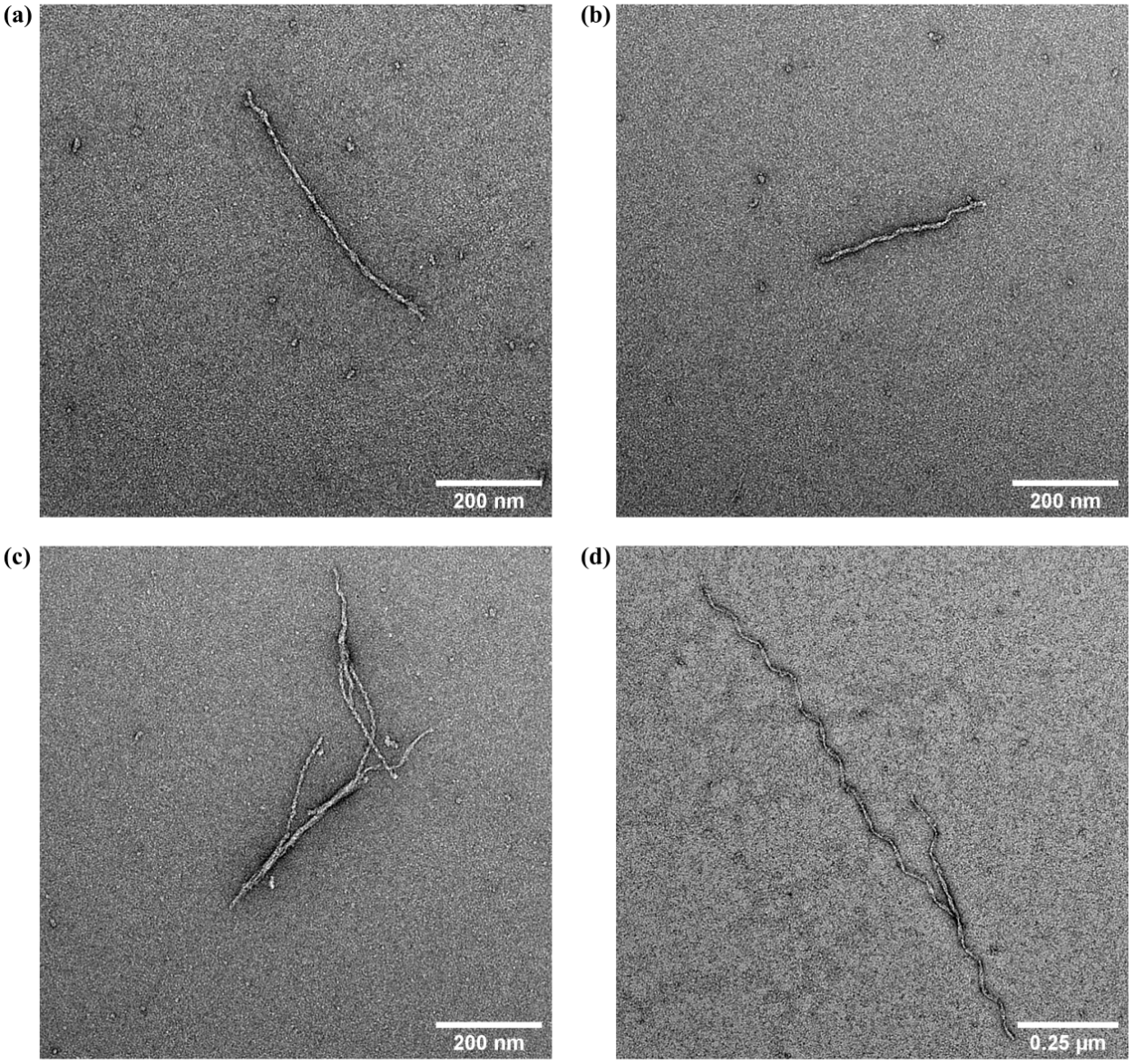

Figure 5.8: NS-EM of 2 μM Aβ(1-42) fibrillisation at an ionic strength of 530 mM (part 1). Panels (a-d) show representative images of Aβ(1-42) fibrils and oligomers formed in a 10 mM sodium phosphate buffer (pH 8) containing 200 μM NaN_3, 200 μM EDTA, 20 μM ThT, and 500 mM NaCl, sampled at the ThT half-time.

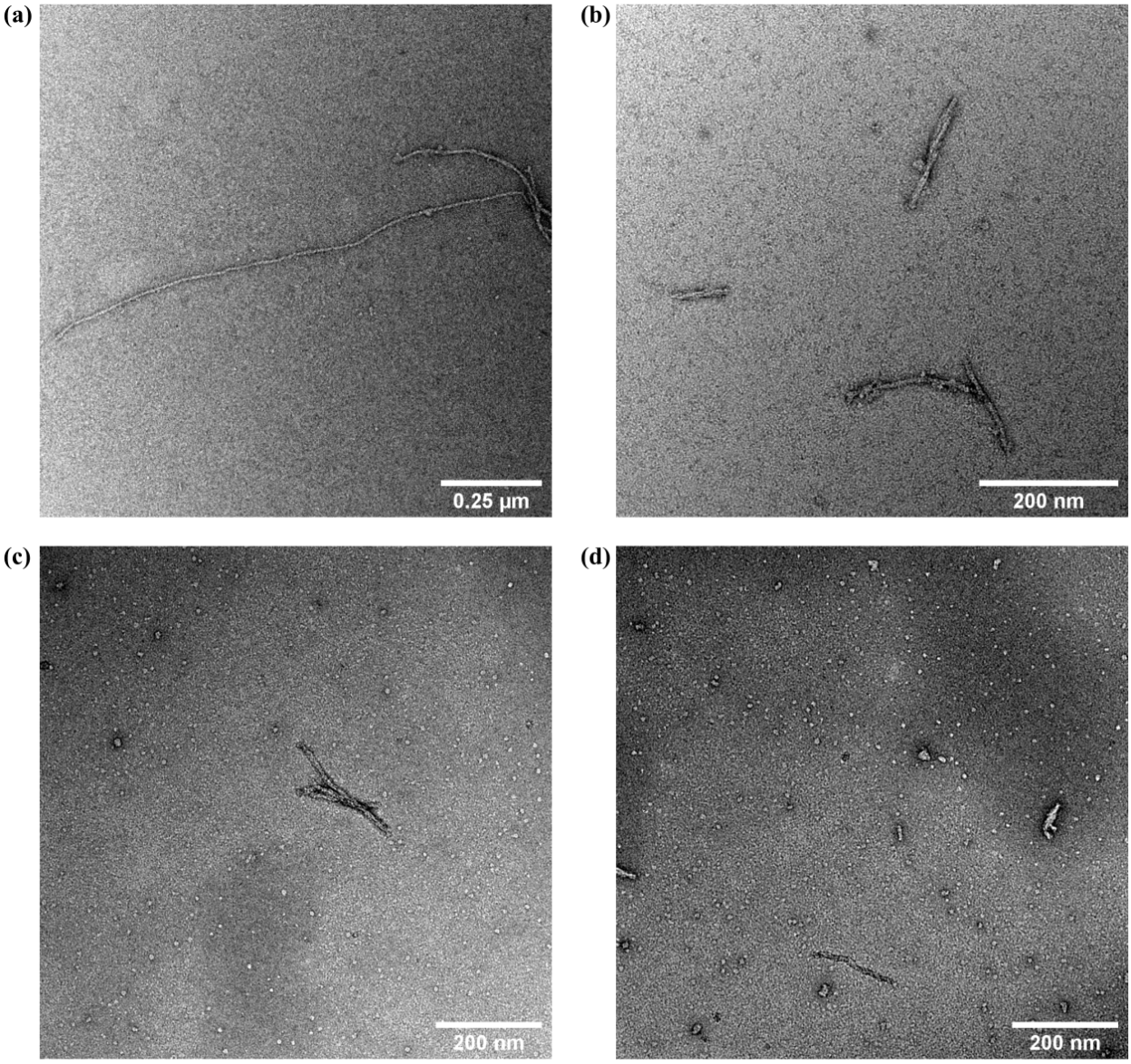

Figure 5.9: NS-EM of 2 μM Aβ(1-42) fibrillisation at an ionic strength of 530 mM (part 2). Panels (a-d) show representative images of Aβ(1-42) fibrils and oligomers formed in a 10 mM sodium phosphate buffer (pH 8) containing 200 μM NaN_3, 200 μM EDTA, 20 μM ThT, and 500 mM NaCl, sampled at the end of the growth phase as determined by ThT fluorescence.

of different polymorphs were calculated. Due to the limited resolution of the images and the high degree of fibril polymorphism, it was necessary to classify polymorphs in relatively broad terms. Therefore, fibrils were split into two classes: those with clearly defined twisted ribbon or helical morphology, and those without. Fibrils were considered to have a twisted ribbon morphology if they exhibited clear, periodic width variations along their length, indicating that they were not only twisted, but also had a non-circular cross-section. While it is possible that apparently tubular fibrils may have actually been twisted ribbons with an approximately circular cross-section, the resolution of the technique does not allow such a distinction to be made with any confidence; therefore, fibrils without periodic width variations or helical morphology were treated as members of a heterogeneous second class. As shown in Fig. 5.10(a), increasing the ionic strength caused a clear reduction in the proportion of the first class, indicating that fibrils formed at higher salt were less ordered, less twisted, had a more circular cross-section, or a combination of all three.

In addition to polymorphism, the NS-EM images were analysed to evaluate the effect of ionic strength on the fibril length distribution at different sampling times. The mean fibril lengths are shown in Fig. 5.10(b), and violin plots showing the median, quartiles, and estimated fibril length distributions are shown in Fig. 5.10(c-e). At all time points, there was an inverse correlation between the ionic strength and the mean fibril length, indicating that faster fibrillisation at high ionic strength was due to enhanced nucleation, rather than elongation. This salt-induced reduction in length is unlikely to be due to fragmentation alone, as fibrils did not show a significant decrease in length between the end of the growth phase and 10000 s after that point, indicating that fragmentation was slow on that timescale; in addition, in the ThT experiments, the maximum rate of fluorescence gain is reached close to or before the half-time (Fig. 5.1-5.2), indicating that the dominant secondary process is a high-order process such as secondary nucleation, rather than fragmentation. Therefore, in the absence of excess fragmentation, the mean fibril length is controlled by the balance between nucleation and elongation, with an increase in nucleation tending to promote the formation of larger numbers of shorter fibrils, and an increase in elongation promoting the formation of smaller numbers of longer fibrils. Thus, ionic strength affects nucleation more strongly than elongation, in agreement with the results of previous work on Aβ(M1-42) [5].

5.3.3 Quantitative analysis of the effects of ionic strength on Aβ(1-42) self-assembly

As an initial measure to evaluate the relative effects of ionic strength on primary versus secondary nucleation, lag times τ_{lag} and maximum fibrillisation rates ν_{max} were calculated for ThT curves acquired at a range of different Aβ(1-42) concentrations, as described in Section 2.5.2. When varying some other factor, in this case the initial monomer concentration $m(0)$, the τ_{lag} and ν_{max} of amyloids have previously

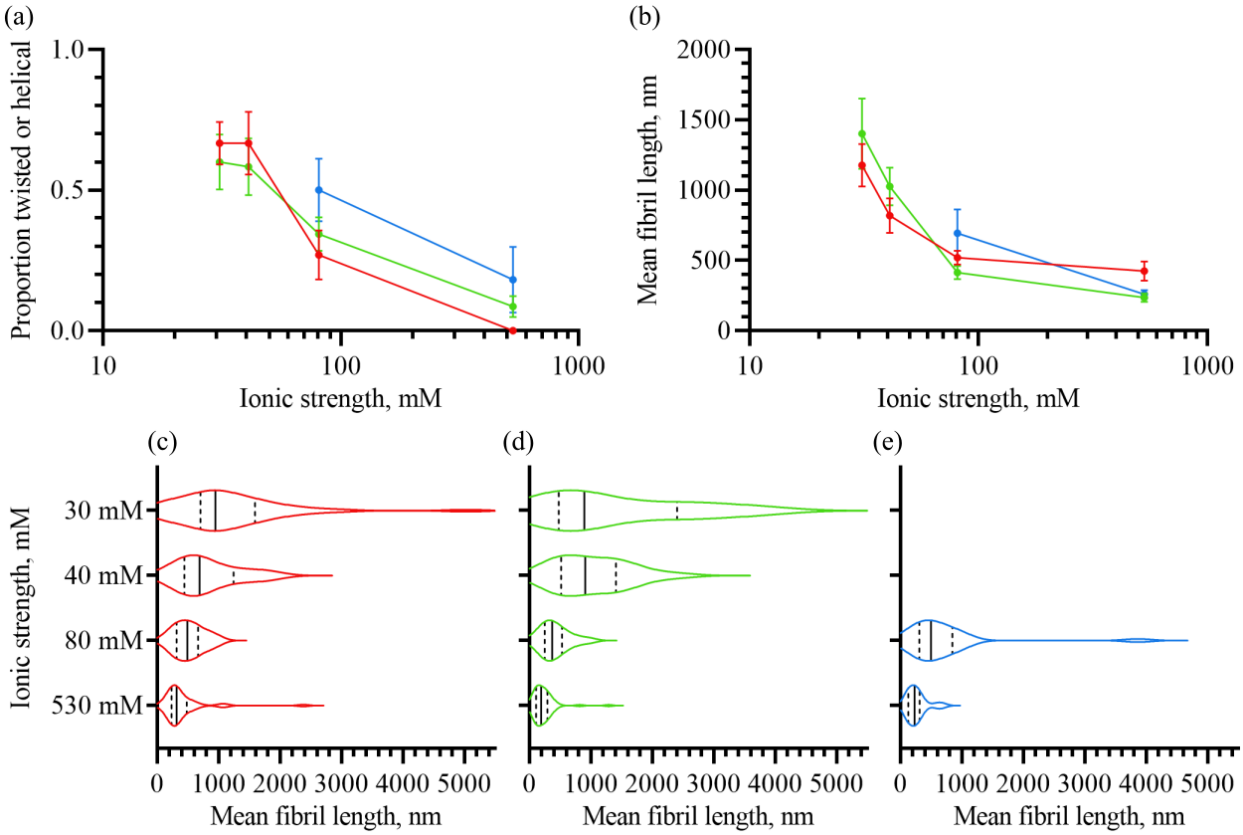

Figure 5.10: Analysis of Aβ(1-42) polymorphism and length distributions, from the NS-EM images in Fig. 5.4-5.9. (a) The proportion of fibrils imaged by NS-EM that had a clearly visible twisted ribbon or helical appearance, as a function of the ionic strength of the fibrillisation buffer. The remainder lacked obvious twisting, although limitations of the imaging method cannot be ruled out. The colour scheme corresponds to the stage of the ThT experiments at which samples were taken and negatively stained: red, half-time; green, end of growth phase, as determined by levelling of the ThT fluorescence; blue, 10000 s after end of growth phase. Error bars represent the standard error of the mean, estimated as described in Section 5.2.3. (b) The mean fibril length as a function of the ionic strength of the fibrillisation buffer. As with panel (a), the colour scheme represents the sampling time in the corresponding ThT experiments, and the error bars represent the standard error of the mean. (c-e) Violin plots showing the estimated fibril length distributions at (c) the half-time, (d) the end of the growth phase, and (e) 10000 s after the end of the growth phase; all three panels have the same *y*-axis, as shown on the left. The median is represented as a solid black line, and the quartiles as dashed black lines; the thickness of the 'violin' represents the kernel density estimation (KDE) of the fibril length distribution (Section 5.2.3), with greater thickness corresponding to higher estimated frequency. The blue datasets in panels (a), (b), and (e) have gaps at ionic strengths of 30 mM and 40 mM as the necessary images were not obtained. Analyses of polymorph frequencies are based on images of 292 separate fibrils (average of 48.6 per data point), while analyses of 273 separate fibrils (average of 45.5 per data point or estimated length distribution).

been shown to co-vary according to the scaling law [555],

$$\tau_{\text{lag}} = \alpha \nu_{\text{max}}^{-\Gamma}, \tag{5.55}$$

where α is a proportionality constant, and Γ is the scaling exponent relating the two quantities. In the original publication, it was assumed that $\Gamma = 1$; however, examination of the fits in that paper suggests that a value in the range $0 < \Gamma < 1$ would be empirically more appropriate. The correspondence between τ_{lag} and ν_{max} for fibrillisation at a variety of $m(0)$ values, in a 20 mM sodium phosphate buffer containing 1 mM NaN_3, 200 μM EDTA, 20 μM ThT and varying concentrations of NaCl is shown in Fig. 5.11. In this figure, the variation in τ_{lag} and ν_{max} at each ionic strength is due to variation in $m(0)$, as well as individual experimental variation. As shown in Fig. 5.11(a), increasing the ionic strength causes a progressive reduction in τ_{lag} and increase in ν_{max}. In addition, the $m(0)$-dependence of the data is reduced at higher ionic strengths, as the range of $m(0)$ values was the same in all datasets (1-10 μM), but there is a broader spread of τ_{lag} and ν_{max} values at lower ionic strengths. Examination of the variation in τ_{lag} and ν_{max} at individual ionic strengths, shown separately in Fig. 5.11(b-h), revealed that the two quantities appeared linearly correlated when plotted against one another on double-logarithmic axes at ionic strengths from 59-260 mM, confirming the existence of a power-law relationship between the two as described by Eq. (5.55). At $I = 360$ mM, a kink appeared in this plot, indicating that a fundamental change in the underlying mechanism had occurred, such that increases in τ_{lag} were not accompanied by further increases in ν_{max}. Nonlinear least-squares fitting of Eq. (5.55) to the datasets acquired at ionic strengths of 59-260 mM, with α values fitted individually and Γ shared globally, gave an estimated $\Gamma = 0.75$. Comparison with fits obtained with the constraint $\Gamma = 1$ supported a non-unitary value of Γ (ΔAICc $= 267.2$), confirming that the proportionality between τ_{lag} and ν_{max} is not exactly inverse (ie. $\Gamma \neq 1$). This may be due to the fact that primary and secondary nucleation can have different reaction orders, and τ_{lag} is slightly more dependent on primary nucleation than ν_{max}, which is mostly influenced by secondary nucleation. In addition, as shown in Fig. 5.11(i), a reduction in α was observed with increasing ionic strength, indicating that changing the ionic strength had a greater effect on τ_{lag} than on ν_{max}. The fits are shown in Fig. 5.11(b-g), and the corresponding fitted parameters, constrained parameters, and diagnostic statistics are shown in Table 5.1.

To more precisely determine the relative effects of ionic strength on primary and secondary nucleation, ThT curves obtained in the 10 mM sodium phosphate buffer at $m(0) = 2$ μM and a variety of ionic strengths were non-globally fitted to Eq. (1.41), which yields the quantities $\lambda^2 = 2k_n' k_e^+ m(0)^{n_c}$ and $\kappa^2 = 2k_2' k_e^+ m^{n_s+1}$, where k_n' and k_s' are the apparent primary and secondary nucleation rate parameters accounting for the effects of saturation, k_e^+ is the bidirectional elongation rate parameter, and n_c and n_s are the effective reaction orders of primary and secondary nucleation, with respect to the monomer. Representative fits are shown in Fig.

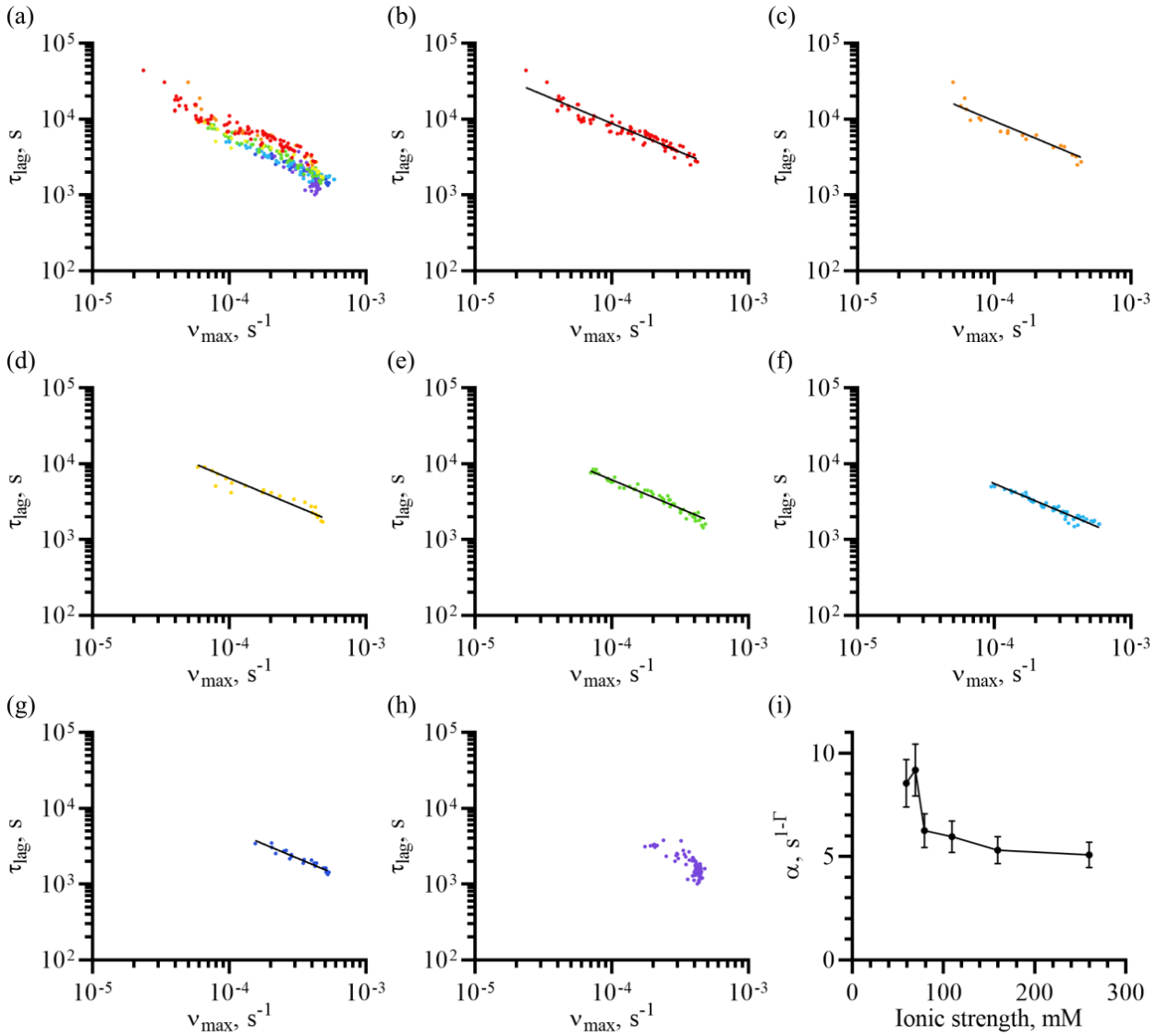

Figure 5.11: Relationship between ν_{max} and τ_{lag} at varying ionic strengths. Panels (a-h) show the relationship between these two quantities for ThT curves obtained at a variety of monomer concentrations and ionic strengths. The colour scheme represents the ionic strength: red, 59 mM; orange, 69 mM; yellow, 79 mM; green, 109 mM; cyan, 160 mM; blue, 260 mM; indigo, 360 mM. Variations in ν_{max} and τ_{lag} within each dataset are due to varying initial monomer concentration. Panel (a) shows an overlay of all ionic strengths, and panels (b-h) show individual ionic strengths globally fitted to Eq. (5.55), as described in the text. The fitted parameters, constrained parameters, and diagnostic statistics from these fits are shown in Table 5.1. Panel (i) plots the effect of ionic strength on the fitted parameter α, with greater values indicating a longer lag phase relative to the growth phase; for a more detailed discussion of the meaning of this parameter, see the text. Error bars represent the standard error of the mean.

Parameter	**Model**	**Value**					
I, mM	—	59	69	79	109	160	260
[NaCl], mM	—	0	10	20	50	100	200
α, $s^{1-\Gamma}$	$\Gamma \neq 1$	8.54	9.18	6.26	5.97	5.31	5.09
	$\Gamma = 1$	0.95	1.04	0.78	0.73	0.70	0.72
Γ	$\Gamma \neq 1$	0.75					
	$\Gamma = 1$	$= 1$					
AICc	$\Gamma \neq 1$	-953.8					
	$\Gamma = 1$	-237.2	-53.2	-56.4	-185.6	-174.0	-100.8
R^2	$\Gamma \neq 1$	0.857	0.806	0.874	0.933	0.909	0.917
	$\Gamma = 1$	0.634	0.782	0.516	0.854	0.621	0.794

Table 5.1: Fitted parameters, constrained parameters, and diagnostic statistics from fitting of the data presented in Fig. 5.11. Two models were tested: Eq. (5.55) with unshared α and shared Γ, as indicated by $\Gamma \neq 1$ in the second column; and Eq. (5.55) with unshared α and the constraint $\Gamma = 1$, as indicated by $\Gamma = 1$ in the second column. The ionic strength I and NaCl concentration [NaCl] are the independent variables, whereas α and Γ are the fitted and/or constrained parameters, and the AICc and R^2 values are diagnostic parameters indicating fit quality. Note that AICc values are only meaningful in a comparative sense, with lower AICc indicating a higher probability, and the fact that the AICc values are negative is not meaningful. As the $\Gamma = 1$ model has no shared parameters, each set of experimental conditions has its own AICc; however, the overall ΔAICc between the two models is 267.2, favouring the $\Gamma \neq 1$ model with $> 99.99\%$ probability.

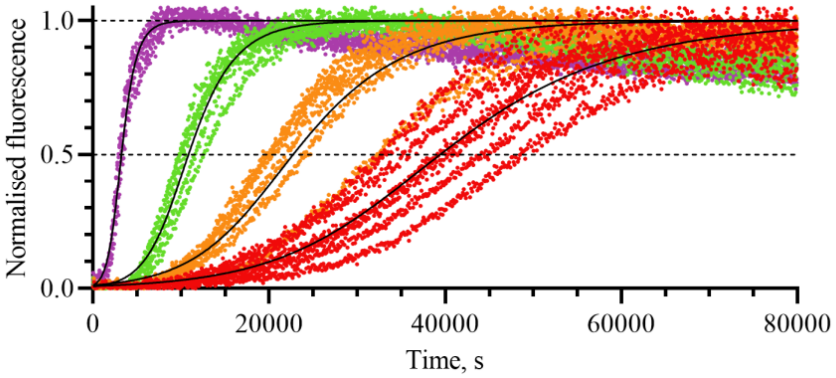

Figure 5.12: Representative ThT curves collected in a 10 mM sodium phosphate buffer (pH 8) containing 200 μM NaN_3, 200 μM EDTA, 20 μM ThT, and varying NaCl, fitted to Eq. (1.41) to extract λ and κ. The colour scheme represents the NaCl concentration and ionic strength: red, 0 m NaCl ($I = 30$ mM); orange, 10 mM NaCl ($I = 40$ mM); green, 50 mM NaCl ($I = 80$ mM); violet, 500 mM NaCl ($I = 530$ mM). The Aβ(1-42) concentration in all experiments was 2 μM. For a description of the fitting procedure, see the text.

5.12. As data were only obtained at a limited range of $m(0)$ in the 10 mM sodium phosphate buffer, global fitting to determine the precise reaction orders and any saturation behaviour was not possible; therefore, the value $n_c = n_s = 2$ was used, which is supported by previous work [54, 519] in the non-saturating limit. As fitting of λ and κ mainly depends on the half-time and maximal rate, which are not particularly sensitive to n_c and n_s, constraining these reaction orders is not expected to strongly affect estimates of the relative variation in λ and κ across different ionic strengths [5]. As shown in Fig. 5.13(a), increasing the ionic strength causes a general increase in λ and κ in the 10 mM sodium phosphate buffer, and the same relationship was also observed in the 20 mM sodium phosphate buffer. The fact that λ and κ exhibit a similar variation with ionic strength indicates there is either a change in the elongation rate constant, which would affect both λ and κ alike, or ionic strength has a similar effect on both primary and secondary nucleation.

The question of whether this effect is due to nucleation or elongation can be settled by closer examination of the fibril length distributions. For the data obtained in 10 mM sodium phosphate buffer, there were corresponding NS-EM data giving average fibril lengths at the end of the growth phase, as presented in Fig. 5.10. Since the Knowles model is able to predict the average fibril lengths at this time, it was possible to combine the measurements to separate out the effects on elongation and primary and secondary nucleation, as described in Section 5.2.3. The relative rate parameters $R'_n(I) = k'_n(I)/k'_n(30\text{ mM})$, $R'_s(I) = k'_s(I)/k'_s(30\text{ mM})$, and $R^+_e(I) = k^+_e(I)/k^+_e(30\text{ mM})$, where the absolute rate parameters are treated as functions of the ionic strength I and normalised against their values at $I = 30$ mM, are shown in Fig. 5.13(b). This analysis confirms that the dependence of the elongation rate on the ionic strength is very weak, meaning that the effect of ionic strength on λ and κ is due to an effect on nucleation. This result is consistent with the notion that primary and secondary nucleation have a similar mechanism, and involve a conformational transition state

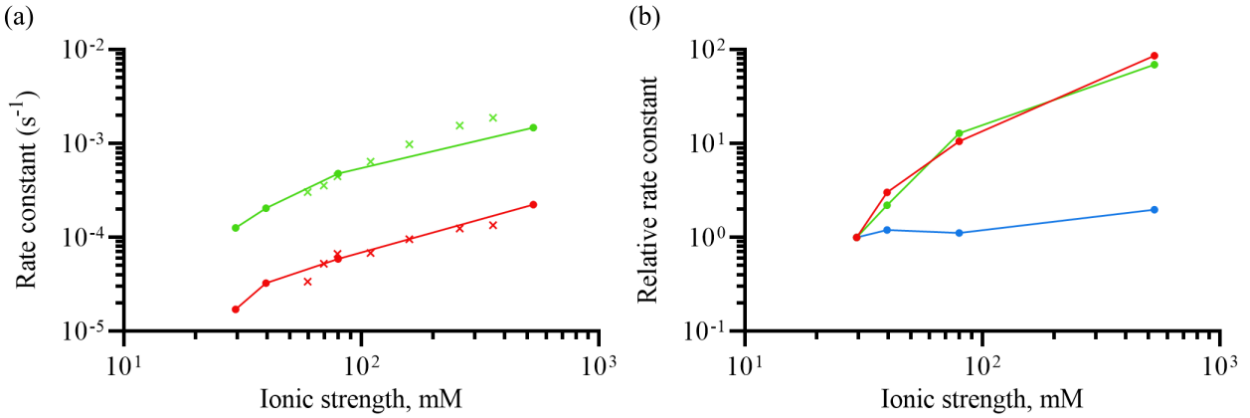

Figure 5.13: Effect of ionic strength on the rate constants of 2 μM Aβ(1-42) self-assembly. (a) The effect of the ionic strength on the macroscopic rate constants λ (red) and κ (green) determined by fitting to Eq. (1.41). Circles and crosses represent the macroscopic rate constants of fibrillisation in a 10 mM sodium phosphate buffer and 20 mM sodium phosphate buffer, respectively, with 1 mM NaN_3 (or 200 μM in 10 mM sodium phosphate buffer), 200 μM EDTA, 20 μM ThT, and varying concentrations of NaCl (pH 8). (b) The effect of the ionic strength on the relative values of the effective nucleation rate parameters R'_n (red) and R'_s (green), and the elongation rate parameter R_e^+ (blue). Data in this panel are all calculated from λ and κ values in the 10 mM sodium phosphate buffer (see previous panel), in conjunction with fibril length distributions from the corresponding NS-EM images.

with a higher net charge than elongation, resulting in a greater ionic strength-dependence [5].

While the analysis in Fig. 5.12-5.13 shows that increasing the ionic strength affects nucleation more strongly than elongation, it does not account for the possible quantitative effects of saturation of nucleation at high ionic strengths and/or monomer concentrations. Saturable secondary nucleation has been suggested for both Aβ(M1-40) [4] and Aβ(M1-42) [5], and saturable primary nucleation due to surface catalysis has recently been suggested for Aβ(M1-40) [6]. Therefore, a broader picture of the $m(0)$-dependence of Aβ(1-42) self-asembly at different ionic strengths was needed to determine whether saturation was occurring, and more accurately quantify the variation in the primary and secondary nucleation rate parameters. Fig. 5.14 shows an analysis of the τ_{50}, τ_{lag}, and ν_{max} of Aβ(1-42) fibrillisation, and the $m(0)$-dependence of these quantities, in the 20 mM sodium phosphate buffer at a range of ionic strengths. For the purpose of this analysis, it is assumed that any observed saturation of these quantities is due to nucleation, as elongation has previously been shown not to saturate at these Aβ(1-42) concentrations and ionic strengths [5], and the data presented in Fig. 5.13 show that $R_e^+(I)$ varies very weakly with I. While τ_{50} appears to exhibit a relatively simple saturation with increasing $m(0)$ or I (Fig. 5.14(a,d)), the pattern with τ_{lag} (Fig. 5.14(b,e)) and ν_{max} (Fig. 5.14(c,f)) is more complex. At low I, τ_{lag} initially levels out with increasing $m(0)$, which is most likely due to saturation of one of the nucleation processes, before the concentration-dependence increases again somewhat, which is most likely due to competition from the non-saturated nucleation process. With

increasing I, there is a decrease in the $m(0)$ at which the initial saturation occurs, but further saturation also begins to appear at the higher $m(0)$ values, indicating that the competing nucleation process also begins to saturate. The behaviour of $\nu_{\max}$ broadly agrees with this scenario at ionic strengths of 59-160 mM, with two regions of changing concentration-dependence; one at $m(0)$ values of 1.5-3 μM, where $\log \nu_{\max}$ is a convex function of $\log m(0)$, and one at $m(0)$ values of 4-10 μM, where $\log \nu_{\max}$ is a concave function of $\log m(0)$. The former suggests competing nucleation processes, while the latter suggests saturation of the nucleation process that dominates at those concentrations. However, at higher ionic strengths ($\gtrapprox$ 260 mM) and initial monomer concentrations ($\gtrapprox$ 3 μM), a new pattern emerges, which is not consistent with the behaviour of τ_{lag}. Rather than simply saturating, $\nu_{\max}$ reverses somewhat, before continuing to increase. This effect was highly reproducible, and the very small experimental variation at this ionic strength and Aβ(1-42) concentration means the effect is significant compared to typical expected variation in $\nu_{\max}$. Therefore, it appears that there is a fundamental change in the self-assembly mechanism at high ionic strengths, which may be incipient at $I = 260$ mM or even lower, and this change of mechanism is responsible for the sharp deviation from expected scaling between τ_{lag} and $\nu_{\max}$, shown in Fig. 5.11(i). The change of mechanism is also associated with weak scaling of the characteristic times and $\nu_{\max}$; as shown in Fig. 5.14(g), at ionic strengths of 260-360 mM and in the 6-10 μM range of initial Aβ(1-42) concentrations, the scaling exponent $\gamma_{50} = -\partial \log \tau_{50} / \partial \log m(0)$ is well below 0.5, the theoretical lower limit if only secondary nucleation is saturable [4], although saturation of primary nucleation could contribute to this effect.

While the data indicate that Aβ(1-42) self-assembly cannot be described by simple saturation at high ionic strengths ($\gtrapprox$ 260 mM) and initial monomer concentrations, global analysis of the saturation behaviour across monomer concentrations is still possible at lower ionic strengths. Therefore, ThT curves acquired in the 20 mM sodium phosphate buffer at ionic strengths of 59-160 mM were non-globally fitted to Eq. (1.41) in order to extract λ and κ values, in the same manner as previously carried out with data collected using the 10 mM sodium phosphate buffer. Fits to representative datasets are shown in Fig. 5.15; to allow comparisons, the 0 mM NaCl ($I = 59$ mM) dataset is the same as that previously shown in Section 3.3.9, and an example of the fibrillisation curves obtained at 300 mM NaCl ($I = 360$ mM), which were not fitted for the reasons discussed above, is shown in Fig. 5.15(d).

Nonlinear regression confirmed that the variations in τ_{50}, τ_{lag}, and $\nu_{\max}$ can be attributed to similar variations in λ and κ, as shown in Fig. 5.16(a-c). To determine whether changes in the concentration-dependence of λ and κ were consistent with saturation of the primary and secondary nucleation processes, respectively, the best-fit λ and κ values were fitted to Eq. (1.49) and (1.50), which describe the cases where both forms of nucleation become independent of the free monomer concentration at high $m(t)$, although κ retains a residual dependence on $m(0)$ due to its additional dependence on the fibrillar monomer concentration. Schematics of these models are shown in Fig. 5.17. In addition, the λ and κ values were fitted to equations describing

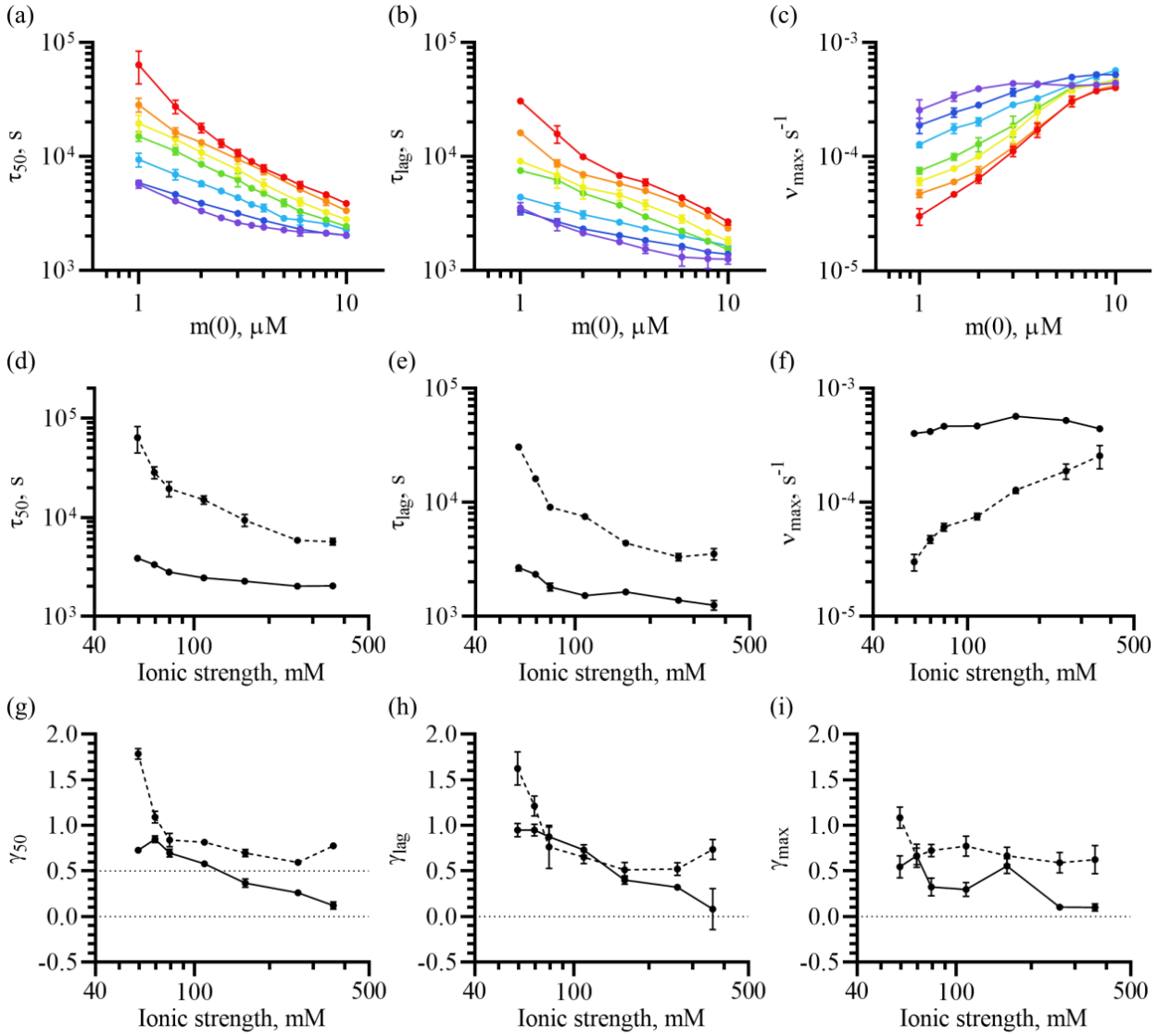

Figure 5.14: Effects of initial monomer concentration and ionic strength on τ_{50}, τ_{lag}, and ν_{max}. Panels (a-c) show the relationship between the initial monomer concentration and (a) τ_{50}, (b) τ_{lag}, or (c) ν_{max} in a 20 mM sodium phosphate buffer (pH 8) containing 1 mM NaN_3, 200 μM EDTA, 20 μM ThT, and varying concentrations of NaCl. The colour scheme represents the NaCl concentration and ionic strength: red, 0 mM NaCl ($I = 59$ mM); orange, 10 mM NaCl ($I = 69$ mM); yellow, 20 mM NaCl ($I = 79$ mM); green, 50 mM NaCl ($I = 109$ mM); cyan, 100 mM NaCl ($I = 160$ mM); blue, 200 mM NaCl ($I = 260$ mM); indigo, 300 mM NaCl ($I = 360$ mM). Error bars represent a single standard deviation. Panels (d-f) show the relationship between the ionic strength and (d) τ_{50}, (e) τ_{lag}, or (f) ν_{max} of 1 μM (black dashed line) or 10 μM (black solid line) Aβ(1-42), from the data in panels (a-c). Error bars represent a single standard deviation. Panels (g-i) show the relationship between the ionic strength and the scaling exponents (g) $\gamma_{50} = -\partial_{\log m(0)} \log \tau_{50}$, (h) $\gamma_{\text{lag}} = -\partial_{\log m(0)} \log \tau_{\text{lag}}$, and (i) $\gamma_{\text{max}} = \partial_{\log m(0)} \log \nu_{\text{max}}$. The dashed black lines show the fitted scaling exponents for 1 μM $\leq m(0) \leq$ 2μM, and the solid black lines show the fitted scaling exponents for 6 μM $\leq m(0) \leq$ 10μM; both are derived from the data in panels (a-c), and the error bars represent the standard error of the fit.

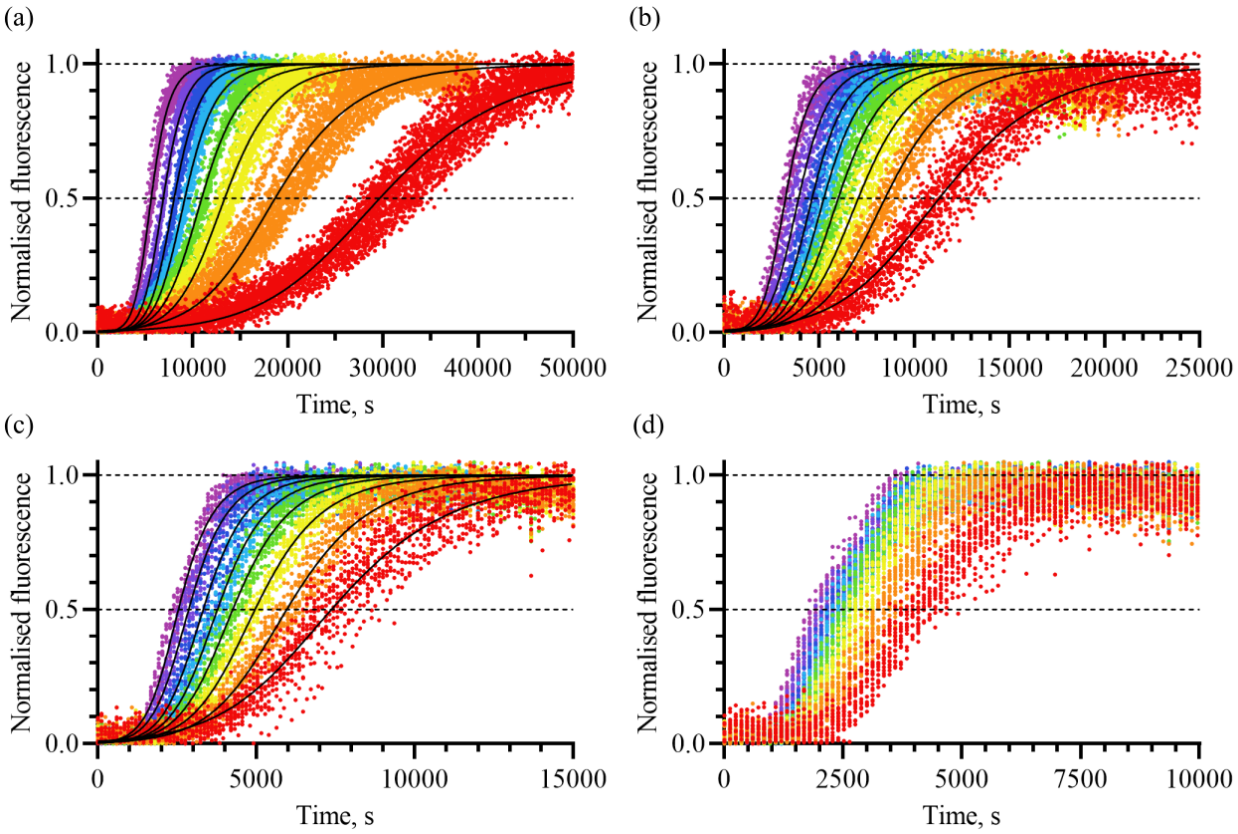

Figure 5.15: Representative ThT curves collected in a 20 mM sodium phosphate buffer (pH 8) containing 1 mM NaN_3, 200 μM EDTA, 20 μM ThT, and varying NaCl, fitted to Eq. (1.41) to extract λ and κ. Panels show sets of concentration-dependent ThT curves at different NaCl concentrations and ionic strengths: (a) 0 mM NaCl ($I = 59$ mM), (b) 50 mM NaCl ($I = 109$ mM), (c) 100 mM NaCl ($I = 160$ mM), and (d) 300 mM NaCl ($I = 360$ mM). The colour scheme represents the initial Aβ(1-42) monomer concentration: red, 1.5 μM; orange, 2 μM; yellow, 2.5 μM; green, 3 μM; cyan, 3.5 μM; blue, 4 μM; indigo, 5 μM; violet, 6 μM. For the purpose of comparison, the data shown in panel (a) are the same as those presented in Section 3.3.9. For reasons discussed in the text, datasets with more than 100 mM NaCl are not fitted, which is why fits are not shown for panel (d). For more detail on the fits, see the text.

cases where primary and secondary nucleation retain a residual dependence on the free monomer concentration under saturating conditions, reflecting scenarios where there are additional steps in the process that do not saturate and whose rate continues to vary with the free monomer concentration. These models were evaluated as possible alternatives to the aforementioned models as the fitted macroscopic rate constants, particularly λ (Fig. 5.16(b, d)), did not appear to level out at the expected concentration-dependence in the saturating limit, despite showing clear signs of a reduction in concentration-dependence across the range of $m(0)$ values investigated. As an example of a mechanism that might result in such a behaviour, if monomers were able to saturate the sites on catalytic surfaces (for heterogeneous primary nucleation) or fibrils (for secondary nucleation) where nucleation occured, but the release of on-pathway oligomers from these sites still required additional monomer-dependent steps such as growth of the surface-bound oligomers, there would be a residual dependence on the free monomer concentration. In these scenarios, the rates of primary and secondary nucleation are

$$\Phi_n(t) = k_n m(t)^{n_c} \frac{K_{M,n}}{K_{M,n} + m(t)^{n_c - \varepsilon_c}}, \tag{5.56}$$

and

$$\Phi_s(t) = k_s m(t)^{n_s} M(t) \frac{K_{M,s}}{K_{M,s} + m(t)^{n_s - \varepsilon_s}}, \tag{5.57}$$

respectively, where $K_{M,n}$ and $K_{M,s}$ are the effective Michaelis constants for the saturable part of the process, and ε_c and ε_n are the residual dependence of $\Phi_n(t)$ and $\Phi_s(t)$ on $m(t)$ in the saturated limit. In Michaelis-Menten kinetics, this is equivalent to introducing an additional dependence of $V_{\max}$ on the concentration of precursor, with a corresponding concentration-dependent effect on the catalytic efficiency; at low $m(t)$, $\partial \log \Phi_n(t) / \partial \log m(t) = n_c$ and $\partial \log \Phi_s(t) / \partial \log m(t) = n_s$, whereas at high m_t, $\partial \log \Phi_n(t) / \partial \log m(t) = \varepsilon_c$ and $\partial \log \Phi_s(t) / \partial \log m(t) = \varepsilon_s$. Following the approach applied by Dear *et al.* [6], the macroscopic rate constants have the expressions

$$\lambda = \sqrt{2 k_n k_e^+ m(0)^{n_c} \frac{K_{M,n}}{K_{M,n} + m(0)^{n_c - \varepsilon_c}}}, \tag{5.58}$$

and

$$\kappa = \sqrt{2 k_s k_e^+ m(0)^{n_s + 1} \frac{K_{M,s}}{K_{M,s} + m(0)^{n_s - \varepsilon_s}}}. \tag{5.59}$$

At low $m(0)$, $\partial \log \lambda / \partial \log m(0) = n_c/2$ and $\partial \log \kappa / \partial \log m(0) = (n_s + 1)/2$; at high m_0, $\partial \log \lambda / \partial \log m(0) = \varepsilon_c/2$ and $\partial \log \kappa / \partial \log m(0) = (\varepsilon_s + 1)/2$. It should be noted that Eq. (1.49-1.50), which describe the cases where saturation with respect to the free monomer concentration is complete, can be considered as special cases of Eq. (5.58-5.59) for which $\varepsilon_c = \varepsilon_s = 0$. Both Eq. (1.49-1.50) and Eq. (5.58-5.59) were fitted to the

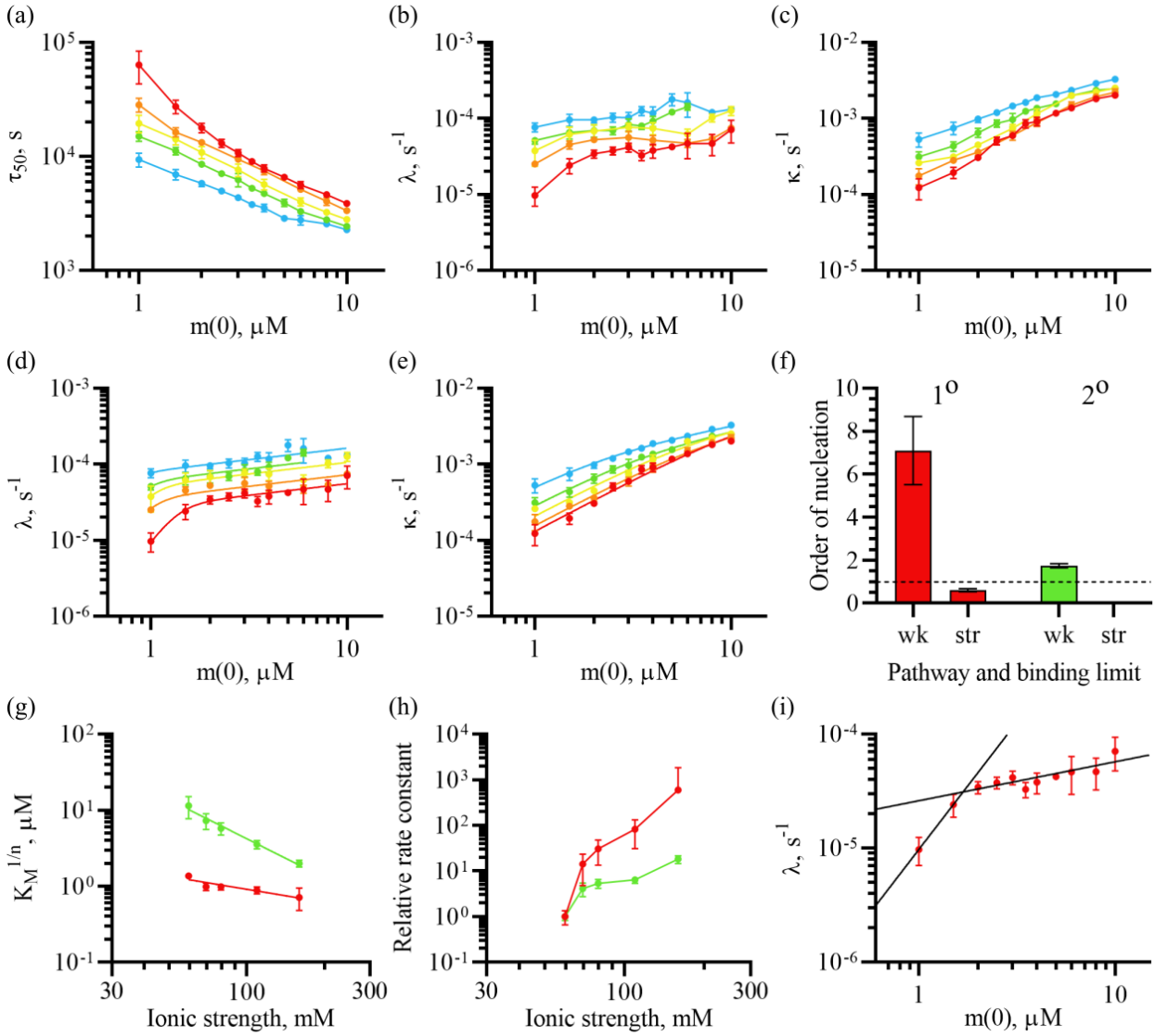

Figure 5.16: Effects of initial monomer concentration and ionic strength on primary and secondary pathways. Panels (a-c) show the relationship between the initial monomer concentration and (a) τ_{50}, (b) λ, or (c) κ in a 20 mM sodium phosphate buffer (pH 8) containing 1 mM NaN_3, 200 μM EDTA, 20 μM ThT, and varying concentrations of NaCl. The colour scheme represents the NaCl concentration and ionic strength: red, 0 mM NaCl ($I = 59$ mM); orange, 10 mM NaCl ($I = 69$ mM); yellow, 20 mM NaCl ($I = 79$ mM); green, 50 mM NaCl ($I = 109$ mM); cyan, 100 mM NaCl ($I = 160$ mM). Error bars represent a single standard deviation. The data in panel (a) are the same as those in Fig. 5.14(a), minus the ionic strengths at which fitting was not performed, and have been included for reference. Panels (d-e) show the same data as panels (b-c), but have been fitted to Eq. (5.58) and Eq. (1.50), respectively. Panels (f-h) show parameters extracted from these fits: (f) the free monomer-dependence of primary (red, $\partial_{\log m(t)} \log \Phi_n$) and secondary (green, $\partial_{\log m(t)} \log \Phi_n$) nucleation in the weak (wk, $m(t) \ll K_M$; n_c and n_s) and strong (str; $m(t) \gg K_M$; ε_c and $\varepsilon_s = 0$) binding limits; (g) the effective Michaelis constants $K_M^{1/n}$ of primary (red, $K_M = K_{M,n}$ and $n = n_c - \varepsilon_c$) and secondary (green, $K_M = K_{M,s}$ and $n = n_s - \varepsilon_s = n_s$) nucleation, fitted to a power law; and (h) the relative rate parameters $R_n R_e^+$ (red) and $R_s R_e^+$ (green). The error bars represent the standard error of the fit. Panel (i) shows the 0 mM NaCl ($I = 59$ mM) dataset from panels (b, d) fitted to two separate non-saturable scaling laws in the $m(0) \leq 1.5$ μM and $m(0) \geq 2$ μM range, respectively.

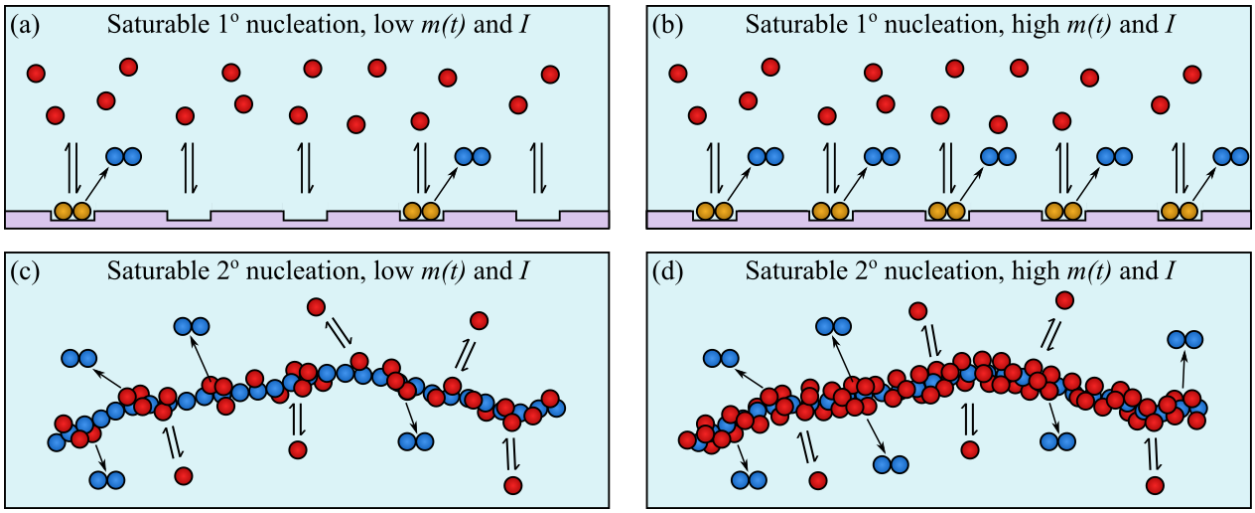

Figure 5.17: Models of saturable primary and secondary nucleation. Panels (a-b) show a possible model of saturable primary nucleation at (a) low $m(t)$ and ionic strength, and (b) high $m(t)$ and ionic strength. Similarly, panels (c-d) show saturable secondary nucleation at (c) low $m(t)$ and ionic strength, and (d) high $m(t)$ and ionic strength. In both panels, the colour scheme corresponds to the monomer conformation: red, soluble; gold, surface-associated; blue, fibrillar. Adsorption of monomers to a catalytic surface, which is either a heterogeneous surface (a-b) or the surface of a fibril (c-d), catalyses the formation of fibril nuclei. Saturation of this surface (b, d) explains saturation of the nucleation rate.

best-fit λ and κ values shown in Fig. 5.16, with global fitting of the Michaelis constants and reaction orders across ionic strengths (with the reaction orders constrained to take non-negative values wherever fitted), and non-global fitting of $k_n k_e^+$ and $k_s k_e^+$. The fits were then compared using the AICc and extra-sum-of-squares F-test; the globally fitted parameters and diagnostic statistics are presented in Table 5.2, and the fits that were ultimately favoured (residual $m(t)$-dependence for λ, no residual $m(t)$-dependence for κ) are shown in Fig. 5.16(d-e).

For λ, a non-zero value of $\varepsilon_c = 0.61$ (95% CI 0.47-0.75) was strongly preferred by both tests, with ΔAICc $= 13.06$ between Eq. (5.58) and Eq. (1.49), indicating a 99.85% probability that the former rather than the latter would have produced the data, and the F-test also supporting the former ($p = 0.0002$); thus, primary nucleation exhibits partial saturation across the investigated range of $m(0)$ values. For κ, the situation was less clear, as the AICc only weakly preferred a non-zero value of $\varepsilon_s = 0.29$ (95% CI 0-0.59), with a ΔAICc $= 0.2004$ between Eq. (5.59) and Eq. (1.50), indicating only a 52.5% probability that the former would have produced the data; in contrast, the F-test weakly favoured the $\varepsilon_s = 0$ model ($p = 0.1261$). Since neither test strongly favours $\varepsilon_s \neq 0$, the unconstrained value of ε_s is close to zero anyway, and this form of incomplete saturation does not appear to have been described elsewhere in the literature, $\Phi_s(t)$ is considered hereafter to fully saturate.

While there is ambiguity with secondary nucleation, it is clear from Fig. 5.16(d) that the primary path-

Parameter		Models of λ			Models of κ	
		Fully saturable	**Partly saturable**	**Change of nucleus size**	**Fully saturable**	**Partly saturable**
		Eq. (1.49)	**Eq. (5.58)**	**Eq. (1.35)**	**Eq. (1.50)**	**Eq. (5.59)**
n_c	best-fit	1.49	7.10	4.47	—	—
	95% CI	1.00 – 1.98	3.96 – 10.23	1.85 – 6.57	—	—
ε_c	best-fit	—	0.61	0.68	—	—
	95% CI	—	0.47 – 0.75	0.50 – 1.11	—	—
n_s	best-fit	—	—	—	1.75	1.90
	95% CI	—	—	—	1.56 – 1.94	1.58 – 2.22
ε_s	best-fit	—	—	—	—	0.29
	95% CI	—	—	—	—	0.00 – 0.59
AICc		-527.9	-540.9	—	-757.5	-757.7
R^2		0.832	0.886	—	0.965	0.966
p		0.0002		—	0.1261	

Table 5.2: Globally fitted parameters and diagnostic statistics from fitting of the data presented in Fig. 5.16. Models of λ treat primary nucleation as fully saturable, partly saturable, or involving an abrupt change of nucleus size. Models of κ treat secondary nucleation as fully or partly saturable. The best-fit and 95% CI values of the fitted parameters are presented below. The diagnostic statistics are the AICc, R^2, and p values; these statistics were not calculated for the model involving a change of nucleus size, as this model was fitted over a different range of ionic strengths and so was not comparable. Note that AICc values are only meaningful in a comparative sense, with lower AICc indicating a higher probability, and the fact that the AICc values are negative is not meaningful. The p values are derived from F-tests and refer to comparisons between fully and partly saturable models of nucleation, where the former is treated as the null hypothesis.

way does not fully saturate, and the statistical tests strongly support this. Therefore, the best fit of Eq. (5.58) to the λ values is shown in Fig. 5.16(d), the best fit of Eq. (1.50) to the κ values is shown in Fig. 5.16(e), and the reaction orders, effective Michaelis constants, and relative rate parameters of these fits ($R_n R_e^+ = k_n(I)k_e^+(I)/k_n(59\text{ mM})k_e^+(59\text{ mM})$ and $R_s R_e^+ = k_s(I)k_e^+(I)/k_s(59\text{ mM})k_e^+(59\text{ mM})$) are shown in Fig. 5.16(f-h). The results of fitting Eq. (1.50) to κ broadly agree with previous studies supporting saturable secondary nucleation, with an unsaturated reaction order of $n_s = 1.75$ (95% CI 1.56-1.94) when $\varepsilon_s = 0$. This indicates that secondary nucleation can be described as the formation of stable on-pathway dimers at saturable sites on the fibril surface, as depicted in Fig. 5.17(d). However, while previous studies assuming that primary nucleation is non-saturable have found that $n_c \approx 2$, the results of this analysis suggest that this is an apparent reaction order caused by saturation of a much higher order process, with a fitted value of $n_c = 7.10$ (95% CI 3.96-10.23). However, due to the fact that saturation typically occurs towards the lower end of the investigated range of $m(0)$ values, the confidence intervals on this value are rather broad, and additional experiments will be need to ascertain the exact reaction order at low concentrations. In addition, despite saturation at high $m(0)$ and I, a residual concentration-dependence remains, reflected in the value of $\varepsilon_c = 0.61$ (95% CI 0.47-0.75) discussed above. This is an effective reaction order rather than reflecting the true number of Aβ(1-42) monomers involved in the non-saturable part of the process; however, the existence of a residual dependence on $m(t)$ indicates that soluble monomers may play a role in the release of surface-bound oligomers as well as their formation. Two possible models for this are represented in Fig. 5.18(a-d).

Alternatively, the change in the concentration-dependence of $\Phi_n(t)$ might not reflect true saturation behaviour, but instead a rapid shift in the size of the critical nucleus due to a change in the relative height of two successive free energy barriers along the self-assembly pathway, with each free energy barrier associated with a pre-fibrillar oligomer of a different size. While the barrier occurring at greater aggregate size would dominate at low $m(0)$, the barrier occurring at lesser aggregate size would dominate at high $m(0)$, due to the $m(0)$-dependence of the free energy function. A similar effect would be expected for ionic strength, as a larger aggregate would have a greater net charge, which would make its free energy more sensitive to the ionic strength. In this interpretation, n_c and ε_c are the effective reaction orders of crossing these two free energy barriers. Such a mechanism would produce a relatively sharp change in concentration-dependence, so that n_c and and ε_c are best determined by fitting to separate non-saturable scaling laws in the $m(0) \leq 1.5$ μM and $m(0) \geq 2$ μM range, respectively (as shown in Fig. 5.16(i)), rather than a single Michaelis-Menten saturation law. Unfortunately, since fitting of n_c involves only two data points, there is a high level of uncertainty on that parameter. Nonetheless, this uncertainty can be quantified by considering the asymmetric 95% confidence intervals; in future, better constraints on n_c could be obtained by collecting more points in this range, although extending the range to significantly lower $m(0)$

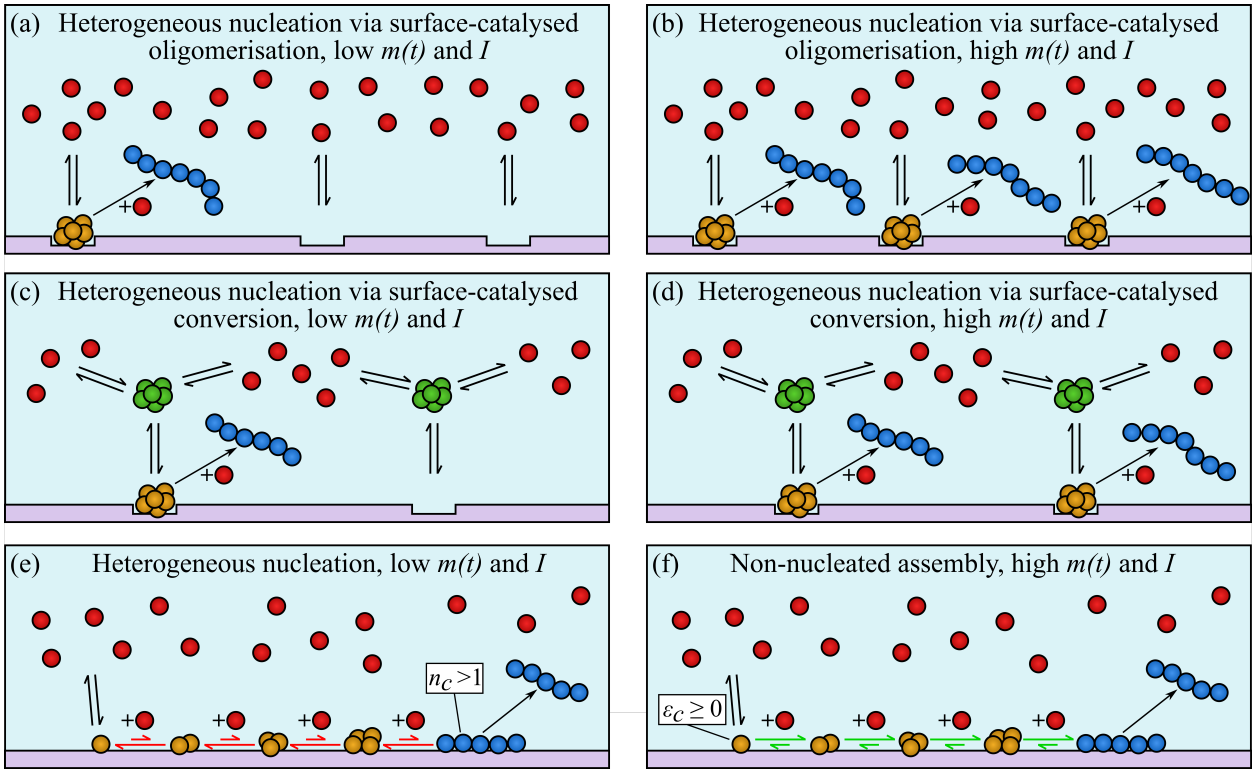

Figure 5.18: Saturable primary nucleation models with a residual monomer dependence at high concentrations. Panels (a-b), (c-d), and (e-f) show three possible mechanisms by which the primary nucleation rate could saturate, but still have a residual monomer-dependence in the strong binding limit ($K_M \gg m(0)$); while panels (a, c, e) show the behaviour at low $m(t)$ and I, panels (b, d, f) show the behaviour at high $m(t)$ and I. In panels (a-b), oligomers form at saturable active sites on a surface, and the residual monomer dependence is due to a growth-dependent transition from a surface-bound monomer to a growing fibril seed. In panels (c-d), the model is very similar, but the oligomers form in solution before binding to and saturating the active sites. In panels (e-f), the decrease in the order of primary nucleation is not due to saturation of active sites, but a shift from nucleated polymerisation to non-nucleated assembly, occurring at the point when the surface-bound critical nucleus becomes more stable than the soluble monomer. In all panels, the colour scheme corresponds to the monomer conformation: red, soluble; gold, surface-bound; green, soluble intermediate; blue, fibrillar.

is probably not feasible due to the experimental challenges of experiments at low Aβ(1-42) concentrations. The fitted scaling exponents were $n_c = 4.47$ (95% CI 1.85-6.57) and $\varepsilon_c = 0.68$ (95% CI 0.50-1.11). Thus, although the fitting of n_c is rather uncertain, and it cannot be said with complete confidence that $n_c > 2$, it is clear that there is a drop in concentration-dependence, and that $\varepsilon_c < 2$. The low value of ε_c suggests two possible models: rate-determining conformational conversion of the monomer (expected $\varepsilon_c = 1$), or surface-catalysed nucleation (expected $\varepsilon_c \geq 0$). Rate-determining conformational conversion of the monomer would require an unstable monomer conformer that persisted for timescales of ~ 0.1 s, which is not supported by the literature, given that the Aβ(1-42) monomer is highly dynamic and samples conformations on sub-μs timescales [232, 236, 238]. Thus, the low value of ε_s implies that the critical nucleus at sufficiently high $m(0)$ and I, and possibly also the critical nucleus at lower $m(0)$ and I, is a surface-bound species. A possible model for this is represented in Fig. 5.18(e-f).

Although the data at present do not provide enough information to determine which model in Fig. 5.18 is correct, all possible models require a surface-bound critical nucleus under 'saturating' conditions, in agreement with the conclusion of Chapter 4 that primary nucleation of Aβ(1-42) is surface-dependent, even in PEG plates, as well as the recent suggestion that Aβ(M1-40) nucleation is also surface-dependent in the same plates [6]. In future, collection of more finely spaced data points around the apparent $K_{M,n}$ values will allow better model discrimination; however, at present, it is not completely certain which model is correct, so the fitted $K_{M,n}$ and $R_n R_e^+$ values should be treated with caution.

The same is not true for the $K_{M,s}$ and $R_s R_e^+$ values, which were fitted completely independently. As shown in Fig. 5.16(g), the best-fit $K_{M,s}$ values exhibit a power-law variation with the ionic strength. This result is interesting, as it implies that the free energy of fibril-bound prefibrillar oligomers contains a term proportional to the logarithm of the ionic strength, but its significance is not entirely clear, as a dependence of the free energy on the square root of the ionic strength would be more consistent with Debye-Hückel theory [549]. Nonetheless, Debye-Hückel theory is only valid at low ionic strengths ($\lessapprox 100$ mM at best), and would not be expected to apply here.

In addition, as shown in Fig. 5.16(h), the relative rate parameter $R_s R_e^+$ exhibits a complex relationship with the ionic strength, which the fitted $R_n R_e^+$ values also appear to follow. The previous finding that changes in λ and κ are due to effects on secondary nucleation rather than elongation is still valid here, so the variation in $R_n R_e^+$ and $R_s R_e^+$ probably reflects a similar variation in R_n and R_s, and thus k_n and k_s. Although uncertain model discrimination means that the exact relationship between I and $R_n R_e^+$ is unclear, the fact that Fig. 5.13 shows a sustained increase in R'_n under 'saturating' conditions, whichever model is considered, means that R_n must be enhanced by ionic strength as well as R_s. Thus, by different routes of reasoning, there is a positive correlation between I and both k_n and k_s. Since both processes are surface-dependent, this could be caused by enhanced dissociation of on-pathway oligomers from their formation sites; such a mechanism

might well rely on enhanced growth or structural maturation of these oligomers that encourages release, as in the absence of these effects the greater ionic strength would be expected to reduce dissociation of these oligomers. Alternatively, it has been proposed that the majority of Aβ(M1-42) oligomers produced by primary or secondary nucleation ultimately disassemble to monomer rather than successfully converting to fibrils [469], so that stabilisation of these oligomers would result in more efficient nucleation and thus higher k_n and k_s values.

5.3.4 Accumulation of amyloid-like oligomers at high $m(0)$ and I

5.3.4.1 Analysis of the ThT time courses reveals biphasic self-assembly kinetics

Although the Knowles model provides a good fit for the self-assembly kinetics at low monomer concentration and ionic strength, the quality of the fits deteriorates as these quantities increase, as shown in Fig. 5.19. The cause of this deterioration appears to be the development of a kinked curve shape implying that two phases of ThT fluorescence gain occur in rapid succession. In addition, as previously discussed, $\nu_{\max}$ also exhibits unusual scaling behaviours at high $m(0)$ and I. A closer view of this scaling is provided in Fig. 5.20, which shows the τ_{50}, τ_{lag}, and $\nu_{\max}$ of varying concentrations of Aβ(1-42) in 20 mM sodium phosphate buffers containing 1 mM NaN_3, 200 μM EDTA, 20 μM ThT, and either 0 mM NaCl, 100 mM NaCl, 300 mM NaCl, or 300 mM NaCl. This figure has some overlap with Fig. 5.14, but also includes NaF and extends to higher $m(0)$. Consistent with results previously presented in this chapter, NaCl and NaF have approximately the same effect on the self-assembly kinetics, indicating that ionic strength remains the main determining factor. While the scaling of the characteristic times and $\nu_{\max}$ with $m(0)$ is consistent with the Knowles model at ionic strengths of 59 mM and 160 mM, and there is no clear sign of unusual behaviour of τ_{lag} at any ionic strength, both τ_{50} and $\nu_{\max}$ exhibit a reversed concentration-dependence at high $m(0)$ and $I = 360$ mM, with the reversed scaling of the former probably caused by reversed scaling of the latter. As previously described for NaCl alone, after the initial reversal of $\partial \log \nu_{\max} / \partial \log m(0)$ in the 3-6 μM range, $\partial \log \nu_{\max} / \partial \log m(0)$ recovers the expected positive value. However, by 20 μM Aβ(1-42), there appears to have been a further reversal, indicating that complex processes are occurring that are associated with the change in curve shape, and reduce $\nu_{\max}$.

To gain a more detailed view of the changing curve shape at high $m(0)$ and I, and investigate the cause of the reduction in $\nu_{\max}$, the first derivative was calculated for the average fluorescence intensities of a set of repeat experiments performed in rapid succession, with the same instrument gain, so that the non-normalised intensities could be used instead of the normalised intensities. It was desirable to use non-normalised intensities, as this allowed overlaying of datasets obtained at different $m(0)$ and I, and comparison of the relative intensities of any phases of ThT fluorescence gain. These derivatives are shown in Fig. 5.21 and Fig. 5.22,

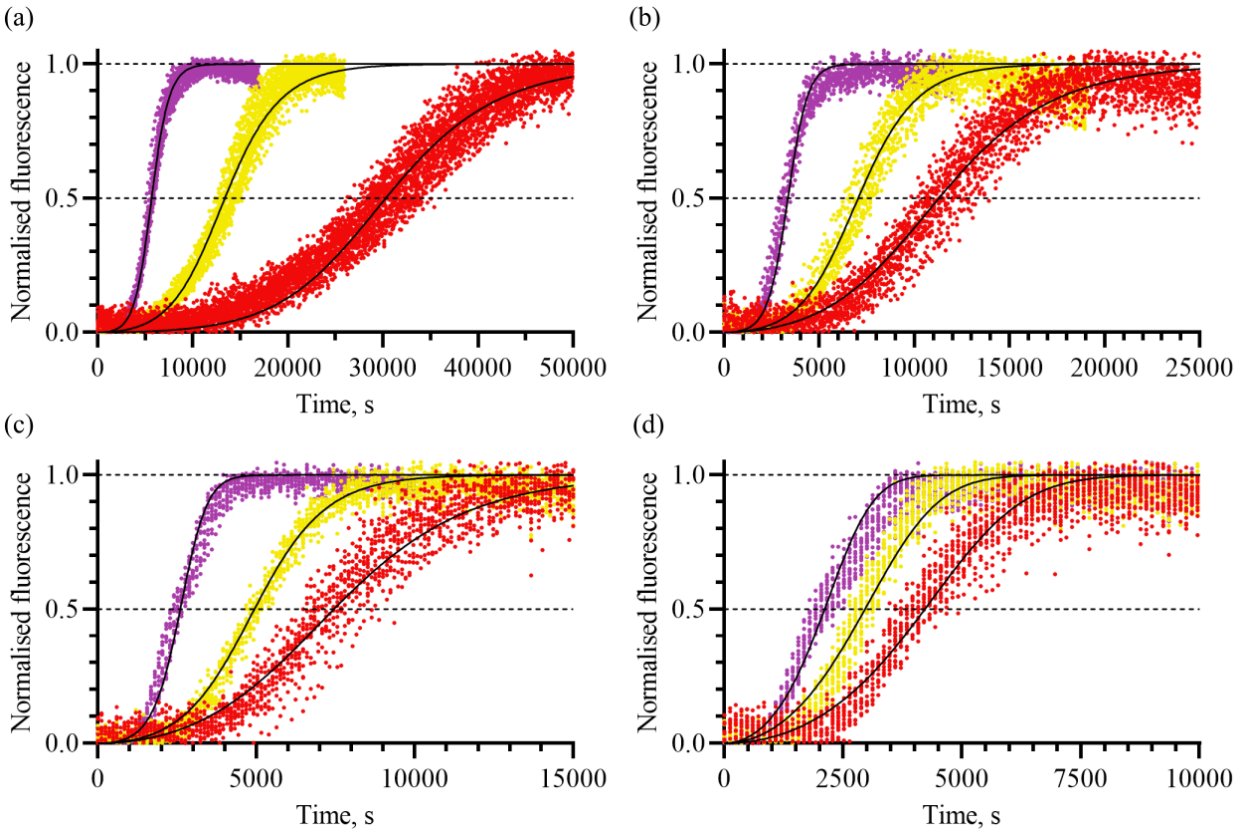

Figure 5.19: The Knowles model does not fit the curve shape at high $m(0)$ and I. Panels show non-global fits of Eq. (1.41) to the same data as in Fig. 5.15, but with fewer $m(0)$ values shown and fits at all I, to show the deterioration of fit quality with increasing $m(0)$ and I. All ThT curves were obtained in a 20 mM sodium phosphate buffer (pH 8) containing 1 mM NaN_3, 200 μM EDTA, 20 μM ThT, and varying NaCl. Panels show sets of concentration-dependent ThT curves at different NaCl concentrations and ionic strengths: (a) 0 mM NaCl ($I = 59$ mM), (b) 50 mM NaCl ($I = 109$ mM), (c) 100 mM NaCl ($I = 160$ mM), and (d) 300 mM NaCl ($I = 360$ mM). The colour scheme represents the initial Aβ(1-42) monomer concentration: red, 1.5 μM; yellow, 2.5 μM; violet, 6 μM. For the purpose of comparison, the data shown in panel (a) are the same as those presented in Section 3.3.9.

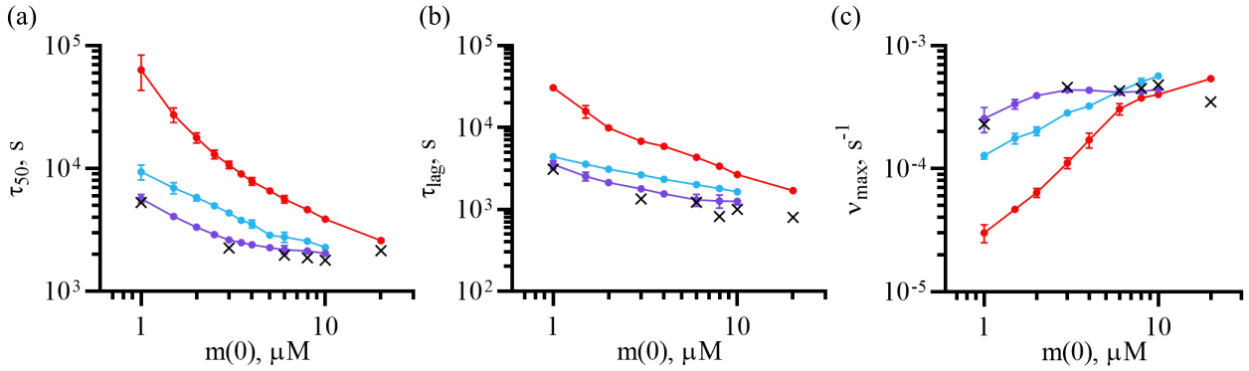

Figure 5.20: Weak scaling of τ_{50}, τ_{lag}, and ν_{max} at high $m(0)$ and I. Panels show the relationship between the initial monomer concentration and (a) τ_{50}, (b) τ_{lag}, or (c) ν_{max} in a 20 mM sodium phosphate buffer (pH 8) containing 1 mM NaN_3, 200 μM EDTA, 20 μM ThT, and varying concentrations of NaCl or NaF. The colour scheme represents the salt concentration and ionic strength: red, 0 mM NaCl ($I = 59$ mM); cyan, 100 mM NaCl ($I = 160$ mM); indigo, 300 mM NaCl ($I = 360$ mM); black crosses, 300 mM NaF ($I = 360$ mM). Error bars represent a single standard deviation across collated replicates from repeat experiments, which was too small to represent in many cases.

which show two different datasets of this sort that were acquired approximately a year apart, with different buffer and a different batch of microplates, explaining the small difference in rate between the two; the latter dataset was acquired to obtain a broader and more detailed characterisation of the effect of $m(0)$ on the curve shape at $I = 360$ mM. While there is a single phase of ThT fluorescence gain at $I = 59$ mM (Fig. 5.21(a)), the kinetics are clearly biphasic at intermediate $m(0)$ (3-7 μM) when $I = 360$ mM (Fig. 5.21(d), Fig. 5.22), and the kinetics at higher $m(0)$ (8-10 μM) and $I = 360$ mM do not show a return to uniphasic kinetics, but more likely the appearance of additional phases that are hard to disentangle (Fig. 5.22). Surprisingly, the first derivatives show that the kinetics are biphasic at much lower ionic strengths than previously suspected, with clear biphasic character at ~ 4 μM Aβ(1-42) when $I = 160$ mM (Fig. 5.21(c)), and possible, but inconclusive, indications of biphasic kinetics at $I = 109$ mM (Fig. 5.21(b)). The transition to a biphasic self-assembly process explains the reduction in ν_{max}, since ν_{max} usually only reflects the normalised amplitude of the first phase of fluorescence gain, and as the ThT curve becomes biphasic, the first phase accounts for progressively less of the total fluorescence intensity change.

As a control to test whether the biphasic kinetics were caused by seeding of the Aβ(1-42) samples, the same experiments were repeated with Aβ(1-42) that had been purified according to the SEC protocol previously described by Hellstrand *et al.* [479]. In summary, 50 μl of Aβ(1-42) dissolved in 50 mM NaOH was loaded onto a Superdex-75 column in a 20 mM sodium phosphate (pH 8) mobile phase, with 1 mM NaN_3, 200 μM EDTA, and 300 mM NaCl. The fraction eluting from 14-15 min (at 1 ml/min) was collected on ice, diluted variably (60%, 80%, or 100%, ie. undiluted) in the elution buffer to give a range of concentrations, supplemented with 20 μM ThT from a concentrated stock, and used in ThT assays. The full

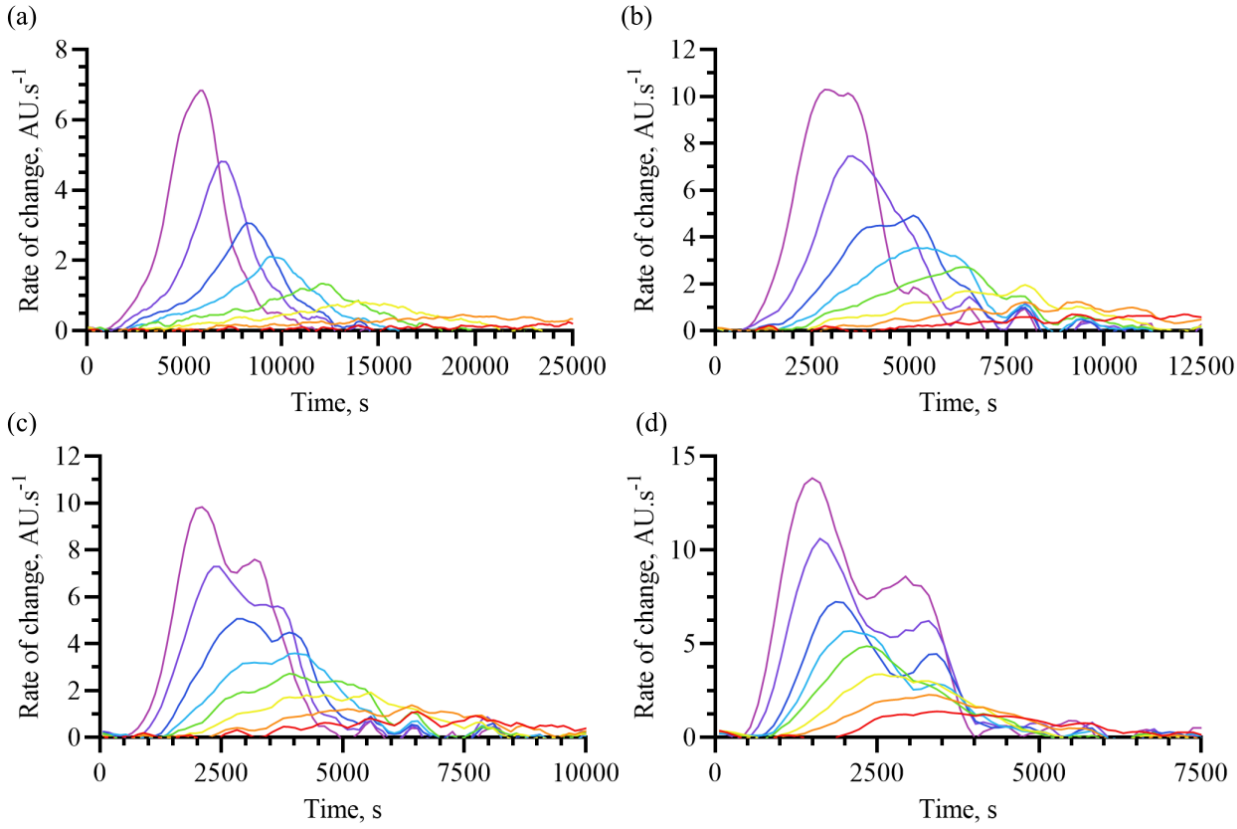

Figure 5.21: Poor fitting of the Knowles model is due to biphasic kinetics (part 1). Panels show the first derivatives of the mean non-normalised fluorescence intensities at varying $m(0)$ and I. All ThT curves were obtained in a 20 mM sodium phosphate buffer (pH 8) containing 1 mM NaN_3, 200 μM EDTA, 20 μM ThT, and varying NaCl. Panels show sets of concentration-dependent ThT curves at different NaCl concentrations and ionic strengths: (a) 0 mM NaCl ($I = 59$ mM), (b) 50 mM NaCl ($I = 109$ mM), (c) 100 mM NaCl ($I = 160$ mM), and (d) 300 mM NaCl ($I = 360$ mM). The colour scheme represents the initial Aβ(1-42) monomer concentration: red, 1.5 μM; orange, 2 μM; yellow, 2.5 μM; green, 3 μM; cyan, 3.5 μM; blue, 4 μM; indigo, 5 μM; violet, 6 μM.

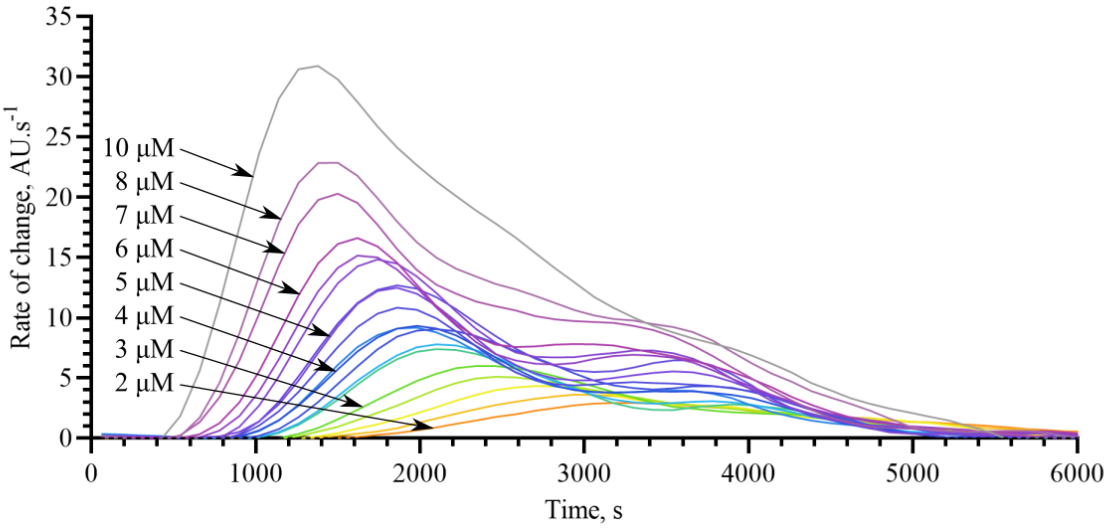

Figure 5.22: Poor fitting of the Knowles model is due to biphasic kinetics (part 2). Panels show the first derivatives of the mean non-normalised fluorescence intensities at varying $m(0)$ and I. All ThT curves were obtained in a 20 mM sodium phosphate buffer (pH 8) containing 1 mM NaN_3, 200 μM EDTA, 20 μM ThT, and 300 mM NaCl ($I = 360$ mM). The colour scheme represents the initial Aβ(1-42) monomer concentration, and corresponds to that used in Fig. 5.21(d), although a large number of intermediate concentrations are present in this figure, and have been given intermediate colours. The concentrations are: 2 μM (orange), 2.25 μM, 2.5 μM (yellow), 2.75 μM, 3 μM (green), 3.25 μM, 3.5 μM (cyan), 3.75 μM, 4 μM (blue), 4.25 μM, 4.5 μM, 4.75 μM, 5 μM (indigo), 5.25 μM, 5.5 μM, 6 μM (violet), 7 μM, 8 μM, 10 μM (gray). To help with distinguishing individual curves, several of the concentrations have been annotated.

details of this experiment, which is similar to the experiment shown in Fig. 3.14 in Section 3.3.5, are given in Section 5.2.4. The purification was carried out several times, with reproducible results. A representative elugram is shown in Fig. 5.23(a), showing a strong monomer peak at $\sim$ 14.5 min, and representative ThT curves are shown in 5.23(b), with the same curve shape as unpurified samples. The first derivatives of the mean fluorescence intensities of the 60%, 80%, and 100% diluted samples, which are shown in Fig. 5.23(c), remained biphasic despite the purification, although variations in concentration of the collected eluent between repeat experiments meant that the averaged derivatives were somewhat blurred, which made the biphasic kinetics slightly less obvious. In addition, as shown in Fig. 5.23(d), the fibrillisation half-times of the purified samples overlaid closely with the half-times of un-purified peptide, having the same rate and concentration-dependence. Thus, the low concentration-dependence and biphasic curve shape observed at high ionic strengths are not affected by further purification of samples, and are unlikely to be caused by seeding.

5.3.4.2 CD spectroscopy supports biphasic self-assembly at high $m(0)$ and I

To test whether the transition to biphasic ThT kinetics was accompanied by a change in the development of the peptide's secondary structure, combined ThT-CD experiments were performed. In each of these experiments, a ThT assay was set up in a microplate containing a large number of replicate wells with identical contents, and the wells were periodically sacrificed and their contents examined by CD. The Aβ(1-42) concentration was 10 μM Aβ(1-42) and the buffer was 20 mM sodium phosphate (pH 8) containing 1 mM NaN_3, 200 μM EDTA, 20 μM ThT, and either 0 mM ($I = 59$ mM) or 300 mM NaF ($I = 360$ mM). As shown in Fig. 5.24(a), in the absence of NaF, the Aβ(1-42) began the self-assembly process in a predominantly disordered state, with molar residue ellipticities (MREs) of $[\Theta]_{\mathrm{MR}} = -9400$ deg.cm^2.dM^{-1} at $\lambda = 200$ nm and $[\Theta]_{\mathrm{MR}} = -1900$ deg.cm^2.dM^{-1} at $\lambda = 222$ nm, consistent with the collapsed disordered PMG state proposed by Uversky and colleagues [225,227], as well as the results of several other CD studies of Aβ monomer [4, 230, 231, 233, 234]. As self-assembly progressed, the CD spectrum revealed a progressive increase in β-sheet content, and after 8680 s of self-assembly, the spectrum had mostly levelled out with MREs of $[\Theta]_{\mathrm{MR}} = -1900$ deg.cm^2.dM^{-1} at $\lambda = 200$ nm and $[\Theta]_{\mathrm{MR}} = -3100$ deg.cm^2.dM^{-1} at $\lambda = 222$ nm, suggesting a mixture of β-sheet and disordered regions. This spectrum is consistent with the findings of structural models of Aβ(1-42) and many other amyloid fibrils, which typically have a β-sheet core surrounded by an extensive halo of unstructured polypeptide [144, 167, 172–175, 556], particularly the N-terminus in the case of Aβ. In addition, the convoluted tertiary structures of many Aβ polymorphs have large numbers of turns and non-β-strand structural elements in the cross-β core [136, 143, 144]. Nonetheless, it is interesting to observe that a futher slow change in CD spectrum occurred throughout the plateau phase (up to 17440 s), characterised by a decrease in MRE at both 200 nm and 222 nm, indicating that the

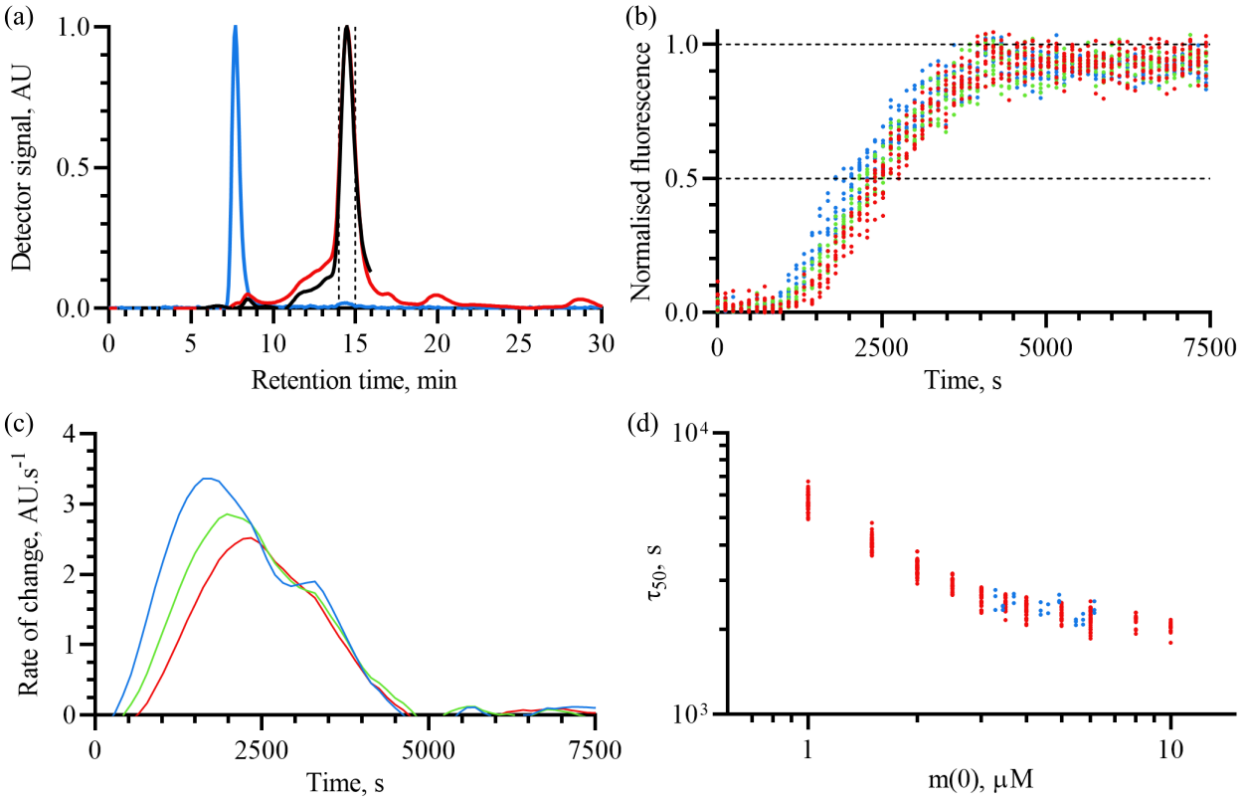

Figure 5.23: Biphasic self-assembly kinetics are not caused by seeding, Aβ(1-42) was purified using a Superdex-75 column and then used in ThT assays at 37°C. The buffer used for elution and ThT assays was sodium phosphate (pH 8) containing 1 mM NaN_3, 200 μM EDTA, and 300 mM NaCl, and the sample was eluted at 1 ml/min. (a) Detector outputs from a typical SEC-MALS run of Aβ(1-42) prepared in 50 mM NaOH. Colour scheme: black, RI; red, UV_{280}; blue, LS 90°. Dashed vertical lines demarcate the fraction (14-15 min) that was collected for ThT assays. (b) Normalised ThT curves of purified Aβ(1-42). Colour scheme indicates Aβ(1-42) concentration as a percentage of the eluent concentration: red, 60% (∼3.5 μM); green, 80% (∼4.6 μM); blue, 100% (∼5.8 μM). (c) First derivatives of the mean normalised ThT fluorescence intensities. (d) Similarity between the fibrillisation half-times of unpurified (red) and purified (blue) Aβ(1-42) in the same buffer.

fibrils gradually became more structured after the initial assembly process. Excluding this later time point and focusing on the growth phase alone (2440-8680 s), the CD spectra acquired in this time period had an isodichroic point at $\lambda \approx 210$ nm, indicating that the structural transition occurring in the growth phase was predominantly a two-state process. In addition, as shown in Fig. 5.24(c), when the MREs at 199 nm were plotted against the ThT signal of the experiment from which the samples were taken, and rescaled so that their start and end values were aligned, the two growth curves overlaid almost perfectly, indicating that the change in ThT signal was accounted for by the structural transition from the PMG-like to the fibril state. The same effect was observed across all wavelengths, although a wavelength of 199 nm is used here as that was where the MRE was initially most negative. Thus, the time course data indicate that, at low ionic strength ($I = 59$ nm), there are three assembly states that accumulate to detectable quantities: a disordered monomer, perhaps similar to a PMG; a newly assembled fibril, characterised by a ThT response and a mixture of β-sheet and disordered regions; and a more ordered state probably representing fibrils that have undergone some structural maturation process.

In the presence of 300 mM NaF, the ThT-CD time course showed a number of key differences. Firstly, as shown in Fig. 5.24(b), the peptide began self-assembly in a slightly more ordered state, with MREs of $[\Theta]_{\mathrm{MR}} = -7700$ deg.cm^2.dM^{-1} at $\lambda = 200$ nm and $[\Theta]_{\mathrm{MR}} = -1700$ deg.cm^2.dM^{-1} at $\lambda = 222$ nm. This is still consistent with a PMG monomer [225], but it does suggest a higher secondary structure content than was observed at lower ionic strength. Possible explanations for this could include a more collapsed monomer, or an increased tendency for rapid oligomerisation after dilution into the fibrillisation buffer, although available measurements of the polymerisation rate under similar conditions indicate that oligomer formation is still limited prior to the start of the 'growth phase' [5]. The fibrillar end point was similar to that observed in the absence of NaF, but did have a less negative MRE in the 215-220 nm range, indicating that the β-sheet content was lower. This could be consistent with the observation that amyloid fibrils formed at high ionic strength appear less structured at a mesoscale level than those formed at lower ionic strength (Section 5.3.2). In addition, there was no obvious isodichroic point, which could have been because the initial and final CD spectra were relatively similar at wavelengths above ~ 215 nm, or alternatively because a simple two-state model could not describe the CD data.

However, the most striking effect of ionic strength was revealed when the MREs at 199 nm were overlaid against the fluorescence intensities from the corresponding ThT experiment, as shown in Fig. 5.24(d). While the corresponding datasets had overlapped almost perfectly in the absence of NaF, the ThT and CD data obtained in the presence of 300 mM NaF had completely different 'growth phases' that occurred at very different rates, despite reporting on self-assembly in the exact same experiment. The ThT signal reached a maximum rate of change at around 1400 s, and had a half-time of 1700 s; however, the MRE at 199 nm appeared to have a maximum rate of change somewhere in the 2800-4120 s range, and a half time of around

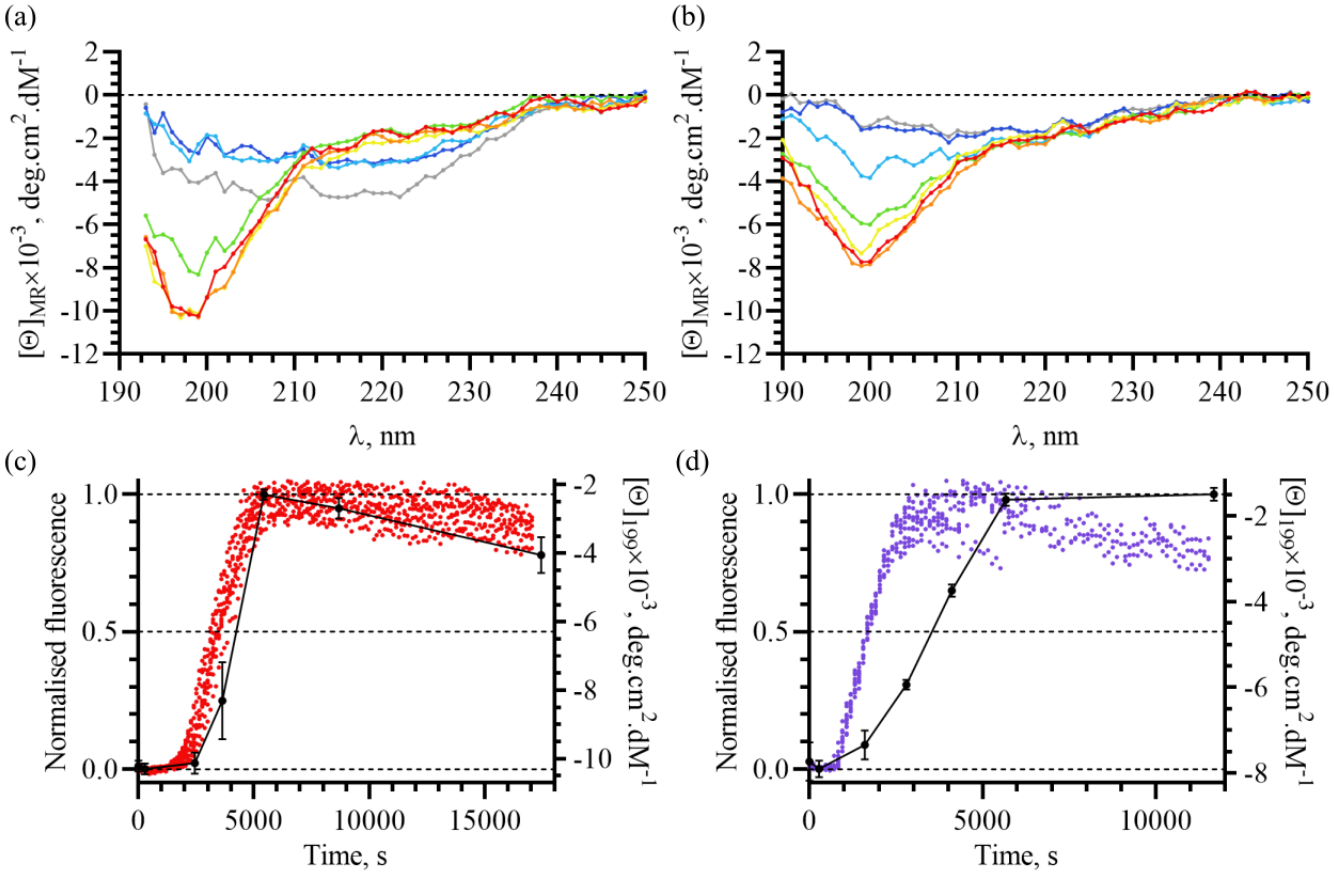

Figure 5.24: Combined ThT-CD time course of Aβ(1-42) self-assembly. Panels (a-b) show overlaid blank-subtracted CD spectra of Aβ(1-42) samples extracted periodically from ThT assays with 10 μM peptide in a 20 mM sodium phosphate buffer (pH 8) containing 1 mM NaN_3, 200 μM EDTA, 20 μM ThT, and either (a) 0 mM NaF ($I = 59$ mM) or (b) 300 mM NaF ($I = 360$ mM). The colour scheme indicates the time point at which Aβ(1-42) was extracted. For panel (a), the colour scheme is: red, 0 s; orange, 280 s; yellow, 2440 s; green, 3640 s; cyan, 5440 s; blue, 8680 s; gray, 17440 s. For panel (b), the colour scheme is: red, 0 s; orange, 280 s; yellow, 1600 s; green, 2800 s; cyan, 4120 s; blue, 5680 s; gray, 11680 s. Each CD spectrum is an average of 3 concordant replicates; in the buffer without NaF, ellipticities at wavelengths below 193 nm were excluded due to poor signal-to-noise. Panels (c-d) show the fluorescence of the unextracted wells in the corresponding ThT experiments, overlaid with the CD-derived molar residue ellipticity of extracted Aβ(1-42) samples at a wavelength of 199 nm, which was where the signal was most negative in the first time point. Panel (c) shows the ThT fluorescence (red) and ellipticity (black) for fibrillisation in the buffer with 0 mM NaCl ($I = 59$ mM). Panel (d) shows the ThT fluorescence (indigo) and ellipticity (black) for fibrillisation in the buffer with 300 mM NaCl ($I = 360$ mM). The colour scheme of the ThT data in panels (c-d) does not correspond to the colouring in panels (a-c), but instead corresponds to the ionic strength-based colouring used in other figures in this chapter. The error bars on the ellipticities in panels (c-d) correspond to the standard error of the mean.

3500 s. After self-assembly for 1600 s, the ThT fluorescence intensity had reached almost half its final value (Fig. 5.24(d)), whereas the CD spectrum was almost unchanged from its starting point (Fig. 5.24(b)); similarly, after 2800 s, the ThT signal had almost reached a plateau, whereas the CD spectrum had only just begun to change significantly. This result is reproducible; although the experiment with the highest signal-to-noise has been presented here, the result was confirmed by a separate control experiment with lower time resolution, as well as a repeat with higher time resolution but lower signal-to-noise performed by Mr. Xander Arscott-Barber.

Interestingly, the time at which the MRE at 199 nm changed the most, ~ 3500 s, was approximately the same as the time at which the second phase of ThT fluorescence intensity change occurred at lower Aβ(1-42) concentrations (Fig. 5.21, Fig. 5.22). As previously discussed, although the biphasic character of the ThT curves is not particularly obvious at $m(0) = 10$ μM, the first derivatives indicate that this is not due to the disappearance of the second phase, but merely an increase in the complexity of the processes that occur after the first phase, as the first derivatives maintain a long, uneven tail after their initial peak (Fig. 5.22). Thus, it is likely that the slow change in MREs occurring after the main ThT growth phase corresponds to the slow increase in ThT signal at this time, and probably the sharper, more distinct second phase occurring at lower $m(0)$. This indicates that the initial increase in ThT fluorescence is caused by formation of a species with a low secondary structure content, which nonetheless causes a ThT response. The fact that there are further increases in ThT signal after the first phase indicates that the species responsible for this initial change either does not produce as strong a ThT response as mature amyloid fibrils, or does not accumulate to quite as high a level, so that the subsequent changes in ThT fluorescence and the CD spectrum represent the gradual replacement of this relatively disordered, ThT-positive species with a more structured species that either causes a somewhat stronger ThT response, or has a lower critical concentration for formation.

Thus, the changes in the ThT and CD signal occurring in the growth phase in the presence of 300 mM NaF cannot be explained by a two-state model. Instead, a minimum of three states are needed to explain this growth phase: a relatively disordered state characterised by a low secondary structure content and a lack of ThT response, which is probably monomer but may include rapidly formed globular oligomers; a state that has a low secondary structure content, but has fibril-like self-assembly kinetics and causes a ThT response; and a final state, probably corresponding to newly formed amyloid fibrils, which has an intermediate secondary structure content and causes a ThT response. At present, it is unclear whether further extending the time course would reveal a slow plateau-phase ordering process similar to that observed in the absence of NaF.

5.3.4.3 A non-fibrillar aggregate accounts for the first phase of self-assembly

Although, at first glance, it seems odd to propose that the ThT 'growth phase' could be accounted for by a species that has a strong ThT response and fibril-like self-assembly kinetics, but a monomer-like secondary structure content, closer examination of the data and the literature reveals that this is not only plausible, but supported by existing studies. To begin with, it should be noted that the data do not suggest that this species has an identical CD spectrum to the monomer, but merely that it is similar; for example, the small change in the CD spectrum by 1600 s could be mostly accounted for by formation of the non-fibrillar species, rather than small quantities of amyloid fibrils. In addition, it is unsurprising that a non-fibrillar aggregate could have a similar CD spectrum to the monomer. Although the formation of non-fibrillar aggregates is often associated with a large change in secondary structure content, this is not always the case, and as previously discussed in Section 1.4.2, partly ordered, globular Aβ oligomers are relatively common, and have a β-strand content (10-40%) [290, 304] very close to that of the monomer (10-30%) [219, 221, 230–232]. Thus, neither the monomer nor the globular oligomers are completely devoid of secondary structure, although the structure of the former is typically highly dynamic, with individual secondary structure elements only persisting for short time scales [221, 230, 232, 236] in a manner consistent with Uversky's concept of a PMG [225, 227]. The CD data presented in this section give secondary structure estimates consistent with the above figures. In the presence of 300 mM NaF, analysis of the 0 s, 280 s, and 1600 s time points gives an estimated β-strand content of $\sim 40\%$ in all cases, with negligible helical structure (see Section 5.2.5). For the initial time point, this is a little high for pure monomer, and may support some degree of rapid oligomerisation after dilution into the fibrillisation buffer; alternatively, it could represent a salt-induced ordering process. For the 1600 s time point, the figure of $\sim 40\%$ is entirely consistent with a mixture of monomer and globular oligomers, given the likely error in the estimated secondary structure content. Thus, it is not surprising that a non-fibrillar aggregate should have a similar secondary structure content to the monomer, and both states have sufficient β-strand content to form small β-sheets, with the exception that the monomer does not form long-lasting β-sheets due to its rapid conformational dynamics, and is obviously incapable of forming intermolecular β-sheets.

Although the data suggest that there is only a small increase in β-structure content from the monomer to the non-fibrillar aggregate, there would have to be a significant change in the nature of the β-sheets to cause a fibril-like ThT response. In the monomer, β-sheets typically manifest as transiently formed β-hairpins, particularly involving the hydrophobic CHC and CTR regions of the peptide [219, 232, 236, 238, 305]. In globular oligomers, a more diverse range of β-sheets have been reported, both intramolecular and intermolecular, and both antiparallel and parallel [220, 278, 290, 303]. Furthermore, even in globular oligomers with a relatively low β-strand content, 'subdomains' with amyloid-like secondary structure and long-lasting

tertiary and quaternary contacts have been observed [216, 290, 296, 303]. Thus, it is not implausible that a globular oligomer with a low secondary structure content should cause a ThT response, and ThT binding has previously been reported for oligomers formed by Aβ(1-40) [278] and Aβ(1-42) [279], despite the oligomers reported in both those studies having an irregular, spheroidal morphology indicative of a lack of long-range molecular order.

This raises the question of what sort of β-sheets would be required to bind ThT. Despite its widespread use as an indicator for amyloid, ThT is neither completely specific nor completely sensitive to amyloid, having been shown to bind some globular proteins [557, 558], and to fail to detect some amyloids [559]. In addition, the results presented earlier in this thesis provide other examples of non-fibrillar aggregates that can bind ThT, including the HMW species identified in Chapter 3, and the films formed on polystyrene, which were presented in Chapter 4. Nonetheless, there is a growing understanding of the binding mode of ThT which means that it is possible to draw tentative conclusions regarding the likely structure of species that cause a ThT response. A more detailed discussion of amyloid-ThT interactions is provided in the reviews by Biancalana and Koide [93] and Groenning [94], but the main points are summarised here. Prevailing models propose that ThT binds a stretch of at least ~ 4 aligned β-strands, with the long axis of the dye oriented parallel to the fibril axis. Most ThT binding sites are easily accessible, requiring β-sheets close to the solvent, and binding is encouraged by the presence of a groove formed by aligned amino acid sidechains; while aromatics and hydrophobics typically encourage binding, unfavourable electrostatics can ablate binding [560–562]. Thus, the factors that distinguish amyloid β-sheets from those found in globular proteins are their extent, the high degree of alignment of the sidechains, and the comparatively low rate of twist. This means that the poor dye binding characteristics of some amyloids can be explained in terms of their unusual surface structure [559], and conversely the false positives obtained for some non-amyloid proteins and supramolecular assemblies can be attributed to the presence of binding pockets that mimic the surface of amyloid fibrils [557, 558]. Although the Aβ monomer transiently forms β-hairpins [219], they do not possess the required characteristics to bind ThT. At the same time, the weak ThT response elicited by the surface films presented in Chapter 4 suggests that there may be some degree of β-sheet formation and molecular alignment close to the solvent, although the specific fluorescence intensity of those films is low compared to that of fibrils.

The fact that the partly ordered aggregates cause a similar ThT response to mature amyloid fibrils suggests that the main ThT binding site is similar, even if the rest of the structure is different. This is consistent with models of the structure of globular Aβ oligomers, in which the motifs present in the core of the final cross-β structure form early in the oligomers, before ordering of most of the polypeptide chain or development of a fibrillar morphology [278, 286, 290]. Without more detailed structural data, it is not possible to say with a high level of certainty which regions of the molecule might be involved in this structure. Nonethe-

less, the CHC region of the peptide would be a prime suspect. This region contains the hydrophobic LVFFA sequence, which is part of the cross-β structure of most fibril polymorphs that have been characterised in atomic detail [111, 136, 143, 144, 160], as well as the ordered subdomains of many partly structured Aβ oligomers [278, 290, 303], indicating that it is usually one of the first regions of the peptide to develop cross-β structure. Although ThT binding is likely to be distributed across the entire fibril surface to some extent, the LVFFA sequence is probably the best candidate for a high-affinity binding site, as it is typically positioned close to the solvent in fibril structures [111, 136, 143, 144], and almost always creates a hydrophobic surface groove between V18 and either F20 or A21 [111, 136, 143, 144]. Thus, if the non-fibrillar aggregates observed in the ThT-CD experiments contained even a short intermolecular β-sheet in the VFFA region, similar to the subdomains in many oligomers that have already been characterised [278, 290, 303], they might be able to elicit a fibril-like ThT response.

5.3.4.4 Morphology of the non-fibrillar aggregate

To obtain a better characterisation of the non-fibrillar species and more generally the morphology of Aβ(1-42) aggregates formed under these conditions, samples were extracted from ThT assays containing 10 μM Aβ(1-42) in a 20 mM sodium phosphate buffer, with 1 mM NaN_3, 200 μM EDTA, 20 μM ThT, and 300 mM NaCl, and examined by NS-EM. The NS-EM data presented in Section 5.3.2 had revealed oligomeric species and changes in fibril polymorphism that were consistent with the results of the ThT-CD experiments, but the conditions had not been exactly comparable, which is why this experiment was performed. The ThT curve had a similar rate and shape to that shown in Fig. 5.24(d), and representative images of samples extracted after 0 s, 2400 s, 3600 s, or 4800 s are shown in Fig. 5.25-5.26. For samples taken after 0 s, ie. after dilution into the fibrillisation buffer followed by immediate staining (Fig. 5.25(a-b)), fibrils were not observed, although small oligomeric species were relatively abundant, supporting the hypothesis that some of the monomer may have rapidly formed oligomers. After incubation for 2400 s, the ThT signal had reached $\sim 65\%$ of its final value, and in the corresponding ThT-CD experiment the MRE at 199 nm was only $\sim 25\%$ of the way from its minimum value of -7900 deg.cm^2.dM^{-1} to its final value of -1500 deg.cm^2.dM^{-1}. In the NS-EM images (Fig. 5.25(c-d)), small fibrils were observed, but at much lower abundance than typically observed during the growth phase at lower ionic strength (Fig. 3.12(c-d), Fig. 5.4, Fig. 5.6), and globular oligomers with a spheroidal or irregular appearance and typical diameter of no more than 10 nm were very abundant. The scarcity of amyloid fibrils agrees with the disordered CD spectra obtained around this time point in the corresponding ThT-CD experiments, and supports the idea that oligomers, rather than fibrils, are responsible for the ThT signal.

After incubation for 3600 s, the ThT signal had reached $\sim 90\%$ of its maximum value, while in the corresponding ThT-CD experiment the MRE at 199 nm was only $\sim 50\%$ of the way between its minimum

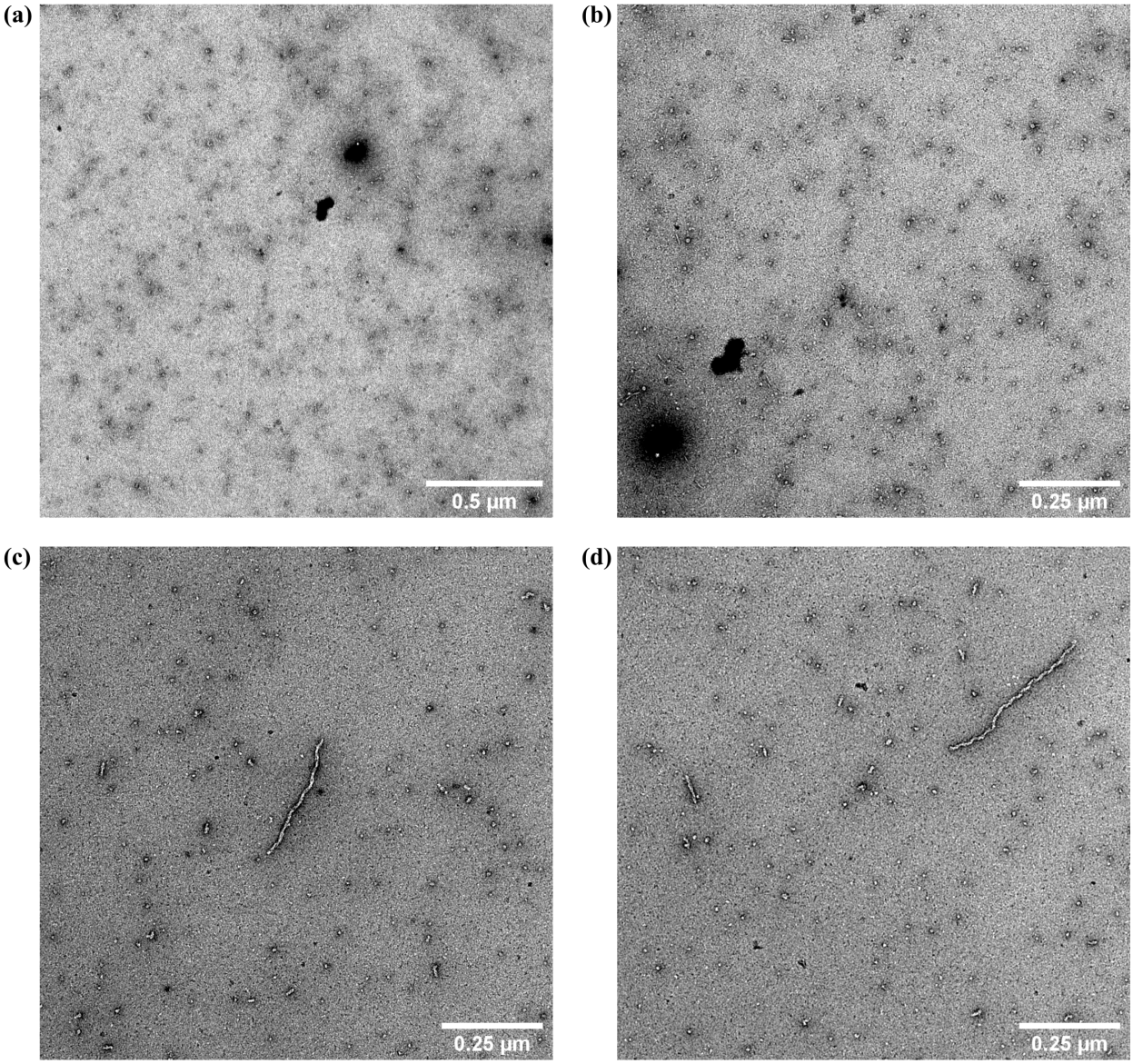

Figure 5.25: NS-EM of 10 μM Aβ(1-42) fibrillisation at $I = 360$ mM (part 1). Panels (a-b) show representative images of Aβ(1-42) aggregates formed immediately after dilution into fibrillisation buffer, and panels (c-d) show representative images of aggregates formed after incubation in fibrillisation buffer for 2400 s, under standard conditions for the ThT assays in this chapter (PEG-treated plates, 37°C). The buffer was 20 mM sodium phosphate (pH 8) containing 1 mM NaN_3, 200 μM EDTA, 20 μM ThT, and 300 mM NaCl.

and maximum values. In the NS-EM images (Fig. 5.26(a-b)), fibrils were more abundant than at 2400 s, and generally had an apparently tubular or irregular morphology. Nonetheless, small, globular oligomers remained relatively abundant. Lastly, after 4800 s incubation, the ThT signal had reached $\sim 100\%$ of its maximum value and in the corresponding ThT-CD experiment the MRE at 199 nm was $\sim 80\%$ of the way from its minimum to its maximum value. The NS-EM images (Fig. 5.26(c-d)) revealed fibrils with a broadly similar morphology to those observed at 3600 s, although fibrils with a helical appearance were observed. Oligomers were still present, but were greatly reduced in size, rarely surpassing 5 nm in diameter.

Collectively, the ThT, CD, and NS-EM data indicate that the dominant Aβ(1-42) self-assembly states differ markedly between $I = 59$ mM and $I = 360$ mM. In the former, the sample begins in a mostly monomeric state with a PMG-like secondary structure content, and the growth phase reflects the incorporation of the monomer into growing fibrils with a mixture of β-sheet and disordered regions, which later undergo further structural changes. Although oligomers are often observed under conditions associated with uniphasic ThT kinetics (Fig. 3.12(c-d), Fig. 5.4), they are never particularly abundant, and do not appear to make a major contribution to either the CD or ThT signal. At high $m(0)$ and I, however, the transition to biphasic self-assembly kinetics is associated with a change in the sequence of dominant species present at different stages of the self-assembly process. The ThT growth phase is not associated with the formation of large quantities of amyloid fibrils, but instead partly ordered, globular oligomers, which are likely to have amyloid-like structural motifs in order to induce a ThT response. The slower CD growth phase, which is associated with a smaller change in ThT signal, sees the shrinkage of these oligomers and the appearance of amyloid fibrils with a more ordered CD spectrum, indicating that oligomers disassemble to maintain a monomer reservoir for fibril growth. After this point, it is possible there may be further slow structural changes in the fibril population, as seen at lower ionic strengths.

5.3.5 Salt-induced oligomers are secondary nucleation intermediates

Although the experimental data report on the sequence in which various species appear during self-assembly, they do not directly reveal on the mechanism by which the ThT-positive oligomers form. Nonetheless, they provide a wealth of timescales and scaling behaviours that can be used to assess possible models. To begin with, the inflection times were calculated for the various self-assembly phases shown in Fig. 5.21(a) and Fig. 5.22, defined as the times at which the rate of ThT fluorescence gain reached a maximum. For the uniphasic data in Fig. 5.21(a), which were obtained at 0 mM NaCl ($I = 59$ mM), there was a single maximum, and the time at which this was reached scaled approximately inversely with $m(0)$, as shown in Fig. 5.27(a) ($\gamma_{\text{inf}} = 1.02$, 95% CI 0.92-1.12). However, for the data in Fig. 5.22, which were obtained at 300 mM NaCl ($I = 360$ mM), there were often two inflection times, reflecting the biphasic nature of the kinetics. Both inflection times were calculated wherever there were obvious corresponding peaks, and the

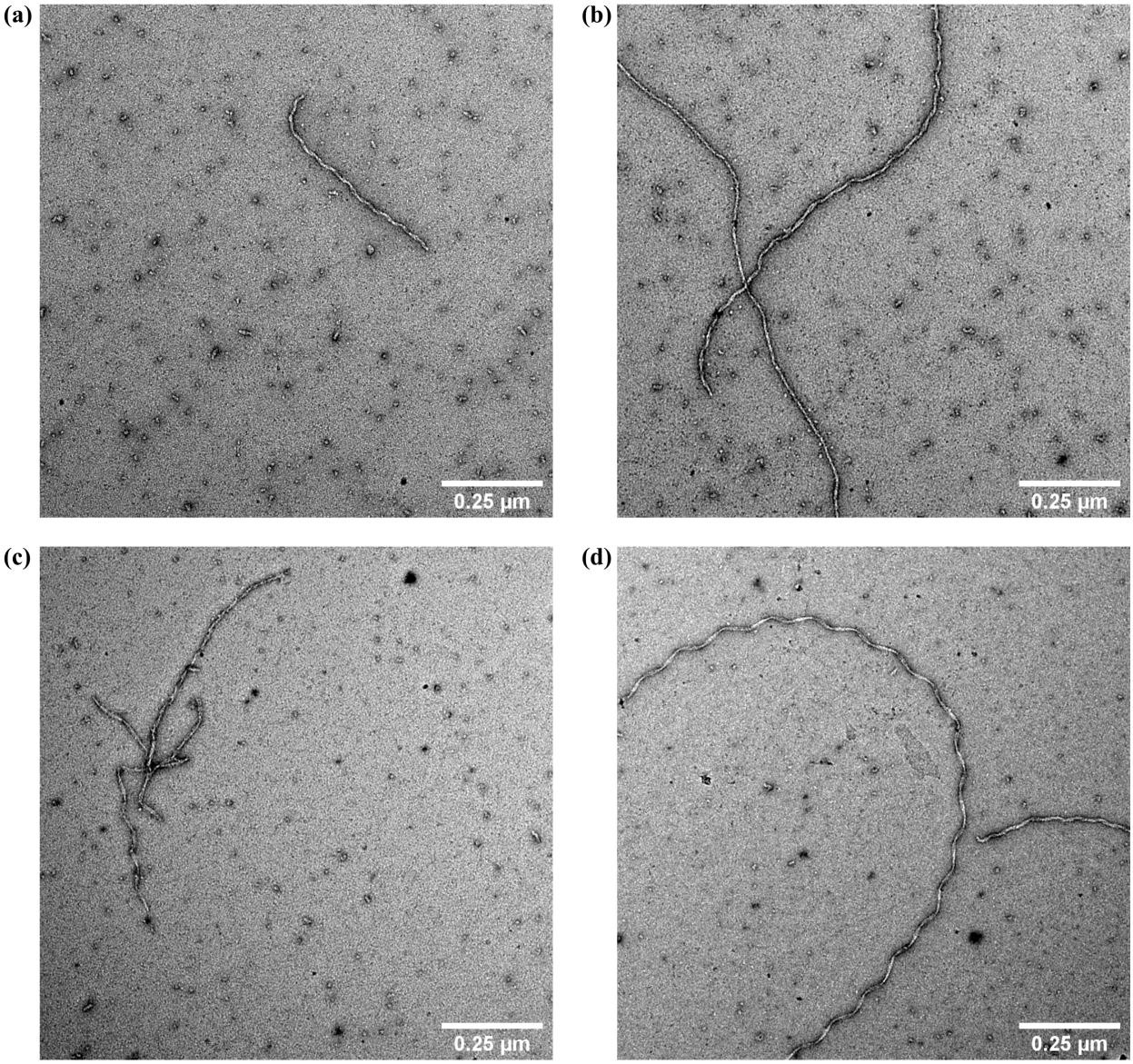

Figure 5.26: NS-EM of 10 μM Aβ(1-42) fibrillisation at $I = 360$ mM (part 2). Panels (a-b) show representative images of Aβ(1-42) aggregates formed after incubation in fibrillisation buffer for 3600 s, and panels (c-d) show representative images of aggregates formed after incubation in fibrillisation buffer for 4800 s. Samples were incubated under standard conditions for ThT assays in this chapter (PEG-treated plates, 37°C), and the fibrillisation buffer was 20 mM sodium phosphate (pH 8) containing 1 mM NaN_3, 200 μM EDTA, 20 μM ThT, and 300 mM NaCl.

times at which these peaks occurred could be determined with sufficient accuracy, and these times are plotted in both panels of Fig. 5.27. While the inflection time of the first phase could be calculated in almost all cases, the inflection time of the second phase could only be calculated in the $3.25\ \mu\text{M} \leq m(0) \leq 5.5\ \mu\text{M}$ range; below this range, there appeared to be no obvious biphasic character, and above this concentration range, the tail of the first derivatives became more complex, so that it was not possible to easily identify a single second inflection time. While a constant concentration-dependence of the inflection time had been observed at 0 mM NaCl, a change in concentration-dependence of the inflection time of the first phase was observed at 300 mM NaCl, with $\gamma_{\text{inf}} = 0.80$ (95% CI 0.67-0.93) for $2\ \mu\text{M} \leq m(0) \leq 3.5\ \mu\text{M}$, and $\gamma_{\text{inf}} = 0.23$ (95% CI 0.12-0.33) for $5.5\ \mu\text{M} \leq m(0) \leq 10\ \mu\text{M}$. Similar scaling exponents were also obtained for the half-times, with $\gamma_{50} = 0.71$ (95% CI 0.65-0.78) for $2\ \mu\text{M} \leq m(0) \leq 3.5\ \mu\text{M}$, and $\gamma_{50} = 0.17$ (95% CI 0.07-0.26) for $5.5\ \mu\text{M} \leq m(0) \leq 10\ \mu\text{M}$, although the γ_{50} values are considered less accurate as they include mixed contributions from the first and second phases. The change in concentration-dependence is associated with the transition from a regime where the first phase is primarily accounted for by fibril formation (eg. Fig. 5.8) to one where globular oligomer formation predominates (Fig. 5.24-5.26). As shown in the inset in Fig. 5.27(a), if this change in self-assembly behaviour and kinetic scaling were due to competition, an increase in concentration-dependence would be expected, representing the overtaking of the pre-existing first phase by a more concentration-dependent self-assembly pathway. However, a very significant reduction in concentration-dependence occurs instead, which is more consistent with saturation or a similar mechanistic change affecting the same pre-existing pathway. In addition, there was a brief inversion of the concentration-dependence around $m(0) \approx 3\ \mu\text{M}$, which can also be seen in the corresponding first derivatives in Fig. 5.22.

The reduction in concentration-dependence of the first phase indicates that the change in self-assembly mechanism is not caused by the emergence of a competing, more concentration-dependent self-assembly pathway, but a change in the pre-existing self-assembly pathway, which affects the predominant species produced by the microscopic processes responsible for the growth phase, and affects the concentration-dependence of this pathway correspondingly. In other words, the globular oligomers appear to be formed by the same process that produces the majority of fibrils, which is secondary nucleation. If the globular oligomers were formed by a separate pathway from that which forms fibrils, they would be unable to outcompete the fibrils as $m(0)$ increased, due to their weaker $m(0)$-dependence. This indicates that increasing $m(0)$ and I causes the cycle of autocatalytic processes usually responsible for fibril formation to increasingly produce ThT-positive globular oligomers, with fibril-like structural elements but a generally lower secondary structure content, and reduced mesoscale order as a result. This also answers the question of how the formation of globular oligomers can have high-order kinetics early during self-assembly, with a well-defined lag phase and growth phase. In the absence of an autocatalytic process, the kinetics of globular oligomer formation might be expected to have either linear early-time kinetics, if nucleation was a single-

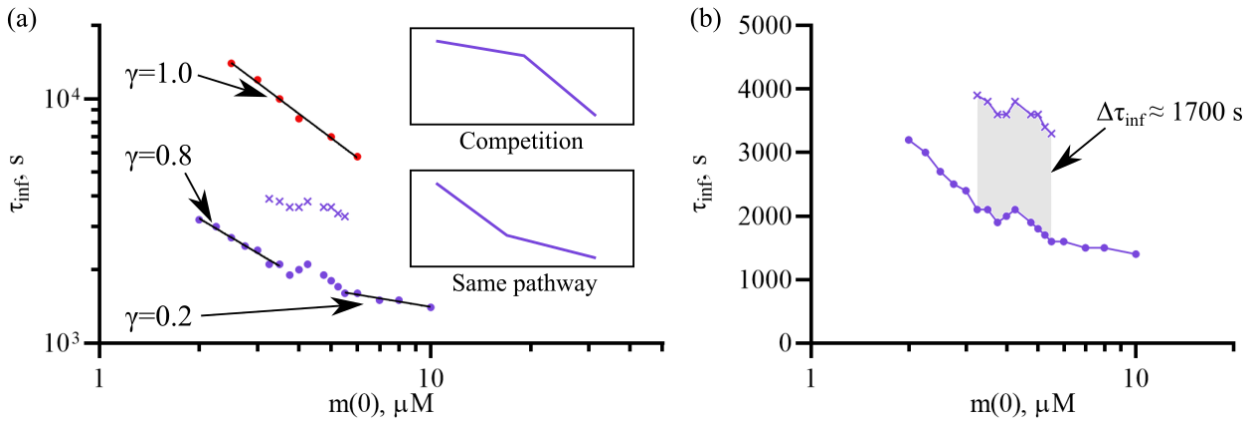

Figure 5.27: The transition between regimes is due to changes in the existing pathway, rather than competing pathways. (a) The inflection time (ie. time of maximum rate of change) of ThT curves as a function of $m(0)$, in a 20 mM sodium phosphate buffer (pH 8) containing 1 mM NaN_3, 200 μM EDTA, 20 μM ThT, and either 0 mM or 300 mM NaCl. Colour scheme: red, inflection time with 0 mM NaCl ($I = 59$ mM); purple dots, inflection time of the first phase with 300 mM NaCl ($I = 360$ mM); purple crosses, inflection time of the second phase with 300 mM NaCl ($I = 360$ mM). Regions of the datasets have been fitted to the relation $\tau_{inf} \propto m(0)^{-\gamma_{inf}}$, which measures the concentration-dependence. The inset panels show the expected appearance of the data on the same axes if the change in regimes is due to competing pathways or a process affecting the pre-existing self-assembly pathway. (b) Examining the same data on a linear time axis shows that the difference between the inflection times of the two phases observed at 300 mM NaCl is independent of $m(0)$, and has a value of $\Delta\tau_{inf} \approx 1700$ s.

step process and growth was restricted, Oosawa-like early-time kinetics if growth was linear [425, 426], or kinetics described by the KJMA equation, if growth occurred three-dimensionally [563]. Although the latter equation would predict sufficiently high-order kinetics in the early time ($\sim t^4$) to approximately fit the ThT curves, the relatively restricted size of the globular oligomers ($d \approx 5$ nm, suggesting a very approximate size of $\sim$ 6-mer based on density constraints) indicates that KJMA-like growth is unlikely. In addition, the observed decrease in concentration-dependence at the transition between regimes suggests that the pathway responsible for globular oligomer formation is the same as that responsible for fibril formation, and thus unlikely to involve KJMA-type self-assembly kinetics. Instead, the high-order early-time scaling is probably a result of the fact that the pathway that forms both globular oligomers and fibrils is autocatalytic, resulting in exponential early-time kinetics. Furthermore, as will be shown subsequently, if the globular oligomers and fibrils were formed by the same cycle of autocatalytic processes, they would have the same concentration-dependence, so any reduction in concentration-dependence associated with increasing oligomer production, regardless of the reason for this reduction, would similarly reduce the concentration-dependence of fibril formation, explaining why fibrils do not outcompete the oligomers at higher concentrations.

If the structural and kinetic changes affecting the first phase represented the diversion of reactive flux towards metastable oligomer formation rather than fibril formation, the second phase would reflect the gradual replacement of those metastable oligomers with fibrils, consistent with the fact that the main change in the CD signal occurs after the first phase of ThT fluorescence gain. Regardless of whether the oligomers can be considered 'on-pathway', or a non-productive by-product of secondary nucleation, replacement of the oligomer population is likely to predominantly involve disassembly, rather than direct conversion to fibrils. This is because conversion is typically proposed to be a slow, rare event, whereas once even a small population of fibrils had formed, they would rapidly deplete the soluble monomer and thus destabilise the remaining oligomers. A predominantly disassembly-based mechanism of replacement is supported by the observation that the oligomers appear to shrink around the time at which the CD signal changes the most (Fig. 5.26). In addition, if direct conversion were the main mechanism by which the oligomer population were replaced with fibrils, the result would be large quantities of small, oligomer-sized fibrils, rather than the smaller quantity of fibrils, each many times the size of an oligomer, that was observed by NS-EM. This mechanism is also supported by analysis of the manner in which the second phase appears (Fig. 5.22), and the time difference $\Delta\tau_{\text{inf}}$ between the inflection times associated with the first and second phases (Fig. 5.27(b)). Rather than splitting off from the first phase, the separation between the two phases is relatively independent of $m(0)$, with an average $\Delta\tau_{\text{inf}} \approx 1700$ s across all $m(0)$ for the data in Fig. 5.22 and Fig. 5.27(b). Thus, as can be seen in Fig. 5.22, at low $m(0)$ it is the amplitude of the second phase that changes, rather than the relative timing. This is consistent with disassembly-limited fibril formation in an environment where the soluble monomer concentration is restricted by the critical concentration for oligomer stability,

and suggests that the amplitude of the second phase is likely to be approximately proportional to the quantity of oligomeric material produced by the first phase. A similar estimate of $\Delta\tau_{\text{inf}} \approx 1550$ s was obtained for the data in Fig. 5.21(d) (also 300 mM NaCl, $I = 360$ mM, with the slight change in $\Delta\tau_{\text{inf}}$ probably reflecting the slight difference in rate between the experiments), and an estimate of $\Delta\tau_{\text{inf}} \approx 1100$ s was obtained for the data in Fig. 5.21(c) (100 mM NaCl, $I = 160$ mM), suggesting that ionic strength stabilises the globular oligomers and reduces their disassembly rate. It is worth noting that, although the lifetime of the oligomers close to their critical concentration is likely to be $\sim \Delta\tau_{\text{inf}}$, disassembly of oligomers is unlikely to be a simple one-step process, explaining why the second phase often has a well-defined peak, rather than occurring as an exponential tail on the first derivative of the ThT signal.

The conclusion that the globular oligomers must be formed by the same autocatalytic pathway as fibrils, in order to produce the required early-time scaling and change in concentration-dependence, entails that globular oligomers are formed by a fibril-dependent process similar to, or perhaps the same as, secondary nucleation. The notion that secondary nucleation should produce globular oligomers is not at all surprising; the first kinetic analysis to demonstrate secondary nucleation in Aβ(1-42) also showed that secondary nucleation resulted in the formation of toxic oligomers, and these oligomers were also suspected to be on-pathway intermediates for secondary fibril formation [54]. However, the main difference between this work and that previously presented is the extent to which secondary oligomers accumulate. While secondary oligomers identified in previous studies have only been present at low levels [54, 469], due to the fact that they are formed at a low rate and are perhaps also inherently unstable at the $m(0)$ and I used in those studies, in the high ionic strength data presented in this chapter the oligomers accumulate until they deplete most of the soluble monomer. This indicates that the there is either a marked increase in oligomer production, or a switch from being unstable fluctuations to metastable aggregates, above a certain $m(t)$ and I. Nonetheless, it is possible that different sub-populations of secondary oligomers could make different contributions to fibril formation, so the secondary oligomers found to accumulate in this chapter could still be functionally off-pathway.

To test whether secondary oligomers would have the right self-assembly kinetics to explain the data, and whether the data better support an on- or off-pathway role, four mechanistic models were proposed. These models represent binary combinations of two pairs of extreme possibilities: oligomers are either completely on-pathway, or completely off-pathway; and oligomers either have a very short lifetime that limits their accumulation, or a long lifetime that allows greater accumulation. In reality, the situation is likely to be more intermediate, but examining these extreme cases simplifies the mathematics, and makes it possible to determine which scenario describes the data best. Schematics of the four models are shown in Fig. 5.28, and full details of the mathematical analysis are provided in Section 5.2.7. In brief, the early-time kinetics of each model were analysed in order to obtain approximate solutions for the concentration of oligomers

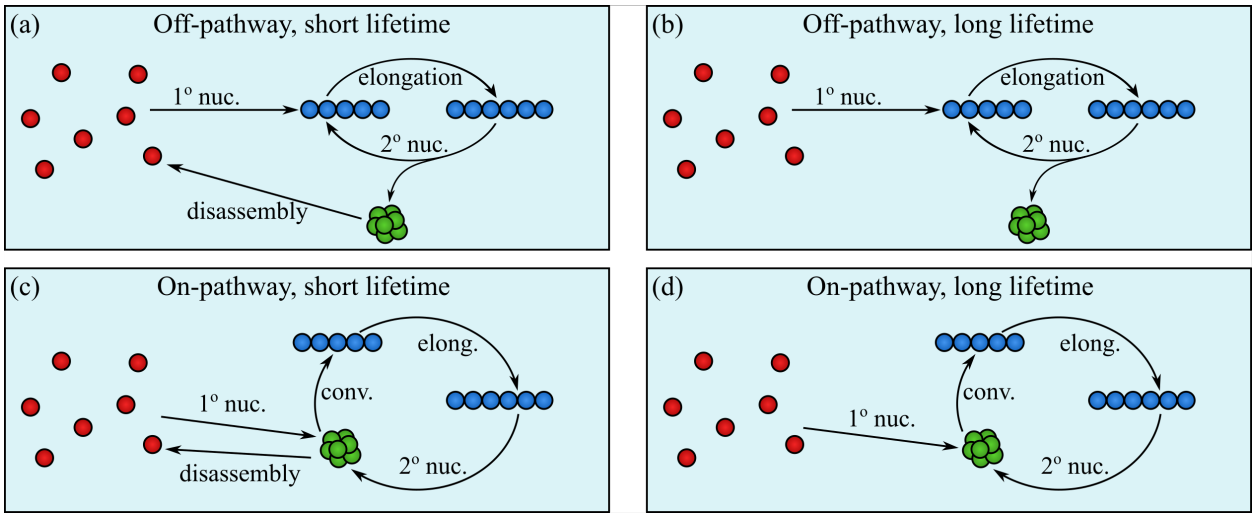

Figure 5.28: Schematics of possible models of secondary oligomer generation. Panels represent different mechanistic models. Circles represent Aβ(1-42) monomers, with the colour scheme representing the conformational state: red, free monomer; green, globular oligomer; blue, fibrillar. The arrows represent the microscopic molecular processes, with the labels meaning: 1° nuc., primary nucleation; 2° nuc., secondary nucleation; conv., conversion; elong., elongation. In the models in panels (a) and (c), oligomers are assumed to rapidly reach a pseudo-steady-state concentration defined by the balance of nucleation and disassembly processes. In the models in panels (b) and (d), oligomers accumulate continuously due to nucleation with negligible disassembly. All these models can be considered extreme cases of the same general reaction scheme, which is similar but not identical to that recently proposed by Michaels *et al.* [469].

and fibrils, the relative ratio of the two, and the generalised scaling exponent γ in secondary-dominated self-assembly pathways, which is expected to be approximately equal to γ_{inf} and γ_{50}. In all models, the analysis confirmed that the oligomer and fibrillar mass concentrations both increase exponentially over time, and have the same effective rate constant, so that an approximately constant ratio of the two is expected throughout the first phase.

In the first model, excess oligomers produced at high $m(0)$ and I are off-pathway, and have a short lifetime so that their concentration is determined by the balance of fibril-dependent formation and disassembly (Fig. 5.28(a)). Thus, their concentration is approximately

$$G(t) \approx \frac{\lambda^2 k'_g m(0)}{2\kappa^2 k'_d} e^{\kappa t}, \tag{5.60}$$

where $G(t)$ is the globular oligomer concentration, k'_g is the pseudo-first-order rate constant for formation of oligomers at a rate proportional to $M(t)$, and k'_d is the effective rate constant for oligomer disassembly, which is assumed for convenience to be a one-step process. The values of λ and κ are given by Eq. (5.58) and Eq. (1.50), so that primary nucleation exhibits a residual $m(t)$-dependence as established in Section 5.3.3. It is assumed from extrapolation of the data in Fig. 5.16(g) that $m(0) \gg K_{M,n}$ and $m(0) \gg K_{M,s}$, so

that both primary and secondary nucleation are maximally saturated; since the bulk of oligomer formation is proposed to occur via a process mechanistically similar to secondary nucleation, k'_g is also treated as $m(t)$-independent. Although it is likely that k'_d will vary with $m(t)$, and this effect is expected to become relevant towards the end of the growth phase when $m(t)$ is highly depleted, there are no experimental data to constrain this variation, so k'_d is here treated as constant for the duration of the early-time kinetics that this model covers.

It should also be noted that the oligomer disassembly rate is independent of the fibril mass concentration, in line with the experimental observations of Michaels *et al.* [469] on a related, although probably distinct, population of secondary oligomers. In that paper, the oligomers were shown to dissociate from the fibrils after their formation, and then spontaneously disassemble in solution. Thus, disassembly was not the simple opposite of oligomer formation, a conclusion that was supported by molecular simulations as well as experimental observations. Although surprising, such a cyclic mechanism is possible in systems that are sufficiently far from equilibrium, and it should be noted that self-assembly experiments and molecular simulations of Aβ(1-42) are both typically performed under conditions of high supersaturation, and experiments contain additional thermal gradients that may help to drive such a process [445]. Alternatively, in some cases, fibril-independence of the disassembly rate could be consistent with an oligomer population that remained predominantly associated with fibrils; although the NS-EM data indicate that this is not likely to be the case at high $m(0)$ and I (Fig. 5.25-5.26), it may well be the case for the smaller oligomer populations formed under uniphasic self-assembly conditions. The self-assembly kinetics do indicate that any rapidly disassembling secondary nucleation intermediate must have a fibril-independent self-assembly rate in order to produce the observed kinetics, requiring one of the above explanations, as the oligomer population would otherwise be insensitive to the fibril mass population, preventing positive feedback. This is not an issue with slowly disassembling oligomer populations, which are considered in models two and four.

The ratio of oligomer to fibril mass can be calculated by multiplying $G(t)$ by the average size of oligomers $\langle N \rangle$, and dividing by the corresponding solution for the fibril mass concentration (Section 5.2.7). In the first model (Fig. 5.28(a)), the ratio of oligomer to fibril mass is

$$\frac{\langle N \rangle G(t)}{M(t)} \approx \frac{\langle N \rangle k'_g}{k'_d}, \tag{5.61}$$

so that oligomers will be the dominant species responsible for the first phase if $\langle N \rangle k'_g \gg k'_d$. If secondary pathways dominate over primary pathways, as can reasonably be expected for all four models evaluated here, the concentration-dependence will be

$$\gamma \approx \frac{1}{2}. \tag{5.62}$$

In the second model, k'_d is negligible, so the oligomers accumulate beyond the level expected from a sim-

ple balance between formation and disassembly (Fig. 5.28(b)). In this model, exponential scaling is still observed, and the exponent is unchanged; the only change is in the definition of the pre-exponential factor. The concentration of oligomers will be

$$G(t) \approx \frac{\lambda^2 k_g' m(0)}{2\kappa^3} e^{\kappa t}, \tag{5.63}$$

where λ and κ are still given by Eq. (5.58) and Eq. (1.50). The ratio of oligomer to fibril mass will be

$$\frac{\langle N \rangle G(t)}{M(t)} \approx \frac{\langle N \rangle k_g'}{\kappa}, \tag{5.64}$$

so that so that oligomers will be the dominant species responsible for the first phase if $\langle N \rangle k_g' \gg \kappa$, and the concentration-dependence will be unchanged from the previous model. In the third model (Fig. 5.28(c)), the oligomer concentration is once again determined by the balance between nucleation and disassembly, but the oligomers are now positioned as an obligate intermediate in both primary and secondary nucleation. This gives the same result as the first model, except that the primary and secondary nucleation rate constants are now given definitions in terms of the conversion rate k_c' per whole oligomer,

$$k_n = \frac{k_0' k_c'}{K_{M,n}(k_c' + k_d')}, \tag{5.65}$$

$$k_s = \frac{k_g' k_c'}{K_{M,s}(k_c' + k_d')}, \tag{5.66}$$

where k_0' is the effective $\varepsilon_c^{\text{th}}$-order rate constant for fibril-independent oligomer generation, and it is assumed that primary and secondary nucleation are both maximally 'saturated', and described by Eq. (5.56) and (1.45), respectively. It is also assumed that k_c' is sufficiently small that elongation is still the main contributor to fibril mass. Lastly, in the fourth model (Fig. 5.28(d)), oligomers are an obligate nucleation intermediate but they persist for a long time, so that losses due to disassembly and conversion are negligible over the course of the growth phase. This results in a different rate of oligomer accumulation,

$$G(t) \approx \frac{k_0' m(0)^{\varepsilon_c}}{3\kappa} e^{\kappa t}, \tag{5.67}$$

where there is a new expression for κ,

$$\kappa = \left[2 k_g' k_c' k_e^+ m(0)\right]^{1/3}, \tag{5.68}$$

which is now the geometric mean of three pseudo-first-order rate constants (k_g', k_c', $2k_e^+ m(0)$), rather than two as in the previous models. This change in the definition of κ accounts for the fact that there are now

three unsteady quantities ($G(t)$, $P(t)$, and $M(t)$) in the autocatalytic cycle, rather than two ($P(t)$, and $M(t)$). The ratio of oligomer to fibrillar mass will be

$$\frac{\langle N\rangle G(t)}{M(t)} \approx \langle N\rangle \left[\frac{(k_g')^2}{2k_c'k_e^+ m(0)}\right]^{1/3}, \tag{5.69}$$

so that oligomers will be the dominant species responsible for the first phase if $\langle N\rangle^{3/2}k_g' \gg \sqrt{2k_c'k_e^+ m(0)}$. More crucially, the change in definition of κ results in a new definition of γ,

$$\gamma \approx \frac{1}{3}. \tag{5.70}$$

Thus, a transition to a regime where on-pathway oligomers have a significantly longer lifetime than the growth phase would result in accumulation of those oligomers, with the possibility that they might become more abundant than fibrils, as well as causing a reduction in the concentration-dependence of both oligomer and fibril mass accumulation. The values of $\gamma_{\text{inf}} = 0.23$ (95% CI 0.12-0.33) and $\gamma_{50} = 0.17$ (95% CI 0.07-0.26) for $5.5\,\mu\text{M} \leq m(0) \leq 10\,\mu\text{M}$ could be consistent with the prediction of the fourth model that $\gamma \approx 1/3$, especially given that there is also likely to be a small contribution from saturable primary nucleation, which would further reduce the concentration-dependence towards a theoretical limit of ~ 0.2. In addition, if other processes were occurring, such as off-pathway oligomerisation prior to the ThT growth phase, saturation of elongation, and rate-determining growth or conformational conversion of the on-pathway oligomers, they would reduce the concentration-dependence further, although prior work suggests that the amplitude of such effects is likely to be small [5]. Thus, in order to achieve such a low concentration-dependence, this analysis suggests that secondary nucleation must involve at least one accumulating intermediate whose concentration does not reach a steady state between formation and loss processes on the timescale required for monomer depletion; the fact that this drop in concentration-dependence is accompanied by a transition to biphasic kinetics strongly implicates the oligomer formed in the first phase as this intermediate.

While model four is probably the most accurate description of kinetics in the biphasic limit, one of models one to three is probably more accurate in the uniphasic limit. This is because there is a wealth of literature to suggest that steady-state approximations are valid for any extant nucleation intermediates under conditions where uniphasic kinetics are observed [4–6, 54, 529, 564]. This includes the particularly diagnostic observation that $\partial \log \kappa / \partial \log m(0)$ saturates at $\sim 1/2$ under such conditions [4, 529, 564], which is corroborated by the analysis in Section 5.3.3, and indicates that there are only two non-steady processes (nucleation and elongation) in the pathway. Although Michaels *et al.* [469] did recently report a population of long-lasting secondary oligomers at low ionic strength, which, if on-pathway, would justify a scenario similar to the fourth model, the authors did not provide evidence that the oligomers were on-pathway, merely

that they were secondary in origin. It should also be noted that the authors used an experimental approach that would be incapable of identifying short-lived oligomers ($1/k'_d \lessapprox 250$ s), their proposed on-pathway model provided a numerically poor fit for inhibitor data presented in the same paper, and the number and reaction order of the processes in that model were incompatible with the saturation behaviours reported in the rest of the literature, as well as this thesis. Therefore, in balance, it remains by far the simplest empirically justifiable scenario that any intermediates present under uniphasic conditions are at a local equilibrium or pseudo-steady-state, favouring one of models one to three. These models all predict $\gamma \approx 1/2$, which is consistent with the observed values of $\gamma_{\text{inf}} = 0.80$ (95% CI 0.67-0.93) and $\gamma_{50} = 0.71$ (95% CI 0.65-0.78), given that complete saturation was assumed in the above analysis, but would not realistically be achieved at $m(0) \leq 3.5$ μM. It should be noted that, so long as the proportion of oligomers is small, all three models are expected to produce identical fibril mass accumulation kinetics to the saturable version of the Knowles model [4, 6]; therefore, the fitting in Section 5.3.3 already validates their use under uniphasic conditions. Out of these models, model three (Fig. 5.28(c)) is the most likely to be correct at low $m(0)$ and I, as the oligomers do not appear to accumulate to high levels in the uniphasic regime, the kinetics of the transition between regimes imply that the oligomers that are observed during biphasic self-assembly are derived from a pre-existing pathway, rather than arising by competition with a pathway that does not involve intermediates, and there is already evidence that transient oligomers formed under similar conditions play an on-pathway role, or at least a proportion of the oligomer population does [54]. Therefore, the uniphasic regime is probably characterised by limited accumulation of on-pathway oligomers due to the short lifespan of those oligomers, so that the transition from uniphasic to biphasic kinetics is caused by a transition from a regime where oligomers do not accumulate (ie. are unstable at $m(t) = m(0)$, as in Fig. 5.28(c)) to one where they do (ie. are metastable at $m(t) = m(0)$, with an extreme case shown in Fig. 5.28(d)).

5.3.6 The role of oligomer disassembly in the transition between regimes

The identification of these two different regimes raises the question of how, and why, the transition between regimes occurs. The main difference between the extreme cases in Fig. 5.28(c-d) is that in one case the oligomers disassemble rapidly, and in the other they exhibit negligible disassembly in the early growth phase. However, technically the criterion for non-steady oligomer accumulation is $1/(k'_c + k'_d) \gg 1/\kappa$, as this ensures that the timescale $1/(k'_c + k'_d)$ on which oligomer populations adjust to an increasing formation rate is significantly longer than the timescale $1/\kappa$ on which oligomer and fibril populations are collectively amplified. Thus, it is probably not a coincidence that the amplitude of the second phase begins to increase around $m(0)$ values for which $1/\kappa$ and $\Delta\tau_{\text{inf}}$ are similar, since $\Delta\tau_{\text{inf}}$ may be close to the value of $1/k'_d$ earlier in the growth phase, and the NS-EM data suggest that $k'_d \gg k'_c$. For example, in the presence of 100 mM NaCl ($I = 160$ mM), when $\Delta\tau_{\text{inf}} \approx 1100$ s, the kinetics become biphasic when $m(0) \approx 3.5$ μM, at which

point $1/\kappa \approx 600$ s (although the transition to biphasic kinetics is likely to cause some error in estimation of κ). Thus, the transition to biphasic kinetics and decrease in concentration-dependence may be caused by two factors: the general increase in κ with increasing $m(0)$ or I, and a general decrease in k_d' with increasing I, and perhaps also $m(0)$. At very low $m(0)$ and I, $1/\kappa$ will be large and $1/(k_c' + k_d')$ will be small; as a result, the oligomer population will rapidly reach a value determined by the balance between formation and loss processes, but the extent of accumulation compared to the fibril population will be small. At higher $m(0)$ and I, $1/\kappa$ will be smaller and $1/(k_c' + k_d')$ will be larger. In this case, the oligomer population will undergo unbounded accumulation for a longer period, resulting in a larger oligomer population, biphasic kinetics, and a lower concentration-dependence due to an extended period in which there are more than two processes occurring at a non-steady rate.

There are two outstanding issues related to the size of the oligomer population in the growth phase that need to be addressed. Firstly, although an increase in the oligomer population relative to the fibril population would add to the ThT signal in the growth phase, so that $m(0)$-dependent reductions in k_d' might add to the concentration-dependence and thus increase γ, this effect only manifests as a small logarithmic term in the characteristic time, and so its effect on γ is expected to be small (Section 5.2.7). Secondly, it should be noted that Eq. (5.69) predicts an inverse relationship between $m(0)$ and the concentration of monomers incorporated into oligomers as a proportion of that incorporated into fibrils. However, this dependence is very weak ($\sim m(0)^{-1/3}$) and is only expected to be apparent at high $m(0)$, when the effect of $m(0)$ on k_d' is negligible; thus, it does not prevent the emergence of biphasic kinetics with increasing $m(0)$, but does predict a recovery of uniphasic kinetics at $m(0)$ values above the current experimental range.

5.3.7 The possibility of non-equilibrium criticality

Although k_d' is likely to be the dominant cause of the transition between regimes, it is also possible that a reduction in k_c' contribute to the lifetime of oligomers. Recently published theory work by myself and co-authors [8], conducted in parallel to the experimental work presented in this thesis, has demonstrated that the competition between growth and conversion of oligomeric or protofibrillar nucleation intermediates may lead to sharp changes in the time taken for the intermediates to convert to mature, growing fibrils. Counterintuitively, a key conclusion of the work is that conditions that promote the proliferation of on-pathway intermediates can significantly delay this transition. In addition, such systems exhibit abrupt changes in the size and abundance of oligomers that resemble the effects of a nonequilibrium critical point. The paper is not presented in full in this thesis as its scope is considerably broader than the topic addressed by the experimental work here, but relevant points that may explain aspects of the Aβ(1-42) self-assembly kinetics are summarised in this subsection.

The basic premise of the model is that growth and conformational change of pre-fibrillar intermediates

are often progressive processes that can occur on similar timescales [278, 295, 333, 565–567], which leads to competition. Schematics of these processes are shown in Fig. 5.29. While conversion is often assumed to be a cooperative transition involving the entire intermediate [224, 380, 418], there is evidence that conversion of many intermediates proceeds through a local conformational change that 'initiates' at a particular site within the intermediate, and then propagates throughout the remainder of the intermediate by templated conformational change [224, 347, 565, 568, 569]. This mechanism of conversion, which we have termed the 'initiation-propagation' (IP) mechanism, is represented in Fig. 5.29(b). Crucially, while growth of intermediates enhances initiation by creating new sites where the mature fibril structure can develop 5.29(c), in cases where templated structural rearrangement is slow, or growth is particularly fast, the continued growth of aggregates can extend the time taken for propagation to occur, and thus impede the transition to a mature fibril 5.29(d). This is because elongation of a newly formed amyloid fibril, which involves the direct incorporation of free monomers into the cross-β structure, requires the fibril ends to be exposed to the solvent. The emergence of fibril ends from the intermediate can be prevented by the continued deposition of non-fibrillar monomers in an intermediate conformational state, if that state undergoes templated conformational change less readily than the soluble monomer. Instead, the result is a mixed aggregate containing domains of fibril-like structure occluded from the solvent by less ordered pre-fibrillar monomers, which prevent elongation of the nascent fibril seeds 5.29(d). This competition fully or partly negates the ability of growth to promote conversion, by restricting the sites where a growing fibril can successfully develop. As a result, under conditions where growth is rapid compared to propagation, intermediates are expected to be large, long-lived, and contain domains of occluded fibril-like structure; conversely, if growth of intermediates is slow compared to propagation, the intermediates are expected to be small, lack fibril-like structural domains, and have a short lifetime that restricts their accumulation. Although the most detailed mathematical analysis so far has been carried out for protofibrillar intermediates, it was shown that spheroidal intermediates exhibited a similar behaviour, and argued that the competition underlying this change in behaviour is sufficiently general to be relevant to intermediates of most morphologies, under appropriate conditions [8].

An example of a rejection-free kinetic Monte Carlo (rfKMC) prediction of the lifetime of intermediates is shown in Fig. 5.30. The lifetime, which is here defined as the time taken to produce an amyloid fibril capable of elongation, is given in relative units as $k_c\langle\tau_s\rangle$, where k_c is the rate parameter for initiation of a domain of amyloid-like structure per monomer in the intermediate, and $\langle\tau_s\rangle$ is the average time for the emergence of a growing fibril end. This process is taken to be complete when the growing fibril ends become exposed to the solvent (Fig. 5.29(b)), as this is when the shift to a mechanism of elongation by addition of soluble monomers can occur. It is important to note that k_c is not the same as k_c', which is effectively $1/\langle\tau_s\rangle$. The lifetime of the intermediates varies with μ/D, a dimensionless parameter describing the balance between propagation and growth. A value of $\mu/D < 0$ means that the new, amyloid-like phase

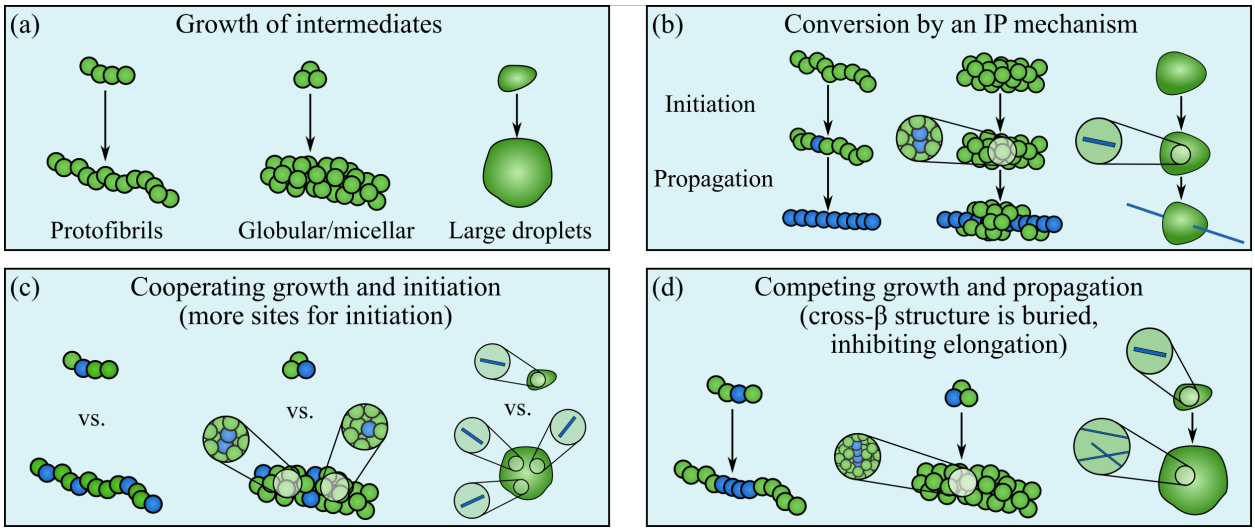

Figure 5.29: Effects of the growth of nucleation intermediates on conformational conversion via an initiation-propagation (IP) mechanism. (a) Schematics of the growth of intermediates with different morphologies: left, protofibrillar, eg. Brown *et al.* [335]; centre, globular or micellar, eg. Lomakin *et al.* [285]; right, large, droplet-like intermediates, eg. Luo *et al.* [295]. See Section 1.4 for a discussion of the development and morphology of these intermediates, and Sections 1.5.2 and 1.5.6 for a discussion of their role in primary and secondary nucleation. (b) Schematics of the IP mechanism of conformational conversion, adapted to a variety of morphologies. The stable amyloid phase originates by conformational conversion of one or more monomers within the intermediate to form a fibril seed (initiation), and then spreads through the intermediate by templated conformational conversion of the remaining monomers (propagation). The propagation step is considered to be complete when the growing ends of the new fibril emerge from the intermediate, allowing the adoption of a fibrillar growth mode; until this occurs, aggregated monomers occlude the fibril end from the solvent, and growth of the fibril seed involves propagation, ie. templated conversion of aggregated monomers, rather than canonical elongation by monomer addition. (c) Growth enhances initiation by increasing the number of sites where cross-β structure can originate, in agreement with the predictions of previous studies [224, 347]. (d) Growth competes with propagation by burying newly formed cross-β structure within amorphous material, occluding growing fibril ends and preventing the emergence of a fibrillar growth mode. In all panels, spheres represent self-assembled monomers, with the colour corresponding to the conformational state: green, intermediate; blue, amyloid. For large, droplet-like intermediates, individual constituent monomers are not represented, as these intermediates are sufficiently large to be functionally continuous. Magnified regions show 'inside' views of the intermediates, ie. regions that are hidden from view in the full schematic. Based on the model and discussion in Taylor *et al.* [8].

propagates through the intermediate faster than the growth of the pre-fibrillar phase, whereas a value of $\mu/D > 0$ means that growth of the pre-fibrillar phase is more rapid, and $\mu/D = 0$ means that the system is critically poised between the two regimes. Increases in either $m(0)$ or I would be expected to cause a corresponding increase in μ/D, with the potential to move the system from a regime where propagation is faster ($\mu/D < 0$) to one where growth is faster ($\mu/D > 0$). Thus, the variation of $k_c\langle\tau_s\rangle$ with respect to μ/D in Fig. 5.30 reflects a similar variation in $1/k_c'$ as a function of $m(0)$ or I. Increasing k_p/k_c, a parameter that represents the extent to which conformational templating by fibrillar monomers accelerates conversion of adjacent monomers in the intermediate, causes a shorter intermediate lifetime in the slowly growing regime ($\mu/D < 0$), and a less smooth transition to the rapidly growing regime ($\mu/D > 0$) (see Fig. 5.30). In the limit where conversion is strongly templated ($k_p/k_c \to \infty$), there is an abrupt change in $\partial k_c\langle\tau_s\rangle/\partial(\mu/D)$ resembling a continuous phase transition, described by the asymptotic relation

$$k_c\langle\tau_s\rangle = \begin{cases} 0, & \mu/D \leq 0, \\ \frac{2\mu}{2D+\mu}, & \mu/D > 0. \end{cases} \tag{5.71}$$

In practice, it is not physically possible to reach this limit, but biopolymer systems are predicted to frequently exhibit large k_p/k_c values (eg. $k_p = 10^3 k_c$) that result in highly nonlinear behaviour when $\mu/D \approx 0$ [8]. Although the macroscopic self-assembly kinetics have not yet been solved for models where the oligomers are generated by secondary nucleation, the results are expected to be broadly similar to those observed for primary nucleation, where an abrupt increase in the lifetime of the oligomers causes a similarly abrupt increase in the time required for oligomer populations to reach a steady state (Fig. 5.31(a)). For oligomers produced by secondary nucleation, the equivalent effect would be a shift from a regime described by Fig. 5.28(c), where the oligomer population is defined by the balance between fibril-dependent formation and losses due to conversion and disassembly, to one described by Fig. 5.28(d), where oligomer accumulation remains exponential but a steady-state approximation cannot be made for secondary nucleation. Concurrent with the increase in the lifetime of intermediates, there is an abrupt increase in the size and abundance of the intermediates (Fig. 5.31(b)). In addition, it is interesting to note that a temporary reduction or even inversion in γ occurs at the transition between regimes (Fig. 5.31(b-c)), reflecting the delaying of fibril formation with increasing $m(0)$ due to a rapid drop in the conversion rate [8]. Although further investigation will be needed to confirm this, it is possible that the brief inversion of γ_{inf} around $m(0) = 3.5$ μM (see Fig. 5.27(b)), which was accompanied by a similar behaviour in γ_{50} and was reproducible across repeat experiments, could be the kinetic signature of a similar transition.

Several features of the macroscopic self-assembly kinetics of Aβ(1-42) at high ionic strength are consistent with near-critical behaviour resulting from a competition between growth and propagation. These

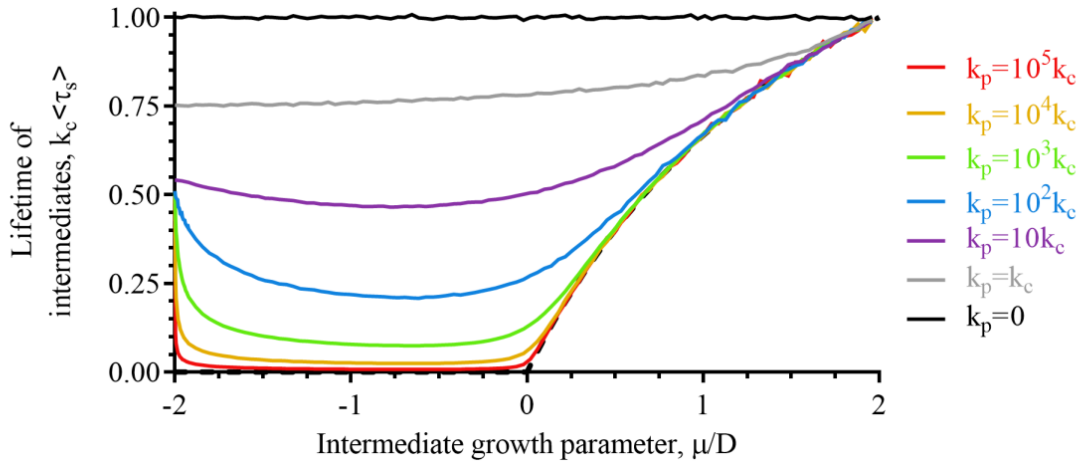

Figure 5.30: The interplay between growth and conformational conversion results in non-equilibrium criticality. The time $k_c\langle\tau_s\rangle$ required for an intermediate to give rise to a growing amyloid fibril, specifically for the growing end of the fibril to become exposed to the solvent, is plotted against the parameter μ/D, which describes the competition between growth of the intermediate phase and propagation of the stable amyloid phase through the intermediate. When $\mu/D < 0$, the amyloid phase propagates through the intermediate faster than the intermediate can grow; when $\mu/D > 0$, spreading of the amyloid phase is slow compared to growth of the intermediate, so that newly formed fibril seeds risk being buried by amorphous or otherwise non-fibrillar material. Each solid curve represents the results of a series of rfKMC simulations at a particular value of k_p/k_c, and varying μ/D. The parameter k_p/k_c represents the extent to which conversion of monomers within fibrils is reliant on conformational templating by adjacent monomers that have already converted. When $k_p \ll k_c$, separate monomers within the intermediate largely convert independently of one another, with little conformational templating. When $k_p \gg k_c$, aggregated monomers that have converted to the amyloid state strongly template the conversion of adjacent monomers. Large values of k_p/k_c are thermodynamically highly plausible [8]. The colour scheme of the solid curves corresponds to the value of k_p/k_c at which the series of simulations was carried out; the dashed black curve is the asymptotic scaling law given by Eq. 5.71, valid for the limit $k_p/k_c \to \infty$. The non-smooth change in gradient in the asymptote resembles a continuous phase transition. Figure adapted with permission from Taylor *et al.* [8].

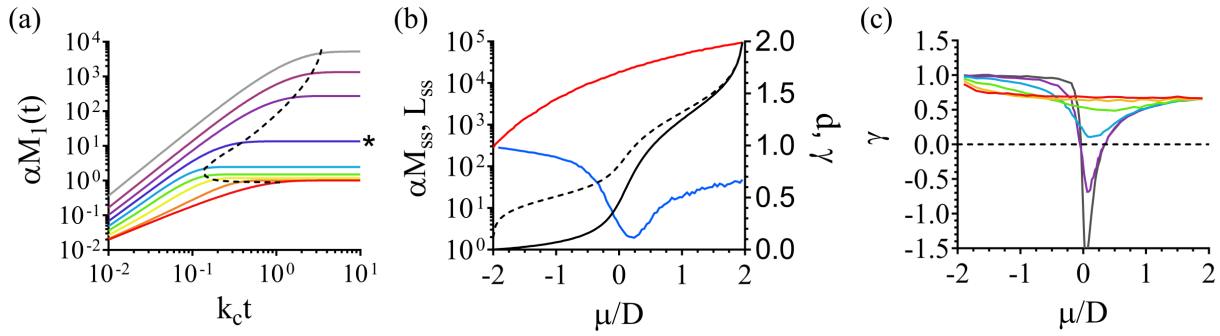

Figure 5.31: Varying μ/D close to the critical point results in highly nonlinear changes in the macroscopic self-assembly kinetics. (a) Accumulation of mass of intermediates $\alpha M_1(t)$, where α is a normalisation constant, and $M_1(t)$ is equivalent to the quantity $\langle N \rangle G(t)$ discussed in this chapter. Time is given in relative units of $k_c t$. The colour corresponds to the value of μ/D: red, -2; orange, -1.9; yellow, -1.5; green, -1; cyan, -0.5; blue, 0 (critical, marked with asterisk); indigo, 0.5; violet, 1; gray, 1.5. The dashed line plots the values of $(k_c t, \alpha M_1(t))$ at which $\alpha M_1(t)$ reaches 90% of its steady-state value, for varying μ/D. (b) Effect of varying μ/D on steady-state oligomer populations and the concentration-dependence of fibril mass accumulation. The steady-state oligomer mass concentration αM_{ss} (solid black) and steady-state mean oligomer size L_{ss} (dashed black) are plotted on the left axis, which uses a logarithmic scale. The scaling exponent γ, which has the same definition as the quantity discussed in Section 5.3.5, is represented by the blue line, plotted on the right axis. The scaling exponent has the limits $\gamma = 1$ when $\mu/D = -2$ and $\gamma = 2/3$ when $\mu/D = 2$, but exhibits a depression at the transition between regimes, rather than a monotonic shift from one to the other. Note that the absolute values of γ in the limits are not relevant to this chapter, as the other microscopic processes were different to those considered here; it is the depression in γ at the transition between regimes that is important. The red curve is not relevant to the discussion in this chapter. (c) Effect of μ/D on γ for different values of k_p/k_c: red, $k_p = 0$; amber, $k_p = 9k_c$; green, $k_p = 99k_c$; blue, $k_p = 999k_c$; indigo, $k_p = 9999k_c$; gray, $k_p = 99999k_c$. As with the previous panel, the absolute values of γ in the limits are not relevant to this chapter; it is the depression in γ at the transition between regimes that is important. All data in this figure are derived from the results of rfKMC simulations, with additional numerical processing. Figure reproduced with permission from Taylor *et al.* [8].

include the relatively abrupt transition from a regime where intermediates do not accumulate to one where they do, the apparent presence of amyloid-like domains within these oligomers, and the temporary inversion of the concentration-dependence at the transition between regimes. In addition, the transition between conversion regimes is usually expected to occur close to the concentration at which oligomers transition from being unstable to metastable [8]. Thus, the critical behaviour resulting from the IP mechanism is not necessarily an alternative to simpler behaviours attributable to reductions in k'_d, but rather a complement to such behaviours. Nonetheless, further investigation is needed to properly test this. In particular, size distributions of the intermediates, and the opportunity to isolate and structurally characterise these species, would be highly informative. Unfortunately, attempts to isolate and characterise the intermediates by SEC-MALS and AF4-MALS have so far proved unsuccessful due to the transience of these species and the perturbative nature of both techniques, with the former stimulating excessive aggregation [570], and the latter exerting a more complex effect due to successive concentration and dilution steps [571]. In addition, theory work on the IP mechanism is still ongoing, and quantitative fitting will not be possible until there are analytical solutions for a model where the intermediates are (i) secondary in origin, and (ii) have the appropriate geometry and growth mechanism, features which are partly reliant upon more detailed experimental data. Nonetheless, although theoretical investigations of the IP mechanism and experimental investigations of Aβ(1-42) self-assembly at high ionic strength were originally separate lines of enquiry, the similarities presented above indicate that the former may well be able to explain the more unusual features of the latter.

5.4 Conclusions

The work presented in this chapter leads to several conclusions. Firstly, the main effect of physiological concentrations of salts on Aβ(1-42) self-assembly is due to charge screening, and can often be predicted from the ionic strength alone. There does not appear to be strong evidence for Hofmeister effects at the salt concentrations used, and the effect of iodide at $[I^-] \gtrapprox 100$ mM is probably electroselective, rather than a general effect. Although this conclusion is somewhat unsurprising, it is important as it means that the results of Aβ(1-42) self-assembly experiments conducted in different fibrillisation buffers are likely to be transferrable to conditions with a similar ionic strength. This means that buffers can be substituted to meet specific experimental requirements without yielding significantly different results, and the conclusions of kinetic work carried out under a restricted range of buffers [4, 5, 54, 519] can be transferred to experiments carried out under different conditions. Secondly, changes in ionic strength alter the morphology of species formed during fibril self-assembly, with greater ionic strength resulting in larger oligomer populations, and amyloid fibrils that have a less structured appearance by NS-EM and a slightly lower secondary structure content by CD. Thirdly, both primary and secondary nucleation undergo saturation-like processes at high

ionic strength. While saturable secondary nucleation has already been described for Aβ(1-40) [4] and Aβ(1-42) [5], and saturable primary nucleation was recently suggested for Aβ(1-40) [6], primary nucleation of Aβ(1-42) has historically been assumed to occur homogeneously in the absence of a strongly binding surface. Although the exact mechanism of saturation is not clear from the kinetics, and the kinetics may actually reflect a change in nucleation mechanism rather than true saturation, the low reaction order of primary nucleation in the 'saturating' limit is most consistent with a heterogeneous nucleation mechanism, supporting the conclusions of Chapter 4 that PEG-treated microplates catalyse Aβ(1-42) nucleation.

Lastly, while past treatments of Aβ(1-42) self-assembly at high ionic strength have assumed that a two-state description remains valid even at high $m(0)$ and I [5], the data presented in this Chapter show that even moderate $m(0)$ and I result in a transition to biphasic self-assembly kinetics with a pre-fibrillar intermediate. At least four states are identified: a monomer with a low but significant secondary structure content; an intermediate with a low secondary structure content, but seemingly enough structure to elicit a fibril ThT response; a newly formed fibril with a moderate secondary structure content and a strong ThT response; and a late-stage fibril observed at lower ionic strength, which appears to be more structured. The oligomers are of particular interest, as their kinetics suggest that they are secondary nucleation intermediates. Thus, while secondary nucleation intermediates have historically been difficult to study due to their transience, these species may provide direct insights into the mechanism of secondary nucleation. Intriguingly, the apparently contradictory characteristics of these oligomers may explain the seemingly conflicting observations that secondary nucleation is sequence-specific [458–460], and yet does not preserve fibril polymorphism [459]. Pre-fibrillar globular oligomers with a low secondary structure content, similar to those described here, have previously been suggested to contain 'subdomains' with a higher degree of structure, including intermolecular β-sheets and amyloid-like tertiary and quaternary contacts [216,278,290,296,303]. The presence of domains of amyloid-like structure embedded within largely amorphous oligomers could explain these species' ThT response, especially if the regions that acquire cross-β structure first are the preferred binding sites for ThT in mature fibrils. In addition, if the stability of the oligomers relied on the presence of amyloid-like subdomains, their formation could well be sequence-specific, explaining why Aβ(1-40) and Aβ(1-42) do not cross-seed via secondary nucleation [458–460]. The ability of the fibril surface to stimulate β-sheet formation would agree with the results of MD simulations suggesting a similar mechanism [467]. At the same time, the secondary oligomers lack the extensive secondary structure of mature amyloid fibrils, explaining why secondary nucleation does not conserve fibril polymorphism [459]. Thus, secondary nucleation appears to occur as a two-step heterogeneous nucleation, with the first step being the formation of amyloid-like globular oligomers with ThT-binding regions, and the second the expansion of cross-β structure, and perhaps the simultaneous acquisition of fibril polymorphism.

Based on the above conclusions, it is possible to tentatively construct a non-equilibrium phase diagram

of the different Aβ(1-42) self-assembly regimes at varying $m(0)$ and I. This phase diagram is represented in Fig. 5.32, with schematics of the individual regimes shown in Fig. 5.33. At low $m(0)$ and I (Fig. 5.33(a)), primary nucleation is a high-order process catalysed by available surfaces (see Chapter 4), and secondary nucleation is unsaturated and has $n_s \approx 1.75$. Secondary oligomers are unstable or weakly metastable, exist at a continuously varying concentration determined by the balance between secondary nucleation and disassembly, and sometimes convert to form fibril seeds. At higher $m(0)$ or I (Fig. 5.33(b)), primary nucleation transitions to a lower-order regime, due to either a saturation mechanism or a change in the relative magnitude of two successive free energy barriers along the self-assembly pathway. This particular transition is probably specific to the surface that catalyses secondary nucleation, in this case PEG (see Chapter 4), and may not be physiologically relevant. Increasing $m(0)$ or I further (Fig. 5.33(c)) causes the sites on the fibril surface that produce secondary oligomers to become saturated with monomers, in the manner previously suggested by Šarić *et al.* [348], reducing the apparent reaction order of secondary nucleation. Lastly, at high $m(0)$ and I (Fig. 5.33(d)), secondary oligomers are sufficiently stable and long-lived that their concentration is no longer governed by a pseudo-steady-state between formation and disassembly. Instead, the oligomers undergo unbounded accumulation throughout all or most of the growth phase, and become the predominant cause of the ThT response, despite having a largely disordered CD spectrum. After sufficient depletion of the free monomer, the oligomers become unstable, and disassemble to sustain a monomer reservoir that is consumed by the fibrils. To explain the observed kinetics, the majority of fibrils must form from secondary oligomers; nonetheless, this does not mean that the majority of secondary oligomers convert to fibrils, and most may still disassemble rather than successfully converting to fibrils [156,572]. The sequential processes of oligomerisation and expansion of the fibril population result in biphasic ThT kinetics, with the majority of the change in CD signal coinciding with the second phase observed by ThT. Thus, both the uniphasic and biphasic self-assembly kinetics are results of the same underlying self-assembly pathway, with changes in the stability of the oligomers causing the transition between these regimes.

There are several obvious avenues for future research. Firstly, while it is likely that the transition to biphasic self-assembly kinetics is largely due to slower disassembly of oligomers, it is possible that critical phenomena caused by competing growth and conversion may play a role, something which should be evaluated by future studies. In a parallel with this, work is ongoing to adapt the insights from the IP model [8] to contexts where intermediates are produced by secondary nucleation, and develop a more realistic description of the geometry and conformational and structural dynamics of these intermediates; these steps will be necessary before quantitative fits can be obtained for the data presented in this chapter. Similarly, expanding the analytical models discussed in Section 5.3.5 to approximate the entire self-assembly time course would allow the conclusions of that section to be confirmed by numerical fitting, although the current treatment already allows relatively clear model discrimination on the basis of concentration-dependences alone. There

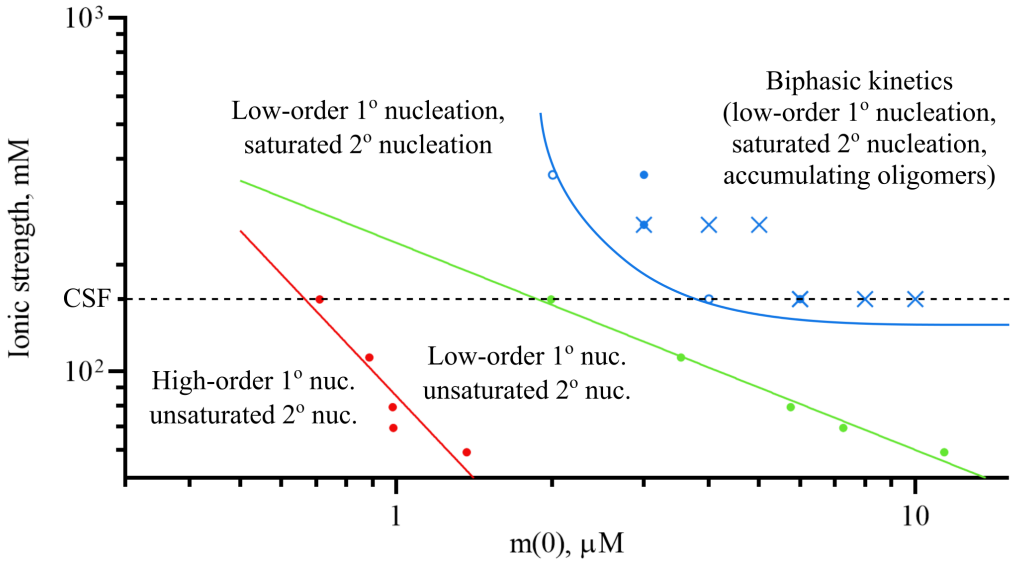

Figure 5.32: A non-equilibrium phase diagram of Aβ(1-42) self-assembly regimes. There are four regimes of self-assembly, occurring at different initial monomer concentration $m(0)$ and ionic strength I. These regimes correspond to the four schematics in Fig. 5.33, which contains a more detailed description of the regimes and the transitions that occur between them. The coloured lines are separatrices approximately indicating where the transitions between regimes occur, and the corresponding circles and crosses are the data points used to place these lines. The red line represents the approximate location of the transition from high-order to low-order primary nucleation, the exact cause of which is unclear; this line was obtained by non-linear power-law regression of the red data points, which are the values of $(K_{M,n}^{1/(n_c-\varepsilon_c)}, I)$ derived from the analysis in Section 5.3.3. Note that the saturation-like model that was used to obtain the $K_{M,n}^{1/(n_c-\varepsilon_c)}$ values may not be correct, but the fitted $K_{M,n}^{1/(n_c-\varepsilon_c)}$ values still give the approximate location of the transition between regimes, at least for low I. The green line represents the effective Michaelis constants for saturation of secondary nucleation sites on the fibril surface, at different I; this line was obtained by non-linear power-law regression of the green data points, which are the $(K_{M,s}^{1/n_s}, I)$ values derived from the analysis in Section 5.3.3. The blue line is the approximate $(m(0), I)$ at which the transition to biphasic kinetics occurs, drawn to enclose the solid blue circles and crosses. The solid blue circles represent the lowest $m(0)$ at which two peaks consistently and clearly occur in the first derivatives of the ThT self-assembly curves, for each value of I. The open blue circles mark lower $m(0)$ values at which biphasic kinetics are inconsistently apparent. The blue crosses mark the lowest I values at which two peaks consistently and clearly occur in the first derivatives of the ThT self-assembly curves, for each value of $m(0)$. All separatrices correspond to the approximate location of continuous transitions, rather than sharp jumps in self-assembly behaviour. As discussed above, the precise location of the red line is model-dependent, and the location of the blue line is approximate; nonetheless, this diagram roughly shows the values of $m(0)$ and I at which different self-assembly regimes occur. The dashed line annotated 'CSF' marks the approximate ionic strength of the CSF, from Elliott and Jasper [542].

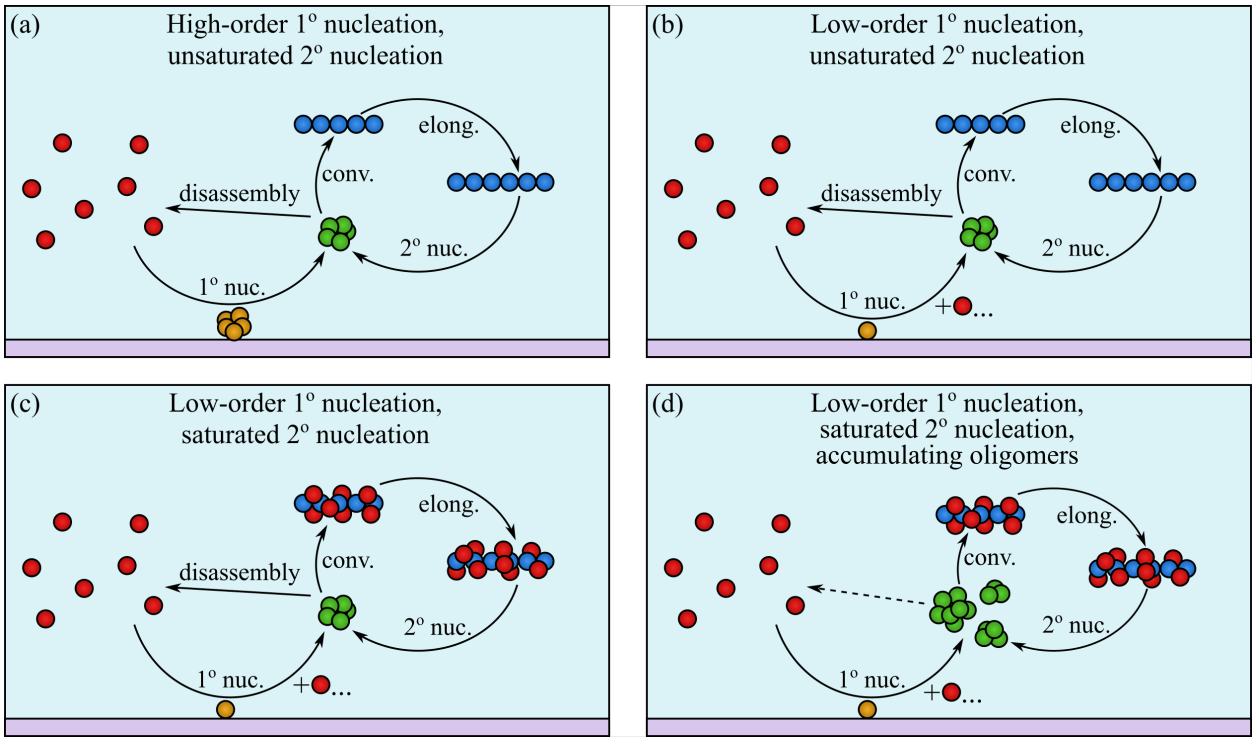

Figure 5.33: Aβ(1-42) self-assembly regimes, based on the conclusions of Chapters 4-5. All regimes are limits of a unified underlying self-assembly pathway. Primary nucleation is a surface-catalysed process, which behaves as a dimerisation or oligomerisation at low $m(0)$ and I, but has a lower reaction order at high $m(0)$ or I due to an uncertain saturation process, or a change in the relative height of two successive free energy barriers that must be crossed for primary nucleation to occur. Secondary nucleation is a two-step process involving the formation of on-pathway oligomers at saturable sites on the fibril surface, and the conformational conversion of those oligomers to amyloid fibrils. Secondary oligomers may also disassemble without successfully converting. Fibrils elongate by incorporating soluble monomers into their structure. There are three apparently continuous transitions between self-assembly regimes: (a) to (b), the transition from high-order to low-order primary nucleation; (b) to (c), saturation of catalytic sites on the fibril surface; and (c) to (d), the transition from a regime where oligomer-mediated secondary nucleation is at a non-equilibrium steady state to one where the oligomeric intermediates undergo unbounded accumulation on timescales comparable to $1/\kappa$, so that no steady-state approximation can be made for secondary nucleation. In all panels, the colour scheme corresponds to the monomer conformation: red, soluble; gold, surface-associated; green, soluble oligomeric intermediate; blue, fibrillar.

is also a need for a more detailed kinetic and structural characterisation of the intermediates, which will help with testing possible mechanistic models. As mentioned in Section 5.3.7, attempts to obtain oligomer size distributions have proved unsuccessful so far, due to the sensitivity of these species to perturbations caused by the fractionation techniques. One possible solution, which is being investigated at present, is to stabilise the intermediates by rapid cross-linking, and then carry out fractionation under denaturing conditions to prevent further aggregation. In addition, there are plans to attempt a more detailed structural characterisation of the intermediates by solution NMR on the non-cross-linked oligomers, in order to test hypotheses regarding the presence of amyloid-like domains. Lastly, future work should investigate whether these intermediates have toxic effects. Oligomers formed by secondary nucleation have previously been shown to result in toxicity in cell-based assays [54], electrophysiology studies on mouse brain slices [55], and membrane models [68]. Incipient biphasic behaviour is observed at $I = 160$ mM, the nominal ionic strength of the CSF [542], and the addition of polyanions and crowding agents would be expected to further promote oligomerisation. Thus, fluctuations in either these factors or the monomer concentration under physiological conditions could result in rapid accumulation of oligomers, and resulting toxicity.

5.5 Acknowledgments

Several Master's students contributed to the experimental data presented in this chapter. The initial observations of the salt-dependence of Aβ(1-42) aggregation, including the low concentration-dependence and biphasic kinetics that occur at high salt concentrations, were made by myself. The ThT and NS-EM experiments with the 10 mM sodium phosphate buffer were carried out by Miss Caitlin Bone, with my supervision. The ThT experiments are repeats of earlier experiments first carried out by myself; these experiments were repeated as they had been performed prior to the optimisations described in Chapter 3. The majority of the ThT experiments with the 20 mM sodium phosphate buffer were carried out by myself or Miss Alanah K. Sheridan. While my dataset had finer sampling of Aβ(1-42) concentrations, Alanah's dataset had finer sampling of salt concentrations; the data were found to be highly concordant, so they were ultimately collated to perform a more detailed analysis. The NS-EM images of aggregates formed in the 20 mM sodium phosphate buffer were collected jointly by myself and Alanah. The dataset shown in Fig. 5.22 was collected by Mr. Xander Arscott-Barber. The remaining experimental work (SEC-MALS, ThT-CD) was carried out by myself. Initial analysis (processing ThT curves, obtaining measurements from NS-EM images) was carried out by the relevant experimentalists with my supervision, using a data analysis pipeline I devised at the start of the work. Further analyses, data fitting, and mathematical modelling were carried out by myself. Some of the data presented in this chapter have been presented by the aforementioned students in their Master's theses [571, 573, 574]. Many thanks to all contributors for making this a more detailed,

reproducible, and comprehensive investigation of the Aβ(1-42) self-assembly kinetics.

The model discussed in Section 5.3.7 has been published in the Journal of Chemical Physics [8]. Co-authors on the paper were Miss Lianne D. Gahan, Dr. Buddhapriya Chakrabarti, and Dr. Rosemary Staniforth. An author contributions statement was included in the publication, and reads: "A.I.P.T. developed the model, carried out the numerical simulations, and obtained the analytical results. L.D.G. verified the analytical results. All authors interpreted the results and contributed to writing the manuscript." Many thanks to all co-authors for their contributions to the work.

In addition, thanks to Dr. Svetomir Tzokov for assistance and expertise in electron microscopy, Dr. Barbara Ciani for loan of a Superdex 75 column, Prof. Tim Dafforn for productive conversations regarding the CD data, and Postnova Analytics (Landsberg am Lech, Germany) for loan of an in-line MALS detector. Many thanks to the members of the Staniforth lab and the wider NMR group, especially Dr. Peter Davis and Dr. Rosemary Staniforth, for useful advice regarding the work in this chapter.

Chapter 6

Conclusions and Future Work

Kinetic studies of Aβ self-assembly can shed light on the factors that cause this peptide to aggregate, the mechanisms by which aggregation occurs, and the manner in which toxic species are generated. These insights are expected to allow the development of better therapeutics for Alzheimer's disease, and other conditions in which Aβ is implicated, such as Parkinson's disease [27] and Down's syndrome [61]. Moreover, as highlighted in Chapter 1, there are numerous similarities between the aggregates and aggregation mechanisms of Aβ and those of other amyloidogenic polypeptides, which result from underlying physical principles that govern the aggregation and polymerisation of proteins. As a result, insights into Aβ self-assembly are often transferrable to other conditions caused by the aggregation of disordered peptides and IDPs, such as Huntington's disease [16] and type-II diabetes [575]. In addition, there is broader interest surrounding amyloids due to their functional role in many organisms, potential for use in biotechnology, and importance in the fundamental study of protein folding and misfolding [9,41], and studies of Aβ contribute to a wider body of research that is essential for these purposes. Nonetheless, there are several remaining gaps in our understanding of Aβ self-assembly, as outlined in Section 1.6. This study aimed to address three major areas of uncertainty surrounding Aβ nucleation and nucleated polymerisation: the extent to which surfaces are required for primary nucleation, the mechanisms of primary and secondary nucleation, and the cause of several poorly understood aspects of the macroscopic self-assembly kinetics, such as low concentration-dependence of the half-time and lag time, which point to flaws in existing mechanistic models.

To address these questions, macroscopic self-assembly kinetics from ThT assays were combined with measurements and observations from complementary techniques such as NS-EM, AFM, and CD spectroscopy, and theoretical approaches such as nonlinear regression and mathematical modelling. In addition to addressing the above questions, it was necessary to establish protocols for solubilisation and standardisation of Aβ monomer preparations, and the insights from this work underlined the importance of carefully handling the peptide in order to prevent seeding or off-pathway aggregation, which may explain many of

the inconsistencies in the literature (Chapter 3). By comparing self-assembly behaviours in the presence of a variety of experimentally relevant surfaces, it was determined that primary nucleation is catalysed by most experimental surfaces (Chapter 4); moreover, primary nucleation can be catalysed by comparatively weakly binding surfaces, indicating that a diverse range of physiological surfaces may stimulate the process *in vivo*. In this sense, primary nucleation resembles secondary nucleation, which is also a surface-dependent process in which the fibril surface acts as the catalyst. Although the precise mechanistic details of primary nucleation in the presence of many surfaces remain unclear, it is clear that different surfaces result in different nucleation intermediates, and thus have different mechanisms. While the intermediate formed in the presence of PEG-treated polystyrene appears to be a small oligomer, ThT-binding multilayer films act as nucleation intermediates in the presence of untreated polystyrene. For secondary nucleation, the fortuitous discovery that the corresponding intermediate is stabilised at moderate to high ionic strength (Chapter 5) led to the recognition that this species is a small oligomer, around the size of the ADDLs described by Lambert *et al.* [71], or other globular oligomers [289, 290, 304]. This oligomer has a β-strand content of $\sim 40\%$, lower than fibrils but typical of Aβ oligomers [290], and binds ThT, similar to some other spheroidal oligomers [278, 279] and implying the presence of amyloid-like β-sheets. Thus, while many details of the mechanisms of primary and secondary nucleation are yet to be discerned, the results of this thesis strongly support the notion that both are surface-catalysed, multi-step processes in which the molecular environment of the surface controls the structural properties of the resulting intermediate, and thus the kinetics of nucleation.

The existence of nucleation intermediates also explains the biphasic character and weak monomer-dependence of the self-assembly kinetics under some conditions, such as in the presence of strongly binding surfaces (Chapter 4) or at high ionic strength (Chapter 5). Existing mechanistic models assume a two-state system, with significant quantities of monomer and fibrils and negligible quantities of intermediates [1–3, 381, 425, 426]; as a result, they are unable to accurately describe scenarios where nucleation intermediates accumulate to high levels. Under these conditions, biphasic self-assembly kinetics result from the fact that there are distinct stages of aggregation, with depletion of the soluble monomer to form a ThT-positive intermediate preceding a second step in which the intermediate is replaced by mature amyloid fibrils. There is not necessarily a single cause of weak monomer-dependence under these conditions. In the case where the intermediate is formed by interactions with non-fibrillar surfaces (Chapter 4), it is only the second phase that exhibits weak scaling, and this is a result of prior monomer depletion. However, when the intermediate is produced by secondary nucleation (Chapter 5), both phases exhibit weak scaling as a result of the positive feedback inherent to secondary processes, which ensures that all species in the same autocatalytic cycle exhibit asymptotically exponential mass accumulation kinetics with the same proportional rate. For the same reason, the intermediates of autocatalytic secondary processes can be generally expected to exhibit exponential early-time kinetics similar to their fibrillar end-products, making them difficult to

distinguish on the basis of ThT data alone. Thus, the identification of such intermediates is likely to require careful analysis of the self-assembly kinetics, beyond data fitting alone, and the use of complementary biophysical techniques that provide orthogonal measurements of the abundance and structural state of species present in solution.

The observation that Aβ(1-42) nucleation is a surface-catalysed, multi-step process suggests that there is a general mechanism for this process, even if the specific structural details of the intermediates are conditioned by the particular catalytic surface. Diverse surfaces are able to stimulate this form of nucleation, as summarised in Fig. 6.1; in this study, catalytic effects were observed for PEG-treated polystyrene, untreated polystyrene, the fibril surface, and probably also glass and the air-water interface. Elsewhere in the literature, studies have supported similar multi-step nucleation mechanisms catalysed by lipid bilayers [313, 357, 531] and a variety of non-biological surfaces [353, 362, 363, 576]. At the same time, it must be conceded that not *every* instance of primary nucleation may be surface-catalysed; in particular, at high concentrations and in the absence of a more rapid alternative, quasi-homogeneous nucleation may occur in micellar oligomers [285, 317], although the possibility that surfaces may be required for the formation of these species does not appear to have been evaluated, and such a result would not be surprising given the importance of surfaces in condensation of similar phases in non-biological systems [385]. It is interesting to note that all the above mechanisms involve a condensed, non-amyloid intermediate, which usually undergoes a slow structural conversion to the fibrillar state (Fig. 6.1). While it is difficult to argue that *all* Aβ nucleation involves a non-fibrillar intermediate, as intermediates are not reported by all studies, and may sometimes be transient and difficult to identify, several relevant points were noted in Section 1.5.2. Firstly, the complexity of the transition to the amyloid state, the instability of cross-β structure in small oligomers, and the favourable attributes of larger oligomers for nucleation of cross-β structure indicate that aggregation may initially precede the development of amyloid structure [268, 315, 410–412]. In a similar vein, the rapid relaxation of small, fibrillar oligomers to a non-amyloid state [410–412] can only be reconciled with the low reaction order of nucleation if small, non-fibrillar oligomers are on-pathway. It is also interesting that both this study and others [353, 357, 362, 363] have found that intermediates formed at surfaces have a ThT response and/or detectable β-sheet content; although these intermediates are non-amyloid, this general observation suggests that partly ordered intermediates that form at surfaces provide a favourable environment for the development of cross-β structure. Thus, the nucleation of Aβ fibrils is probably preceded by non-amyloid aggregation involving partly structured intermediates. Although this does not necessarily entail that aggregation is a multi-step process, as the transition to the amyloid state may sometimes occur continuously with increasing aggregate size, rather than involving an activated state [409], conversion of intermediates formed by Aβ [216, 278, 295, 345] and many other polypeptides [217, 251, 335, 346, 401] is slow, and the same finding is supported by this study. Slow conversion implies the existence of a free energy barrier sepa-

rating pre-fibrillar intermediates from amyloids, and is consistent with the observation that the mature fibril structure is highly cooperative, containing large numbers of mutually supportive interactions (see Section 1.3). Thus, the results presented in this thesis add to a growing body of literature supporting the proposal that disordered polypeptides nucleate amyloids via a two-step condensation-ordering transition [268, 394, 399], in which initial nonspecific aggregation creates a dynamic, condensed phase that provides a favourable environment for the nucleation of cross-β structure.

At the same time, while theoretical models typically consider the condensation step as a homogeneous process occurring in solution [268, 309, 399], it is clear from this study that interfaces are the preferred environment for condensation. This should not be surprising, as nucleation of condensed phases is usually favoured or catalysed by surfaces, particularly when close to the binodal [403]. However, the conclusion that even weakly-binding surfaces can catalyse nucleation, and the type of surface affects the intermediate formed, has far-reaching consequences for our understanding of amyloid nucleation *in vivo*. Viable catalysts for primary nucleation may extend beyond membranes alone, encompassing other biological surfaces such as oligosaccharides and ECM components, and changes in the properties of physiological surfaces may affect the variety of oligomers produced. In addition, instead of being a distinct form of nucleation requiring a separate mechanism, secondary nucleation is simply a special case of the same process, which occurs when the catalyst itself is an amyloid fibril. The results of this study also hint that there may be a higher degree of specificity in the intermediates than the above model would suggest. Both of the intermediates that accumulated to directly measurable quantities had a ThT signal; while this does not necessitate the existence of a mature cross-β structure, it does suggest some structural similarities to mature amyloid fibrils, in agreement with the finding that on-pathway oligomers and other intermediates often develop fibril-like tertiary and quaternary contacts prior to the final transition to the amyloid state [216,278,290,296,303]. In addition, the fact that secondary oligomers cause a ThT response raises the question of whether the fibril surface templates the formation of early amyloid-like structure in the secondary oligomers, stabilising them and predisposing them to on-pathway aggregation. At present, there is too little mechanistic information to determine whether this is the case; future evaluation of this question will require a more detailed characterisation of both the structure of the secondary oligomers, and their kinetics of formation and conversion.

In summary, the results of this study suggest that Aβ nucleation occurs as a two-step process at physiological concentrations: firstly, the monomer undergoes a surface-catalysed condensation to form an aggregated, partly structured intermediate; and, secondly, cross-β structure nucleates in the favourable molecular environment provided by this intermediate. Future work should aim to provide a more detailed investigation of the structure and formation kinetics of Aβ nucleation intermediates, especially those produced by secondary nucleation or physiological surfaces; in particular, time-dependent size distributions would allow determination of the rates of nucleation, growth, and conversion, and spectroscopic techniques such

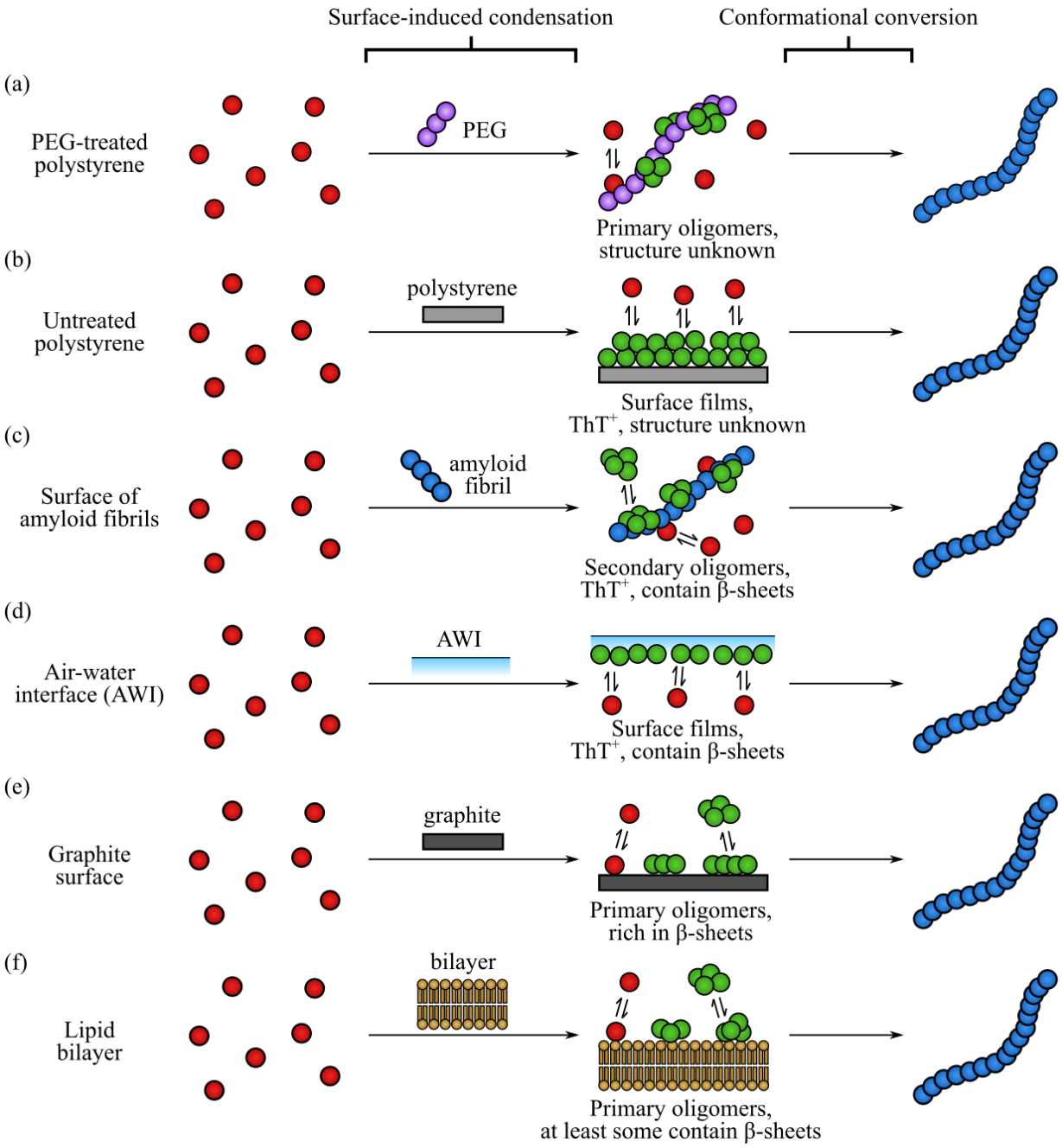

Figure 6.1: Surface-catalysed multi-step nucleation of Aβ fibrils. Panels (a-f) depict the nucleation of Aβ amyloid fibrils in the presence of different surfaces shown to catalyse multi-step nucleation, in this study and others: (a), PEG-treated polystyrene microplates, as shown in Chapters 4-5; (b), untreated polystyrene surfaces, as shown in Chapter 4; (c), amyloid fibrils, ie. secondary nucleation, as first described by Cohen *et al.* [54] and explored further in Chapter 5; (d), the air-water interface (AWI), which is implicated in Chapter 4 and supported by previous work [353, 362]; (e), graphite surfaces, as demonstrated by Yu *et al.* [363]; and (f), lipid bilayers, for which multi-step mechanisms have been supported by several studies [313, 357, 531]. In all panels, the colour scheme corresponds to the monomer conformation: red, soluble; green, soluble *or* surface-associated intermediate; blue, fibrillar. In all the above processes, there appears to be a multi-step mechanism involving at least two steps: surface-induced condensation to form a partly ordered, often β-rich intermediate; and slow conformational conversion of this intermediate to a mature amyloid fibril.

as NMR or fluorescence spectroscopy might provide information about the structural characteristics and development of these species. These data would allow better model discrimination, and clarify the extent to which different surfaces alter the structural and functional properties of the intermediates. In addition, future experimental work should investigate whether the findings of this study are applicable to other amyloids formed by large peptides or IDPs, such as poly-Q, α-syn, Tau, and Ure2p, for which the same arguments can be made regarding the relative merits of monomers and globular oligomers as nucleation sites for cross-β structure [268], and for which there is plentiful evidence to support a multi-step nucleation mechanism [217,251,335,346,393]. Lastly, the finding that secondary nucleation intermediates accumulate to high levels under near-physiological conditions means that mathematical treatments of amyloid self-assembly must increasingly explore multi-state models, where the fibril is not the only aggregate that accumulates to high levels, and steady-state approximations cannot necessarily be made for nucleation. While these scenarios are more challenging to interpret, analytical solutions for the macroscopic self-assembly kinetics, or at the very least efficient numerical simulations, will be a powerful tool for the interrogation of kinetic data. In addition, the results of recent analytical work show that, despite the complexity of such models, general analytical solutions and universal scaling laws can still be obtained [8, 380, 469]; results of this type are more generally applicable than specific analytical solutions, and will be particularly important under conditions where the precise values of various microscopic rate parameters are difficult to disentangle, or the experimental data do not permit model discrimination by nonlinear regression alone. Together, these experimental and theoretical insights will lead to more realistic models of amyloid self-assembly and the generation of toxic species *in vivo*, allowing the development of more effective therapeutics for Alzheimer's disease and other diseases caused by amyloid formation.

Bibliography

[1] Knowles, T. P. J, Waudby, C. A, Devlin, G. L, Cohen, S. I. A, Aguzzi, A, Vendruscolo, M, Terentjev, E. M, Welland, M. E, & Dobson, C. M. (2009) An analytical solution to the kinetics of breakable filament assembly. *Science* **326**, 1533–1537.

[2] Cohen, S. I. A, Vendruscolo, M, Welland, M. E, Dobson, C. M, Terentjev, E. M, & Knowles, T. P. J. (2011) Nucleated polymerization with secondary pathways. I. Time evolution of the principal moments. *J. Chem. Phys.* **135**, 065105.

[3] Cohen, S. I. A, Vendruscolo, M, Dobson, C. M, & Knowles, T. P. J. (2011) Nucleated polymerization with secondary pathways. II. Determination of self-consistent solutions to growth processes described by non-linear master equations. *J. Chem. Phys.* **135**, 065106.

[4] Meisl, G, Yang, X, Hellstrand, E, Frohm, B, Kirkegaard, J. B, Cohen, S. I. A, Dobson, C. M, Linse, S, & Knowles, T. P. J. (2014) Differences in nucleation behavior underlie the contrasting aggregation kinetics of the Aβ40 and Aβ42 peptides. *Proc. Natl. Acad. Sci. U. S. A.* **111**, 9384–9389.

[5] Meisl, G, Yang, X, Dobson, C. M, Linse, S, & Knowles, T. P. J. (2017) Modulation of electrostatic interactions to reveal a reaction network unifying the aggregation behaviour of the Aβ42 peptide and its variants. *Chem. Sci.* **8**, 4352–4362.

[6] Dear, A. J, Meisl, G, Michaels, T. C. T, Zimmermann, M. R, Linse, S, & Knowles, T. P. J. (2020) The catalytic nature of protein aggregation. *J. Chem. Phys.* **152**, 045101.

[7] Hong, L & Yong, W.-A. (2013) Simple moment-closure model for the self-assembly of breakable amyloid filaments. *Biophys. J.* **104**, 533–540.

[8] Taylor, A. I. P, Gahan, L. D, Chakrabarti, B, & Staniforth, R. A. (2020) A two-step biopolymer nucleation model shows a nonequilibrium critical point. *J. Chem. Phys.* **153**, 025102.

[9] Michaels, T. C. T, Šarić, A, Habchi, J, Chia, S, Meisl, G, Vendruscolo, M, Dobson, C. M, & Knowles, T. P. J. (2018) Chemical kinetics for bridging molecular mechanisms and macroscopic measurements of amyloid fibril formation. *Annu. Rev. Phys. Chem.* **69**, 273–298.

[10] Glenner, G. G & Wong, C. G. (1984) Alzheimer's disease: Initial report of the purification and characterization of a novel cerebrovascular amyloid protein. *Biochem. Biophys. Res. Commun.* **120**, 895–890.

[11] Glenner, G. G & Wong, C. G. (1984) Alzheimer's disease and Down's syndrome: sharing of a unique cerebrovascular amyloid fibril protein. *Biochem. Biophys. Res. Commun.* **122**, 1131–1135.

[12] Masters, C. L, Simms, G, Weinman, N. A, Multhaup, G, McDonald, B. L, & Beyreuther, K. (1985) Amyloid plaque core protein in Alzheimer's disease and Down syndrome. *Proc. Natl. Acad. Sci. U. S. A.* **82**, 4245–4249.

[13] Hardy, J. A & Higgins, G. A. (1992) Alzheimer's disease: The amyloid cascade hypothesis. *Science* **156**, 184–185.

[14] Selkoe, D. J & Schenk, D. (2003) Alzheimer's disease: Molecular understanding predicts amyloid-based therapeutics. *Annu. Rev. Pharmacol. Toxicol.* **43**, 545–584.

[15] Spillantini, M. G, Schmidt, M. L, Lee, V. M, Trojanowski, J. Q, Jakes, R, & Goedert, M. (1997) α-Synuclein in Lewy bodies. *Nature* **388**, 839–840.

[16] Perutz, M. F. (1999) Glutamine repeats and neurodegenerative diseases: molecular aspects. *Trends Biochem. Sci.* **24**, 58–63.

[17] Brookmeyer, R, Johnson, E, Ziegler-Graham, K, & Arrighi, H. M. (2007) Forecasting the global burden of Alzheimer's disease. *Alzheimer's Dement.* **3**, 186–191.

[18] Prince, M, Wilmo, A, Guerchet, M, Ali, G. C, Wu, Y.-T, Prina, M, & Alzheimer's Disease International. (2015) World Alzheimer report 2015: The global impact of dementia., (Alzheimer's Disease International.), Technical report.

[19] World Health Organization. (2017) Global action plan on the public health response to dementia., (World Health Organization), Technical report.

[20] Wittenberg, R, Hu, B, Barraza-Araiza, L, & Rehill, A. (2019) Projections of older people with dementia and costs of dementia care in the United Kingdom, 2019-2040. *Age Ageing* **49**, 264–269.

[21] Alzheimer's Assoc. (2020) 2020 Alzheimer's disease facts and figures. *Alzheimer's Dement.* **16**, 391–460.

[22] Goedert, M, Wischik, C. M, Crowther, R. A, Walker, J. E, & Klug, A. (1988) Cloning and sequencing of the cDNA encoding a core protein of the paired helical filament of Alzheimer disease: identification as the microtubule-associated protein tau. *Proc. Natl. Acad. Sci. U. S. A.* **85**, 4051–4055.

[23] Yoshimoto, M, Iwai, A, Kang, D, Otero, D. A, Xia, Y, & Saitoh, T. (1995) NACP, the precursor protein of the non-amyloid β/A4 protein (Aβ) component of Alzheimer disease amyloid, binds Aβ and stimulates Aβ aggregation. *Proc. Natl. Acad. Sci. U. S. A.* **92**, 9141–9145.

[24] Giasson, B. I, Forman, M. S, Higuchi, M, Golbe, L. I, Graves, C. L, Kotzbauer, P. T, Trojanowski, J. Q, & Lee, V. M.-Y. (2003) Initiation and synergistic fibrillization of tau and alpha-synuclein. *Science* **300**, 636–640.

[25] Guo, J. L, Covell, D. J, Daniels, J. P, Iba, M, Stieber, A, Zhang, B, Riddle, D. M, Kwong, L. K, Xu, Y, Trojanowski, T. Q, & Lee, V. M. Y. (2013) Distinct α-synuclein strains differentially promote tau inclusions in neurons. *Cell* **154**, 103–117.

[26] Laurén, J, Gimbel, D. A, Nygaard, H. B, Gilbert, J. W, & Strittmatter, S. M. (2009) Cellular prion protein mediates impairment of synaptic plasticity by amyloid-beta oligomers. *Nature* **457**, 1128–1132.

[27] Masliah, E, Rockenstein, E, Veinbergs, I, Sagara, Y, Mallory, M, Hashimoto, M, & Mucke, L. (2001) β-amyloid peptides enhance α-synuclein accumulation and neuronal deficits in a transgenic mouse model linking Alzheimer's disease and Parkinson's disease. *Proc. Natl. Acad. Sci. U. S. A.* **98**, 12245–12250.

[28] Tycko, R. (2015) Amyloid polymorphism: Structural basis and neurobiological relevance. *Neuron* **86**, 632–645.

[29] Knowles, T. P. J, Vendruscolo, M, & Dobson, C. M. (2014) The amyloid state and its association with protein misfolding diseases. *Nat. Rev. Mol. Cell Biol.* **15**, 384–396.

[30] Hartl, F. U & Hayer-Hartl, M. (2009) Converging concepts of protein folding *in vitro* and *in vivo*. *Nat. Struct. Mol. Biol.* **16**, 574–581.

[31] Chiti, F, Webster, P, Taddei, N, Clark, A, Stefani, M, Ramponi, G, & Dobson, C. M. (1999) Designing conditions for *in vitro* formation of amyloid protofilaments and fibrils. *Proc. Natl. Acad. Sci. U. S. A.* **96**, 3590–3594.

[32] Astbury, W. T & Dickinson, S. (1935) The X-ray interpretation of denaturation and the structure of the seed globulins. *Biochem. J.* **29**, 2351–2360.1.

[33] Eanes, E. D & Glenner, G. G. (1968) X-ray diffraction studies on amyloid filaments. *J. Histochem. Cytochem.* **16**, 673–677.

[34] Guijarro, J. I, Sunde, M, Jones, J. A, Campbell, I. D, & Dobson, C. M. (1998) Amyloid fibril formation by an SH3 domain. *Proc. Natl. Acad. Sci. U. S. A.* **95**, 4224–4228.

[35] Litvinovich, S. V, Brew, S. A, Aota, S, Akiyama, S. K, Haudenschild, C, & Ingham, K. C. (1999) Formation of amyloid-like fibrils by self-association of a partially unfolded fibronectin type III module. *J. Mol. Biol.* **280**, 245–258.

[36] Fändrich, M & Dobson, C. M. (2002) The behaviour of polyamino acids reveals an inverse side chain effect in amyloid structure formation. *EMBO J.* **21**, 5682–5690.

[37] Bradford, V. J & Iverson, B. L. (2008) Amyloid-like behavior in abiotic, amphiphilic foldamers. *J. Am. Chem. Soc.* **130**, 1517–1524.

[38] Baldwin, A. J, Knowles, T. P. J, Tartaglia, G. G, Fitzpatrick, A. W, Devlin, G. A, Shammas, S. L, Waudby, C. A, Mossuto, M. F, Meehan, S, Gras, S. L, Christodoulou, J. Anthony-Cahill, S. J, Barker, P. D, Vendruscolo, M, & Dobson, C. M. (2011) Metastability of native proteins and the phenomenon of amyloid formation. *J. Am. Chem. Soc.* **133**, 14160–14163.

[39] Varela, A. E, Lang, J. F, Wu, Y, Dalphin, M. D, Stangl, M. D, Okuno, Y, & Cavagnero, S. (2018) Kinetic trapping of folded proteins relative to aggregates under physiologically relevant conditions. *J. Phys. Chem. B* **122**, 7682–7698.

[40] Anfinsen, C. B. (1973) Principles that govern the folding of protein chains. *Science* **181**, 223–230.

[41] Ke, P. C, Zhou, R, Serpell, L. C, Riek, R, Knowles, T. P. J, Lashuel, H, Gazit, E, Hamley, I. W, Davis, T. P, Fändrich, M, Otzen, D. E, Chapman, M. R, Dobson, C. M, Eisenberg, D. S, & Mezzenga, R. (2020) Half a century of amyloids: past, present and future. *Chem. Soc. Rev.* **49**, 5473–5509.

[42] Krishnan, R, Tsubery, H, Proschitsky, M. Y, Asp, E, Lulu, M, Gilead, S, Gartner, M, Waltho, J. P, Davis, P. J, Hounslow, A. M, Kirschner, D. A, Inouye, H, Myszka, D. G, Wright, J, Solomon, B, & Fisher, R. A. (2014) A bacteriophage capsid protein provides a general amyloid interaction motif (GAIM) that binds and remodels misfolded protein assemblies. *J. Mol. Biol.* **426**, 2500–2519.

[43] Chapman, M. R, Robinson, L. S, Pinkner, J. S, Roth, R, Heuser, J, Hammar, M, Normark, S, & Hultgren, S. J. (2002) Role of *Escherichia coli* curli operons in directing amyloid fiber formation. *Science* **295**, 851–855.

[44] Cox, B. (1965) ψ, a cytoplasmic suppressor of super-suppressor in yeast. *Heredity* **20**, 505–521.

[45] Patino, M. M, Liu, J. J, Glover, J. R, & Lindquist, S. (1996) Support for the prion hypothesis for inheritance of a phenotypic trait in yeast. *Science* **273**, 622–626.

[46] Masison, D. C & Wickner, R. B. (1995) Prion-inducing domain of yeast Ure2p and protease resistance of Ure2p prion-containing cells. *Science* **270**, 93–95.

[47] Maddelein, M. L, Dos Reis, S, Duvesin-Caubet, S, Coulary-Salin, B, & Saupe, S. J. (2002) Amyloid aggregates of the HET-s prion protein are infectious. *Proc. Natl. Acad. Sci. U. S. A.* **99**, 7402–7407.

[48] McGlinchey, R. P, Shewmaker, F, McPhie, P, Monterroso, B, Thurber, K, & Wickner, R. B. (2009) The repeat domain of the melanosome fibril protein Pmel17 forms the amyloid core promoting melanin synthesis. *Proc. Natl. Acad. Sci. U. S. A.* **106**, 13731–13736.

[49] Lotz, G. P & Legleiter, J. (2013) The role of amyloidogenic protein oligomerization in neurodegenerative disease. *J. Mol. Med.* **91**, 653–664.

[50] Walsh, D. M, Klyubin, I, Fadeeva, J. V, Cullen, W. K, Anwyl, R, Wolfe, M. S, Rowan, M. J, & Selkoe, D. J. (2002) Naturally secreted oligomers of amyloid β protein potently inhibit hippocampal long-term potentiation *in vivo*. *Nature* **416**, 535–539.

[51] Kayed, R, Sokolov, Y, Edmonds, B, McIntire, T. M, Milton, S. C, Hall, J. E, & Glabe, C. G. (2004) Permeabilization of lipid bilayers is a common conformation-dependent activity of soluble amyloid oligomers in protein misfolding diseases. *J. Biol. Chem.* **279**, 46363–46366.

[52] Yoshiike, Y, Akagi, T, & Takashima, A. (2007) Surface structure of amyloid-β fibrils contributes to cytotoxicity. *Biochemistry* **46**, 9805–9812.

[53] Willander, H, Presto, J, Askarieh, G, Biverstål, H, Frohm, B, Knight, S. D, Johansson, J, & Linse, S. (2012) BRICHOS domains efficiently delay fibrillation of amyloid β-peptide. *J. Biol. Chem.* **287**, 31608–31617.

[54] Cohen, S. I. A, Linse, S, Luheshi, L. M, Hellstrand, E, White, D. A, Rajah, L, Otzen, D. E, Vendruscolo, M, Dobson, C. M, & Knowles, T. P. J. (2013) Proliferation of amyloid-β42 aggregates occurs through a secondary nucleation mechanism. *Proc. Natl. Acad. Sci. U. S. A.* **110**, 9758–9763.

[55] Cohen, S. I. A, Arosio, P, Presto, J, Kurudenkandy, F. R, Biverstål, H, Dolfe, L, Dunning, C, Yang, X, Frohm, B, Vendruscolo, M, Johansson, J, Dobson, C. M, Fisahn, A, Knowles, T. P. J, & Linse, S. (2015) A molecular chaperone breaks the catalytic cycle that generates toxic Aβ oligomers. *Nat. Struct. Mol. Biol.* **22**, 207–213.

[56] Gaspar, R, Meisl, G, Buell, A. K, Young, L, Kaminski, C. F, Knowles, T. P. J, Sparr, E, & Linse, S. (2016) Secondary nucleation of monomers on fibril surface dominates α-synuclein aggregation and provides autocatalytic amyloid amplification. *Q. Rev. Biophys.* **50**, e6.

[57] Jakob-Roetne, R & Jacobsen, H. (2009) Alzheimer's disease: From pathology to therapeutic approaches. *Angew. Chem. Int. Ed.* **48**, 3030–3059.

[58] Hamley, I. W. (2012) The amyloid beta peptide: A chemist's perspective. Role in Alzheimer's and fibrillization. *Chemical Reviews* **112**, 5147–5192.

[59] Goate, A, Charter-Harlin, M.-C, Mullan, M, Brown, J, Crawford, F, Fidani, L, Giuffra, L, Haynes, A, Irving, N, James, L, Mant, R, Newton, P, Rooke, K, Roques, P, Talbot, C, Pericak-Vance, M, Roses, A, Williamson, R, Rossor, M, Owen, M, & Hardy, J. (1991) Segregation of a missense mutation in the amyloid precursor protein gene with familial Alzheimer's disease. *Nature* **349**, 704–706.

[60] Sherrington, R, Rogaev, E. I, Liang, Y, Rogaeva, E. A, Levesque, G, Ikeda, M, Chi, H, Lin, C, Li, G, Holman, K, Tsuda, T, Mar, L, Foncin, J. F, Bruni, A. C, Montesi, M. P, Sorbi, S, Rainero, I, Pinessi, L, Nee, L, Chumakov, I, Pollen, D, Brookes, A, Sanseau, P, Polinsky, R. J, Wasco, W, Da Silva, H. A, Haines, J. L, Perkicak-Vance, M. A, Tanzi, R. E, Roses, A. D, Fraser, P. E, Rommens, J. M, & St George-Hyslop, P. H. (1995) Cloning of a gene bearing missense mutations in early-onset familial Alzheimer's disease. *Nature* **29**, 754–760.

[61] Goldgaber, D, Lerman, M. I, McBride, W. O, Saffiotti, U, & Gajdusek, D. C. (1987) Isolation, characterization, and chromosomal localization of human brain cDNA clones coding for the precursor of the amyloid of brain in Alzheimer's disease, Down's syndrome and aging. *J. Neural Transm. Suppl.* **24**, 23–28.

[62] Näslund, J, Schierhorn, A, Hellman, U, Lannfelt, L, Roses, A. D, Tjernberg, L. O, Silberring, J, Gandy, S. E, Winblad, B, Greengard, P, Nordstedt, C, & Terenius, L. (1994) Relative abundance of Alzheimer Aβ amyloid peptide variants in Alzheimer disease and normal aging. *Proc. Natl. Acad. Sci. U. S. A.* **91**, 8378–8382.

[63] Rhee, S. K, Quist, A. P, & Lal, R. (1998) Amyloid β protein-(1–42) forms calcium-permeable, Zn2+-sensitive channel. *J. Biol. Chem.* **273**, 13379–13382.

[64] Quist, A, Doudevski, I, Lin, H, Azimova, R, Ng, D, Frangione, B, Kagan, B, Ghiso, J, & Lal, R. (2005) Amyloid ion channels: A common structural link for protein-misfolding disease. *Proc. Natl. Acad. Sci. U. S. A.* **102**, 10427–10432.

[65] Kayed, R, Pensalfini, A, Margoi, L, Sokolov, Y, Sarsoza, F, Head, E, , Hall, J. E, & Glabe, C. G. (2009) Annular protofibrils are a structurally and functionally distinct type of amyloid oligomer. *J. Biol. Chem.* **284**, 4230–4237.

[66] Jang, H, Arce, F. T, Ramachandran, S, Capone, R, Azimova, R, Kagan, B. L, Nussinov, R, & Lal, R. (2010) Truncated β-amyloid peptide channels provide an alternative mechanism for Alzheimer's disease and Down syndrome. *Proc. Natl. Acad. Sci. U. S. A.* **107**, 6538–6543.

[67] Williams, T. L, Johnson, B. R. G, Urbanc, B, Jenkins, A. T. A, Connell, S. D. A, & Serpell, L. C. (2011) Aβ42 oligomers, but not fibrils, simultaneously bind to and cause damage to ganglioside-containing lipid membranes. *Biochem. J.* **439**, 67–77.

[68] Flagmeier, P, De, S, Michaels, T. C. T, Yang, X, Dear, A. J, Emanuelsson, C, Vendruscolo, M, Linse, S, Klenerman, D, Knowles, T. P. J, & Dobson, C. M. (2020) Direct measurement of lipid membrane disruption connects kinetics and toxicity of Aβ42 aggregation. *Nat. Struct. Mol. Biol.* **27**, 886–891.

[69] Kim, J. H, Anwyl, R, Suh, Y. H, Djamgoz, M. B, & Rowan, M. J. (2001) Use-dependent effects of amyloidogenic fragments of β-amyloid precursor protein on synaptic plasticity in rat hippocampus in vivo. *J. Neurosci.* **21**, 1327–1333.

[70] Jin, M, Shepardson, N, Yang, T, Chen, G, Walsh, D, & Selkoe, D. J. (2011) Soluble amyloid beta-protein dimers isolated from Alzheimer cortex directly induce Tau hyperphosphorylation and neuritic degeneration. *Proc. Natl. Acad. Sci. U. S. A.* **108**, 5819–5824.

[71] Lambert, M. P, Barlow, A. K, Chromy, B. A, Edwards, C, Freed, R, Liosatos, M, Morgan, T. E, Rozovsky, I, Trommer, B, Viola, K. L, Wals, P, Zhang, C, Finch, C. E, Krafft, G. A, & Klein, W. L. (1998) Diffusible, nonfibrillar ligands derived from Aβ1–42 are potent central nervous system neurotoxins. *Proc. Natl. Acad. Sci. U. S. A.* **95**, 6448–6453.

[72] Hartley, D. M, Walsh, D. M, Ye, C. P, Diehl, T, Vasquez, S, Vassilev, P. M, Teplow, D. B, & Selkoe, D. J. (1999) Protofibrillar intermediates of amyloid β-protein induce acute electrophysiological changes and progressive neurotoxicity in cortical neurons. *J. Neurosci.* **15**, 8876–8884.

[73] Benilova, I, Karran, E, & De Strooper, B. (2012) The toxic Aβ oligomer and Alzheimer's disease: an emperor in need of new clothes. *Nat. Neurosci.* **12**, 349–357.

[74] Ruschak, A. M & Miranker, A. D. (2007) Fiber-dependent amyloid formation as catalysis of an existing reaction pathway. *Proc. Natl. Acad. Sci. U. S. A.* **104**, 12341–12346.

[75] Frankel, R, Törnquist, M, Meisl, G, Hansson, O, Andreasson, U, Zetterberg, H, Blennow, K, Frohm, B, Cedervall, T, Knowles, T. P. J, Leidig, T, & Linse, S. (2010) Autocatalytic amplification of Alzheimer associated Aβ42 peptide aggregation in human cerebrospinal fluid. *Commun. Biol.* **2**, 365.

[76] Dawkins, E & Small, D. H. (2014) Insights into the physiological function of the β-amyloid precursor protein: beyond Alzheimer's disease. *J. Neurochem.* **129**, 756–769.

[77] Iadanza, M. G, Jackson, M. P, Hewitt, E. W, Ranson, N. A, & Radford, S. E. (2018) A new era for understanding amyloid structures and disease. *Nat. Rev. Mol. Cell Biol.* **19**, 755–773.

[78] Virchow, R. (1854) Zur Cellulose. *Archiv. Pathol. Anat.* **6**, 416–426.

[79] Sipe, J. D & Cohen, A. S. (2000) Review: History of the amyloid fibril. *J. Struct. Biol.* **130**, 88–89.

[80] Friedrich, N & Kekulé, A. (1859) Zur Amyloidfrage. *Virchows Arch. Pathol. Anat. Physiol.* **16**, 50–65.

[81] Bennhold, H. (1922) Specific staining of amyloid by Congo red. *Münch. Med. Wochenschr.* **69**, 1537–1538.

[82] Divry, P. (1927) Étude histochimique des plaques. *J. Belge de Neurologie et de Psychiatrie* **27**, 643–657.

[83] Divry, P & Florkin, M. (1927) Sur les propriétés optiques de l'amyloïde. *Comptes Rendus des Sèances de la Sociètè de Biologie et de ses Filiales.* **97**, 1808–1810.

[84] Ladewig, P. (1945) Double-refringence of the amyloid-Congo-red-complex in histological sections. *Nature* **156**, 81–82.

[85] Puchtler, H, Sweat, F, & Levine, M. (1962) On the binding of Congo red by amyloid. *J. Histochem. Cytochem.* **10**, 355–364.

[86] Astbury, W. T & Street, A. (1935) X-ray studies of the structure of hair, wool and related fibres. I. General. *Phil. Trans. R. Soc.* **230**, 75–101.

[87] Romhanyi, G. (1949) Über die submikroskopische Struktur des Amyloids. *Schweiz Ztschr. Path. u. Bakt.* **12**, 253–262.

[88] Cohen, A. S & Calkins, E. (1959) Electron microscopic observations on a fibrous component in amyloid of diverse origins. *Nature* **183**, 1202–1203.

[89] Movat, H. Z. (1960) The fine structure of the glomerulus in amyloidosis. *Arch. Path.* **69**, 323–332.

[90] Makin, O. S, Atkins, E, Sikorski, P, Johansson, J, & Serpell, L. C. (2005) Molecular basis for amyloid fibril formation and stability. *Proc. Natl. Acad. Sci. U. S. A.* **102**, 315–320.

[91] Aliyan, A, Cook, N. P, & Martí, A. A. (2019) Interrogating amyloid aggregates using fluorescent probes. *Chem. Rev.* **119**, 11819–11856.

[92] LeVine, H. R. (1993) Thioflavine T interaction with synthetic Alzheimer's disease beta-amyloid peptides: detection of amyloid aggregation in solution. *Protein Sci.* **2**, 404–410.

[93] Biancalana, M & Koide, S. (2010) Molecular mechanism of thioflavin-T binding to amyloid fibrils. *Biochim. Biophys. Acta* **1804**, 1405–1412.

[94] Groenning, M. (2010) Binding mode of thioflavin T and other molecular probes in the context of amyloid fibrils - current status. *J. Chem. Biol.* **3**, 1–18.

[95] Toyama, B. H & Weissman, J. S. (2011) Amyloid structure: Conformational diversity and consequences. *Annu. Rev. Biochem.* **80**, 557–585.

[96] Tycko, R. (2011) Solid-state NMR studies of amyloid fibril structure. *Annu. Rev. Phys. Chem.* **62**, 279–299.

[97] Nelson, R, Sawaya, M. R, Balbirnie, M, Madsen, A. O, Riekel, C, Grothe, R, & Eisenberg, D. (2005) Structure of the cross-β spine of amyloid-like fibrils. *Nature* **45**, 773–778.

[98] Sawaya, M. R, Sambashivan, S, Nelson, R, Ivanova, M. I, Sievers, S. A, Apostol, M. I, Thompson, M. J, Balbirnie, M, Wiltzius, J. J. W, McFarlane, H. T, Madsen, A. O, Riekel, C, & Eisenberg, D. (2007) Atomic structures of amyloid cross-beta spines reveal varied steric zippers. *Nature* **447**, 453–457.

[99] Wiltzius, J. J. W, Landau, M, Nelson, R, Sawaya, M. R, Apostol, M. I, Goldschmidt, L, Soriaga, A. B, Cascio, D, Rajashankar, K, & Eisenberg, D. (2009) Molecular mechanisms for protein-encoded inheritance. *Nat. Struct. Mol. Biol.* **16**, 973–978.

[100] Rodriguez, J. A, Eisenberg, D. S, & Gonen, T. (2017) Taking the measure of microED. *Curr. Opin. Struct. Biol.* **46**, 79–86.

[101] Siemer, A. B, Arnold, A. A, Ritter, C, Westfield, T, Ernst, M, Riek, R, & Meier, B. H. (2006) Observation of highly flexible residues in amyloid fibrils of the HET-s prion. *J. Am. Chem. Soc.* **128**, 13224–13228.

[102] Toyama, B. H, Kelly, M. J, Gross, J. D, & Weissman, J. S. (2007) The structural basis of yeast prion strain variants. *Nature* **449**, 233–237.

[103] Orlova, E. V & Saibil, H. R. (2011) Structural analysis of macromolecular assemblies by electron microscopy. *Chem. Rev.* **111**, 7710–7748.

[104] Kühlbrandt, W. (2014) Cryo-EM enters a new era. *eLife* **3**, e03678.

[105] Bai, X.-C, McMullan, G, & Scheres, S. (2015) How cryo-EM is revolutionizing structural biology. *Trends Biochem. Sci.* **40**, 49–57.

[106] Binnig, G, Quate, C. F, & Gerber, C. (1986) Atomic force microscope. *Phys. Rev. Lett.* **56**, 930–933.

[107] Lutter, L, Serpell, C. J, Tuite, M. F, Serpell, L. C, & Xue, W.-F. (2020) Three-dimensional reconstruction of individual helical nano-filament structures from atomic force microscopy topographs. *BioMol. Concepts* **11**, 102–115.

[108] Hu, X & Li, H. (2014) Force spectroscopy studies on protein-ligand interactions: a single protein mechanics perspective. *FEBS Lett.* **588**, 3613–3620.

[109] Sweers, K. K. M, Bennink, M. L, & Subramaniam, V. (2012) Nanomechanical properties of single amyloid fibrils. *J. Phys.: Condens. Matter* **24**, 243101.

[110] Ruggeri, F. S, Šneideris, T, Vendruscolo, M, & Knowles, T. P. J. (2019) Atomic force microscopy for single molecule characterisation of protein aggregation. *Arch. Biochem. Biophys.* **664**, 134–148.

[111] Paravastu, A. K, Leapman, R. D, Yau, W.-M, & Tycko, R. (2008) Molecular structural basis for polymorphism in β-amyloid fibrils. *Proc. Natl. Acad. Sci. U. S. A.* **105**, 18349–18354.

[112] Bertini, I, Connelli, L, Luchinat, C, Mao, J, & Nesi, A. (2011) A new structural model of Aβ40 fibrils. *J. Am. Chem. Soc.* **133**, 16013–16022.

[113] Iwata, K, Fujiwara, T, Matsuki, Y, Akutsu, H, Takahashi, S, Naiki, H, & Goto, Y. (2006) 3D structure of amyloid protofilaments of β2-microglobulin fragment probed by solid-state NMR. *Proc. Natl. Acad. Sci. U. S. A.* **103**, 18119–18124.

[114] Mizuno, N, Baxa, U, & Steven, A. C. (2011) Structural dependence of HET-s amyloid fibril infectivity assessed by cryoelectron microscopy. *Proc. Natl. Acad. Sci. U. S. A.* **108**, 3252–3257.

[115] Dearborn, A, Wall, J. S, Cheng, N, Heymann, J. B, Kajava, A. V, Varkey, J, Langen, R, & Steven, A. C. (2016) Kinetic diversity of amyloid oligomers. *J. Biol. Chem.* **291**, 2310–2318.

[116] Walsh, D. M, Lomakin, A, Benedek, G. B, Condron, M. M, & Teplow, D. B. (1997) Amyloid β-protein fibrillogenesis: Detection of a protofibrillar intermediate. *J. Biol. Chem.* **272**, 22364–22372.

[117] Wasmer, C, Lange, A, Van Melckebeke, H, Siemer, A. B, Riek, R, & Meier, B. H. (2008) Amyloid fibrils of the HET-s(218–289) prion form a β solenoid with a triangular hydrophobic core. *Science* **319**, 1523–1526.

[118] Wasmer, C, Schütz, A, Loquet, A, Buhtz, C, Greenwald, J, Riek, R, Böckmann, A, & Meier, B. H. (2009) The molecular organization of the fungal prion HET-s in its amyloid form. *J. Mol. Biol.* **394**, 119–127.

[119] Van Melckebeke, H, Wasmer, C, Lange, A, AB, E, Loquet, A, Böckmann, A, & Meier, B. (2010) Atomic-resolution three-dimensional structure of HET-s(218-289) amyloid fibrils by solid-state NMR spectroscopy. *J. Am. Chem. Soc.* **132**, 13765–13775.

[120] Vázquez-Fernández, E, Vos, M. R, Afanasyev, P, Cebey, L, Sevillano, A. M, Vidal, E, Rosa, I, Renault, L, Ramos, A, Peters, P. J, Fernández, J. J, van Heel, M, Young, H. S, Requena, J. R, & Wille, H. (2016) The structural architecture of an infectious mammalian prion using electron cryomicroscopy. *PLOS Pathog.* **12**, e1005835.

[121] Fitzpatrick, A. W, Knowles, T. P. J, Waudby, C. A, Vendruscolo, M, & Dobson, C. M. (2011) Inversion of the balance between hydrophobic and hydrogen bonding interactions in protein folding and aggregation. *PLOS Comput. Biol.* **7**, e1002169.

[122] Perutz, M. F, Johnson, T, Suzuki, M, & Finch, J. T. (1994) Glutamine repeats as polar zippers: their possible role in inherited neurodegenerative diseases. *Proc. Natl. Acad. Sci. U. S. A.* **91**, 5355–5358.

[123] Thirumalai, D, Reddy, G, & Straub, J. E. (2012) Role of water in protein aggregation and amyloid polymorphism. *Acc. Chem. Res.* **45**, 83–92.

[124] Rauscher, S, Baud, S, Miao, M, Keeley, F. W, & Pomès, R. (2006) Proline and glycine control protein self-organization into elastomeric or amyloid fibrils. *Structure* **14**, 1667–1676.

[125] Krysmann, M. J, Castelletto, V, Kelarakis, A, Hamley, I. W, Hule, R. A, & Pochan, D. J. (2008) Self-assembly and hydrogelation of an amyloid peptide fragment. *Biochemistry* **47**, 4597–4605.

[126] Madine, J, Jack, E, Stockley, P. G, Radford, S. E, Serpell, L. C, & Middleton, D. A. (2008) Structural insights into the polymorphism of amyloid-like fibrils formed by region 20-29 of amylin revealed by solid-state NMR and X-ray fiber diffraction. *J. Am. Chem. Soc.* **130**, 14990–15001.

[127] Madine, J, Copland, A, Serpell, L. C, & Middleton, D. A. (2009) Cross-β spine architecture of fibrils formed by the amyloidogenic segment NFGSVQFV of medin from solid-state NMR and X-ray fiber diffraction measurements. *Biochemistry* **48**, 3089–3099.

[128] Fitzpatrick, A. W. P, Falcon, B, He, S, Murzin, A. G, Murshudov, G, Garringer, H. J, Crowther, R. A, Ghetti, B, Goedert, M, & Scheres, S. H. W. (2017) Cryo-EM structures of tau filaments from Alzheimer's disease. *Nature* **547**, 185–190.

[129] Iadanza, M. G, Silvers, R, Boardman, J, Smith, H. I, Karamanos, T. K, Debelouchina, G. T, Su, Y, Griffin, R. G, Ranson, N. A, & Radford, S. E. (2018) The structure of a β2-microglobulin fibril suggests a molecular basis for its amyloid polymorphism. *Nat. Commun.* **9**, 4517.

[130] Liberta, F, Loerch, S, Rennegarbe, M, Schierhorn, A, Westermark, P, Westermark, G. T, Hazenberg, B. P. C, Grigorieff, N, Fändrich, M, & Schmidt, M. (2019) Cryo-EM fibril structures from systemic AA amyloidosis reveal the species complementarity of pathological amyloids. *Nat. Commun.* **10**, 1104.

[131] Schmidt, M, Wiese, S, Adak, V, Engler, J, Agarwal, S, Fritz, G, Westermark, P, Zacharias, M, & Fändrich, M. (2019) Cryo-EM structure of a transthyretin-derived amyloid fibril from a patient with hereditary ATTR amyloidosis. *Nat. Commun.* **10**, 5008.

[132] Lu, J, Cao, Q, Hughes, M. P, Sawaya, M. R, Boyer, D. R, Cascio, D, & Eisenberg, D. S. (2020) CryoEM structure of the low-complexity domain of hnRNPA2 and its conversion to pathogenic amyloid. *Nat. Commun.* **11**, 4090.

[133] Chan, J. C. C, Oyler, N. A, Yau, W.-M, & Tycko, R. (2005) Parallel β-sheets and polar zippers in amyloid fibrils formed by residues 10–39 of the yeast prion protein Ure2p. *Biochemistry* **44**, 10669–10680.

[134] Sivanandam, V. N, Jayaraman, M, Hoop, C. L, Kodali, R, Wetzel, R, & van der Wel, P. C. A. (2011) The aggregation-enhancing huntingtin N-terminus is helical in amyloid fibrils. *J. Am. Chem. Soc.* **133**, 4558–4566.

[135] Tuttle, M. D, Comellas, G, Nieuwkoop, A. J, Covell, D. J, Berthold, D. A, Kloepper, K. D, Courtney, J. M, Kim, J. K, Barclay, A. M, Kendall, A, Wan, W, Stubbs, G, Schwieters, C. D, Lee, V. M. Y,

George, J. M, & Rienstra, C. M. (2016) Solid-state NMR structure of a pathogenic fibril of full-length human α-synuclein. *Nat. Struct. Mol. Biol.* **23**, 409–415.

[136] Wälti, M. A, Ravotti, F, Arai, H, Glabe, C. G, Wall, J. S, Böckmann, A, Güntert, P, Meier, B. H, & Riek, R. (2016) Atomic-resolution structure of a disease-relevant Aβ(1–42) amyloid fibril. *Proc. Natl. Acad. Sci. U. S. A.* **113**, E4976–E4984.

[137] Guerrero-Ferreira, R, Taylor, N. M. I, Mona, D, Ringler, P, Lauer, M. E, Riek, R, Britschgi, M, & Stahlberg, H. (2018) Cryo-EM structure of alpha-synuclein fibrils. *eLife* **7**, e36402.

[138] Guerrero-Ferreira, R, Taylor, N. M. I, Arteni, A.-A, Kumari, P, Mona, D, Ringler, P, Britschgi, M, Lauer, M. E, , Makky, A, Verasdonck, J, Riek, R, Melki, R, Meier, B. H, Böckmann, A, Bousset, L, , & Stahlberg, H. (2019) Two new polymorphic structures of human full-length alpha-synuclein fibrils solved by cryo-electron microscopy. *eLife* **8**, e48907.

[139] Röder, C, Vettore, N, Mangels, L. N, Gremer, L, Ravelli, R. B. G, Willbold, D, Hoyer, W, Buell, A. K, & Schröder, G. (2019) Atomic structure of PI3-kinase SH3 amyloid fibrils by cryo-electron microscopy. *Nat. Commun.* **10**, 3754.

[140] Cao, Q, Boyer, D. R, Sawaya, M. R, Ge, P, & Eisenberg, D. S. (2020) Cryo-EM structure and inhibitor design of human IAPP (amylin) fibrils. *Nat. Struct. Mol. Biol.* **27**, 653–659.

[141] Glynn, C, Sawaya, M. R, Ge, P, Gallagher-Jones, M, Short, C. W, Bowman, R, Apostol, M, Zhou, Z. H, Eisenberg, D. S, & Rodriguez, J. A. (2020) Cryo-EM structure of a human prion fibril with a hydrophobic, protease-resistant core. *Nat. Struct. Mol. Biol.* **27**, 417–423.

[142] Röder, C, Kupreichyk, T, Gremer, L, Schäfer, L. U, Pothula, K. R, Ravelli, R. B. G, Willbold, D, Hoyer, W, & Schröder, G. (2020) Cryo-EM structure of islet amyloid polypeptide fibrils reveals similarities with amyloid-β fibrils. *Nat. Struct. Mol. Biol.* **27**, 660–667.

[143] Xiao, Y, Ma, B, Parthasarathy, S, Long, F, Hoshi, M, Nussinov, R, & Ishii, Y. (2015) Aβ(1–42) fibril structure illuminates self-recognition and replication of amyloid in Alzheimer's disease. *Nat. Struct. Mol. Biol.* **22**, 499–505.

[144] Gremer, L, Schölzel, D, Schenk, C, Reinartz, E, Labahn, J, Ravelli, R. B. G, Tusche, M, Lopez-Iglesias, C, Hoyer, W, Heise, H, Willbold, D, & Schröder, G. F. (2017) Fibril structure of amyloid-β(1-42) by cryoelectron microscopy. *Science* **358**, 116–119.

[145] Li, Y, Zhao, C, Luo, F, Liu, Z, Gui, X, Luo, Z, Zhang, X, Li, D, Liu, C, & Li, X. (2018) Amyloid fibril structure of α-synuclein determined by cryoelectron microscopy. *Cell Res.* **28**, 897–903.

[146] Li, B, Ge, P, Murray, K. A, Sheth, P, Zhang, M, Nair, G, Sawaya, M. R, Shin, W. S, Boyer, D. R, Ye, S, Eisenberg, D. S, Zhou, Z. H, & Jiang, L. (2018) Cryo-EM of full-length α-synuclein reveals fibril polymorphs with a common structural kernel. *Nat. Commun.* **9**, 3609.

[147] Boyer, D. R, Li, B, Sun, C, Fan, W, Sawaya, M. R, Jiang, L, & Eisenberg, D. S. (2019) Structures of fibrils formed by α-synuclein hereditary disease mutant H50Q reveal new polymorphs. *Nat. Struct. Mol. Biol.* **26**, 1044–1052.

[148] Radamaker, L, Lin, Y.-H, Annamalai, K, Huhn, S, Hegenbart, U, Schönland, S. O, Fritz, G, Schmidt, M, & Fändrich, M. (2019) Cryo-EM structure of a light chain-derived amyloid fibril from a patient with systemic AL amyloidosis. *Nat. Commun.* **10**, 1103.

[149] Swuec, P, Lavatelli, F, Tasaki, M, Paissoni, C, Rognoni, P, Maritan, M, Brambilla, F, Milani, P, Mauri, P, Camilloni, C, Palladini, G, Merlini, G, Ricagno, S, & Bolognesi, M. (2019) Cryo-EM structure of cardiac amyloid fibrils from an immunoglobulin light chain AL amyloidosis patient. *Nat. Commun.* **10**, 1269.

[150] Zhao, K, Lim, Y.-J, Liu, Z, Long, H, Sun, Y, Hu, J.-J, Zhao, C, Tao, Y, Zhang, X, Li, D, Li, Y.-M, & Liu, C. (2020) Parkinson's disease-related phosphorylation at Tyr39 rearranges α-synuclein amyloid fibril structure revealed by cryo-EM. *Proc. Natl. Acad. Sci. U. S. A.* **117**, 20305–20315.

[151] Trovato, A, Chiti, F, Maritan, A, & Seno, F. (2006) Insight into the structure of amyloid fibrils from the analysis of globular proteins. *PLOS Comput. Biol.* **2**, e170.

[152] Petkova, A. T, Buntkowsky, G, Dyda, F, Leapman, R. D, Yau, W. M, & Tycko, R. (2004) Solid state NMR reveals a pH-dependent antiparallel beta-sheet registry in fibrils formed by a beta-amyloid peptide. *J. Mol. Biol.* **335**, 247–260.

[153] Balbach, J. J, Ishii, Y, Antzutkin, O. N, Leapman, R. D, Rizzo, N. W, Dyda, F, Reed, J, & Tycko, R. (2000) Amyloid fibril formation by Aβ16-22, a seven-residue fragment of the Alzheimer's β-amyloid peptide, and structural characterization by solid state NMR. *Biochemistry* **39**, 13748–13759.

[154] Bu, Z, Shi, Y, Callaway, D. J. E, & Tycko, R. (2007) Molecular alignment within β-sheets in Aβ14-23 fibrils: Solid-state NMR experiments and theoretical predictions. *Biophys. J.* **92**, 594–602.

[155] Boatz, J. C, Piretra, T, Lasorsa, A, Matlahov, I, Conway, J. F, & van der Wel, P. C. A. (2020) Protofilament structure and supramolecular polymorphism of aggregated mutant Huntingtin exon 1. *J. Mol. Biol.* **432**, 4722–4744.

[156] Dear, A. J, Michaels, T. C. T, Meisl, G, Klenerman, D, Wu, S, Perrett, S, Linse, S, Dobson, C. M, & Knowles, T. P. J. (2020) Kinetic diversity of amyloid oligomers. *Proc. Natl. Acad. Sci. U. S. A.* **117**, 12087–12094.

[157] Peralta, M. D. R, Karsai, A, Ngo, A, Sierra, C, Fong, K. T, Hayre, N. R, Mirzaee, N, Ravikumar, K. M, Kluber, A. J, Chen, X, Liu, G. Y, Toney, M. D, Singh, R. R, & Cox, D. L. (2015) Engineering amyloid fibrils from β-solenoid proteins for biomaterials applications. *ACS Nano* **9**, 449–463.

[158] Peng, Z, Peralta, M. D. R, Cox, D. L, & Toney, M. D. (2020) Bottom-up synthesis of protein-based nanomaterials from engineered β-solenoid proteins. *PLOS ONE* **15**, e0229319.

[159] Colvin, M. T, Silvers, R, Ni, Q. Z, Can, T. V, Sergeyev, I, Rosay, M, Donovan, K. J, Michael, B, Wall, J, Linse, S, & Griffin, R. (2016) Atomic resolution structure of monomorphic Aβ42 amyloid fibrils. *J. Am. Chem. Soc.* **138**, 9663–9674.

[160] Kollmer, M, Close, W, Funk, L, Rasmussen, J, Bsoul, A, Schierhorn, A, Schmidt, M, Sigurdson, C. J, Jucker, M, & Fändrich, M. (2019) Cryo-EM structure and polymorphism of Aβ amyloid fibrils purified from Alzheimer's brain tissue. *Nat. Commun.* **10**, 4760.

[161] Hervas, R, Rau, M. J, Park, Y, Zhang, W, Murzin, A. G, Fitzpatrick, J. A. J, Scheres, S. H. W, & Si, K. (2020) Cryo-EM structure of a neuronal functional amyloid implicated in memory persistence in Drosophila. *Science* **367**, 1230–1234.

[162] Schütz, A. K, Vagt, T, Huber, M, Ovchinnikova, O. Y, Cadalbert, R, Wall, J, Güntert, P, Böckmann, A, Glockshuber, R, & Meier, B. H. (2015) Atomic-resolution three-dimensional structure of amyloid β fibrils bearing the Osaka mutation. *Angew. Chem. Int. Ed.* **54**, 331–335.

[163] Petkova, A. T, Ishii, Y, Balbach, J. J, Antzutkin, O. N, Leapman, R. D, Delaglio, F, & Tycko, R. (2002) A structural model for Alzheimer's β-amyloid fibrils based on experimental constraints from solid state NMR. *Proc. Natl. Acad. Sci. U. S. A.* **99**, 16742–16747.

[164] Lührs, T, Ritter, C, Adrian, M, Riek-Loher, D, Bohrmann, B, Döbeli, H, Schubert, D, & Riek, R. (2005) 3D structure of Alzheimer's amyloid-β(1–42) fibrils. *Proc. Natl. Acad. Sci. U. S. A.* **102**, 17342–17347.

[165] Ban, T, Hoshino, M, Takahashi, S, Hamada, D, Hasegawa, K, Naiki, H, & Goto, Y. (2004) Direct observation of Aβ amyloid fibril growth and inhibition. *J. Mol. Biol.* **344**, 757–767.

[166] Young, L. J, Kaminski Schierle, G. S, & Kaminski, C. F. (2017) Imaging Aβ(1–42) fibril elongation reveals strongly polarised growth and growth incompetent states. *Phys. Chem. Chem. Phys.* **19**, 27987–27996.

[167] Balbach, J. J, Petkova, A. T, Oyler, N. A, Antzutkin, O. N, Gordon, D. J, Meredith, S. C, & Tycko, R. (2002) Supramolecular structure in full-length Alzheimer's β-amyloid fibrils: Evidence for a parallel β-sheet organization from solid-state nuclear magnetic resonance. *Biophys. J.* **83**, 1205–1216.

[168] Jaroniec, C. P, MacPhee, C. E, Astrof, N. S, Dobson, C. M, & Griffin, R. G. (2002) Molecular conformation of a peptide fragment of transthyretin in an amyloid fibril. *Proc. Natl. Acad. Sci. U. S. A.* **99**, 16748–16753.

[169] Heise, H, Hoyer, W, Becker, S, Andronesi, O. C, Riedel, D, & Baldus, M. (2005) Molecular-level secondary structure, polymorphism, and dynamics of full-length α-synuclein fibrils studied by solid-state NMR. *Proc. Natl. Acad. Sci. U. S. A.* **102**, 15871–15876.

[170] Bateman, D. A, Tycko, R, & Wickner, R. B. (2011) Experimentally derived structural constraints for amyloid fibrils of wild-type transthyretin. *Biophys. J.* **101**, 2485–2492.

[171] Kryndushkin, D. S, Wickner, R. B, & Tycko, R. (2011) The core of Ure2p prion fibrils is formed by the N-terminal segment in a parallel cross-β structure: Evidence from solid-state NMR. *J. Mol. Biol.* **409**, 263–277.

[172] Sachse, C, Fändrich, M, & Grigorieff, N. (2008) Paired β-sheet structure of an Aβ(1-40) amyloid fibril revealed by electron microscopy. *Proc. Natl. Acad. Sci. U. S. A.* **105**, 7462–7466.

[173] Schmidt, M, Sachse, C, Richter, W, Xu, C, Fändrich, M, & Grigorieff, N. (2009) Comparison of Alzheimer Aβ(1–40) and Aβ(1–42) amyloid fibrils reveals similar protofilament structures. *Proc. Natl. Acad. Sci. U. S. A.* **106**, 19813–19818.

[174] Scheidt, H. A, Morgado, I, Rothemund, S, & Huster, D. (2012) Dynamics of amyloid β fibrils revealed by solid-state NMR. *J. Biol. Chem.* **287**, 2017–2021.

[175] Schmidt, M, Rohou, A, Lasker, K, Yadav, J. K, Schiene-Fischer, C, Fändrich, M, & Grigorieff, N. (2015) Peptide dimer structure in an Aβ(1–42) fibril visualized with cryo-EM. *Proc. Natl. Acad. Sci. U. S. A.* **112**, 11858–11863.

[176] Jiménez, J. L, Guijarro, J. I, Orlova, E, Zurdo, J, Dobson, C. M, Sunde, M, & Saibil, H. R. (1999) Cryo-electron microscopy structure of an SH3 amyloid fibril and model of the molecular packing. *EMBO J.* **18**, 815–821.

[177] Zhang, R, Hu, Z, Khant, H, Ludtke, S. J, Chiu, W, Schmid, M. F, Frieden, C, & Lee, J. M. (2009) Interprotofilament interactions between Alzheimer's Aβ1–42 peptides in amyloid fibrils revealed by cryoEM. *Proc. Natl. Acad. Sci. U. S. A.* **106**, 4653–4658.

[178] Zhang, S, Andreasen, M, Nielsen, J. T, Liu, L, Nielsen, E. H, Song, J, Ji, G, Sun, F, Skrydstrup, T, Besenbacher, F, Nielsen, N. C, Otzen, D. E, & Dong, M. (2013) Coexistence of ribbon and helical fibrils originating from hIAPP20–29 revealed by quantitative nanomechanical atomic force microscopy. *Proc. Natl. Acad. Sci. U. S. A.* **110**, 2798–2803.

[179] Adamcik, J, Sánchez-Ferrer, A, Ait-Bouziad, N, Reynolds, N. P, Lashuel, H. A, & Mezzenga, R. (2016) Microtubule-binding R3 fragment from tau self-assembles into giant multistranded amyloid ribbons. *Angew. Chem. Int. Ed.* **55**, 618–622.

[180] Reynolds, N. P, Adamcik, J, Berryman, J. T, Handschin, S, Zanjani, A. A. H, Li, W, Liu, K, Zhang, A, & Mezzenga, R. (2017) Competition between crystal and fibril formation in molecular mutations of amyloidogenic peptides. *Nat. Commun.* **8**, 1338.

[181] Seuring, C, Verasdonck, J, Ringler, P, Cadalbert, R, Stahlberg, H, Böckmann, A, Meier, B. H, & Riek, R. (2017) Amyloid fibril polymorphism: Almost identical on the atomic level, mesoscopically very different. *J. Phys. Chem. B* **121**, 1783–1792.

[182] Jiménez, J. L, Nettleton, E. J, Bouchard, M, Robinson, C. V, Dobson, C. M, & Saibil, H. R. (2002) The protofilament structure of insulin amyloid fibrils. *Proc. Natl. Acad. Sci. U. S. A.* **99**, 9196–9201.

[183] Fitzpatrick, A. W. P, Debelouchina, G. T, Bayro, M. J, Clare, D. K, Caporini, M. A, Bajaj, V. S, Jaroniec, C. P, Wang, L, Ladizhansky, V, Müller, S. A, MacPhee, C. E, Waudby, C. A, Mott, H. R, De Simone, A, Knowles, T. P. J, Saibil, H. R, Vendruscolo, M, Orlova, E. V, Griffin, R. G, & Dobson, C. M. (2013) Atomic structure and hierarchical assembly of a cross-β amyloid fibril. *Proc. Natl. Acad. Sci. U. S. A.* **110**, 5468–5473.

[184] Schmidt, A, Annamalai, K, Schmidt, M, Grigorieff, N, & Fändrich, M. (2016) Cryo-EM reveals the steric zipper structure of a light chain-derived amyloid fibril. *Proc. Natl. Acad. Sci. U. S. A.* **113**, 6200–6205.

[185] Close, W, Neumann, M, Schmidt, A, Hora, M, Annamalai, K, Schmidt, M, Reif, B, Schmidt, V, Grigorieff, N, & Fändrich, M. (2018) Physical basis of amyloid polymorphism. *Nat. Commun.* **6**, 699.

[186] Adamcik, J & Mezzenga, R. (2018) Amyloid polymorphism in the protein folding and aggregation energy landscape. *Angew. Chem. Int. Ed.* **57**, 8370–8382.

[187] Meinhardt, J, Sachse, C, Hortschansky, P, Grigorieff, N, & Fändrich, M. (2009) Aβ(1-40) fibril polymorphism implies diverse interaction patterns in amyloid fibrils. *J. Mol. Biol.* **386**, 869–877.

[188] Pellarin, R, Schuetz, P, Guarnera, E, & Caflisch, A. (2010) Amyloid fibril polymorphism is under kinetic control. *J. Am. Chem. Soc.* **32**, 14960–14970.

[189] Krotee, P, Rodriguez, J. A, Sawaya, M. R, Cascio, D, Reyes, F. E, Shi, D, Hattne, J, Nannenga, B. L, Oskarsson, M. E, Philipp, S, Griner, S, Jiang, L, Glabe, C. G, Westermark, G. T, Gonen, T, & Eisenberg, D. S. (2017) Atomic structures of fibrillar segments of hIAPP suggest tightly mated β-sheets are important for cytotoxicity. *eLife* **6**, e19273.

[190] Perutz, M. F, Staden, R, Moens, L, & De Baere, I. (1993) Polar zippers. *Curr. Biol.* **3**, 249–253.

[191] Gallagher-Jones, M, Glynn, C, Boyer, D. R, Martynowicz, M. W, Hernandez, E, Miao, J, Zee, C.-T, Novikova, I. V, Goldschmidt, L, McFarlane, H. T, Helguera, G. F. Evans, J. E, Sawaya, M. R, Cascio, D, Eisenberg, D. S, Gonen, T, & Rodriguez, J. A. (2018) Sub-ångström cryo-EM structure of a prion protofibril reveals a polar clasp. *Nat. Struct. Mol. Biol.* **25**, 131–134.

[192] Miller, Y, Ma, B, & Nussinov, R. (2011) The unique Alzheimer's β-amyloid triangular fibril has a cavity along the fibril axis under physiological conditions. *J. Am. Chem. Soc.* **133**, 2742–2748.

[193] McDonald, M, Box, H, Bian, W, Kendall, A, Tycko, R, & Stubbs, G. (2012) Fiber diffraction data indicate a hollow core for the Alzheimer's Aβ three-fold symmetric fibril. *J. Mol. Biol.* **423**, 454–461.

[194] Knowles, T. P. J, Smith, J. F, Craig, A, Dobson, C. M, & Welland, M. E. (2006) Spatial persistence of angular correlations in amyloid fibrils. *Phys. Rev. Lett.* **96**, 238301.

[195] Knowles, T. P. J, Fitzpatrick, A. W, Meehan, S, Mott, H. R, Vendruscolo, M, Dobson, C. M, & Welland, M. E. (2007) Role of intermolecular forces in defining material properties of protein nanofibrils. *Science* **318**, 1900–1903.

[196] Periole, X, Huber, T, Bonito-Oliva, A, Aberg, K. C, van der Wel, P. C. A, Sakmar, T. P, & Marrink, S. J. (2018) Energetics underlying twist polymorphisms in amyloid fibrils. *J. Phys. Chem. B* **122**, 1081–1091.

[197] Chothia, C. (1973) Conformation of twisted beta-pleated sheets in proteins. *J. Mol. Biol.* **75**, 295–302.

[198] Lovell, S. C, Davis, I. W, Arendall, W. B. I, de Bakker, P. W, Word, J. M, Prisant, M. G, Richardson, J. S, & Richardson, D. C. (2003) Structure validation by Cα geometry: φ, ψ and Cβ deviation. *Proteins* **50**, 437–450.

[199] Adamcik, J, Jung, J.-M, Flakowski, J, De Los Rios, P, Dietler, G, & Mezzenga, R. (2011) Understanding amyloid aggregation by statistical analysis of atomic force microscopy images. *Nat. Nanotechnol.* **5**, 423–428.

[200] Adamcik, J & Mezzenga, R. (2011) Adjustable twisting periodic pitch of amyloid fibrils. *Soft Matter* **7**, 5437–5443.

[201] Assenza, S, Adamcik, J, Mezzenga, R, & De Los Rios, P. (2014) Universal behavior in the mesoscale properties of amyloid fibrils. *Phys. Rev. Lett.* **113**, 268103.

[202] Usov, I, Adamcik, J, & Mezzenga, R. (2013) Polymorphism complexity and handedness inversion in serum albumin amyloid fibrils. *ACS Nano* **7**, 10465–10474.

[203] Riley, K. F, Hobson, M. P, & Bence, S. J. (2006) *Mathematical Methods for Physics and Engineering.* (Cambridge University Press, Cambridge, UK).

[204] Landau, L. D & Lifshitz, E. M. (1979) *Course of Theoretical Physics*. (Pergamon Press, Oxford, UK) Vol. 5.

[205] Petkova, A. T, Leapman, R. D, Guo, Z, Yau, W. M, Mattson, M. P, & Tycko, R. (2005) Self-propagating, molecular-level polymorphism in Alzheimer's β-amyloid fibrils. *Science* **307**, 262–265.

[206] Yagi, H, Ban, T, Morigaki, K, Naiki, H, & Goto, Y. (2007) Visualization and classification of amyloid β supramolecular assemblies. *Biochemistry* **46**, 15009–15017.

[207] Qiang, W, Kelley, K, & Tycko, R. (2013) Polymorph-specific kinetics and thermodynamics of β-amyloid fibril growth. *J. Am. Chem. Soc.* **135**, 6860–6871.

[208] Qiang, W, Yau, W.-M, Lu, J.-X, Collinge, J, & Tycko, R. (2017) Structural variation in amyloid-β fibrils from Alzheimer's disease clinical subtypes. *Nature* **541**, 217–221.

[209] Goldsbury, C, Frey, P, Olivieri, V, Aebi, U, & Müller, S. A. (2005) Multiple assembly pathways underlie amyloid-β fibril polymorphisms. *J. Mol. Biol.* **352**, 282–298.

[210] Lazo, N. D & Downing, D. T. (1998) Amyloid fibrils may be assembled from β-helical protofibrils. *Biochemistry* **37**, 1731–1735.

[211] Li, Y, Darden, T. A, Bartolotti, L, Kominos, D, & Pedersen, L. G. (1999) An atomic model for the pleated β-sheet structure of Aβ amyloid protofilaments. *Biophys. J.* **76**, 2871–2878.

[212] Tjernberg, L. O, Callaway, D. J. E, Tjernberg, A, Hahne, S, Lilliehook, C, Terenius, L, Thyberg, J, & Nordstedt, C. (1999) A molecular model of Alzheimer amyloid beta-peptide fibril formation. *J. Biol. Chem.* **274**, 12619–12625.

[213] Serpell, L. C & Smith, J. M. (2000) Direct visualisation of the β-sheet structure of synthetic Alzheimer's amyloid. *J. Mol. Biol.* **299**, 225–231.

[214] Benzinger, T. L. S, Gregory, D. M, Burkoth, T. S, Miller-Auer, H, Lynn, D. G, Botto, R. E, & Meredith, S. C. (1998) Propagating structure of Alzheimer's β-amyloid(10–35) is parallel β-sheet with residues in exact register. *Proc. Natl. Acad. Sci. U. S. A.* **95**, 13407–13412.

[215] Antzutkin, O. N, Balbach, J. J, Leapman, R. D, Rizzo, N. W, Reed, J, & Tycko, R. (2000) Multiple quantum solid-state NMR indicates a parallel, not antiparallel, organization of β-sheets in Alzheimer's β-amyloid fibrils. *Proc. Natl. Acad. Sci. U. S. A.* **97**, 13045–13050.

[216] Ahmed, M, Davis, J, Aucoin, D, Sato, T, Ahuja, S, Aimoto, S, Elliott, J. I, van Nostrand, W. E, & Smith, S. O. (2010) Structural conversion of neurotoxic amyloid-β1–42 oligomers to fibrils. *Nat. Struct. Mol. Biol.* **17**, 561.

[217] Yang, J, Dear, A. J, Michaels, T. C. T, Dobson, C. M, Knowles, T. P. J, Wu, S, & Perrett, S. (2018) Direct observation of oligomerization by single molecule fluorescence reveals a multistep aggregation mechanism for the yeast prion protein Ure2. *J. Am. Chem. Soc.* **140**, 2493–2503.

[218] Petkova, A. T, Yau, W. M, & Tycko, R. (2006) Experimental constraints on quaternary structure in Alzheimer's β-amyloid fibrils. *Biochemistry* **45**, 498–512.

[219] Yang, M & Teplow, D. B. (2008) Amyloid β-protein monomer folding: Free-energy surfaces reveal alloform-specific differences. *J. Mol. Biol.* **384**, 450–464.

[220] Urbanc, B, Betnel, M, Cruz, L, Bitan, G, & Teplow, D. B. (2010) Elucidation of amyloid β-protein oligomerization mechanisms: Discrete molecular dynamics study. *J. Am. Chem. Soc.* **132**, 4266–4280.

[221] Vitalis, A & Caflisch, A. (2010) Micelle-like architecture of the monomer ensemble of Alzheimer's amyloid-β peptide in aqueous solution and its implications for Aβ aggregation. *J. Mol. Biol.* **403**, 148–165.

[222] Barz, B & Urbanc, B. (2014) Minimal model of self-assembly: Emergence of diversity and complexity. *J. Phys. Chem. B* **118**, 3761–3770.

[223] Barz, B, Olubiyi, O. O, & Strodel, B. (2014) Early amyloid β-protein aggregation precedes conformational change. *Chem. Commun.* **50**, 5373.

[224] Šarić, A, Michaels, T. C. T, Zaccone, A, Knowles, T. P. J, & Frenkel, D. (2016) Kinetics of spontaneous filament nucleation via oligomers: Insights from theory and simulation. *J. Chem. Phys.* **145**, 211926.

[225] Uversky, V. N & Fink, A. L. (2004) Conformational constraints for amyloid fibrillation: the importance of being unfolded. *Biochim. Biophys. Acta* **1698**, 131–153.

[226] Thirumalai, D, O'Brien, E. P, Morrison, G, & Hyeon, C. (2010) Theoretical perspectives on protein folding. *Annu. Rev. Biophys.* **39**, 159–183.

[227] Uversky, V. N. (2002) Natively unfolded proteins: A point where biology waits for physics. *Protein Sci.* **11**, 739–756.

[228] Dyson, H. J & Wright, P. E. (2005) Intrinsically disordered proteins and their functions. *Nat. Rev. Mol. Cell Biol.* **6**, 197–208.

[229] Holehouse, A. S & Pappu, R. V. (2018) Collapse transitions of proteins and the interplay among backbone, sidechain, and solvent interactions. *Annu. Rev. Biophys.* **47**, 19–39.

[230] Danielsson, J, Jarvet, J, Damberg, P, & Gräslund, A. (2005) The Alzheimer β-peptide shows temperature-dependent transitions between left-handed 3(1)-helix, β-strand and random coil secondary structures. *FEBS J.* **272**, 3938–3949.

[231] Nichols, M. R, Moss, M. A, Reed, D. K, Cratic-McDaniel, S, Hoh, J. H, & Rosenberry, T. L. (2005) Amyloid-β protofibrils differ from amyloid-β aggregates induced in dilute hexafluoroisopropanol in stability and morphology. *J. Biol. Chem.* **280**, 2471–2480.

[232] Rosenman, D. J, Connors, C. R, Chen, W, Wang, C, & García, A. E. (2013) Aβ monomers transiently sample oligomer and fibril-like configurations: Ensemble characterization using a combined MD/NMR approach. *J. Mol. Biol.* **425**, 3338–3359.

[233] Wolff, M, Unuchek, D, Zhang, B, Gordeliy, V, Willbold, D, & Nagel-Steger, L. (2015) Amyloid β oligomeric species present in the lag phase of amyloid formation. *PLOS ONE* **10**, e0127865.

[234] Kedia, N, Almisry, M, & Bieschke, J. (2017) Glucose directs amyloid-beta into membrane-active oligomers. *Phys. Chem. Chem. Phys.* **19**, 18036.

[235] Baumketner, A, Bernstein, S. L, Wyttenbach, T, Bitan, G, Teplow, D. B, Bowers, M. T, & Shea, J.-E. (2006) Amyloid β-protein monomer structure: A computational and experimental study. *Protein Sci.* **15**, 420–428.

[236] Sgourakis, N. G, Yan, Y, McCallum, S. A, Wang, C, & Garcia, A. E. (2007) The Alzheimer's peptides Aβ40 and 42 adopt distinct conformations in water: A combined MD / NMR study. *J. Mol. Biol.* **368**, 1448–1457.

[237] Brovchenko, I, Burri, R. R, Krukau, A, Oleinikova, A, & Winter, R. (2008) Intrinsic thermal expansivity and hydrational properties of amyloid peptide Aβ42 in liquid water. *J. Chem. Phys.* **129**, 195101.

[238] Carballo-Pacheco, M & Strodel, B. (2017) Comparison of force fields for Alzheimer's Aβ42: A case study for intrinsically disordered proteins. *Protein Sci.* **26**, 174–185.

[239] Bernadó, P, Bertoncini, C. W, Griesinger, C, Zweckstetter, M, & Blackledge, M. (2005) Defining long-range order and local disorder in native α-synuclein using residual dipolar couplings. *J. Am. Chem. Soc.* **127**, 17968–17969.

[240] Morar, A. S, Olteanu, A, Young, G. B, & Pielak, G. J. (2001) Solvent-induced collapse of α-synuclein and acid-denatured cytochrome. *Protein Sci.* **10**, 2195–2199.

[241] Dukor, R. K & Keiderling, T. A. (1991) Reassessment of the random coil conformation: vibrational CD study of proline oligopeptides and related polypeptides. *Biopolymers* **31**, 1747–1761.

[242] Wilson, G, Hecht, L, & Barron, L. D. (1996) Residual structure in unfolded proteins revealed by Raman optical activity. *Biochemistry* **35**, 12518–12525.

[243] Park, S. H, Shalongo, W, & Stellwagen, E. (1997) The role of PII conformations in the calculation of peptide fractional helix content. *Protein Sci.* **6**, 1694–1700.

[244] Kelly, M. A, Chellgren, B. W, Rucker, A. L, Troutman, J. M, Fried, M. G, Miller, A. F, & Creamer, T. P. (2001) Host-guest study of left-handed polyproline II helix formation. *Biochemistry* **40**, 14376–14383.

[245] Shi, Z, Olson, C. A, Rose, G. D, Baldwin, R. L, & Kallenback, N. R. (2002) Polyproline II structure in a sequence of seven alanine residues. *Proc. Natl. Acad. Sci. U. S. A.* **99**, 9190– 9195.

[246] Shi, Z, Woody, N, & Kallenback, N. R. (2002) Is polyproline II a major backbone conformation in unfolded proteins? *Adv. Protein Chem.* **62**, 163–140.

[247] Syme, C. D, Blanch, E. W, Holt, C, Jakes, R, Goedert, M, Hecht, L, & Barron, L. D. (2002) A Raman optical activity study of rheomorphism in caseins, synucleins and tau. New insight into the structure and behaviour of natively unfolded proteins. *Eur. J. Biochem.* **269**, 148–156.

[248] Avbelj, F & Baldwin, R. L. (2003) Role of backbone solvation and electrostatics in generating preferred peptide backbone conformations: distributions of phi. *Proc. Natl. Acad. Sci. U. S. A.* **100**, 5742–5747.

[249] Chellgren, B. W, Miller, A. F, & Creamer, T. P. (2006) Evidence for polyproline II helical structure in short polyglutamine tracts. *J. Mol. Biol.* **361**, 362–371.

[250] Mukrasch, M. D, Markwick, P, Biernat, J, vin Bergen, M, Bernadó, P, Griesinger, C, Mandelkow, E, Zweckstetter, M, & Blackledge, M. (2007) Highly populated turn conformations in natively unfolded Tau protein identified from residual dipolar couplings and molecular simulation. *J. Am. Chem. Soc.* **129**, 5235–5243.

[251] Thakur, A. K, Jayaraman, M, Mishra, R, Thakur, M, Chellgren, V. M, Byeon, I.-J. L, Anjum, D. H, Kodali, B, Creamer, T. P, Conway, J. F, Gronenborn, A. M, & Wetzel, R. (2009) Polyglutamine disruption of the huntingtin exon 1 N terminus triggers a complex aggregation mechanism. *Nat. Struct. Mol. Biol.* **16**, 380–389.

[252] Blanch, E. W, Morozova-Roche, L. A, Cochran, D. A. E, Doig, A. J, Hecht, L, & Barron, L. D. (2000) Is polyproline II helix the killer conformation? A Raman optical activity study of the amyloidogenic prefibrillar intermediate of human lysozyme. *J. Biol. Chem.* **301**, 553–563.

[253] Fauvet, B, Mbefo, M. K, Fares, M.-B, Desobry, C, Michael, S, Ardah, M. T, Tsika, E, Coune, P, Prudent, M, Lion, N, Eliezer, D, Moore, D. J, Schneider, B, Aebischer, P, El-Agnaf, O. M, Masliah, E, & Lashuel, H. A. (2012) α-synuclein in central nervous system and from erythrocytes, mammalian cells, and *Escherichia coli* exists predominantly as disordered monomer. *J. Biol. Chem.* **287**, 15345–15364.

[254] Goldsbury, C, Goldie, K, Pellaud, J, Seelig, J, Frey, P, Müller, S. A, Kistler, J, Cooper, G. J. S, & Aebi, U. (2000) Amyloid fibril formation from full-length and fragments of amylin. *J. Struct. Biol.* **130**, 352–362.

[255] Dupuis, N. F, Wu, C, Shea, J.-E, & Bowers, M. T. (2009) Human islet amyloid polypeptide monomers form ordered β-hairpins: A possible direct amyloidogenic precursor. *J. Am. Chem. Soc.* **131**, 18283–18292.

[256] Karamanos, T. K, Jackson, M. P, Calabrese, A. N, Goodchild, S. C, Cawood, E. E, Thompson, G. S, Kalverda, A. P, Hewitt, E. W, & Radford, S. E. (2019) Structural mapping of oligomeric intermediates in an amyloid assembly pathway. *eLife* **8**, e46574.

[257] Karamanos, T. K, Pashley, C. L, Kalverda, A. P, Thompson, G. S, Mayzel, M, Orekhov, V. Y, & Radford, S. E. (2016) A population shift between sparsely populated folding intermediates determines amyloidogenicity. *J. Am. Chem. Soc.* **138**, 6271–6280.

[258] Staniforth, R. A, Giannini, S, Higgins, L. D, Conroy, M. J, Hounslow, A. M, Jerala, R, Craven, C. J, & Waltho, J. P. (2001) Three-dimensional domain swapping in the folded and molten-globule states of cystatins, an amyloid-forming structural superfamily. *EMBO J.* **20**, 4774–4781.

[259] Khurana, R, gillespie, J. R, Talapatra, A, Minert, L. J, Ionescu-Zanetti, C, Millett, I, & Fink, A. L. (2001) Partially folded intermediates as critical precursors of light chain amyloid fibrils and amorphous aggregates. *Biochemistry* **40**, 3525–3535.

[260] Fezoui, Y & Teplow, D. B. (2002) Kinetic studies of amyloid β-protein fibril assembly. *J. Biol. Chem.* **277**, 36948–36954.

[261] Lazo, N. D, Grant, M. A, Condron, M. C, Rigby, A. C, & Teplow, D. B. (2005) On the nucleation of amyloid β-protein monomer folding. *Protein Sci.* **14**, 1581–1596.

[262] Williamson, J. A & Miranker, A. D. (2007) Direct detection of transient α-helical states in islet amyloid polypeptide. *Protein Sci.* **16**, 110–117.

[263] Ferrone, F. A. (2015) Assembly of Aβ proceeds via monomeric nuclei. *J. Mol. Biol.* **427**, 287–290.

[264] Chen, S, Berthelier, V, Yang, W, & Wetzel, R. (2001) Polyglutamine aggregation behavior *in vitro* supports a recruitment mechanism of cytotoxicity. *J. Mol. Biol.* **311**, 174–182.

[265] Uversky, V. N, Li, J, & Fink, A. L. (2001) Metal-triggered structural transformations, aggregation and fibril formation of human α-synuclein. a possible molecular link between Parkinson's disease and heavy metal exposure. *J. Biol. Chem.* **276**, 44284–44296.

[266] Chen, S, Ferrone, F. A, & Wetzel, R. (2002) Huntington's disease age-of-onset linked to polyglutamine aggregation nucleation. *Proc. Natl. Acad. Sci. U. S. A.* **99**, 11884–11889.

[267] Mukhopadhyay, S, Krishnan, R, Lemke, E. A, Lindquist, S, & Deniz, A. A. (2007) A natively unfolded yeast prion monomer adopts an ensemble of collapsed and rapidly fluctuating structures. *Proc. Natl. Acad. Sci. U. S. A.* **104**, 2649–2654.

[268] Vitalis, A, Lyle, N, & Pappu, R. V. (2009) Thermodynamics of β-sheet formation in polyglutamine. *Biophys. J.* **97**, 303–311.

[269] Jain, N, Bhattacharya, M, & Mukhopadhyay, S. (2011) Chain collapse of an amyloidogenic intrinsically disordered protein. *Biophys. J.* **101**, 1720–1729.

[270] Vitalis, A, Wang, X, & Pappu, R. V. (2007) Quantitative characterization of intrinsic disorder in polyglutamine: Insights from analysis based on polymer theories. *Biophys. J.* **93**, 1923–1937.

[271] Tran, H. T, Mao, A, & Pappu, R. V. (2008) Role of backbone-solvent interactions in determining conformational equilibria of intrinsically disordered proteins. *J. Am. Chem. Soc.* **130**, 7380–7392.

[272] Kim, S, Takeda, T, & Klimov, D. K. (2010) Globular state in the oligomers formed by Aβ peptides. *J. Chem. Phys.* **132**, 225101.

[273] Yun, S, Urbanc, B, Cruz, L, Bitan, G, Teplow, D. B, & Stanley, H. E. (2007) Role of electrostatic interactions in amyloid β-protein (Aβ) oligomer formation: A discrete molecular dynamics study. *Biophys. J.* **92**, 4064–4077.

[274] Barz, B & Urbanc, B. (2012) Dimer formation enhances structural differences between amyloid β-protein (1–40) and (1–42): An explicit-solvent molecular dynamics study. *PLOS ONE* **7**, e34345.

[275] Meral, D & Urbanc, B. (2013) Discrete molecular dynamics study of oligomer formation by N-terminally truncated amyloid β-protein. *J. Mol. Biol.* **425**, 2260–2275.

[276] Arya, S & Mukhopadhyay, S. (2014) Ordered water within the collapsed globules of an amyloidogenic intrinsically disordered protein. *J. Phys. Chem. B* **118**, 9191–9198.

[277] Dahlgren, K. N, Manelli, A. M, Stine, W. B. J, Baker, L. K, Krafft, G. A, & LaDu, M. J. (2002) Oligomeric and fibrillar species of amyloid-β peptides differentially affect neuronal viability. *J. Biol. Chem.* **277**, 32046–32053.

[278] Chimon, S, Shaibat, M. A, Jones, C. R, Calero, D. C, Aizezi, B, & Ishii, Y. (2007) Evidence of fibril-like β-sheet structures in a neurotoxic amyloid intermediate of Alzheimer's β-amyloid. *Nat. Struct. Mol. Biol.* **14**, 1157–1164.

[279] Nichols, M. R, Colvin, B. A, Hood, E. A, Paranjape, G. S, Osborn, D. C, & Terrill-Usery, S. E. (2015) Biophysical comparison of soluble amyloid-β(1-42) protofibrils, oligomers, and protofilaments. *Biochemistry* **54**, 2193–2204.

[280] Kotler, S. A, Brender, J. R, Vivekanandan, S, Suzuki, Y, Yamamoto, K, Monette, M, Krishnamoorthy, J, Walsh, P, Cauble, M, Holl, M. M. B, Marsh, E. N. G, & Ramamoorthy, A. (2015) High-resolution NMR characterization of low abundance oligomers of amyloid-β without purification. *Sci. Rep.* **5**, 11811.

[281] Janowski, R, Kozak, M, Jankowska, E, Z., G, Grubb, A, Abrahamson, M, & Jaskolski, M. (2001) Human cystatin C, an amyloidogenic protein, dimerizes through three-dimensional domain swapping. *Nat. Struct. Biol.* **8**, 316–320.

[282] Sanders, A, Craven, C. J, Higgins, L. D, Giannini, S, Conroy, M. J, Hounslow, A. M, Waltho, J. P, & Staniforth, S. A. (2004) Cystatin forms a tetramer through structural rearrangement of domain-swapped dimers prior to amyloidogenesis. *J. Mol. Biol.* **336**, 165–178.

[283] Serio, T. R, Cashikar, A. G, Kowal, A. S, Sawicki, G. J, Moslehi, J. J, Serpell, L, Arnsdorf, M. F, & Lindquist, S. L. (2000) Nucleated conformational conversion and the replication of conformational information by a prion determinant. *Science* **289**, 1317–1321.

[284] Krishnan, R & Lindquist, S. L. (2005) Structural insights into a yeast prion illuminate nucleation and strain diversity. *Nature* **435**, 765–772.

[285] Lomakin, A, Chung, D. S, Benedek, G. B, Kirschner, D. A, & Teplow, D. B. (1996) On the nucleation and growth of amyloid β-protein fibrils: Detection of nuclei and quantitation of rate constants. *Proc. Natl. Acad. Sci. U. S. A.* **93**, 1125–1129.

[286] Huang, T. H. J, Yang, D.-S, Plaskos, N. P, Go, S, Yip, C. M, Fraser, P. E, & Chakrabarty, A. (2000) Structural studies of soluble oligomers of the Alzheimer β-amyloid peptide. *J. Mol. Biol.* **297**, 73–87.

[287] Bitan, G, Lomakin, A, & Teplow, D. B. (2001) Amyloid β-protein oligomerization. *J. Biol. Chem.* **276**, 35176–35184.

[288] Hoshi, M, Sato, M, Matsumoto, S, Noguchi, A, Yasutake, K, Yoshida, N, & Sato, K. (2003) Spherical aggregates of β-amyloid (amylospheroid) show high neurotoxicity and activate tau protein kinase I/glycogen synthase kinase-3β. *Proc. Natl. Acad. Sci. U. S. A.* **100**, 6370–6375.

[289] Barghorn, S, Nimmrich, V, Striebinger, A, Krantz, C, Keller, P, Janson, B, Bahr, M, Schmidt, M, Bitner, R. S, Harlan, J, Barlow, E, Ebert, U, & Hillen, H. (2005) Globular amyloid β-peptide 1-42 oligomer - a homogenous and stable neuropathological protein in alzheimer's disease. *J. Neurochem.* **95**, 834–847.

[290] Sandberg, A, Luheshi, L. M, Söllvander, S, de Barros, T. P, Macao, B, Knowles, T. P. J, Biverstål, H, Lendel, C, Ekholm-Petterson, F, Dubnovitsky, A, Lannfelt, L, Dobson, C. M, & Härd, T. (2010) Stabilization of neurotoxic Alzheimer amyloid-β oligomers by protein engineering. *Proc. Natl. Acad. Sci. U. S. A.* **107**, 15595–15600.

[291] Sarroukh, R, Cerf, E, Derclaye, S, Dufrêne, Y. F, Goormaghtigh, E, Ruysschaert, J.-M, & Raussens, V. (2011) Transformation of amyloid β(1–40) oligomers into fibrils is characterized by a major change in secondary structure. *Cell. Mol. Life Sci.* **68**, 1429–1438.

[292] Corsale, C, Carrotta, R, Mangione, M. R, Vilasi, S, Provenzano, A, Cavallaro, G, Bulone, D, & San Biagio, P. L. (2012) Entrapment of Aβ1-40 peptide in unstructured aggregates. *J. Phys.: Condens. Matter* **24**, 244103.

[293] Yusko, E. C, Prangkio, P, Sept, D, Rollings, R. C, Li, J, & Mayer, M. (2012) Single-particle characterization of Aβ oligomers in solution. *ACS Nano* **6**, 5909–5919.

[294] Garai, K & Frieden, C. (2013) Quantitative analysis of the time course of Aβ oligomerization and subsequent growth steps using tetramethylrhodamine-labeled Aβ. *Proc. Natl. Acad. Sci. U. S. A.* **110**, 3321–3326.

[295] Luo, J, Wärmländer, S. K. T. S, Gräslund, A, & Abrahams, J. P. (2014) Alzheimer peptides aggregate into transient nanoglobules that nucleate fibrils. *Biochemistry* **53**, 6302–6308.

[296] Potapov, A, Yau, W.-M, Ghirlando, R, Thurber, K. R, & Tycko, R. (2015) Successive stages of amyloid-β self-assembly characterized by solid-state nuclear magnetic resonance with dynamic nuclear polarization. *J. Am. Chem. Soc.* **137**, 8294–8307.

[297] Conway, K. A, Harper, J. D, & Lansbury, P. T. J. (2000) Fibrils formed in vitro from α-synuclein and two mutant forms linked to parkinson's disease are typical amyloid. *Biochemistry* **39**, 2552–2563.

[298] Apetri, M. M, Maiti, N. C, Zagorski, M. G, Carey, P. R, & Anderson, V. E. (2006) Secondary structure of α-synuclein oligomers: Characterization by Raman and atomic force microscopy. *J. Mol. Biol.* **355**, 63–71.

[299] Lorenzen, N, Nielsen, S. B, Buell, A. K, Kaspersen, J. D, Arosio, P, Vad, B. S, Paslawski, W, Christiansen, G, Valnickova-Hansen, Z, Andreasen, M, Enghild, J. J, Pedersen, J. S, Dobson, C. M, Knowles, T. P. J, & Otzen, D. E. (2014) The role of stable α-synuclein oligomers in the molecular events underlying amyloid formation. *J. Am. Chem. Soc.* **136**, 3859–3868.

[300] Williamson, J. A, Loria, J. P, & Miranker, A. D. (2009) Helix stabilization precedes aqueous and bilayer-catalyzed fiber formation in islet amyloid polypeptide. *J. Mol. Biol.* **393**, 383–396.

[301] Dupuis, N. F, Wu, C, Shea, J.-E, & Bowers, M. T. (2011) The amyloid formation mechanism in human IAPP: Dimers have β-strand monomer-monomer interfaces. *J. Am. Chem. Soc.* **133**, 7240–7243.

[302] Poirier, M. A, Li, H, Macosko, J, Cai, S, Amzel, M, & Ross, C. A. (2002) Huntingtin spheroids and protofibrils as precursors in polyglutamine fibrilization. *J. Biol. Chem.* **277**, 41032–41037.

[303] Yu, L, Edalji, R, Harlan, J. E, Holzman, T. F, Lopez, A. P, Labkovsky, B, Hillen, H, Barghorn, S, Ebert, U, Richardson, P. L, Miesbauer, L, Solomon, L, Bartley, D, Walter, K, Johnson, R. W, Hajduk, P. J, & Olejniczak, E. T. (2009) Structural characterization of a soluble amyloid β-peptide oligomer. *Biochemistry* **48**, 1870–1877.

[304] Bitan, G, Kirkitadze, M. D, Lomakin, A, Vollers, S. S, Benedek, G. B, & Teplow, D. B. (2003) Amyloid β-protein (Aβ) assembly: Aβ40 and Aβ42 oligomerize through distinct pathways. *Proc. Natl. Acad. Sci.* **100**, 330–335.

[305] Xi, W, Vanderford, E. K, & Hansmann, U. H. E. (2018) Out-of-register Aβ42 assemblies as models for neurotoxic oligomers and fibrils. *J. Chem. Theory Comput.* **14**, 1099–1110.

[306] Buchanan, L. E, Dunkelberger, E. B, Tran, H. Q, Cheng, P.-N, Chiu, C.-C, Cao, P, Raleigh, D. P, de Pablo, J. J, Nowick, J. S, & Zanni, M. T. (2013) Mechanism of IAPP amyloid fibril formation involves an intermediate with a transient β-sheet. *Proc. Natl. Acad. Sci. U. S. A.* **110**, 19285–19290.

[307] Tanaka, M, Machida, Y, Nishikawa, Y, Akagi, T, Hashikawa, T, Fujisawa, T, & Nukina, N. (2003) Expansion of polyglutamine induces the formation of quasi-aggregate in the early stage of protein fibrillization. *J. Biol. Chem.* **278**, 34717–34724.

[308] Wacker, J. L, Zareie, M. H, Fong, H, Sarikaya, M, & Muchowski, P. J. (2004) Hsp70 and Hsp40 attenuate formation of spherical and annular polyglutamine oligomers by partitioning monomer. *Nat. Struct. Mol. Biol.* **11**, 1215–1222.

[309] Pellarin, R & Caflisch, A. (2006) Interpreting the aggregation kinetics of amyloid peptides. *J. Mol. Biol.* **360**, 882–892.

[310] Bellesia, G & Shea, J.-E. (2009) Effect of β-sheet propensity on peptide aggregation. *J. Chem. Phys.* **130**, 145103.

[311] Auer, S & Kashchiev, D. (2010) Phase diagram of α-helical and β-sheet forming peptides. *Phys. Rev. Lett.* **104**, 168105.

[312] Barz, B, Wales, D. J, & Strodel, B. (2014) A kinetic approach to the sequence-aggregation relationship in disease-related protein assembly. *J. Phys. Chem. B* **118**, 1003–1011.

[313] Brown, A. M & Bevan, D. R. (2016) Molecular dynamics simulations of amyloid β-peptide (1-42): Tetramer formation and membrane interactions. *Biophys. J.* **111**, 937–949.

[314] Barz, B & Strodel, B. (2018) Pathways of amyloid-β aggregation depend on oligomer shape. *J. Am. Chem. Soc.* **140**, 319–327.

[315] Zheng, W, Tsai, M.-Y, Chen, M, & Wolynes, P. (2016) Exploring the aggregation free energy landscape of the amyloid-β protein (1–40). *Proc. Natl. Acad. Sci. U. S. A.* **113**, 11835–11840.

[316] Yong, W, Lomakin, A, Kirkitadze, M. D, Teplow, D. B, Chen, S.-H, & Benedek, G. B. (2002) Structure determination of micelle-like intermediates in amyloid β-protein fibril assembly by using small angle neutron scattering. *Proc. Natl. Acad. Sci. U. S. A.* **99**, 150–154.

[317] Sabaté, R & Estelrich, J. (2005) Evidence of the existence of micelles in the fibrillogenesis of β-amyloid peptide. *J. Phys. Chem. B* **109**, 11027–11032.

[318] Leonil, J, Hendy, G, Jouanneau, D, Delage, M.-M, Forge, V, & Putaux, J.-L. (2008) Kinetics of fibril formation of bovine κ-casein indicate a conformational rearrangement as a critical step in the process. *J. Mol. Biol.* **381**, 1267–1280.

[319] Dear, A. J, Šarić, A, Michaels, T. C. T, Dobson, C. M, & Knowles, T. P. J. (2018) Statistical mechanics of globular oligomer formation by protein molecules. *J. Phys. Chem. B* **122**, 11721–11730.

[320] Zampagni, M, Cascella, R, Casamenti, F, Grossi, C, Evangelisti, E, Wright, D, Becatti, M, Liguri, G, Mannini, B, Campioni, S, Chiti, F, & Cecchi, C. (2011) A comparison of the biochemical modifications caused by toxic and non-toxic protein oligomers in cells. *J. Cell. Mol. Med.* **15**, 2106–2116.

[321] Jang, H, Connelly, L, Arce, F. T, Ramachandran, S, Lal, R, Kagan, B. L, & Nussinov, R. (2013) Alzheimer's disease: which type of amyloid-preventing drug agents to employ? *Phys. Chem. Chem. Phys.* **15**, 8868.

[322] Fang, Y.-S, Tsai, K.-J, Chang, Y.-J, Kao, P, Woods, R, Kuo, P.-H, Wu, C.-C, Liao, J.-Y, Chou, S.-C, Lin, V, Jon, L.-W, Yuan, H. S, Cheng, I. H, Tu, P.-H, & Chen, Y.-R. (2014) Full-length TDP-43 forms toxic amyloid oligomers that are present in frontotemporal lobar dementia-TDP patients. *Nat. Commun.* **5**, 4824.

[323] Laganowsky, A, Liu, C, Sawaya, M. R, Whitelegge, J. P, Park, J, Zhao, M, Pensalfini, A, Soriaga, A. B, Landau, M, Teng, P. K, Cascio, D, Glabe, C, & Eisenberg, D. (2012) Atomic view of a toxic amyloid small oligomer. *Science* **335**, 1228–1231.

[324] Lendel, C, Bjerring, M, Dubnovitsky, A, Kelly, R. T, Filippov, A, Antzutkin, O. N, Nielsen, N. C, & Härd, T. (2014) A hexameric peptide barrel as building block of amyloid-β protofibrils. *Angew. Chem. Int. Ed.* **53**, 12756–12760.

[325] Bernstein, S. L, Dupuis, N. F, Lazo, N. F, Wyttenback, T, Condron, M. M, Bitan, G, Teplow, D. B, Shea, J. E, Ruotolo, B. T, Robinson, C. V, & Bowers, M. T. (2009) Amyloid-β protein oligomerization and the importance of tetramers and dodecamers in the aetiology of Alzheimer's disease. *Nat. Chem.* **1**, 316–331.

[326] Kayed, R, Head, E, Thompson, J. L, McIntire, T. M, Milton, S. C, Cotman, C. W, & Glabe, C. G. (2003) Common structure of soluble amyloid oligomers implies common mechanism of pathogenesis. *Science* **300**, 486–489.

[327] Yoshiike, Y, Kayed, R, Milton, S. C, Takashima, A, & Glabe, C. G. (2007) Pore-forming proteins share structural and functional homology with amyloid oligomers. *Neuromolecular Med.* **9**, 270–275.

[328] Tomic, J. L, Pensalfini, A, Head, E, & Glabe, C. G. (2009) Soluble fibrillar oligomer levels are elevated in Alzheimer's disease brain and correlate with cognitive dysfunction. *Neurobiol. Dis.* **35**, 352–358.

[329] Gosal, W. S, Morten, I. J, Hewitt, E. W, Smith, A. D, Thomson, N. H, & Radford, S. E. (2005) Competing pathways determine fibril morphology in the self-assembly of β2-microglobulin into amyloid. *J. Mol. Biol.* **351**, 850–864.

[330] Holm, N. K, Jespersen, S. K, Thomassen, L. V, Wolff, T. Y, Sehgal, P, Thomsen, L. A, Christiansen, G, Andersen, C. B, Knudsen, A. D, & Otzen, D. E. (2007) Aggregation and fibrillation of bovine serum albumin. *Biochim. Biophys. Acta* **1774**, 1128–1138.

[331] Harper, J. D, Wong, S. S, Lieber, C. M, & Lansbury, P. T. J. (1997) Observation of metastable Aβ amyloid protofibrils by atomic force microscopy. *Chem. Biol.* **4**, 119–125.

[332] Lee, C. H, Kim, H. J, Lee, J.-H, Cho, H.-J, Kim, J, Chung, K. C, Jung, S, & Paik, S. R. (2006) Dequalinium-induced protofibril formation of β-synuclein. *J. Biol. Chem.* **281**, 3463–3472.

[333] Kumar, S & Udgaonkar, J. B. (2009) Structurally distinct amyloid protofibrils form on separate pathways of aggregation of a small protein. *Biochemistry* **48**, 6441–6449.

[334] Keller, A, Fritzsche, M, Yu, Y.-P, Liu, Q, Li, Y.-M, Dong, M, & Besenbacher, F. (2011) Influence of hydrophobicity on the surface-catalyzed assembly of the islet amyloid polypeptide. *ACS Nano* **5**, 2770–2778.

[335] Brown, J. P. W, Meisl, G, Knowles, T. P. J, Buell, A. K, Dobson, C. M, & Galvagnion, C. (2018) Kinetic barriers to α-synuclein protofilament formation and conversion into mature fibrils. *Chem. Commun.* **54**, 7854–7857.

[336] Harper, J. D, Wong, S. S, Lieber, C. W, & Lansbury, P. T. J. (1999) Assembly of Aβ amyloid protofibrils: An in vitro model for a possible early event in Alzheimer's disease. *Biochemistry* **38**, 8972–8980.

[337] Srinivasan, R, Jones, E. M, Liu, K, Ghiso, J, Marchant, R. E, & Zagorski, M. G. (2003) pH-dependent amyloid and protofibril formation by the ABri peptide of familial british dementia. *J. Mol. Biol.* **333**, 1003–1023.

[338] Relini, A, Torrassa, S, Ferrando, R, Rolandi, R, Campioni, S, Chiti, F, & Gliozzi, A. (2010) Detection of populations of amyloid-like protofibrils with different physical properties. *Biophys. J* **98**, 1277–1284.

[339] Miti, T, Mulaj, M, Schmit, J. D, & Muschol, M. (2014) Stable, metastable, and kinetically trapped amyloid aggregate phases. *Biomacromolecules* **16**, 326–335.

[340] Lashuel, H. A, Lai, Z, & Kelly, J. W. (1998) Characterization of the transthyretin acid denaturation pathways by analytical ultracentrifugation: Implications for wild-type, V30M, and L55P amyloid fibril formation. *Biochemistry* **37**, 17851–17864.

[341] Nilsberth, C, Westlind-Danielsson, A, Eckman, C. B, Condron, M. M, Axelman, K, Forsell, C, Stenh, C, Luthman, J, Teplow, D. B, Younkin, S. G, Näslund, J, & Lannfelt, L. (2001) The 'Arctic' APP mutation (E693G) causes Alzheimer's disease by enhanced Aβ protofibril formation. *Nat. Neurosci.* **4**, 887–893.

[342] Kheterpal, I, Lashuel, H. A, Hartley, D. M, Walz, T, Lansbury, P. T. J, & Wetzel, R. (2003) Aβ protofibrils possess a stable core structure resistant to hydrogen exchange. *Biochemistry* **42**, 14092–14098.

[343] Chiricotto, M, Melchionna, S, Derreumaux, P, & Sterpone, F. (2019) Multiscale aggregation of the amyloid Aβ16-22 peptide: From disordered coagulation and lateral branching to amorphous prefibrils. *J. Phys. Chem. Lett.* **10**, 1594–1599.

[344] Bitan, G, Tarus, B, Vollers, S. S, Lashuel, H. A, Condron, M. M, Straub, J. E, & Teplow, D. B. (2003) A molecular switch in amyloid assembly: Met35 and amyloid β-protein oligomerization. *J. Am. Chem. Soc.* **125**, 15359–15365.

[345] Lee, J, Culyba, E. K, Powers, E. T, & Kelly, J. W. (2011) Amyloid-β forms fibrils by nucleated conformational conversion of oligomers. *Nat. Chem. Biol.* **7**, 602–609.

[346] Iljina, M, Garcia, G. A, Horrocks, M. H, Tosatto, L, Choi, M. L, Ganzinger, K. A, Abramov, A. Y, Gandhi, S, Wood, N. W, Cremades, N, Dobson, C. M, Knowles, T. P. J, & Klenerman, D. (2016) Kinetic model of the aggregation of alpha-synuclein provides insights into prion-like spreading. *Proc. Natl. Acad. Sci. U. S. A.* **7**, E1206–E1205.

[347] Auer, S, Ricchiuto, P, & Kashchiev, D. (2012) Two-step nucleation of amyloid fibrils: Omnipresent or not? *J. Mol. Biol.* **422**, 723–730.

[348] Šarić, A, Buell, A. K, Meisl, G, Michaels, T. C. T, Dobson, C. M, Linse, S, Knowles, T. P. J, & Frenkel, D. (2016) Physical determinants of the self-replication of protein fibrils. *Nat. Phys.* **12**, 874–880.

[349] Zeng, Y, Yang, J, Zhang, B, Gao, M, Su, Z, & Huang, Y. (2020) The structure and phase of tau: from monomer to amyloid filament. *Cell. Mol. Life Sci.* Advance online publication, DOI: 10.1007/s00018-020-03681-x.

[350] Rocha, S, Krastev, R, Thünemann, A. F, Pereira, M. C, Möhwald, H, & Brezesinski, G. (2005) Adsorption of amyloid β-peptide at polymer surfaces: A neutron reflectivity study. *ChemPhysChem* **6**, 2527–2534.

[351] Shen, L, Adachi, T, Vanden Bout, D, & Zhu, X.-Y. (2012) A mobile precursor determines amyloid-β peptide fibril formation at interfaces. *J. Am. Chem. Soc.* **134**, 14172–14178.

[352] Kowalewski, T & Holtzman, D. M. (1999) *In situ* atomic force microscopy study of Alzheimer's β-amyloid peptide on different substrates: New insights into mechanism of β-sheet formation. *Proc. Natl. Acad. Sci. U. S. A.* **96**, 3688–3693.

[353] Morinaga, A, Hasegawa, K, Nomura, R, Ookoshi, T, Osawa, D, Goto, Y, Yamada, M, & Naiki, H. (2010) Critical role of interfaces and agitation on the nucleation of Aβ amyloid fibrils at low concentrations of Aβ monomers. *Biochim. Biophys. Acta* **1804**, 986–995.

[354] Jang, H, Zheng, J, & Nussinov, R. (2007) Models of β-amyloid ion channels in the membrane suggest that channel formation in the bilayer is a dynamic process. *Biophys. J.* **93**, 1938–1949.

[355] Jang, H, Ma, B, Lal, R, & Nussinov, R. (2008) Models of toxic β-sheet channels of protegrin-1 suggest a common subunit organization motif shared with toxic Alzheimer β-amyloid ion channels. *Biophys. J.* **95**, 4631–4642.

[356] Mustata, M, Capone, R, Jang, H, Arce, F. T, Ramachandran, S, Lal, R, & Nussinov, R. (2009) K3 fragment of amyloidogenic β2-microglobulin forms ion channels: Implication for dialysis related amyloidosis. *J. Am. Chem. Soc.* **131**, 14938–14945.

[357] Ikeda, K, Yamaguchi, T, Fukunaga, S, Hoshino, M, & Matsuzaki, K. (2011) Mechanism of amyloid β-protein aggregation mediated by GM1 ganglioside clusters. *Biochemistry* **50**, 6433–6440.

[358] Lasagna-Reeves, C. A, Glabe, C. A, & Kayed, R. (2011) Amyloid-β annular protofibrils evade fibrillar fate in Alzheimer disease brain. *J. Biol. Chem.* **286**, 22122–22130.

[359] Zhu, M, Souillac, P. O, Ionescu-Zanetti, C, Carter, S. A, & Fink, A. L. (2002) Surface-catalyzed amyloid fibril formation. *J. Biol. Chem.* **277**, 50914–50922.

[360] Auer, S, Trovato, A, & Vendruscolo, M. (2009) A condensation-ordering mechanism in nanoparticle-catalyzed peptide aggregation. *PLOS Comput. Biol.* **5**, e1000458.

[361] Coles, M, Bicknell, W, Watson, A. A, Fairlie, D. P, & Craik, D. J. (1999) Solution structure of amyloid β-peptide(1-40) in a water-micelle environment. is the membrane-spanning domain where we think it is? *Biochemistry* **37**, 11064–11077.

[362] Chi, E. Y, Frey, S. L, Winans, A, Lam, K. L. H, Kjaer, K, Majewski, J, & Lee, K. Y. C. (2010) Amyloid-β fibrillogenesis seeded by interface-induced peptide misfolding and self-assembly. *Biophys. J.* **98**, 2299–2308.

[363] Yu, X, Wang, Q, Lin, Y, Zhao, J, Zhao, C, & Zheng, J. (2012) Structure, orientation, and surface interaction of Alzheimer amyloid-β peptides on the graphite. *Langmuir* **28**, 6595–6605.

[364] Morriss-Andrews, A & Shea, J.-E. (2012) Kinetic pathways to peptide aggregation on surfaces: The effects of β-sheet propensity and surface attraction. *J. Chem. Phys.* **136**, 065103.

[365] Zhai, J, Lee, T.-H, Small, D. H, & Aguilar, M.-I. (2012) Characterization of early stage intermediates in the nucleation phase of Aβ aggregation. *Biochemistry* **51**, 1070–1078.

[366] Green, J. D, Kreplak, L, Goldsbury, C, Li Blatter, X, Stolz, M, Cooper, G. S, Seelig, A, Kistler, J, & Aebi, U. (2004) Atomic force microscopy reveals defects within mica supported lipid bilayers induced by the amyloidogenic human amylin peptide. *J. Mol. Biol.* **342**, 877–887.

[367] Jang, H, Arce, F. T, Ramachandran, S, Capone, R, Lal, R, & Nussinov, R. (2010) Structural convergence among diverse, toxic β-sheet ion channels. *J. Phys. Chem. B* **114**, 9445–9451.

[368] Ando, T, Kodera, N, Takai, E, Maruyama, D, Saito, K, & Toda, A. (2001) A high-speed atomic force microscope for studying biological macromolecules. *Proc. Natl. Acad. Sci. U. S. A.* **98**, 12468–12472.

[369] Palitto, M. M & Murphy, R. M. (2001) A mathematical model of the kinetics of β-amyloid fibril growth from the denatured state. *Biophys. J.* **81**, 1805–1822.

[370] He, X, Giurleo, J. T, & Talaga, D. S. (2010) Role of small oligomers on the amyloidogenic aggregation free-energy landscape. *J. Mol. Biol.* **395**, 134–154.

[371] Michaels, T. C. T, Yde, P, Willis, J. C. W, Jensen, M. H, Otzen, D, Dobson, C. M, Buell, A. K, , & Knowles, T. P. J. (2015) The length distribution of frangible biofilaments. *J. Chem. Phys.* **143**, 164901.

[372] Beal, D. M, Tournus, M, Marchante, R, Purton, T. J, Smith, D. P, Tuite, M. F, Doumic, M, & Xue, W.-F. (2020) The division of amyloid fibrils: Systematic comparison of fibril fragmentation stability by linking theory with experiments. *iScience* **23**, 101512.

[373] Cohen, S. I. A, Vendruscolo, M, Dobson, C. M, & Knowles, T. P. J. (2012) From macroscopic measurements to microscopic mechanisms of protein aggregation. *J. Mol. Biol.* **421**, 160–171.

[374] Arosio, P, Knowles, T. P. J, & Linse, S. (2015) On the lag phase in amyloid fibril formation. *Phys. Chem. Chem. Phys.* **17**, 7606–7618.

[375] Ferrone, F. A. (1999) Analysis of protein aggregation kinetics. *Methods Enzymol.* **309**, 256–274.

[376] Ferrone, F. A, Hofrichter, J, Sunshine, H. R, & Eaton, W. A. (1980) Kinetic studies on photolysis-induced gelation of sickle cell hemoglobin suggest a new mechanism. *Biophys. J.* **32**, 361–380.

[377] Scheibel, T, Bloom, J, & Lindquist, S. L. (2004) The elongation of yeast prion fibers involves separable steps of association and conversion. *Proc. Natl. Acad. Sci. U. S. A.* **101**, 2287–2292.

[378] Schreck, J. S & Yuan, J.-M. (2013) A kinetic study of amyloid formation: Fibril growth and length distributions. *J. Phys. Chem. B* **117**, 6574–6583.

[379] Hasecke, F, Miti, T, Perez, C, Barton, J, Schölzel, D, Gremer, L, Grüning, C. S. R, Matthews, G, Meisl, G, Knowles, T. P. J, Willbold, D, Neudecker, P, Heise, H, Ullah, G, Hoyer, W, & Muschol, M. (2018) Origin of metastable oligomers and their effects on amyloid fibril self-assembly. *Chem. Sci.* **9**, 5937–5948.

[380] Garcia, G. A, Cohen, S. I. A, Dobson, C. M, & Knowles, T. P. J. (2014) Nucleation-conversion-polymerization reactions of biological macromolecules with prenucleation clusters. *Phys. Rev. E* **89**, 032712.

[381] Bishop, M. F & Ferrone, F. A. (1984) Kinetics of nucleation-controlled polymerization: A perturbation treatment for use with a secondary pathway. *Biophys. J.* **46**, 631–644.

[382] Come, J. H, Fraser, P. E, & Lansbury, P. T. J. (1993) A kinetic model for amyloid formation in the prion diseases: Importance of seeding. *Proc. Natl. Acad. Sci. U. S. A.* **90**, 5959–5963.

[383] Jarrett, J. T, Berger, E. P, & Lansbury, P. T. J. (1993) The carboxy terminus of the β amyloid protein is critical for the seeding of amyloid formation: Implications for the pathogenesis of Alzheimer's disease. *Biochemistry* **32**, 4693–4697.

[384] Kashchiev, D. (2000) *Nucleation: Basic theory with applications.* (Butterworth Heinemann, Oxford, UK).

[385] Erdemir, D, Lee, A. Y, & Myerson, A. S. (2009) Nucleation of crystals from solution: Classical and two-step models. *Acc. Chem. Res.* **42**, 621–629.

[386] ten Wolde, P. R & Frenkel, D. (1997) Enhancement of protein crystal nucleation by critical density fluctuations. *Science* **277**, 1975–1978.

[387] Nicolis, G & Nicolis, C. (2003) Enhancement of the nucleation of protein crystals by the presence of an intermediate phase: A kinetic model. *Physica A* **323**, 135–154.

[388] Gavezzotti, A. (1999) Molecular aggregation of acetic acid in a carbon tetrachloride solution: A molecular dynamics study with a view to crystal nucleation. *Chem. Eur. J.* **5**, 567–576.

[389] Shore, J. D, Perchak, D, & Shnidman, Y. (2000) Simulations of the nucleation of AgBr from solution. *J. Chem. Phys.* **113**, 6276–6284.

[390] Levin, A, Mason, T. O, Adler-Abramovich, L, Buell, A. K, Meisl, G, Galvagnion, C, Bram, Y, Stratford, S. A, Dobson, C. M, Knowles, T. P. J, & Gazit, E. (2014) Ostwald's rule of stages governs structural transitions and morphology of dipeptide supramolecular polymers. *Nat. Commun.* **5**, 5219.

[391] Galkin, O, Pan, W, Filobelo, L, Hirsch, R. E, Nagel, R. L, & Vekilov, P. G. (2007) Two-step mechanism of homogeneous nucleation of sickle cell hemoglobin polymers. *Biophys. J.* **93**, 902–913.

[392] Pavlova, A, Cheng, C.-Y, Kinnebrew, M, Lew, J, Dahlquist, F. W, & Han, S. (2015) Protein structural and surface water rearrangement constitute major events in the earliest aggregation stages of tau. *Proc. Natl. Acad. Sci. U. S. A.* **113**, E127–E136.

[393] Shammas, S. L, Garcia, G. A, Kumar, S, Kjaergaard, M, Horrocks, M. H, Shivji, N, Mandelkow, E, Knowles, T. P. J, Mandelkow, E, & Klenerman, D. (2015) A mechanistic model of tau amyloid aggregation based on direct observation of oligomers. *Nat. Commun.* **6**, 7025.

[394] Auer, S, Dobson, C. M, & Vendruscolo, M. (2007) Characterization of the nucleation barriers for protein aggregation and amyloid formation. *HFSP J.* **1**, 137–146.

[395] Tarus, B, Straub, J. E, & D., T. (2006) Dynamics of Asp23-Lys28 salt-bridge formation in Aβ10-35 monomers. *J. Am. Chem. Soc.* **128**, 159–168.

[396] Reddy, G, Straub, J. E, & Thirumalai, D. (2010) Dry amyloid fibril assembly in a yeast prion peptide is mediated by long-lived structures containing water wires. *Proc. Natl. Acad. Sci. U. S. A.* **107**, 21459–21464.

[397] Baftizadeh, F, Biarnes, X, Pietrucci, F, Affinito, F, & Laio, A. (2012) Multidimensional view of amyloid fibril nucleation in atomistic detail. *J. Am. Chem. Soc.* **134**, 3886–3894.

[398] Cremades, N, Cohen, S. I. A, Deas, E, Abramov, A. Y, Chen, A. Y, Orte, A, Sandal, M, Clarke, R. W, Dunne, P, Aprile, F. A, Bertoncini, C. W, Wood, N. W, Knowles, T. P. J, Dobson, C. M, & Klenerman, D. (2012) Direct observation of the interconversion of normal and toxic forms of α-synuclein. *Cell* **149**, 1048–1059.

[399] Šarić, A, Chebaro, Y. C, , Knowles, T. P. J, & Frenkel, D. (2014) Crucial role of nonspecific interactions in amyloid nucleation. *Proc. Natl. Acad. Sci. U. S. A.* **111**, 17869–17874.

[400] Zheng, W, Tsai, M.-Y, & Wolynes, P. G. (2017) Comparing the aggregation free energy landscapes of amyloid beta(1-42) and amyloid beta(1-40). *J. Am. Chem. Soc.* **139**, 16666–16676.

[401] Kjaergaard, M, Dear, A. J, Kundel, F, Qamar, S, Meisl, G, Knowles, T. P. J, & Klenerman, D. (2018) Oligomer diversity during the aggregation of the repeat region of Tau. *ACS Chem. Neurosci.* **9**, 3060–3071.

[402] Oxtoby, D. W & Kashchiev, D. (1994) A general relation between the nucleation work and the size of the nucleus in multicomponent nucleation. *J. Chem. Phys.* **100**, 7665.

[403] Sear, R. P. (2007) Nucleation: theory and applications to protein solutions and colloidal suspensions. *J. Phys. Condens. Matt.* **19**, 033101.

[404] Cabriolu, R, Kashchiev, D, & Auer, S. (2010) Atomistic theory of amyloid fibril nucleation. *J. Chem. Phys.* **133**, 225101.

[405] Ising, E. (1925) Beitrag zur Theorie des Ferromagnetismus. *Phys. Zeit.* **31**, 253–258.

[406] Peierls, R & Born, M. (1936) On Ising's model of ferromagnetism. *Math. Proc. Camb. Philos. Soc.* **32**, 477–481.

[407] Zhang, L & Schmit, J. D. (2016) Pseudo-one-dimensional nucleation in dilute polymer solutions. *Phys. Rev. E* **93**, 060401.

[408] Kayed, R, Bernhagen, J, Greenfield, N, Sweimeh, K, Brunner, H, Voelter, W, & Kapurniotu, A. (1999) Conformational transitions of islet amyloid polypeptide (IAPP) in amyloid formation *in vitro*. *J. Mol. Biol.* **287**, 781–796.

[409] Bleiholder, C, Dupuis, N. F, Wyttenbach, T, & Bowers, M. T. (2011) Ion mobility–mass spectrometry reveals a conformational conversion from random assembly to β-sheet in amyloid fibril formation. *Nat. Chem.* **3**, 172–177.

[410] Horn, A. H. C & Sticht, H. (2010) Amyloid-β42 oligomer structures from fibrils: A systematic molecular dynamics study. *J. Phys. Chem. B* **114**, 2219–2226.

[411] Xu, J, Zhang, J. Z. H, & Xiang, Y. (2013) Molecular dynamics simulation and computational two-dimensional infrared spectroscopic study of model amyloid β-peptide oligomers. *J. Phys. Chem. A* **117**, 6373–6379.

[412] Urbanc, B, Cruz, L, Ding, F, Sammond, D, Khare, S, Buldyrev, S. V, Stanley, H. E, & Dokholyan, N. V. (2004) Molecular dynamics simulation of amyloid β dimer formation. *Biophys. J.* **87**, 2310–2321.

[413] Kakkar, V, Månsson, C, de Mattos, E. P, Bergink, S, van der Zwaag, M, van Waarde, M. A. W. H, Kloosterhuis, N. J, Melki, R, van Cruchten, R. T. P, Al-Karadaghi, S, Arosio, P, Dobson, C. M, Knowles, T. P. J, Bates, G. P, van Deursen, J. M, Linse, S, van de Sluis, B, Emanuelsson, C, & Kampinga, H. H. (2016) The S/T-rich motif in the DNAJB6 chaperone delays polyglutamine aggregation and the onset of disease in a mouse model. *Mol. Cell* **62**, 272–283.

[414] Pellarin, R, Guarnera, E, & Caflisch, A. (2007) Pathways and intermediates of amyloid fibril formation. *J. Mol. Biol.* **374**, 917–924.

[415] Latshaw, D. C, Cheon, M, & Hall, C. K. (2014) Effects of macromolecular crowding on amyloid beta (16-22) aggregation using coarse-grained simulations. *J. Phys. Chem.* **118**, 13513–13526.

[416] Luiken, J. A & Bolhuis, P. G. (2015) Primary nucleation kinetics of short fibril-forming amyloidogenic peptides. *J. Phys. Chem. B* **119**, 12568–12579.

[417] Ilie, I. M, den Otter, W. K, & Briels, W. J. (2016) A coarse grained protein model with internal degrees of freedom. Application to α-synuclein aggregation. *J. Chem. Phys.* **144**, 085103.

[418] Lee, C. T & Terentjev, E. M. (2017) Mechanisms and rates of nucleation of amyloid fibrils. *J. Chem. Phys.* **147**, 105103.

[419] Chen, X, Chen, M, Schafer, N. P, & Wolynes, P. G. (2020) Exploring the interplay between fibrillization and amorphous aggregation channels on the energy landscapes of tau repeat isoforms. *Proc. Acad. Sci. U. S. A.* **117**, 4125–4130.

[420] Han, W & Schulten, K. (2014) Fibril elongation by Aβ17-42: Kinetic network analysis of hybrid resolution molecular dynamics simulations. *J. Am. Chem. Soc.* **136**, 12450–12460.

[421] Esler, W. P, Stimson, E. R, Ghilardi, J. R, Vinters, H. V, Lee, J. P, Mantyh, P. W, & Maggio, J. E. (1996) *In vitro* growth of alzheimer's disease β-amyloid plaques displays first-order kinetics. *Biochemistry* **35**, 749–757.

[422] Kusumoto, Y, Lomakin, A, Teplow, D. B, & Benedek, G. B. (1998) Temperature dependence of amyloid β-protein fibrillization. *Proc. Natl. Acad. Sci. U. S. A.* **95**, 12277–12282.

[423] Xu, Y, Safari, M. S, Ma, W, Schafer, N. P, Wolynes, P. G, & Vekilov, P. G. (2019) Steady, symmetric, and reversible growth and dissolution of individual amyloid-β fibrils. *ACS Chem. Neurosci.* **19**, 2967–2976.

[424] Konno, H, Watanabe-Nakayama, T, Uchihashi, T, Okuda, M, Zhu, L, Kodera, N, Kikuchi, Y, Ando, T, & Taguchi, H. (2020) Dynamics of oligomer and amyloid fibril formation by yeast prion Sup35 observed by high-speed atomic force microscopy. *Proc. Natl. Acad. Sci. U. S. A.* **117**, 7831–7836.

[425] Oosawa, F & Kasai, M. (1962) A theory of linear and helical aggregations of macromolecules. *J. Mol. Biol.* **4**, 10–21.

[426] Oosawa, F & Asakura, S. (1975) *Thermodynamics of the Polymerization of Protein.* (Academic Press, New York).

[427] Schwierz, N, Frost, C. V, Geissler, P. L, & Zacharias, M. (2015) Dynamics of seeded Aβ40-fibril growth from atomistic molecular dynamics simulations: Kinetic trapping and reduced water mobility in the locking step. *J. Am. Chem. Soc.* **138**, 527–539.

[428] Buell, A. K, Dhulesia, A, White, D. A, Knowles, T. P. J, Dobson, C. M, & Welland, M. E. (2012) Detailed analysis of the energy barriers for amyloid fibril growth. *Angew. Chem. Int. Ed.* **51**, 5247–5251.

[429] Röder, K & Wales, D. J. (2018) Energy landscapes for the aggregation of Aβ17-42. *J. Am. Chem. Soc.* **140**, 4018–4027.

[430] Lee, C. F, Loken, J, Jean, L, & Vaux, D. J. (2009) Elongation dynamics of amyloid fibrils: A rugged energy landscape picture. *Phys. Rev. E* **80**, 041906.

[431] Schmit, J. (2013) Kinetic theory of amyloid fibril templating. *J. Chem. Phys.* **138**, 185102.

[432] Wördehoff, M. M, Bannach, O, Shaykhalishahi, H, Kulawik, A, Schiefer, S, Willbold, D, Hoyer, W, & Birkmann, E. (2015) Single fibril growth kinetics of α-synuclein. *J. Mol. Biol.* **427**, 1428–1435.

[433] Rojas, A, Liwo, A, Browne, D, & Scheraga, H. A. (2010) Mechanism of fiber assembly: Treatment of Aβ peptide aggregation with a coarse-grained united-residue force field. *J. Mol. Biol.* **404**, 537–552.

[434] Morriss-Andrews, A, Bellesia, G, & Shea, J.-E. (2012) β-sheet propensity controls the kinetic pathways and morphologies of seeded peptide aggregation. *J. Chem. Phys.* **137**, 145104.

[435] Gurry, T & Stultz, C. M. (2014) Mechanism of amyloid-β fibril elongation. *Biochemistry* **53**, 6981–6991.

[436] Rodriguez, R. A, Chen, L. Y, Plascencia-Villa, G, & Perry, G. (2018) Thermodynamics of amyloid-β fibril elongation: Atomistic details of the transition state. *ACS Chem. Neurosci.* **9**, 783–789.

[437] Bernacki, J. P & Murphy, R. M. (2009) Model discrimination and mechanistic interpretation of kinetic data in protein aggregation studies. *Biophys. J.* **96**, 2871–2887.

[438] Gillam, J. E & MacPhee, C. E. (2013) Modelling amyloid fibril formation kinetics: mechanisms of nucleation and growth. *J. Phys. Condens. Matter* **25**, 373101.

[439] Wakabayashi, K, Hotani, H, & Asakura, S. (1969) Polymerization of *Salmonella* flagellin in the presence of high concentrations of salts. *Biochim. Biophys. Acta* **175**, 195–203.

[440] Bonfils, C, Bec, N, Lacroix, B, Harricane, M.-C, & Larroque, C. (2007) Kinetic analysis of tubulin assembly in the presence of the microtubule-associated protein TOGp. *J. Biol. Chem.* **282**, 5570–5581.

[441] Tobacman, L. S & Korn, E. D. (1983) The kinetics of actin nucleation and polymerization. *J. Biol. Chem.* **258**, 3207–3214.

[442] Michaels, T. C. T, Dear, A. J, & Knowles, T. P. J. (2016) Scaling and dimensionality in the chemical kinetics of protein filament formation. *Int. Rev. Phys. Chem.* **35**, 679–703.

[443] Flyvberg, H, Jobs, E, & Leibler, S. (1996) Kinetics of self-assembling microtubules: an "inverse problem" in biochemistry. *Proc. Natl. Acad. Sci. U. S. A.* **93**, 5975–5979.

[444] Michaels, T. C. T, Liu, L. X, Meisl, G, & Knowles, T. P. J. (2017) Physical principles of filamentous protein self-assembly kinetics. *J. Phys. Condens. Matter* **29**, 153002.

[445] Törnquist, M, Michaels, T. C. T, Sanagavarapu, K, Yang, X, Meisl, G, Cohen, S. I. A, Knowles, T. P. J, & Linse, S. (2018) Secondary nucleation in amyloid formation. *Chem. Commun.* **54**, 8667–8684.

[446] Nielsen, L, Khurana, R, Coats, A, Frokjaer, S, Brange, J, Vyas, S, Uversky, V. N, & Fink, A. L. (2001) Effect of environmental factors on the kinetics of insulin fibril formation: elucidation of the molecular mechanism. *Biochemistry* **40**, 6036–6046.

[447] Zhu, L, Zhang, X.-J, Wang, L.-Y, Zhou, J.-M, & Perrett, S. (2003) Relationship between stability of folding intermediates and amyloid formation for the yeast prion Ure2p: a quantitative analysis of the effects of pH and buffer system. *J. Mol. Biol.* **328**, 235–254.

[448] Collins, S. R, Douglass, A, Vale, R. D, & Weissmann, J. S. (2004) Mechanism of prion propagation: Amyloid growth occurs by monomer addition. *PLOS Biol.* **2**, e321.

[449] Wright, C. F, Teichmann, S. A, Clarke, J, & Dobson, C. M. (2005) The importance of sequence diversity in the aggregation and evolution of proteins. *Nature* **438**, 878–881.

[450] Xue, W.-F, Homans, S. W, & Radford, S. E. (2008) Systematic analysis of nucleation-dependent polymerization reveals new insights into the mechanism of amyloid self-assembly. *Proc. Natl. Acad. Sci. U. S. A.* **105**, 8926–8931.

[451] Nicoud, L, Lazzari, S, Barragán, D. B, & Morbidelli, M. (2015) Fragmentation of amyloid fibrils occurs in preferential positions depending on the environmental conditions. *J. Phys. Chem. B.* **119**, 4644–4652.

[452] Zaccone, A, Terentjev, I, Herling, T. W, Knowles, T. P. J, Aleksandrova, A, & Terentjev, E. M. (2016) Kinetics of fragmentation and dissociation of two-strand protein filaments: Coarse grained simulations and experiments. *J. Chem. Phys.* **145**, 105101.

[453] Hill, T. L. (1983) Length dependence of rate constants for end-to-end association and dissociation of equilibrium linear aggregates. *Biophys. J.* **44**, 285–288.

[454] Wang, Y.-Q, Buell, A. K, Wang, X.-Y, Welland, M. E, Dobson, C. M, Knowles, T. P. J, & Perrett, S. (2011) Relationship between prion propensity and the rates of individual molecular steps of fibril assembly. *J. Biol. Chem.* **286**, 12101–12107.

[455] Michaels, T. C. T & Knowles, T. P. J. (2014) Role of filament annealing in the kinetics and thermodynamics of nucleated polymerization. *J. Chem. Phys.* **140**, 214904.

[456] Huseby, C. J, Bundschuh, R, & Kuret, J. (2019) The role of annealing and fragmentation in human tau aggregation dynamics. *J. Biol. Chem.* **294**, 4728–4737.

[457] Yang, S, Griffin, M. D. W, Binger, K. J, Schuck, P, & Howlett, G. J. (2012) An equilibrium model for linear and closed-loop amyloid fibril formation. *J. Mol. Biol.* **421**, 364–377.

[458] Cukalevski, R, Yang, X, Meisl, G, Weininger, U, Bernfur, K, Frohm, B, Knowles, T. P. J, & Linse, S. (2015) The Aβ40 and Aβ42 peptides self-assemble into separate homomolecular fibrils in binary mixtures but cross-react during primary nucleation. *Chem. Sci.* **6**, 4215–4233.

[459] Brännström, K, Islam, T, Gharibyan, A. L, Iakovleva, I, Nilsson, L, Lee, C. C, Sandblad, L, Pamrén, A, & Olofsson, A. (2018) The properties of amyloid-β fibrils are determined by their path of formation. *J. Mol. Biol.* **430**, 1940–1949.

[460] Törnquist, M, Cukalevski, R, Weininger, U, Meisl, G, Knowles, T. P. J, Leiding, T, Malmendal, A, Akke, M, & Linse, S. (2020) Ultrastructural evidence for self-replication of Alzheimer-associated Aβ42 amyloid along the sides of fibrils. *Proc. Natl. Acad. Sci. U. S. A.* **117**, 11265–11273.

[461] Weber, P, Reznicek, L, Mitteregger, G, Kretzschmar, H, & Giese, A. (2008) Differential effects of prion particle size on infectivity in vivo and in vitro. *Biochem. Biophys. Res. Commun.* **369**, 924–928.

[462] Xue, W.-F, Hellewell, A. L, Gosal, W. S, Homans, S. W, Hewitt, E. W, & Radford, S. E. (2009) Fibril fragmentation enhances amyloid cytotoxicity. *J. Biol. Chem.* **284**, 34272–34282.

[463] Botsaris, G. D. (1976) in *Industrial Crystallization*. (Springer, Berlin), pp. 3–22.

[464] Arosio, P, Cukalevski, R, Frohm, B, Knowles, T. P. J, & Linse, S. (2014) Quantification of the concentration of Aβ42 propagons during the lag phase by an amyloid chain reaction assay. *J. Am. Chem. Soc.* **136**, 219–225.

[465] Michaels, T. C. T, Cohen, S. I. A, Vendruscolo, M, Dobson, C. M, & Knowles, T. P. J. (2016) Hamiltonian dynamics of protein filament formation. *Phys. Rev. Lett.* **116**, 038101.

[466] Andersen, C. B, Yagi, H, Manno, M, Martorana, V, Ban, T, Christiansen, G, Otzen, D. E, Goto, Y, & Rischel, C. (2000) Branching in amyloid fibril growth. *Biophys. J.* **96**, 1529–1536.

[467] Barz, B & Strodel, B. (2016) Understanding amyloid-β oligomerization at the molecular level: The role of the fibril surface. *Chem. Eur. J.* **22**, 8768–8772.

[468] Scheidt, T, Łapińska, U, Kumita, J. R, Whiten, D. R, Klenerman, D, Wilson, M. R, Cohen, S. I. A, Linse, S, Vendruscolo, M, Dobson, C. M, Knowles, T. P. J, & Arosio, P. (2019) Secondary nucleation and elongation occur at different sites on Alzheimer's amyloid-β aggregates. *Sci. Adv.* **5**, eaau3112.

[469] Michaels, T. C. T, Šarić, A, Curk, S, Bernfur, K, Arosio, P, Meisl, G, Dear, A. J, Cohen, S. I. A, Dobson, C. M, Vendruscolo, M, Linse, S, & Knowles, T. P. J. (2020) Dynamics of oligomer populations formed during the aggregation of Alzheimer's Aβ42 peptide. *Nat. Chem.* **12**, 445–451.

[470] Peduzzo, A, Linse, S, & Buell, A. K. (2020) The properties of α-synuclein secondary nuclei are dominated by the solution conditions rather than the seed fibril strain. *ACS Chem. Neurosci.* **11**, 909–918.

[471] Linse, S. (2017) Monomer-dependent secondary nucleation in amyloid formation. *Biophys. Rev.* **9**, 329–338.

[472] Richards, F. J. (1959) A flexible growth function for empirical use. *J. Exp. Bot.* **10**, 290–301.

[473] Gompertz, B. (1825) On the nature of the function expressive of the law of human mortality, and on a new mode of determining the value of life contingencies. *Philos. Trans. R. Soc.* **115**, 513–585.

[474] Rabe, M, Soragni, A, Reynolds, N. P, Verdes, D, Liverani, E, Riek, R, & Seeger, S. (2012) On-surface aggregation of α-synuclein at nanomolar concentrations results in two distinct growth mechanisms. *ACS Chem. Neurosci.* **4**, 408–417.

[475] Vácha, R, Linse, S, & Lund, M. (2014) Surface effects on aggregation kinetics of amyloidogenic peptides. *J. Am. Chem. Soc.* **136**, 11776–11782.

[476] Zagorski, M. G, Yang, J, Shao, H, Ma, K, Zeng, H, & Hong, A. (1999) Methodological and chemical factors affecting amyloid β peptide amyloidogenicity. *Methods Enzymol.* **309**, 189–204.

[477] Gasteiger, E, Hoogland, C, Gattiker, A, Duvaud, S, Wilkins, M. R, Appel, R. D, & Bairoch, A. (2005) in *The Proteomics Protocols Handbook*, ed. Walker, J. (Humana Press, Totowa, NJ).

[478] Zhao, H, Brown, P. H, & Schuck, P. (2011) On the distribution of protein refractive index increments. *Biophys. J.* **100**, 2309–2317.

[479] Hellstrand, E, Boland, B, Walsh, D. M, & Linse, S. (2010) Amyloid β-protein aggregation produces highly reproducible kinetic data and occurs by a two-phase process. *ACS Chem. Neurosci.* **1**, 13–18.

[480] Hasselbalch, K. A. (1917) Die Berechnung der Wasserstoffzahl des Blutes aus der freien und gebundenen Kohlensäure desselben, und die Sauerstoffbindung des Blutes als Funktion der Wasserstoffzahl. *Biochem. Z.* **78**, 112–144.

[481] Green, A. A. (1933) The preparation of acetate and phosphate buffer solutions of known pH and ionic strength. *J. Am. Chem. Soc.* **55**, 2331–2336.

[482] Schindelin, J, Arganda-Carreras, I, Frise, E, Kaynig, V, Longair, M, Pietzsch, T, Preibisch, S, Rueden, C, Saalfeld, S, Schmid, B, Tivenez, J.-Y, White, J. D, Eliceiri, K, Tomancak, P, & Cardona, A. (2012) Fiji: an open-source platform for biological-image analysis. *Nat. Methods* **9**, 676–682.

[483] Rueden, C. T, Schindelin, J, Hiner, M. C. DeZonia, B. E, Walter, A. E, Arena, E. T, & Eliceiri, K. W. (2017) ImageJ2: ImageJ for the next generation of scientific image data. *BMC Bioinformatics* **18**, 529.

[484] Lin, H, Zhu, Y. J, & Lal, R. (1999) Amyloid β protein (1-40) forms calcium-permeable, Zn2+-sensitive channel in reconstituted lipid vesicles. *Biochemistry* **38**, 11189–11196.

[485] Sánchez, L, Madurga, S, Pukala, T, Vilaseca, M, López-Iglesias, C, Robinson, C. V, Giralt, E, & Carulla, N. (2011) Aβ40 and Aβ42 amyloid fibrils exhibit distinct molecular recycling properties. *J. Am. Chem. Soc.* **133**, 6505–6508.

[486] Matheou, C. J, Younan, N. D, & Viles, J. H. (2015) Cu2+ accentuates distinct misfolding of Aβ(1–40) and Aβ(1–42) peptides, and potentiates membrane disruption. *Biochem. J.* **466**, 233–242.

[487] Hortschansky, P, Schroeckh, V, Christopeit, T, Zandomeneghi, G, & Fändrich, M. (2005) The aggregation kinetics of Alzheimer's β-amyloid peptide is controlled by stochastic nucleation. *Protein Sci.* **14**, 1753–1759.

[488] Nagata-Uchiyama, M, Yaguchi, M, Hirano, Y, & Ueda, T. (2007) Expression and purification of uniformly N-15-labelled amyloid-β peptide 1-40 in *Escherichia coli*. *Protein Peptide Lett.* **14**, 788–792.

[489] Shahnawaz, M, Thapa, A, & Park, I. S. (2007) Stable activity of a deubiquitylating enzyme (Usp2-cc) in the presence of high concentrations of urea and its application to purify aggregation-prone peptides. *Biochem. Biophys. Res. Commun.* **359**, 801–805.

[490] Macao, B, Hoyer, W, Sandberg, A, Brorsson, A. C, Dobson, C, & Härd, T. (2008) Recombinant amyloid-β peptide production by coexpression with an affibody ligand. *BMC Biotechnol.* **8**, 11.

[491] Thapa, A, Shahnawaz, M, Karki, P, Dahal, G. R, Sharoar, M. G, Shin, S. Y, Lee, J. S, Cho, B, & Park, I. S. (2008) Purification of inclusion body-forming peptides and proteins in soluble form by fusion to *Escherichia coli* thermostable proteins. *BioTechniques* **44**, 787–796.

[492] Garai, K, Crick, S. L, Mustafi, S. M, & Frieden, C. (2009) Expression and purification of amyloid-β peptides from *Escherichia coli*. *Protein Expr. Purif.* **66**, 107–112.

[493] Utsumi, M, Yamaguchi, Y, Sasakawa, H, Yamamoto, N, Yanagisawa, K, & Kato, K. (2009) Up-and-down topological mode of amyloid-β peptide lying on hydrophilic/hydrophobic interface of ganglioside clusters. *Glycoconj. J.* **26**, 999–1006.

[494] Walsh, D. M, Thulin, E, Minogue, A. M, Gustavsson, N, Pang, E, Teplow, D. B, & Linse, S. (2009) A facile method for expression and purification of the Alzheimer's disease-associated amyloid β-peptide. *FEBS J.* **276**, 1266–1281.

[495] Finder, V. H, Vodopivec, I, Nitsch, R. M, & Glockshuber, R. (2010) The recombinant amyloid-β peptide Aβ1–42 aggregates faster and is more neurotoxic than synthetic Aβ1–42. *J. Mol. Biol.* **396**, 9–18.

[496] O'Malley, T. T, Linse, S, & Walsh, D. (2018) Production and use of recombinant Aβ for aggregation studies. *Methods Mol. Biol.* **1777**, 307–320.

[497] Garai, K, Sahoo, B, Sengupta, P, & Maiti, S. (2008) Quasihomogeneous nucleation of amyloid beta yields numerical bounds for the critical radius, the surface tension, and the free energy barrier for nucleus formation. *J. Chem. Phys.* **128**, 045102.

[498] Friedemann, M, Helk, E, Tiiman, A, Zovo, K, Palumaa, P, & Tõugu, V. (2015) Effect of methionine-35 oxidation on the aggregation of amyloid-β peptide. *Biochem. Biophys. Rep.* **3**, 94–99.

[499] Sato, T, Kienlen-Campard, P, Ahmed, M, Liu, W, Li, H, Elliot, J. I, Aimoto, S, Constantinescu, S. N, Octave, J.-N, & Smith, S. O. (2006) Inhibitors of amyloid toxicity based on β-sheet packing of Aβ40 and Aβ42. *Biochemistry* **45**, 5503–5516.

[500] Lee, M.-C, Yu, W.-C, Shih, Y.-H, Chen, C.-Y, Guo, Z.-H, Huang, S.-J, Chan, J. C. C, & Chen, Y.-R. (2018) Zinc ion rapidly induces toxic, off-pathway amyloid-β oligomers distinct from amyloid-β derived diffusible ligands in Alzheimer's disease. *Sci. Rep.* **8**, 4772.

[501] Whalen, B. M, Selkoe, D. J, & Hartley, D. M. (2005) Small non-fibrillar assemblies of amyloid β-protein bearing the arctic mutation induce rapid neuritic degeneration. *Neurobiol. Dis.* **20**, 254–266.

[502] Jan, A, Hartley, D. M, & Lashuel, H. A. (2010) Preparation and characterization of toxic Aβ aggregates for structural and functional studies in Alzheimer's disease research. *Nat. Protoc.* **5**, 1186–1209.

[503] Matheou, C. J, Younan, N. D, & Viles, J. H. (2016) The rapid exchange of zinc 2+ enables trace levels to profoundly influence amyloid-β misfolding and dominates assembly outcomes in Cu 2+/Zn 2+ mixtures. *J. Mol. Biol.* **428**, 2832–2846.

[504] Williams, A. J. (2014) Ph.D. thesis (Department of Molecular Biology and Biotechnology, University of Sheffield, UK).

[505] Aubrey, L. (2018) Ph.D. thesis (Department of Molecular Biology and Biotechnology, University of Sheffield, UK).

[506] Wahlund, K. G & Giddings, J. C. (1987) Properties of an asymmetrical flow field-flow fractionation channel having one permeable wall. *Anal. Chem.* **59**, 1332–1339.

[507] Cölfen, H & Antonietti, M. (2000) in *New Developments in Polymer Analytics I. Advances in Polymer Science*, ed. Schmidt, M. (Springer, Berlin) Vol. 150, pp. 67–187.

[508] Giddings, J. C. (1965) A new separation concept based on a coupling of concentration and flow nonuniformities. *Sep. Sci.* **1**, 123–125.

[509] Giddings, J. C. (1978) Displacement and dispersion of particles of finite size in flow channels with lateral forces: Field-flow fractionation and hydrodynamic chromatography. *Sep. Sci. Technol.* **13**, 241–254.

[510] Young, R. J & Lovell, P. A. (2011) *Introduction to polymers.* (CRC Press, Boca Raton, Florida), 3 edition.

[511] Andersson, M, Wittgren, B, & Wahlund, K.-G. (2013) Accuracy in multiangle light scattering measurements for molar mass and radius estimations. Model calculations and experiments. *Anal. Chem.* **75**, 4279–4291.

[512] Debye, P. (1947) Molecular-weight determination by light scattering. *J. Phys. Colloid Chem.* **51**, 18–32.

[513] Zimm, B. H. (1948) Apparatus and methods for measurement and interpretation of the angular variation of light scattering: Preliminary results on polystyrene solutions. *J. Chem. Phys.* **16**, 1099–1116.

[514] Berry, G. C. (1966) Thermodynamic and conformational properties of polystyrene. I. Light-scattering studies on dilute solutions of linear polystyrenes. *J. Chem. Phys.* **44**, 4550–4564.

[515] Wyatt, P. (1993) Light scattering and the absolute characterisation of macromolecules. *Anal. Chim. Acta* **272**, 1–40.

[516] Burnham, K. P & Anderson, D. R. (2002) *Model Selection and Multimodel Inference: A practical information-theoretic approach.* (Springer, Berlin).

[517] Pachahara, S. K, Chaudhary, N, Subbalakshmi, C, & Nagaraj, R. (2012) Hexafluoroisopropanol induces self-assembly of β-amyloid peptides into highly ordered nanostructures. *J. Pept. Sci.* **18**, 233–241.

[518] Solntseva, E. I & Bukanova, J. V. (2017) Use-dependent inhibition of glycine-activated chloride current in rat neurons by β-amyloid peptide pretreated with hexafluoroisopropanol. *NeuroReport* **28**, 579–583.

[519] Silvers, R, Colvin, M. T, Frederick, K. K, Jacavone, A. C, Lindquist, S, Linse, S, & Griffin, R. G. (2017) Aggregation and fibril structure of AβM01-42 and Aβ1-42. *Biochemistry* **56**, 4850–4859.

[520] Fezoui, Y, Hartley, D. M, Harper, J. D, Khurana, R, Walsh, D. M, Condron, M. M, Selkoe, D. J, Lansbury, P. T. J, Fink, A. L, & Teplow, D. B. (2000) An improved method of preparing the amyloid beta-protein for fibrillogenesis and neurotoxicity experiments. *Amyloid* **7**, 166–178.

[521] Grüning, C. S. R, Klinker, S, Wolff, M, Schneider, M, Toksöz, K, Klein, A. N, Nagel-Steger, L, Willbold, D, & Hoyer, W. (2013) The off-rate of monomers dissociating from amyloid-β protofibrils. *J. Biol. Chem.* **288**, 37104–37111.

[522] Carotta, R, Manno, M, Bulone, D, Martorana, V, & San Biagio, P. L. (2005) Protofibril formation of amyloid β-protein at low pH via a non-cooperative elongation mechanism. *J. Biol. Chem.* **280**, 30001–30008.

[523] Hayden, E. Y, Hoi, K. K, Inayathullah, M, Condron, M. M, & Teplow, D. B. (2017) Identification of key regions and residues controlling Aβ folding and assembly. *Sci. Rep.* **7**, 12434.

[524] Colvin, M. T, Silvers, R, Frohm, B, Su, Y, Linse, S, & Griffin, R. G. (2015) High resolution structural characterization of Aβ42 amyloid fibrils by magic angle spinning NMR. *J. Am. Chem. Soc.* **137**, 7509–7518.

[525] Bayer, T. A & Wirths, O. (2014) Focusing the amyloid cascade hypothesis on N-truncated Abeta peptides as drug targets against Alzheimer's disease. *Acta Neuropathol.* **127**, 787–801.

[526] Mital, M, Wezynfeld, N. E, Frączyk, T, Wiloch, M. Z, Wawrzyniak, U. E, Bonna, A, Tumpach, C, Barnham, K. J, Haigh, C. L, Bal, W, & Drew, S. C. (2015) A functional role for Aβ in metal

homeostasis? N-truncation and high-affinity copper binding. *Angew. Chem. Int. Ed.* **54**, 10460–10464.

[527] Wulff, M, Baumann, M, Thümmler, A, Yadav, J. K, Heinrich, L, Knüpfer, U, Schlenzig, D, Schierhorn, A, Rahfeld, J.-U, Horn, U, Balbach, J, Demuth, H.-U, & Fändrich, M. (2016) Enhanced fibril fragmentation of N-terminally truncated and pyroglutamyl-modified Aβ peptides. *Angew. Chem. Int. Ed.* **55**, 5081–5084.

[528] Szczepankiewicz, O, Linse, B, Meisl, G, Thulin, E, Frohm, B, Frigerio, C. S, Colvin, M. T, Jacavone, A. C, Griffin, R. G, Knowles, T, Walsh, D. M, & Linse, S. (2015) N-terminal extensions retard Aβ42 fibril formation but allow cross seeding and coaggregation with Aβ42. *J. Am. Chem. Soc.* **137**, 14673–14685.

[529] Yang, X, Meisl, G, Frohm, B, Thulin, E, Knowles, T. P. J, & Linse, S. (2018) On the role of sidechain size and charge in the aggregation of Aβ42 with familial mutations. *Proc. Natl. Acad. Sci. U. S. A.* **115**, E5849–E5858.

[530] Weiffert, T, Meisl, G, Flagmeier, P, De, S, Dunning, C. J. R, Frohm, B, Zetterberg, H, Blennow, K, Portelius, E, Klenerman, D, Dobson, C. M, Knowles, T. P. J, & Linse, S. (2019) Increased secondary nucleation underlies accelerated aggregation of the four-residue N-terminally truncated Aβ42 species Aβ5-42. *ACS Chem. Neurosci.* **10**, 2374–2384.

[531] Habchi, J, Chia, S, Galvagnion, C, Michaels, T. C. T, Bellaiche, M. M. J, Ruggeri, F. S, Sanguanini, M, Idini, I, Kumita, J. R, Sparr, E, Linse, S, Dobson, C. M, Knowles, T. P. J, & Vendruscolo, M. (2018) Cholesterol catalyses Aβ42 aggregation through a heterogeneous nucleation pathway in the presence of lipid membranes. *Nat. Chem.* **10**, 673–683.

[532] Brambilla, D, Verpillot, R, Le Droumaguet, B, Nicolas, J, Taverna, M, Kóňa, J, Lettiero, B, Hashemi, S. H, De Kimpe, L, Canovi, M, Gobbi, M, Nicolas, V, Scheper, W, Moghimi, S. M, Tvaroška, I, Couvreur, P, & Andrieux, K. (2012) PEGylated nanoparticles bind to and alter amyloid-beta peptide conformation: Toward engineering of functional nanomedicines for Alzheimer's disease. *ACS Nano* **6**, 5897–5908.

[533] Taylor, A. I. P. (2015) Master's thesis (Department of Molecular Biology and Biotechnology, University of Sheffield, UK).

[534] Bartsch, H.-J. (1974) *Handbook of mathematical formulas.* (Academic Press, New York).

[535] Necas, D & Klapetek, P. (2012) Gwyddion: an open-source software for SPM data analysis. *Cent. Eur. J. Phys.* **10**, 181–188.

[536] Eden, K, Morris, R, Gillam, J, MacPhee, C. E, & Allen, R. J. (2015) Competition between primary nucleation and autocatalysis in amyloid fibril self-assembly. *Biophys. J.* **108**, 632–643.

[537] Michaels, T. C. T, Dear, A. J, Kirkegaard, J. B, Saar, K. L, Weitz, D. A, & Knowles, T. P. J. (2016) Fluctuations in the kinetics of linear protein self-assembly. *Phys. Rev. Lett.* **116**, 258103.

[538] Stroud, J. C, Liu, C, Teng, P. K, & Eisenberg, D. (2012) Toxic fibrillar oligomers of amyloid-β have cross-β structure. *Proc. Natl. Acad. Sci. U. S. A.* **109**, 7717–7722.

[539] Jeong, J. S, Ansaloni, A, Mezzenga, R, Lashuel, H, & Dietler, G. (2013) Novel mechanistic insight into the molecular basis of amyloid polymorphism and secondary nucleation during amyloid formation. *J. Mol. Biol.* **425**, 1765–1781.

[540] O'Malley, T. T, Oktaviani, N. A, Zhang, D, Lomakin, A, O'Nuallain, B, Linse, S, Benedek, G. B, Rowan, M. J, Mulder, F. A. A, & Walsh, D. M. (2014) Aβ dimers differ from monomers in structural propensity, aggregation paths and population of synaptotoxic assemblies. *Biochem. J.* **461**, 413–426.

[541] Goebel-Stengel, M, Stengel, A, Taché, Y, & Reeve, J. R. J. (2011) The importance of using the optimal plastic and glassware in studies involving peptides. *Anal. Biochem.* **414**, 38–46.

[542] Elliott, K. A. C & Jasper, H. H. (1949) Physiological salt solutions for brain surgery. *J. Neurosurg.* **6**, 140–152.

[543] Munishkina, L. A, Henriques, J, Uversky, V. N, & Fink, A. L. (2004) Role of protein-water interactions and electrostatics in α-synuclein fibril formation. *Biochemistry* **42**, 3289–3300.

[544] Pedersen, J. S, Fink, J. M, Dikov, D, & Otzen, D. E. (2006) Sulfates dramatically stabilize a salt-dependent type of glucagon fibrils. *Biophys. J.* **90**, 4181–4194.

[545] Jain, S & Udgaonkar, J. B. (2010) Salt-induced modulation of the pathway of amyloid fibril formation by the mouse prion protein. *Biochemistry* **49**, 7615–7624.

[546] Brown, L. D, Cai, T. T, & DasGupta, A. (2001) Interval estimation for a binomial proportion. *Stat. Sci.* **16**, 101–133.

[547] Wiedemann, C, Bellstedt, P, & Görlach, M. (2013) CAPITO - a web server based analysis and plotting tool for circular dichroism data. *Bioinformatics* **29**, 1750–1757.

[548] Raaflaub, J. (1956) Applications of metal buffers and metal indicators in biochemistry. *Methods Biochem. Anal.* **3**, 301–324.

[549] Debye, P & Hückel, E. (1923) Zur Theorie der Elektrolyte. *Phys. Zeit.* **24**, 185–206.

[550] Ferrone, F. A, Hofrichter, J, & Eaton, W. A. (1985) Kinetics of sickle hemoglobin polymerization II. A double nucleation mechanism. *J. Mol. Biol.* **183**, 611–631.

[551] Hofmeister, F. (1888) On the understanding of the effects of salts. On regularities in the precipitating effect of salts and their relationship to their physiological behavior. *Arch. Exp. Pathol. Pharmakol. (Leipzig)* **24**, 247–260.

[552] McBain, J. W. (1950) *Colloid Science*. (D. C. Heath and Co., New York).

[553] Gregor, H. P, Belle, J, & Marcus, R. A. (1955) Studies on ion-exchange resins. XIII. selectivity coefficients of quaternary base anion-exchange resins toward univalent anions. *J. Am. Chem. Soc.* **77**, 2713–2719.

[554] Gjerde, D. T, Schmuckler, G, & Fritz, J. S. (1980) Anion chromatography with low-conductivity eluents. 2. *J. Chromatograph.* **187**, 35–45.

[555] Fändrich, M. (2007) Absolute correlation between lag time and growth rate in the spontaneous formation of several amyloid-like aggregates and fibrils. *J. Mol. Biol.* **365**, 1266–1270.

[556] Gallardo, R, Ranson, N. A, & Radford, S. E. (2020) Amyloid structures: much more than just a cross-β fold. *Curr. Opin. Struct. Biol.* **60**, 7–16.

[557] Harel, M, Sonoda, L. K, Silman, I, Sussman, J. L, & Rosenberry, T. L. (2008) Crystal structure of thioflavin T bound to the peripheral site of *Torpedo californica* acetylcholinesterase reveals how thioflavin T acts as a sensitive fluorescent reporter of ligand binding to the acylation site. *J. Am. Chem. Soc.* **130**, 7856–7861.

[558] Sen, P, Fatima, S, Ahmad, B, & Khan, R. H. (2009) Interactions of thioflavin T with serum albumins: spectroscopic analyses. *Spectrochim. Acta A Mol. Biomol. Spectrosc.* **74**, 94–99.

[559] Sabaté, R, Lascu, I, & Saupe, S. J. (2008) On the binding of thioflavin-T to HET-s amyloid fibrils assembled at pH 2. *J. Struct. Biol.* **162**, 387–396.

[560] Wu, C, Wang, Z, Lei, H, Duan, Y, Bowers, M. T, & Shea, J. E. (2008) The binding of thioflavin T and its neutral analog BTA-1 to protofibrils of the Alzheimer's disease Aβ(16-22) peptide probed by molecular dynamics simulations. *J. Mol. Biol.* **384**, 718–729.

[561] Biancalana, M, Makabe, K, Koide, A, & Koide, S. (2009) Molecular mechanism of thioflavin-T binding to the surface of β-rich peptide self-assemblies. *J. Mol. Biol.* **385**, 1052–1063.

[562] Wu, C, Biancalana, M, Koide, S, & Shea, J. E. (2009) Binding modes of thioflavin-T to the single-layer β-sheet of the peptide self-assembly mimics. *J. Mol. Biol.* **394**, 627–633.

[563] Avrami, M. (1939) Kinetics of phase change. I. General theory. *J. Chem. Phys.* **7**, 1103–1112.

[564] Thacker, D, Sanagavarapu, K, Frohm, B, Meisl, G, Knowles, T. P. J, & Linse, S. (2020) The role of fibril structure and surface hydrophobicity in secondary nucleation of amyloid fibrils. *Proc. Natl. Acad. Sci. U. S. A.* **117**, 25272–25283.

[565] Auer, S, Dobson, C. M, Vendruscolo, M, & Maritan, A. (2008) Self-templated nucleation in peptide and protein aggregation. *Phys. Rev. Lett.* **101**, 258101.

[566] Li, D. W, Mohanty, S, Irbäck, A, & Huo, S. (2008) Formation and growth of oligomers: A Monte Carlo study of an amyloid Tau fragment. *PLoS Comput. Biol.* **4**, e1000238.

[567] Chen, S. W, Drakulic, S, Deas, E, Ouberai, M, Aprile, F. A, Arranz, R, Ness, S, Roodveldt, C, Guilliams, T, De-Genst, E. J, Klenerman, D, Wood, N. W, Knowles, T. P. J, Alfonso, C, Rivas, G, Abramov, A. Y, Valpuesta, J. M, Dobson, C. M, & Cremades, N. (2015) Structural characterization of toxic oligomers that are kinetically trapped during α-synuclein fibril formation. *Proc. Natl. Acad. Sci. U. S. A.* **112**, E1194–E2003.

[568] Ding, F, LaRocque, J. J, & Dokholyan, N. V. (2005) Direct observation of protein folding, aggregation, and a prion-like conformational conversion. *J. Biol. Chem.* **280**, 40235–40240.

[569] Lipfert, J, Franklin, J, Wu, F, & Doniach, S. (2005) Protein misfolding and amyloid formation for the peptide GNNQQNY from yeast prion protein Sup35: Simulation by reaction path annealing. *J. Mol. Biol.* **349**, 648–658.

[570] Taylor, A. I. P. (2019). *Unpublished data, not included due to space constraints and the absence of an interpretable result.*

[571] Arscott-Barber, A. (2020) Master's thesis (Department of Molecular Biology and Biotechnology, University of Sheffield, UK).

[572] Dear, A. J, Meisl, G, Šarić, A, Michaels, T. C. T, Kjaergaard, M, Linse, S, & Knowles, T. P. J. (2020) Identification of on- and off-pathway oligomers in amyloid fibril formation. *Chem. Sci.* **11**, 6236–6247.

[573] Bone, C. (2018) Master's thesis (Department of Molecular Biology and Biotechnology, University of Sheffield, UK).

[574] Sheridan, A. K. (2019) Master's thesis (Department of Molecular Biology and Biotechnology, University of Sheffield, UK).

[575] Westermark, P, Andersson, A, & Westermark, G. T. (2011) Islet amyloid polypeptide, islet amyloid, and diabetes mellitus. *Physiol. Rev.* **91**, 795–826.

[576] Lucas, M. J & Keitz, B. K. (2018) Influence of zeolites on amyloid-β aggregation. *Langmuir* **34**, 9789–9797.